Crystal clues to the inner lives of volcanoes *p. 822*

Conservation science comes into its own *p. 826*

Watching shrinking gold particles in situ *p. 874*

# Science

$15
18 NOVEMBER 2016
sciencemag.org

AAAS

## PHOTOSYNTHESIS IN CROPS

Speeding adjustment from light to shadow boosts yield *pp. 816 & 857*

# CONTENTS

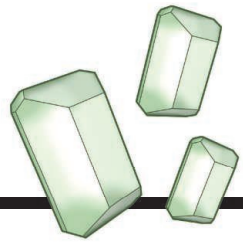

822
Telltale crystals

18 NOVEMBER 2016 • VOLUME 354 • ISSUE 6314

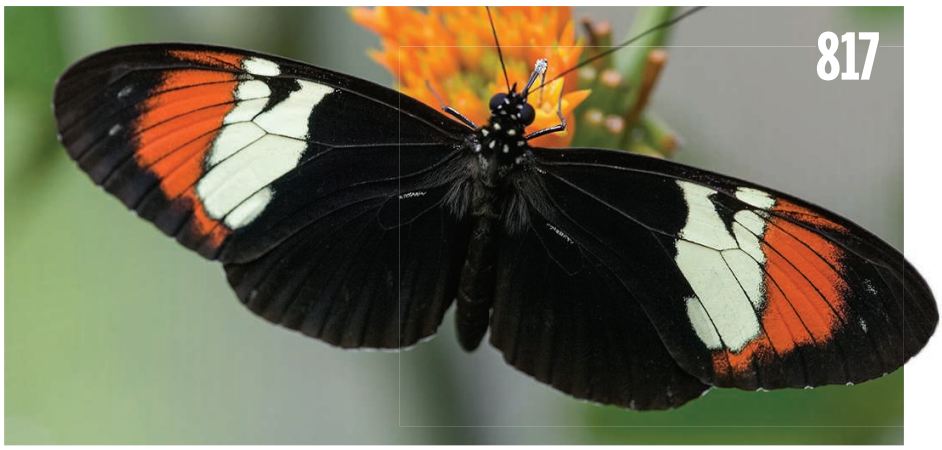


## NEWS

### IN BRIEF

808 News at a glance

### IN DEPTH

811 **SCIENTISTS START TO PARSE A TRUMP PRESIDENCY**
Fears for climate and social science research, hopes for infrastructure boost *By J. Mervis*

813 **A NEW EVOLUTIONARY CLASSIC**
At least a dozen times, rove beetles independently evolved the ability to invade and steal from army ant nests *By E. Pennisi*

814 **JAPAN REBOOTS X-RAY PROBE–AND MISSION MANAGEMENT**
After a series of mission failures, Japan's space science agency aims to overhaul lax oversight *By D. Normile*

815 **NO NEED TO APPLY, DUTCH SCIENCE ACADEMY TELLS MEN**
Two special elections seek to address gender imbalance by admitting only women *By M. Enserink*

816 **ENGINEERED CROPS COULD HAVE IT MADE IN THE SHADE**
Modified tobacco plants quickly speed up photosynthesis when bright light dims, boosting yields *By E. Stokstad*
▸ RESEARCH ARTICLE P. 857; VIDEO

### FEATURES

817 **SHAKING UP THE TREE OF LIFE**
Hybrids are turning up everywhere, blurring species lines *By E. Pennisi*

818 **A shortcut to a species**
*By E. Pennisi*
▸ PODCAST

822 **CRYSTAL CLOCKS**
How smudged crystals offer windows into a volcano's eruptive past *By J. Rosen*
▸ VIDEO

## INSIGHTS

### BOOKS *ET AL.*

826 **WHERE SCIENCE MEETS ART**
Scientific methods inform conservation efforts in the quest to preserve cultural heritage *By R. Ploeger and A. Shugar*

### PERSPECTIVES

829 **PLANT METABOLONS ASSEMBLED ON DEMAND**
Proteins interact at an intracellular membrane to form dynamic metabolons that increase metabolic flux *By M. Dastmalchi and P. J. Facchini*
▸ REPORT P. 890

830 **FIXING CARBON, UNNATURALLY**
A synthetic enzymatic pathway is more energy efficient than natural aerobic carbon fixation pathways
*By F. Gong and Y. Li*
▸ REPORT P. 900

832 **LIGHT-SENSING PHYTOCHROMES FEEL THE HEAT**
Plant phytochrome activity is governed not just by light, but also by prevailing temperature *By K. J. Halliday and S. J. Davis*
▸ REPORTS PP. 886 & 897

833 **NEURAL CIRCUITRY GETS REWIRED**
Former parasympathetic innervations of organs are now claimed sympathetic
*By I. Adameyko*
▸ REPORT P. 893

835 **DIAMOND DEFECTS COOPERATE VIA LIGHT**
Silicon-vacancy centers in diamond show single-photon switching and superradiance *By R. Hanson*
▸ RESEARCH ARTICLE P. 847

836 **REVEALING THE DYNAMICS OF A LARGE IMPACT**
Drilling into the Chicxulub crater provides constraints on how it formed
*By P. Barton*
▸ REPORT P. 878

### POLICY FORUM

838 **TOWARD A NATIONAL, SUSTAINED U.S. ECOSYSTEM ASSESSMENT**
Pieces are in place, but need coordination and policy focus
*By S. T. Jackson* et al.

### LETTERS

840 **THE DUAL COMPONENTS OF MENTAL HEALTH**
*By J. W. Reich*

840 **RESPONSE**
*By J. Cilliers* et al.

840 **NIH'S MENTORING MAKES PROGRESS**
*By J. Vishwanatha* et al.

Downloaded from http://science.sciencemag.org/ on November 22, 2016



Published by AAAS

# CONTENTS

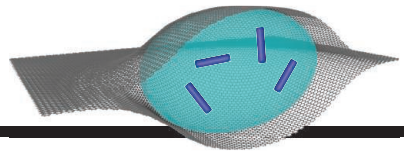

874 Watching particles dissolve

18 NOVEMBER 2016 • VOLUME 354 • ISSUE 6314

## RESEARCH

### IN BRIEF

**843** From *Science* and other journals

### REVIEW

**846 APPLIED OPTICS**
Optically resonant dielectric nanostructures *A. I. Kuznetsov* et al.
REVIEW SUMMARY; FOR FULL TEXT: dx.doi.org/10.1126/science.aag2472

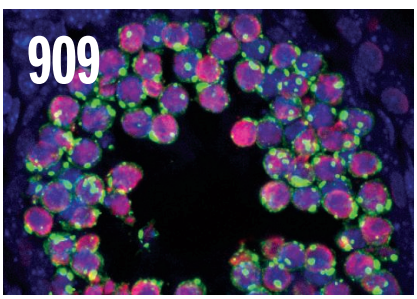


### RESEARCH ARTICLES

**847 QUANTUM OPTICS**
An integrated diamond nanophotonics platform for quantum-optical networks *A. Sipahigil* et al.
▸ PERSPECTIVE P. 835

**851 ORGANIC CHEMISTRY**
A general catalytic β-C–H carbonylation of aliphatic amines to β-lactams *D. Willcox* et al.

**857 PLANT SCIENCE**
Improving photosynthesis and crop productivity by accelerating recovery from photoprotection *J. Kromdijk* et al.
▸ NEWS STORY P. 816

### REPORTS

**861 SOLAR CELLS**
Perovskite-perovskite tandem photovoltaics with optimized band gaps *G. E. Eperon* et al.

**865 ORGANIC CHEMISTRY**
Asymmetric synthesis of batrachotoxin: Enantiomeric toxins show functional divergence against $Na_V$ *M. M. Logan* et al.

**869 GEOPHYSICS**
Coseismic rupturing stopped by Aso volcano during the 2016 $M_w$ 7.1 Kumamoto earthquake, Japan *A. Lin* et al.

**874 NANOMATERIALS**
Single-particle mapping of nonequilibrium nanocrystal transformations *X. Ye* et al.

**878 GEOLOGY**
The formation of peak rings in large impact craters *J. V. Morgan* et al.
▸ PERSPECTIVE P. 836

**882 ACTIVE MATTER**
Command of active matter by topological defects and patterns *C. Peng* et al.

**886 PLANT SCIENCE**
Phytochromes function as thermosensors in *Arabidopsis* *J.-H. Jung* et al.
▸ PERSPECTIVE P. 832; REPORT P. 897

**890 PLANT SCIENCE**
Characterization of a dynamic metabolon producing the defense compound dhurrin in sorghum *T. Laursen* et al.
▸ PERSPECTIVE P. 829

**893 NEURODEVELOPMENT**
The sacral autonomic outflow is sympathetic *I. Espinosa-Medina* et al.
▸ PERSPECTIVE P. 833

**897 PLANT SCIENCE**
Phytochrome B integrates light and temperature signals in *Arabidopsis* *M. Legris* et al.
▸ PERSPECTIVE P. 832; REPORT P. 886

**900 SYNTHETIC BIOLOGY**
A synthetic pathway for the fixation of carbon dioxide in vitro *T. Schwander* et al.
▸ PERSPECTIVE P. 830

**904 NEURODEGENERATION**
Site-specific phosphorylation of tau inhibits amyloid-β toxicity in Alzheimer's mice *A. Ittner* et al.

**909 DNA METHYLATION**
The DNA methyltransferase DNMT3C protects male germ cells from transposon activity *J. Barau* et al.

### DEPARTMENTS

**807 EDITORIAL**
Reunifying America
*By Jeremy Berg*

**934 WORKING LIFE**
Selling out science?
*By Kevin F. Boehnke*

### ON THE COVER

Soybean plants at sunset. Leaves protect themselves against too much sunlight by dissipating excess absorbed energy as heat. When leaves are suddenly shaded by clouds or other leaves, this photoprotective dissipation continues for many minutes, although the energy could be used for photosynthesis. By accelerating the recovery from photoprotection, Kromdijk *et al.* increased productivity in a field crop. See pages 816 and 857. *Photo: © Igor Stevanovic/500px*

*Science* Staff ..... 806
New Products ..... 913
*Science* Careers ..... 914

**SCIENCE (ISSN 0036-8075) is published weekly on Friday, except the last week in December, by the American Association for the Advancement of Science, 1200 New York Avenue, NW, Washington, DC 20005.** Periodicals mail postage (publication No. 484460) paid at Washington, DC, and additional mailing offices. Copyright © 2016 by the American Association for the Advancement of Science. The title SCIENCE is a registered trademark of the AAAS. Domestic individual membership and subscription (51 issues): $165 ($74 allocated to subscription). Domestic institutional subscription (51 issues): $1522; Foreign postage extra: Mexico, Caribbean (surface mail) $55; other countries (air assist delivery) $89. First class, airmail, student, and emeritus rates on request. Canadian rates with GST available upon request, GST #1254 88122. Publications Mail Agreement Number 1069624. **Printed in the U.S.A.**
**Change of address:** Allow 4 weeks, giving old and new addresses and 8-digit account number. **Postmaster:** Send change of address to AAAS, P.O. Box 96178, Washington, DC 20090–6178. **Single-copy sales:** $15.00 current issue, $20.00 back issue prepaid includes surface postage; bulk rates on request. **Authorization to photocopy** material for internal or personal use under circumstances not falling within the fair use provisions of the Copyright Act is granted by AAAS to libraries and other users registered with the Copyright Clearance Center (CCC) Transactional Reporting Service, provided that $35.00 per article is paid directly to CCC, 222 Rosewood Drive, Danvers, MA 01923. The identification code for *Science* is 0036-8075. *Science* is indexed in the *Reader's Guide to Periodical Literature* and in several specialized indexes.



*Published by AAAS*

Downloaded from http://science.sciencemag.org/ on November 22, 2016

Science
AAAS
1200 New York Avenue, NW, Washington, DC 20005
Clarendon House, Clarendon Road, Cambridge, UK CB2 8FH

**Editor-in-Chief** Jeremy Berg
**Executive Editor** Monica M. Bradford **News Editor** Tim Appenzeller
**Deputy Editors** Lisa D. Chong, Andrew M. Sugden(UK), Valda J. Vinson, Jake S. Yeston

## Research and Insights

**DEPUTY EDITOR, EMERITUS** Barbara R. Jasny **SR. EDITORS** Caroline Ash(UK), Gilbert J. Chin, Julia Fahrenkamp-Uppenbrink(UK), Pamela J. Hines, Stella M. Hurtley(UK), Paula A. Kiberstis, Marc S. Lavine(Canada), Kristen L. Mueller, Ian S. Osborne(UK), Beverly A. Purnell, L. Bryan Ray, Guy Riddihough, H. Jesse Smith, Jelena Stajic, Peter Stern(UK), Phillip D. Szuromi, Sacha Vignieri, Brad Wible, Nicholas S. Wigginton, Laura M. Zahn **ASSOCIATE EDITORS** Brent Grocholski, Priscilla Kelly,Keith T. Smith **ASSOCIATE BOOK REVIEW EDITOR** Valerie B. Thompson **LETTERS EDITOR** Jennifer Sills **LEAD CONTENT PRODUCTION EDITORS** Harry Jach, Lauren Kmec **CONTENT PRODUCTION EDITORS** Jeffrey E. Cook, Chris Filiatreau, Cynthia Howe, Barbara P. Ordway, Catherine Wolner **SR. EDITORIAL COORDINATORS** Carolyn Kyle, Beverly Shields **EDITORIAL COORDINATORS** Aneera Dobbins, Joi S. Granger, Jeffrey Hearn, Lisa Johnson, Maryrose Madrid, Anita Wynn **PUBLICATIONS ASSISTANTS** Nida Masiulis, Dona Mathieu, Le-Toya Mayne Flood, Shannon McMahon, Scott Miller, Jerry Richardson, Alice Whaley(UK), Gwen Grant(UK), Brian White **EXECUTIVE ASSISTANT** Anna Bashkirova **ADMINISTRATIVE SUPPORT** Janet Clements(UK), Lizanne Newton(UK), Sarah Harrison (UK)

## News

**NEWS MANAGING EDITOR** John Travis **INTERNATIONAL EDITOR** Richard Stone **DEPUTY NEWS EDITORS** Elizabeth Culotta, David Grimm, Eric Hand David Malakoff, Leslie Roberts **CONTRIBUING EDITOR** Martin Enserink(Europe) **SR. CORRESPONDENTS** Daniel Clery(UK), Jeffrey Mervis, Elizabeth Pennisi **NEWS WRITERS** Adrian Cho, Jon Cohen, Jennifer Couzin-Frankel, Carolyn Gramling, Jocelyn Kaiser, Catherine Matacic, Kelly Servick, Robert F. Service, Erik Stokstad(Cambridge, UK), Paul Voosen, Meredith Wadman **INTERNS** Jessica Boddy, Ben Panko **CONTRIBUTING CORRESPONDENTS** John Bohannon, Warren Cornwall, Ann Gibbons, Mara Hvistendahl, Sam Kean, Eli Kintisch, Kai Kupferschmidt(Berlin), Andrew Lawler, Mitch Leslie, Charles C. Mann, Eliot Marshall, Virginia Morell, Dennis Normile(Shanghai). Heather Pringle, Tania Rabesandratana(London), Emily Underwood, Gretchen Vogel(Berlin), Lizzie Wade(Mexico City) **CAREERS** Donisha Adams, Rachel Bernstein(Editor), Maggie Kuo **COPY EDITORS** Julia Cole, Dorie Chevlen, Jennifer Levin (Chief) **ADMINISTRATIVE SUPPORT** Jessica Adams

**Executive Publisher** Rush D. Holt
**Publisher** Bill Moran **Chief Digital Media Officer** Rob Covey

**BUSINESS OPERATIONS AND PORTFOLIO MANAGEMENT DIRECTOR** Sarah Whalen **PRODUCT DEVELOPMENT DIRECTOR** Will Schweitzer **PRODUCT DEVELOPMENT ASSOCIATE** Hannah Heckner **BUSINESS SYSTEMS AND FINANCIAL ANALYSIS DIRECTOR** Randy Yi **SENIOR SYSTEMS ANALYST** Nicole Mehmedovich **DIRECTOR, BUSINESS OPERATIONS & ANALYSIS** Eric Knott **MANAGER, BUSINESS OPERATIONS** Jessica Tierney **SENIOR BUSINESS ANALYST** Cory Lipman **BUSINESS ANALYSTS** David Garrison, Michael Hardesty Meron Kebede, Sandy Kim **FINANCIAL ANALYST** Drew Sher **DIRECTOR, COPYRIGHTS LICENSING SPECIAL PROJECTS** Emilie David **PERMISSIONS ASSOCIATE** Elizabeth Sandler **RIGHTS, CONTRACTS, AND LICENSING ASSOCIATE** Lili Kiser **RIGHTS & PERMISSIONS ASSISTANT** Alexander Lee

**MARKETING DIRECTOR** Elise Swinehart **ASSOCIATE MARKETING DIRECTOR** Stacey Burke Bowers **MARKETING ASSOCIATE** Steven Goodman **CREATIVE DIRECTOR** Scott Rodgerson **SENIOR ART ASSOCIATES** Paula Fry **ART ASSOCIATE** Kim Huynh

**FULFILLMENT SYSTEMS AND OPERATIONS** membership@aaas.org **MANAGER, MEMBER SERVICES** Pat Butler **SPECIALISTS** Terrance Morrison, Latasha Russell **MANAGER, DATA ENTRY** Mickie Napoleoni **DATA ENTRY SPECIALISTS** Brenden Aquilino, Fiona Giblin **MARKETING ASSOCIATE** Isa Sesay-Bah

**DIRECTOR, INSTITUTIONAL LICENSING** David Celano **PUBLISHER RELATIONS, EASTERN REGION** Keith Layson **PUBLISHER RELATIONS, WESTERN REGION** Ryan Rexroth **ASSOCIATE DIRECTOR, INSTITUTIONAL LICENSING OPERATIONS** Iquo Edim **SENIOR OPERATIONS ANALYST** Lana Guz **MANAGER, AGENT RELATIONS & CUSTOMER SUCCESS** Judy Lillibridge

**WEB TECHNOLOGIES PORTFOLIO MANAGER** Trista Smith **TECHNICAL MANAGER** Chris Coleman **PROJECT MANAGER** Nick Fletcher **DEVELOPERS** Elissa Heller, Ryan Jensen, Jimmy Marks, Brandon Morrison

**DIGITAL MEDIA DIRECTOR OF ANALYTICS** Enrique Gonzales **DIGITAL REPORTING ANALYST** Eric Hossinger **SR. MULTIMEDIA PRODUCER** Sarah Crespi **MANAGING DIGITAL PRODUCER** Alison Crawford **PRODUCER** Liana Birke **VIDEO PRODUCER** Chris Burns, Nguyên Khôi Nguyễn **DIGITAL SOCIAL MEDIA PRODUCER** Brice Russ

**DIRECTOR OF OPERATIONS PRINT AND ONLINE** Lizabeth Harman **DIGITAL/PRINT STRATEGY MANAGER** Jason Hillman **QUALITY TECHNICAL MANAGER** Marcus Spiegler **PROJECT ACCOUNT MANAGER** Tara Kelly **DIGITAL PRODUCTION MANAGER** Lisa Stanford **ASSISTANT MANAGER DIGITAL/PRINT** Rebecca Doshi **SENIOR CONTENT SPECIALISTS** Steve Forrester, Antoinette Hodal, Lori Murphy, Anthony Rosen **CONTENT SPECIALISTS** Jacob Hedrick, Kimberley Oster **ADVERTISING OPERATIONS SPECIALIST** Ashley Jeter

**DESIGN DIRECTOR** Beth Rakouskas **DESIGN EDITOR** Marcy Atarod **SENIOR DESIGNER** Chrystal Smith **DESIGNER** Christina Aycock **GRAPHICS MANAGING EDITOR** Alberto Cuadra **GRAPHICS EDITOR** Garvin Grullón **SENIOR SCIENTIFIC ILLUSTRATORS** Chris Bickel, Katharine Sutliff **SCIENTIFIC ILLUSTRATOR** Valerie Altounian **INTERACTIVE GRAPHICS EDITOR** Jia You **SENIOR GRAPHICS SPECIALISTS** Holly Bishop, Nathalie Cary **PHOTOGRAPHY MANAGING EDITOR** William Douthitt **PHOTO EDITOR** Emily Petersen

**DIRECTOR, GLOBAL COLLABORATION, CUSTOM PUBLICATIONS, ADVERTISING** Bill Moran **EDITOR, CUSTOM PUBLISHING** Sean Sanders: 202-326-6430 **ASSISTANT EDITOR, CUSTOM PUBLISHING** Jackie Oberst: 202-326-6463 **ADVERTISING MARKETING MANAGER** Justin Sawyers: 202-326-7061 science_advertising@aaas.org **ADVERTISING SUPPORT MANAGER** Karen Foote: 202-326-6740 **ADVERTISING PRODUCTION OPERATIONS MANAGER** Deborah Tompkins **SR. PRODUCTION SPECIALIST/GRAPHIC DESIGNER** Amy Hardcastle **SR. TRAFFIC ASSOCIATE** Christine Hall **SALES COORDINATOR** Shirley Young **ASSOCIATE DIRECTOR, COLLABORATION, CUSTOM PUBLICATIONS/CHINA/TAIWAN/KOREA/SINGAPORE** Xiaoying Chu: +86-186 0082 9345, xchu@aaas.org **COLLABORATION/CUSTOM PUBLICATIONS/JAPAN** Adarsh Sandhu + 81532-81-5142 asandhu@aaas.org **EAST COAST/E. CANADA** Laurie Faraday: 508-747-9395, FAX 617-507-8189 **WEST COAST/W. CANADA** Lynne Stickrod: 415-931-9782, FAX 415-520-6940 **MIDWEST** Jeffrey Dembksi: 847-498-4520 x3005. Steven Loerch: 847-498-4520 x3006 **UK EUROPE/ASIA** Roger Goncalves: TEL/FAX +41 43 243 1358 **JAPAN** Katsuyoshi Fukamizu(Tokyo): +81-3-3219-5777 kfukamizu@aaas.org **DIRECTOR, GLOBAL COLLABORATION AND PUBLISHING SERVICES CHINA/TAIWAN** Yan Xiang: +86-186 0082 9345, yxiang@aaas.org

**WORLDWIDE ASSOCIATE DIRECTOR OF SCIENCE CAREERS** Tracy Holmes: +44 (0) 1223 326525, FAX +44 (0) 1223 326532 tholmes@science-int.co.uk **CLASSIFIED** advertise@sciencecareers.org **U.S. SALES** Tina Burks: 202-326-6577, Nancy Toema: 202-326-6578 **EUROPE/ROW SALES** Sarah Lelarge **SALES ASSISTANT** Kelly Grace **JAPAN** Hiroyuki Mashiki(Kyoto): +81-75-823-1109 hmashiki@aaas.org **CHINA/TAIWAN** Yan Xiang: +86-186 0082 9345 yxiang@aaas.org **MARKETING MANAGER** Allison Pritchard **MARKETING ASSOCIATE** Aimee Aponte

**AAAS BOARD OF DIRECTORS, CHAIR** Geraldine L. Richmond **PRESIDENT** Barbara A. Schaal **PRESIDENT-ELECT** Susan Hockfield **TREASURER** David Evans Shaw **CHIEF EXECUTIVE OFFICER** Rush D. Holt **BOARD** Cynthia M. Beall, May R. Berenbaum, Carlos J. Bustamante, Stephen P.A. Fodor, Claire M. Fraser, Michael S. Gazzaniga, Laura H. Greene, Elizabeth Loftus, Mercedes Pascual

**SUBSCRIPTION SERVICES** For change of address, missing issues, new orders and renewals, and payment questions: 866-434-AAAS (2227) or 202-326-6417, FAX 202-842-1065. Mailing addresses: AAAS, P.O. Box 96178, Washington, DC 20090-6178 or AAAS Member Services, 1200 New York Avenue, NW, Washington, DC 20005

**INSTITUTIONAL SITE LICENSES** 202-326-6730 **REPRINTS:** Author Inquiries 800-635-7181 **COMMERCIAL INQUIRIES** 803-359-4578 **PERMISSIONS** 202-326-6765, permissions@aaas.org **AAAS Member Services** 202-326-6417 or http://membercentral.aaas.org/discounts

*Science* serves as a forum for discussion of important issues related to the advancement of science by publishing material on which a consensus has been reached as well as including the presentation of minority of conflicting points of view. Accordingly, all articles published in *Science*—including editorials, news and comment, and book reviews—are signed and reflect the individual views of the authors and not official points of view adopted by AAAS or the institutions with which the authors are affiliated.

**INFORMATION FOR AUTHORS** See pages 624 and 625 of the 5 February 2016 issue or access www.sciencemag.org/authors/science-information-authors

**SENIOR EDITORIAL BOARD**
**Gary King,** *Harvard University,* **Susan M. Rosenberg,** *Baylor College of Medicine,*
**Ali Shilatifard,** *Northwestern University Feinberg School of Medicine*

**BOARD OF REVIEWING EDITORS** (Statistics board members indicated with **(S)**)

**Adriano Aguzzi,** *U. Hospital Zürich*
**Takuzo Aida,** *U. of Tokyo*
**Leslie Aiello,** *Wenner-Gren Foundation*
**Judith Allen,** *U. of Edinburgh*
**Sonia Altizer,** *U. of Georgia*
**Sebastian Amigorena,** *Institut Curie*
**Meinrat O. Andreae,** *Max-Planck Inst. Mainz*
**Paola Arlotta,** *Harvard U.*
**Johan Auwerx,** *EPFL*
**David Awschalom,** *U. of Chicago*
**Clare Baker,** *University of Cambridge*
**Nenad Ban,** *ETH Zurich*
**Franz Bauer,** *Pontificia Universidad Católica de Chile*
**Ray H. Baughman,** *U. of Texas, Dallas*
**David Baum,** *U. of Wisconsin*
**Carlo Beenakker,** *Leiden U.*
**Kamran Behnia,** *ESPCI-ParisTech*
**Yasmine Belkaid,** *NIAID, NIH*
**Philip Benfey,** *Duke U.*
**May Berenbaum,** *U. of Illinois*
**Gabriele Bergers,** *U. of California, San Francisco*
**Bradley Bernstein,** *Massachusettes General Hospital*
**Peer Bork,** *EMBL*
**Bernard Bourdon,** *Ecole Normale Supérieure de Lyon*
**Chris Bowler,** *École Normale Supérieure*
**Ian Boyd,** *U. of St. Andrews*
**Emily Brodsky,** *U. of California, Santa Cruz*
**Ron Brookmeyer,** *U. of California Los Angeles* **(S)**
**Christian Büchel,** *U. Hamburg-Eppendorf*
**Joseph A. Burns,** *Cornell U.*
**Carter Tribley Butts,** *U. of California, Irvine*
**Gyorgy Buzsaki,** *New York U. School of Medicine*
**Blanche Capel,** *Duke U.*
**Mats Carlsson,** *U. of Oslo*
**Ib Chorkendorff,** *U. of Denmark*
**David Clapham,** *Children's Hospital Boston*
**Joel Cohen,** *Rockefeller U., Columbia U.*
**James J. Collins,** *MIT*
**Robert Cook-Deegan,** *Duke U.*
**Lisa Coussens,** *Oregon Health & Science U.*
**Alan Cowman,** *Walter & Eliza Hall Inst.*
**Robert H. Crabtree,** *Yale U.*
**Roberta Croce,** *Vrije Universiteit*
**Janet Currie,** *Princeton U.*
**Jeff L. Dangl,** *U. of North Carolina*
**Tom Daniel,** *U. of Washington*
**Frans de Waal,** *Emory U.*
**Stanislas Dehaene,** *Collège de France*
**Robert Desimone,** *MIT*
**Claude Desplan,** *New York U.*
**Sandra Diaz,** *Universidad Nacional de Cordoba*
**Dennis Discher,** *U. of Pennsylvania*
**Gerald W. Dorn II,** *Washington U. School of Medicine*
**Jennifer A. Doudna,** *U. of California, Berkeley*
**Bruce Dunn,** *U. of California, Los Angeles*
**William Dunphy,** *Caltech*
**Christopher Dye,** *WHO*
**Todd Ehlers,** *U. of Tuebingen*
**David Ehrhardt,** *Carnegie Inst. of Washington*
**Tim Elston,** *U. of North Carolina at Chapel Hill*
**Jennifer Elisseeff,** *Johns Hopkins U.*
**Gerhard Ertl,** *Fritz-Haber-Institut, Berlin*
**Barry Everitt,** *U. of Cambridge*
**Ernst Fehr,** *Johns Hopkins U.*
**Anne C. Ferguson-Smith,** *U. of Cambridge*
**Michael Feuer,** *The George Washington U.*
**Toren Finkel,** *NHLBI, NIH*
**Kate Fitzgerald,** *U. of Massachusetts*
**Peter Fratzl,** *Max-Planck Inst.*
**Elaine Fuchs,** *Rockefeller U.*
**Daniel Geschwind,** *UCLA*
**Karl-Heinz Glassmeier,** *TU Braunschweig*
**Ramon Gonzalez,** *Rice U.*
**Elizabeth Grove,** *U. of Chicago*
**Nicolas Gruber,** *ETH Zurich*
**Kip Guy,** *St. Jude's Children's Research Hospital*
**Taekjip Ha,** *U. of Illinois at Urbana-Champaign*
**Wolf-Dietrich Hardt,** *ETH Zurich*
**Christian Haass,** *Ludwig Maximilians U.*
**Sharon Hammes-Schiffer,** *U. of Illinois at Urbana–Champaign*
**Michael Hasselmo,** *Boston U.*
**Martin Heimann,** *Max-Planck Inst. Jena*
**Yka Helariutta,** *U. of Cambridge*
**James A. Hendler,** *Rensselaer Polytechnic Inst.*
**Janet G. Hering,** *Swiss Fed. Inst. of Aquatic Science & Technology*
**Kai-Uwe Hinrichs,** *U. of Bremen*
**David Hodell,** *U. of Cambridge*
**Lora Hooper,** *UT Southwestern Medical Ctr. at Dallas*
**Tamas Horvath,** *Yale University*
**Raymond Huey,** *U. of Washington*
**Fred Hughson,** *Princeton U.*
**Auke Ijspeert,** *EPFL Lausanne*
**Stephen Jackson,** *USGS and U. of Arizona*
**Steven Jacobsen,** *U. of California, Los Angeles*
**Seema Jayachandra,** *Northwestern U.*
**Kai Johnsson,** *EPFL Lausanne*
**Peter Jonas,** *Inst. of Science & Technology (IST) Austria*
**Matt Kaeberlein,** *U. of Washington*
**William Kaelin Jr.,** *Dana-Farber Cancer Inst.*
**Daniel Kahne,** *Harvard U.*
**Daniel Kammen,** *U. of California, Berkeley*
**Abby Kavner,** *U. of California, Los Angeles*
**Hitoshi Kawakatsu,** *U. of Tokyo*
**Masashi Kawasaki,** *U. of Tokyo*
**V. Narry Kim,** *Seoul National U.*
**Robert Kingston,** *Harvard Medical School*
**Etienne Koechlin,** *Ecole Normale Suprieure*
**Alexander Kolodkin,** *Johns Hopkins U.*
**Thomas Langer,** *U. of Cologne*
**Mitchell A. Lazar,** *U. of Pennsylvania*
**David Lazer,** *Harvard U.*
**Thomas Lecuit,** *IBDM*
**Virginia Lee,** *U. of Pennsylvania*
**Stanley Lemon,** *U. of North Carolina at Chapel Hill*
**Ottoline Leyser,** *Cambridge U.*
**Wendell Lim,** *U.C. San Francisco*
**Marcia C. Linn,** *U. of California, Berkeley*
**Jianguo Liu,** *Michigan State U.*
**Luis Liz-Marzan,** *CIC biomaGUNE*
**Jonathan Losos,** *Harvard U.*
**Ke Lu,** *Chinese Acad. of Sciences*
**Christian Lüscher,** *U. of Geneva*
**Laura Machesky,** *CRUK Beatson Inst. for Cancer Research*
**Anne Magurran,** *U. of St. Andrews*
**Oscar Marin,** *CSIC & U. Miguel Hernández*
**Charles Marshall,** *U. of California, Berkeley*
**C. Robertson McClung,** *Dartmouth College*
**Rodrigo Medellin,** *U. of Mexico*
**Graham Medley,** *U. of Warwick*
**Jane Memmott,** *U. of Bristol*
**Tom Misteli,** *NCI*
**Yasushi Miyashita,** *U. of Tokyo*
**Mary Ann Moran,** *U. of Georgia*
**Richard Morris,** *U. of Edinburgh*
**Alison Motsinger-Reif,** *NC State U.* **(S)**
**Thomas Murray,** *The Hastings Center*
**Daniel Neumark,** *U. of California, Berkeley*
**Kitty Nijmeijer,** *U. of Twente*
**Helga Nowotny,** *European Research Advisory Board*
**Rachel O'Reilly,** *Warwick U.*
**Joe Orenstein,** *U. of California Berkeley & Lawrence Berkeley National Lab*
**Harry Orr,** *U. of Minnesota*
**Pilar Ossorio,** *U. of Wisconsin*
**Andrew Oswald,** *U. of Warwick*
**Isabella Pagano,** *Istituto Nazionale di Astrofisica*
**Margaret Palmer,** *U. of Maryland*
**Steve Palumbi,** *Stanford U.*
**Jane Parker,** *Max-Planck Inst. of Plant Breeding Research*
**Giovanni Parmigiani,** *Dana-Farber Cancer Inst.* **(S)**
**John H. J. Petrini,** *Memorial Sloan-Kettering Cancer Center*
**Samuel Pfaff,** *Salk Institute for Biological Studies*
**Kathrin Plath,** *U. of California, Los Angeles*
**Joshua Plotkin,** *U. of Pennsylvania*
**Albert Polman,** *FOM Institute AMOLF*
**Philippe Poulin,** *CNRS*
**Jonathan Pritchard,** *Stanford U.*
**Wim van der Putten,** *Netherlands Institute of Ecology*
**David Randall,** *Colorado State U.*
**Sarah Reisman,** *Caltech*
**Felix Rey,** *Institut Pasteur*
**Trevor Robbins,** *U. of Cambridge*
**Jim Roberts,** *Fred Hutchinson Cancer Research Ctr.*
**Amy Rosenzweig,** *Northwestern University*
**Mike Ryan,** *U. of Texas, Austin*
**Mitinori Saitou,** *Kyoto U.*
**Shimon Sakaguchi,** *Kyoto U.*
**Miquel Salmeron,** *Lawrence Berkeley National Lab*
**Jürgen Sandkühler,** *Medical U. of Vienna*
**Alexander Schier,** *Harvard U.*
**Vladimir Shalaev,** *Purdue U.*
**Robert Siliciano,** *Johns Hopkins School of Medicine*
**Denis Simon,** *Arizona State U.*
**Uri Simonsohn,** *U. of Pennsylvania*
**Alison Smith,** *John Innes Centre*
**Richard Smith,** *U. of North Carolina* **(S)**
**John Speakman,** *U. of Aberdeen*
**Allan C. Spradling,** *Carnegie Institution of Washington*
**Jonathan Sprent,** *Garvan Inst. of Medical Research*
**Eric Steig,** *U. of Washington*
**Paula Stephan,** *Georgia State U. and National Bureau of Economic Research*
**Molly Stevens,** *Imperial College London*
**V. S. Subrahmanian,** *U. of Maryland*
**Ira Tabas,** *Columbia U.*
**Sarah Teichmann,** *Cambridge U.*
**John Thomas,** *North Carolina State U.*
**Shubha Tole,** *Tata Institute of Fundamental Research*
**Christopher Tyler-Smith,** *The Wellcome Trust Sanger Inst.*
**Herbert Virgin,** *Washington U.*
**Bert Vogelstein,** *Johns Hopkins U.*
**David Wallach,** *Weizmann Inst. of Science*
**Ian Walmsley,** *U. of Oxford*
**Jane-Ling Wang,** *U. of California, Davis* **(S)**
**David Waxman,** *Fudan U.*
**Jonathan Weissman,** *U. of California, San Francisco*
**Chris Wikle,** *U. of Missouri* **(S)**
**Ian A. Wilson,** *The Scripps Res. Inst.* **(S)**
**Timothy D. Wilson,** *U. of Virginia*
**Rosemary Wyse,** *Johns Hopkins U.*
**Jan Zaanen,** *Leiden U.*
**Kenneth Zaret,** *U. of Pennsylvania School of Medicine*
**Jonathan Zehr,** *U. of California, Santa Cruz*
**Len Zon,** *Children's Hospital Boston*
**Maria Zuber,** *MIT*

**BOOK REVIEW BOARD**
**David Bloom,** *Harvard U.*, **Samuel Bowring,** *MIT,* **Angela Creager,** *Princeton U.,*
**Richard Shweder,** *U. of Chicago,* **Ed Wasserman,** *DuPont*



*Published by AAAS*

EDITORIAL

# Reunifying America

*Editor-in-Chief,* Science *Journals*

I was in Berlin on the night of the United States presidential election, waiting for the Falling Walls conference to begin on 9 November. The bruising 2016 presidential campaign revealed societal fragmentation across the nation. Being in Berlin to absorb the election news had some unique resonances. Here, history has shown that there can be grave dangers in division and benefits of unification. Yet countries everywhere are showing signs of deep polarization. We must understand more fully these divisions. Communities at all levels and across sectors must work hard on drawing citizenry, and the world, together. The scientific community must recognize its important role in helping to break down barriers and find solutions that will build better lives for everyone.

Falling Walls is where scientists from around the world have convened for the past 8 years to discuss how to tackle society's major challenges. The name of the conference is derived from the fall of the Berlin Wall on 9 November 1989, which reunified East and West Germany. Germany, Europe, and the world have benefitted greatly from the reunification. Ironically, this date also corresponds to the anniversary of Kristallnacht, the Night of the Broken Glass, when, in 1938, Nazi soldiers and civilians rampaged across Germany, destroying Jewish businesses and synagogues. This fragmentation of society foreshadowed horrors yet to come. These events are not meant to imply a comparison of leaders, but rather, to provide clear markers of the power of unity and the dangers of division.

Deep discontent and substantial differences in opinion now exist across America. Much of this discord is centered around the impact of globalization. Voting patterns changed in regions where, for example, there were once traditional centers of heavy industry and domestic manufacturing jobs. The election results and exit polling also revealed that the United States is sharply divided along lines of gender, race, and educational attainment.

And yet, historically, Americans have always shared many important characteristics, including a strong work ethic; a willingness to take risks; an acceptance, if at times quite grudging, of welcoming immigrants to build better lives for themselves and for all of us; and an ability to invent and discover, with tremendous societal and economic benefits. Many of the discussions that I had in Berlin have shown how these features are highly regarded and respected by other countries. These qualities may unravel if the nation's societal distress is not carefully examined.

The scientific enterprise embodies many of these cherished characteristics, and its own history and culture of problem-solving and collaboration may help bridge the divides. Research requires hours of hard work, often frustrating and seemingly fruitless. Exploring new areas or translating results into practical benefits requires expenditure of time and effort and, sometimes, considerable financial risk. This enterprise has been global for a long time, and the United States gains tremendously from individuals who begin or extend their scientific careers in this country. Many "American" Nobel laureates came to the United States from abroad. What is the output? Technological innovation and unimagined discoveries that drive progress, open new opportunities, and improve societal well-being.

***"Moving ahead productively will be an important test...for everyone."***

It is important to understand the basis for the divisions across the United States and elsewhere. The tools of social science should be harnessed to better examine these divides. This will require careful listening to avoid missing important cues. While such a diagnostic phase is under way, scientists must continue to reach out and offer insights and mechanisms that provide the factual foundations for a collective path forward. The United States now ventures into somewhat uncharted territory with a president-elect who will come into office with no experience in governing and relatively vague positions about many aspects of domestic and foreign policy. Moving ahead productively will be an important test not only for American institutions, but for everyone.

**– Jeremy Berg**

10.1126/science.aal3815

PHOTO: DAN MOORE/ISTOCK PHOTO

Downloaded from http://science.sciencemag.org/ on November 22, 2016



Published by AAAS

# NEWS

> “These are figures which really we should be ashamed of.”
>
> **Shekhar Saxena, director of mental health and substance abuse at the World Health Organization in Geneva, Switzerland**, noting this week at the Society for Neuroscience that only 1% of total global development assistance is spent on mental health.

IN BRIEF

The magnitude-7.8 earthquake, which produced landslides and caused extensive infrastructure damage, occurred on a little studied fault.

PHOTO: MARK MITCHELL/NEW ZEALAND HERALD/POOL VIA AP PHOTO

## New Zealand earthquake rattles experts

A magnitude-7.8 earthquake struck New Zealand’s South Island shortly after midnight local time on 14 November, killing two people. The U.S. Geological Survey placed the epicenter of the quake near Kaikoura, a coastal tourist town 92 kilometers northeast of Christchurch, at a depth of about 23 kilometers. The shallow quake triggered landslides and caused extensive damage to infrastructure. New Zealand straddles the collision zone between the Australia and Pacific tectonic plates. The country’s earthquake hazard maps anticipate strong quakes emanating from the complex faults in those boundaries, which run off the east coast of the North Island and along the west coast of the South Island, says Kevin McCue, an engineering seismologist at Australia’s Central Queensland University in Rockhampton. But the epicenter of Sunday’s quake was on a little studied intraplate fault on the east coast of the South Island—like the strong temblors that struck Christchurch in 2010 and 2011. That suggests this region has more risk than thought, and New Zealand’s earthquake hazard maps, which affect building codes, must be reconsidered, McCue says. He also worries that the quake might increase stress on the plate boundaries, where a rupture could produce an even stronger earthquake.

AROUND THE WORLD

### Experiment to raise dead blocked

BENGALURU, INDIA | The Indian Council of Medical Research (ICMR) has derailed a controversial experiment that would seek to revive brain-dead accident victims. On 11 November, ICMR’s National Institute of Medical Statistics removed the “ReAnima” trial from India’s clinical trial registry, noting several regulatory lapses in the trial. In May, Himanshu Bansal, an orthopedic surgeon at Anupam Hospital in Uttarakhand in India, announced plans to give about 20 brain-dead people a mix of interventions including injections of mesenchymal stem cells and peptides said to help regenerate brain cells, as well as transcranial laser stimulation and median nerve stimulation, techniques shown to improve cognition in patients with traumatic brain injury. Bansal said he wanted to bring brain-dead individuals to a state in which they show flickers of consciousness.

Downloaded from http://science.sciencemag.org/ on November 22, 2016



Published by AAAS

Scientists and physicians have raised ethical concerns, noting that the mix of interventions has not been tested in animals and that the effort could distress family members. The team says that the trial's deregistration is a temporary setback for the project. http://scim.ag/ReAnimablock

## Canada seeks new science adviser

OTTAWA | The Canadian government will issue an open call for nominations for the position of national science adviser, Minister of Science Kirsty Duncan said last week at an annual science policy conference in Canada's capital city. The position was axed in 2008 by then–Prime Minister Stephen Harper; when Prime Minister Justin Trudeau was elected in October 2015, he promised to resurrect it. Nominations for the position may come from researchers, institutions such as universities, and average Canadians, Duncan says. "We want to hear from Canadians across the country." Meanwhile, rumors are swirling among Canada's scientific community that a review of federal financial support for fundamental research will recommend creating a military research body akin to the United States's Defense Advanced Research Projects Agency. The review is being conducted by a nine-member panel led by David Naylor, former president of the University of Toronto in Canada. http://scim.ag/Canadaadviser

## La Niña returns

WASHINGTON, D.C. | Winter is coming—at least to the U.S. northwest. The U.S. National Weather Service (NWS) and the National Oceanic and Atmospheric Administration Climate Prediction Center last week said they had observed weak but persistent La Niña conditions, including cooler-than-normal surface water temperatures, in the eastern and central equatorial Pacific throughout October and early November. La Niña, known as the "cool" phase of the El Niño/Southern Oscillation, brings wetter-than-normal conditions to much of the globe during the Northern Hemisphere winter, from Indonesia to southeastern Africa to northern Australia, and tends to make the southeast United States—already suffering a drought—warmer and drier than normal in winter; the reverse is true for the northwestern United States. La Niña also tends to increase Indian monsoon rainfall during the Northern Hemisphere summer, but this weak La Niña likely won't last past February, NWS says.

La Niña brought powerful snowstorms to California in December 2010.

CREDITS: (PHOTO) RICH PEDRONCELLI/AP PHOTO; (GRAPHIC) C. SMITH/*SCIENCE*

## Animal travel ban paralyzes labs

CANARY ISLANDS, IN SPAIN | The decision by two major Spanish airlines to stop transporting laboratory animals from mainland Spain to the Canary Islands is threatening 30 biomedical research projects across the archipelago. Now, some politicians plan to ask the Spanish government to intervene, according to a story in Spanish newspaper *El País* last week. Since Air Europa stopped flying research animals last year and Iberia followed suit in March, several groups have put their research with transgenic mice on hold; 29 animals ordered from the United States by the University Hospital of the Canary Islands on Tenerife have been stranded in Madrid since September. The uncertainty could affect island researchers' chances of winning grants, says Javier Castro, a rheumatological disease researcher at the Tenerife hospital. Iberia cited safety reasons for its ban, including the risk that escaped mice could damage to the aircraft cables. But the European Animal Research Association believes the companies gave in to pressure from animal activists. http://scim.ag/Canarymice

NEWSMAKERS

## Who's influencing brain science?

When it comes to influential neuroscience research, University College London (UCL) has a lot to boast about. That's not the opinion of a human, but rather the output of a computer program that has parsed the content of 2.5 million neuroscience articles, mapped all the citations between them, and calculated a score for each author's influence on the rest. Three of its top 10 most influential neuroscientists hail from UCL: **Karl Friston** (first), **Raymond Dolan** (second), and **Chris Frith** (seventh). The

## Ballot initiatives across the country

Donald Trump's victory in the presidential election last week helped usher in a new era of Republican rule in Washington, D.C. But voters also weighed in on several science-related state ballot items. Here's a roundup of the results.

PASSED DID NOT PASS

**Monroe County, in Florida**
Release genetically modified mosquitoes to combat mosquito-borne disease?
57%

**Washington**
Establish the first U.S. carbon tax—in exchange for a sales tax cut and working families tax rebate?
41%

**California**
Raise cigarette taxes by $2 per pack, give money to public health programs?
63%

**Colorado**
Raise cigarette taxes by $2 per pack, give money to public health programs and research?
47%

**Montana**
Spend $20 million over 10 years on a biomedical research authority for disease research grants?
42%

**Oregon**
Crack down on wildlife trafficking by banning sales and purchases of animal parts from 12 species?
69%

**Florida**
Allow consumers to own or lease solar equipment on their property—to generate power specifically for their own use? (Sixty percent support was needed to pass.)
51%

**POT WINS HIGH MARKS**

**Arkansas, California, Florida, Maine, Massachusetts, Nevada, North Dakota**
Legalize recreational or medicinal marijuana?

Marijuana had a good day at the ballot box. Voters in California, Maine, Massachusetts, and Nevada approved measures legalizing recreational marijuana and regulating or taxing it to various degrees. Only in Arizona was recreational marijuana turned back. Arkansas, Florida, and North Dakota voted to legalize marijuana for certain medicinal uses, and Montana voted to expand its 2004 medical marijuana law.

Downloaded from http://science.sciencemag.org/ on November 22, 2016



Published by AAAS

secret of their success? "We got into human functional brain imaging very early," Frith says, which made it possible to "be first to do many of the obvious studies." The program, called Semantic Scholar, is an online tool built at the Allen Institute for Artificial Intelligence (AI2) in Seattle, Washington. When Semantic Scholar looks at a paper published online, what does it actually see? Much more than the typical academic search engine, says Oren Etzioni, CEO of AI2, who has led the project. "We are using machine learning, natural language processing, and [machine] vision to begin to delve into the semantics." For the complete list of Semantic Scholar's "top 10," visit: **http://scim.ag/10neuro.**

## Three Qs

A linguist is the unlikely hero of the sci-fi popcorn movie *Arrival*, released this week. Linguistics professor Louise Banks, played by Amy Adams, is recruited by the U.S. military to communicate with alien spacecraft that appear in Earth's skies. The aliens' written language has a strange (to humans) structure: Entire sentences are constructed instantaneously as impossibly complex circles. To save humanity, Banks must decipher this puzzle. *Science* asked linguist **Jennifer Nycz** of Georgetown University in Washington, D.C., for her take on the movie. **http://scim.ag/ArrivalQA**

**Q: Was linguistics portrayed accurately?**
**A:** Most of the characters in the film are concerned with translation, which is not really a core focus of academic linguistics; most linguists are interested in understanding how language works at a deeper level. There is a concept from linguistics that is really excellently deployed in terms of the storytelling—but to say anything else would be a big spoiler!

**Q: How would you expect extraterrestrials to communicate?**
**A:** Language on Earth is both physically and socially embedded. … Variation within and across human languages reflects these physical and cognitive constraints. I'd expect alien language to do the same. So I'd have to know something about their physiology, their cognition, and their society to even begin to speculate.

**Q: What did you think of the movie overall?**
**A:** I really liked it! Does the language learning (on both the human and alien sides) happen improbably fast? Yes. Is it a cinéma vérité portrayal of how linguists work in the field? No. [But] there's a lot regarding the experience of being a linguist that rang true: For example, [the] other characters expect the linguist to just *know* all the languages, including the alien one. None of us [is] C-3PO!

The El Tor cholera pandemic began in the 1960s and arrived in Haiti in 2010 via U.N. troops.

PHOTO: KENA BETANCUR/REUTERS/NEWSCOM

## How today's cholera pandemic was born

The world is in the grip of its seventh great cholera pandemic, begun in the 1960s and currently burning through developing countries like Haiti and the Democratic Republic of the Congo. Strain No. 7 of cholera was a harmless microbe when it was first identified in a laboratory in El Tor, Egypt, in 1897. But over time, it morphed into a deadly pathogen. This week in the *Proceedings of the National Academy of Sciences*, scientists report using DNA from cholera samples stored in laboratories around the world to trace the origin of the current pandemic. Cholera, caused by the bacterium *Vibrio cholerae*, is marked by watery diarrhea that can lead to dehydration and death. By comparing the samples' genomes, the researchers defined six stages in the modern strain's evolution that helped it gain toxic properties and its ability to spread. At some point El Tor picked up a gene called *tcpA*, which helps it cling to the wall of the small intestine and so live longer in the gut. Between 1903 and 1908, a phage—a virus that infects bacteria—transferred a genetic trait from the sixth cholera pandemic that causes watery diarrhea, accelerating the disease's spread. In Makassar, Indonesia, El Tor gained more genes that increased transmissibility. And, eventually, in 1961, it became a true pandemic, spreading around the world.

### BY THE NUMBERS

**13%**

Fatality rate for acute and delayed deaths due to West Nile virus, reports a study of more than 4000 patients. The Centers for Disease Control and Prevention previously estimated the acute fatality rate at 4% (American Society of Tropical Medicine and Hygiene conference).

**0.2%**

Projected increase in global carbon emissions from burning fossil fuels for 2016, a break from the rapid growth of 2.3% per year this decade until 2013 (*Earth System Science Data*).

**4.20 million**

Reduction in the number of global deaths in children younger than 5 in 2015, compared with 2000, mainly because of fewer deaths due to pneumonia, diarrhea, childbirth deaths, malaria, and measles (*The Lancet*).

Downloaded from http://science.sciencemag.org/ on November 22, 2016



Published by AAAS

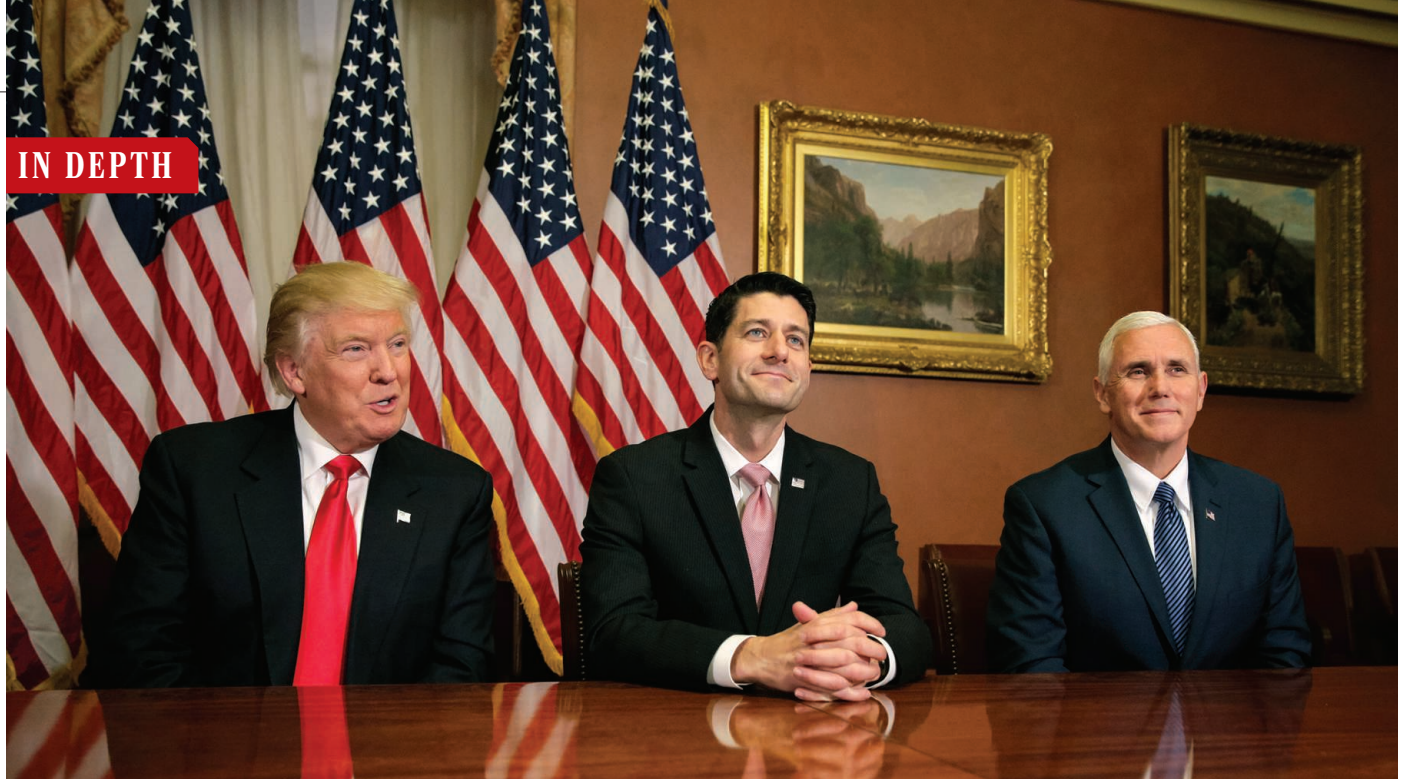

President-elect Donald Trump (left) and Vice President–elect Mike Pence (right) meet with Representative Paul Ryan (R–WI), the speaker of the House of Representatives.

PHOTO: JOSHUA ROBERTS

U.S. POLITICS

# *Scientists start to parse a Trump presidency*

## Fears for climate and social science research, hopes for infrastructure boost

*By* **Jeffrey Mervis**

Donald Trump's surprising victory last week over Hillary Clinton has profoundly altered the U.S. political landscape. Many scientists were no less confounded by the outcome, which delivered the White House to a man many academics opposed and maintained Republican control of both the Senate and the House of Representatives.

Even so, the science establishment has already begun to coalesce behind a common message: Don't stick your head in the sand, and don't assume the worst. Continue making the case to the incoming administration and Congress that research contributes to the prosperity and security of the nation.

The community's initial sense of despair stemmed in part from Trump's public comments questioning the validity of such bedrock scientific concepts as vaccination and climate change, and the absence of any science-savvy advisers on his campaign team. "Already wary of Trump's support for science, the scientific community will be watching closely to see if President Trump is able to transcend his early rhetoric and find a way to demonstrate that he will respect and take science seriously," says Tobin Smith, vice president for policy at the Association of American Universities, a Washington, D.C.–based consortium of the nation's top research universities.

One worry is how the new president will wield his immense executive powers. With a stroke of a pen, for example, Trump could undo Obama-era executive orders easing controls on human embryonic stem cell research and undermine high-profile regulations aimed at reducing U.S. greenhouse gas emissions and protecting small waterways.

A second concern is that a Republican president is less likely to threaten to veto legislation produced by a Republican Congress. That threat is often enough to derail legislation before it reaches the Oval Office. In recent years, President Barack Obama used it to fight proposals that the scientific community also opposed, including plans to alter peer review at the National Science Foundation (NSF), curb research in the earth, environmental, and social sciences at NSF and NASA, and weaken environmental rules. In addition, Obama has actually vetoed a dozen bills, one-third of which involved climate or environmental issues.

Then there is the question of how a Trump administration will affect federal funding of research. The encouraging news is that, regardless of which party controls Congress and the White House, spending on science has for decades remained steady as a portion of the overall federal budget—about 10% of nondefense discretionary spending, to use one common metric. In addition, fields such as biomedical research enjoy broad bipartisan support. But other fields—including climate and the environmental and social sciences—are unpopular with many Republicans, and are likely to be squeezed.

History has shown, however, that having the same party control both the White House and Congress is no guarantee of legislative harmony. Sharp differences could arise after Trump's initial list of priorities—creating jobs, restricting immigration, and repealing and replacing the Affordable Care Act—are translated into proposed legislation. Some of Trump's goals could even create opportunities for science advocates, such as his campaign pledge to pump hundreds of billions of dollars into repairing roads and bridges, harbors, airports, and rail systems. Scientific groups would like to see cyber and scientific infrastructure included in any bill.

Increased infrastructure spending is attractive to members of both parties. "Anything that will encourage economic growth and create jobs, this will make America bet-

Downloaded from http://science.sciencemag.org/ on November 22, 2016



Published by AAAS

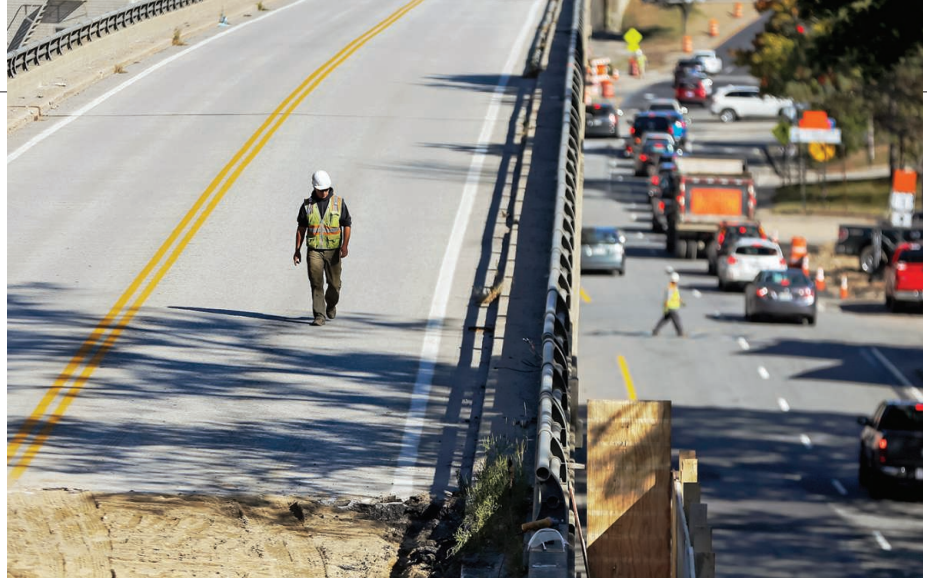

Scientists hope any new infrastructure spending bill will include money for scientific facilities.

PHOTO: PORTLAND PRESS HERALD

ter," says former Republican Senate Majority Leader Trent Lott, now a senior fellow at the Bipartisan Policy Center in Washington, D.C. But Lott and others say that finding a way to pay for any infrastructure program will be a major sticking point.

If that problem is solved, an infrastructure bill may be the best chance for science advocates to secure a short-term rise in federal research funding. Their model is the 2009 economic stimulus package, passed shortly after Obama took office, which included $21 billion for several research agencies.

Absent such an initiative, science spending is likely to remain flat. One big reason is that a 2011 law aimed at reducing the federal deficit over 10 years by limiting overall discretionary spending remains in force. That law triggered the across-the-board cuts known as sequestration in 2013, and the politics of deficit reduction haven't gotten any easier since then.

Trump may try to alter that law to boost defense spending, something that many congressional Republicans also want, without also increasing domestic budgets. Under the current law, any increase in defense spending would require cuts to domestic programs, a category that includes every science agency outside the defense and homeland security departments. Most congressional Democrats would vehemently oppose that move, and in the Senate they have the 40 votes necessary to block a vote (assuming the Republican majority doesn't change the so-called filibuster rules).

At some point the new administration will also have to weigh in on a disagreement between House and Senate Republicans over NSF's approach to funding research. In the House, Representative Lamar Smith (R–TX), chairman of the House science committee, has enraged many scientists by writing NSF reauthorization measures that propose cuts to the geosciences and social sciences, as well as changes in NSF's vaunted system of peer review to choose the best ideas. Smith says he simply wants to put scarce dollars to their best use, whereas scientists say he wants to impose his own views over those of experts. Obama's White House has threatened to veto Smith's legislation because it "could cast a shadow over the value of basic research … [and] would add nothing to accountability in Federal funding for scientific research, while needlessly adding to bureaucratic burdens."

The Senate also has not embraced Smith's vision. Instead, this past June, a Senate panel supported NSF's current practices in its version of a reauthorization bill. Science lobbyists hope that the Senate's view will prevail in current negotiations to iron out differences between the two bodies.

Looking at the big picture, the new administration's attitude toward science remains a mystery. Trump's transition team hasn't yet said who it has selected to review policies and appointments at key science agencies, including the National Institutes of Health, NSF, and NASA. That does not mean science advocates should despair, says lobbyist Joel Widder of Federal Science Partners in Washington, D.C. "Until you know who you're talking to [in the Trump transition], I'd keep the message simple—support for basic research generates new knowledge that can fuel economic growth and provides the talent that industry needs," says Widder, a former longtime NSF government affairs manager and congressional staffer.

Widder offers similar advice to those worried that Trump will drag his feet on appointing a presidential science adviser, or choose someone not highly regarded by the scientific community. Fairly or not, science politicos believe that a lengthy delay in the appointment means science is an afterthought—or worse—in a new president's administration. "I think they will be able to find someone of [good] stature eventually," says Widder about the Trump administration. "I just don't think it's high on their list of things to do right now."

David Goldston of the Natural Resources Defense Council in Washington, D.C., and a former chief of staff for the House science committee, even suggests that scientists may be happier if Trump doesn't name someone with far-reaching authority to coordinate research policy. "Benign neglect is not always the worst" outcome, he says, if it means more flexibility for science agencies. ■

*With reporting by the* Science *news staff.*

## A longer spending freeze

*By* **Jeffrey Mervis**

This week Congress returned for a short lame-duck session. And the first thing Republican leaders did was delay completion of a 2017 spending bill until after Donald Trump takes office—a decision that forces science agencies to tread water.

All agency budgets are now frozen at 2016 levels under what is called a continuing resolution (CR), which prohibits starting new programs or expanding existing initiatives. Congressional spending panels have spent months working on a dozen bills that would fund the government through September 2017. But those measures would also have needed to pass muster with President Barack Obama. So the Republican leadership decided to extend the CR, which expires on 9 December, until 31 March, which is two months into the Trump administration. A separate bill to spur drug development and bolster biomedical research remains in limbo.

A longer CR will likely stall high-profile Obama initiatives in precision medicine, neuroscience, and cancer at the National Institutes of Health, and delay boosts to high performance computing and a new neutrino experiment within the Department of Energy. It also complicates a planned upgrading of the academic research fleet by the National Science Foundation: A House spending panel has declined to fund the request for two ships, while a Senate panel wants to build three ships. ■

Downloaded from http://science.sciencemag.org/ on November 22, 2016



Corrected 18 November 2016. See full text.



Published by AAAS

ECOLOGY

# A new evolutionary classic

## At least a dozen times, rove beetles independently evolved the ability to invade and steal from army ant nests

*By* **Elizabeth Pennisi**

An army ant colony does not welcome outsiders. Not only are the ants notoriously fierce, but they specialize in coordinating mass attacks. Yet within the nests of all 340 known species of army ants, quietly stealing nourishment from their unwitting hosts, live tiny beetles. These flea-sized parasites have lost their "beetleness" and look, smell, and behave so much like their ants that they can pilfer food or eat ant young with impunity.

You might think that the adaptations of these rove beetles, as they are known, amount to an improbable feat of evolution, never to be repeated. But you would be wrong, a new study suggests. By genetically analyzing 40 beetle species from army ant gatherings around the world, entomologists Joseph Parker of Columbia University and Munetoshi Maruyama of the Kyushu University Museum in Fukuoka, Japan, show that the beetles adapted to live with army ants not once, as some investigators thought, but at least a dozen times. Together, says Daniel Kronauer, an evolutionary biologist at The Rockefeller University in New York City, the beetles offer "amazing examples of parallel evolution in deep time."

There are other classic examples of parallel evolution—a tiny marine fish called the stickleback evolved the same changes multiple times after it repeatedly became trapped in freshwater, and anole lizards developed similar adaptations on the different Caribbean islands they invaded. But those species had a recent common ancestor and likely tapped very similar genetic toolboxes as they evolved in parallel. The rove beetle species, in contrast, had already been diverging for tens of millions of years before they took up independently with army ants. "It is a textbook example of morphological convergence," says Terry Ord, an evolutionary biologist at the University of New South Wales in Sydney, Australia. "It is likely to become a classic."

With 61,000 named species, rove beetles outnumber any other group of multicellular animals, yet most live hidden in leaf litter in the tropics and other obscure places. But several groups have adopted a lifestyle that, though riskier, promises richer rewards: parasitizing ant and termite nests. "A social insect colony is a little bit like Manhattan, a very energy-packed resource with lots of different niches," Kronauer explains. "If you manage to get in, the payoff is very high."

The parasites aren't easy to study. Parker and Maruyama spent almost a decade following army ant trails to collect fresh specimens, hampered both by the aggressive ants and the scarcity of the beetles, which number roughly one for every 1000 ants. In the end the duo had enough to sequence DNA from five beetle genes, combine it with data from other studies, and build a family tree. The analysis, reported 30 September in a preprint posted to bioRxiv, revealed that all the ant-associated beetles and their free-living relatives shared a common ancestor 105 million years ago. Since then, the beetles took up with army ants at least 12 times.

The beetles were prepared in at least one way to evolve their unusual lifestyle, the study suggests. Earlier work had shown that the common ancestor of the parasitic lineages had already evolved a gland at the tip of the abdomen that squirts noxious compounds called quinones at any attackers. "It's a preadaptation that allows you to undergo some extreme adaptations," Parker says. Since then, some parasitic beetles have evolved new glands and new functions. One group now sprays ant alarm pheromones that cause would-be attackers to scatter. Others secrete what are likely the same chemicals that ants themselves use to recognize colony mates. With the help of still other features, including a narrowed waist, longer legs, antennae with antlike elbow joints, and even an antlike gait, the interlopers effectively fool their hosts into feeding, protecting, and transporting them.

Taro Eldredge, a graduate student at the University of Kansas in Lawrence, believes a similar story holds for the many rove beetle species that have taken up residence with termites. Investigators haven't done a DNA analysis to work out the evolutionary history of these beetles, as even fewer specimens have been collected. But Eldredge, Maruyama, and Taisuke Kanao from Kyoto University in Japan have proposed a scenario for how the beetles came to live with termites. The termite dwellers share a curious feature with another group of rove beetles, which live and hunt on shorelines. To protect their heads as they force their way through sand grains, these beetles have a kind of visor, formed from an enlarged thorax. The parasitic beetles have similar armor, and in a 27 October preprint on bioRxiv, the researchers propose that it was key to enabling them to withstand attack as they began encroaching on termite nests.

At first, the beetles might have hung out at the mound entrances, eating injured colony members. But gradually some weaseled their way in, and found a jackpot. In time, say Eldredge and colleagues, some species evolved physical features and other ways to fool their hosts and live among them: a termite-like body with a bulging abdomen and termitelike body odors and behaviors.

Eldredge doesn't know whether this remarkable mimicry evolved repeatedly, as it did for ants. But he suspects that, as with the ant parasites, evolution displayed its virtuosity more than once. As Kronauer puts it, in the story of the rove beetles, "you feel the power of evolution—of natural selection—staring you in the eye." ■

A rove beetle (right) tails a Malaysian army ant. Its antlike look and behavior let it parasitize ants with impunity.

PHOTO: TAKASHI KOMATSU

Downloaded from http://sciencemag.org/ on November 22, 2016



Published by AAAS

SPACE SCIENCE

# Japan reboots x-ray probe—and mission management

## After a series of mission failures, Japan's space science agency aims to overhaul lax oversight

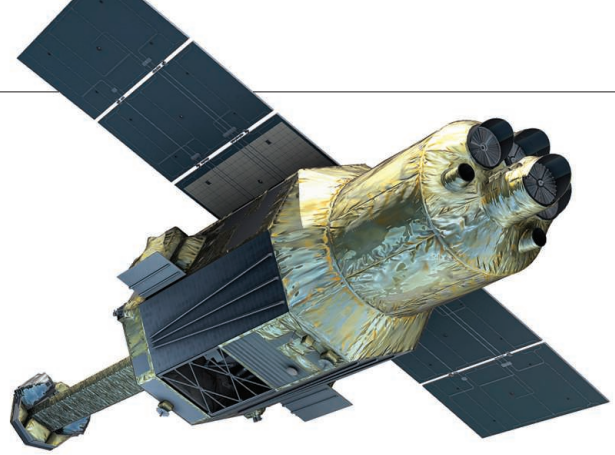

After a month in orbit, ASTRO-H broke apart. Failures in the probe's control systems were to blame.

*By* **Dennis Normile**, *in Sagamihara, Japan*

When Japan launched the ASTRO-H x-ray satellite on 17 February, the astrophysics community held its collective breath. Two previous Japanese-U.S. x-ray missions had failed, and scientists hungered for the detailed view of the x-ray sky that ASTRO-H promised. The new satellite seemed to beat the odds, getting into orbit. But 5 weeks later, it suddenly broke apart—leaving astrophysicists heartbroken yet again.

Now, after a report detailing the flaws that doomed the $300 million satellite, renamed Hitomi after launch, Japanese scientists are laying plans to try again. "We have to fulfill our responsibility" to put an x-ray observatory in orbit, says Saku Tsuneta, director general of the Institute of Space and Astronautical Science (ISAS) here, a division of the Japan Aerospace Exploration Agency (JAXA).

Before a reboot can begin, ISAS must convince funding agencies and international partners that it will rectify management shortcomings that contributed to the demise of Hitomi, which suffered a cascading series of failures that sent it into a fatal spin. Japan's education ministry is on board. It has included funding to start work on a replacement mission in its 2017 budget request, expected to be approved by Japan's parliament next month. And NASA, which provided Hitomi's key instrument—the Soft X-Ray Spectrometer (SXS)—is discussing with JAXA the possibility of building a replacement, says NASA astrophysics spokesperson Felicia Chou in Washington, D.C. Tsuneta says the mission, slated for launch in 2021, will be simpler and cheaper, carrying two instruments instead of the four on Hitomi.

Hitomi's loss left a gaping hole in x-ray astronomy studies, which can only be done from space and provide a window into the universe's hottest and most violent corners. In 2000, a launch failure sent Japan's ASTRO-E x-ray satellite crashing into the Pacific. Its replacement, Suzaku, lost a key instrument several weeks after its 2005 launch. X-ray astronomers have had to rely on aging instruments launched in 1999: the European Space Agency's (ESA's) X-ray Multi-Mirror Mission and NASA's Chandra X-ray Observatory. That's why scientists lined up behind a Hitomi replacement so quickly, says Dan McCammon, a space physicist at the University of Wisconsin in Madison, who worked on the SXS.

Unlike previous x-ray missions, which were tuned to image point sources such as black holes and neutron stars, Hitomi promised extremely high resolution—by energy levels—of the x-rays emanating from superheated gases around black holes and in galaxy clusters and supernova remnants. It got off to a promising start. After a smooth launch, operators spent a month testing and tuning its instruments. The SXS "was performing exceptionally well," says ASTRO-H science working group member Andrew Fabian, a theoretical astrophysicist at the University of Cambridge in the United Kingdom. Then, early on 26 March, mission control lost contact. After concluding the satellite had broken up, JAXA abandoned the mission on 28 April.

Investigators from JAXA, ISAS, and mission contractors pieced together a failure scenario using telemetry data, analyses, and simulations. After observing the Crab Nebula on 25 March, the spacecraft aimed at an active galactic nucleus, using a star tracker for attitude control. Faulty star tracker data led the attitude control system to conclude that Hitomi was rotating when it was, in fact, stable. The craft activated a reaction wheel to counter the perceived rotation. As a result, Hitomi actually started rotating. A second malfunction made it spin faster. The probe fired thrusters to counteract it, but because of a faulty control program the thrusters fired in the wrong direction, accelerating the rotation until the solar panels snapped off. In an 8 July report, investigators blamed the failures on

## Star-crossed missions

High-profile cancellations and failures, including ASTRO-H (see above), have prompted Japan's space science institute to take a hard look at its management style.

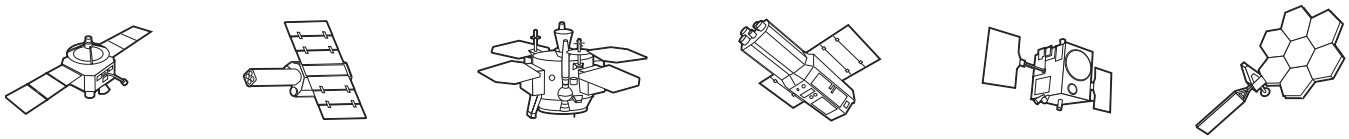

**Nozomi**
**Orbiter to study martian atmosphere**
Failed to enter orbit

**ASTRO-E**
**Joint mission with NASA for x-ray astronomy**
Lost because of launch rocket failure

**LUNAR-A**
**Orbiter with two penetrators to study the internal structure of the moon**
Canceled in 2007 because of development problems

**Suzaku**
**Joint mission with NASA for x-ray astronomy**
Liquid helium coolant leak after launch crippled the main instrument, an x-ray spectrometer

**Akatsuki**
**Probe to study the venusian climate**
Failed to enter orbit on first pass in 2010, succeeded on second try in 2015

**ASTRO-G**
**Radio astronomy**
Canceled in 2011 because of development problems

1998 2000 2002 2004 2006 2008 2010 2012

CREDITS: (PHOTO) JAXA; (GRAPHIC) G. GRULLÓN/*SCIENCE*

Downloaded from http://science.sciencemag.org/ on November 22, 2016



Published by AAAS

"insufficient project management oversight of safety, reliability, and satellite safety and system design."

To prevent such lapses in the future, the investigators recommended a raft of measures including better data sharing with contractors and thorough documentation during spacecraft testing. The most critical issue the investigators flagged is mission management. According to Tsuneta, ISAS typically appoints one senior professor as "a god" for a mission. That person is responsible not only for the science, but also for spacecraft and instrument engineering and coordination among partners and contractors.

ISAS had taken that approach since it was formed by a group of space buffs from a University of Tokyo engineering department who launched missions on shoestring budgets. But as missions grew more ambitious, costly, and complex, "there is some threshold," Tsuneta says, where that management style "is no longer an optimal system." In most of ISAS's spacecraft failures, he says, the mission teams succeeded with the complex scientific instruments but failed on routine spacecraft operations. Hitomi drove home the point. Its instruments "worked beautifully," Tsuneta says, yet the spacecraft had the defective attitude control, which "should be perfect."

For future missions, ISAS will separate the roles of the principal investigator, who will focus on the science, and the project manager, who will wrestle with cost constraints, instrument specifications, and keep the mission on track, Tsuneta says. A new position, system manager, will ensure a mission's technical soundness. That's similar to how ESA and NASA manage missions, Tsuneta says.

The management overhaul gets a qualified thumbs-up from Japan's scientific community. "The ISAS reformation plan will surely reinforce upcoming projects," says Makoto Tashiro, a University of Tokyo astrophysicist who was on the Hitomi science team. Kozo Fujii, a former ISAS aerospace engineer now at Tokyo University of Science, hopes that new bureaucratic rules don't stifle the institute's academic culture, bottom-up decision-making, and investigator-driven emphasis on cutting-edge missions. The reforms must not cloud ISAS's science vision, adds Junichiro Kawaguchi, who led ISAS's Hayabusa asteroid sample return mission. Historically, he says, ISAS scientists and engineers nurtured satellite building and operating skills through their own intimate involvement in projects, not by simply managing contractors.

Tsuneta says he wants to preserve good aspects of the ISAS way, including bottom-up mission proposals and a close interaction between scientists and engineers. But more rigorous management is essential, he says. "We cannot go back to the earlier days." ■

PHOTO: MILETTE RAATS

DIVERSITY

# No need to apply, Dutch science academy tells men

## Two special elections seek to address gender imbalance by admitting only women

*By* **Martin Enserink**, *in Amsterdam*

Sorry guys—this time it's women only. That's the message the Royal Netherlands Academy of Arts and Sciences (KNAW) here has for male researchers during two special elections. In order to reduce its perpetual gender imbalance—87% of its 556 members are men—the academy seeks to recruit 10 new members in 2017 and six more in 2018, all with two X chromosomes.

Dutch academy President José van Dijck says electing more women won't come at the expense of male candidates.

It's about as bold a step as any science academy has taken to address the underrepresentation of women—and for some it raises concerns. "I don't think we would do that," says Marcia McNutt, a geophysicist who became the first female president of the U.S. National Academy of Sciences (NAS) in Washington, D.C., earlier this year. "Other people might feel that women elected this way somehow did not meet the same standards as their male counterparts, or even other women elected through the regular process," McNutt says. But KNAW President José van Dijck says the process will be "just as rigorous as always."

KNAW's headquarters, a palatial 17th century mansion on one of Amsterdam's oldest canals, is hardly the only bastion of male power among science academies. A study based on data from 2013 and 2014, published in February by the Academy of Science of South Africa and the InterAcademy Partnership, found that only 12% of the members of 63 academies surveyed worldwide were women. NAS, like KNAW, had about 13%, although McNutt says the number today is 15.4%. The German and U.K. academies came in at 10% and 6%, respectively, whereas Cuba topped the list with 27%. Only 60% of academies had a specific policy or document addressing gender balance.

Because most academies grant membership for life, their existing makeup partly reflects past biases. Among current members of the Dutch academy who are below the retirement age (fewer than half the total), women have better representation, at 24%. At NAS, about a quarter of newly elected members are women as well, McNutt says.

One common approach to redressing the disparity, championed by the late Ralph Cicerone, McNutt's predecessor at NAS, is to find more qualified women to nominate, then have them compete in the regular election process. But Van Dijck, herself the first female president in KNAW's 208-year history, says the Dutch academy wants to move faster. The idea for special elections came from two male board members, she says: "I can't claim credit but I embraced it lovingly."

The plan "does not come at men's expense," Van Dijck stresses, because regular election rounds, which allow 16 members annually into the pinnacle of Dutch academe, will continue. The proposal was approved by a 73% majority during an academy-wide vote earlier this year.

"I think it's truly remarkable. I know of no similar example in any academy," says social anthropologist Frances Henry, an emeritus professor of York University in Toronto, Canada, who co-authored this year's survey. Henry applauds KNAW's plan. "If you want to move women forward, you have to provide the extra space," Henry says. "Otherwise, we're going to sit here for another two generations." ■

Downloaded from http://science.sciencemag.org/ on November 22, 2016



Published by AAAS

PLANT BIOTECHNOLOGY

# Engineered crops could have it made in the shade

## Modified tobacco plants quickly speed up photosynthesis when bright light dims, boosting yields

*By* **Erik Stokstad**

Just because plants photosynthesize doesn't mean they can't get a form of sunburn—damage caused by overexposure to light. That's why all plants rely on a mechanism that defends against excessively bright sunlight by converting photons into harmless heat. But like someone who is slow to doff their sunglasses indoors, this botanical sun shield is slow to turn off when a shadow passes over a leaf. The result: Photosynthesis stays depressed.

Now, plant biologists seeking improved photosynthesis—and, ultimately, more bountiful crops—have cleverly manipulated plants to adjust more quickly to shade. Genetically engineered into tobacco plants, the faster response yielded up to a 20% increase in biomass. The proof-of-concept study, described on p. 857, is "ground-breaking" and the first convincing field trial in the hot area of engineering photosynthesis, says Robert Furbank, an integrative plant biologist at the Australian National University in Canberra.

Traditional plant breeding has greatly boosted yields of popular crops. During the green revolution, for example, Norman Borlaug and others nearly doubled wheat yields by creating plants with short, sturdy stems that could hold a greater load of grain. Nowadays, breeders can get crops to put about 50% to 60% of their biomass into seeds. But the gains have stagnated at less than 1% per year because plant growth is now limited by the efficiency of photosynthesis itself.

Research teams are trying to break the bottleneck in multiple ways. One long-held dream is taking a high-power type of photosynthesis found in corn and three other crops, called the C4 pathway, and putting it into rice. Another goal is improving RuBisCO, the notoriously sluggish enzyme that catalyzes early stages in the conversion of carbon dioxide into useful organic molecules.

Manipulating how tobacco plants recover from overly bright sunshine boosted photosynthesis and overall yield.

More recently, a few researchers have contemplated streamlining an aspect of photosynthesis called photoprotection. To guard themselves from bright light—as well as balance their metabolic processes—plants rely on a mechanism called nonphotochemical quenching (NPQ), in which chloroplasts divert photons from their light-harvesting molecules and simply waste them as heat. In dim conditions, plants can turn off NPQ to boost photosynthetic efficiency. But although they can raise the shield in a few minutes, lowering the defenses can take hours, which limits photosynthesis in the shade.

This time lag isn't a problem for wild plants, for which survival and reproduction are paramount, but it's a disadvantage for farmers who want to maximize biomass. In 2004, plant physiologist Stephen Long of the University of Illinois in Urbana and colleagues calculated that NPQ operating under typical conditions for a midlatitude farm can reduce the amount of carbon dioxide turned into sugars by up to 30%.

After reading Long's paper, geneticist Krishna Niyogi of the University of California, Berkeley, had an idea for how to turn off NPQ faster. The strategy was to add extra copies of three genes whose proteins are responsible for relaxing the protection. The higher protein levels should speed the response to shade. Niyogi, Long, and their postdocs took these genes from the widely studied mustard *Arabidopsis thaliana* and inserted them into tobacco plants, which are relatively easy to modify. After lab and greenhouse testing, they planted them in a test field near the University of Illinois. The modified tobacco bulked up their leaves, stems, and roots, weighing 14% to 20% more than unmodified plants after 22 days.

"To see something like that increase in a field trial was astonishing," Niyogi says. The bonus came without apparent side effects, although the researchers could not test for any loss of disease resistance or stress tolerance in such a small field trial.

The big question is whether similar manipulations in food crops will mean more consumable yield. To find out, Niyogi and Long have already started to put the genes into elite breeding lines of rice and maize, and other crops could follow. Long also predicts that researchers will find ways to turn off NPQ even faster, and perhaps generate even more biomass. "We think this could still be bigger than we have now."

It's also possible that the same effect could be achieved without moving genes between species, which might ease regulatory approval or improve consumer acceptance. Plants normally silence any extra copies of their own genes, but editing the genes or promoters using CRISPR or another technique could get around that barrier, allowing researchers to work with a species's own genetic material.

Regardless of how it's done, boosting photosynthesis could help researchers answer critics of plant biotechnology who complain that genetically modified plants have not boosted harvests, says Dario Leister, a plant molecular biologist at Ludwig-Maximilian University of Munich in Germany. "Making plants that yield more: That is something that everyone should be happy about." ■

PHOTO: BLOOMBERG

Downloaded from http://science.sciencemag.org/ on November 22, 2016



Published by AAAS

Two captive *Heliconius* species mate, illustrating the rampant hybridization among plants and animals in nature.

PHOTO: RAUL GONZÁLEZ ALEGRÍA

# SHAKING UP THE TREE OF LIFE

## Species were once thought to keep to themselves. Now, hybrids are turning up everywhere, challenging evolutionary theory

*By* **Elizabeth Pennisi**

In 2010, a comparison between the genomes of a Neandertal and people today settled what anthropologists and geneticists had debated for decades: Our ancestors had indeed mated with their archaic cousins, producing hybrid children. They, in turn, had mated with other modern humans, leaving their distant descendants—us—with a permanent Neandertal legacy. Not long afterward, DNA from another archaic human population, the Denisovans, also showed up in the modern human genome, telling a similar story (*Science*, 23 December 2011, p. 1629).

For researchers and the public alike, this evidence of interbreeding among distinct human populations—so different some still argue there was more than one species—created a shock wave. Suddenly hybridization "just captured our imagination," says Michael Arnold, an evolutionary biologist at the University of Georgia in Athens. "That genomic information overturned the assumption that everyone had."

The techniques that revealed the Neandertal and Denisovan legacy in our own genome are now making it possible to peer into the genomic histories of many organisms to check for interbreeding. The result: "Almost every genome study where people use sensitive techniques for detecting hybridization, we find [it]—we are finding hybridization events where no one expected them," says Loren Reiseberg, an evolutionary biologist at the University of British Columbia in Vancouver, Canada.

Downloaded from http://science.sciencemag.org/ on November 22, 2016



Published by AAAS

"Big Bird," a hybrid Darwin's finch, could be on its way to becoming a new species.

PHOTO: PETER GRANT

# A shortcut to a species

*By* **Elizabeth Pennisi**

A hefty finch with an outsized head is the poster child for a recently recognized source of new species: hybridization. For decades, biologists have explored how cross-species matings can accelerate evolution by introducing genetic novelty into the parent lineages (see main story, p. 817). But they now realize that the hybrid offspring themselves can thrive and set off on their own evolutionary path. "Big Bird," one of Darwin's finches on the Galápagos Islands, may be the best documented animal example.

Peter and Rosemary Grant, evolutionary biologists at Princeton University, and their graduate student Trevor Price noticed the unusual male in 1981, after he arrived on the Galápagos island of Daphne Major. Weighing 28 grams instead of the typical 18 grams for male finches, sporting a big head, and singing an unusual song, Big Bird was probably born on neighboring Santa Cruz Island from a mating between a cactus finch and medium ground finch. At first, the immigrant and its young consorted with Daphne Major's medium ground finches. But after a severe drought from 2003 to 2005 killed 90% of the island's avian inhabitants, the two Big Bird descendants that survived and their 26 offspring crowded into one corner of the island and have kept to themselves ever since.

This group breeds just among their own kind, and even though male Big Bird finches are very territorial, they react aggressively only when other Big Bird males infringe, suggesting they don't see those other male finches as reproductive rivals. They also have a distinctive food source: Thanks to their intermediate-sized beaks, they are able to crack certain seed cases that other birds can't. "It's been going on like that for a few generations," Peter Grant says.

Until recently, biologists insisted that a species has to be reproductively isolated—unable to produce viable offspring when it mates with another species. The Big Birds are far from meeting that definition, but since many scientists no longer insist on it, "It's provocative to call [these birds] a new species," Peter Grant says. Still, the Grants are unwilling make that final call on the Big Birds.

DNA analysis is turning up more examples of hybrid species. Between 4% and 10% of plant species appear to have arisen this way. And researchers are finding new examples among birds, insects, fish, and marine mammals. The clymene dolphin (*Stenella clymene*), found in the Atlantic Ocean, emerged from dalliances between the striped and spinner dolphins, and at least two of five cichlid species—a group known for being very diverse—in Africa's Lake Victoria originated from hybrids.

Among birds, the Italian sparrow is recognized as a distinct species—it's a hybrid of the Spanish and house sparrows. The Hawaiian duck is descended from a hybridization event 10,000 years ago between the mallard (*Anas platyrhynchos*) and Laysan ducks (*A. laysanensis*). And the root-knot nematode, a deadly plant pest, adds another layer of complexity: One of its parent species was itself a hybrid species.

As evolutionary biologist Scott Taylor of the University of Colorado in Boulder puts it, hybridization is "making it seem that speciation is more complex than we thought." ■

All these data belie the common idea that animal species can't hybridize or, if they do, will produce inferior or infertile offspring—think mules. Such reproductive isolation is part of the classic definition of a species. But many animals, it is now clear, violate that rule: Not only do they mate with related species, but hybrid descendants are fertile enough to contribute DNA back to a parental species—a process called introgression.

None of this came as a surprise to James Mallet, a Harvard University evolutionary biologist who decades ago began quantifying hybridization among butterflies. He, Arnold, and a few other biologists have long argued that hybridization is pervasive and plays an important role in evolution. In addition to research on plants, where hybridization has long been documented, they pointed to studies of animals including Darwin's finches in the Galápagos Islands, tropical butterflies, and mosquitoes. Yet most other evolutionary biologists regarded these organisms as anomalies. "We thought that hybridization was kind of rare and therefore not that significant," says Carole Smadja, an evolutionary biologist at the National Center for Scientific Research's Institute of Evolutionary Biology based at the University of Montpellier in France. Now, says Stuart Baird, an evolutionary biologist at the Academy of Sciences of the Czech Republic in Studenec, "You can't deny it because it's in our own family tree."

Biologists long ago accepted that microbes can swap DNA, and they are now coming to terms with rampant gene flow among more complex creatures. "A large percent of the genome is free to move around," notes Chris Jiggins, an evolutionary biologist at the University of Cambridge in the United Kingdom. This "really challenges our concept of what a species is." As a result, where biologists once envisioned a tree of life, its branches forever distinct, many now see an interconnected web.

Hybridization, says Mallet, "has become big news and there's no escaping it."

**IN 1949**, botanist Edgar Anderson suggested that plants could take on genes from other species through hybridization and back crosses, where the hybrid mates with the parent species. He based this then-radical proposal on genetic crosses and morphological studies of flowering plants and ferns suggesting mixtures of genes from different species in individual genomes. Five years later, with fellow botanist G. Ledyard Stebbins, he argued such gene exchange could lead to new plant species. Their ideas quickly hit home with other plant researchers, but not with zoologists. "There was a very different conventional view in botany

Downloaded from http://science.sciencemag.org/ on November 22, 2016



Published by AAAS

than in zoology," Rieseberg says.

Most of those who studied animals had instead bought into the argument by the famous mid-20th century evolutionary biologist Ernst Mayr that the formation of a new species requires reproductive isolation. Mayr and his contemporaries thought that the offspring of any hybrids would be less fit or even infertile, and would not persist. To be sure, captive animals could be interbred: Breeders crossed the African serval cat with domestic cats to produce the Savannah cat, and the Asian leopard cat with domestic breeds to produce the Bengal cat. There's even a "liger," the result of a zoo mating of a tiger and a lion. But like male mules, male ligers are sterile, supporting the notion that in nature, hybridization is mostly a dead end.

By the early 1990s, however, these ideas "weren't reflective of all the information out there," recalls Arnold, who has championed the importance of hybridization in animals in four scientific books. Support for his view had already begun rolling in from some of evolution's most iconic creatures, the Galápagos finches that Darwin observed as he developed his ground-breaking ideas. Princeton University evolutionary biologists Peter and Rosemary Grant were making annual visits to a small Galápagos island called Daphne Major and observing the Darwin's finches (*Geospiza*) there. They recorded matings, how many young survived, and what the birds ate. Early on, they noticed that 1% to 3% of the pairs consisted of a male of one species and a female of another. Such hybridization surprised them, Rosemary Grant recalls. "Our mind frame was that it wasn't happening."

The hybrid offspring varied quite a bit, in traits including beak size and shape. That variation came in handy when drought or floods destroyed the bird's usual food plants, leaving behind seeds ill suited to the parents' original beak size. Far from being less fit, the hybrids with their intermediate-sized beaks thrived. There were even hints that hybridization was leading to new species of finches (see sidebar, p. 818). In 1992, the Grants surveyed the avian literature and found that Darwin's finches were far from unique. Almost 10% of all bird species failed to respect species boundaries, they reported. Ducks and geese were the most promiscuous, with reports of half the species exchanging genes. Woodpeckers, hawks, grouse, partridges, and hummingbirds also interbred. "That flew in the face of the current wisdom," Peter Grant says.

What the Grants saw in birds, Mallet saw in butterflies. Tropical butterflies belonging to the genus *Heliconius* have wing patterns that generally vary widely from species to species, but entomologists long ago noticed some striking exceptions, in which certain species and subspecies closely resemble one another. Mostly scientists chalked up the similarities to independent, but parallel, evolution. But 50 years ago, Larry Gilbert threw together multiple species of Costa Rican *Heliconius* in an insectary at the University of Texas in Austin and found that they interbred, swapping wing patterns and sometimes generating entirely new ones. Mallet and Jiggins, his graduate student at the time, found the same to be true a decade ago when they let *Heliconius* from Ecuador interbreed.

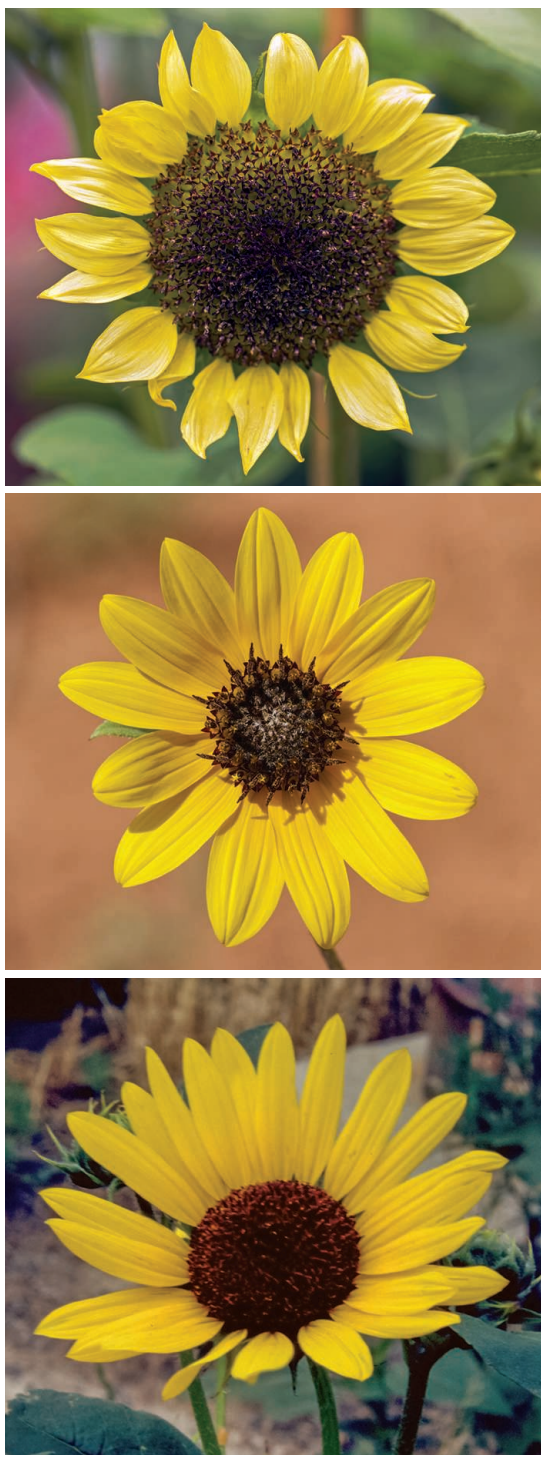

Studies of sunflowers have driven home the importance of hybridization. Matings between the top two species yielded a new one, *Helianthus anomalus* (bottom).

PHOTOS: (TOP TO BOTTOM) KEITH WHEELER/SCIENCE SOURCE; DAVID HOSKING/FLPA/SCIENCE SOURCE; W. D. AND DOPHIA BRANSFORD/LADY BIRD JOHNSON WILDFLOWER CENTER

Intrigued, Mallet surveyed all the examples of *Heliconius* he could find in museum collections around the world and calculated, based on wing patterns, that more than 30% of the *Heliconius* species had formed hybrids. His writings persuaded some animal biologists that hybridization isn't just important for plants. "Jim is recognized as an evolutionary zoologist, so when he wrote about it, [others] sat up and said, 'Wow, that's cool, it's about animals,' while there'd already been a few of us who have been saying this for 20 years," Arnold says. "He's been very influential in a good way."

**NOW**, cheaper DNA sequencing is enabling researchers to track the genetic impact of all this crisscrossing. In 2012, the Grants teamed up with Leif Andersson at Uppsala University in Sweden, sending him 120 blood samples from all Darwin's finches and two close relatives for DNA sequencing. The Swedish team "showed the genetic underpinning" of the Galápagos field observations, says Rosemary Grant, proving that many of the 18 species interbred with one another. The mixing was so great that, genetically speaking, two different finch species on any particular island were more similar to each other than to the same species on a different island.

Moreover, the Grants' many years of field data enabled them to show that just a few introgressed genes could have a very strong effect. In their surveys, they took multiple measurements of each bird, as if fitting it for a suit, noting features such as the size and shape of the beak. Just by looking for variants of a gene called *ALX1* in the DNA from each individual, the Uppsala team was able to sort the birds into two groups that perfectly matched the two major beak shapes. Birds that had acquired two different variants of the gene, from ancestors belonging to distinct species, had an intermediate beak shape, suggesting

Downloaded from http://science.sciencemag.org/ on November 22, 2016



Published by AAAS

a tight connection between genetics and morphology. The finding, reported last year in *Nature*, showed that the hybridization the Grants had observed over the decades had taken place throughout the finches' million-year history.

Genome analytical tools originally developed to gauge how much DNA passed between humans and Neandertals have enabled researchers to track gene flow between various species in more detail. Working with butterfly genomes sequenced by a consortium including Mallet, Jiggins, and Kanchon Dasmahapatra, now at the University of York in the United Kingdom, showed significant gene flow on 11 of 21 chromosomes in two butterfly subspecies living in the same place in Peru. Butterfly gene exchange is "promiscuous," the consortium reported in a 2012 *Nature* paper.

Similar genome analyses have since documented significant gene flow in many groups of mammals, including cats, says William Murphy, a geneticist at Texas A&M University in College Station. By surveying the nuclear and mitochondrial DNA of 38 cat species, his team found that at least three neotropical cat species had interbred over their 3-million-year history, they reported last year in *Genome Research*. In North America, they found bobcats and lynx have frequently hybridized and continue to do so today along the U.S.-Canada border.

The blurring of species lines can complicate conservation. A recent genomic study showed that the red wolf, an endangered species, and the eastern wolf are both relatively recent hybrids of coyotes and gray wolves. The result, reported in July in *Science Advances* by Robert Wayne of the University of California, Los Angeles, and his colleagues, could suggest that the two wolf varieties don't qualify for protection under the Endangered Species Act. Then there are the "pizzlies" and "grolars," as hybrids between polar and brown bears are known. Extensive genomic studies of the two bear species indicate they have long had dalliances. But as polar bears are driven southward by climate change, such unions are producing more offspring. In the United States, hunting polar bears is illegal, except for Native Alaskans, but a hybrid of the bears is not protected.

**AS EXAMPLES** of hybridization have multiplied, so has evidence that, at least in nature, swapping DNA has its advantages. When one toxic butterfly species acquires a gene for warning coloration from another toxic species, both species benefit, as a single encounter with either species is now enough to teach predators to avoid both. Among canids, interbreeding with domestic dogs has given wolves in North America a variant of the gene for an immune protein called β-defensin. The variant gives wolf-dog hybrids and their descendants a distinctive black pelt and better resistance to canine distemper, Wayne says. In Asia, wolf-dog matings may have helped Tibetan mastiffs cope with the thin air at high altitudes. And interspecies gene flow has apparently allowed insecticide resistance to spread among malaria-carrying mosquitoes and the black flies that transmit river blindness.

In each case, the beneficial genetic changes unfolded faster than they would have by the normal process of mutation, which often changes DNA just one base at a time. Given the ability of hybridization and introgression to speed adaptive changes, says Baird, "closing that door [with reproductive isolation] is not necessarily going to be a good thing for your longterm survival."

A fair number of biologists remain uneasy with this picture of unchecked gene swapping. "Some people are going way overboard in saying that everything is hybridizing with everything else," says Joel Cracraft of the American Museum of Natural History in New York City. "It's a little hyperbol[ic] to say it's wiping away species boundaries."

The Grants think the divide over the importance of hybridization and its effect on speciation is partly cultural. They and other field biologists accept that a species can be legitimate even if it can sometimes mate with others. In contrast, says Rosemary Grant, "Some people in museums only [recognize] a species when it's absolutely certain there's complete genetic incompatibility." A species may have to evolve for tens of millions of years before it can meet that definition—if it happens at all.

"We always like to put things in boxes. We are removing people's boxes," Baird adds. What's more, widespread gene swapping threatens a standard approach to building the tree of life: comparing DNA from different species. "That would [work] if the truth were trees, but that's not the truth," Baird says. Because of hybridization, disparate species can share similar sequences. As Baird puts it, evolving species "don't form trees, they form nets."

The malaria-carrying *Anopheles gambiae* mosquito and its relatives drive home how challenging it can be to build a phylogenetic tree when hybridization runs amok. Last year in *Science*, evolutionary biologists Nora Besansky of the University of Notre Dame in Indiana, Matthew Hahn from Indiana University in Bloomington, and their colleagues reported that gene flow among six mosquito species was so extensive that only 2% of the insects' genomes—mostly in the X chromosome—reflected those mos-

## Hybridization shapes evolution

When two species mate and produce fertile offspring, evolution can take new turns: Backcrossing introduces new genes into the parent species' genomes (introgression) or hybrids start to breed only with other hybrids, forming new species.

### Two species comingling

**Hybridization**
Animals can hybridize more successfully than once thought.

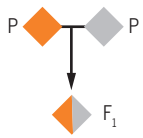


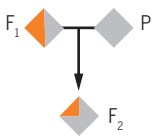


**Introgression**
New DNA joins the parent's (P) genome if a hybrid ($F_1$) mates back with a parent.

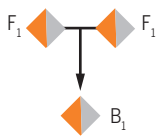


**Speciation**
Hybrids mating among themselves can lead to a new species ($B_1$).

### Accelerating genetic change

Introgression quickly introduces much more genetic variation than can random mutations and can help organisms adapt better to changing environments.

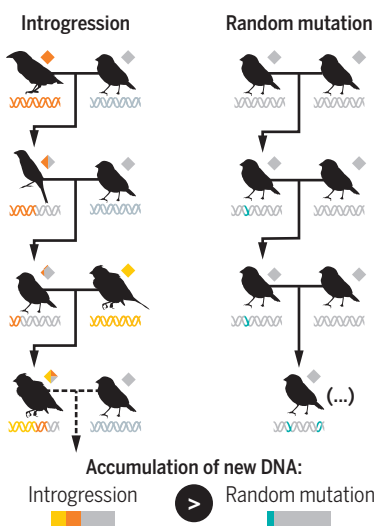


### From tree of life to a web

Hybridization creates new connections between branches on the tree of life and can lead to new species.

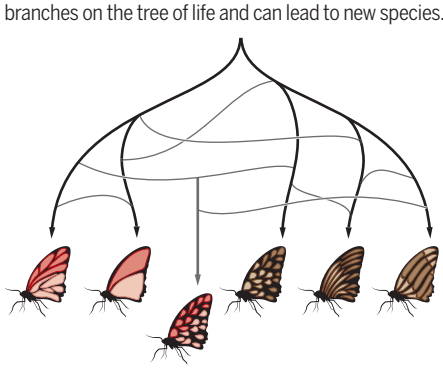

CREDITS: (GRAPHIC) V. ALTOUNIAN/*SCIENCE*; (DATA) MICHAEL ARNOLD/UNIVERSITY OF GEORGIA

Downloaded from http://science.sciencemag.org/ on November 22, 2016



Published by AAAS

PHOTOS: (CLOCKWISE FROM TOP LEFT) REUTERS/CHRISTIAN CHARISIUS/ALAMY STOCK PHOTO; GARY NAFIS; JUAN GILLERMO MONTAÑES AND MAURICIO LIÑARES; KEVIN SCHAFER/MINDEN PICTURES; EPA EUROPEAN PRESSPHOTO AGENCY B.V./ALAMY STOCK PHOTO

**Hybrids are everywhere on the tree of life. (Clockwise from top left): liger (lion/tiger), barred salamander hybrid (Western/California barred salamanders), *Heliconius heurippa (H. cydno/H. melpomene)*; Hawaiian duck (mallard/Laysan duck), pizzlies (polar/brown bear).**

quitoes' true history. "It is really a beautiful story that no doubt has Ernst Mayr hyperventilating in his grave," Besansky says.

The resulting "net" for the mosquitoes showed that the two most important human malaria vectors split off early in the evolution of this group, and later likely shared through hybridization the genes that make them suitable hosts for the malarial parasite and, consequently, so dangerous to people. Such introgression could also explain why it's so difficult to sort out the exact history of the early explosion of birds or of mammals millions of years ago.

The Grants believe that complete reproductive isolation is outdated as a definition of a species. They have speculated that when a species is no longer capable of exchanging genes with any other species, it loses evolutionary potential and may become more prone to extinction.

This idea has yet to be proven, and even Mallet concedes that biologists don't fully understand how hybridization and introgression drive evolution—or how to reconcile these processes with the traditional picture of species diversifying and diverging over time. Yet for him and for others, these are heady times. "It's the world of hybrids," Rieseberg says. "And that's wonderful." ■

Downloaded from http://science.sciencemag.org/ on November 22, 2016



Published by AAAS

PHOTO: MARTIN RIETZE/SCIENCE SOURCE

Downloaded from http://sciencesciencemag.org/ on November 22, 2016

# CRYSTAL CLOCKS

## How smudged crystals offer windows into a volcano's eruptive past

*By* **Julia Rosen**

Between the jungle and the rice paddies, Fidel Costa struggled to find bare rock on the slopes of Mount Gede, a towering volcano near the western tip of the Indonesian island of Java. But an abandoned quarry hewn into the mountainside offered a rare chance to nab a few samples. So on a muggy day in 2011, Costa, a volcanologist at the Earth Observatory of Singapore, scrambled up the steep wall to some rocks, marbled like rye bread, which he pried loose with a hammer. Four thousand years ago, they erupted from Gede and fell out of a cloud of hot ash.

There are no accounts of that eruption, let alone records of any seismic tremors or burps of gas leading up to it—the clues scientists now use to infer what's brewing deep beneath a volcano. Indeed, the volcano's last outburst occurred in 1957, long before modern monitoring efforts began, so scientists know little about its temperament. What signs portend Gede's eruptions, and how much warning do they give? For the millions of people living on its flanks, as well as in the nearby cities of Jakarta and Bandung, the answers are critical. There's no indication that Gede will erupt anytime soon. But when it does, Costa says, "anything that happens there is going to be a big mess."

From the rocks released by that 4000-year-old eruption, however, Costa and his colleagues at the Center for Volcanology and Geological Hazard Mitigation of Indonesia in Bandung were able to glean some crucial clues about Gede's behavior. The clues were locked in crystals, most smaller than lentils, embedded in the rocks. Each crystal grew in a soup of magma deep underground, accreting layers that bore witness to the events that preceded the eruption, and—most importantly—how fast they unfolded.

These crystal clocks told Costa's team that Gede's 4000-year-old eruption came



Published by AAAS

Crystal clocks have helped reveal the multichambered plumbing under Italy's Mount Etna, shown erupting in 2012.

roughly 4 weeks after the injection of a fresh batch of magma beneath the volcano. Crystals from four more ancient eruptions gave similar answers. The pattern gives planners an idea of what to expect in the future: When sensors detect signs of magma stirring below the slumbering giant, an eruption may follow within weeks. "It might be uncertain, but it's much better than not knowing anything," Costa says.

Costa has spent years learning to coax such stories out of tiny volcanic crystals with a technique he helped develop, known as diffusion chronometry. And it's catching on. "It's one of those techniques that is about to explode in popularity," says Tom Sisson, a volcanologist at the U.S. Geological Survey in Menlo Park, California.

Already, the few researchers adept at using the technique have found that magma can tear through the crust at searing velocities, and that volcanoes can gurgle to life in a geologic instant. Instead of taking centuries or millennia, these processes can unfold in a matter of decades or years, sometimes even months, says Kari Cooper, a volcano geochemist at the University of California, Davis. The results help explain why geophysicists haven't found simmering magma chambers under volcanoes like Yellowstone, and why some eruptions are more violent than others. "This is something that has the potential to really be a game changer in a lot of ways," she says.

**BACK IN HIS LAB** in Singapore, Costa gleans his volcano histories from cellophane-thin slices of rock. Backlit under a microscope, minerals in the slices—including plagioclase, olivine, and pyroxene—burst into focus: polygonal islands swimming in a dark sea of rock. Many have concentric bands like tree rings, which formed as the crystals grew in an ever-changing bath of liquid magma.

The chemistry of each new band records the evolving composition of the magma, or changes in its temperature or pressure. Costa uses an instrument called an electron microprobe to map the chemical variations along the crystal faces, making a measurement every few microns. In the Gede crystals, the microprobe revealed higher concentrations of magnesium and iron in the outermost layers, which suggested that a fresh burst of magma rich in these elements bubbled up beneath Gede shortly before the eruption—potentially triggering it. But how shortly? That's where Costa and Daniel Krimler, a graduate student at the observatory, turned to diffusion chronometry, which converts the chemical smudging between the rim and the crystal's core into an estimate of time.

> ***"It's one of those techniques that is about to explode in popularity."***
>
> **Tom Sisson**, U.S. Geological Survey

Researchers first developed the technique, originally dubbed geospeedometry, in the 1960s. They used it to estimate cooling rates in meteorites and rocks that have been subjected to extreme heat and pressure. The method relies on the premise that nature rarely abides sharp gradients. Just as a few drops of food coloring will diffuse throughout a glass of water—no stirring required—so, too, will diffusion shuffle atoms from areas of high concentration to low concentration within a solid crystal lattice.

In the Gede crystals, diffusion moved atoms of magnesium and iron from the crystal rims to the cores, and shuttled other elements in the opposite direction to fill the vacancies left by these atoms. It transformed an abrupt, steplike change in chemical composition into a more gradual curve. By knowing how fast magnesium and iron diffuse through specific minerals, Costa and Krimler could calculate how long diffusion went on after the magma injection and before the volcano erupted, freezing the chemical profile in place. They had a stopwatch.

It's not quite that simple, of course. Diffusion rates depend not only on the element and mineral in question, but on the temperature, pressure, and oxidation state the crystal experienced, which researchers estimate from other clues in the crystals. In the 1980s, pioneers like Sumit Chakraborty, a geologist at Ruhr University in Bochum, Germany, began the tedious work of pinning down these diffusion parameters across a range of conditions. That meant long hours in the lab torturing natural and synthetic crystals with heat and pressure and then watching diffusion proceed. At first, single experiments could take weeks, but the results gave diffusion chronometry teeth.

Curiously though, the technique didn't catch on with volcanologists until the turn of the century. By the time Costa published his first paper on the topic in 2003, applying diffusion techniques to volcanic crystals from the San Pedro volcano in Chile, several other researchers were having similar epiphanies. It was an idea whose time had come.

One appeal of diffusion chronometry lies in its ability to track a wide range of volcanic processes. Any time a new zone forms within a crystal, diffusion chronometry can theoretically exploit it. And that allows scientists to target many stages leading up to an eruption, including when magma rises from the mantle, when it collects in crustal reservoirs and mixes with other magmas, and when it barrels up through the plumbing of the volcano toward the surface.

Take the initial ascent of magma from the mantle. Terry Plank, a geochemist at Columbia University's Lamont-Doherty Earth Observatory in Palisades, New York, and a former postdoctoral researcher in her lab, Philipp Ruprecht, wanted to understand the origin of magma in a famous eruption of the Irazú volcano in Costa Rica that lasted from 1963 to 1965. In certain olivine crystals, the researchers noted variations in nickel concentrations inside the crystal cores that appeared to have formed in the mantle.

The fact that the chemical variations survived the ascent through the crust implied that diffusion had little time to smear them out. Plank and Ruprecht concluded that the magma must have risen through roughly 35 kilometers of crust in just months, or at most, a few years. "That was a surprise," Plank says. The results—suggesting the pos-

Downloaded from http://science.sciencemag.org/ on November 22, 2016



Published by AAAS

sibility of a direct connection between the mantle and the surface—contradicted the widespread idea that magma follows a tortuous path upward, pooling in magma chambers along the way before finally erupting.

In many cases, though, it appears that magma does spend millennia loitering a few kilometers beneath the surface, only to mobilize rapidly before an eruption. At Mount Hood in Oregon, for example, Cooper examined rocks from the volcano's last two eruptions, 1500 and 220 years ago. She focused on plagioclase crystals that formed in shallow magma chambers in the crust. By measuring the concentrations of uranium and its radioactive daughter elements, she found that these crystals were born at least 20,000 years ago.

Many of these plagioclase crystals also had numerous layers with different chemical compositions, which they acquired over their long lifetimes. When Cooper looked closely at the boundaries between these layers, she found something startling: They were only slightly smudged, suggesting that in spite of their age, the crystals had only a brief sojourn in hot, liquid magma. In 2014, she and Adam Kent of Oregon State University in Corvallis explained their discovery by proposing that the magma spent as much as 99% of its time in storage at temperatures too cool to erupt and too cool for diffusion. Instead, it existed in a mostly solid crystalline mush beneath Mount Hood.

The results support the so-called "mush model," which has gained traction in the last decade or so. Cooper's work suggests that magma may liquefy and erupt even more quickly than many researchers thought. "It's a bit of a subtle shift, but it's very important, because all of a sudden, everything you want to do"—mixing and assembling the final pot of magma that erupts—"all that has to happen really quickly," Cooper says. Crystal clocks from a 3600-year-old

## The clock is ticking

Researchers are using a technique called diffusion chronometry to help them decipher the clocks hidden inside volcanic crystals. The crystals tell them, for example, how soon a volcano erupts after a last pulse of magma. The research suggests that many volcanic processes happen much faster than previously thought. It may also help researchers understand the eruptive tendencies of a volcano, even where there are no historical records.

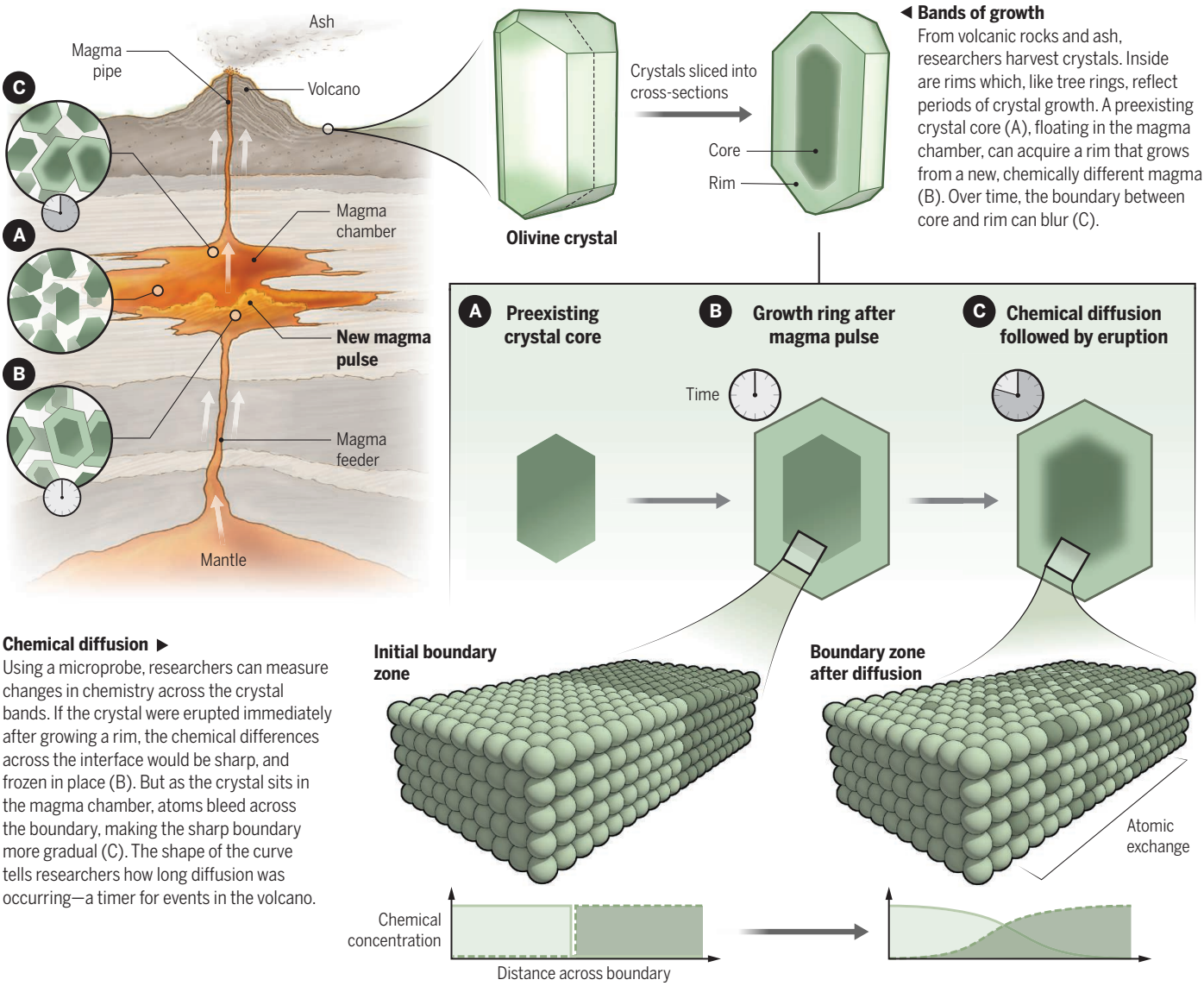


**◀ Bands of growth**
From volcanic rocks and ash, researchers harvest crystals. Inside are rims which, like tree rings, reflect periods of crystal growth. A preexisting crystal core (A), floating in the magma chamber, can acquire a rim that grows from a new, chemically different magma (B). Over time, the boundary between core and rim can blur (C).

**Chemical diffusion ▶**
Using a microprobe, researchers can measure changes in chemistry across the crystal bands. If the crystal were erupted immediately after growing a rim, the chemical differences across the interface would be sharp, and frozen in place (B). But as the crystal sits in the magma chamber, atoms bleed across the boundary, making the sharp boundary more gradual (C). The shape of the curve tells researchers how long diffusion was occurring—a timer for events in the volcano.

PHOTO: C. BICKEL/SCIENCE

Downloaded from http://science.sciencemag.org/ on November 22, 2016



Published by AAAS

eruption of the Greek volcano Santorini, which had been dormant for 18,000 years, suggest that it awakened in a century or less. If other volcanoes behave similarly, it would explain why researchers have struggled to find evidence for large molten magma chambers on Earth today—such vats of liquid magma may only exist immediately prior to an eruption.

When an eruption finally happens, magma races from its subterranean source to the surface. Plank's current quest is to understand whether the speed of that ascent influences how explosively a volcano erupts—causing Hawaii's Kilauea, for example, to erupt gently today in spite of explosive outbursts in the past. Plank and others suspect that, all else being equal, a slowly rising magma has more time to lose dissolved gases—and therefore erupts less violently—than magma that gushes toward the surface. "It's not the gas in the seltzer bottle, it's how fast you open the seltzer bottle," she says.

But how does one measure the speed of magma rising deep beneath the ground? Instead of studying diffusion in crystals, Plank has looked at how dissolved volatiles like water and carbon dioxide diffuse through melt tubes, tiny burrows in crystals that fill with liquid magma. As crystals rise toward the surface, the volatiles trapped in a melt tube diffuse toward its mouth, striving to stay in equilibrium with the dropping concentrations in the magma outside the crystal. This produces a diffusion profile along the tube that Plank and others can use as a clock. Because these gases move relatively fast, the technique allows them to time processes that unfold rapidly. They have found that slugs of magma can rise 10 kilometers in roughly 10 minutes. "It's like a freight train," she says.

Her preliminary results from a handful of volcanoes in Alaska, Hawaii, and Central America support the idea that ascent rates correlate with explosivity. She's working now to study more volcanoes, but, she says, "the problem is that most of those eruptions go unsampled." So she's getting creative; when the Pavlof Volcano erupted violently on the Alaska Peninsula in March of this year, she bartered a box of fresh fruit for a trashcan of ash collected by locals. Her team still had to search through it for crystals that meet their criteria—another challenge. "My students pick for hours under a microscope looking for the one olivine that has a weird tube in it," she says. "We published a paper on four of them, that's how rare they are."

**RELYING ON A HANDFUL** of tiny crystals to track an entire body of magma worries some outsiders. "People are making strong interpretations based on not a whole lot of results," Sisson says. Dan Morgan, a petrologist at the University of Leeds in the United Kingdom and an early practitioner of diffusion chronometry, shares that concern. Although there's no way around it in Plank's work, Morgan says researchers should be careful with small sample numbers. "If you find five very photogenic crystals, they will be anomalous," he says. One 2015 study, led by Thomas Shea, a volcanologist at the University of Hawaii in Honolulu, points out that researchers must analyze at least 20 olivine profiles to account for the fact that chemicals diffuse in three dimensions through a crystal.

A quarry on the flanks of Mount Gede, an Indonesian volcano, reveals deposits from past eruptions that are ripe for harvesting crystals.

PHOTO: F. COSTA

So Morgan and others have been working on faster ways to measure and analyze diffusion profiles. One strategy is to skip the slow process of moving point by point across the crystal face with the microprobe, and instead use a technique called backscattered electron microscopy, which essentially snaps a chemical photo of the crystal. The brightness of the image can serve as a proxy for the concentration of iron and magnesium, and the process takes much less time.

Both Morgan and Costa are also developing user-friendly software to help researchers who aren't experts in diffusion modeling interpret their data. Morgan says that when he started out, he could model two or three chemical profiles in a day; his new daily record is 80. By speeding up the process, he hopes researchers can generate more data, "which then starts to tell you things at the scale of the whole magma mass rather than an individual crystal's story."

Others worry about uncertainties in the diffusion rates, especially for less common elements and minerals. But Costa says that it's important to keep perspective. Even if the uncertainties are 100% or more, the clock results can still be meaningful. "If I find 1 month, 100% uncertainty is a few months," he says. "It's still not 100 years."

The biggest challenge, according to experts like Costa and Morgan, isn't calibrating the stopwatch—it's knowing which volcanic processes the crystals are recording. That's why many researchers are studying crystals from eruptions of actively monitored volcanoes. Maren Kahl, a petrologist at the University of Iceland in Reykjavik, has used that approach at one of the best studied volcanoes on Earth, Mount Etna in Italy. She and her colleagues examined crystals from eight well-documented eruptive episodes between 1991 and 2008. The researchers were able to tie monitoring records of earthquakes, ground deformation, and gas emissions to pulses of magma recorded in crystal chemistry, which they dated using diffusion chronometry. The result was an unprecedented picture of the volcano's multichambered plumbing, with five different magma zones and three dominant pathways between them. The researchers were even able to create a model of how the volcano erupts based on realistic physics. "We've never been able to quite do that before," Plank says.

As researchers get better at linking the crystals' stories with observations of modern eruptions, Kahl says, they will gain confidence about applying the technique to ancient ones, as Costa is doing at Gede. Of the 1500 potentially active volcanoes on Earth, only a small fraction are actively monitored, and fewer still have erupted since scientists started watching.

With diffusion chronometry, however, researchers can use crystals to learn the histories and personalities of these hibernating volcanoes. "We can go pick up the rocks, study the minerals, and basically get timescale information about an eruption that happened, let's say, 100,000 years ago," Kahl says. And by diving deep into a volcano's past, scientists can gain a glimpse into its future. ■

Downloaded from http://science.sciencemag.org/ on November 22, 2016



Published by AAAS

Downloaded from http://science.sciencemag.org/ on November 22, 2016

CONSERVATION SCIENCE

# *Where science meets art*

## Scientific methods inform conservation efforts in the quest to preserve cultural heritage

*By* **Rebecca Ploeger** *and* **Aaron Shugar**

Fifty years ago on 3 November 1966, after a long stretch of heavy rain, the Levane and La Penna dams in Valdarno, Italy, began to leak, releasing water toward the city of Florence. Fearing that the dams would burst, on 4 November, engineers discharged a massive amount of water that coursed through the city streets at an astonishing 37 miles per hour (*1*). The raging waters covered much of Florence, killing dozens of people, displacing thousands more, and damaging countless books and works of art. Over a million items in the Biblioteca Nazionale Centrale di Firenze alone were completely submerged.

Known collectively as the "angeli del fango" (mud angels), art conservators, scientists, and concerned citizens descended on the beleaguered city to offer assistance. But volunteers were met with daunting challenges, including sparse laboratory space and a general lack of instrumentation for assessing the damage.

In a recent interview, Robert Feller, a renowned American conservation scientist, recounted how improvised equipment was assembled on site. "I was looking for a polarizing microscope, something to see the minerals coming out of the frescoes," he recalls (*2*). "I went downtown and bought two polarizing sunglasses and I made a polarizing microscope."

When the flood hit, scientific technolo-

PHOTO: DAVE YODER/NATIONAL GEOGRAPHIC CREATIVE



Published by AAAS

Alberto Felici searches for gaps in a Vasari mural that experts can probe without causing further damage.

gies were starting to become permanent fixtures in museums and cultural institutions. In the years since, art conservation science has developed into a full-fledged discipline, using state-of-the-art instrumentation to analyze and treat works of art.

## SCIENCE MEETS THE HIDDEN PROFESSION

In 1899, Edward Waldo Forbes purchased a 15th-century panel painting by the Italian artist Girolamo di Benvenuto on behalf of the Fogg Museum at Harvard for $100. Its condition was so poor that no one else could see its potential, yet he found himself moved by it (*3*).

When Forbes became the director of the museum, his interest in restoring this and other paintings in the museum's collection led him to establish a new department—the Department for Technical Studies—composed of conservators, historians, and scientists, including George Stout and Sheldon Keck. [Stout and Keck would go on to serve as "monuments men," tasked with recovering cultural objects stolen by Nazis during World War II. In his 13 months of service in Europe, Stout alone aided in recovering tens of thousands of cultural objects (*4*).]

The Department for Technical Studies was dedicated to the scientific study of art and began disseminating information about its work in a new publication entitled *Technical Studies in the Field of the Fine Arts*. The idea of conservation as a hidden profession with carefully guarded treatment methods soon began to fade. Forbes is widely credited with laying the foundation for modern conservation science.

In the mid-20th century, scientists who worked with museums and at cultural heritage sites typically trained in biology, chemistry, physics, and engineering and were drawn to scientific aspects of art and conservation out of their own curiosity and interest. A greater awareness and appreciation of art, as well as the development of more advanced scientific instrumentation, led to a growing recognition of conservation science as a discipline unto itself. Soon, cultural institutions in North America, Great Britain, and Europe began creating or expanding their own scientific laboratories. This quickly led to collaborations with research institutions and the chemical industry, which sought to characterize existing conservation materials and develop new ones specifically for the maturing field.

*Department of Art Conservation, State University of New York College at Buffalo, Buffalo, NY 14222, USA. Email: ploeger@buffalostate.edu*

When the Florence flood hit in 1966, museums and cultural institutions around the world were ready to provide assistance. Samples of accretions from frescoes were sent to the Mellon Institute of Industrial Research in Pittsburgh for x-ray diffractometry, and optical microscopy was employed extensively to inspect paintings, sculptures, and frescoes for damage.

## STRIKING THE RIGHT BALANCE

Historically, conservation scientists mainly focused on paintings, where visual aesthetics were a key factor and the critical eye of a conservator often aligned with the goals of the scientist. This union led to the development of a number of new synthetic varnishes and adhesives for the conservation of paintings (*5*).

But conservation scientists face unique challenges—for example, the need to balance scientific rigor with museum policies that limit physical alterations to works of art. These two requirements sometimes clash, and the challenge of obtaining comprehensive data from limited samples can be incredibly difficult.

Different philosophies, protocols, or ideas about which treatments should be pursued can also arise. In postflood Florence, for example, Italian, American, and British experts reportedly disagreed on what type of processes to use to treat mold in library collections and salvaged materials (*6*). Experts from Harvard recommended thymol, and the United States sent large quantities to Florence for the American volunteers to use. However, experts from the British Museum recommended topane and advocated its use over thymol because "it was possible to grow mould on a thymol treated paper (*1*)." Yet, topane was known to be a skin irritant. One could speculate that the disagreement may have had more to do with reputation than with science.

## SCIENCE IN SITU

When a cultural material cannot travel to the laboratory for analysis—because it is on display, or it is too fragile to be moved, or the expense and risk associated with off-site transportation and storage are prohibitive—conservation efforts are often performed on site. Small, portable instruments now allow conservation scientists to conduct quick assessments and analyses on items in the field or on permanent display and on large sculptures and frescoes.

Launched in 2004, the Mobile Laboratory (MOLAB) was the first state-of-the-art collection of portable scientific instruments dedicated to the preservation of cultural heritage in Europe. To date, MOLAB instruments have been used for a variety of purposes on a wide range of collections—from identifying pigments on Old Master paintings to studying modern synthetic polymeric binding media. It has also been instrumental in monitoring the conservation state of various cultural objects, including Michelangelo's *David* (*7*, *8*).

Fifty years ago, a devastating flood damaged countless works of art and cultural objects in Florence, Italy.

PHOTO: ASSOCIATED PRESS

Downloaded from http://science.sciencemag.org/ on November 22, 2016



Published by AAAS

## CONSERVATION GETS PERSONAL(IZED)

Risk assessment and preventive conservation methods are now a standard practice in cultural institutions and are tailored to each institution's unique collection, location, and climate. Natural disaster recovery protocols, cultural sensitivities, and energy sustainability goals are also considered in these assessments.

A culturally sensitive example of such a program can be found in Luang Prabang, Laos, where conservation professionals funded by the British Library have partnered with Buddhist monks to preserve a rich archive of photographs depicting monastic life. Rather than imposing a strict climate-control system in the modest temple that houses the collection, a system was developed in which caretakers actively monitor for insects and other issues. Local craftsmen were charged with building the archival cabinetry and housing as a way to ensure sustainable construction and increase awareness of the collection in surrounding communities (*9*).

Mud-covered volunteers retrieve a painting from the murky Florence flood waters on 7 November 1966.

## ART AND SCIENCE: STRONGER TOGETHER

Cross-fertilization between disciplines has facilitated greater accessibility to instrumentation and expertise, prompting novel applications of existing technologies in the examination of art. An excellent example is tomography, which allows researchers to examine the internal structures of mummified remains and works of art. The fragile En-Gedi scroll, for example, was recently digitally unfurled with computerized tomography, revealing text from the first eight verses of the Book of Leviticus (*10*). Likewise, hyperspectral imaging, developed for military and geographic applications, was recently applied to a panel painting by the early-Renaissance artist Cosimo Tura in order to map paint binding media and identify pigments without the need for physical sampling (*11*). Proteomics, an invaluable tool for medicine and biology, is also currently used for species identification of modern and ancient leathers, furs, and parchments (*12*).

The study of traditional material has also led to improvements in scientific techniques. For example, a recent study revealed that the luminescent properties of micronized Egyptian blue pigment provide a sharper contrast between dark backgrounds and bright fingerprints than ultraviolet-based dusting powders, enabling the detection of latent fingerprints on patterned and reflective surfaces (*13*).

Always searching for new and novel scientific methods, conservation science has begun to employ spectroscopic mapping—especially elemental mapping with micro x-ray fluorescence (μXRF)—where advances in array detectors are enabling quick and comprehensive analysis of works of art. Elemental mapping of Edgar Degas's *Portrait of a Woman* was recently completed with the help of a Maia 384 detector array and the XRF microscopy beamline at the Australian Synchrotron, for example. The results yielded an exciting revelation: The image long known to be concealed behind the famous portrait is, in fact, a portrait of another woman (*14*).

## VALUING CULTURAL HERITAGE

Technical studies of works of art were historically motivated by the need to confirm a piece's authenticity or provenance or to aid in a conservator's treatment decision. But many museums now incorporate scientific and technical analyses into public outreach, exhibition catalogs, and education programs. Programs like the BBC's *Fake or Fortune?*, in which investigators team up with conservators and scientists to determine whether works of art are authentic, reinforce the idea that there is a growing interest in this field among the general public.

Days before the 1944 invasion of northern Europe, General Eisenhower released a memorandum that stated "… in the path of our advance will be found historical monuments and cultural centers which symbolize to the world all that we are fighting to preserve. It is the responsibility of every commander to protect and respect these symbols whenever possible" (*15*). Just over 20 years later, museums and other institutions around the world came together again when Florence's cultural heritage was in trouble. Today, new and continuing threats, including climate change, natural disasters, and armed conflict, demand a united front when it comes to protecting and preserving rare works of art and cultural objects. As science continues to inform the field of conservation, and vice versa, we stand better prepared than ever to rise to this challenge. ■

### REFERENCES


1. S. Waters, *Waters Rising: Letters from Florence*. (Legacy Press, Ann Arbor, 2016).
2. A. Shugar, R. Ploeger, Oral interview with R. Feller and C. Tahk (2015).
3. F. G. Bewer, *A Laboratory for Art: Harvard's Fogg Museum and the Emergence of Conservation in America, 1900–1950* (Harvard Art Museum, 2010).
4. R. M. Edsel, *Harvard Magazine* (Cambridge, 2010); http://harvardmagazine.com/2010/01/monuments-men-rescuing-art-stolen-by-nazis.
5. E. René de la Rie, C. W. McGlinchey, *Studies in Conservation* **35**, 168 (1990).
6. S. K. Heninger, R. M. Kingdon, M. P. Gilmore, *Renaissance Quarterly* **20**, 81 (1967).
7. C. Miliani, F. Rosi, B. G. Brunetti, A. Sgamellotti, *Accounts Chem. Res.* **43**, 728 (2010).
8. B. Brunetti *et al.*, *Topics Curr. Chem.* **374**, 1 (2016).
9. M. C. Jürgens, in *Topics in Photographic Preservation,* B. Bernier, C. Moore, Eds. (American Institute for Conservation of Historic & Artistic Works, Washington, DC, 2009), vol. 13, pp. 21–36.
10. W. B. Seales *et al.*, *Sci. Adv.* **2**, e1601247 (2016).
11. K. A. Dooley *et al.*, *Analyst* **138**, 4838 (2013).
12. S. Dallongeville, N. Garnier, C. Rolando, C. Tokarski, *Chem. Rev.* **116**, 2 (2015).
13. B. Errington *et al.*, *Dyes Pigments* **132**, 310 (2016).
14. D. Thurrowgood *et al.*, *Sci. Rep.* **6**, 29594 (2016).
15. Dwight D. Eisenhower, General, U.S. Army, "Preservation of Historical Monuments," *Memorandum for G.O.C. in Chief, 21 Army Group; Commanding General, 1st U.S. Army Group; Allied Naval Commander, Expeditionary Force and Air C-in-C, Allied Expeditionary Force.* (Division, General Staff, Supreme Headquarters Allied Expeditionary Forces, Allied Operational and Occupation Headquarters, World War II, RG 331, 1944).


10.1126/science.aai8387

Downloaded from http://science.sciencemag.org/ on November 22, 2016

PHOTO: ASSOCIATED PRESS



Published by AAAS

PHOTO: TOPPYBAKER/ISTOCK PHOTO

There's more than meets the eye in a field of sorghum. The ER membranes in some cells contain metabolons that produce dhurrin, a defensive compound that can be converted by the plant to toxic hydrogen cyanide.

CELL METABOLISM

# *Plant metabolons assembled on demand*

## Proteins interact at an intracellular membrane to form dynamic metabolons that increase metabolic flux

*By* **Mehran Dastmalchi** *and* **Peter J. Facchini**

The concept of a metabolon was first described in 1985 as a supramolecular assembly of enzymatic and structural components able to sequester and channel metabolic pathway intermediates (*1*). Initially, metabolons were proposed for the citric acid cycle, glycolysis, and nucleotide and amino acid biosynthesis as a mechanism to coordinate metabolic flux and reduce kinetic constraints. Although the theory is expedient and has aligned with a vast amount of evidence in support of protein-protein interactions, definitive proof that efficient cellular metabolism is associated with metabolon formation has been elusive. On page 890 of this issue, elegant work from Laursen *et al.* (*2*) provides a functional link between the dynamic interactions of metabolic enzymes and the production of the cyanogenic glucoside, dhurrin, in the cereal crop sorghum. Upon tissue damage by pests, dhurrin is hydrolyzed to toxic hydrogen cyanide as a plant defense mechanism.

Most metabolon models are based on a dynamic, noncovalent aggregation of components on the surface of the endoplasmic reticulum (ER), in complex with cytochrome (CYP) P450 proteins lodged within the membrane (*3*). The cytosolic segments of P450s usually contain the catalytic domain and certain members have been shown to interact with both soluble and membrane-bound proteins. As such, the ER has been described as a metabolic assembly platform studded with P450s tethering soluble protein partners.

Metabolons appear to occur in all living organisms and are particularly relevant to the complex metabolism of plants. An area of continued research has been the photosynthetic Calvin-Benson cycle metabolon (*4*), the importance of which has recently been shown in engineered microorganisms with improved efficiency of enzymes integrated in scaffolds rather than as diffusible proteins (*5*). Other pioneering work on plant-specialized metabolism suggested the channeling of intermediates between the first two enzymes in phenylpropanoid biosynthesis (*6*). Although subsequent studies have yielded contradictory evidence regarding this proposed channeling, an array of evidence supports metabolons in downstream pathways leading to lignin (*7*), flavonoids (*8*), and isoflavonoids (*9*). Metabolon formation has also been implicated in the biosynthesis of sporopollenin polymer, a major constituent of the outer wall of pollen (*10*). These studies have relied on a variety of methods to study protein-protein interactions and to isolate intact complexes. In the dizzying realm of plant specialized me-

*Department of Biological Sciences, University of Calgary, Calgary, Alberta T2N 1N4, Canada. Email: pfacchin@ucalgary.ca*

Downloaded from http://science.sciencemag.org/ on November 22, 2016



Published by AAAS

tabolism—which yields compounds such as cyanogenic glycosides, phenylpropanoids, glucosinolates, terpenoids, and alkaloids—the formation of metabolons to organize and direct flux across biosynthetic networks seems essential.

The work of Laursen *et al.* is a watershed in metabolon research and a pinnacle of earlier groundbreaking work on the dhurrin metabolon (*11*). The authors discovered that the dhurrin metabolon has three biosynthetic proteins anchored in the ER: an essential P450 oxidoreductase (POR), serving as an electron donor, and its pathway-specific P450 partners, CYP79A1 and CYP71E1. The fourth component is a soluble uridine diphosphate–glucosyltransferase (UGT85B1). All four proteins perform in concert to convert the amino acid L-tyrosine to dhurrin. Laursen *et al.* show that CYP79A1 and CYP71E1 form hetero- and homo-oligomers that recruit UGT85B1, which mediates the efficient channeling of intermediates. Tandem P450s have also been reported in lignin (*7*) and isoflavonoid biosynthesis (*9*). Metabolon disassembly results in the release of the antifungal agent aldoxime, a pathway intermediate produced by CYP79A1. The amount of aldoxime converted to cyanohydrin by CYP71E1 increases in the presence of UGT85B1, which yields dhurrin. The formidable efficiency of the metabolon is demonstrated by high dhurrin accumulation in sorghum seedlings despite pathway enzymes representing less than 1% of total membrane protein content.

***"...the membrane itself is an integral part of the metabolon."***

Of critical importance is the demonstration that the membrane itself is an integral part of the metabolon. Key membrane features include the local lipid composition and the overall charge on the ER surface. Remarkably, Laursen *et al.* were able to carve out discrete regions of the ER bilayer and determine the precise phospholipid composition of isolated particles containing the dhurrin metabolon. CYP71E1 activity, in particular, was affected by charges of the cytosolic-facing lipid headgroups. This highlights an important and often overlooked reality that plant ER membranes are heterogeneous. Lipid composition might just be the tip of the iceberg as other structural and accessory features of specific ER domains are investigated. Indeed, attempts to transplant plant metabolic pathways into heterologous hosts, such as the complete reconstitution of opioid biosynthesis in yeast, have been hampered by low yields (*12*). This may be due to differences between plants and microbes in membrane structure and composition. Variations could affect protein stability, anchoring, and function, leading to the disassembly of necessary metabolons.

As compositional changes in the ER are better understood, our appreciation for the flexibility, movement, and functional integrity of membranes is also improving. The ER is no longer seen as a collection of rigid membranes but rather as a cellular network extending outward from the nuclear envelope in a series of cisternal sheets and dynamic tubules. ER movement is driven by the cytoskeleton, and its architecture is constantly being reshaped by proteins. As shown by Laursen *et al.*, integral membrane proteins dynamically diffuse along this network. The coexpression of metabolic partners affected the diffusion coefficients of the ER-bound P450s, but not of the universal electron donor POR. The intimate interaction of enzymes within a metabolon introduces reciprocal constraints on the membrane-anchored components, resulting in slower diffusion rates along the ER, which would be expected to improve metabolon formation and catalytic efficiency.

Also notable in the work of Laursen *et al.* is the use of styrene maleic acid copolymer (*13*) and affinity chromatography to isolate the intact dhurrin metabolon. This method circumvents the need to use detergents that disrupt complexes and fusion tags that alter protein folding. Continued development of this methodology could allow researchers to recover all of the molecular components in metabolons and further define membrane platforms that host metabolic machinery. A plethora of perceived nonmetabolic components that coprecipitate or colocalize with metabolic enzymes (*9*) can be investigated by using similar strategies. ■

## REFERENCES


1. P. A. Srere, *Trends Biochem. Sci.* **10**, 109 (1985).
2. T. Laursen *et al.*, *Science* **354**, 890 (2016).
3. S. Bak *et al.*, *Arabidopsis Book* **9**, e0144 (2011).
4. E. Graciet, S. Lebreton, B. Gontero, *J. Exp. Bot.* **55**, 1245 (2004).
5. C. Singleton, T. P. Howard, N. Smirnoff, *J. Exp. Bot.* **65**, 1947 (2014).
6. G. Hrazdina, G. J. Wagner, *Arch. Biochem. Biophys.* **237**, 88 (1985).
7. J. E. Bassard *et al.*, *Plant Cell* **24**, 4465 (2012).
8. I. E. Burbulis, B. Winkel-Shirley, *Proc. Natl. Acad. Sci. U.S.A.* **96**, 12929 (1999).
9. M. Dastmalchi, M. A. Bernards, S. Dhaubhadel, *Plant J.* **85**, 689 (2016).
10. B. Lallemand, M. Erhardt, T. Heitz, M. Legrand, *Plant Physiol.* **162**, 616 (2013).
11. K. A. Nielsen, D. B. Tattersall, P. R. Jones, B. L. Møller, *Phytochemistry* **69**, 88 (2008).
12. S. Galanie, K. Thodey, I. J. Trenchard, M. Filsinger Interrante, C. D. Smolke, *Science* **349**, 1095 (2015).
13. S. C. Lee *et al.*, *Nat. Protoc.* **11**, 1149 (2016).


10.1126/science.aal2948

BIOTECHNOLOGY

# *Fixing carbon, unnaturally*

## A synthetic enzymatic pathway is more energy efficient than natural aerobic carbon fixation pathways

*By* **Fuyu Gong** *and* **Yin Li**

Rising atmospheric carbon dioxide ($CO_2$) concentration as a result of extensive use of fossil fuel resources is one of the main causes of global warming. Natural photosynthesis converts 100 billion tons of $CO_2$ into biomass annually (*1*). Although natural photosynthesis plays a vital role in absorbing $CO_2$ emitted from fossil fuel use, it cannot prevent the net increase of atmospheric $CO_2$ concentration since the Industrial Revolution. Natural $CO_2$ fixation is mainly achieved by a $CO_2$ fixation pathway called the Calvin cycle, in which ribulose 1,5-bisphosphate carboxylase/oxygenase (RuBisCO) is the key enzyme. To date, six $CO_2$ fixation pathways, including the Calvin cycle, have been discovered (*2*). On page 900 of this issue, Schwander *et al.* (*3*) report a synthetic $CO_2$ fixation pathway that is more energy efficient than the Calvin cycle, expanding the capabilities for recapturing atmospheric $CO_2$ for use as a carbon feedstock.

Natural $CO_2$ fixation processes through plants and other autotrophic (carbon fixing) organisms are usually slow. Moreover, it is difficult to genetically engineer plants and autotrophic organisms, which complicates efforts to improve the native $CO_2$ fixation efficiency. Scientists have therefore reconstructed the natural $CO_2$ fixation pathways in heterotrophic microorganisms, which are genetically accessible and metabolically active but cannot naturally fix carbon. By increasing the expression levels of the carbon-fixing enzymes in heterotrophic microorganisms, it is expected that the $CO_2$ fixation rate of the reconstructed $CO_2$ fixation pathways can be increased. However, the configurations of the reconstructed $CO_2$ fixation pathways were not changed, and the energy efficiencies [consumption of adenosine triphosphate (ATP) and the reduced form of nicotinamide

*CAS Key Laboratory of Microbial Physiological and Metabolic Engineering, Institute of Microbiology, Chinese Academy of Sciences, Beijing 100101, China. Email: yli@im.ac.cn*

Downloaded from http://science.sciencemag.org/ on November 22, 2016



Published by AAAS

adenine dinucleotide phosphate (NADPH) per molecule $CO_2$ fixed] therefore also remained the same as in the native pathways (*4*–*7*). Moreover, because carboxylases catalyze the rate-limiting steps of natural $CO_2$ fixation pathways, reconstructing a natural pathway without introducing a new efficient carboxylase or increasing the activity of the existing carboxylase will not increase the overall $CO_2$ fixation efficiency.

Schwander *et al.* now report the construction of a non-natural $CO_2$ fixation cycle—termed the "crotonyl–coenzyme A (CoA)/ethylmalonyl-CoA/hydroxybutyryl-CoA" (CETCH) cycle—that achieves unprecedented in vitro $CO_2$ fixation efficiency. They used the highly efficient enoyl-CoA carboxylase/reductase (ECR) as the starting point for designing a pathway that avoids the carboxylation efficiency bottleneck in the natural $CO_2$ fixation. The authors used stepwise optimization, including engineering of the enzymes involved, to further improve the CETCH cycle. ECR comes from the acetate assimilation ethylmalonyl-CoA pathway (*8*) and shows the highest activity of all carboxylases characterized to date. Its carboxylation activity is 4.3 times that of propanoyl-CoA carboxylase involved in the 3-hydroxypropionate (3HP) bicycle and the 3-hydroxypropionate-4-hydroxybutyrate (3HP-4HB) cycle (*9*), which has the highest carboxylation activity among the three natural aerobic $CO_2$ fixation pathways, and 37 times that of RuBisCO (*9*), the most abundant carboxylase on Earth but notorious for low specific activity.

The CETCH cycle is an aerobic pathway that shares four reactions and five intermediates with the 3HP-4HB cycle (see the figure). However, the 12 enzymes involved in the CETCH cycle come from six organisms across all three domains of life: one from a plant (*Arabidopsis thaliana*), one from humans (*Homo sapiens*), and the other 10 enzymes from microbes, indicating the underestimated potential of natural biodiversity. Usually, the carboxylation reaction is the rate-limiting step in $CO_2$ fixation pathways. Besides ECR, there are other efficient carboxylases (such as pyruvate carboxylase) that are not involved in the six natural $CO_2$ fixation pathways. These carboxylases may also be used as starting points for designing new synthetic $CO_2$ fixation pathways. To increase the efficiency of a natural/synthetic $CO_2$ fixation pathway, one might consider engineering the carboxylase involved, or screening for carboxylase with higher activity, from the vast amount of genomic data available.

The CETCH cycle has the fewest reactions and the lowest requirement for ATP and NADPH among the aerobic $CO_2$ fixation pathways. However, in contrast to the products from the other three aerobic cycles, the product of CETCH, glyoxylate, is a less active (or reductive) metabolic intermediate and its conversion to other metabolites usually needs assistance from acetyl-CoA (AcCoA) or propanoyl-CoA. Furthermore, glyoxylate has fewer connections with other major metabolic pathways. Therefore, incorporation of the CETCH cycle into the central metabolic pathway of a biological cell may not be as easy as it is for the natural $CO_2$ fixation pathways. Moreover, using a complex enzyme cocktail to convert $CO_2$ into useful products on a large scale is not economically realistic.

## $CO_2$ fixation pathways

Six natural biological $CO_2$ fixation pathways are known (*2*). Schwander *et al.* now report the CETCH cycle, a synthetic $CO_2$ fixation pathway. This cycle shares some elements of the aerobic 3HP-4HB cycle. However, it is more energy efficient than this and the other two known aerobic cycles.

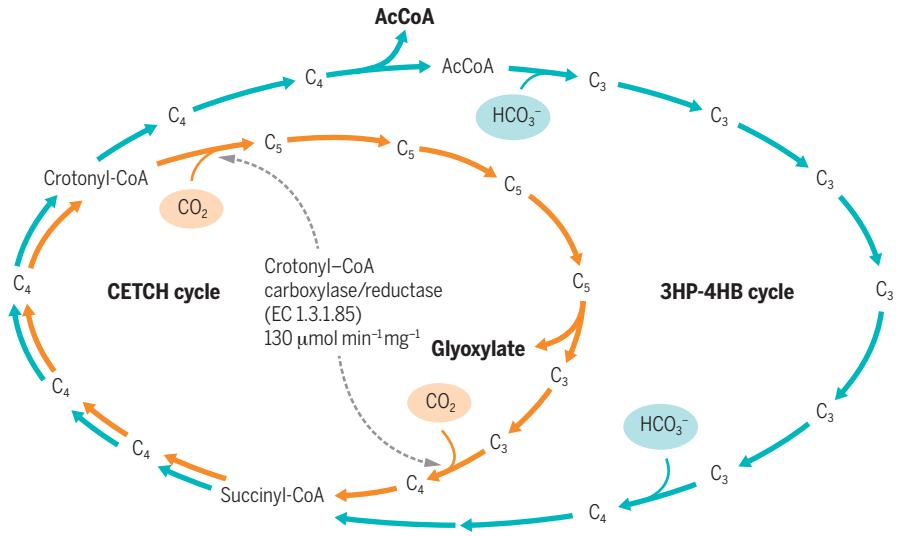


*"...it is possible to use natural elements to construct a more efficient synthetic pathway."*

Transplantation of the CETCH cycle into a living organism, with the hope to develop robust whole-cell biocatalysts capable of using $CO_2$ as feedstock, is thus a logical next step. To that end, it remains challenging to select the chassis organism, regulate the expression level of each enzyme, and identify and accelerate the rate-limiting steps to increase the overall flux of the CETCH cycle. Nevertheless, the in vitro demonstration of a functional CETCH cycle is a breakthrough, showing that it is possible to use natural elements to construct a more efficient synthetic pathway.

Efficient supply of energy and reducing power is key to the efficient reduction of $CO_2$. The in vitro operation of the CETCH cycle is driven by ATP and NADPH added to the buffered reaction system, which is not feasible for a practical $CO_2$ fixation process because ATP and NADPH are expensive. Efficient supply of cheap energy and reducing power is thus crucial for achieving efficient $CO_2$ fixation. Sunlight is a cheap, readily available energy source and widely used by plants, algae, and cyanobacteria. The energy efficiency of using light can be improved by artificial photosynthesis (*10*). However, energy loss associated with light penetration remains a big problem for large-scale light-driven $CO_2$ fixation. Electricity is also a readily available (and potentially cheap) energy source. Integrated use of electricity for carbon fixation has been achieved (*11*), but direct biological use of electricity is still challenging. Future efforts should focus on improving the energy efficiency of using light and designing novel biocatalysts that can directly use electricity for carbon fixation. ■


**REFERENCES**

1. M. Peplow, *Nat. Biotechnol.* **33**, 1123 (2015).
2. F. Gong *et al.*, *Sci. China Life Sci.* **59**, 1106 (2016).
3. T. Schwander *et al.*, *Science* **354**, 900 (2016).
4. F. Gong *et al.*, *Biotechnol. Biofuels* **8**, 86 (2015).
5. N. Antonovsky *et al.*, *Cell* **166**, 115 (2016).
6. M. D. Mattozzi *et al.*, *Metab. Eng.* **16**, 130 (2013).
7. M. W. Keller *et al.*, *Proc. Natl. Acad. Sci. U.S.A.* **110**, 5840 (2013).
8. T. J. Erb *et al.*, *Proc. Natl. Acad. Sci. U.S.A.* **104**, 10631 (2007).
9. B. Even *et al.*, *Proc. Natl. Acad. Sci. U.S.A.* **107**, 8889 (2010).
10. K. K. Sakimoto *et al.*, *Science* **351**, 74 (2016).
11. H. Li *et al.*, *Science* **335**, 1596 (2012).


10.1126/science.aal1559

GRAPHIC: C. BICKEL/*SCIENCE*

Downloaded from http://science.sciencemag.org/ on November 22, 2016



*Published by AAAS*

PLANT BIOLOGY

# Light-sensing phytochromes feel the heat

## Plant phytochrome activity is governed not just by light, but also by prevailing temperature

*By* **Karen J. Halliday**[1] *and* **Seth J. Davis**[2]

Plants expect light and warmth during the day and darkness and coolness at night. But dim, overcast days and unusually warm nights also occur. How is the perception of this variability integrated into more regular daily cycles? Phytochromes constitute a major class of plant photoreceptors that respond to brightness and color ratio. In so doing, they coordinate growth and development. Phytochromes are therefore a vital surveillance system that enables plants to adapt to a changing environment. Two reports in this issue, by Legris *et al.* (*1*) on page 897 and Jung *et al.* (*2*) on page 886, now implicate phytochrome B (phyB) in the thermal regulation of the light-sensing pathways.

Phytochromes are chromic proteins that must operate under both predictable and unpredictable conditions, which can span, for example, an ~30°C range in temperature (*3*). Responding to the sometimes massive, daily fluctuations in temperature under a mostly predictable light environment is a major challenge. Phytochromes have intriguing properties that allow them to sense changes in light quality and quantity. Like other phytochromes, phyB exists as dimers in inactive Pr and active Pfr forms. Red light drives the photoconversion of Pr to Pfr, whereas far-red light switches it back (see the figure). In this way, changes in light quality lead to different proportions of active Pfr to inactive Pr. The amount of active Pfr also depends upon light-independent thermal (or dark) reversion back to Pr. Mathematical modeling of phytochrome kinetics indicates that dark reversion is essential for accurate detection of light quantity (*4*). A simple and quantitative readout of phytochrome action is hypocotyl (seedling stem) length, which inversely correlates with Pfr. Phytochrome signaling operates in part by negatively regulating transcription factors, such as those in the PHYTOCHROME INTERACTING FACTOR (PIF) family. This is achieved by triggering PIF proteolysis and through direct binding to PIFs at target promoters (*5, 6*). As such, phytochrome binding to PIFs is thought to be important in transcriptional regulation. Indeed, Jung *et al.* could detect phyB at DNA sites where PIFs target genes that control an array of responses, including hypocotyl growth.

The active phytochrome Pfr accumulates in nuclear bodies. Small nuclear bodies form at fluence rates that generate low levels of Pfr, whereas large nuclear bodies form when Pfr levels exceed a higher threshold (*7*). Pfr-Pfr constitutes the main dimeric form in nuclear bodies and most likely represents the "active" form (*8*). By using nuclear body size as a proxy for active Pfr levels, Legris *et al.* conducted multivariate analysis with wild-type and dark reversion–defective phytochrome variants, grown in varying light quality, quantity, and temperature to examine the relationship of dark reversion to thermal inputs and nuclear body dimensions. The simple correlation between spectroscopic Pfr and temperature was not observed for nuclear body size, suggesting that nuclear body dynamics capture additional temperature characteristics. However, a consistent feature, not observed in dark reversion variants, was the reduction in number of large nuclear bodies at high temperatures. By mathematically modeling nuclear body size as a function of Pfr amount, warmth was shown to deplete Pfr levels in a dark reversion–dependent manner. Although this analysis delineates a key role for dark reversion in nuclear body thermal stability, as nuclear body constituents have not been fully determined, other factors could contribute to this response.

Both Legris *et al.* and Jung *et al.* establish that phytochrome signaling is thermally controlled. The importance of phyB thermal reversion was demonstrated in regulating phytochrome activity during the early night (*2*) and in dim daylight conditions (*1*). Jung *et al.* showed that temperature effects on post-dusk Pfr result in a phyB enrichment at PIF-associated target promoters when plants experience cooler temperatures. These data imply that at permissive temperatures, phyB

## See the light, feel the heat

Plant phytochromes sense light. The phytochrome phyB can also sense temperature, linking the detection of light and heat.

**Pathways affecting active phytochromes**

Phytochromes exist as dimers. Red light drives the production of the active dimer (Pfr-Pfr), whereas far-red light favors the inactive dimer (Pr-Pr). The active dimer pool is also influenced by thermal (or dark) reversion, a two-step (kr1, kr2) process that converts Pfr-Pfr back to inactive Pr-Pr.

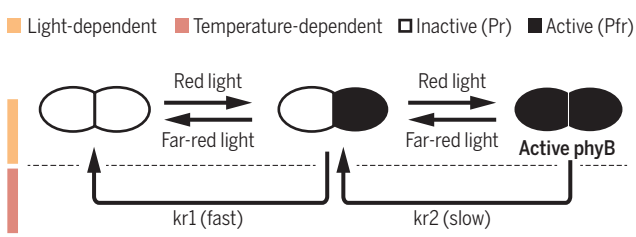


**Short day, low light, be cool**

Plants lacking phytochrome are tall under short days (time of light exposure is limited) whether the temperature is warm or cool. In wild-type plants, the stem grows tall only when it is warm. Thus, phytochrome is required to sense temperatures, at least under short photoperiods or low light.

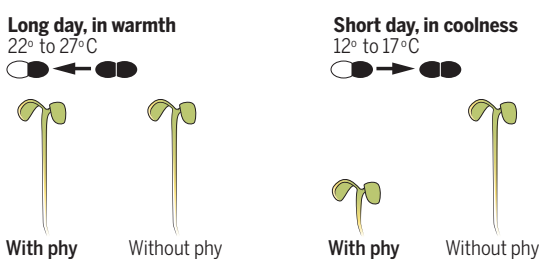


[1]*SynthSys, School of Biological Sciences, CH Waddington Building, University of Edinburgh, Edinburgh EH9 3BF, UK.* [2]*Department of Biology, University of York, York YO10 5DD, UK. Email: karen.halliday@ed.ac.uk; seth.davis@york.ac.uk*

Downloaded from http://science.sciencemag.org/ on November 24, 2016

CREDITS: (GRAPHIC) V. ALTOUNIAN/*SCIENCE*; (PHOTO) KAREN HALLIDAY



Published by AAAS

inhibits PIF activity through direct binding at target promoters. In this way, phyB conveys temperature information to PIFs. These results indicate that the phytochrome active state, Pfr, determines the receptor's signaling and that this is dependent on the ambient temperatures during the first hours of darkness.

Further, Legris *et al.* show that temperature profoundly affects the abundance of active Pfr under low-light conditions. This study considers that phytochrome exists as a dimer and that dark reversion is a two-part process comprising a slow step from Pfr-Pfr to Pfr-Pr (*3*), and a fast step from Pfr-Pr to Pr-Pr (*1*, *8*). Legris *et al.* demonstrate how these dark reversion–rate kinetics underlie thermal regulation. At very low light levels, there is a higher proportion of the Pfr-Pr heterodimer, but the balance tips toward Pfr-Pfr as light intensity increases (*8*). Critically, the authors showed that temperature was particularly effective in reducing Pfr at very low light levels, which suggests that Pfr-Pr to Pr-Pr dark reversion kinetics are more temperature sensitive than Pfr-Pfr to Pfr-Pr. This illustrates that active phytochrome is particularly sensitive to temperature at very low levels of light typical under a dense canopy. Nonetheless, using hypocotyl growth as an indicator of phyB action, temperature effects on phyB were also observed at higher intensities. The active phytochrome pool is therefore highly dynamic, as determined by both light-activated Pr-to-Pfr photoconversion and thermal reversion.

Together, the studies of Legris *et al.* and Jung *et al.* suggest that phytochrome signaling is perturbed by heat. Sensitivity to temperature is particularly acute under conditions that impede conversion to Pfr-Pfr, such as very low-light, far red–rich canopy shade, or warmth during early night darkness. These studies support the idea that cool temperatures boost phyB action, which may be important for restricting stem elongation growth and adjusting metabolism to cope with cold spells or cooler seasons (*3*). Future work could reveal the different molecular circuit architectures that respond to or protect from temperature changes. ■

## REFERENCES


1. M. Legris *et al.*, *Science* **354**, 897 (2016).
2. J.-H. Jung *et al.*, *Science* **354**, 886 (2016).
3. C. R. McClung, S. J. Davis, *Curr. Biol.* **20**, R1086 (2010).
4. J. Rausenberger *et al.*, *PLOS ONE* **5**, e10721 (2010).
5. J. F. Martínez-García, E. Huq, P. H. Quail, *Science* **288**, 859 (2000).
6. E. Park *et al.*, *Plant J.* **72**, 537 (2012).
7. M. Chen, R. Schwab, J. Chory, *Proc. Natl. Acad. Sci. U.S.A.* **100**, 14493 (2003).
8. C. Klose *et al.*, *Nat. Plants* **1**, 15090 (2015).


10.1126/science.aaj1918

PHOTO: RYAN NEELY

Dust-sized wireless sensors could be used as "electroceuticals" to stimulate nerves, muscles, and organs.

NEUROSCIENCE

# Neural circuitry gets rewired

## Former parasympathetic innervations of organs are now claimed sympathetic

*By* **Igor Adameyko**[1,2]

Our body organs are well integrated into a control framework that is represented by coordinated neural and hormonal signals. The key component of this system is the circuitry of the autonomic nervous system, which regulates bodily functions that are not consciously directed. Historically, this system is divided into sympathetic and parasympathetic subdivisions—a yin and yang control mechanism for stress responses (fight or flight) and homeostasis (rest and digest), respectively. On page 893 of this issue, Espinosa-Medina *et al.* (*1*) clearly demonstrate that, contrary to current dogma, certain autonomic neural circuitry does not belong in the parasympathetic subdivision. This finding provokes a serious shift in textbook knowledge, and, as with any fundamental discovery, it brings important practical implications for neuroanatomists, evolutionary-developmental specialists, and possibly a new era of health care based on "electroceuticals."

In vertebrates, the sympathetic and parasympathetic subdivisions are formed by specialized structures with a number of canonical functions, circuitry characteristics, and evolutionary and developmental origins (*2*). Three major components of an autonomic compartment include preganglionic motor fibers originating from

[1]*Department of Physiology and Pharmacology, Karolinska Institutet, 17177 Stockholm, Sweden.* [2]*Center for Brain Research, Medical University Vienna, 1090 Vienna, Austria. Email: igor.adameyko@ki.se*

Downloaded from http://science.sciencemag.org/ on November 24, 2016



Published by AAAS

inhibits PIF activity through direct binding at target promoters. In this way, phyB conveys temperature information to PIFs. These results indicate that the phytochrome active state, Pfr, determines the receptor's signaling and that this is dependent on the ambient temperatures during the first hours of darkness.

Further, Legris *et al.* show that temperature profoundly affects the abundance of active Pfr under low-light conditions. This study considers that phytochrome exists as a dimer and that dark reversion is a two-part process comprising a slow step from Pfr-Pfr to Pfr-Pr (*3*), and a fast step from Pfr-Pr to Pr-Pr (*1*, *8*). Legris *et al.* demonstrate how these dark reversion–rate kinetics underlie thermal regulation. At very low light levels, there is a higher proportion of the Pfr-Pr heterodimer, but the balance tips toward Pfr-Pfr as light intensity increases (*8*). Critically, the authors showed that temperature was particularly effective in reducing Pfr at very low light levels, which suggests that Pfr-Pr to Pr-Pr dark reversion kinetics are more temperature sensitive than Pfr-Pfr to Pfr-Pr. This illustrates that active phytochrome is particularly sensitive to temperature at very low levels of light typical under a dense canopy. Nonetheless, using hypocotyl growth as an indicator of phyB action, temperature effects on phyB were also observed at higher intensities. The active phytochrome pool is therefore highly dynamic, as determined by both light-activated Pr-to-Pfr photoconversion and thermal reversion.

Together, the studies of Legris *et al.* and Jung *et al.* suggest that phytochrome signaling is perturbed by heat. Sensitivity to temperature is particularly acute under conditions that impede conversion to Pfr-Pfr, such as very low-light, far red–rich canopy shade, or warmth during early night darkness. These studies support the idea that cool temperatures boost phyB action, which may be important for restricting stem elongation growth and adjusting metabolism to cope with cold spells or cooler seasons (*3*). Future work could reveal the different molecular circuit architectures that respond to or protect from temperature changes. ■

## REFERENCES


1. M. Legris *et al.*, *Science* **354**, 897 (2016).
2. J.-H. Jung *et al.*, *Science* **354**, 886 (2016).
3. C. R. McClung, S. J. Davis, *Curr. Biol.* **20**, R1086 (2010).
4. J. Rausenberger *et al.*, *PLOS ONE* **5**, e10721 (2010).
5. J. F. Martínez-García, E. Huq, P. H. Quail, *Science* **288**, 859 (2000).
6. E. Park *et al.*, *Plant J.* **72**, 537 (2012).
7. M. Chen, R. Schwab, J. Chory, *Proc. Natl. Acad. Sci. U.S.A.* **100**, 14493 (2003).
8. C. Klose *et al.*, *Nat. Plants* **1**, 15090 (2015).


10.1126/science.aaj1918

PHOTO: RYAN NEELY

Dust-sized wireless sensors could be used as "electroceuticals" to stimulate nerves, muscles, and organs.

NEUROSCIENCE

# *Neural circuitry gets rewired*

## Former parasympathetic innervations of organs are now claimed sympathetic

*By* **Igor Adameyko**[1,2]

Our body organs are well integrated into a control framework that is represented by coordinated neural and hormonal signals. The key component of this system is the circuitry of the autonomic nervous system, which regulates bodily functions that are not consciously directed. Historically, this system is divided into sympathetic and parasympathetic subdivisions—a yin and yang control mechanism for stress responses (fight or flight) and homeostasis (rest and digest), respectively. On page 893 of this issue, Espinosa-Medina *et al.* (*1*) clearly demonstrate that, contrary to current dogma, certain autonomic neural circuitry does not belong in the parasympathetic subdivision. This finding provokes a serious shift in textbook knowledge, and, as with any fundamental discovery, it brings important practical implications for neuroanatomists, evolutionary-developmental specialists, and possibly a new era of health care based on "electroceuticals."

In vertebrates, the sympathetic and parasympathetic subdivisions are formed by specialized structures with a number of canonical functions, circuitry characteristics, and evolutionary and developmental origins (*2*). Three major components of an autonomic compartment include preganglionic motor fibers originating from

[1]*Department of Physiology and Pharmacology, Karolinska Institutet, 17177 Stockholm, Sweden.* [2]*Center for Brain Research, Medical University Vienna, 1090 Vienna, Austria. Email: igor.adameyko@ki.se*

Downloaded from http://science.sciencemag.org/ on November 22, 2016



Published by AAAS

the central nervous system, peripheral autonomic ganglia innervated by those preganglionic fibers and, finally, the organ controlled by the neurons from autonomic ganglia. There are a few exceptions to this rule, such as the integrated presence of sensory and interneurons in the enteric nervous system of the gut (*3*).

Historically, long cranial and pelvic preganglionic nerves originating from the central nervous system were considered to be very similar and largely parasympathetic in nature. Therefore, all peripheral ganglia in the body innervated by those lengthy nerves were thought to be parasympathetic and similar in terms of how they control inner organs (including the large intestine, colon, bladder, and reproductive organs). However, several recent studies have challenged this paradigm (*4*). For example, the dorsal or ventral position of the nerve exit point from the central nervous system is different between cranial and pelvic nerves. Thus, pelvic nerves are more similar in that sense to the thoracic preganglionic sympathetic nerve fibers.

During development, neural crest cells migrate directly from the dorsal neural tube (precursor of the brain and spinal cord) to produce sympathetic ganglia, whereas precursors of parasympathetic ganglia are nerve-dependent, glia-like, and are delivered to the site of the future ganglion formation by parasympathetic preganglionic nerves. These glia-like precursors express both transcription factors SRY-Box 10 (Sox10) and paired-like homeobox 2b (Phox2b) (*5*, *6*).

Espinosa-Medina *et al*. examined the circuitry that arises from the so-called "sacral parasympathetic nucleus" in the spinal cord of the mouse. This region is located in the sacrum, the base of the spinal column where the pelvis is situated. These parasympathetic nerves are commonly referred to as the pelvic splanchnic nerves. The authors found that glia-like precursor cells associated with these pelvic preganglionic neurons express the transcription factor Sox10, but not Phox2b. Moreover, the formation of pelvic parasympathetic ganglia turned out to be nerve-independent because ablation of the corresponding pelvic splanchnic nerves did not influence the formation of pelvic ganglia; this is similar to the nerve-independent nature of sympathetic ganglia. Pelvic ganglia thus appear to be unlike parasympathetic ganglia that fail to form in the absence of preganglionic nerve fibers (*5*, *6*). The transcription factor signature of neurons inhabiting pelvic ganglia also had a sympathetic identity on the basis of their transcription factor expression profile, which included insulin gene enhancer protein (Isl1), GATA binding protein 3 (Gata3), and heart and neural crest derivatives expressed 1 (Hand1), but not the transcription factors H6 family homeobox 2 (Hmx2) and H6 family homeobox 3 (Hmx3); the authors identified the latter pair as markers of parasympathetic ganglia.

This discovery is very important for neuroanatomists and evolutionary-developmental biologists because it renders cranial nerves as unique. Indeed, cranial nerves are extraordinarily complex in terms of their branching, evolution, and afferent–efferent composition. Pelvic nerves were considered to be similarly complex, despite numerous other differences compared with cranial nerves. Espinosa-Medina *et al*. have now resolved this historical controversy. They and others (*5*–*7*) have shown that only cranial nerves ontogenetically give rise to the whole parasympathetic system by recruiting nerve-associated glia-like progenitor cells into parasympathetic ganglia. At the same time, the classical sympathetic system and newly relabeled sympathetic pelvic ganglia are shown to have a different origin that is solely dependent on early neural crest cell migration (*8*).

A recent exciting trend has emerged in the innovative field of biomedicine—electroceuticals (see the photo) (*9*). The idea is to directly modulate or imitate the electric stimuli that control the operation of internal organs. This approach may improve a number of health issues—for example, problems with stomach acidity, activity of kidneys, or control of sexual organs and bladder. The concept suggests that homeostasis-related problems can be addressed by harnessing the electrical activity of the body through a capacity called "neural dust" (*10*, *11*). Neural dust includes tiny autonomic electric machines with microprocessors that emit encoded signals to stimulate the autonomic nerves or even organs directly. This is conceptually similar to the highly successful approach of using brain-controlled prostheses, such as robotic arms and legs (*12*). With the findings of Espinosa-Medina *et al*., we can envision advances in this arena. To engineer working solutions, designers need to know whether local autonomic innervation is sympathetic or parasympathetic, as this is directly related to the particular molecular modulators of neuron activity, function, and information processing by the peripheral ganglia. The study of Espinosa-Medina *et al*. suggests that certain internal organs receive only sympathetic, not parasympathetic, stimuli. This new fundamental information about the neural circuitry associated with organ control may help to manipulate circuits with implantable microdevices rather than through pharmacology (see the figure). Additionally, if cell-based therapies ever reach a wide clinical stage, data about particular sympathetic–parasympathetic neuronal identity will be essential for developing cell-replacement strategies for patients with specific neuronal damage (such as loss of pelvic ganglia) as a result of trauma, cancer, or any other pathology. ■

## Electroceutical treatment

An electronic microdevice (neural dust) may replace local innervation by ganglia to control organ function.

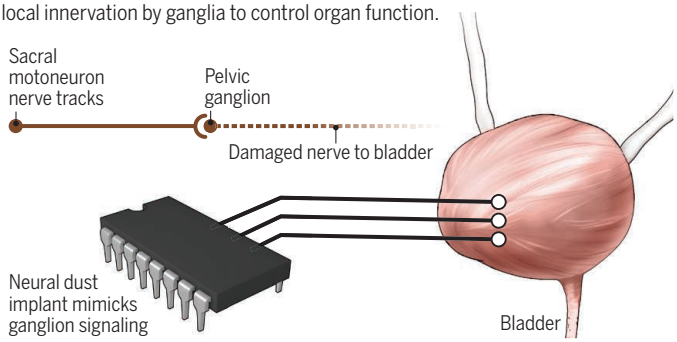


GRAPHIC: V. ALTOUNIAN/*SCIENCE*

***"This finding...brings important practical implications for...a new era of health care based on 'electroceuticals.'"***


**REFERENCES**

1. I. Espinosa-Medina *et al*., *Science* **354**, 893 (2016).
2. L. McCorry, *Am. J. Pharm. Educ.* **4**, 71 (2007).
3. M. Costa, S. J. H. Brookes, G. W. Hennig, *Gut* **47**, iv15 (2000).
4. J. R. Keast, *Int. Rev. Cytol.* **248**, 141 (2006).
5. V. Dyachuk *et al*., *Science* **345**, 82 (2014).
6. I. Espinosa-Medina *et al*., *Neurodev. Sci.* **345**, 87 (2014).
7. E. Ivashkin, E. E. Voronezhskaya, I. Adameyko, *Zoology (Jena)* **117**, 293 (2014).
8. P. Kulesa, R. McLennan, *F1000Prime Rep.* **7**, 2 (2015).
9. S. Reardon, *Nature* **511**, 393 (2014).
10. S. Makin, *Sci. Am.* (8 August 2016).
11. D. Seo *et al*., *Neuron* **91**, 529 (2016).
12. L. R. Hochberg *et al*., *Nature* **442**, 164 (2006).


10.1126/science.aal2810

Downloaded from http://science.sciencemag.org/ on November 22, 2016



Published by AAAS

QUANTUM OPTICS

# Diamond defects cooperate via light

## Silicon-vacancy centers in diamond show single-photon switching and superradiance

*By* **Ronald Hanson**

Quantum light–matter interfaces operating at optical wavelengths are key to emerging applications in quantum information processing such as distributed quantum computing and secure quantum communication (*1*). In the past decade, such interfaces have been successfully implemented across platforms ranging from trapped atoms and ions to quantum dots to defect centers in diamond. On the other hand, integrating and optically coupling several optical emitters within a single device has proven to be a more demanding goal. On page 847 of this issue, Sipahigil *et al.* (*2*) report on an all-diamond nanophotonics platform that enables efficient coupling of quantum emitters to on-chip cavities and waveguides. These results could pave the way for large on-chip quantum networks and novel quantum science experiments.

So far, most of the work with defect centers in diamond has been on the nitrogen-vacancy (NV) center. Its intrinsic spin-photon quantum interface—similar to that of trapped ions (*3*)—has been used to create quantum-entangled states of widely separated spins (*4*), which has enabled, for example, teleportation between separate diamonds (*5*). One drawback of the NV center is the broadness of its emission spectrum. For quantum information applications, photons must be coherent, and only 3% of the emission from NV centers is coherent—a major reason that entangling rates of distant spins have been low. Many efforts are ongoing to enhance this fraction through coupling to optically confined modes in cavities (*6*).

Unlike the NV center, the silicon-vacancy (SiV) center (*7*) emits roughly half of its photons coherently and, in the absence of a cavity, is more efficient as a single-photon source than the NV center. The SiV center also couples much more strongly to confined optical modes than the NV center does, making it the emitter of choice for Sipahigil *et al.* to realize the basic ingredients of an on-chip optical quantum network.

The reliable optical coupling of single defects to solid-state optical structures has been hindered by two major challenges. The emitter and the optical mode need to overlap spatially with accuracy much better than the optical wavelength within the structure, a requirement hampered by the limited accuracy of nanofabrication and placement of single emitters. Sipahigil *et al.* combine state-of-the-art nanofabrication (*8*) with Si ion implantation at specific locations within the diamond nanostructures. The positioning uncertainty of this implanting is ~40 nm, well below the SiV optical wavelength of ~300 nm within diamond. Converting implanted Si ions to SiV centers is not efficient (a few percent), precluding a fully deterministic fabrication procedure. Nonetheless, many SiVs could achieve efficient coupling of a single SiV center to a nanobeam cavity, as evidenced by an observed cooperativity near unity. These capabilities were exploited to create a device in which a single photon can open an optical transmission channel.

Another challenge toward integrated devices is the large inhomogeneous spread of emitter line widths within nanostructures caused by enhanced strain and uncontrolled surface charge. Most applications will require the photons to be indistinguishable (and therefore have the same wavelength). NV centers in separate bulk diamonds have been efficiently tuned onto resonance using local electric fields (*4*, *5*). SiV centers are less sensitive to electric fields because they are internally more symmetric than their NV-center cousin, which results in less spectral diffusion but also inhibits electrical tuning to compensate strain.

Sipahigil *et al.* solved this problem by using Raman photons instead of resonant photons. The emitters are virtually excited with a Raman laser beam that is far detuned from the optical transition, and the resulting spontaneous emission is of a photon whose wavelength can be tuned by varying the Raman laser's wavelength. Because the emitters are embedded in a waveguide structure, this process is relatively efficient, resulting in a tuning range of tens of linewidths, comparable to the variation observed for SiV centers.

With this nanophotonics platform in hand, Sipahigil *et al.* demonstrate a novel two-photon correlation effect that results from two SiV centers within a single waveguide being made to emit indistinguishable Raman photons. The key idea is that when a single photon is detected, there is no way of determining which of the two SiV centers emitted that photon. In case both SiV centers were initially prepared in the bright state so that they could both be the source of

### Superradiance in diamond

Silicon-vacancy defects in a one-dimensional diamond waveguide possess an electronic spin. Excitation of the defect with laser light leads to emission of a photon. The rate of photon emission depends on quantum entanglement.

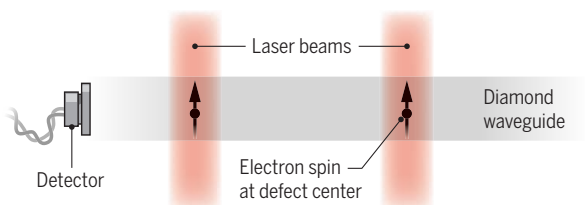


There is equal probability for each emitter to produce a photon and thereby flip the spin from up to down. If the transitions are not in resonance, the photons are distinguishable, and emission of the second photon occurs at rate Γ.

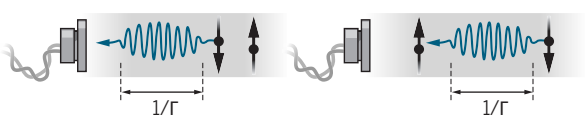


If the lasers are tuned so that the transitions are in resonance, the emitted photons are indistinguishable. Detecting the first emitted photon entangles the spins—we cannot tell which center emitted it.

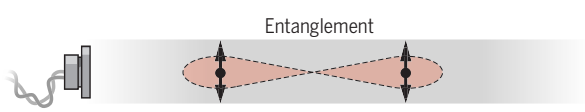


The next photon comes out of the entangled spin state at double the rate 2Γ.

GRAPHIC: C. BICKEL/*SCIENCE*

*QuTech and Kavli Institute of Nanoscience Delft, Delft University of Technology, P.O. Box 5046, 2600 GA Delft, Netherlands. Email: r.hanson@tudelft.nl*

Downloaded from http://science.sciencemag.org/ on November 22, 2016



*Published by AAAS*

the photon, quantum theory dictates that the detected photon—in retrospect—came out of a superposition of both SiV centers having emitted it. This leaves those centers in a specific entangled state that is superradiant: A second Raman photon will be emitted at a rate twice that of a single SiV center because of the coherent phase relation between the emitters. In this ideal scenario, entanglement between the two SiV centers is thus heralded by the detection of the first Raman photon.

The experiment of Sipahigil *et al.* shows a crucial step toward such on-chip heralded entanglement. Careful tuning of the Raman photon energies results in a distinctive feature in the two-photon intensity correlation measurements; the antibunching dip that is characteristic of single emitters completely vanishes once the emitted photons are made indistinguishable. Control experiments convincingly demonstrate that this feature is indeed caused by the formation of a superradiant state (see the figure). With future improvements in the initialization of the spin and charge state of SiV centers and longer spin coherence times, this procedure could yield rapid high-fidelity entanglement across the on-chip network.

Although these experiments show much potential, more research is needed to turn it into a truly scalable platform. First, if the yield of Si to SiV conversion could be increased, tens of defects could be coupled within a single integrated device. Second, the coherence time of the emitters—tens of nanoseconds for SiV centers at 4 K and limited by stimulated phonon transitions—must be improved by many orders of magnitude. One approach may be to operate at even lower temperatures, where the relevant phonon occupation is diminished (*9*). Another approach could be to apply the same platform to other defect centers. For instance, although the NV center is more susceptible to charge fluctuations, NV spin coherence times above tens of milliseconds are now routinely observed. If these challenges can be met, the result could be a versatile and powerful platform that marries fast optically mediated entanglement between long-lived quantum systems, opening the door to a new generation of quantum optics experiments and large-scale quantum information processing devices. ■

## REFERENCES


1. H. J. Kimble, *Nature* **453**, 1023 (2008).
2. A. Sipahigil *et al.*, *Science* **354**, 847 (2016).
3. C. Monroe, J. Kim, *Science* **339**, 1164 (2013).
4. B. Hensen *et al.*, *Nature* **526**, 682 (2015).
5. W. Pfaff *et al.*, *Science* **345**, 532 (2014).
6. M. Lončar, A. Faraon, *Mater. Res. Soc. Bull.* **38**, 144 (2013).
7. G. Burkard, *Physics* **7**, 131 (2014).
8. M. J. Burek *et al.*, *Nat. Commun.* **5**, 5718 (2014).
9. K. D. Jahnke *et al.*, *New J. Phys.* **17**, 043011 (2015).


10.1126/science.aak9836

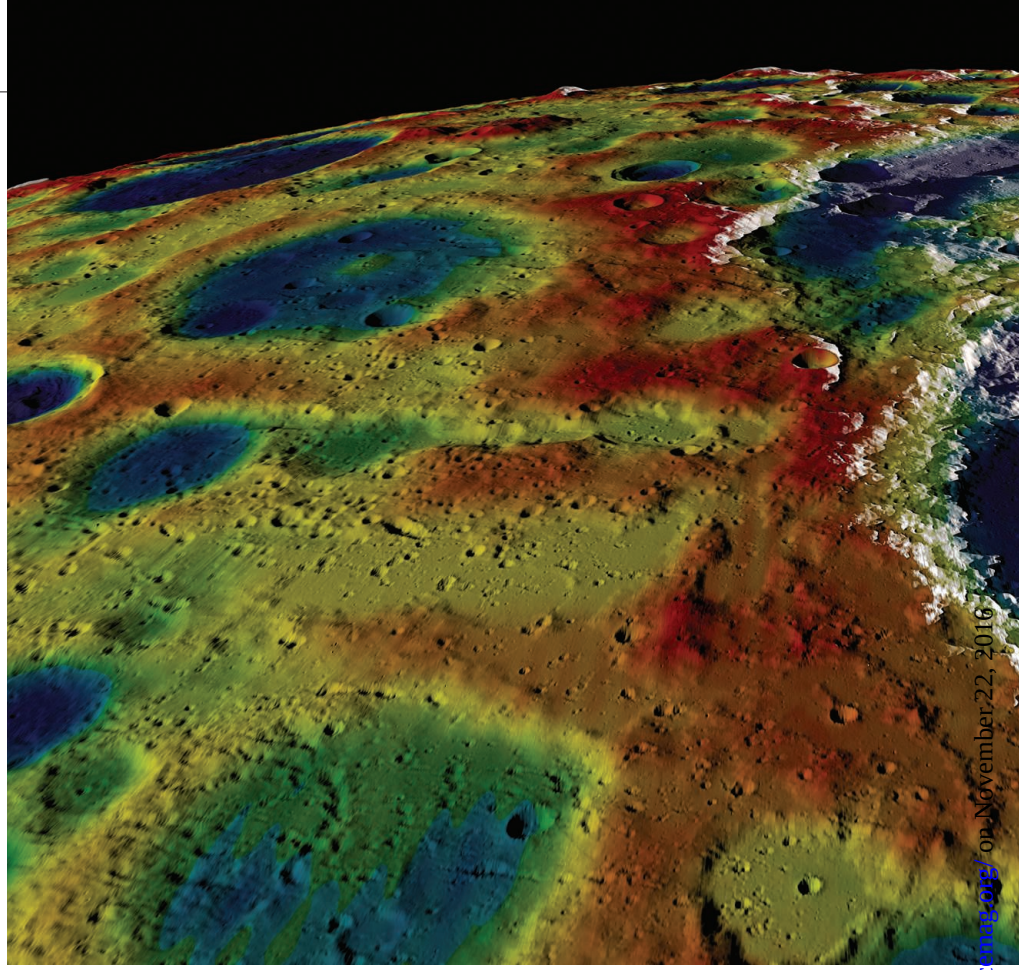

ILLUSTRATION: NASA'S SCIENTIFIC VISUALIZATION STUDIO

Downloaded from http://science.sciencemag.org/ on November 22, 2016

GEOPHYSICS

# *Revealing the dynamics of a large impact*

## Drilling into the Chicxulub crater provides constraints on how it formed

*By* **Penny Barton**

Steady as a rock. We all know what to expect of rock. Rocks deform infinitesimally slowly. Earth scientists get excited at the prospect of "rapid" plate movements that average the same speed at which our fingernails grow. Humans don't make much impact on rocks, except at the most puny of scales. Sometimes nature does experiments for us that we could never do for ourselves: When a large meteorite hits the planet, interactions occur that are far outside our normal experience. The outer surface is deformed with a force and strain rate that we cannot begin to reproduce; rocks flow like fluid, very fast and on a huge scale. On page 878 of this issue, Morgan *et al.* (*1*) present results from a drilling expedition into the Chicxulub crater that reveal how the formation of peak rings in large impact craters occurs. Numerical simulations of the impact model the time scale of events: a rim of mountains, higher than the Himalayas, adjacent to a void 25 km deep and about 70 km wide, forming and collapsing within the first three minutes; the central fluidized peak rising and collapsing in minutes 3 to 4; and a shakedown period in minutes 5 to 10, leaving a shallow crater at the surface, an intensely deformed impact zone extending through the thickness of the Earth's crust and beyond, and the world changed forever.

We see widespread evidence of meteorite impact on the rocky planets in our solar system—generally, those without active

*Department of Earth Sciences and Homerton College, University of Cambridge, Cambridge CB2 3EQ UK. Email: pb29@cam.ac.uk*



Published by AAAS

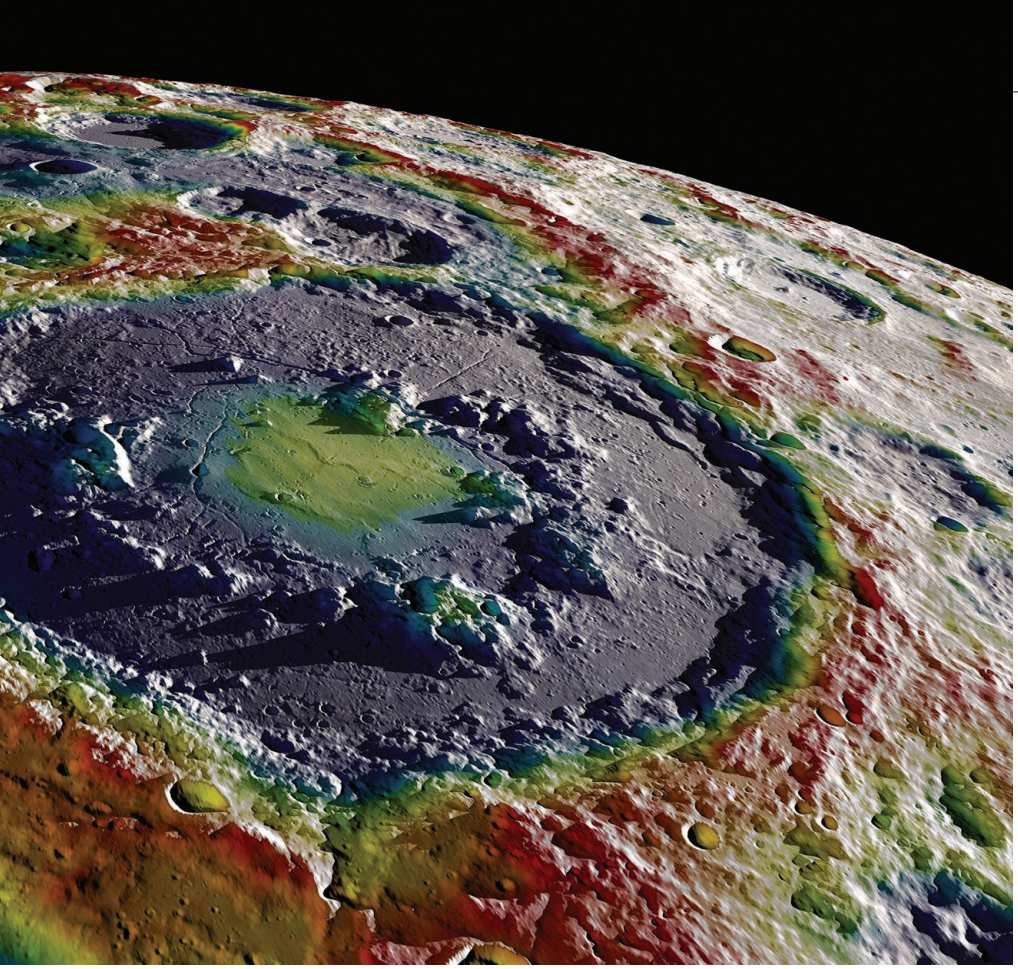

The Schrödinger crater on the Moon, from NASA's GRAIL project. Terrain image overlaid by free-air gravity field, as described in (*3*). The more continuous outer ring is the crater rim, and the discontinuous, uneven inner ring surrounding the central greenish-yellow area is the peak ring, similar to the feature drilled at Chicxulub and described by Morgan *et al*.

atmospheres or mobile surfaces. Cratering has been categorized and modeled in terms of size, and various features are observed depending on the scale of the impact (*2*). Medium-sized impacts often exhibit a central peak, which is thought to be the collapsed remnant of a rising column formed by material rushing inward to fill the void formed by the impact—much like dropping a lump of sugar into a cup of tea. At larger scales, this central peak seems to be replaced by a "peak ring," an uneven ring of rocky hills within the crater bowl (see the figure) (*3*). Because we cannot witness these processes firsthand (and would not survive them if we did), modeling provides a vital tool in understanding the environmental effects of impact (*4*). The validation and calibration of such models relies on them being able to predict all the evidence that we are able to collect, one of the most contentious aspects being the origin and formation of the peak ring.

The surface of Earth is constantly being eroded and renewed and is protected by a combustible atmosphere, so that relatively few craters are formed, and even fewer are preserved. The Chicxulub crater, which straddles the current coastline of the Yucatan region of Mexico, is a uniquely well-preserved example of a peak ring crater on Earth; its intact preservation is due to being buried under a kilometer or so of limestone, but the downside of this is that this pristine crater is very hard to access, even though it is on the same planet as we are.

Until the recent drilling expedition led by Morgan and Gulick, investigations of the Chicxulub crater principally relied on remote geophysical methods. These were used to map the crater's internal and external morphology (*5*). This morphology includes a distinct peak ring on the buried crater floor, consisting of an uneven ring of hills a few hundred meters high and a few tens of kilometers wide. Modeling suggested that the peak ring would be composed of rocks from deep within the crust, usually characterized by having a high density and transmission speed for seismic waves, which can be measured remotely. However, geophysical methods showed anomalously low transmission velocities within the peak ring rocks. The implication of this finding was that either the rocks in the peak ring were from much nearer the surface than the dynamic collapse cratering models infer, suggesting that the models were fundamentally wrong, or that the deeper crustal rocks were so comprehensively deformed that they no longer resembled their original material. The lowered transmission velocities have been correlated with rocks that have been subjected to maximum shock pressure (*6*), although exactly what mechanism would lower the seismic transmission velocity of the shocked rocks so profoundly and permanently is not yet clear. The drilling program was initiated to resolve this puzzle.

Therefore, it is a great surprise that the rocks found in this drilling program are recognizably crystalline granite basement rocks showing much of the original structure of an intrusive igneous rock from the midcontinental crust. The rocks in the drill core are crosscut by faults, dyke injections, shear zones, and shatter cones but have not been completely melted during the impact—otherwise, they would not retain their coarse crystalline texture (which takes time to form) or be able to support the numerous deformation features described. So, they do appear to come from the midcrust as predicted by the modeling. But what causes their lowered seismic velocity, as compared with that of normal rocks of this type, is not yet clear: Are the large-scale deformation features sufficient, or is there some pervasive change to the crystalline fabric of the rock, invisible to the eye?

In the shocked hours and days after the impact, tidal waves would have oscillated in and out onto the central pool of melt (*7*), causing a dramatic firework display in the otherwise sterilized landscape. The massive radiation blast was followed by global reentry of glowing ejecta from the upper atmosphere, itself turbulent from being punched through by the bolide. Conditions for some forms of life would have been drastically affected worldwide, leading to the famous end-Cretaceous mass extinction and ultimately the conditions favorable for the evolution of mammals and hence humans. At the same time, the crater itself provided a crucible for the recolonization of life, a process that has also been recorded in the rocks of this drill hole. Thus far, the findings from this project seem to validate the dynamic collapse models featured in this paper for the formation of the peak ring but, as in all the best scientific investigations, open up many new questions for further work on these exciting samples. ■

## REFERENCES


1. J. V. Morgan *et al.*, *Science* **354**, 878 (2016).
2. J. Melosh, *Impact Cratering: A Geologic Process* (Oxford Univ. Press, 1989).
3. S. Goossens *et al.*, *Geophys. Res. Lett.* **41**, 3367 (2014).
4. G. S. Collins, *J. Geophys. Res.* **119**, 2600 (2014).
5. J. V. Morgan *et al.*, *Earth Planet. Sci. Lett.* **183**, 347 (2000).
6. J. V. Morgan *et al.*, *J. Geophys. Res.* **116**, B06303 (2011).
7. P. J. Barton *et al.*, *GSA Spec. Pap.* **465**, 103 (2010).


10.1126/science.aak9802

Downloaded from http://science.sciencemag.org/ on November 22, 2016



Published by AAAS

POLICY FORUM

Land by this Little Laramie River branch, Wyoming, gives ecosystem services and cultural benefits.

ECOLOGY

# *Toward a national, sustained U.S. ecosystem assessment*

## Pieces are in place, but need coordination and policy focus

*By* **Stephen T. Jackson,[1,2] Clifford S. Duke,[3] Stephanie E. Hampton,[4] Katharine L. Jacobs,[2] Lucas N. Joppa,[5] Karim-Aly S. Kassam,[6] Harold A. Mooney,[7] Laura A. Ogden,[8] Mary Ruckelshaus,[7] Jason F. Shogren[9]**

The massive investment of resources devoted to monitoring and assessment of economic and societal indicators in the United States is neither matched by nor linked to efforts to monitor and assess the ecosystem services and biodiversity that support economic and social well-being. Although national-scale assessments of biodiversity (*1*) and ecosystem indicators (*2*) have been undertaken, nearly a decade has elapsed since the last systematic assessment (*2*). A 2011 White House report called for a national biodiversity and ecosystem services assessment (*3*), but the initiative has stalled. Our aim here is to stimulate the process and outline a credible framework and pathway for an ongoing assessment of ecosystem functioning (see the photo). A national assessment should engage diverse stakeholders from multiple sectors of society and should focus on metrics and analyses of direct relevance to policy decisions, from local to national levels. Although many technical or science-focused components are in place, they need to be articulated, distilled, and organized to address policy issues.

[1]*United States Geological Survey, Tucson, AZ 85721, USA.* [2]*University of Arizona, Tucson, AZ 85721, USA.* [3]*Ecological Society of America, Washington, DC 20036, USA.* [4]*Washington State University, Pullman, WA 99164, USA.* [5]*Microsoft Research, Redmond, WA 98052, USA.* [6]*Cornell University, Ithaca, NY 14850, USA.* [7]*Stanford University, Stanford, CA 94305, USA.* [8]*Dartmouth College, Hanover, NH 03755, USA.* [9]*University of Wyoming, Laramie, WY 82071, USA. Email:* stjackson@usgs.gov

### ASSESSMENT: THE MISSING ELEMENT

The Obama Administration, recognizing societal threats from rapid environmental change and stressors, charged the President's Council of Advisors on Science and Technology (PCAST) with identifying priorities in research, informatics, and institutional arrangements. The 2011 report (*3*) made a series of recommendations, the first of which called for a "Quadrennial Ecosystem Services Trends (QuEST) Assessment," incorporating current conditions (including biodiversity), predicted trends, syntheses linking ecosystem properties to ecosystem services, existing and emerging threats, and potential policy responses (*3*). This assessment was intended to serve as a foundation for the other recommendations, which were that the U.S. federal government (i) identify actions and policies affecting ecosystem services and biodiversity; (ii) incorporate ecosystem-services impacts into planning and management decisions; (iii) integrate, disseminate, and use relevant data and data products; and (iv) support and participate in relevant international initiatives. Substantial progress has been made on all of these recommendations except the national assessment; continued progress on the other recommendations is hampered in its absence. A systematic national assessment program is needed to identify potential risks, determine priorities, identify trends, and evaluate decisions and actions.

A government-wide milestone deriving from the PCAST report was a 2015 White House memorandum instructing federal agencies to incorporate ecosystem services into decision-making (*4*). Yet without context and reference points provided by a comprehensive national assessment, it will be difficult to assess government decisions aimed at enhancing or protecting ecosystem services.

The PCAST report (*3*) laid out an ambitious vision for Ecoinformatics-based Open Resources and Machine Accessibility (EcoINFORMA) to support and coordinate government-wide informatics related to biodiversity and ecosystem services and to facilitate assessments and other integrative activities. A Web-based platform has been established with three hubs to leverage partnerships with universities, nongovernmental organizations (NGOs), and other entities outside government. However, the national assessment they were intended to facilitate has failed to ma-

PHOTO: S. T. JACKSON

Downloaded from http://science.sciencemag.org/ on November 22, 2016



Published by AAAS

terialize. EcoINFORMA would benefit from more comprehensive integration and direction of the kind provided by an assessment program. For example, the Biodiversity Information Serving Our Nation (BISON) hub provides an excellent resource for researchers, but is not designed to deliver products or metrics of direct use to decision-makers.

PCAST recommended U.S. participation in and support for international initiatives, notably the Intergovernmental Science-Policy Platform on Biodiversity and Ecosystem Services (IPBES) (*5*). The United States has been involved in IPBES; the Department of State is recruiting U.S. scientists to participate. Scientists from federal agencies are involved in IPBES, including regional and global assessments. These assessments were intended to build on national assessments, and the regional assessment of the Americas (covering the entire Western Hemisphere) cannot substitute for a national assessment focused specifically on national policy concerns. Several countries have recently conducted ecosystem, ecosystem services, or biodiversity assessments (*6*–*9*) that have informed policy (*10*). By failing to implement a national assessment, the United States is missing an opportunity to provide leadership and contribute to and benefit from IPBES.

Most important, the accelerating pace of environmental change lends urgency to a comprehensive national assessment program. The 2012 RESTORE Act (*11*) includes objectives for ecosystem recovery in the Gulf of Mexico region, and better baselines are needed. Persistent drought in southwestern states is driving widespread forest dieback and disturbance (*12*) and placing severe stresses on water delivery systems (*13*). Rapid decline of native bees in Hawai'i has led to their recent listing under the Endangered Species Act (*14*). These and other dramatic changes in the past few years—largely dealt with on an ad hoc basis as they arise—speak to the need for systematic and comprehensive monitoring, which will help anticipate problems before they reach crisis stage and will identify losses and restoration targets when crises emerge. A national assessment would organize and aggregate baseline information that can prove useful in a crisis, and analyses of trends in indicators aggregated at local, regional, and national scales would help identify potential threats.

## AWAITING A CONDUCTOR AND A SCORE

To date, no champions have emerged from within the federal government with sufficient resources for a national assessment at a meaningful scale. Progress has been made in characterizing ecosystem services (*15*) and identifying how they can be incorporated into federal decision-making (*16*, *17*). Individual federal science agencies, enforcement agencies, and resource-management agencies administer diverse monitoring and inventory programs. A 2013 White House directive (*18*) is driving development of platforms for data sharing and delivery in federal science agencies, which could be integrated into a national assessment program. Many states, tribes, NGOs, and private-sector entities have monitoring and analytical capacities, and the National Science Foundation supports ecological monitoring programs. Yet a centralized process—guided by policy-relevant questions, methodologies, and reporting structures—is lacking. A fully instrumented orchestra is seated in the concert hall, awaiting a conductor and a coherent score.

The transition to a new presidential administration represents a unique opportunity. A successful and well-vetted model for a national assessment was developed by the Federal Advisory Committee that prepared the third National Climate Assessment (NCA) report. Its members debated alternative structures, concluding that a sustained process, partnering government and nongovernment entities, would yield stakeholder-relevant products, capacity-building, and scientific credibility (*19*). This model was used in the third NCA, which provides a number of lessons for other assessments (*20*, *21*). On the basis of this recent example, we suggest that a national ecosystem assessment can be more scientifically rigorous and more useful to decision-makers if it is developed as an ongoing process involving external partners, rather than a periodic event owned and prescribed entirely by the federal government. The goal is to achieve an evolving record of conditions, documented using well-articulated methodologies, in contrast to periodic assessments that may comprise shifting arrays of methods, assumptions, and priorities.

Although federal government leadership will be critical in providing links to policy and furnishing national-scale infrastructure and capacity, a biodiversity and ecosystem services assessment could be developed in a partnership between NGOs; philanthropic foundations; private-sector entities; agencies of the U.S. government; and selected state, local, and tribal agencies. A sustained assessment effort can be strategically phased to require relatively low levels of resources on an annual basis, with topical and regional assessments phasing in and out, and real-time links to NCA reports and public databases via EcoINFORMA. Inclusion of multiple institutional partners can bring an array of in-kind and funding resources, ensuring a stable future from a resource perspective (*20*).

Such an approach requires long-term commitment to the process and strong integration with at least one and preferably multiple federal science agencies. The community will need to be creative in bridging the public-private divide and should look to innovative models (e.g., the National Park Foundation).

Historically, the United States has been a leader in responsible management of public lands, stewardship of water and timber, conservation of migratory and endangered species, and protection of air and water quality. Similarly, it has led development and application of key indicators of economic performance, social welfare, and public health. We call on the White House transition team, and colleagues in government, academic, NGO, and business sectors, to build on this legacy by launching a national biodiversity assessment commensurate with our natural and cultural heritage and with our needs to preserve the natural systems that sustain us. ■

## REFERENCES AND NOTES


1. B. A. Stein, L. S. Kutner, J. S. Adams, Eds., *Precious Heritage: The Status of Biodiversity in the United States* (Oxford Univ. Press, New York, 2000).
2. The H. John Heinz III Center for Science, Economics, and the Environment, *The State of the Nation's Ecosystems* (Island Press, Washington, DC, 2008).
3. PCAST, "Report to the president: Sustaining environmental capital: Protecting society and the economy" (White House, Washington, DC, 2011).
4. S. Donovan, C. Goldfuss, J. Holdren, "Incorporating Ecosystem Services into Federal Decision Making" (White House, Washington, DC, 2015); http://bit.ly/2el5SE7.
5. S. Díaz *et al.*, *Curr. Opin. Environ. Sustain.* **14**, 1 (2015).
6. Z. Ouyang *et al.*, *Science* **352**, 1455 (2016).
7. J. Sarukhán, L. Curzio, W. Reed, R. Dirzo, "Natural capital of Mexico, Synopsis: Current knowledge, evaluation, and prospects for sustainability" (Comisión Nacional para el Conocimiento y Uso de la Biodiversidad, Mexico City, 2010).
8. Sistema Nacional de Áreas de Conservación (SINAC), "V Informe nacional al convenio sobre la diversidad biológica, Costa Rica" (Global Environment Facility–United Nations Development Programme, San José, Costa Rica, 2014)
9. U.K. Department for Environment, Food, and Rural Affairs, "Biodiversity 2020: A strategy for England's wildlife and ecosystem services" (Defra, London, 2015); www.gov.uk/defra.
10. J. Sarukhán, R. Jiménez, *Curr. Opin. Environ. Sustain.* **19**, 153 (2016).
11. Resources and Ecosystems Sustainability, Tourist Opportunities, and Revived Economies of the Gulf Coast States Act, Pub. L. No. 112-141, §1604 (2012).
12. C. I. Millar, N. L. Stephenson, *Science* **349**, 823 (2015).
13. W. Yardley, *LA Times*, 6 July 2016; http://lat.ms/2eDAKuR.
14. S. Guertin, "Endangered and threatened wildlife and plants; endangered status for 49 species from the Hawaiian Islands: A rule by the Fish and Wildlife Service on 09/30/2016." *Fed. Regist.* **81**, 67786 (2016).
15. W. R. Munns Jr. *et al.*, *Integr. Environ. Assess. Manag.* **12**, 522 (2016).
16. L. Scarlett, J. Boyd, *Ecol. Econ.* **115**, 3 (2015).
17. M. Schaefer, E. Goldman, A. M. Bartuska, A. Sutton-Grier, J. Lubchenco, *Proc. Natl. Acad. Sci. U.S.A.* **112**, 7383 (2015).
18. Office of Science Technology and Policy, "Memorandum for the heads of executive departments and agencies: Increasing access to the results of federally funded scientific research" (Executive Office of the President, Washington, DC, 2013).
19. J. L. Buizer *et al.*, "Preparing the nation for change: Building a sustained national climate assessment process" (National Climate Assessment Development and Advisory Committee, U.S. Global Change Research Program, Washington, DC, 2013).
20. J. L. Buizer *et al.*, *Clim. Change* **135**, 23 (2016).
21. S. C. Moser *et al.*, *Clim. Change* **135**, 187 (2016).


## ACKNOWLEDGMENTS

This paper was supported by the NSF (grant DBI-1415669). We thank K. Quach for assistance in preparing the manuscript and R. Sayre and anonymous reviewers for valuable comments.

10.1126/science.aah5750

Downloaded from http://science.sciencemag.org/ on November 22, 2016



Published by AAAS

LETTERS

*Edited by* **Jennifer Sills**

# The dual components of mental health

IN THEIR RESEARCH Article "Reconciling after civil conflict increases social capital but decreases individual well-being" (13 May, p. 787), J. Cilliers *et al.* found that although reconciliation techniques helped communities in war-torn Sierra Leone recover from conflicts, individuals suffered negative mental health consequences. This disturbing conclusion raises questions about what might be a valuable social intervention. However, Cilliers *et al.*'s assessment may not tell the whole story because it is based on a one-dimensional model of mental health.

Mental health has dual, relatively independent components (*1*). Cilliers *et al.* assessed negative components such as post-traumatic stress disorder, depression, and anxiety, but they did not assess positive components such as happiness, optimism, purpose in life, gratitude, and mindfulness. These variables are powerful buffers, enhancing human resilience in the face of stressful life events (*2*). The presence of negative components does not mean the absence of positive components (*3*).

The reconciliation program in Sierra Leone may well have had favorable effects on the mental health of the individuals experiencing it, in addition to the negative effects found by Cilliers *et al.* The call for policy-makers to restructure reconciliation processes to "reduce their negative psychological costs" is indeed a valuable suggestion. That said, it seems prudent to withhold judgment until a more effective assessment is performed.

***John W. Reich***

Department of Psychology, Arizona State University, Tempe, AZ 85282, USA. Email: john.reich@asu.edu

**REFERENCES**

1. A. J. Zautra, C. A. Guarnaccia, J. W. Reich, *J. Consult. Clin. Psychol.* **56**, 514 (1988).
2. M. Kent, M. C. Davis, J. W. Reich, Eds., *The Resilience Handbook: Approaches to Stress and Trauma* (Routledge, 2014).
3. J. W. Reich, A. J. Zautra, M. C. Davis. *Rev. Gen. Psychol.* **7**, 66 (2003).

10.1126/science.aah5251

## Response

REICH SUGGESTS THAT we should look at other psychological outcomes. He posits that if we had examined positive psychological outcomes, we might have uncovered opposite effects. For example, happiness may have increased even though people were more depressed, anxious, and traumatized. Although we think scholars should continue probing other outcomes, we believe that this particular scenario is unlikely.

Decades of psychology research cited in Reich's own review (*1*) suggest that responses in the positive and negative domains either move inversely to produce effects in the same direction (*2*–*4*) or that they do not move together at all (*5*–*7*). This evidence suggests that we likely would have found that happiness had fallen or remained unchanged in conjunction with increased depression and anxiety after community reconciliation in Sierra Leone.

Of course, there are exceptions. For example, individuals may reappraise negative events as positive events if they survive crises and believe that survival fosters personal growth and resilience (*8*, *9*). However, in Reich's own assessment, "perceptions of positive gain from negative experiences may be mostly illusionary" [(*7*), p. 127]. Indeed, individuals who reappraised negative outcomes as positive for reasons like personal growth were not found to be less vulnerable to future stressors (*10*). This suggests that in studying reconciliation, if we look at outcomes such as life satisfaction, where positive effects may appear, we should also verify how these outcomes relate to measures like psychological resilience, to fully interpret the effects.

Even if other positive effects do exist, we find it difficult to agree with Reich's conclusion that one should "withhold judgment" about the effects of the reconciliation project. The effects we documented—increased depression, anxiety, and post-traumatic stress disorder—are all important measures of psychological well-being. If other positive effects exist (beyond those that we show for forgiveness), these would still have to be balanced against the existing negative effects. This trade-off underscores our call to policy-makers: Reconciliation processes should be restructured so as to minimize their negative consequences.

***Jacobus Cilliers,[1] Oeindrila Dube,[2]* Bilal Siddiqi[3]***

[1]McCourt School of Public Policy, Georgetown University, Washington, DC 20057, USA. [2]Harris School of Public Policy, University of Chicago, Chicago, IL 60637, USA. [3]World Bank, Washington, DC 20433, USA.

*Corresponding author. Email: odube@uchicago.edu

**REFERENCES**

1. J. W. Reich, A. J. Zautra, M. C. Davis. *Rev. Gen. Psychol.* **7**, 66 (2003).
2. C. Wang *et al.*, *J. Clin. Endocrin. Metab.* **81**, 3578 (1996).
3. A. A. Stone, E. Kennedy-Moore, J. M. Neale, *Health Psychol.* **14**, 341 (1995).
4. M. van Eck, N. A. Nicolson, J. Berkhof, J. Sulon, *Biol. Psychol.* **43**, 69 (1996).
5. B. Knutson *et al.*, *Am. J. Psychiatr.* **155**, 373 (1998).
6. J. T. Cacioppo, W. L. Gardner, G. G. Berntson, *J. Personal. Soc. Psychol.* **76**, 839 (1999).
7. A. K. Zautra, J. W. Reich, *J. Commun. Psychol.* **11**, 121 (1983).
8. B. A. Baldwin, *Am. J. Orthopsychiat.* **48**, 538 (1978).
9. G. Caplan, *Principles of Preventive Psychiatry* (Basic Books, New York, 1964).
10. D. Goodhart, "Cognitive resolution of ordinary life crises and psychological well-being," Doctoral dissertation (Arizona State University, 1980).

10.1126/science.aai7397

People walk through the town of Kailahun in Sierra Leone in 2012. Reconciliation efforts in the wake of the country's vicious civil war have been found to have complex and sometimes counterintuitive effects on mental health.

PHOTO: FINBARR O'REILLY/REUTERS

# NIH's mentoring makes progress

A 2012 REPORT by the National Institutes of Health (NIH) Advisory Committee to the Director highlighted the unacceptable lack of diversity among biomedical and

Downloaded from http://science.sciencemag.org/ on November 22, 2016



Published by AAAS

behavioral researchers and recommended a comprehensive strategy, including a call to improve research mentoring and career preparation (*1*). We commend NIH for launching and supporting the Diversity Program Consortium, which includes the National Research Mentoring Network (NRMN) (*2*), as one response to this critical need. As J. Mervis points out in his News Feature "Mentoring's moment" (2 September, p. 980), measurable change in the workforce's demographic composition takes time and cannot be achieved solely by one program. Despite the challenges, NRMN leaders, and all of those working toward its success, are deeply committed to implementing a national mentoring program to advance a more inclusive research training enterprise.

NRMN has made progress. In 2 years, more than 2000 mentors have participated in NRMN mentor training and 2500 mentees (75% from underrepresented groups) have engaged in NRMN, 225 of them with NRMN's intensive grantsmanship coaches. NRMN has developed and implemented a multifaceted program to enhance national efforts to increase, size, quality, diversity, and research productivity of the biomedical workforce. NRMN programs match and link mentees across career stages to mentors and coaches; train mentors, coaches, and mentees to more effectively navigate their relationships, with a focus on cultural responsivity; refer mentees to career and research resources; and promote the value of career mentoring. Initial feedback has been positive: Mentors trained by NRMN have indicated that both their knowledge of targeted mentoring competencies and their confidence have substantially increased. We hope to build on this success by refining and expanding our training program in the future.

***Jamboor Vishwanatha,[1] Christine Pfund,[2] Elizabeth Ofili,[3] Kolawole Okuyemi[4]****

[1]Texas Center for Health Disparities, University of North Texas Health Science Center, Fort Worth, TX 76107, USA. [2]Center for the Improvement of Mentored Experiences in Research, University of Wisconsin-Madison, Madison, WI 53706, USA. [3]Clinical Research Center, Morehouse School of Medicine, Atlanta, GA 30310, USA. [4]Department of Family Medicine and Community Health, University of Minnesota Medical School, Minneapolis, MN 55414, USA.

*Corresponding author. Email: kokuyemi@umn.edu

## REFERENCES

1. NIH, "Draft Report of the Advisory Committee to the Director Working Group on Diversity in the Biomedical Research Workforce" (2012); http://acd.od.nih.gov/diversity%20in%20the%20biomedical%20research%20workforce%20report.pdf.
2. National Research Mentoring Network (www.nrmnet.net).

10.1126/science.aal1898



Published by AAAS

Downloaded from http://science.sciencemag.org/ on November 22, 2016

# RESEARCH

Magnetic dipoles can manipulate light at the nanoscale

*Kuznetsov* et al., *p. 846*

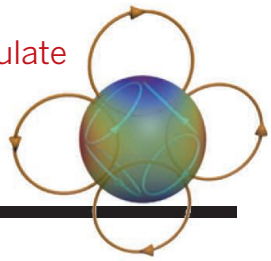

## IN *SCIENCE* JOURNALS

*Edited by* **Stella Hurtley**

A small-scale eruption of Mount Aso was also recorded in April 2016.

GEOPHYSICS

### A volcanic end to an earthquake

The dangerous and active Aso volcanic cluster appears to have put an early end to the damaging magnitude 7.1 Kumamoto earthquake that struck Japan in April 2016. Lin *et al.* found that the fault rupture stopped underneath the Aso caldera. The unzipping of the fault ended where the rocks went from cold and brittle to a more liquid-like magmatic mush. This distinctive example shows how abrupt changes in rock properties can terminate fault rupture and cap the size of an earthquake. —BG

*Science*, this issue p. 869

PLANT SCIENCE

### Faster light adaptation improves productivity

Crop plants protect themselves from excess sunlight by dissipating some light energy as heat, readjusting their systems when shadier conditions prevail. But the photosynthetic systems do not adapt to fluctuating light conditions as rapidly as a cloud passes overhead, resulting in suboptimal photosynthetic efficiency. Kromdijk *et al*. sped up the adaptation process by accelerating interconversion of violaxanthin and zeaxanthin in the xanthophyll cycle and by increasing amounts of a photosystem II subunit. Tobacco plants tested with this system showed about 15% greater plant biomass production in natural field conditions. —PJH

*Science*, this issue p. 857

PLANT SCIENCE

### Metabolite channeling by a dynamic metabolon

The specialized metabolite dhurrin breaks down into cyanide when plant cell walls have been chewed, deterring insect pests. Laursen *et al*. found that the enzymes that synthesize dhurrin in sorghum assemble as a metabolon in lipid membranes (see the Perspective by Dsatmaichi and Facchini). The dynamic nature of metabolon assembly and disassembly provides dhurrin on an as-needed basis. Membrane-anchored cytochrome P450s cooperated with a soluble glucosyltransferase to channel intermediates toward efficient dhurrin production. —PJH

*Science*, this issue p. 890; see also p. 829

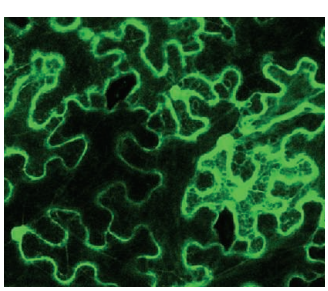

**Dhurrin synthetic enzyme (green) revealed in plant cells**

ORGANIC CHEMISTRY

### Pluses and minuses of BTX behavior

Batrachotoxin is a potent neurotoxin produced by the endangered Colombian poison dart frog and is an agonist of voltage-gated sodium ion channels (NaVs). Logan *et al*. developed a chemical synthesis of this molecule, denoted (−)-BTX, by taking advantage of a tin hydride–mediated radical cyclization to stitch together the polycyclic framework. Using an analogous route, they also prepared the non-natural mirror image, (+)-BTX. Conversely to the natural product, (+)-BTX antagonized NaVs. —JSY

*Science*, this issue p. 865

CREDITS (FROM TOP): KUZNETSOV *ET AL.*; KYODO KYODO/REUTERS PICTURES; LAURSEN *ET AL.*



Published by AAAS

ACTIVE MATTER

## Directing traffic with patterns

Biological entities, such as bacteria, may direct their motion in response to their environment, but this usually does not lead to large-scale patterns or collective behavior. Peng *et al*. found that the orientational ordering of a liquid crystal could direct the flow of self-propelling bacteria, which in turn influenced the patterning of the liquid crystal molecules. Patterns on a substrate caused surface anchoring of the liquid crystals that transmitted to the ordering of the bacteria, thus imparting control on what would otherwise be chaotic out-of-equilibrium behavior. —MSL

*Science*, this issue p. 882

DNA METHYLATION

## Combating parasitic DNA by methylation

DNA methylation plays an important role in repressing the expression of "parasitic" DNAs, such as transposable elements, which have invaded our genomes. Mammals have three DNA methyltransferase enzymes. Barau *et al*. discovered a fourth DNA methyltransferase enzyme in mice. The enzyme DNMT3C is a duplication of DNMT3B and is found in male germ cells. There it targets evolutionarily young transposons, of which there is a heavy burden in the mouse genome. DNMT3C methylates and silences the young transposons, preserving male fertility. —GR

*Science*, this issue p. 909

NEURODEGENERATION

## Tau phosphorylation—not all bad

Alzheimer's disease presents with amyloid-β (Aβ) plaques and tau tangles. The prevailing idea in the field is that Aβ induces phosphorylation of tau, which in turn mediates neuronal dysfunction. Working in Alzheimer's disease mouse models, Ittner *et al*. found evidence for a protective role of tau in early Alzheimer's disease. This protection involves specific tau phosphorylation at threonine 205 at the postsynapse. A protective role of phosphorylated tau in disease challenges the dogma that tau phosphorylation only mediates toxic processes. —SMH

*Science*, this issue p. 904

DRUG DELIVERY

## Toward malaria eradication

Even though we know how to prevent malaria, we have failed to eliminate this damaging disease. Bellinger et al. designed an easy-to-administer device that provides long-lasting delivery of an antimalarial drug. A star-shaped, drug-containing material is packaged into a capsule. When swallowed, the capsule dissolves in the stomach and the star unfolds, assuming a shape that cannot pass further down the intestine. The star delivers the anti-malarial drug for weeks, but eventually falls apart and passes harmlessly out of the body. —KLK

*Sci. Transl. Med.* **8**, 365ra157 (2016).

TYPE 1 DIABETES

## Exhausting autoimmunity

In the case of autoimmune diseases, such as type 1 diabetes, so-called "exhausted" T cells may be the answer to stopping disease. Long et al. report that the best responses in type 1 diabetics treated with teplizumab, a monoclonal antibody against CD3, were associated with $CD8^+$ T cells with features of exhausted T cells. These cells recognized a broad spectrum of autoantigens but proliferated less than nonexhausted cells ex vivo. However, they were not terminally exhausted: Stimulation with a ligand for the inhibitory receptor TIGIT further down-regulated their activation. Inducing T cell exhaustion may thus represent a potential therapeutic approach in type 1 diabetes. —ACC

*Sci. Immunol.* **1**, eaai7793 (2016).

# IN OTHER JOURNALS

*Edited by* **Caroline Ash** *and* **Jesse Smith**

Hubble eXtreme Deep Field view of distant galaxies

URBAN ECOLOGY

## $C_4$ plants in the heat of the city

Cities tend to have a warmer microclimate than their surroundings—the so-called "urban heat island" effect. The elevated temperature, along with other aspects of the urban environment, can have a marked influence on the organisms that live in cities. Duffy and Chown find that plants with $C_4$ photosynthetic metabolism, a trait that is favored in warmer herbaceous communities, are more common in European cities than in adjacent nonurban habitats. They predict that under further climatic warming, $C_4$ species may become generally more widespread in temperate habitats, compared with $C_3$ species that are adapted to cooler conditions. —AMS

*J. Ecol.* **104**, 1618 (2016).

METABOLISM

## Small RNA regulates glucose homeostasis

Noncoding RNAs, such as microRNAs, regulate gene expression through RNA silencing and posttranscriptional gene regulation. Lin *et al.* show that miR-155 is important for glucose homeostasis and insulin sensitivity. When miR-155 is

Higher temperatures in cities select for $C_4$ plants.

PHOTOS: (FROM TOP) NASA, ESA, G. ILLINGWORTH, D. MAGEE, AND P. OESCH, R. BOUWENS, HUDF09 TEAM; MATTHIAS SCHOLZ/ALAMY STOCK PHOTO



Published by AAAS

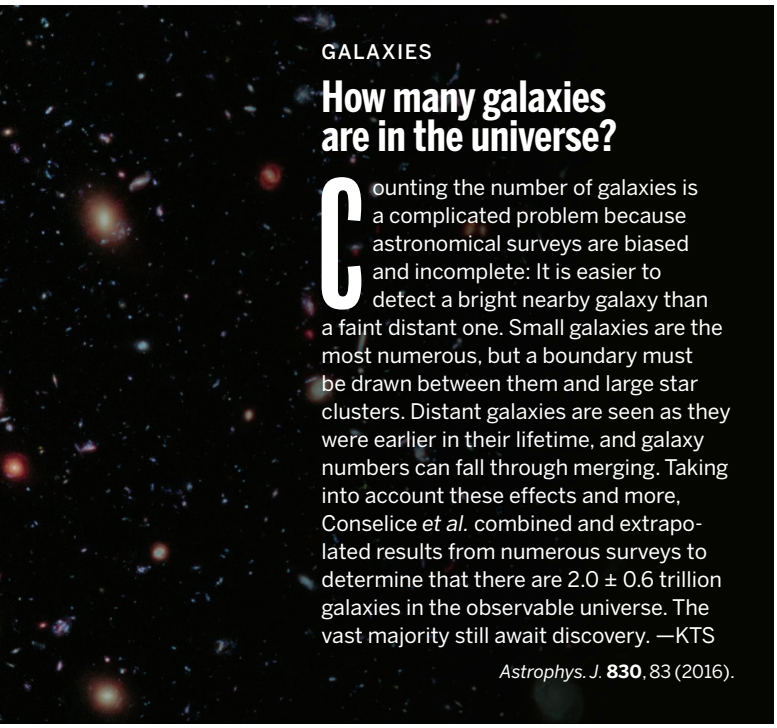

GALAXIES

## How many galaxies are in the universe?

Counting the number of galaxies is a complicated problem because astronomical surveys are biased and incomplete: It is easier to detect a bright nearby galaxy than a faint distant one. Small galaxies are the most numerous, but a boundary must be drawn between them and large star clusters. Distant galaxies are seen as they were earlier in their lifetime, and galaxy numbers can fall through merging. Taking into account these effects and more, Conselice *et al.* combined and extrapolated results from numerous surveys to determine that there are 2.0 ± 0.6 trillion galaxies in the observable universe. The vast majority still await discovery. —KTS

*Astrophys. J.* **830**, 83 (2016).

overexpressed in mice, they become hypoglycemic, whereas if miR-155 is deleted, the result is hyperglycemia and insulin resistance. miR-155 does not seem to alter pancreas morphology or β-cell function; instead, it appears to act on negative regulators of insulin signaling, such as C/EPBb, HDAC4, and SOCS1. Patients with type 2 diabetes show reduced miR-155, suggesting that it may also be involved in human insulin signaling. The discovery of this microRNA function opens a window of opportunity for the treatment of diabetes through glycemic control. —BAP

*PLOS Genet.* 10.1371/journal.pgen.1006308 (2016).

TISSUE REPAIR

## Getting one's joint out of nose

Articular cartilage lubricates joints and is essential for pain-free movement. Unlike other tissues, injured cartilage does not repair on its own. One common treatment involves harvesting cartilage-secreting cells called chondrocytes from the injured joint, expanding the cells in culture for a few weeks, and then implanting them back into the joint. Animal studies suggest that chondrocytes from a different tissue source, the nose, are better at regenerating articular cartilage. Mumme *et al.* tested this less invasive procedure in a pilot study of 10 patients with knee injuries. In all cases, they successfully produced cartilage tissue ex vivo by using chondrocytes taken from the nasal septum. All patients reported an improvement in clinical scores for pain, knee function, and quality of life. —PAK

*Lancet* **388**, 1985 (2016).

PALEOANTHROPOLOGY

## Farmer-foragers went west

Humans began to settle and combine farming with foraging about 12,000 years ago. Over the next 2000 to 3000 years, they moved west from the Fertile Crescent into Anatolia, although it seems, from the distribution of obsidian flints, that the eastern and western populations kept in contact. Kılınç *et al.* obtained genome sequence data from nine Neolithic individuals from two ancient village sites in Anatolia. The settlers from the older site were distinct from their European forager counterparts but, like them, showed little genetic diversity, indicating a small population. The later farmer-settlers, who had acquired pottery-making skills, were genetically more diverse. These data point to an additional wave of migration from the Fertile Crescent or the Levant that brought new genes and promoted further westward expansion before the mobile hunter-gatherers of the northern steppes added their genes to the European mix. —CA

*Curr. Biol.* **26**, 2659 (2016).

CATALYSIS

## Longer lifetimes for a metal oxide

Although heterogeneous molybdenum catalysts can convert cyclohexene to its epoxide with high conversion and selectivity, the catalysts deactivate quickly because the Mo species leach into solution. Noh *et al.* show that a more stable catalyst can be made by depositing Mo via a metallorganic complex onto the zirconium oxide nodes within the metal organic framework (MOF) NU-1000. After exposure to air to form the Mo oxide species, this catalyst showed activity comparable to that of epoxidation of Mo supported on $ZrO_2$. However, the $ZrO_2$ support lost 80% of its Mo after reaction, whereas no loss of Mo occurred for the MOF catalyst. Density functional theory calculations indicate that the loss of Mo(VI) from the MOF Zr node is energetically unfavorable. —PDS

*J. Am. Chem. Soc.* 10.1021/jacs.6b08898 (2016).

ANTIBIOTIC RESISTANCE

## No silver bullet for wastewater treatment

The spread of antibiotic resistance is a major public health concern. Czekalski *et al.* investigate whether ozonation of wastewater can help to combat this spread by eliminating resistant bacteria. In laboratory experiments, ozone doses that can be used in full-scale applications disrupted intracellular resistance genes. However, ozonation of secondary effluent at a wastewater treatment plant did not affect the abundance of intracellular resistance genes, and multiresistant bacteria partly regrew after ozonation. The results have important implications for wastewater treatment plants that are planning to implement ozonation. —JFU

*Environ. Sci. Technol.* 10.1021/acs.est.6b02640 (2016).

**Fragment of a clay pot discovered at Tepecik Çiftlik, Turkey**

PHOTO: IMAGES & STORIES/ALAMY STOCK PHOTO



Published by AAAS

## ALSO IN *SCIENCE* JOURNALS

*Edited by* **Stella Hurtley**

APPLIED OPTICS

### A clear approach to nanophotonics

The resonant modes of plasmonic nanoparticle structures made of gold or silver endow them with an ability to manipulate light at the nanoscale. However, owing to the high light losses caused by metals at optical wavelengths, only a small fraction of plasmonics applications have been realized. Kuznetsov *et al*. review how high-index dielectric nanoparticles can offer a substitute for these metals, providing a highly flexible and low-loss route to the manipulation of light at the nanoscale. —ISO

*Science*, this issue p. 846

QUANTUM OPTICS

### Integrated quantum nanophotonics

Technologies that exploit the rules of quantum mechanics offer a potential advantage over classical devices in terms of sensitivity. Sipahigil *et al*. combined the quantum optical features of silicon-vacancy color centers with diamond-based photonic cavities to form a platform for integrated quantum nanophotonics (see the Perspective by Hanson). They could thus generate single photons from the color centers, optically switch light in the cavity by addressing the state of the color center, and quantum-mechanically entangle two color centers positioned in the cavity. The work presents a viable route to develop an integrated platform for quantum networks. —ISO

*Science*, this issue p. 847; see also p. 835

ORGANIC CHEMISTRY

### CO takes the lead to make β-lactam rings

Strained β-lactam rings are a key feature of penicillin and some other drugs. Willcox *et al*. designed a versatile route to these four-membered ring motifs through the palladium-catalyzed coupling of carbon monoxide with secondary amines. The bulky carboxylate ligand appears to facilitate preliminary CO incorporation into a Pd anhydride, which is then attacked by the amine to set up ring closure via C–H activation. This approach broadens the substrate scope compared with a previous scheme in which C–H activation preceded CO insertion. —JSY

*Science*, this issue p. 851

SOLAR CELLS

### Tandem perovskite cells

The ready processability of organic-inorganic perovskite materials for solar cells should enable the fabrication of tandem solar cells, in which the top layer is tuned to absorb shorter wavelengths and the lower layer to absorb the remaining longer-wavelength light. The difficulty in making an all-perovskite cell is finding a material that absorbs the red end of the spectrum. Eperon *et al*. developed an infrared-absorbing mixed tin-lead material that can deliver 14.8% efficiency on its own and 20.3% efficiency in a four-terminal tandem cell. —PDS

*Science*, this issue p. 861

NANOMATERIALS

### Watching it all fall apart

The control of the shape and size of metal nanoparticles can be very sensitive to the growth conditions of the particles. Ye *et al*. studied the reverse process: They tracked the dissolution of gold nanoparticles in a redox environment inside a liquid cell within an electron microscope, controlling the particle dissolution with the electron beam. Tracking short-lived particle shapes revealed structures of greater or lesser stability. The findings suggest kinetic routes to particle sizes and shapes that would otherwise be difficult to generate. —MSL

*Science*, this issue p. 874

GEOLOGY

### Drilling into Chicxulub's formation

The Chicxulub impact crater, known for its link to the demise of the dinosaurs, also provides an opportunity to study rocks from a large impact structure. Large impact craters have "peak rings" that define a complex crater morphology. Morgan *et al*. looked at rocks from a drilling expedition through the peak rings of the Chicxulub impact crater (see the Perspective by Barton). The drill cores have features consistent with a model that postulates that a single over-heightened central peak collapsed into the multiple-peak-ring structure. The validity of this model has implications for far-ranging subjects, from how giant impacts alter the climate on Earth to the morphology of crater-dominated planetary surfaces. —BG

*Science*, this issue p. 878; see also p. 836

NEURODEVELOPMENT

### Sacral neurons reassigned

The autonomic nervous system regulates the function of internal organs such as the gut. The parasympathetic and sympathetic arms of this system tend to operate antagonistically. Espinosa-Medina *et al*. used anatomical and molecular analyses to reevaluate the assignment of neurons in the sacral autonomic nervous system (see the Perspective by Adameyko). Previously categorized as parasympathetic, these neurons are now identified as sympathetic. The results resolve a persistent confusion about how the two systems developed and open the avenue to more predictable outcomes in developing treatments targeted to the pelvic autonomic nervous system. —PJH

*Science*, this issue p. 893; see also p. 833

SYNTHETIC BIOLOGY

### Optimizing designer metabolisms in vitro

Biological carbon fixation requires several enzymes to turn $CO_2$ into biomass. Although this pathway evolved in plants, algae, and microorganisms over billions of years, many reactions and enzymes could aid in the production of desired chemical products instead of biomass. Schwander *et al*. constructed an optimized synthetic carbon fixation pathway in vitro by using 17 enzymes—including three engineered enzymes—from nine different organisms across all three domains of life (see the Perspective by Gong and Li). The pathway is up to five times more efficient than the in vivo rates of the most common natural carbon fixation pathway. Further optimization of this and other metabolic pathways by using similar approaches may lead to a host of biotechnological applications. —NW

*Science*, this issue p. 900; see also p. 830

PHARMACOLOGY

### A kinase makes its own inhibitor

The kinase GSK-3 is a promising drug target for treating neurodegenerative disorders, including Alzheimer's disease. However, most GSK-3 inhibitors have not reached the clinic because they also inhibit other kinases. Licht-Murava *et al*. discovered a peptide that was converted by the catalytic site of GSK-3 to an inhibitor of the kinase. This peptide was highly selective for GSK-3, inhibited GSK-3 in cells and animals, and improved



Published by AAAS

cellular symptoms, cognitive function, and social behaviors in a mouse model of Alzheimer's disease. This new mechanism of inhibition may finally enable effective and selective GSK-3 inhibitors to reach the clinic. —NRG

*Sci. Signal.* **9**, ra110 (2016).

PLANT SCIENCE

## Combining heat and light responses

Plants integrate a variety of environmental signals to regulate growth patterns. Legris *et al*. and Jung *et al*. analyzed how the quality of light is interpreted through ambient temperature to regulate transcription and growth (see the Perspective by Halliday and Davis). The phytochromes responsible for reading the ratio of red to far-red light were also responsive to the small shifts in temperature that occur when dusk falls or when shade from neighboring plants cools the soil. —PJH

*Science*, this issue p. 897, p. 886; see also p. 832



*Published by AAAS*

REVIEW SUMMARY

APPLIED OPTICS

# Optically resonant dielectric nanostructures

**Arseniy I. Kuznetsov, Andrey E. Miroshnichenko, Mark L. Brongersma,* Yuri S. Kivshar,* Boris Luk'yanchuk***

**BACKGROUND:** Nanoscale optics is usually associated with plasmonic structures made of metals such as gold or silver. However, plasmonics suffers from high losses of metals, heating, and incompatibility with complementary metal oxide semiconductor fabrication processes. Recent developments in nanoscale optical physics have led to a new branch of nanophotonics aiming at the manipulation of optically induced Mie resonances in dielectric and semiconductor nanoparticles with high refractive indices. Such particles offer unique opportunities for reduced dissipative losses and large resonant enhancement of both electric and magnetic near-fields. Semiconductor nanostructures also offer longer excited-carrier lifetimes and can be electrically doped and gated to realize subwavelength active devices. These recent developments revolve closely around the nature of the optical resonances of the structures and how they can be manipulated in individual entities and in complex particle arrangements such as metasurfaces. Resonant high-index dielectric nanostructures form new building blocks to realize unique functionalities and novel photonic devices.

**ADVANCES:** We discuss the key advantages of resonant high-index nanostructures, associated new physical effects, and applications for nanoantennas, optical sensors, nonlinear devices, and flat optics. For a subwavelength high-index dielectric particle illuminated by a plane wave, electric and magnetic dipole resonances have comparable strengths. The resonant magnetic response results from a coupling of incoming light to the circular displacement currents of the electric field, when the wavelength inside the particle becomes comparable to its diameter $d = 2R \approx \lambda/n$, where $R$ is the nanoparticle radius, $n$ is its refractive index, and $\lambda$ is the wavelength of light. At the wavelength of a magnetic resonance, the excited magnetic dipole mode of a high-index dielectric sphere may provide a dominant contribution to the scattering efficiency exceeding the contribution of other multipoles by orders of magnitude.

Nanophotonic structures composed of dielectric resonators can exhibit many of the same features as plasmonic nanostructures, including enhanced scattering, high-frequency magnetism, and negative refractive index. The specific design and parameter engineering of all-dielectric nanoantennas and metasurfaces give rise to superior performance in comparison to their lossy plasmonic counterparts. Spectral signatures of the Mie-type resonances of these structures are revealed by using far-field spectroscopy while tuning geometrically their resonance properties. A special case is realized when the electric and magnetic resonances spectrally overlap; the impedance matching eliminates the backward scattering, leading to unidirectional scattering and Huygens metasurfaces. A variety of nanoparticle structures have been studied, including dielectric oligomers as well as metasurfaces and metadevices. The magnetic resonances lead to enhanced nonlinear response, Raman scattering, a novel Brewster effect, sharp Fano resonances, and highly efficient sensing and photodetection.

ON OUR WEBSITE

Read the full article at http://dx.doi.org/10.1126/science.aag2472

**OUTLOOK:** The study of resonant dielectric nanostructures has been established as a new research direction in modern nanophotonics. Because of their unique optically induced electric and magnetic resonances, high-index nanophotonic structures are expected to complement or even replace different plasmonic components in a range of potential applications. The unique low-loss resonant behavior allows reproduction of many subwavelength resonant effects demonstrated in nanophotonics without much energy dissipation into heat. In addition, the coexistence of strong electric and magnetic resonances, their interference, and resonant enhancement of the magnetic field in dielectric nanoparticles bring entirely novel functionalities to simple geometries largely unexplored in plasmonic structures, especially in the nonlinear regime or in optoelectronic device applications. ■

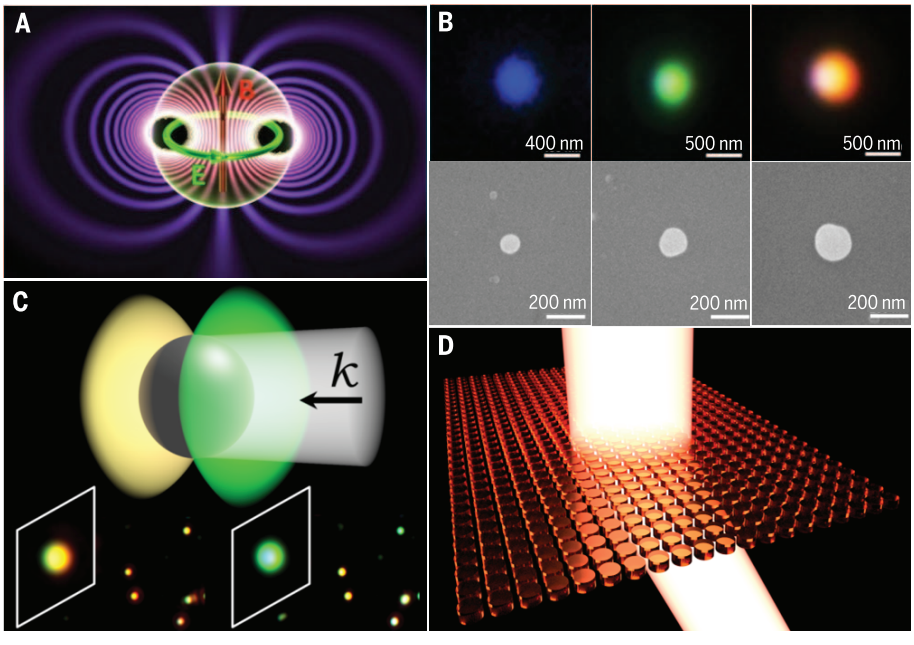


**Manifestations of all-dielectric resonant nanophotonics.** (**A**) Structure of the fields near the magnetic dipole resonance. (**B**) Experimental demonstration of optical magnetic response shown through optical dark-field and scanning electron microscope images (top and bottom, respectively). (**C**) Unidirectional light scattering by a single dielectric nanoparticle for overlapping electric and magnetic dipole resonances, where **k** is the wave vector of the incident white light. (**D**) Light manipulation with highly transparent Huygens metasurfaces.

The list of author affiliations is available in the full article online.
*Corresponding author. Email: ysk@internode.on.net (Y.S.K.); boris_l@dsi.a-star.edu.sg (B.L.); brongersma@stanford.edu (M.L.B.)
Cite this article as A. I. Kuznetsov *et al.*, *Science* **354**, aag2472 (2016). DOI: 10.1126/science.aag2472

Downloaded from http://science.sciencemag.org/ on November 22, 2016

REVIEW

APPLIED OPTICS

# Optically resonant dielectric nanostructures

Arseniy I. Kuznetsov,[1] Andrey E. Miroshnichenko,[2] Mark L. Brongersma,[3]* Yuri S. Kivshar,[2]* Boris Luk'yanchuk[1,4]*

**Rapid progress in nanophotonics is driven by the ability of optically resonant nanostructures to enhance near-field effects controlling far-field scattering through intermodal interference. A majority of such effects are usually associated with plasmonic nanostructures. Recently, a new branch of nanophotonics has emerged that seeks to manipulate the strong, optically induced electric and magnetic Mie resonances in dielectric nanoparticles with high refractive index. In the design of optical nanoantennas and metasurfaces, dielectric nanoparticles offer the opportunity for reducing dissipative losses and achieving large resonant enhancement of both electric and magnetic fields. We review this rapidly developing field and demonstrate that the magnetic response of dielectric nanostructures can lead to novel physical effects and applications.**

Ever since Lord Rayleigh clarified why our sky is blue, the study of light scattering by nanoparticles has been an important part of optical science. Later, Gustav Mie explained a variation in colors of colloidal solutions of gold nanoparticles in terms of their size distribution, thereby opening up the possibility of using resonant nanoscale scatterers to control an optical response. Recent decades have witnessed a growing interest in the study of plasmonic nanoparticles made of gold or silver (*1*). The resonant optical modes supported by such structures endow them with an ability to manipulate light at the nanoscale. This notion has stimulated the development of a diverse set of applications including biosensors, thermotherapy, solar cells, and information storage. However, up to now only a small fraction of plasmonics applications have been realized in practice, mainly due to high losses of metals at visible frequencies and their incompatibility with complementary metal oxide semiconductor (CMOS) fabrication processes. Whereas new materials with improved plasmonic properties have been proposed (*2*), there has been a growing understanding that the optical resonances of high-index dielectric and semiconductor nanostructures can also facilitate light manipulation below the free-space diffraction limit. These structures offer very low optical losses, a wealth of distinct optical resonances, and an opportunity to manipulate the resonances by electrical doping and gating of the mobile carrier density. Many dielectrics and semiconductors are also materials that are compatible with semiconductor device technologies.

For these reasons, it is of great value to analyze how such high-index dielectric structures can be used as building blocks with unique optical functionalities for real metadevices and novel structures. It remains to be determined where exactly they can add much value to their metallic counterparts. Studies currently in progress derive inspiration from century-old studies on light scattering while also advancing our knowledge of photonic crystals and metamaterials. Logically, these studies revolve closely around the nature of the optical resonances of the nanostructures and how they can be manipulated in individual entities as well as complex particle arrangements. We review the basic optical properties of nanostructures composed of resonant high-index nanoparticles, analyze recent advances in this area, and provide a perspective that will help to direct future research.

## Mie resonances in subwavelength particles

To illustrate the fundamental properties of light scattering by nanoparticles, we consider the case of a spherical particle illuminated by a plane wave, for which an exact analytical solution of Maxwell's equations exists. According to Mie theory (*3*), both metallic and dielectric spherical particles can possess strong scattering resonances (Fig. 1A). In the case of lossless and nonmagnetic materials, their scattering properties depend only on two parameters: the dielectric permittivity $\varepsilon$ and a size parameter $q$ that is proportional to the ratio between the nanoparticle radius $R$ and the wavelength of light $\lambda$ ($q = 2\pi R/\lambda$). For a fixed size parameter, the difference between metallic and dielectric particles is in the sign of the dielectric permittivity, which is negative for metals and positive for dielectrics. Small metallic spheres ($q < 1$) produce only localized surface plasmon resonances of an electric type—dipole, quadrupole, etc.—while their magnetic response remains almost negligible because of a vanishing field inside the sphere (Fig. 1A). To generate a magnetic response from metallic structures, the particle's geometry should be changed. For example, a split-ring resonator (*4*) works similarly to an effective LC circuit (i.e., inductor-capacitor circuit) with the enhancement of the magnetic field in the center. For dielectric particles, we can observe both electric- and magnetic-type responses of comparable strengths (Fig. 1A). The resonant magnetic dipole response results from a coupling of incoming light to the circular displacement currents of the electric field, owing to the field penetration and phase retardation inside the particle. This occurs when the wavelength inside the particle becomes comparable to the particle's diameter $2R \approx \lambda/n$ (Fig. 1B). The field structure of the four major resonant modes in high-index dielectric particles—magnetic dipole, electric dipole, magnetic quadrupole, and electric quadrupole—is shown in Fig. 1C. At the wavelength of a magnetic resonance, the excited magnetic dipole mode of a high-index dielectric sphere may provide a major contribution to the scattering efficiency, exceeding that of other multipoles by orders of magnitude.

From Mie theory, it follows that the maximum achievable scattering efficiency for a specific multipolar excitation of a subwavelength particle depends only on the resonance frequency and not the type of material (*5*). This suggests that many plasmonic effects observed for the scattering of light by metallic nanoparticles can be realized with high-index dielectric nanoparticles. Figure 1B shows the scaling of different resonances with respect to the refractive index $n$. For $n > 2$, all main multipoles are well defined, and their spectral positions correspond to a fixed ratio of the wavelength inside the particle, $\lambda/n$, to its diameter, $2R$. The scattering efficiency of all multipoles also increases with increasing $n$ (*6*–*9*).

Strong, optically induced magnetic dipole resonances in high-index dielectric nanoparticles can be achieved not only for spheres but also for spheroids (*10*, *11*), disks and cylinders (*12*), rings (*13*), and many other geometries (*14*). This provides important opportunities for designing a variety of all-dielectric nanostructures with desirable spectral positions of the resonances. By changing the geometrical parameters of the particles, the spectral positions of both electric and magnetic dipole resonances can be tuned independently, interchanging or overlapping spectrally at a single frequency for simple geometries (*11*, *12*, *15*).

## Observation of optical magnetic resonances in dielectric nanoparticles

Experimental observation of magnetic resonances in dielectric particles at optical frequencies

[1]Data Storage Institute, A*STAR (Agency for Science, Technology and Research), 138634 Singapore. [2]Nonlinear Physics Centre, Research School of Physics and Engineering, Australian National University, Canberra, ACT 2601, Australia. [3]Geballe Laboratory for Advanced Materials, Stanford University, Stanford CA 94305, USA. [4]Division of Physics and Applied Physics, School of Physical and Mathematical Sciences, Nanyang Technological University, 637371 Singapore.
*Corresponding author. Email: ysk@internode.on.net (Y.S.K.); boris_l@dsi.a-star.edu.sg (B.L.); brongersma@stanford.edu (M.L.B.)

Downloaded from http://science.sciencemag.org/ on November 22, 2016

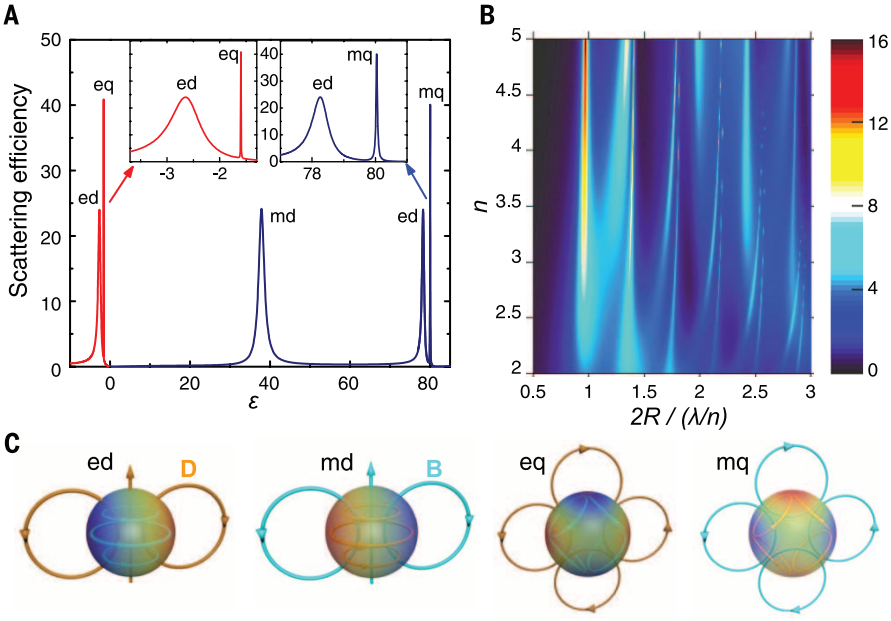


**Fig. 1. Mie resonances of a spherical particle.** (**A**) Scattering efficiency (dimensionless ratio of scattering cross section to geometrical cross section of the particle) versus dielectric permittivity ε (lossless particle, $q$ = 0.5) for plasmonic (ε < 0) and dielectric (ε > 0) materials. Abbreviations for resonances: ed, electric dipole; eq, electric quadrupole; md, magnetic dipole; mq, magnetic quadrupole. Higher-order multipole modes are not shown for the sake of simplicity. (**B**) Scattering efficiency of a lossless dielectric particle (color scale at right) as a function of refractive index $n$ and size parameter. (**C**) Illustration of electric and magnetic field structures for different electric and magnetic resonances supported by a spherical dielectric particle.

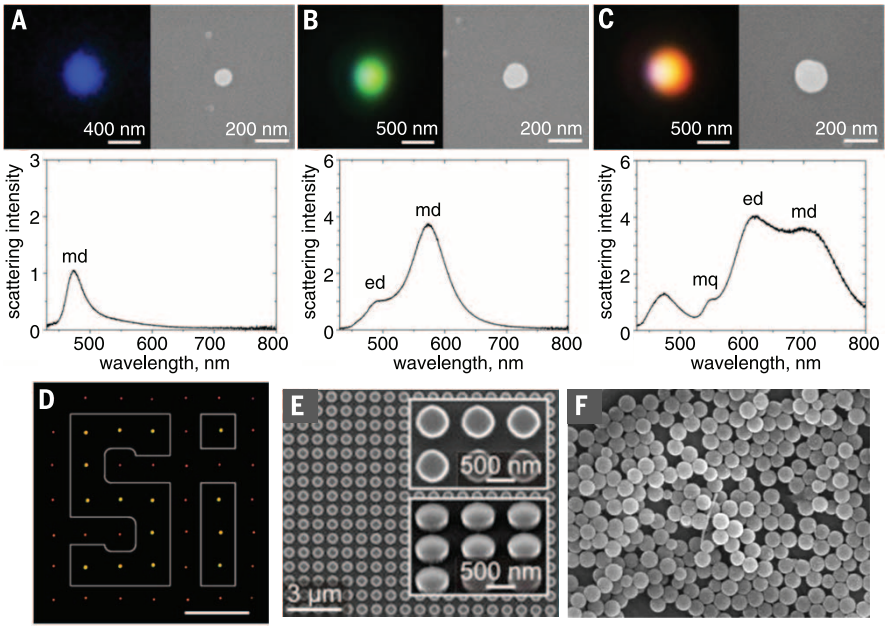


**Fig. 2. Demonstration of optical magnetic response and examples of resonant silicon nanostructures.** (**A** to **C**) Dark-field optical microscope images (top left), scanning electron microscope (SEM) images (top right), and dark-field scattering spectra (bottom) of spherical Si nanoparticles with approximate diameters of 100 nm (A), 140 nm (B), and 180 nm (C) (*8*). Abbreviations for resonances are as in Fig. 1. (**D**) Dark-field microscope image of laser-printed Si nanoparticle arrays. Si is crystallized inside the marked areas by additional laser irradiation, producing a change in color (*22*); scale bar, 10 μm. (**E**) Lithographically fabricated Si nanodisk arrays with varied spectral positions of the electric and magnetic resonances (*15*). (**F**) Monodispersed silicon nanoparticles resonant at near-IR frequencies prepared by chemical synthesis (*25*).

[mid-infrared (IR)] was reported for silicon carbide microrods (*16*). Later, dielectric and semiconductor microrods and nanorods were observed to exhibit scattering resonances in the visible and near-IR spectral range [see, e.g., (*17*–*19*)]. It was also pointed out (*6*, *7*) that silicon (Si) nanospheres with sizes ranging from 100 to 300 nm support strong magnetic and electric dipole resonances in the visible and near-IR spectral range. Although Si is not a completely loss-free material, its absorption in the visible spectrum is much lower than that of metals, making it a good material for the study of Mie resonances.

An experimental demonstration of electric and magnetic dipole resonances at visible wavelengths was first reported for spherical Si nanoparticles fabricated by femtosecond laser ablation on silicon and glass substrates (*8*, *20*). Different colors observed in dark-field microscope images (Fig. 2, A to C) correspond to magnetic dipole resonances of almost perfect spherical Si nanoparticles with sizes ranging from 100 to 200 nm (*8*). A recently developed laser-induced transfer method allows the generation of arrays of resonant nanoparticles with almost perfect spherical shape (Fig. 2D) (*21*, *22*). However, from the viewpoint of practical applications, conventional electron beam lithography and photolithography provide much better reproducibility and control over the structural parameters (Fig. 2E) (*15*, *17*). Soft-imprint lithography (*23*), nanosphere lithography (*24*), and chemical synthesis (Fig. 2F) (*25*) were also used for generating silicon nanostructures with the required parameters to display strong scattering resonances in the visible and near-IR spectrum. Apart from silicon, group IV and group III-V semiconductors with refractive indices above 2 might have similar optical properties depending on their absorption and refractive index in a specific wavelength range. For example, magnetic and electric dipole resonances were recently observed experimentally in gallium arsenide (GaAs) nanodisks in the visible spectrum (*26*) and tellurium (Te) cubes in the mid-IR spectrum (*27*).

## Directional scattering of light

Any particle much smaller than the wavelength of light ($R$ << λ) behaves as an electric dipole that scatters light symmetrically in the plane transverse to the dipole axis. To achieve an asymmetry in the light scattering, interference effects of a few or several different modes can be exploited. For plasmonic particles, the asymmetric scattering may be attributable to the Fano resonance resulting from interference of a broad electrical dipole and narrow quadrupole (or higher-order) modes (*28*, *29*). However, losses of typical plasmonic metals are too large and preclude a clear observation of this effect in a single spherical nanoparticle. In high-index dielectric nanospheres, strong directional scattering of light results from the interference of magnetic and electric dipole responses excited simultaneously in the nanoparticle with comparable strength. Using Mie theory for a spherical dielectric nanoparticle, it can be shown that when

Downloaded from http://science.sciencemag.org/ on November 22, 2016

electric ($a_1$) and magnetic ($b_1$) dipole coefficients (*3*) coincide ($a_1 = b_1$) and other higher-order modes are negligible, the backward scattering vanishes (Fig. 3, A to C) (*11*, *30*, *31*). This is conceptually similar to the condition for the zero-backward scattering derived by Kerker *et al.* in 1983 (*32*) for a particle having similar electric and magnetic properties, $\varepsilon = \mu$, often called the first Kerker condition. Although the total suppression of the forward scattering is forbidden by the optical theorem (*33*), it is also possible to find the other condition for a minimal ratio of the forward and backward scattering, often called the second Kerker condition (*34*).

Experimental verification of the Kerker-type asymmetry in the scattering of electromagnetic waves by high-index dielectric particles was reported in the microwave regime (*35*) for spherical ceramic particles with diameter of 18 mm and refractive index of 4. Microwave experiments allowed direct measurements of angular scattering patterns (Fig. 3D). Asymmetric scattering by Si nanoparticles at visible frequencies was demonstrated shortly thereafter (Fig. 3E) (*10*). This strong scattering asymmetry results in different colors of the same nanoparticles when observed in the dark-field microscope in transmission or reflection mode (insets in Fig. 3E) (*10*). Suppression of the backward scattering was also observed for single GaAs nanodisks (*26*).

The interference effects between electric and magnetic dipole resonances of dielectric nanoparticles may have multiple applications, including efficient nanoantenna structures, Huygens metasurfaces, and unconventional Brewster angle behavior.

## Dielectric nanoantennas

Light control at the nanoscale is important for many emerging applications, including 3D optical interconnects in multilayer chips, enhancement of fluorescence signals in bioimaging, high-resolution spatial light modulators, and light energy concentration in heat-assisted magnetic recording. At the subwavelength scale, conventional optical elements are not applicable, and nanoscale elements such as optical nanoantennas (*36*) offer a conceptually new approach for the design of nanoscale photonic devices. The study of nanoantennas is a rapidly growing area of research, and various geometries have been demonstrated successfully for nonclassical light emission, fluorescence enhancement, high-harmonic generation, nanoscale photodetectors, and single-molecule detection (*36*). Despite this progress, plasmonic nanoantennas working in optics are still far from attaining the same good characteristics as conventional antennas at radio frequencies, primarily because of losses in metallic elements. Therefore, all-dielectric nanoantennas are viewed as a reasonable alternative to plasmonic structures. At microwave frequencies, the so-called dielectric resonator antennas (*37*), made of ceramic components of various shapes, are commonly used. The use of dielectrics leads to many advantages such as low loss, small size, light weight, high radiation efficiency, and reasonable bandwidth. At optical frequencies, typical dielectrics may have low losses similar to those at microwave frequencies, but their refractive indices are limited to smaller numbers ($n \sim 4$), which imposes limitations on the size of the nanoantenna devices scaling proportionally to $\lambda/n$.

For a single-particle nanoantenna excited by a localized light source, the optimal conditions for the directional scattering differ from plane-wave excitation. They depend not only on the frequency but also on the relative distance between the source dipole and the nanoparticle (*38*). Thus, a single dielectric nanoparticle can either reflect or collect the light emitted by a photon source (*39*). The directivity can be tuned by controlling the distance between the emitter and the nanoparticle at the scale of $\lambda/6n$ (*38*). By using an array of nanoparticles, it is possible to enhance the overall directivity of optical nanoantennas, including the emission maximum (*38*) and direction (*40*), in more versatile ways. An all-dielectric analog of the well-known Yagi-Uda nanoantenna was shown to exhibit high directivity together with higher radiation efficiency than that of its plasmonic counterpart (*41*). This concept was verified experimentally in the microwave regime (*42*) by using spherical ceramic particles with a refractive index close to that of Si in the visible range.

Another important property of nanoantennas is their ability to concentrate electromagnetic energy at the nanoscale. Plasmonic nanoantennas may achieve high enhancement of the electric near-field while only weakly affecting the magnetic near-field. In contrast, resonant dielectric nanostructures not only can enhance electric near-fields (*43*, *44*) but can also behave like magnetic near-field concentrators. It was predicted theoretically (*45*) and demonstrated experimentally for microwaves (*46*) and visible wavelengths (*47*) that a dimer composed of two high-index dielectric nanoparticles with a subwavelength gap can enhance the magnetic field intensity by as much as two orders of magnitude. At the same time, the electric near-field intensity can also be enhanced (Fig. 4A). Magnetic hotspots, in addition to the electric hotspots, result in an increase of the local optical density of states, and thus can modify the magnetic transition rates of molecules or quantum emitters with an enhancement of the Purcell factor (*39*, *45*, *48*). The mode structure of dielectric dimer nanoantennas has been further investigated using spectroscopic (*49*) and cathodoluminescence (*50*) techniques. Recently, silicon dimers have been used for high surface-enhanced Raman scattering and surface-enhanced fluorescence without generating heat; nanoantennas using such components are suitable for detection of heat-sensitive biological species (*51*).

The overall scattering efficiency is also of prime importance. It was recently demonstrated that certain arrangements of nanoparticles, such

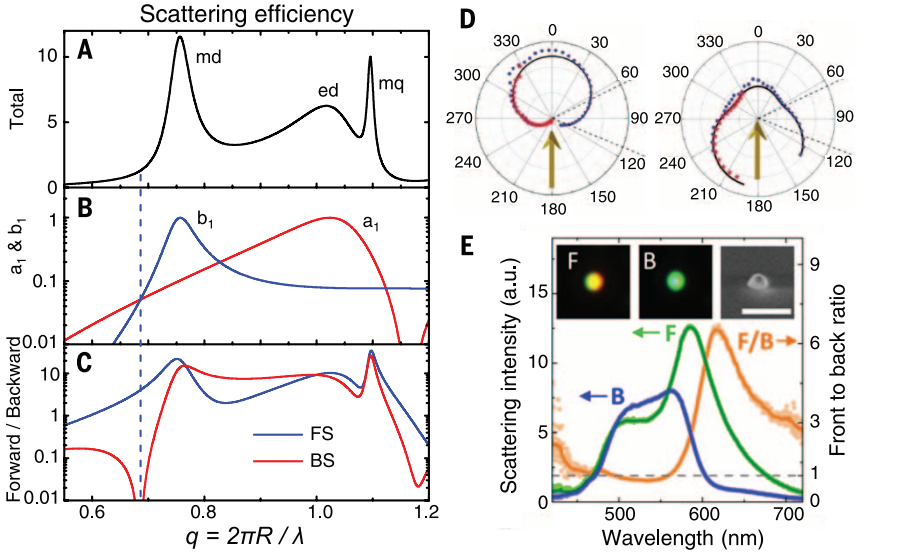


**Fig. 3. Directional scattering of light by a single dielectric nanoparticle.** (**A**) Scattering efficiency of a dielectric sphere calculated by Mie theory versus size parameter $q$ for refractive index $n = 4$. Abbreviations for resonances are as in Fig. 1. (**B**) Electric $a_1$ and magnetic $b_1$ dipole scattering coefficients of the sphere (log scale). (**C**) Forward (FS) and backward (BS) scattering efficiencies of the sphere (log scale). The dashed line in (A) to (C) marks the wavelength at which the first Kerker condition is realized. (**D**) Experimental forward and backward scattering from a subwavelength spherical dielectric particle with diameter of 18 mm, recorded using a 3D angular measurement setup in the microwave spectral range at $\lambda = 84$ mm (left) and 69 mm (right). Dots are experimental data points; solid curves are Mie theory calculations (*35*). (**E**) Experimentally measured forward (green) and backward (blue) scattering spectra and forward-to-backward ratio (orange) of a near-spherical Si nanoparticle with a diameter of about 150 nm placed on a glass substrate (a.u., arbitrary units). Insets show transmission (F) and reflection (B) dark-field microscope images and a SEM image of the nanoparticle (*10*); scale bar for SEM image, 500 nm.

Downloaded from http://science.sciencemag.org/ on November 22, 2016

as oligomers, can lead to resonant suppression of the total scattering efficiency, a phenomenon associated with Fano resonances (*28*, *29*). A Fano resonance typically arises from the interference of broad and narrow spectral lines. In the case of plasmonic oligomers, most of the incident excitation is absorbed by nanoparticles. A new route for achieving Fano resonances in nanoparticle oligomers is now possible through the use of electric and magnetic resonances in lossless high-index dielectric nanoparticles (Fig. 4B) (*52*, *53*). The origin of the observed Fano resonances is interference of the optically induced magnetic dipole mode of the central particle with the collective mode of the nanoparticle structure (*52*). Fano resonance can also be observed in simpler geometries such as an individual silicon nanostripe (*54*).

Because of their low losses and strong magnetic response, resonant dielectric nanoparticles offer a unique playground to demonstrate new nanophotonic effects. One of them is the existence of a nonradiating anapole (i.e., poleless) mode recently observed in silicon nanodisks. In classical electrodynamics, the anapole mode is strongly related to the existence of a toroidal dipole excitation. In general, the toroidal response is produced by currents flowing on the surface of a torus along its meridians (*55*). Despite a scale factor, the polarization and angular distribution of the radiated fields of the dynamic toroidal dipoles are exactly the same as those of conventional electric dipoles. As a result, a particular superposition of electric and toroidal dipole moments can cause the complete destructive interference of the corresponding far-field radiation contributions. Such a vanishing electromagnetic field produced by a nontrivial current source is a classical analog of the radiationless anapole initially introduced by Zel'dovich in nuclear physics. Interestingly, such peculiar induced currents can be naturally excited inside dielectric nanoparticles.

The anapole mode was recently demonstrated within an individual dielectric nanoparticle in the visible spectrum (*56*). In particular, a silicon nanodisk with a height of 50 nm and diameter of 310 nm was observed to exhibit a pronounced dip in the far-field scattering and a simultaneous near-field enhancement inside and around the disk (Fig. 4C) (*56*). These particles become nearly invisible in the far-field at the wavelength of anapole excitation. At the same time, the electric field energy is maximized inside the particles at the same wavelength; this was recently confirmed by third-harmonic generation experiments (*57*). Although the anapole in the dielectric nanodisks originates from mere interference, it provides new perspective for investigations into electromagnetic properties of various charge-current distributions.

Potential areas of application for low-loss dielectric nanoantennas not yet explored in the literature also include optoacoustics and elastodynamics.

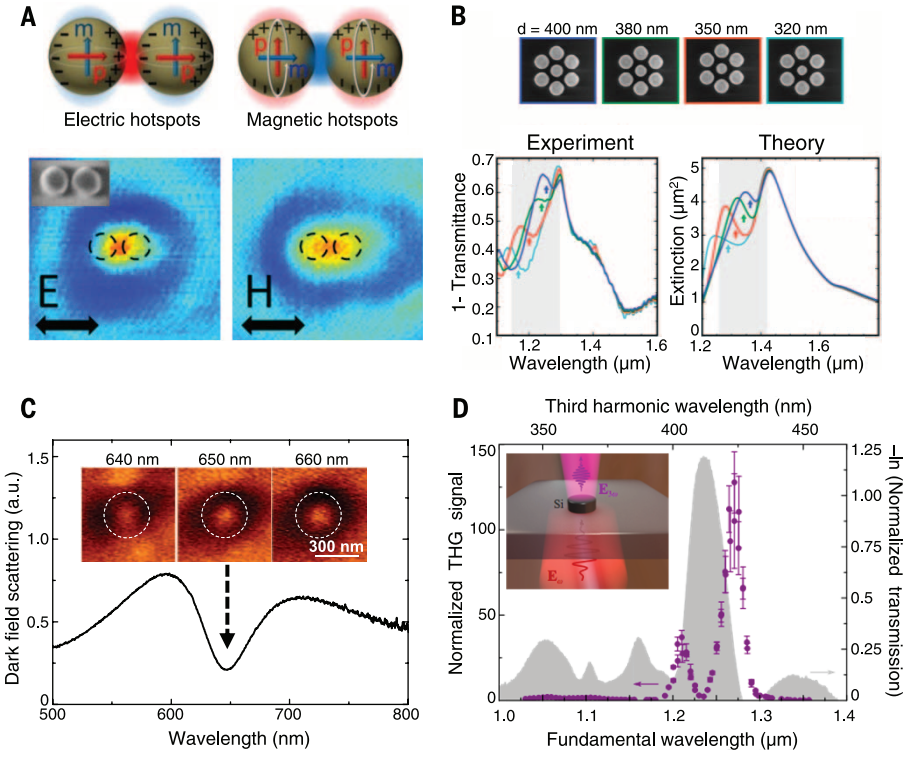


**Fig. 4. Dielectric nanoantennas.** (**A**) Magnetic and electric near-field enhancement in a nanogap between two silicon nanocylinders (height, 150 nm; diameter, 140 nm; gap, 30 nm). Top: Schematics of the measured system; p and m indicate electric and magnetic dipole moments, respectively. Bottom: Scanning near-field optical microscopy images for the two orthogonal excitation polarizations (*47*). Arrows indicate polarization direction for electric (**E**) and magnetic (**H**) fields. Color varies from minimal (blue) to maximal (red) values. Dashed circles mark the positions of silicon nanocylinders. Inset shows a SEM image of the studied dimer nanoantenna. (**B**) Magnetic Fano resonance in all-dielectric oligomers (*53*). Top: SEM images of fabricated heptamer for different diameters (d) of the central Si disk. Bottom: Theoretical and experimental demonstrations of the magnetic Fano resonances. Blue, green, red, and cyan curves correspond to different diameters of the central Si nanodisk: 400 nm, 380 nm, 350 nm, and 320 nm, respectively. Arrows indicate the spectral positions of the Fano resonance. (**C**) Nonradiating anapole mode in silicon nanodisks (*56*): Experimental dark-field scattering spectra of an amorphous Si nanodisk (diameter, 310 nm; height, 50 nm) on a quartz substrate. A strong dip in the nanodisk scattering at the wavelength of anapole excitation is clearly observed. Inset shows experimental near-field scanning optical microscopy images of the anapole mode at three different wavelengths (640, 650, and 660 nm) near the scattering minimum. White dashed circles indicate the nanodisks' positions. (**D**) Nonlinear spectroscopy of an array of Si nanodisks (*58*). Shown is the negative logarithm of the normalized transmission spectrum of a sample marked by a gray area indicating a resonance at 1.24 μm. The third-harmonic generation (THG) spectrum of the sample normalized over the spectrum of the substrate (purple dots) is strongly enhanced within the spectral band of the resonance. The inset shows a schematic of the THG at a single silicon nanodisk.

## Nonlinear optics with resonant dielectric nanostructures

Near-field enhancement of electric and magnetic response in all-dielectric nanostructures may lead to novel nonlinear effects. In particular, second- and third-harmonic generation (SHG and THG), self-action of light, and Raman scattering are affected by strong confinement resulting from geometrical resonances. Plasmonic resonances that enhance local electric fields in hotspots are known to boost nonlinear optical effects in metal nanostructures. In contrast to plasmonics, resonances of high-index dielectric nanoparticles provide a mode volume that is not limited to interfaces and thus may lead to higher conversion efficiencies.

The enhanced THG from Si nanodisks exhibiting both electric and magnetic dipole resonances was observed experimentally (*58*) through third-harmonic microscopy and spectroscopy, with the TH signal enhanced in the vicinity of the magnetic dipole resonance (Fig. 4D). The field localization at the magnetic resonance results in an enhancement of the harmonic intensity by two orders of magnitude with respect to unstructured bulk Si, with the conversion efficiency limited only by the two-photon absorption in the substrate (*58*). Strong THG has also been reported from Si-based metasurfaces (*59*). Combining the Kerr effect with a high–quality factor resonance in the metasurface linear transmittance

Downloaded from http://science.sciencemag.org/ on November 22, 2016

spectrum, the authors demonstrated THG conversion efficiency of $1.18 \times 10^{-6}$ at a peak pump intensity of 3.2 GW/cm$^2$. This corresponds to $1.5 \times 10^5$ enhancement of the THG signal relative to that from an unstructured Si film with the same thickness. Recent demonstrations also include enhancement of SHG in resonant nanopillars made of the high-index noncentrosymmetric III-V semiconductors GaAs (*60*) and AlGaAs (*61*). An enhancement factor of $10^4$ relative to unstructured GaAs films is shown with total conversion efficiency of $2 \times 10^{-5}$ at a pump intensity of 3.4 GW/cm$^2$. Strong quadratic nonlinear processes pave the way for the enhanced generation of entangled photon pairs through spontaneous parametric downconversion (SPDC) with dielectric nanoresonators and experimental realization of nanoscale quantum-entangled light sources that use optical nonlinearity.

Apart from the harmonic generation, efficient tuning of optical properties of high-index nanoparticles near magnetic Mie-type resonances by means of femtosecond laser irradiation has also been demonstrated (*62*). The effect is based on ultrafast (<100 fs) photoinjection of dense electron-hole plasma within such nanoparticles, drastically changing their transient dielectric permittivity. Reflectance changes up to 20% have been achieved. In a similar experiment, ultrafast all-optical switching in subwavelength nonlinear dielectric nanostructures exhibiting localized magnetic resonances has been shown (*63*). Pump-probe measurements have revealed that switching in the nanodisks can be governed by pulse-limited 65-fs two-photon absorption, which is enhanced by a factor of 80 with respect to the unstructured silicon film (*63*).

These experimental demonstrations indicate great promise for the rapidly developing field of nonlinear and quantum nanophotonics. The main advantage of resonant dielectric nanostructures over plasmonics is the localization and strong enhancement of optical fields inside the particles, which promotes strong volumetric nonlinearities and allows for large conversion efficiencies.

## Metamaterials and metasurfaces based on resonant dielectric nanostructures

Electromagnetic properties of media composed of resonant dielectric scatterers were discussed in many theoretical works starting from Lewin (*64*). Magnetic response of purely dielectric particles with very high refractive index (close to 50) was also studied theoretically (*65*). During the previous decade, this problem was reconsidered in connection to metamaterials (*16*, *66*, *67*). Some earlier theoretical results, as well as the first experimental demonstrations of such composite media at gigahertz frequencies, are reviewed in (*68*). In the visible and near-IR spectral ranges, practical materials such as Si and germanium (Ge) have the highest refractive index, around 4, which is substantially lower than the values available at microwave frequencies. Therefore, 3D periodic structures composed of such nanoparticles should demonstrate the properties of photonic crystals and are not suitable for the homogenization of parameters (*69*), with the exception of zero-index materials (*70*).

Resonant dielectric nanoparticles can also be used for creating planar single-layer arrays known as metasurfaces (*71*). Metasurfaces offer the possibility of engineered resonant electric and magnetic optical response combined with low losses of thin-layer structures, and hence they demonstrate many useful properties of metadevices. One of the major functionalities of metasurfaces is control of the phase of reflected and transmitted light. The idea of using dielectrics structured at the subwavelength scale for wavefront control was actively discussed two decades ago in the context of blazing gratings (*72*). Similar ideas have also been pursued more recently (*73*–*76*) to achieve the 2π phase accumulation. This approach does not directly rely on resonances of single elements and requires relatively tall nanopillars (on the order of a free-space wavelength) and a high aspect ratio, sometimes reaching 10:1. At the same time, it provides the highest efficiencies to date for operation in the transmission mode, in the range of 80 to 90%.

Another approach to achieving phase control was proposed in the early 2000s, and it relies on metallic or dielectric subwavelength gratings with different orientations to control the circularly polarized light through a geometric Pancharatnam-Berry (PB) phase (*77*, *78*). A recent work based on this principle demonstrated flat silicon lenses and axicons operating at visible wavelengths (Fig. 5A) (*79*). The structure is generated by patterning 120-nm-wide nanoantennas into a 100-nm-thick Si film. It could be reduced in thickness relative to previous PB-phase elements by exploiting resonances in the Si structures. This approach was further extended to highly efficient operation at visible wavelengths by using transparent titanium dioxide ($TiO_2$) as the metasurface material (*80*). Beam focusing with efficiency of >66% at selected wavelengths in blue, red, and green regions has been experimentally demonstrated. In contrast to the previous example, this design was achieved with a relatively large height of $TiO_2$ structures (600 nm), which imposes greater restrictions on the nanofabrication.

A novel approach to creating dielectric metasurfaces is to use electric and magnetic dipole resonances of dielectric nanoparticles to control the phase of incoming light (*81*). Each of the dipoles is capable of shifting the phase from 0 to π near the resonance. Combining the response of both dipoles at the same wavelength makes it possible to achieve the whole 0 to 2π phase coverage (*82*). This overlap of resonances provides not only the required phase shifts but also near-unity transmission of the metasurface, due to the

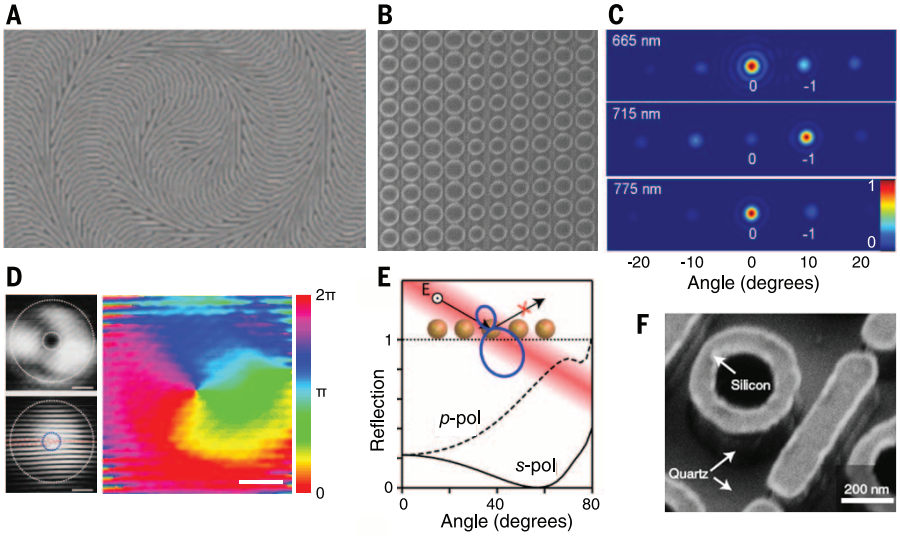


**Fig. 5. Dielectric metasurfaces.** (**A**) SEM image of a dielectric metasurface constructed from >$10^4$ Si nanoantennas and serving as an optical axicon (*79*). (**B** and **C**) Beam deflection with a Huygens silicon metasurface (*84*): (B) SEM image of a 130-nm-thick gradient resonant metasurface; (C) back focal plane image of light transmitted through the metasurface showing close to 50% total deflection efficiency at 715 nm. "0" and "−1" labels indicate the angular positions of the corresponding diffraction orders. (**D**) Vortex beam generated by a Huygens dielectric metasurface in transmission (*85*). Left: Logarithmic intensity profile of the generated vortex beam (top); interferogram showing the characteristic fork structure (bottom). Right: Reconstructed phase of the vortex beam imaged at 4 cm beyond the sample. All scale bars are 200 μm. (**E**) Demonstration of the generalized Brewster effect with a silicon metasurface. Simulated reflection of p- and s-polarized light at a wavelength of 710 nm from a square array of silicon spheres with diameter of 180 nm and pitch of 300 nm shows Brewster angle behavior for s polarization. Inset at top illustrates how electric and magnetic dipoles interfere to cancel the reflection of s-polarized incident light through scattering cancellation in the reflection direction (*90*). (**F**) SEM image of a unit cell of the silicon metasurface, demonstrating electromagnetically induced transparency behavior in the near-IR spectral range (*92*).

Downloaded from http://science.sciencemag.org/ on November 22, 2016

enhanced forward scattering by each of the nanoparticles, and suppression of backward scattering, due to the first Kerker condition. Such designs are conceptually similar to Huygens metasurfaces proposed in plasmonics (*83*), but they have much higher transmission efficiencies due to lower losses in transparent dielectric materials. Recently, silicon-based visible-range metasurfaces with resonant transmission greater than 85% have been experimentally demonstrated (*84*). These devices are only 130 nm thick, corresponding to less than one-fifth of the free-space wavelength, and are capable of controlling the wavefront of light and performing beam deflection with close to 50% efficiency in transmission (Fig. 5, B and C). Similar concepts were also used to achieve efficient vortex beam generation (*85*, *86*) (Fig. 5D). Because of the low thickness and low aspect ratio of the nanodisks (around 1:2), this approach, despite slightly lower efficiency, might be promising for practical applications relying on large-scale nanofabrication techniques such as nanoimprinting.

Apart from transmission phase manipulation, dielectric metasurfaces can also be used as almost perfect reflectors exceeding the performance of conventional metallic and dielectric mirrors (*6*, *24*, *87*). In contrast to high-transmissivity arrays, which are based on disks with an aspect ratio of approximately 1:2 and have overlapped electric and magnetic dipole resonances, high reflectance can be achieved with spheres or cylinders with an aspect ratio close to 1:1, whose electric and magnetic dipole resonances are spectrally separated. This effect arises from the coherent interaction of magnetic or electric dipoles excited by an external radiation in each nanoparticle. A recent experiment demonstrated very high reflectance (up to 99.7%) in the near-IR spectral range from a dense array of Si nanoparticles (*24*). This high-reflectance behavior is conceptually similar to that observed earlier in high-contrast subwavelength gratings [see (*88*) and references therein].

Interfering electric and magnetic dipoles may lead to phenomena that cannot be observed with conventional dielectrics or metals. One such effect is magnetic mirror–like behavior, when the dielectric metasurface acts as a perfect magnetic conductor flipping the phase of an incident magnetic field with no effect on the phase of the electric field (*89*). Another example is the generalized Brewster effect (*90*). In contrast to the conventional Brewster effect, which is limited to p-polarized incidence and angles above 45° (a Brewster angle below 45° is always accompanied by total internal reflection at higher angles), the generalized Brewster effect can be achieved for any polarization (both p and s) and any angle of incidence (both below and above 45° without having total internal reflection) (Fig. 5E). It appears as a result of interference of electric and magnetic resonances in the array and cancellation of their scattering in the reflection direction.

Another approach to dielectric metasurfaces is to use dielectrics for the plasmonic-inspired designs with a substantial reduction of losses. Examples are the spectrally selective Fano metasurfaces (*91*) and metasurface analogs of electromagnetically induced transparency (*92*) (Fig. 5F). In the latter case, because of extremely low absorption loss and coherent interaction of neighboring nanoparticles, a resonance quality factor of 483 is observed, leading to a refractive index sensor with a figure of merit of 103. Furthermore, it was shown that dielectric metasurfaces can be engineered to confine the optical field in either the Si resonator or the environment, allowing one to tailor light-matter interaction at the nanoscale (*92*).

Dielectric metasurfaces hold promise for real-world applications to novel ultracompact optical components and wearable photonic devices because of their high efficiency, ease of fabrication, and CMOS compatibility. A key to their success may lie in development of their broadband operation and active switching capabilities. Recent experimental demonstrations of a silicon metasurface operating at three different wavelengths (*93*), active tuning of the spectral position of dielectric metasurface resonances by liquid crystals (*94*), and theoretical prediction of the retardation phase tunability of InSb metasurfaces by charge injection (*95*) are the first important steps in this direction.

The field of dielectric metamaterials is developing very rapidly. Additional information related to zero-index and anisotropic all-dielectric metamaterials can be found in (*96*).

## Optoelectronic devices using resonant semiconductor nanostructures

Advances in nanotechnology and semiconductor electronics enable the realization of complex device architectures constructed from nanoscale semiconductor elements. This progress has opened up tremendous opportunities for nanophotonics because at this size scale, the semiconductor structures naturally possess optical resonances that can be used to manipulate light-material interactions for a wide range of applications. Although the study of resonances in high-index nanostructures has a long history, only recently have researchers started to use these resonances to enhance the performance of optoelectronic devices such as photodetectors (*97*–*99*), optical sources (*100*), and thermal emitters based on individual nanostructures (*101*), as well as large-area nanostructured devices such as solar cells (*23*, *102*–*105*) and photoelectrochemical devices (*106*).

Figure 6A shows a single semiconductor nanowire photodetector that capitalizes on its optical resonances to achieve an absorption cross section $\sigma_{abs}$ that exceeds its geometric cross section $\sigma_{geom}$ (*97*, *98*). The high absorption efficiency $Q_{abs} = \sigma_{abs}/\sigma_{geom}$ enables more efficient, high-speed, low-noise photodetection schemes. Photocurrent spectra taken from single Ge nanowire detectors with different radii show peaks that are not visible in the intrinsic materials absorption of Ge and are attributed to the excitation of optical resonances that enhance absorption (Fig. 6B). These spectra qualitatively agree well with the predicted absorption features of Ge nanowires with the corresponding radii (Fig. 6C) in terms of the number of absorption peaks and their spectral location. Conversely, it has also been

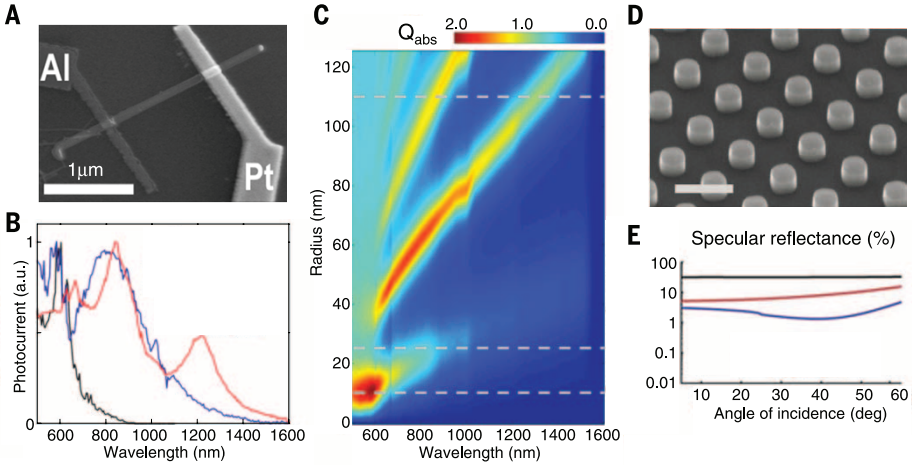


**Fig. 6. Nanophotonic devices based on semiconductor nanoantennas.** (**A**) SEM image of a photodetector using an optically resonant Ge nanowire with asymmetric metallic contacts [one side ohmic (Al), the other side Schottky (Pt)] (*98*). (**B**) Photocurrent spectra of individual Ge nanowires with radii of 10 nm (black), 25 nm (blue), and 110 nm (red) (*97*). (**C**) Two-dimensional plot of the calculated absorption efficiency $Q_{abs}$ as a function of wavelength and radius of the nanowire. The dashed gray lines indicate the radii for which the spectral photocurrent is shown in (B) (*97*). (**D**) SEM image of an array of Si Mie resonators that serves as an antireflection coating on a Si substrate (*23*). Scale bar, 1 μm. (**E**) Measurement of the specular reflectance at 632 nm as a function of the angle of incidence for a bare Si wafer (black), a 60-nm-thick $Si_3N_4$ antireflection coating (red), and an array of Mie resonators as shown in (D) coated with a 60-nm-thick $Si_3N_4$ layer (blue) (*23*).

Downloaded from http://science.sciencemag.org/ on November 22, 2016

demonstrated that subwavelength structures can emit via their size-tunable resonances, affording new levels of control over the spectral emission (*100*, *101*).

Large arrays of Mie resonators can also be realized on top of devices—for example, as a high-performance antireflection coating (Fig. 6, D and E) (*23*). Here, the Mie resonators can assist in increasing the flow of light into a high-index solar cell. Alternatively, a layer of judiciously shaped Mie resonators can be used to create ultrathin metafilms with designer absorption spectra (*107*). From a device perspective, some key advantages of resonant semiconductors over metals are the natural materials compatibility with semiconductor device technology, the longer lifetimes of excited carriers, an ability to electrically gate carrier densities, and the possibility of defining device functions (such as p-n junctions) inside the resonant structures.

## Further developments and outlook

Because of their unique optically induced electric and magnetic resonances, high-index dielectric nanostructures are expected to complement or even replace plasmonic components in a range of potential applications. The unique low-loss resonant behavior makes it possible to realize many subwavelength resonant effects demonstrated in nanophotonics without much energy dissipation into heat. In addition, the coexistence of strong electric and magnetic resonances, their interference, and the resonant enhancement of the magnetic field in dielectric nanoparticles bring entirely new functionalities to simple geometries largely unexplored in plasmonic structures, especially in the nonlinear and quantum regimes.

In the visible range, the main materials of choice are silicon, germanium, $TiO_2$, GaAs, and other semiconductors with high values of the optical refractive index. These materials are extensively used in current device technologies, enabling many novel functionalities offered by the subwavelength physics of high-index resonant dielectric nanostructures to be transferred directly into existing industrial production lines.

## REFERENCES AND NOTES


1. L. Novotny, B. Hecht, *Principles of Nano-optics* (Cambridge Univ. Press, 2012).
2. A. Boltasseva, H. A. Atwater, Low-loss plasmonic metamaterials. *Science* **331**, 290–291 (2011). doi: 10.1126/science.1198258; pmid: 21252335
3. C. F. Bohren, D. R. Huffman, *Absorption and Scattering of Light by Small Particles* (Wiley, 1983).
4. J. B. Pendry, A. J. Holden, D. J. Robbins, W. J. Stewart, Magnetism from conductors and enhanced nonlinear phenomena. *IEEE Trans. Microw. Theory Tech.* **47**, 2075–2084 (1999). doi: 10.1109/22.798002
5. J. A. Schuller, M. L. Brongersma, General properties of dielectric optical antennas. *Opt. Express* **17**, 24084–24095 (2009). doi: 10.1364/OE.17.024084; pmid: 20052120
6. A. B. Evlyukhin, C. Reinhardt, A. Seidel, B. S. Luk'yanchuk, B. N. Chichkov, Optical response features of Si-nanoparticle arrays. *Phys. Rev. B* **82**, 045404 (2010). doi: 10.1103/PhysRevB.82.045404
7. A. García-Etxarri *et al*., Strong magnetic response of submicron silicon particles in the infrared. *Opt. Express* **19**, 4815–4826 (2011). doi: 10.1364/OE.19.004815; pmid: 21445117
8. A. I. Kuznetsov, A. E. Miroshnichenko, Y. H. Fu, J. Zhang, B. Luk'yanchuk, Magnetic light. *Sci. Rep.* **2**, 492 (2012). doi: 10.1038/srep00492; pmid: 22768382
9. Y. Zhang, M. Nieto-Vesperinas, J. J. Sáenz, Dielectric spheres with maximum forward scattering and zero backscattering: A search for their material composition. *J. Opt.* **17**, 105612 (2015). doi: 10.1088/2040-8978/17/10/105612
10. Y. H. Fu, A. I. Kuznetsov, A. E. Miroshnichenko, Y. F. Yu, B. Luk'yanchuk, Directional visible light scattering by silicon nanoparticles. *Nat. Commun.* **4**, 1527 (2013). doi: 10.1038/ncomms2538; pmid: 23443555
11. B. S. Luk'yanchuk, N. V. Voshchinnikov, R. Paniagua-Dominguez, A. I. Kuznetsov, Optimum forward light scattering by spherical and spheroidal dielectric nanoparticles with high refractive index. *ACS Photonics* **2**, 993–999 (2015). doi: 10.1021/acsphotonics.5b00261
12. A. B. Evlyukhin, C. Reinhardt, B. N. Chichkov, Multipole light scattering by nonspherical nanoparticles in the discrete dipole approximation. *Phys. Rev. B* **84**, 235429 (2011). doi: 10.1103/PhysRevB.84.235429
13. M. A. van de Haar, J. van de Groep, B. J. M. Brenny, A. Polman, Controlling magnetic and electric dipole modes in hollow silicon nanocylinders. *Opt. Express* **24**, 2047–2064 (2016). doi: 10.1364/OE.24.002047; pmid: 26906780
14. J. Zhang, K. F. MacDonald, N. I. Zheludev, Near-infrared trapped mode magnetic resonance in an all-dielectric metamaterial. *Opt. Express* **21**, 26721–26728 (2013). doi: 10.1364/OE.21.026721; pmid: 24216893
15. I. Staude *et al*., Tailoring directional scattering through magnetic and electric resonances in subwavelength silicon nanodisks. *ACS Nano* **7**, 7824–7832 (2013). doi: 10.1021/nn402736f; pmid: 23952969
16. J. A. Schuller, R. Zia, T. Taubner, M. L. Brongersma, Dielectric metamaterials based on electric and magnetic resonances of silicon carbide particles. *Phys. Rev. Lett.* **99**, 107401 (2007). doi: 10.1103/PhysRevLett.99.107401; pmid: 17930407
17. L. Cao, P. Fan, E. S. Barnard, A. M. Brown, M. L. Brongersma, Tuning the color of silicon nanostructures. *Nano Lett.* **10**, 2649–2654 (2010). doi: 10.1021/nl1013794; pmid: 20507083
18. G. Brönstrup *et al*., Optical properties of individual silicon nanowires for photonic devices. *ACS Nano* **4**, 7113–7122 (2010). doi: 10.1021/nn101076t; pmid: 21080685
19. K. Seo *et al*., Multicolored vertical silicon nanowires. *Nano Lett.* **11**, 1851–1856 (2011). doi: 10.1021/nl200201b; pmid: 21413684
20. A. B. Evlyukhin *et al*., Demonstration of magnetic dipole resonances of dielectric nanospheres in the visible region. *Nano Lett.* **12**, 3749–3755 (2012). doi: 10.1021/nl301594s; pmid: 22703443
21. A. I. Kuznetsov, J. Koch, B. N. Chichkov, Laser-induced backward transfer of gold nanodroplets. *Opt. Express* **17**, 18820–18825 (2009). doi: 10.1364/OE.17.018820; pmid: 20372615
22. U. Zywietz, A. B. Evlyukhin, C. Reinhardt, B. N. Chichkov, Laser printing of silicon nanoparticles with resonant optical electric and magnetic responses. *Nat. Commun.* **5**, 3402 (2014). doi: 10.1038/ncomms4402; pmid: 24595073
23. P. Spinelli, M. A. Verschuuren, A. Polman, Broadband omnidirectional antireflection coating based on subwavelength surface Mie resonators. *Nat. Commun.* **3**, 692 (2012). doi: 10.1038/ncomms1691; pmid: 22353722
24. P. Moitra *et al*., Large-scale all-dielectric metamaterial perfect reflectors. *ACS Photonics* **2**, 692–698 (2015). doi: 10.1021/acsphotonics.5b00148
25. L. Shi *et al*., Monodisperse silicon nanocavities and photonic crystals with magnetic response in the optical region. *Nat. Commun.* **4**, 1904 (2013). doi: 10.1038/ncomms2934; pmid: 23695698
26. S. Person *et al*., Demonstration of zero optical backscattering from single nanoparticles. *Nano Lett.* **13**, 1806–1809 (2013). doi: 10.1021/nl4005018; pmid: 23461654
27. J. C. Ginn *et al*., Realizing optical magnetism from dielectric metamaterials. *Phys. Rev. Lett.* **108**, 097402 (2012). doi: 10.1103/PhysRevLett.108.097402; pmid: 22463666
28. B. Luk'yanchuk *et al*., The Fano resonance in plasmonic nanostructures and metamaterials. *Nat. Mater.* **9**, 707–715 (2010). doi: 10.1038/nmat2810; pmid: 20733610
29. A. E. Miroshnichenko, S. Flach, Y. S. Kivshar, Fano resonances in nanoscale structures. *Rev. Mod. Phys.* **82**, 2257–2298 (2010). doi: 10.1103/RevModPhys.82.2257
30. M. Nieto-Vesperinas, R. Gómez-Medina, J. J. Sáenz, Angle-suppressed scattering and optical forces on submicrometer dielectric particles. *J. Opt. Soc. Am. A* **28**, 54–60 (2011). doi: 10.1364/JOSAA.28.000054; pmid: 21200411
31. R. Gómez-Medina *et al*., Electric and magnetic dipolar response of germanium nanospheres: Interference effects, scattering anisotropy, and optical forces. *J. Nanophotonics* **5**, 053512 (2011). doi: 10.1117/1.3603941
32. M. Kerker, D. Wang, G. Giles, Electromagnetic scattering by magnetic spheres. *J. Opt. Soc. Am.* **73**, 765–767 (1983). doi: 10.1364/JOSA.73.000765
33. A. Alu, N. Engheta, How does zero forward-scattering in magnetodielectric nanoparticles comply with the optical theorem? *J. Nanophotonics* **4**, 041590 (2010). doi: 10.1117/1.3449103
34. B. García-Cámara, J. M. Saiz, F. González, F. Moreno, Nanoparticles with unconventional scattering properties: Size effects. *Opt. Commun.* **283**, 490–496 (2010). doi: 10.1016/j.optcom.2009.10.027
35. J. M. Geffrin *et al*., Magnetic and electric coherence in forward- and back-scattered electromagnetic waves by a single dielectric subwavelength sphere. *Nat. Commun.* **3**, 1171 (2012). doi: 10.1038/ncomms2167; pmid: 23132021
36. L. Novotny, N. van Hulst, Antennas for light. *Nat. Photonics* **5**, 83–90 (2011). doi: 10.1038/nphoton.2010.237
37. R. K. Mongia, P. Bhartia, Dielectric resonator antennas—a review and general design relations for resonant frequency and bandwidth. *Int. J. Microwave Mill.* **4**, 230–247 (1994).
38. B. Rolly, B. Stout, N. Bonod, Boosting the directivity of optical antennas with magnetic and electric dipolar resonant particles. *Opt. Express* **20**, 20376–20386 (2012). doi: 10.1364/OE.20.020376; pmid: 23037088
39. M. K. Schmidt *et al*., Dielectric antennas—a suitable platform for controlling magnetic dipolar emission. *Opt. Express* **20**, 13636–13650 (2012). doi: 10.1364/OE.20.013636; pmid: 22714428
40. L. Zou *et al*., Dielectric resonator nanoantennas at visible frequencies. *Opt. Express* **21**, 1344–1352 (2013). doi: 10.1364/OE.21.001344; pmid: 23389028
41. A. E. Krasnok, A. E. Miroshnichenko, P. A. Belov, Y. S. Kivshar, All-dielectric optical nanoantennas. *Opt. Express* **20**, 20599–20604 (2012). doi: 10.1364/OE.20.020599
42. D. S. Filonov *et al*., Experimental verification of the concept of all-dielectric nanoantennas. *Appl. Phys. Lett.* **100**, 201113 (2012). doi: 10.1063/1.4719209
43. S. Hayashi, R. Koh, Y. Ichiyama, K. Yamamoto, Evidence for surface-enhanced Raman scattering on nonmetallic surfaces: Copper phthalocyanine molecules on GaP small particles. *Phys. Rev. Lett.* **60**, 1085–1088 (1988). doi: 10.1103/PhysRevLett.60.1085; pmid: 10037937
44. M. M. Sigalas, D. A. Fattal, R. S. Williams, S. Y. Wang, R. G. Beausoleil, Electric field enhancement between two Si microdisks. *Opt. Express* **15**, 14711–14716 (2007). doi: 10.1364/OE.15.014711; pmid: 19550752
45. P. Albella *et al*., Low-loss electric and magnetic field-enhanced spectroscopy with subwavelength silicon dimers. *J. Phys. Chem. C* **117**, 13573–13584 (2013). doi: 10.1021/jp4027018
46. G. Boudarham, R. Abdeddaim, N. Bonod, Enhancing the magnetic field intensity with a dielectric gap antenna. *Appl. Phys. Lett.* **104**, 021117 (2014). doi: 10.1063/1.4861166
47. R. M. Bakker *et al*., Magnetic and electric hotspots with silicon nanodimers. *Nano Lett.* **15**, 2137–2142 (2015). doi: 10.1021/acs.nanolett.5b00128; pmid: 25686205
48. B. Rolly, B. Bebey, S. Bidault, B. Stout, N. Bonod, Promoting magnetic dipolar transition in trivalent lanthanide ions with lossless Mie resonances. *Phys. Rev. B* **85**, 245432 (2012). doi: 10.1103/PhysRevB.85.245432
49. U. Zywietz *et al*., Electromagnetic resonances of silicon nanoparticle dimers in the visible. *ACS Photonics* **2**, 913–920 (2015). doi: 10.1021/acsphotonics.5b00105
50. J. van de Groep, T. Coenen, S. A. Mann, A. Polman, Direct imaging of hybridized eigenmodes in coupled silicon nanoparticles. *Optica* **3**, 93–99 (2016). doi: 10.1364/OPTICA.3.000093
51. M. Caldarola *et al*., Non-plasmonic nanoantennas for surface enhanced spectroscopies with ultra-low heat conversion. *Nat. Commun.* **6**, 7915 (2015). doi: 10.1038/ncomms8915; pmid: 26238815
52. A. E. Miroshnichenko, Y. S. Kivshar, Fano resonances in all-dielectric oligomers. *Nano Lett.* **12**, 6459–6463 (2012). doi: 10.1021/nl303927q; pmid: 23170879
53. K. E. Chong *et al*., Observation of Fano resonances in all-dielectric nanoparticle oligomers. *Small* **10**, 1985–1990 (2014). doi: 10.1002/smll.201303612; pmid: 24616191


Downloaded from http://science.sciencemag.org/ on November 22, 2016

54. P. Fan, Z. Yu, S. Fan, M. L. Brongersma, Optical Fano resonance of an individual semiconductor nanostructure. *Nat. Mater.* **13**, 471–475 (2014). doi: 10.1038/nmat3927; pmid: 24747781
55. N. Papasimakis, V. A. Fedotov, V. Savinov, T. A. Raybould, N. I. Zheludev, Electromagnetic toroidal excitations in matter and free space. *Nat. Mater.* **15**, 263–271 (2016). doi: 10.1038/nmat4563; pmid: 26906961
56. A. E. Miroshnichenko *et al*., Nonradiating anapole modes in dielectric nanoparticles. *Nat. Commun.* **6**, 8069 (2015). doi: 10.1038/ncomms9069; pmid: 26311109
57. G. Grinblat, Y. Li, M. P. Nielsen, R. F. Oulton, S. A. Maier, Enhanced third harmonic generation in single germanium nanodisks excited at the anapole mode. *Nano Lett.* **16**, 4635–4640 (2016). doi: 10.1021/acs.nanolett.6b01958; pmid: 27331867
58. M. R. Shcherbakov *et al*., Enhanced third-harmonic generation in silicon nanoparticles driven by magnetic response. *Nano Lett.* **14**, 6488–6492 (2014). doi: 10.1021/nl503029j; pmid: 25322350
59. Y. Yang *et al*., Nonlinear Fano-resonant dielectric metasurfaces. *Nano Lett.* **15**, 7388–7393 (2015). doi: 10.1021/acs.nanolett.5b02802; pmid: 26501777
60. S. Liu *et al*., Resonantly enhanced second-harmonic generation using III-V semiconductor all-dielectric metasurfaces. *Nano Lett.* **16**, 5426–5432 (2016). doi: 10.1021/acs.nanolett.6b01816; pmid: 27501472
61. V. F. Gili *et al*., Monolithic AlGaAs second-harmonic nanoantennas. *Opt. Express* **24**, 15965–15971 (2016). doi: 10.1364/OE.24.015965; pmid: 26259100
62. S. Makarov *et al*., Tuning of magnetic optical response in a dielectric nanoparticle by ultrafast photoexcitation of dense electron-hole plasma. *Nano Lett.* **15**, 6187–6192 (2015). doi: 10.1021/acs.nanolett.5b02534; pmid: 26259100
63. M. R. Shcherbakov *et al*., Ultrafast all-optical switching with magnetic resonances in nonlinear dielectric nanostructures. *Nano Lett.* **15**, 6985–6990 (2015). doi: 10.1021/acs.nanolett.5b02989; pmid: 26393983
64. L. Lewin, The electrical constants of a material loaded with spherical particles. *Proc. Inst. Electr. Eng.* **94**, 65–68 (1947).
65. G. Videen, W. S. Bickel, Light-scattering resonances in small spheres. *Phys. Rev. A* **45**, 6008–6012 (1992). doi: 10.1103/PhysRevA.45.6008; pmid: 9907700
66. S. O'Brien, J. B. Pendry, Photonic bandgap effects and magnetic activity in dielectric composites. *J. Phys. Condens. Matter* **14**, 4035–4044 (2002). doi: 10.1088/0953-8984/14/15/317
67. C. L. Holloway, E. F. Kuester, J. Baker-Jarvis, P. Kabos, A double negative (DNG) composite medium composed of magnetodielectric spherical particles embedded in a matrix. *IEEE Trans. Antenn. Propag.* **51**, 2596–2603 (2003). doi: 10.1109/TAP.2003.817563
68. Q. Zhao, J. Zhou, F. Zhang, D. Lippens, Mie resonance-based dielectric metamaterials. *Mater. Today* **12**, 60–69 (2009). doi: 10.1016/S1369-7021(09)70318-9
69. M. V. Rybin *et al*., Phase diagram for the transition from photonic crystals to dielectric metamaterials. *Nat. Commun.* **6**, 10102 (2015). doi: 10.1038/ncomms10102; pmid: 26626302
70. P. Moitra *et al*., Realization of an all-dielectric zero-index optical metamaterial. *Nat. Photonics* **7**, 791–795 (2013). doi: 10.1038/nphoton.2013.214
71. N. Yu, F. Capasso, Flat optics with designer metasurfaces. *Nat. Mater.* **13**, 139–150 (2014). doi: 10.1038/nmat3839; pmid: 24452357
72. P. Lalanne, S. Astilean, P. Chavel, E. Cambril, H. Launois, Design and fabrication of blazed binary diffractive elements with sampling periods smaller than the structural cutoff. *J. Opt. Soc. Am. A* **16**, 1143 (1999). doi: 10.1364/JOSAA.16.001143
73. E. Schonbrun, K. Seo, K. B. Crozier, Reconfigurable imaging systems using elliptical nanowires. *Nano Lett.* **11**, 4299–4303 (2011). doi: 10.1021/nl202324s; pmid: 21923112
74. P. R. West *et al*., All-dielectric subwavelength metasurface focusing lens. *Opt. Express* **22**, 26212–26221 (2014). doi: 10.1364/OE.22.026212; pmid: 25401653
75. A. Arbabi, Y. Horie, M. Bagheri, A. Faraon, Dielectric metasurfaces for complete control of phase and polarization with subwavelength spatial resolution and high transmission. *Nat. Nanotechnol.* **10**, 937–943 (2015). doi: 10.1038/nnano.2015.186; pmid: 26322944
76. S. Kruk *et al*., Broadband highly efficient dielectric metadevices for polarization control. *APL Photonics* **1**, 030801 (2016). doi: 10.1063/1.4949007
77. Z. Bomzon, V. Kleiner, E. Hasman, Pancharatnam-Berry phase in space-variant polarization-state manipulations with subwavelength gratings. *Opt. Lett.* **26**, 1424–1426 (2001). doi: 10.1364/OL.26.001424; pmid: 18049626
78. U. Levy, C.-H. Tsai, H.-C. Kim, Y. Fainman, Design, fabrication and characterization of subwavelength computer-generated holograms for spot array generation. *Opt. Express* **12**, 5345–5355 (2004). doi: 10.1364/OPEX.12.005345; pmid: 19484095
79. D. Lin, P. Fan, E. Hasman, M. L. Brongersma, Dielectric gradient metasurface optical elements. *Science* **345**, 298–302 (2014). doi: 10.1126/science.1253213; pmid: 25035488
80. M. Khorasaninejad *et al*., Metalenses at visible wavelengths: Diffraction-limited focusing and subwavelength resolution imaging. *Science* **352**, 1190–1194 (2016). doi: 10.1126/science.aaf6644; pmid: 27257251
81. Y. Yang *et al*., Dielectric meta-reflectarray for broadband linear polarization conversion and optical vortex generation. *Nano Lett.* **14**, 1394–1399 (2014). doi: 10.1021/nl4044482; pmid: 24547692
82. M. Decker *et al*., High-efficiency dielectric Huygens' surfaces. *Adv. Opt. Mater.* **3**, 813–820 (2015). doi: 10.1002/adom.201400584
83. C. Pfeiffer *et al*., Efficient light bending with isotropic metamaterial Huygens' surfaces. *Nano Lett.* **14**, 2491–2497 (2014). doi: 10.1021/nl5001746; pmid: 24689341
84. Y. F. Yu *et al*., High-transmission dielectric metasurface with $2\pi$ phase control at visible wavelengths. *Laser Photonics Rev.* **9**, 412–418 (2015). doi: 10.1002/lpor.201500041
85. K. E. Chong *et al*., Polarization-independent silicon metadevices for efficient optical wavefront control. *Nano Lett.* **15**, 5369–5374 (2015). doi: 10.1021/acs.nanolett.5b01752; pmid: 26192100
86. M. I. Shalaev *et al*., High-efficiency all-dielectric metasurfaces for ultracompact beam manipulation in transmission mode. *Nano Lett.* **15**, 6261–6266 (2015). doi: 10.1021/acs.nanolett.5b02926; pmid: 26280735
87. J. Du, Z. Lin, S. T. Chui, G. Dong, W. Zhang, Nearly total omnidirectional reflection by a single layer of nanorods. *Phys. Rev. Lett.* **110**, 163902 (2013). doi: 10.1103/PhysRevLett.110.163902; pmid: 23679606
88. C. J. Chang-Hasnain, W. Yang, High-contrast gratings for integrated optoelectronics. *Adv. Opt. Photonics* **4**, 379–440 (2012). doi: 10.1364/AOP.4.000379
89. S. Liu *et al*., Optical magnetic mirrors without metals. *Optica* **1**, 250 (2014). doi: 10.1364/OPTICA.1.000250
90. R. Paniagua-Domínguez *et al*., Generalized Brewster effect in dielectric metasurfaces. *Nat. Commun.* **7**, 10362 (2016). doi: 10.1038/ncomms10362; pmid: 26783075
91. C. Wu *et al*., Spectrally selective chiral silicon metasurfaces based on infrared Fano resonances. *Nat. Commun.* **5**, 3892 (2014). doi: 10.1038/ncomms4892; pmid: 24861488
92. Y. Yang, I. I. Kravchenko, D. P. Briggs, J. Valentine, All-dielectric metasurface analogue of electromagnetically induced transparency. *Nat. Commun.* **5**, 5753 (2014). doi: 10.1038/ncomms6753; pmid: 25511508
93. F. Aieta, M. A. Kats, P. Genevet, F. Capasso, Multiwavelength achromatic metasurfaces by dispersive phase compensation. *Science* **347**, 1342–1345 (2015). doi: 10.1126/science.aaa2494; pmid: 25700175
94. J. Sautter *et al*., Active tuning of all-dielectric metasurfaces. *ACS Nano* **9**, 4308–4315 (2015). doi: 10.1021/acsnano.5b00723; pmid: 25748581
95. P. P. Iyer, N. A. Butakov, J. A. Schuller, Reconfigurable semiconductor phased-array metasurfaces. *ACS Photonics* **2**, 1077–1084 (2015). doi: 10.1021/acsphotonics.5b00132
96. S. Jahani, Z. Jacob, All-dielectric metamaterials. *Nat. Nanotechnol.* **11**, 23–36 (2016). doi: 10.1038/nnano.2015.304; pmid: 26740041
97. L. Cao *et al*., Engineering light absorption in semiconductor nanowire devices. *Nat. Mater.* **8**, 643–647 (2009). doi: 10.1038/nmat2477; pmid: 19578337
98. L. Cao, J.-S. Park, P. Fan, B. Clemens, M. L. Brongersma, Resonant germanium nanoantenna photodetectors. *Nano Lett.* **10**, 1229–1233 (2010). doi: 10.1021/nl9037278; pmid: 20230043
99. M. Garín *et al*., All-silicon spherical-Mie-resonator photodiode with spectral response in the infrared region. *Nat. Commun.* **5**, 3440 (2014). doi: 10.1038/ncomms4440; pmid: 24614644
100. G. Grzela *et al*., Nanowire antenna emission. *Nano Lett.* **12**, 5481–5486 (2012). doi: 10.1021/nl301907f; pmid: 23030698
101. J. A. Schuller, T. Taubner, M. L. Brongersma, Optical antenna thermal emitters. *Nat. Photonics* **3**, 658–661 (2009). doi: 10.1038/nphoton.2009.188
102. L. Cao *et al*., Semiconductor nanowire optical antenna solar absorbers. *Nano Lett.* **10**, 439–445 (2010). doi: 10.1021/nl9036627; pmid: 20078065
103. J. Grandidier, D. M. Callahan, J. N. Munday, H. A. Atwater, Light absorption enhancement in thin-film solar cells using whispering gallery modes in dielectric nanospheres. *Adv. Mater.* **23**, 1272–1276 (2011). doi: 10.1002/adma.201004393; pmid: 21381129
104. M. L. Brongersma, Y. Cui, S. Fan, Light management for photovoltaics using high-index nanostructures. *Nat. Mater.* **13**, 451–460 (2014). doi: 10.1038/nmat3921; pmid: 24751773
105. F. Priolo, T. Gregorkiewicz, M. Galli, T. F. Krauss, Silicon nanostructures for photonics and photovoltaics. *Nat. Nanotechnol.* **9**, 19–32 (2014). doi: 10.1038/nnano.2013.271; pmid: 24390564
106. S. J. Kim *et al*., Light trapping for solar fuel generation with Mie resonances. *Nano Lett.* **14**, 1446–1452 (2014). doi: 10.1021/nl404575e; pmid: 24524658
107. S. J. Kim, P. Fan, J.-H. Kang, M. L. Brongersma, Creating semiconductor metafilms with designer absorption spectra. *Nat. Commun.* **6**, 7591 (2015). doi: 10.1038/ncomms8591; pmid: 26184335


## ACKNOWLEDGMENTS

We thank I. Brener, A. Krasnok, D. Neshev, I. Staude, and J. Valentine for useful discussions and R. Paniagua for help with design of the figures. Supported by the DSI core fund and A*STAR Science and Engineering Research Council Pharos grant 1527000025 (A.I.K. and B.L.); the Australian Research Council (A.E.M. and Y.S.K.); and U.S. Air Force Office of Scientific Research grant FA9550-14-1-0389 and the U.S. Department of Energy (DOE) Light-Material Interactions Energy Frontier Research Center, an Energy Frontier Research Center funded by the DOE Office of Science, Basic Energy Sciences, under award DE-SC0001293 (M.L.B.).

10.1126/science.aag2472

Downloaded from http://science.sciencemag.org/ on November 22, 2016

RESEARCH ARTICLES

QUANTUM OPTICS

# An integrated diamond nanophotonics platform for quantum-optical networks

A. Sipahigil,[1]* R. E. Evans,[1]* D. D. Sukachev,[1,2,3]* M. J. Burek,[4] J. Borregaard,[1] M. K. Bhaskar,[1] C. T. Nguyen,[1] J. L. Pacheco,[5] H. A. Atikian,[4] C. Meuwly,[4] R. M. Camacho,[5] F. Jelezko,[6] E. Bielejec,[5] H. Park,[1,7] M. Lončar,[4] M. D. Lukin[1]†

**Efficient interfaces between photons and quantum emitters form the basis for quantum networks and enable optical nonlinearities at the single-photon level. We demonstrate an integrated platform for scalable quantum nanophotonics based on silicon-vacancy (SiV) color centers coupled to diamond nanodevices. By placing SiV centers inside diamond photonic crystal cavities, we realize a quantum-optical switch controlled by a single color center. We control the switch using SiV metastable states and observe optical switching at the single-photon level. Raman transitions are used to realize a single-photon source with a tunable frequency and bandwidth in a diamond waveguide. By measuring intensity correlations of indistinguishable Raman photons emitted into a single waveguide, we observe a quantum interference effect resulting from the superradiant emission of two entangled SiV centers.**

Efficient interfaces between photons and quantum emitters are central to applications in quantum science (*1*, *2*) but are challenging to implement due to weak interactions between single photons and individual quantum emitters. Despite advances in the control of microwave and optical fields using cavity and waveguide quantum electrodynamics (QED) (*3*–*9*), the realization of integrated quantum devices where multiple qubits are coupled by optical photons remains an outstanding challenge (*10*). In particular, due to their complex environments, solid-state emitters have optical transitions that generally exhibit a large inhomogeneous distribution (*10*, *11*), rapid decoherence (*7*), and substantial spectral diffusion, especially in nanostructures (*12*). Moreover, most solid-state emitters appear at random positions, making the realization of scalable devices with multiple emitters difficult (*11*, *13*).

## Diamond platform for quantum nanophotonics

Our approach uses negatively charged silicon-vacancy (SiV) color centers (*14*) integrated into diamond nanophotonic devices. SiV centers in high-quality diamond crystals show nearly lifetime-broadened optical transitions with an inhomogeneous (ensemble) distribution on the order of the lifetime-broadened linewidth (*15*). These properties arise from the inversion symmetry of the SiV center, which protects the optical transitions from electric field noise in the environment (*16*, *17*).

The stable quantum emitters are integrated into one-dimensional diamond waveguides and photonic-crystal cavities with small mode volumes ($V$) and large quality factors ($Q$). These nanophotonic devices are fabricated using angled reactive-ion etching to scalably create freestanding single-mode structures starting from bulk diamond (*18*, *19*). As an example, Fig. 1C and fig. S3 show structures consisting of a notch for free space-waveguide coupling (at ~1% efficiency), a waveguide section on each side, and a cavity (Fig. 1B). The measured cavity $Q = 7200(500)$ is limited predominantly by decay to the waveguide, so the system has high transmission on resonance. We measure the cavity mode profile and infer $V \sim 2.5(\lambda/n)^3$ using a uniform, high-density SiV ensemble (fig. S4).

To obtain optimal coupling between an individual SiV and the cavity mode, we use a focused ion beam to implant $Si^+$ ions at the center of the cavities, as illustrated in Fig. 1C. To form SiVs and mitigate crystal damage from fabrication and implantation, we subsequently anneal the sample at 1200°C in vacuum (*17*). This targeted implantation technique enables positioning of emitters inside the cavity with close to 40-nm precision in all three dimensions (*19*) and control over the isotope and average number of implanted $Si^+$ ions. We fabricate ~2000 SiV-cavity nodes on a single diamond sample with optimal spatial alignment. For example, Fig. 1D shows fluorescence from the array of cavities implanted with $Si^+$ ions in Fig. 1C. SiV fluorescence is detected at

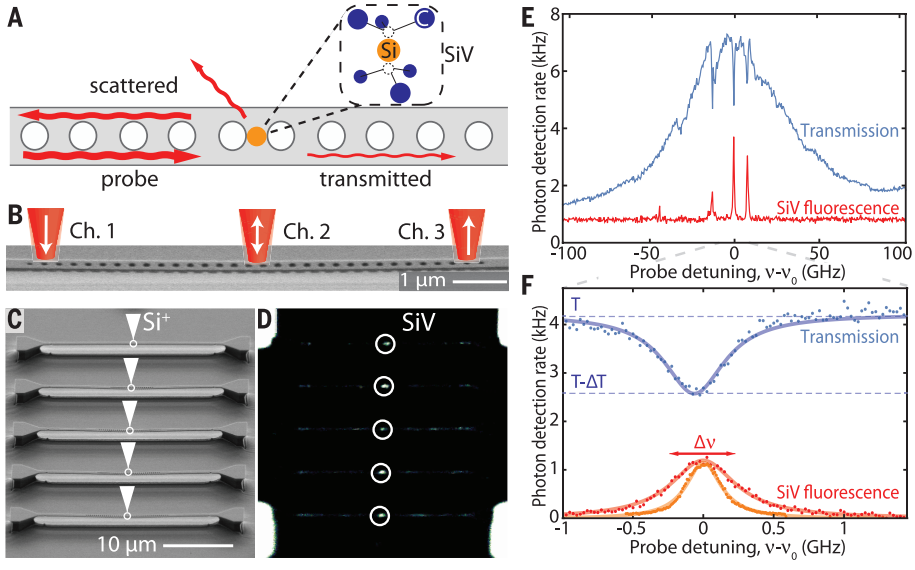


**Fig. 1. Positioning and strong coupling of SiVs in diamond cavities.** (**A**) Schematic of a SiV center in a diamond photonic crystal cavity. (**B**) Scanning electron micrograph (SEM) of a cavity. (**C**) SEM of five cavities fabricated out of undoped diamond. After fabrication, SiV centers are deterministically positioned at the center of each cavity using focused $Si^+$ ion beam implantation. (**D**) SiV fluorescence is detected at the center of each nanocavity shown in (C). (**E**) Measured cavity transmission (blue, Ch. 3) and SiV scattered fluorescence (red, Ch. 2) spectrum. Three SiV centers are coupled to the cavity, and each results in suppressed transmission. (**F**) Strong extinction, $\Delta T/T = 38(3)\%$, of probe transmission from a single SiV center. Optical transition linewidths $\Delta\nu$ are measured with the cavity detuned (orange) and on resonance (red, count rate offset by −150 Hz and multiplied by 3.3) with the SiV transition.

[1]Department of Physics, Harvard University, Cambridge, MA 02138, USA. [2]Russian Quantum Center, Skolkovo, Moscow 143025, Russia. [3]P. N. Lebedev Physical Institute of the Russian Academy of Sciences, Moscow 119991, Russia. [4]John A. Paulson School of Engineering and Applied Sciences, Harvard University, Cambridge, MA 02138, USA. [5]Sandia National Laboratories, Albuquerque, NM 87185, USA. [6]Institute for Quantum Optics, University of Ulm, 89081 Ulm, Germany. [7]Department of Chemistry and Chemical Biology, Harvard University, Cambridge, MA 02138, USA.
*These authors contributed equally to this work. †Corresponding author. Email: lukin@physics.harvard.edu

Downloaded from http://science.sciencemag.org/ on November 22, 2016

the center of each cavity, demonstrating high-yield creation of SiV-cavity nodes. The number of SiVs created varies based on the number of implanted ions and the ~2% conversion yield from $Si^+$ to SiV (*19*). For our experiments, we create an average of ~5 SiVs per cavity. Because each SiV can be resolved in the frequency domain, device creation is nearly deterministic: Most SiV-cavity nodes can be used for the experiments described below.

We characterize the coupled SiV-cavity system at 4 K (*19*). As shown in Fig. 1B and fig. S1, three optical beams are focused on the nanostructure to excite the waveguide mode (Channel 1), to detect fluorescence scattering and to control the SiV (Channel 2), and to detect transmission (Channel 3). In subsequent experiments (Figs. 4 and 5), efficient collection with a tapered optical fiber is employed. We scan the frequency $v$ of the weak excitation laser across the SiV resonance $\nu_0 = 406.706$ THz and monitor the transmitted and scattered field intensities (Fig. 1E). We observe three fluorescence peaks in Channel 2 from three SiV centers in a single cavity (red curve in Fig. 1E) (*19*). At the same time, within the broad cavity transmission spectrum measured in Channel 3, each of these three resonances results in strong extinction of the cavity transmission, indicating that all three SiVs couple to the cavity mode.

The strength of the SiV-cavity coupling is evaluated using the data in Fig. 1F. When the cavity is off-resonant with the emitter, the SiV transition linewidth is $\Delta\nu = 298(5)$ MHz (orange curve) and the excited state lifetime is $\tau_e = 1.8(1)$ ns. This is close to the lifetime-broadening limit of 90 MHz, with additional nonradiative broadening likely due to a combination of finite temperature effects (*20*) and residual spectral diffusion (*17*). When the cavity is tuned into resonance (*19*), the transition is radiatively broadened to $\Delta\nu = 590(30)$ MHz (red curve), with a corresponding measured reduction in lifetime $\tau_e = 0.6(1)$ ns (limited by detection bandwidth). At the same time, we find that a single SiV results in 38(3)% extinction of the probe field in transmission (Fig. 1F, blue curve). Based on the radiative broadening shown in Fig. 1F, we infer a cooperativity of $C = 4g^2/\kappa\gamma = 1.0(1)$ for the SiV-cavity system with cavity QED parameters $\{g, \kappa, \gamma\}/2\pi = \{2.1, 57, 0.30\}$ GHz, where $g$ is the single-photon Rabi frequency, $\kappa$ is the cavity intensity decay rate, and $\gamma$ is the SiV optical transition linewidth (*19*).

## Quantum-optical switch based on a single SiV center

The coupled emitter-cavity system can be used to create strong interactions between single photons and achieve single-photon nonlinearities (*2*, *21*). To probe the nonlinear response of the SiV-cavity system, we repeat the transmission and linewidth measurements of Fig. 1F at increasing probe intensities. As expected (*21*, *22*), we find that the system saturates at a level less than a single photon per Purcell-enhanced excited-state lifetime (Fig. 3A), resulting in power broadening in fluorescence ($\Delta\nu$) and reduced extinction in transmission ($\Delta T/T$) (*19*).

We realize an all-optical switch with memory by optically controlling the metastable orbital states (*23*–*25*) of a single SiV (Fig. 2). Specifically, we use a 30-ns-long gate pulse to optically pump the SiV to an orbital state that is uncoupled ($|u\rangle$, Fig. 2A) or coupled ($|c\rangle$, Fig. 2B) to a weak probe field resonant with the cavity. The response of the system to the probe field after the gate pulse is monitored both in transmission (Fig. 2C) and fluorescence (Fig. 2D). If the gate pulse initializes the system in state $|c\rangle$ (blue curves), the transmission is reduced and the fluorescence scattering is increased. Initializing the system in state $|u\rangle$ (red curves) results in increased transmission and reduced fluorescence scattering. The observed modulation demonstrates switching of a weak probe pulse by a classical gate pulse. The switch memory time is limited by a thermal phonon relaxation process between $|c\rangle$ and $|u\rangle$ that depolarizes the system over $\tau_0 \sim 10$ ns at 4 K (*20*).

To investigate these processes at the single-photon level, we resonantly excite the SiV-cavity system with a weak coherent light and measure photon statistics of the scattered and transmitted fields. To this end, scattered and transmitted light are each split to two detectors (fig. S1), allowing us to measure normalized intensity autocorrelations for the scattered [$g^{(2)}_{SS}(\tau)$, Fig. 3B] and transmitted [$g^{(2)}_{TT}(\tau)$, Fig. 3C] fields, as well as cross-correlations between the two channels [$g^{(2)}_{ST}(\tau)$, Fig. 3D]. At short time scales determined by the excited state lifetime $\tau_e$, we observe strong antibunching of photons scattered by the SiV [$g^{(2)}_{SS}(0) = 0.15(4)$], consistent with scattering from a single emitter. In transmission, the photons are strongly bunched, with $g^{(2)}_{TT}(0) = 1.50(5)$. This photon bunching in transmission results from the interference between the weak probe field and the antibunched resonant scattering from the SiV. The destructive interference for single photons yields preferential transmission of photon pairs and is a direct indication of nonlinear response at the single-photon level (*21*, *22*). In other words, a single photon in an optical pulse switches a second photon, and the

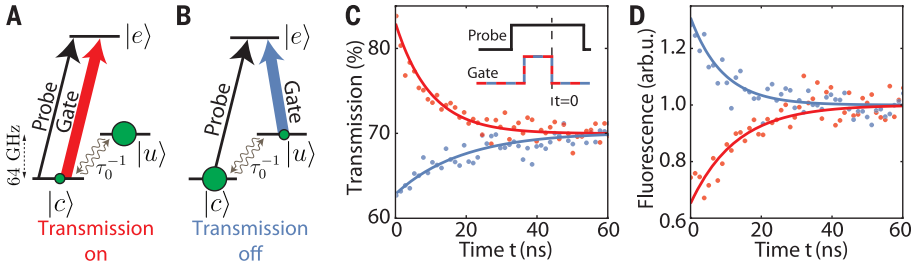


**Fig. 2. An all-optical switch using a single SiV.** (**A** and **B**) The transmission of a probe field is modulated using a gate pulse that optically pumps the SiV to state $|u\rangle$ (A) or $|c\rangle$ (B). (**C**) Probe field transmission measured after the initialization gate pulse. Initialization in state $|u\rangle$ ($|c\rangle$) results in increased (suppressed) transmission and (**D**) suppressed (increased) fluorescence.

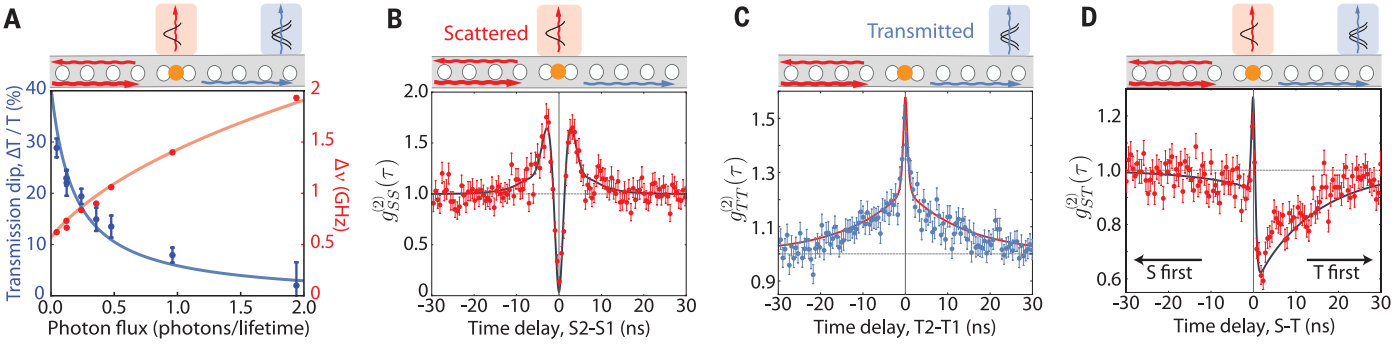


**Fig. 3. Single-photon switching.** (**A**) Cavity transmission and SiV transition linewidth measured at different probe intensities. (**B** and **C**) Intensity autocorrelations of the scattered (fluorescence) and transmitted fields. The scattered field shows antibunching (B), whereas the transmitted photons are bunched with an increased contribution from photon pairs (C). (**D**) Intensity cross-correlation between the scattered and transmitted fields. $g^{(2)}_{SS}$ is measured under different conditions with above-saturation excitation (*19*).

Downloaded from http://science.sciencemag.org/ on November 22, 2016

system acts as a photon number router where single photons are scattered while photon pairs are preferentially transmitted. Finally, both bunching [$g^{(2)}_{ST}(0) = 1.16(5)$] and antibunching are observed for scattering-transmission cross-correlations at fast and slow time scales, respectively.

To understand the system saturation and switching responses in Figs. 2 and 3, we model the quantum dynamics of the SiV-cavity system using the cavity QED parameters measured in Fig. 1 and a three-level model of the SiV (Fig. 2 and fig. S7). The results of our calculation (*19*) are in excellent agreement with our observations (solid curves in Figs. 1 to 3). Specifically, the presence of a second metastable state, $|u\rangle$, reduces the extinction in linear transmission (Fig. 1F) and affects the nonlinear saturation response (*19*, *21*). The metastable state $|u\rangle$ also causes both slow dynamics in photon correlation measurements (Fig. 3) at the metastable orbital relaxation timescale of $\tau_0$ and an asymmetry in cross-correlations. In these measurements, the detection of a transmitted (scattered) photon preferentially prepares the SiV in state $|u\rangle$ ($|c\rangle$), resulting in enhanced (reduced) transmission and reduced (enhanced) scattering for $\tau_0$ (*19*).

## Tunable single-photon source using Raman transitions

A key challenge for building scalable quantum networks using solid-state emitters is the spectral inhomogeneity of their optical transitions. Although the inhomogeneous broadening of SiVs is suppressed by inversion symmetry, SiVs inside nanostructures still display a substantial inhomogeneous distribution (seen in Fig. 1E) due to residual strain from fabrication (*17*). To mitigate this effect, we use Raman transitions between the metastable orbital states of SiV centers. When a single SiV is excited from the state $|u\rangle$ at a detuning $\Delta$ (Fig. 4B), the emission spectrum includes a spontaneous component at frequency $\nu_{ec}$ and a Raman component at frequency $\nu_{ec} - \Delta$ that is tunable by choosing $\Delta$.

Tunable single-photon emission is experimentally realized by implanting SiVs inside a one-dimensional diamond waveguide and continuously exciting the emitters from free space (Fig. 4A). The fluorescence scattering into the diamond waveguide is coupled to a tapered single-mode fiber with ≥70% efficiency using adiabatic mode transfer (*3*, *19*, *26*). As we change the excitation frequency from near-resonance to a detuning of $\Delta = 6$ GHz, we observe a corresponding tuning of the Raman emission frequency $\nu_{ec} - \Delta$, whereas the spontaneous emission frequency remains nearly fixed at $\nu_{ec}$ up to an AC Stark shift (Fig. 4C and fig. S8).

The Raman linewidth can be controlled by both the detuning and the power of the driving laser and is ultimately limited by the ground state coherence between states $|u\rangle$ and $|c\rangle$. At large detunings and low power, we measure a subnatural Raman linewidth of less than 30 MHz (fig. S8). The nonclassical nature of the Raman emission is demonstrated via photon correlation measurements. The Raman photons from a single SiV are antibunched with $g^{(2)}_{single}(0) = 0.16(3)$ (orange curve in Fig. 5D), close to the ideal limit $g^{(2)}_{single}(0) = 0$. For the continuous excitation used here, we detect Raman photons at a rate of ~15 kHz from a single SiV. After a Raman scattering event, the SiV cannot scatter a second photon within the metastable orbital state relaxation time scale $\tau_0$, limiting the Raman emission rate. This rate can be improved using a pulsed excitation scheme, in which the SiV is first prepared in state $|u\rangle$ via optical pumping and subsequently excited with a pulse of desired shape and duration. Unlike previous demonstrations of Raman tuning of solid-state quantum emitters (*27*, *28*), the tuning range demonstrated here is comparable to the inhomogeneous distribution of the SiV ensemble and can thus be used to tune pairs of SiV centers into resonance.

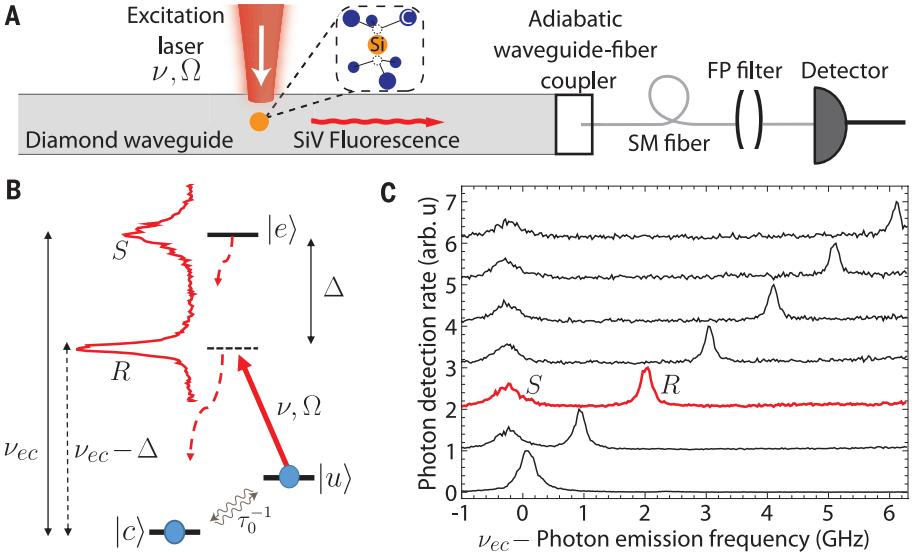


**Fig. 4. Spectrally tunable single photons using Raman transitions.** (**A**) Photons scattered by a single SiV into a diamond waveguide are efficiently coupled to a single-mode (SM) fiber. A scanning Fabry-Perot (FP) cavity is used to measure emission spectra (*19*). (**B**) Under excitation at a detuning $\Delta$, the emission spectrum contains spontaneous emission (labeled *S*) at frequency $\nu_{ec}$ and narrow Raman emission (*R*) at frequency $\nu_{ec} - \Delta$. (**C**) $\Delta$ is varied from 0 to 6 GHz in steps of 1 GHz, and a corresponding tuning of the Raman emission frequency is observed. The red curves in (B) and (C) are the same data.

## Entanglement of SiV centers in a nanophotonic waveguide

Quantum entanglement is an essential ingredient in quantum networks (*1*). Although optical photons were recently used to entangle solid-state qubits over long distances (*29*, *30*), optically mediated entanglement of solid-state qubits in a single nanophotonic device has not yet been observed.

Motivated by the proposals for probabilistic entanglement generation based on interference of indistinguishable photons (*31*), we use two SiV centers inside a diamond waveguide (Fig. 5A), continuously excite each SiV on the $|u\rangle \rightarrow |e\rangle$ transition with a separate laser, and measure photon correlations in the waveguide mode. If the Raman transitions of the two SiVs are not tuned into resonance, the photons are distinguishable, resulting in the measured $g^{(2)}_{dist}(0) = 0.63(3)$ (blue curve in Fig. 5D) close to the conventional limit associated with two single-photon emitters $g^{(2)}_{dist}(0) = 0.5$ (*16*, *19*). Alternatively, if the Raman transitions of the two SiVs are tuned instead into resonance with each other, an interference feature is observed in photon correlations around zero time delay, with $g^{(2)}_{ind}(0) = 0.98(5)$ (red curve in Fig. 5D).

These results can be understood by considering the level diagrams in Fig. 5, B and C, involving the SiV metastable states $|u\rangle$ and $|c\rangle$ (*8*, *32*). Photon correlation measurements probe the conditional dynamics of the two SiVs starting in state $|uu\rangle$ (*19*). In this state, each SiV scatters Raman single photons to the waveguide at a rate $\Gamma_{1D}$. However, when the Raman transitions of the two SiVs are tuned into resonance with each other, it is fundamentally impossible to distinguish which of the two emitters produced a waveguide photon. Thus, emission of an indistinguishable single photon leaves the two SiVs prepared in the entangled state $|B\rangle = (|cu\rangle + e^{i\phi}|uc\rangle)/\sqrt{2}$ (*19*, *31*) (Fig. 5B), where $\phi$ is set by the propagation phase between emitters spaced by $\Delta L$ and the relative phase of the driving lasers, which is constant in each experimental run (fig. S9). This state is a two-atom superradiant Dicke state with respect to the waveguide mode, independent of the value of $\Delta L$ (*19*, *32*). This implies that, although there is only a single excitation stored in the state $|B\rangle$, it will scatter Raman photons at a rate $2\Gamma_{1D}$ that is twice the scattering rate of a single emitter. This enhanced emission rate into the waveguide mode results in the experimentally observed interference peak at short time delays (Fig. 5D) and is a signature of entanglement. Our measured value of $g^{(2)}_{ind}(0) = 0.98(5)$ is close to the ideal limit, where the factor of two enhancement in the emission from the entangled state $|B\rangle$ yields $g^{(2)}_{ind}(0) = 1$.

Downloaded from http://science.sciencemag.org/ on November 22, 2016

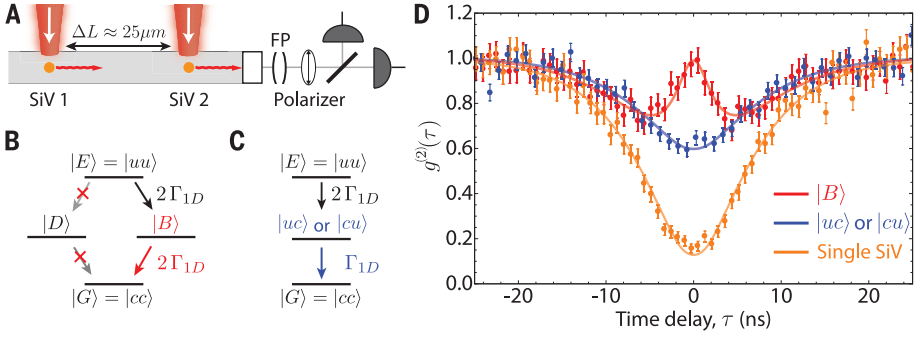


**Fig. 5. Quantum interference and two-SiV entanglement in a nanophotonic waveguide.** (**A**) Photons scattered by two SiV centers into a diamond waveguide are detected after a polarizer. (**B**) After emission of an indistinguishable photon, the two SiVs are in the entangled state $|B\rangle$, which decays at the collectively enhanced rate of $2\Gamma_{1D}$ into the waveguide. (**C**) After emission of a distinguishable photon, the two SiVs are in a classical mixture of states $|uc\rangle$ and $|cu\rangle$, which decays at a rate $\Gamma_{1D}$ into the waveguide. (**D**) Intensity autocorrelations for the waveguide photons. Exciting only a single SiV yields $g^{(2)}_{single}(0) = 0.16(3)$ for SiV1 (orange data), and $g^{(2)}_{single}(0) = 0.16(2)$ for SiV2. Blue: Both SiVs excited; Raman photons are spectrally distinguishable. Red: Both SiVs excited; Raman photons are tuned to be indistinguishable. The observed contrast between the blue and the red curves at $g^{(2)}(0)$ is due to the collectively enhanced decay of $|B\rangle$. The solid curves are fits to a model (*19*).

The visibility of the interference signal in photon correlation measurements in Fig. 5D can be used to evaluate a lower bound on the conditional entanglement fidelity $F = \langle B|\rho|B\rangle$ (*19*). For experimental runs in which we detect a photon coincidence within the interference window (rate ~0.5 Hz), we find that the two SiVs were in an entangled state with $F \geq 82(7)\%$ after the emission of the first photon. This conditional fidelity is primarily limited by laser leakage and scattering from nearby SiVs that yield false detection events (*19*). Our measurements also demonstrate entanglement generation (rate ~30 kHz) after a single Raman photon emission event. As discussed in (*19*), using photon correlation data and steady-state populations of SiV orbital states, we find that a single photon emission results in an entangled state with positive concurrence $\mathcal{C} > 0.090(0.024)$, which is limited by imperfect initialization in state $|uu\rangle$. The width of the interference signal in Fig. 5D can be used to extract a lifetime $T_2^* \approx 2.5$ ns of the entangled state $|B\rangle$. This lifetime is mainly limited by imperfect spectral tuning of the two Raman photons from the two SiVs, resulting in a relative frequency detuning δ. In this regime, emission of a first photon results in a state $|\psi(\tau)\rangle = (|cu\rangle + e^{i(\phi-2\pi\delta\tau)}|uc\rangle)/\sqrt{2}$ that oscillates at frequency δ between states $|B\rangle$ and the subradiant state $|D\rangle = (|cu\rangle - e^{i\phi}|uc\rangle)/\sqrt{2}$. Since $|D\rangle$ does not couple to the waveguide mode due to destructive interference, fluctuations in δ over different realizations result in decay of the collectively enhanced signal (central peak in red curve in Fig. 5D).

In our experiment, the photon propagation time is longer than $T_2^*$ and the entangled state dephases before it can be heralded by detection of the first photon. To generate useful heralded entanglement with high fidelity (*30*, *31*), a pulsed excitation scheme can be employed in which the two SiVs are optically initialized in state $|uu\rangle$ and excited by short pulses. The Raman emission frequencies can be further stabilized using a narrowband reference cavity to extend the lifetime of the entangled state.

## Outlook

The performance of these quantum nanophotonic devices can be improved in several ways. Control over the SiV orbital states is limited by the occupation of ~50 GHz phonons at 4 K, which causes relaxation between the metastable orbital states $|u\rangle$ and $|c\rangle$ and limits their coherence times to less than 50 ns. Phonon relaxation should be strongly suppressed by operating at temperatures below 300 mK or engineering the phononic density of states to enable millisecond-long coherence times (*20*). Even longer-lived quantum memories can potentially be obtained by storing the qubit in the $^{29}$Si nuclear spin (*24*), which is only weakly coupled to the environment (*33*). Furthermore, the demonstrated cooperativity in our nanocavity experiment is lower than the theoretical estimate based on an ideal two-level emitter optimally positioned in a cavity (*19*). The discrepancy is due to a combination of factors, including imperfect spatial and polarization alignment, phonon broadening (*20*), finite quantum efficiency (*13*), the branching ratio of the transition, and residual spectral diffusion (*17*). These imperfections also limit the collection efficiencies obtained in our waveguide experiments. Despite uncertainties in individual contributions, operation at lower temperatures and improved cavity designs with higher $Q/V$ ratios should enable spin-photon interfaces with high cooperativity C >> 1. Furthermore, the efficient fiber-diamond waveguide coupling can be improved to exceed 95% efficiency (*26*).

Our work demonstrates key ingredients required for realizing integrated quantum network nodes and opens up new possibilities for realizing large-scale systems involving multiple emitters strongly interacting via photons. Our fabrication approach can be used to create systems involving many coupled emitters per cavity as well as arrays of multiple atom-cavity nodes. Such a system can be used to implement entanglement generation, quantum memories, and quantum gates for either photonic or spin qubits, paving the way for the realization of scalable quantum networks (*1*, *2*).

## REFERENCES AND NOTES


1. H. J. Kimble, *Nature* **453**, 1023–1030 (2008).
2. D. E. Chang, V. Vuletić, M. D. Lukin, *Nat. Photonics* **8**, 685–694 (2014).
3. T. G. Tiecke *et al.*, *Nature* **508**, 241–244 (2014).
4. A. Reiserer, N. Kalb, G. Rempe, S. Ritter, *Nature* **508**, 237–240 (2014).
5. D. Englund *et al.*, *Nature* **450**, 857–861 (2007).
6. A. Javadi *et al.*, *Nat. Commun.* **6**, 8655 (2015).
7. S. Sun, H. Kim, G. S. Solomon, E. Waks, *Nat. Nanotechnol.* **11**, 539–544 (2016).
8. J. Mlynek, A. Abdumalikov, C. Eichler, A. Wallraff, *Nat. Commun.* **5**, 5186 (2014).
9. B. Casabone *et al.*, *Phys. Rev. Lett.* **111**, 100505 (2013).
10. P. Lodahl, S. Mahmoodian, S. Stobbe, *Rev. Mod. Phys.* **87**, 347–400 (2015).
11. A. Badolato *et al.*, *Science* **308**, 1158–1161 (2005).
12. A. Faraon, C. Santori, Z. Huang, V. M. Acosta, R. G. Beausoleil, *Phys. Rev. Lett.* **109**, 033604 (2012).
13. J. Riedrich-Möller *et al.*, *Nano Lett.* **14**, 5281–5287 (2014).
14. C. Hepp *et al.*, *Phys. Rev. Lett.* **112**, 036405 (2014).
15. L. J. Rogers *et al.*, *Nat. Commun.* **5**, 4739 (2014).
16. A. Sipahigil *et al.*, *Phys. Rev. Lett.* **113**, 113602 (2014).
17. R. E. Evans, A. Sipahigil, D. D. Sukachev, A. S. Zibrov, M. D. Lukin, *Phys. Rev. Applied* **5**, 044010 (2016).
18. M. J. Burek *et al.*, *Nat. Commun.* **5**, 5718 (2014).
19. Materials and methods are available as supplementary materials on *Science* Online.
20. K. D. Jahnke *et al.*, *New J. Phys.* **17**, 043011 (2015).
21. D. E. Chang, A. S. Sørensen, E. A. Demler, M. D. Lukin, *Nat. Phys.* **3**, 807–812 (2007).
22. P. R. Rice, H. J. Carmichael, *IEEE J. Quantum Electron.* **24**, 1351–1366 (1988).
23. B. Pingault *et al.*, *Phys. Rev. Lett.* **113**, 263601 (2014).
24. L. J. Rogers *et al.*, *Phys. Rev. Lett.* **113**, 263602 (2014).
25. J. N. Becker, J. Görlitz, C. Arend, M. Markham, C. Becher, https://arxiv.org/abs/1603.00789 (2016).
26. T. G. Tiecke *et al.*, *Optica* **2**, 70–75 (2015).
27. G. Fernandez, T. Volz, R. Desbuquois, A. Badolato, A. Imamoglu, *Phys. Rev. Lett.* **103**, 087406 (2009).
28. T. M. Sweeney *et al.*, *Nat. Photonics* **8**, 442–447 (2014).
29. B. Hensen *et al.*, *Nature* **526**, 682–686 (2015).
30. A. Delteil *et al.*, *Nat. Phys.* **12**, 218–223 (2015).
31. C. Cabrillo, J. Cirac, P. Garcia-Fernandez, P. Zoller, *Phys. Rev. A* **59**, 1025–1033 (1999).
32. R. Wiegner, S. Oppel, D. Bhatti, J. von Zanthier, G. Agarwal, *Phys. Rev. A* **92**, 033832 (2015).
33. P. C. Maurer *et al.*, *Science* **336**, 1283–1286 (2012).


## ACKNOWLEDGMENTS

We thank D. Twitchen and M. Markham from Element Six Inc. for substrates and K. De Greve and M. Goldman for experimental help. Financial support was provided by the NSF, the Center for Ultracold Atoms, the Air Force Office of Scientific Research Multidisciplinary University Research Initiative (MURI), the Office of Naval Research MURI, the Defense Advanced Research Projects Agency QuINESS program, the Army Research Laboratory, the Vannevar Bush Faculty Fellowship program, the Carlsberg Foundation (J.B.), and the Harvard Quantum Optics Center (M.J.B. and H.A.A.). F.J. is affiliated with the Center for Integrated Quantum Science and Technology (IQst) in Baden-Württemberg, Germany. Devices were fabricated at the Harvard Center for Nanoscale Systems supported under NSF award ECS-0335765. Ion implantation was performed with support from the Laboratory Directed Research and Development Program and the Center for Integrated Nanotechnologies at Sandia National Laboratories, an Office of Science facility operated for the DOE (contract DE-AC04-94AL85000) by Sandia Corporation, a Lockheed Martin subsidiary.

## SUPPLEMENTARY MATERIALS

www.sciencemag.org/content/354/6314/847/suppl/DC1
Materials and Methods
Figs. S1 to S10
References (*34*–*40*)

1 August 2016; accepted 29 September 2016
Published online 13 October 2016
10.1126/science.aah6875

Downloaded from http://science.sciencemag.org/ on November 22, 2016

ORGANIC CHEMISTRY

# A general catalytic β-C–H carbonylation of aliphatic amines to β-lactams

**Darren Willcox,* Ben G. N. Chappell,* Kirsten F. Hogg, Jonas Calleja, Adam P. Smalley, Matthew J. Gaunt†**

**Methods for the synthesis and functionalization of amines are intrinsically important to a variety of chemical applications. We present a general carbon-hydrogen bond activation process that combines readily available aliphatic amines and the feedstock gas carbon monoxide to form synthetically versatile value-added amide products. The operationally straightforward palladium-catalyzed process exploits a distinct reaction pathway, wherein a sterically hindered carboxylate ligand orchestrates an amine attack on a palladium anhydride to transform aliphatic amines into β-lactams. The reaction is successful with a wide range of secondary amines and can be used as a late-stage functionalization tactic to deliver advanced, highly functionalized amine products of utility for pharmaceutical research and other areas.**

The preparation and functionalization of amines is fundamental to a variety of chemical applications, such as the synthesis of medicinal agents, biologically active molecules, and functional materials (*1*). The best-established methods for amine synthesis involve carbon-nitrogen bond–forming processes based on alkylation (*2*), carbonyl reductive amination (*3*), and cross-coupling (*4*–*6*). Although recent advances in olefin hydroamination (*7*, *8*) and biocatalysis (*9*, *10*) have further expanded the toolbox of available transformations, the need for functional amines keeps the development of increasingly general catalytic reactions for amine synthesis at the forefront of synthetic organic chemistry. Inspired by the efficacy with which these well-established methods produce amines, we recognized the potential utility of a general catalytic process capable of directly introducing new functionality onto the framework of readily accessible and simple amines. In particular, we envisioned that their union with carbon monoxide through a selective amine-directed C–H carbonylation would produce a β-lactam feature, the versatile reactivity and biological relevance of which would make the method valuable to practitioners of synthetic and medicinal chemistry (Fig. 1A).

Transition metal catalysts capable of C–H activation have inspired intense research efforts within the synthetic chemistry community (*11*–*14*). Although many advances have been made in the field of aromatic $sp^2$-hybridized C–H [C($sp^2$)–H] bond activation, functionalization of less reactive C($sp^3$)–H bonds in aliphatic molecules continues to present a challenge (*15*). Because of the lower reactivity of C($sp^3$)–H bonds, their activation often relies on the proximity to polar functional groups such as carboxylic acids (*16*, *17*), heteroarenes (*18*), and hydroxyl functionalities (*19*); aliphatic hydrocarbons containing the free-NH amino group, however, continue to cause problems that restrict wider application (*20*).

A number of factors can be identified that impede the development of free-NH aliphatic amine–directed C–H activation with catalysts such as Pd(II) salts (Fig. 1B): The high affinity of a free-NH amine for Pd(II) salts leads to the formation of stable bis(amine)-Pd complexes and can preclude catalysis; β-hydride elimination pathways often lead to oxidative degradation of the amine and catalyst reduction; and other polar functional groups can compete with the amine for coordination to the Pd catalyst, leading to poorly reactive or unselective systems. As a result, successful aliphatic amine–directed C–H activation typically requires the nucleophilicity of the nitrogen atom to be modulated by strongly electron-withdrawing protecting groups (*21*), directing auxiliaries (*22*–*25*), or an intensified steric environment around the NH motif (*26*, *27*). Despite the success of these methods, the additional functional and structural features that need to be incorporated into the amine framework for successful C–H activation can sometimes preclude downstream operations. Taken together, the limitations of current methods give weight to the appeal of a free-NH aliphatic amine–directed C–H activation process (Fig. 1A). Here we report the development of a general process for the catalytic C–H carbonylation of aliphatic amines, wherein readily available unprotected amines are combined with carbon monoxide to generate β-lactams. The design of a reaction pathway for C–H carbonylation controlled by a sterically hindered carboxylate ligand was crucial in overcoming the incompatibility of free-NH aliphatic amines and Pd(II) catalysts. There are a number of specific advantages of this method: First, readily available aliphatic amines can be directly converted into highly functionalized and synthetically versatile small-molecule lactam building blocks; second, by obviating the need for nitrogen-protecting or auxiliary groups, the number of synthetic steps required to access functional amines is greatly reduced; third, C–H carbonylation directed by free-NH amine motifs in pharmaceutical agents or natural products could be used as a potentially powerful late-stage functionalization approach to analog synthesis.

Carbon monoxide (CO) is an abundant chemical feedstock, and metal-catalyzed carbonylation reactions are integral to the laboratory- and manufacturing-scale synthesis of chemical products. Most of these processes involve CO binding to a metal to form a metal-carbonyl complex with well-established reactivity (*28*). Recently, our group described a sterically controlled C–H activation strategy for carbonylation of free-NH aliphatic amines (*26*). Highly hindered amines, displaying fully substituted carbon atoms on either side of the nitrogen motif, underwent C–H carbonylation to yield β-lactams (Fig. 2A). A key factor in the success of this strategy was the sterically induced destabilization of the readily formed bis(amine)-Pd(II) complex, resulting from a clash between the two highly hindered amines, which shifts the equilibrium toward a mono(amine)-Pd(II) species required for C–H activation. The anticipated pathway for these amine-directed reactions had been based on seminal studies by Fujiwara and colleagues (*29*), who outlined a mechanistic blueprint that has underpinned most subsequent directed C–H carbonylation reactions with Pd(II) catalysts: In our case, amine-directed cyclopalladation of the C–H bond formed a four-membered ring complex and was followed by coordination of CO, 1,1-migratory insertion to an acyl-Pd species, and reductive elimination to generate the carbonyl product. However, when the same reaction concept was applied to more commonly encountered, less hindered amines, the reaction failed or was low-yielding and resulted in oxidative degradation and acetylated amine products (Fig. 2A). Furthermore, we were not able to observe any trace of the corresponding four-membered-ring cyclopalladation complex, in contrast to the case for reactions with the hindered amine counterparts. Indeed, we calculated that a transition state for four-membered-ring cyclopalladation on these less hindered amines was too high to be a realistic pathway (*30*). On the basis of these observations, we reconsidered the classical mechanism for C–H carbonylation. CO is a strongly binding ligand, and it is perhaps surprising that it does not interact with the Pd catalyst before C–H activation. Moreover, $Pd(OAc)_2$ (Ac, acetate group) and CO display contrasting redox properties, and their combination predictably leads to catalyst reduction, which can complicate a catalytic process. Intrigued by the apparent paradox of the redox properties of the reagents, we became interested in the mechanism of CO-mediated reduction of $Pd(OAc)_2$, outlined in Fig. 2B. Although little is known about this pathway, studies by

Department of Chemistry, University of Cambridge, Lensfield Road, Cambridge CB2 1EW, UK.
*These authors contributed equally to this work. †Corresponding author. Email: mjg32@cam.ac.uk

Downloaded from http://science.sciencemag.org/ on November 22, 2016

Moiseev and colleagues (*31*) provided clues that led us to propose a simplified model that we supported through computation. Two molecules of CO coordinate to monomeric $Pd(OAc)_2$ (**int-I**) and a calculated Pd–C–O angle of 153.7°, along with a bond distance between the carboxylate and CO of 2.06 Å, suggested an interaction between the two ligands. An attack on one of these CO ligands by a neighboring carboxylate was energetically favorable, leading to a Pd anhydride–type species, **int-II**. The transition state for this step (**int-I** to **int-II**) was calculated to be +11.50 kcal $mol^{-1}$ relative to **int-I**. Coordination of a further CO (**int-III**) could trigger an intermolecular attack of the $\kappa^1$-bound acetate onto the distal carbonyl group of the anhydride, causing the release of $CO_2$, acetic anhydride, and Pd(0). Motivated by the potential reactivity of the putative Pd anhydride **int-II**, we postulated that attack by an amine on the proximal carbonyl would lead to a carbamoyl-Pd species (Fig. 2C), from which C–H activation would be possible. This unorthodox cyclopalladation pathway would lead to C–H activation two carbon atoms away from the nitrogen group—distinct from classical cyclopalladation processes that usually result in activation three carbons from the directing motif.

## Reaction development and mechanistic studies

To test our hypothesis, we reacted amine **1a** under anticipated conditions for C–H carbonylation (Fig. 2D) (*32*, *33*). Although we observed the desired product (β-lactam **2a**) in low yield, the reaction was capricious and accompanied by the formation of acetylated amine and oxidative degradation products (entry 1). On the basis of our mechanistic blueprint, we expected that the attack on the Pd anhydride species at position **a** would lead to $CO_2$ release, reduction of the Pd catalyst, and an acetylated amine side product (Fig. 2B). We speculated that a larger carboxylate would generate a sterically biased Pd anhydride, steering the amine attack to position **b** to form the carbamoyl-Pd species and precluding the deleterious reduction pathway. Accordingly, addition of adamantanoic acid ($AdCO_2H$) to the standard reaction resulted in an increase in yield to 32% (entry 2). A similar improvement was observed when the original reaction was conducted in the presence of benzoquinone (BQ) (entry 3) (*34*). We found that the addition of both $AdCO_2H$ and BQ resulted in a dramatic increase in yield, with the β-lactam isolated in 65% yield (entry 4). The addition of nitrogen-containing ligands, such as quinoline **3a** or quinuclidine **3b**, enabled us to lower the amounts of the other reagents (entries 6, 7, and 9) (*35*). We also found that other hindered carboxylic acids were effective in the reaction (entry 8). An optimized procedure thus involved stirring a 0.1 M solution of amine **1a** in toluene with 10 mole (mol) % $Pd(OAc)_2$, 10 mol % $Cu(OAc)_2$, 100 mol % BQ, 25 mol % adamantanoic acid, and 10 mol % **3a** at 120°C under an atmosphere of CO; this gave an 83% yield of β-lactam **2a** after isolation. To probe the nature of the C–H activation step, we synthesized a derivative (**4**) of the proposed carbamoyl-Pd species (Fig. 2E). Under conditions that would create a similar chemical environment to the reaction (see Fig. 2D, entry 10, where $PPh_3$ is used as an additive), we showed that the β-lactam **2b** could be formed, albeit in low yield, supporting our hypothesis that C–H activation can occur through this carbamoyl-Pd intermediate (*36*).

A number of further preliminary mechanistic experiments were conducted to ascertain the role of the distinctive components of this C–H carbonylation process. First, we confirmed the importance of the sterically bulky carboxylate by comparing the reaction of the acetate- and adamantanoate-derived bis(amine)-Pd(II) carboxylate complexes (**5a** and **5b** in Fig. 3A) in the presence of BQ under a CO atmosphere; the yield of β-lactam from the acetate complex (**5a**) was 25%, compared with 89% from the adamantanoate complex (**5b**), supporting our hypothesis of a sterically controlled attack on the putative Pd anhydride species (Fig. 3A). Second, we identified BQ as essential for the high-yielding formation of **2a** from **5b:** In its absence, the yield drops from 89 to 26%, suggesting that BQ may play a mechanistic role in the pathway beyond that of an oxidant (*35*). Third, we deduced that although quinoline **3a** and quinuclidine **3b** additives increase the yield of β- lactam, they do not substantively affect the rate of the catalytic reaction. Last, we observed a kinetic isotope effect of 1.14 from parallel reaction of **1a** and $\boldsymbol{d^6}$**-1a**, suggesting that C–H activation is not the rate-determining step (Fig. 3B). A close inspection of the reaction of $\boldsymbol{d^6}$**-1a**, using nuclear magnetic resonance (NMR), revealed that hydrogen-deuterium scrambling had occurred in the lactam product **2a** at the

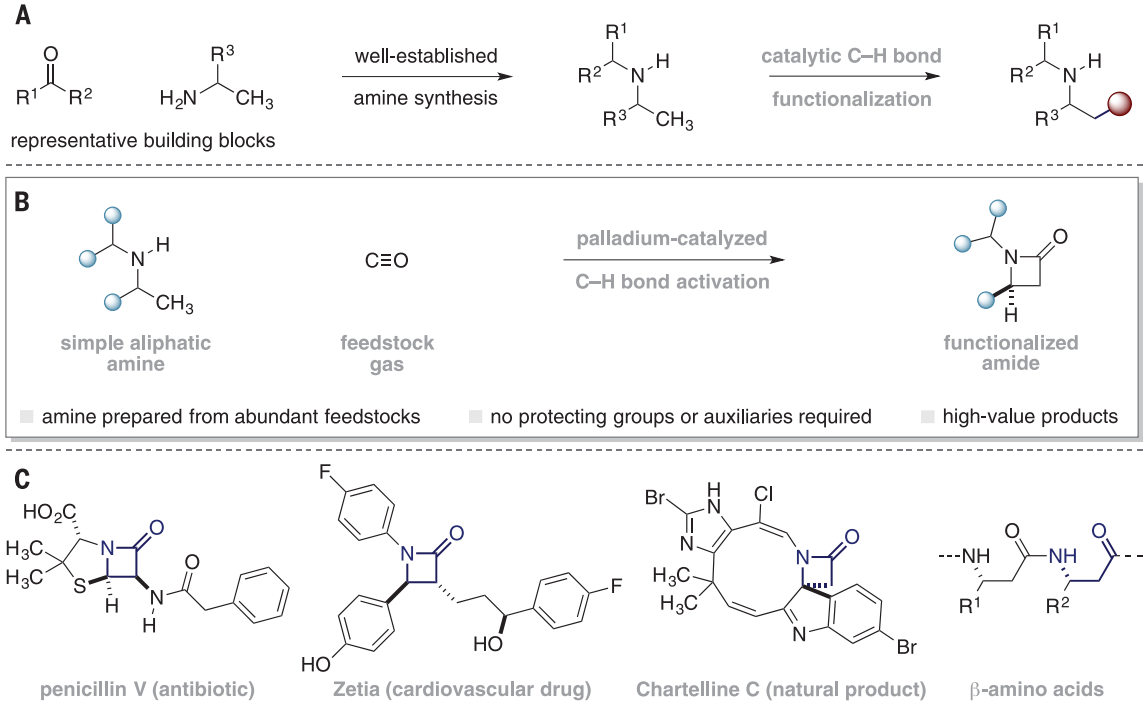


**Fig. 1. A strategy for the catalytic synthesis of functionalized aliphatic amines.** (**A**) Hypothesis: Combining well-established amine synthesis with metal-catalyzed C–H functionalization will lead to the rapid synthesis of functionalized amides. (**B**) Pd-catalyzed $C(sp^3)$–H carbonylation of free-NH amines. A blue circle or R denotes a general organic group. (**C**) The importance of β-lactams.

Downloaded from http://science.sciencemag.org/ on November 22, 2016

methyl group and at the position adjacent to the carbonyl of the amide. However, no hydrogen-deuterium scrambling was observed in the recovered starting material $d^6$-**1a**. These observations indicate that C–H activation is reversible and takes place after an irreversible step.

Taken together, these observations suggest a catalytic cycle for this C–H carbonylation reaction (*30*), which we have supported with a computational study of a simplified system using diisopropylamine **1b** and pivalic acid and without the involvement of **3a** or **3b** (Fig. 3C). The process begins with carboxylate exchange on $Pd(OAc)_2$: Coordination of the sterically hindered acid ($RCO_2H$) (R, *t*-butyl group) forms $Pd(O_2CR)_2$ or a mixed carboxylate complex. Next, amine coordination forms the mono(amine)-Pd(II) complex **int-IV**, which is in equilibrium with the off-cycle bis(amine)-Pd(II) complex (**int-V**); we deemed **int-V**, as the catalyst resting state, to be the energetic reference point. CO binding then forms **int-VI**, from which a viable transition state (**TS1**) to the Pd anhydride complex **int-VII** was determined. On the basis of our kinetic isotope effect and computational studies, we suggest that the attack of the amine at the internal carbonyl of **int-VII** (via **TS2**) to form carbamoyl-Pd species **int-VIII** is irreversible, and from this point, reversible C–H activation takes place through a concerted metalation deprotonation pathway (**TS3**) to form a five-membered-ring cyclopalladation intermediate **int-IX** (see also Fig. 2E). Last, BQ-assisted reductive elimination (via **TS4**) leads to β-lactam **2b** after decomplexation from Pd(0); oxidation of the Pd(0) species with $Cu(OAc)_2$ regenerates the active Pd(II) species. The amine additives **3a** and **3b** may stabilize the Pd(0) species before oxidation by preventing deactivating aggregation (*37*). This effect may be more pronounced toward the end of the reaction, when the concentration of the amine substrate **1** is lower, and possibly explains why **3a** and **3b** have an effect on yield but not on the rate of reaction.

## Substrate scope with simple amines

Having established optimal reaction conditions and validated a possible reaction mechanism, we focused our efforts on establishing the scope of the C–H carbonylation process. In setting a benchmark, we targeted a substrate scope that would encompass all structural classes of aliphatic secondary amines with respect to substitution at the carbon atoms directly connected to the free-NH group. We previously reported a C–H activation strategy for fully substituted aliphatic secondary amines that proceeds via four-membered-ring cyclopalladation—a pathway distinct from

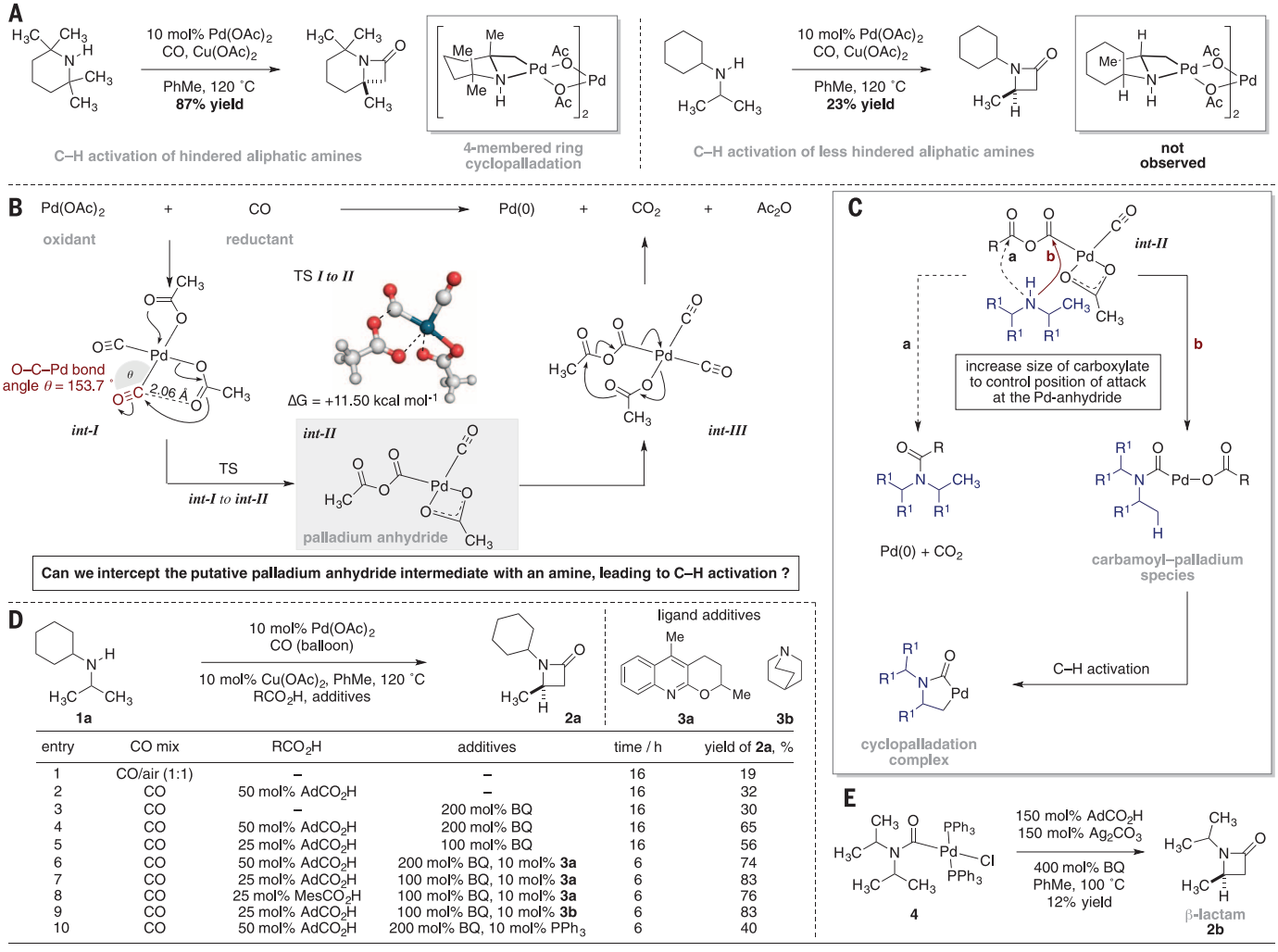


| entry | CO mix | $RCO_2H$ | additives | time / h | yield of **2a**, % |
|---|---|---|---|---|---|
| 1 | CO/air (1:1) | – | – | 16 | 19 |
| 2 | CO | 50 mol% $AdCO_2H$ | – | 16 | 32 |
| 3 | CO | – | 200 mol% BQ | 16 | 30 |
| 4 | CO | 50 mol% $AdCO_2H$ | 200 mol% BQ | 16 | 65 |
| 5 | CO | 25 mol% $AdCO_2H$ | 100 mol% BQ | 16 | 56 |
| 6 | CO | 50 mol% $AdCO_2H$ | 200 mol% BQ, 10 mol% **3a** | 6 | 74 |
| 7 | CO | 25 mol% $AdCO_2H$ | 100 mol% BQ, 10 mol% **3a** | 6 | 83 |
| 8 | CO | 25 mol% $MesCO_2H$ | 100 mol% BQ, 10 mol% **3a** | 6 | 76 |
| 9 | CO | 25 mol% $AdCO_2H$ | 100 mol% BQ, 10 mol% **3b** | 6 | 83 |
| 10 | CO | 50 mol% $AdCO_2H$ | 200 mol% BQ, 10 mol% $PPh_3$ | 6 | 40 |

**Fig. 2. Toward an activation mode for C–H carbonylation of unhindered aliphatic amines.** (**A**) Previous work: C–H carbonylation of hindered aliphatic amines via a four-membered-ring cyclopalladation pathway (left) and poor-yielding C–H carbonylation of less hindered amines (right). (**B**) Reduction of $Pd(OAc)_2$ by CO. (**C**) Design: A sterically controlled ligand-enabled C–H activation. (**D**) Optimization studies. (**E**) C–H activation from a de novo carbamoyl-Pd complex. Computational studies were conducted using Amsterdam Density Functional software at the ZORA:BLYP-D3/TZ2P level with the COSMO solvation model (PhMe) (supplementary materials). Ph, phenyl group; Me, methyl group; Ac, acetate group; BQ, benzoquinone; Ad, adamantyl group; $MesCO_2H$, 2,4,6-trimethylbenzoic acid; Δ*G*, change in Gibbs free energy; TS, transition state; int, intermediate; h, hours; equiv, equivalent.

Downloaded from http://science.sciencemag.org/ on November 22, 2016

this process (*26*). However, the majority of amines in everyday use are represented by less substituted variants. Each class of these amine starting materials can be prepared by classical methods of C–N bond formation, thereby linking the C–H activation process to well-established preparative methods and reliable chemical feedstocks. Figure 4 shows the wide breadth of the substrate scope for this aliphatic amine C–H activation process. We began by assessing amines with five substituents around the nitrogen motif and found that these hindered secondary amines were compatible with the reaction conditions and could be efficiently converted into the corresponding β-lactams in good yields (**2c** to **2i**). In the case of **2d**, classical amine-directed five-membered-ring cyclopalladation could potentially lead to a γ-lactam product; however, only the product formed via the new carbonylation pathway was observed. Amines with an unsymmetrical arrangement of four substituents around the NH motif also worked very well in the C–H activation process (**2j** to **2s**). A variety of useful functional groups were amenable to the reaction conditions, producing the β-lactam products in good yields. The reaction with amines containing two substituents on either side of the free-NH amine motif (**2a**, **2b,** and **2t** to **2af**) tolerated the incorporation of protected hydroxyl motifs (**2u** and **2af**), carbonyls (**2w**), and amine motifs (**2ab**, **2ad**, and **2ae**) into the β-lactam products, providing opportunities for downstream synthetic manipulations of these valuable products. Pyridines (**2y** and **2z**) and thioethers (**2ac**) were tolerated as well, with no adverse effects on regioselectivity or catalyst poisoning (*38*). The reaction of an *N*-aryl amine (to **2ag**), however, was unsuccessful under these conditions, and the starting material was returned unchanged (*39*).

Having demonstrated that the reaction works well on heavily substituted secondary amines, we next sought to investigate the process with less hindered substrates. These types of amines would be expected to form stable bis(amine)-Pd(II) complexes (compare with **int-V**, Fig. 3C), and their high nucleophilicity suggested that selective attack on the putative Pd anhydride complex might be difficult to control. Additionally, each substrate contains up to four C–H bonds that can readily undergo β-hydride–elimination side reactions. Despite these potential pitfalls, we found that a range of amines with three substituents worked very well in the C–H carbonylation (**2ah** to **2aq**) when the reaction was conducted using phenylbenzoquinone, a hindered variant of BQ that prevents deleterious oxidative amination of the quinone scaffold. A substrate with only unfunctionalized alkyl groups worked well (**2ah**), demonstrating that the success of the reaction is not the result of remote functionality influencing the reactivity. A variety of functional groups on the amine substituents were tolerated, including sulfones (**2aj**), esters (**2ak**), aromatic heterocycles (**2al**), and alkenes (**2an**), producing the β-lactams in high yields. Aliphatic heterocycles were also competent substrates for this reaction (**2aq**), thereby providing a simple method by which to functionalize readily available amine building blocks suitable for complex molecule synthesis. Our C–H carbonylation even produced unsubstituted β-lactam products from unbranched secondary amines, albeit in lower

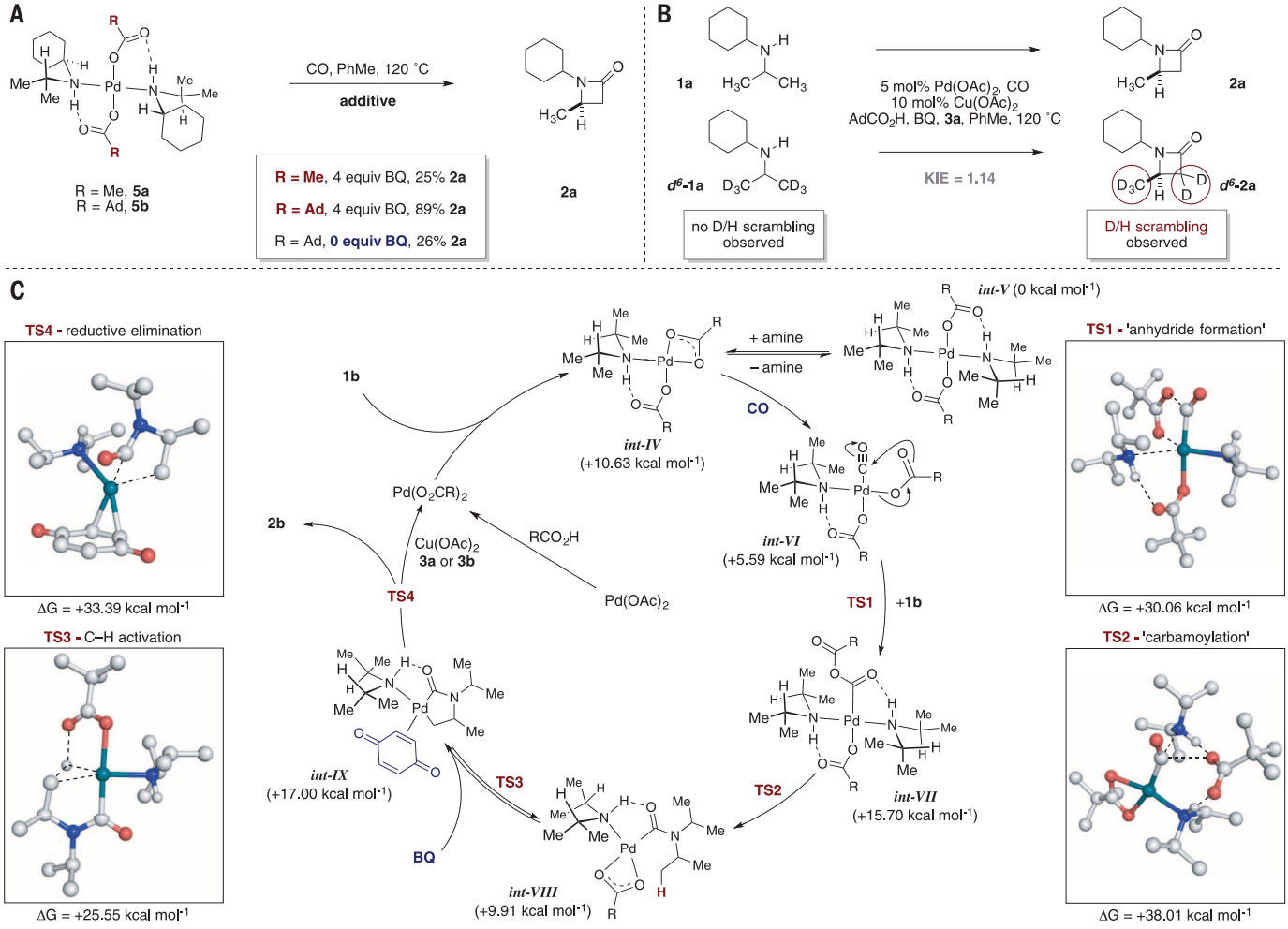


**Fig. 3. Mechanistic evaluation of the C–H carbonylation reaction.** (**A**) Stoichiometric studies. (**B**) Kinetic isotope effect (KIE) studies. (**C**) Proposed mechanism for C–H carbonylation of aliphatic amines. In the insets, blue is nitrogen, teal is palladium, red is oxygen, and light gray is carbon. Dotted lines indicate breaking and forming bonds. Computational studies were conducted as in Fig. 2.

Downloaded from http://science.sciencemag.org/ on November 22, 2016

yields (due in part to by-products formed from *N*-acylation and β-hydride elimination) compared with those from the other amine types (**2ar** to **2as**). As a whole, our scope studies demonstrate that the C–H carbonylation reaction tolerates a wide range of synthetic versatile functional groups spanning more than 40 examples, highlighting the generality of this transformation.

## Application to complex molecules

Aliphatic amine motifs are present in at least 30% of small-molecule pharmaceutical agents and are heavily represented in preclinical candidates (*40*). Therefore, a major benefit of our aliphatic amine C–H carbonylation process is its potential amenability to mid- and late-stage functionalization applications (*41*). In more complex molecules, the competition between numerous Lewis basic functionalities capable of steering C–H activation could cause deactivation or selectivity issues.

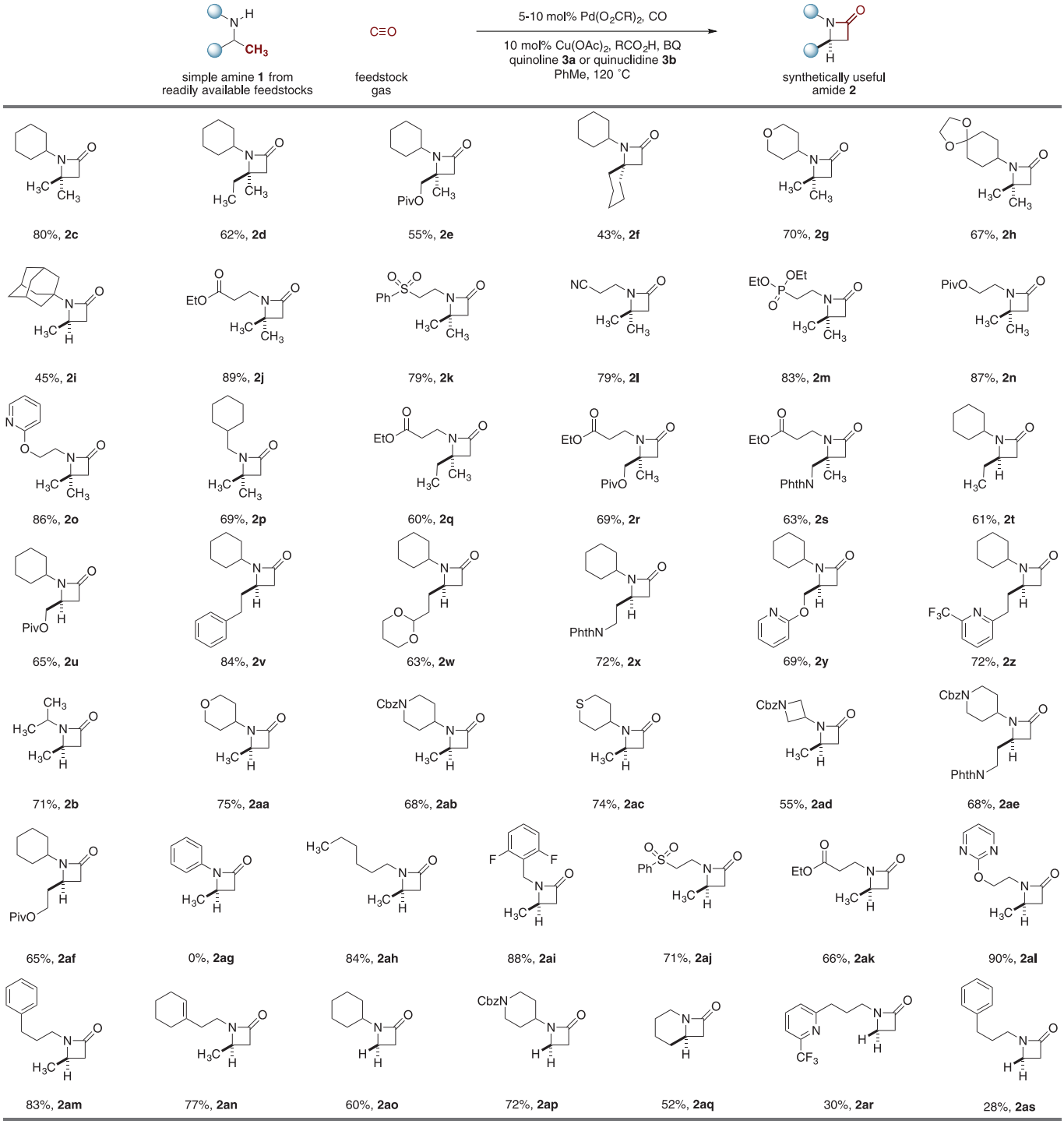


**Fig. 4. The scope of the aliphatic amine C–H carbonylation.** Yields of isolated products are shown. All compounds are racemic. Piv, pivaloyl group; Et, ethyl group; Phth, phthalimido group; Cbz, carbobenzyloxy group.

Downloaded from http://science.sciencemag.org/ on November 22, 2016

To test this, we prepared an amine (**1at**) with three possible sites of C–H activation and found that C–H carbonylation was directed by the aliphatic amine motif (to form **2at**) without any trace of the competitive pyridine-directed C–H activation product (Fig. 5A). To further the potential for late-stage functionalization, we subjected a selection of pharmaceutical derivatives and biologically active molecules to our C–H carbonylation protocol (Fig. 5B). Salbutamol and propranolol are $\beta_2$-adrenergic receptor agonists and are representative of a huge range of marketed pharmaceutical agents with a distinctive secondary amino alcohol. Simple derivatives of these molecules (**6a** and **6b**) effectively underwent C–H carbonylation to form β-lactams (**7a** and **7b**) in synthetically useful yields. A derivative of the acute heart failure drug dobutamine (**6c**) reacted smoothly to afford β-lactam in 72% yield (**7c**). Fenfluramine (**6d**), part of an anti-obesity treatment, was successfully carbonylated to yield a separable mixture of regioisomeric β-lactams (**7d**, 2.5:1), highlighting a moderate selectivity for the branched methyl group. Last, C–H carbonylation on the aza-sterol **6e**, an inhibitor of the hedgehog-activating transmembrane protein Smoothened (*42*), formed the β- lactam **7e** in useful yield, providing access to valuable analogs of this molecule that would be difficult to obtain by other means. A successful late-stage functionalization program would require the delivery of multiple analogs to get the maximum benefit from the strategy; β-lactams support a rich array of chemistry that can transform the amide function into pharmaceutically relevant motifs (*43*). Removal of the hydroxyl-protecting group from β-lactam **7b** yielded alcohol **8**, reductive ring opening afforded β-amino alcohol **9**, and esterification yielded β-amino ester **10** (Fig. 5C). Under certain reductive conditions, the β-lactam could be transformed into azetidine **11**, an important structural feature that is common in many drug development programs (Fig. 5C), underlining the diversity of structural motifs readily available from this aliphatic C–H activation tactic.

## Outlook

We expect this general C–H carbonylation process for aliphatic secondary amines to find broad application among practitioners of synthetic and pharmaceutical chemistry. In addition to the utility of this protocol, we anticipate that the distinct reactivity of free-NH aliphatic amines in combination with Pd catalysts will inspire further advances in a range of C–H activation processes. Moreover, this C–H carbonylation pathway is conceptually distinct from classical cyclopalladation-related approaches and may lead to opportunities for C–H activation reactions in other classes of functionalized aliphatic and aromatic molecules.

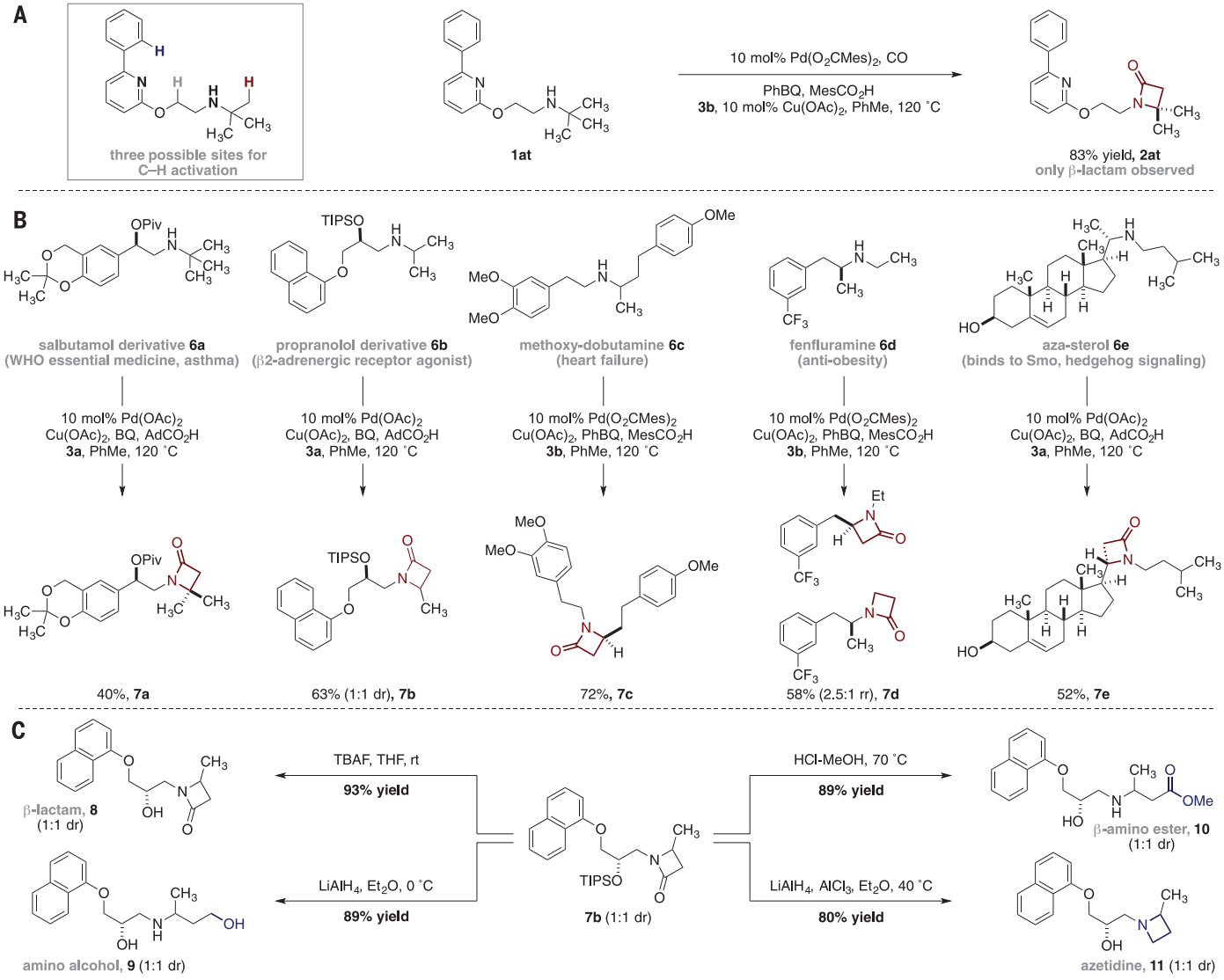


**Fig. 5. Application to complex substrates.** (**A**) Regioselective C–H activation in the presence of competing directing groups. (**B**) Late-stage C–H functionalization on biologically active molecules. (**C**) Derivatizations of the β-lactam framework. TIPS, triisopropylsilyl; WHO, World Health Organization; Smo, Smoothened (protein); TBAF, tetrabutylammonium fluoride; THF, tetrahydrofuran; dr, diastereoisomeric ratio; rr, regioisomeric ratio; rt, room temperature.

Downloaded from http://science.sciencemag.org/ on November 22, 2016

## REFERENCES AND NOTES

1. S. D. Roughley, A. M. Jordan, *J. Med. Chem.* **54**, 3451–3479 (2011).
2. R. N. Salvatore, C. H. Yoon, K. W. Jung, *Tetrahedron* **57**, 7785–7811 (2001).
3. E. W. Baxter, A. B. Reitz, *Org. React.* **59**, 1–714 (2004).
4. J. Bariwal, E. Van der Eycken, *Chem. Soc. Rev.* **42**, 9283–9303 (2013).
5. D. S. Surry, S. L. Buchwald, *Angew. Chem. Int. Ed. Engl.* **47**, 6338–6361 (2008).
6. J. F. Hartwig, *Acc. Chem. Res.* **41**, 1534–1544 (2008).
7. Y. Yang, S.-L. Shi, D. Niu, P. Liu, S. L. Buchwald, *Science* **349**, 62–66 (2015).
8. J. Gui *et al.*, *Science* **348**, 886–891 (2015).
9. C. K. Savile *et al.*, *Science* **329**, 305–309 (2010).
10. F. G. Mutti, T. Knaus, N. S. Scrutton, M. Breuer, N. J. Turner, *Science* **349**, 1525–1529 (2015).
11. J. Yamaguchi, A. D. Yamaguchi, K. Itami, *Angew. Chem. Int. Ed. Engl.* **51**, 8960–9009 (2012).
12. T. W. Lyons, M. S. Sanford, *Chem. Rev.* **110**, 1147–1169 (2010).
13. I. A. I. Mkhalid, J. H. Barnard, T. B. Marder, J. M. Murphy, J. F. Hartwig, *Chem. Rev.* **110**, 890–931 (2010).
14. J. Wencel-Delord, T. Dröge, F. Liu, F. Glorius, *Chem. Soc. Rev.* **40**, 4740–4761 (2011).
15. R. Jazzar, J. Hitce, A. Renaudat, J. Sofack-Kreutzer, O. Baudoin, *Chemistry* **16**, 2654–2672 (2010).
16. H. A. Chiong, Q. N. Pham, O. Daugulis, *J. Am. Chem. Soc.* **129**, 9879–9884 (2007).
17. K. M. Engle, T. S. Mei, M. Wasa, J.-Q. Yu, *Acc. Chem. Res.* **45**, 788–802 (2012).
18. K. J. Stowers, K. C. Fortner, M. S. Sanford, *J. Am. Chem. Soc.* **133**, 6541–6544 (2011).
19. E. M. Simmons, J. F. Hartwig, *Nature* **483**, 70–73 (2012).
20. A. D. Ryabov, *Chem. Rev.* **90**, 403–424 (1990).
21. K. S. L. Chan *et al.*, *Nat. Chem.* **6**, 146–150 (2014).
22. V. G. Zaitsev, D. Shabashov, O. Daugulis, *J. Am. Chem. Soc.* **127**, 13154–13155 (2005).
23. G. He, G. Chen, *Angew. Chem. Int. Ed. Engl.* **50**, 5192–5196 (2011).
24. C. Wang *et al.*, *Chem. Sci.* **6**, 4610–4614 (2015).
25. J. J. Topczewski, P. J. Cabrera, N. I. Saper, M. S. Sanford, *Nature* **531**, 220–224 (2016).
26. A. McNally, B. Haffemayer, B. S. L. Collins, M. J. Gaunt, *Nature* **510**, 129–133 (2014).
27. J. Calleja *et al.*, *Nat. Chem.* **7**, 1009–1016 (2015).
28. X.-F. Wu, H. Neumann, M. Beller, *ChemSusChem* **6**, 229–241 (2013).
29. C. Jia, T. Kitamura, Y. Fujiwara, *Acc. Chem. Res.* **34**, 633–639 (2001).
30. We considered a number of alternative pathways as part of our assessment of possible catalytic cycles. See the supplementary materials for details of these calculations.
31. T. A. Stromnova, M. N. Vargaftik, I. I. Moiseev, *J. Organomet. Chem.* **252**, 113–120 (1983).
32. K. Orito *et al.*, *J. Am. Chem. Soc.* **126**, 14342–14343 (2004).
33. E. J. Yoo, M. Wasa, J.-Q. Yu, *J. Am. Chem. Soc.* **132**, 17378–17380 (2010).
34. K. L. Hull, M. S. Sanford, *J. Am. Chem. Soc.* **131**, 9651–9653 (2009).
35. J. He *et al.*, *Science* **343**, 1216–1220 (2014).
36. C. Tsukano, M. Okuno, Y. Takemoto, *Angew. Chem. Int. Ed. Engl.* **51**, 2763–2766 (2012).
37. B. V. Popp, S. S. Stahl, *Chemistry* **15**, 2915–2922 (2009).
38. Y-J. Liu *et al.*, *Nature* **515**, 389–393 (2015).
39. W. Li *et al.*, *Angew. Chem. Int. Ed. Engl.* **54**, 1893–1896 (2015).
40. N. A. McGrath, M. Brichacek, J. T. Njardarson, *J. Chem. Educ.* **87**, 1348–1349 (2010).
41. J. Wencel-Delord, F. Glorius, *Nat. Chem.* **5**, 369–375 (2013).
42. D. Nedelcu, J. Liu, Y. Xu, C. Jao, A. Salic, *Nat. Chem. Biol.* **9**, 557–564 (2013).
43. B. K. Banik, Ed., *β-Lactams: Unique Structures of Distinction for Novel Molecules* (Springer, 2013).



## ACKNOWLEDGMENTS

We gratefully acknowledge funding from the European Research Council and the UK Engineering and Physical Sciences Research Council (EPSRC) (to D.W., K.F.H., A.P.S., and M.J.G.), the Herchel Smith Trust (to B.G.N.C.), the Marie Curie Foundation (to J.C.), and the Royal Society (Wolfson Merit Award to M.J.G.). Mass spectrometry data were acquired at the EPSRC UK National Mass Spectrometry Facility at Swansea University. Computational work was performed with the Darwin Supercomputer of the University of Cambridge High Performance Computing Service (http://www.hpc.cam.ac.uk/), provided by Dell, using Strategic Research Infrastructure Funding from the Higher Education Funding Council for England. The supplementary materials contain $^{1}$H and $^{13}$C NMR spectra and computational details. Crystallographic data are available free of charge from the Cambridge Crystallographic Data Centre under reference numbers CCDC-1508626 to CCDC-1508631.


## SUPPLEMENTARY MATERIALS

www.sciencemag.org/content/354/6314/851/suppl/DC1
Materials and Methods
Figs. S1 to S3
NMR Spectra
References (*44*–*55*)

26 April 2016; accepted 13 October 2016
10.1126/science.aaf9621

PLANT SCIENCE

# Improving photosynthesis and crop productivity by accelerating recovery from photoprotection

**Johannes Kromdijk,[1]* Katarzyna Głowacka,[1,2]* Lauriebeth Leonelli,[3] Stéphane T. Gabilly,[3] Masakazu Iwai,[3,4] Krishna K. Niyogi,[3,4]† Stephen P. Long[1,5]†**

**Crop leaves in full sunlight dissipate damaging excess absorbed light energy as heat. When sunlit leaves are shaded by clouds or other leaves, this protective dissipation continues for many minutes and reduces photosynthesis. Calculations have shown that this could cost field crops up to 20% of their potential yield. Here, we describe the bioengineering of an accelerated response to natural shading events in *Nicotiana* (tobacco), resulting in increased leaf carbon dioxide uptake and plant dry matter productivity by about 15% in fluctuating light. Because the photoprotective mechanism that has been altered is common to all flowering plants and crops, the findings provide proof of concept for a route to obtaining a sustainable increase in productivity for food crops and a much-needed yield jump.**

According to detailed forecasts of future global food demand, current rates of increase in crop yields per hectare of land are inadequate. Prior model predictions have suggested that the efficiency of the photosynthetic process and thereby crop yield could be improved (*1*). Here, we show improvement of photosynthetic efficiency and crop productivity through genetic manipulation of photoprotection.

Light in plant canopies is very dynamic, and leaves routinely experience sharp fluctuations in levels of absorbed irradiance. When light intensity is too high or increases too fast for photochemistry to use the absorbed energy, several photoprotective mechanisms are induced to protect the photosynthetic antenna complexes from overexcitation (*2*). Excess excitation energy in the photosystem II (PSII) antenna complex can be harmlessly dissipated as heat, which is observable as a process named nonphotochemical quenching of chlorophyll fluorescence (NPQ) (*3*). Changes in NPQ can be fast but are not instantaneous and therefore lag behind fluctuations in absorbed irradiance. In particular, the rate of NPQ relaxation is slower than the rate of induction, and this asymmetry is exacerbated by prolonged or repeated exposure to excessive light conditions (*4*). This slow rate of recovery of PSII antennae from the quenched to the unquenched state implies that the photosynthetic quantum yield of $CO_2$ fixation is transiently depressed by NPQ upon a transition from high to low light intensity (Fig. 1). When this hypothesis was tested in model simulations and integrated for a crop canopy over a diurnal course, corresponding losses of $CO_2$ fixation were estimated to range between 7.5 and 30% (*5*–*7*). On the basis of these computations, increasing the relaxation rate of NPQ appeared to be a very promising strategy for improving crop photosynthetic efficiency and in turn yield (*8*).

Although the exact NPQ quenching site and nature of the quenching mechanisms involved are still debated (*9*), it is clear that for NPQ to occur, PSII-associated antennae need to undergo a conformational change to the quenched state,

[1]Carl R. Woese Institute for Genomic Biology, University of Illinois, 1206 West Gregory Drive, Urbana, IL 61801, USA. [2]Institute of Plant Genetics, Polish Academy of Sciences, Ulica Strzeszyńska 34, 60-479 Poznań, Poland. [3]Howard Hughes Medical Institute, Department of Plant and Microbial Biology, 111 Koshland Hall, University of California Berkeley, Berkeley, CA 94720-3102, USA. [4]Molecular Biophysics and Integrated Bioimaging Division, Lawrence Berkeley National Laboratory, Berkeley, CA 94720, USA. [5]Lancaster Environment Centre, University of Lancaster, Lancaster, LA1 1YX, UK.
*These authors contributed equally to this work. **†Corresponding author. Email: niyogi@berkeley.edu (K.K.N.); slong@illinois.edu (S.P.L.)**

Downloaded from http://science.sciencemag.org/ on November 22, 2016

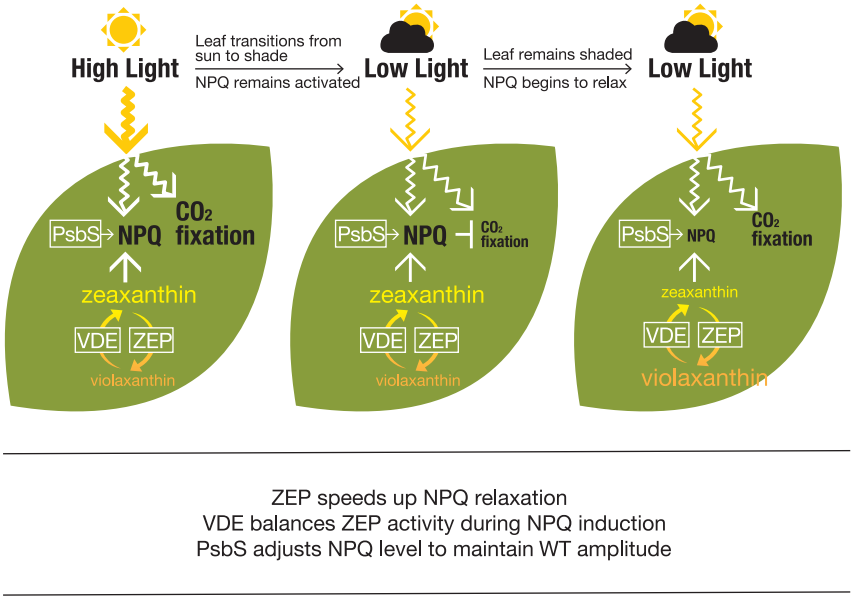


**Fig. 1. Interaction between photoprotection and $CO_2$ fixation during sun-shade transitions.** When leaves are exposed to high light, the rate of $CO_2$ fixation is high, and excessive excitation energy is harmlessly dissipated through NPQ. The level of NPQ is positively correlated with the abundance of PsbS and further stimulated by the de-epoxidation of violaxanthin to zeaxanthin, catalyzed by VDE. Upon transition to low light, $CO_2$ fixation becomes limited by the reduced form of nicotinamide adenine dinucleotide phosphate and adenosine triphosphate derived from photosynthetic electron transport, which in turn is limited by high levels of NPQ. The rate of $CO_2$ fixation therefore remains depressed until relaxation of NPQ is complete. This can take minutes to hours and is correlated with the rate of zeaxanthin epoxidation, catalyzed by ZEP. The text underneath the figure describes the strategy used to accelerate NPQ relaxation compared with WT tobacco.

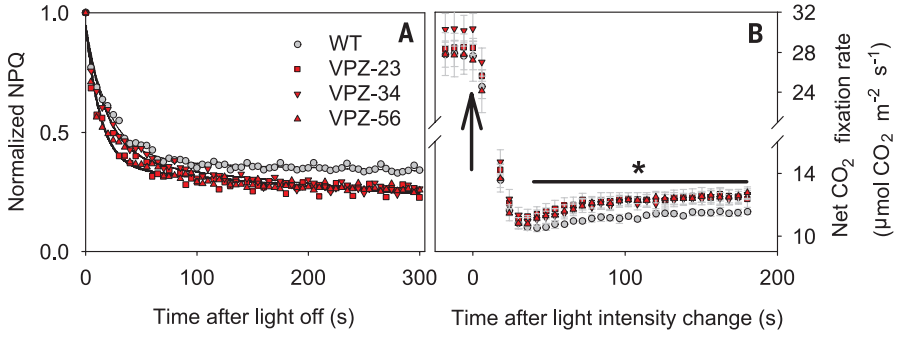


**Fig. 3. Transient adjustment of NPQ and net $CO_2$ assimilation.** (**A**) Dark relaxation of NPQ after exposure to alternating high and low light in young seedlings of wild-type *N. tabacum* (WT) and three lines expressing *AtVDE*, *AtPsbS*, and *AtZEP* (VPZ). SEM were less than symbol size ($n$ = 18 biological replicates). Lines depict best fits of a double exponential model for WT ($\tau_1$ = 21.4 ± 1.2 s and $\tau_2$ = 2641.1 ± 821.2 s), VPZ-23 ($\tau_1$ = 13.3 ± 1.3 s and $\tau_2$ = 792.6 ± 131.7 s), VPZ-34 ($\tau_1$ =19.4 ± 1.4 s and $\tau_2$ = 692.6 ± 77.9 s), and VPZ-56 ($\tau_1$ =13.2 ± 1.0 s and $\tau_2$ = 774.9 ± 94.5 s). (**B**) Time course of net $CO_2$ fixation rate in fully expanded leaves in response to a decrease in light intensity of 2000 to 200 μmol photons $m^{-2}$ $s^{-1}$ at time zero, indicated by the black arrow. Error bars indicate SEM ($n$ = 5 biological replicates). Asterisk indicates significant difference ($\alpha$ = 0.05).

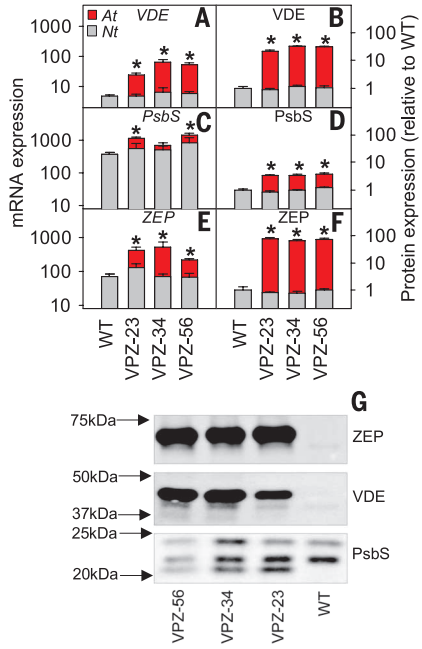


**Fig. 2. Levels of mRNA and protein of VDE, PsbS, and ZEP.** Native (Nt) and transgenic (At) VDE, PsbS, and ZEP in leaves of wild-type *N. tabacum* (WT) and three lines expressing *AtVDE*, *AtPsbS*, and *AtZEP* (VPZ) grown under greenhouse conditions. (**A**, **C**, and **E**) mRNA levels relative to actin and tubulin. (**B**, **D**, and **F**) Protein levels relative to WT, determined from densitometry on immunoblots. Error bars indicate SEM ($n$ = 5 biological replicates), and asterisks indicate significant differences between VPZ lines and WT ($\alpha$ = 0.05). (**G**) Representative immunoblots for VDE, PsbS, and ZEP.

which can be induced by a number of different mechanisms with contrasting time constants (*3*). So-called energy-dependent quenching (qE) (*10*) requires low thylakoid lumen pH and is greatly aided by the presence of PSII subunit S (PsbS) (*11*, *12*) and de-epoxidation of violaxanthin to antheraxanthin and zeaxanthin via the xanthophyll cycle (*13*, *14*). Expression of PsbS strongly affects the amplitude of qE formation, and overexpression results in an increased rate of induction and relaxation of qE (*15*–*17*). As a result, the effects of PsbS overexpression on $CO_2$ fixation and plant growth depend on the prevailing light environment. Enhancement of qE via PsbS overexpression may offer increased photoprotection under high light or rapidly fluctuating conditions (*18*) but can be at the expense of $CO_2$ fixation under less stressful conditions (*15*). An alternative route of NPQ manipulation is to modify xanthophyll cycle kinetics. The xanthophyll cycle de-epoxidation state (DES) influences the level of NPQ (*19*) because of the stimulating effect of zeaxanthin on qE and on zeaxanthin-dependent quenching (qZ) (*20*). qZ has slower relaxation kinetics (10 to 15 min) than qE (10 to 90 s), which are linked to the kinetics of the zeaxanthin pool. *Arabidopsis* mutants with increased xanthophyll-cycle pigment pool size were shown to have slower rates of NPQ formation and relaxation, owing to slower DES kinetics (*21*). Thus, the rate of adjustment of DES appears to be affected by the xanthophyll-cycle pool size relative to the rate of turnover via violaxanthin de-epoxidase (VDE) and zeaxanthin epoxidase (ZEP), which in turn affects the adjustment rate of NPQ.

We hypothesized that by accelerating the xanthophyll cycle and increasing PsbS, NPQ would decline more rapidly on transfer of leaves to shade (Fig. 1), leading to faster restoration of the maximum efficiency of $CO_2$ assimilation that can be achieved at a given light intensity in

Downloaded from http://science.sciencemag.org/ on November 24, 2016

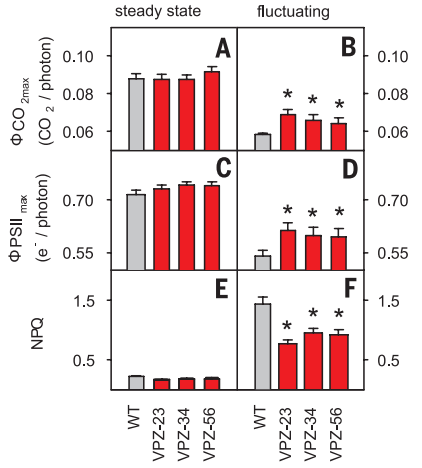


**Fig. 4. Photosynthetic efficiency and NPQ under steady-state and fluctuating light.** (**A**) Quantum efficiency of leaf net $CO_2$ assimilation ($\Phi CO_{2max}$) under steady-state light. (**B**) $\Phi CO_{2max}$ under fluctuating light. (**C**) Quantum efficiency of linear electron transport ($\Phi PSII_{max}$) under steady-state light. (**D**) Quantum efficiency of linear electron transport ($\Phi PSII_{max}$) under fluctuating light. (**E**) Average NPQ corresponding to (A) and (C). (**F**) Average NPQ corresponding to (B) and (D). Data were derived from light-response curves in which light intensity was either increased from low to high photon flux density (PFD), while waiting for steady state at each step (steady-state), or varied from high to low PFD with 4 min of 2000 µmol photons $m^{-2}$ $s^{-1}$ before each light-intensity change (fluctuating). Error bars indicate SEM ($n$ = 6 biological replicates), and asterisks indicate significant differences ($\alpha$ = 0.05) between wild-type *N. tabacum* (WT) and three lines expressing *AtVDE*, *AtPsbS*, and *AtZEP* (VPZ).

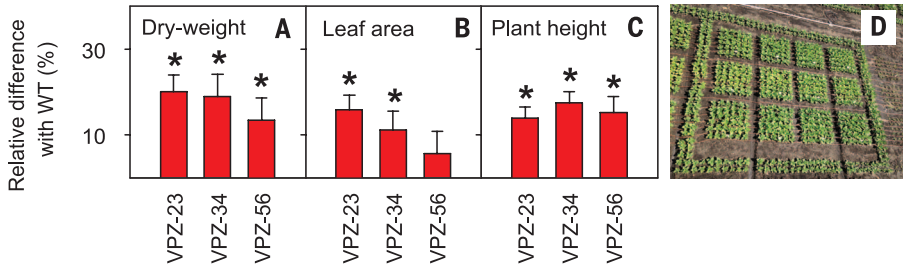


**Fig. 5. Productivity of field-grown *N. tabacum* plants.** Lines expressing *AtVDE*, *AtPsbS*, and *AtZEP* (VPZ) produced 15% larger plants than did the WT. (**A**) Total dry weight. (**B**) Leaf area. (**C**) Plant height. Data were normalized to WT. Error bars indicate SEM ($n$ = 12 blocks), and asterisks indicate significant differences between VPZ lines and WT ($\alpha$ = 0.05). (**D**) Aerial view of the field experiment in Urbana, Illinois (40.11°N, 88.21°W), in the summer of 2016. [Photo: D. Drag]

the shade, which in turn would allow increased productivity.

## Results

### *Transgene mRNA and protein expression*

*Nicotiana tabacum* was transformed with the coding sequences of *Arabidopsis VDE*, *ZEP*, and *PsbS* under the control of different promoters for expression in leaves (fig. S1). Two transformants with a single transfer DNA (T-DNA) integration (VPZ-34 and -56) and one transformant with two T-DNA insertions (VPZ-23) were selected based on a seedling NPQ screen (figs. S2 and S3) and self-pollinated to obtain homozygous T2 progeny for further investigation. All three VPZ lines showed increases in total (transgenic plus native) transcript levels of *VDE* (10-fold), *PsbS* (threefold), and *ZEP* (sixfold) relative to those of the wild type (WT) (Fig. 2, A, C, and E). For *PsbS*, the increase in transcript levels translated into an approximately fourfold-higher PsbS protein level (Fig. 2D), as exemplified in bands at 21 kDa (AtPsbS) and 24 kDa (NtPsbS) (Fig. 2G). For *VDE* and *ZEP*, the increase in transcript levels corresponded to 30-fold for VDE (45 kDa) (Fig. 2, B and G) and 74-fold for ZEP (73 kDa) (Fig. 2, F and G) increases over WT protein levels. Field-grown plants showed similar increases in protein levels (47-, 3-, and 75-fold for VDE, PsbS, and ZEP, respectively) (fig. S4), although increases in transcript levels were less pronounced (4-, 1.2-, and 7-fold for VDE, PsbS, and ZEP, respectively) (fig. S4).

### *Faster relaxation of NPQ and recovery of $CO_2$ fixation rate*

To compare the kinetics of dynamic NPQ adjustment, a double exponential model was fitted to dark relaxation of NPQ in young seedlings after exposure to fluctuating light between 2000 and 200 µmol photons $m^{-2}$ $s^{-1}$ (Fig. 3A). The qZ phase of NPQ relaxation ($\tau_2$) was significantly faster in VPZ lines at an average of 753 versus 2684 s in WT ($P$ < 0.05), and qE relaxation ($\tau_1$) was also noticeably faster at an average of 15 versus 21 s (significant in VPZ-23 and VPZ-56, $P$ < 0.05). To see whether this faster relaxation translated into higher leaf $CO_2$ uptake, leaves were exposed to a sharp transition in light from 2000 to 200 µmol photons $m^{-2}$ $s^{-1}$. $CO_2$ assimilation declined immediately after the decrease in light intensity in both WT and VPZ lines (Fig. 3B), reaching a minimum at 30 s. During the following 150 s, the $CO_2$ fixation rate increased gradually but more rapidly in the VPZ lines as compared with WT, leading to significantly higher $CO_2$ fixation rates, averaging an increase of 9% ($P$ < 0.02).

### *Effects of fluctuating light on the efficiency of photosynthetic $CO_2$ assimilation*

To evaluate the dynamic effect of VPZ overexpression on the response of leaf $CO_2$ uptake to light, light intensity was varied in two different ways. First, light intensity was varied from low to high (fig. S5A), taking care to allow gas exchange and fluorescence to achieve steady state at each light intensity. Second, light intensity was varied in 4-min alternating steps of high to low light (fig. S5B). The resulting steady-state and fluctuating light-response curves of $CO_2$ fixation and linear electron transport rate were distinctly different between WT and VPZ lines. In steady state, the maximum quantum yield of $CO_2$ fixation ($\Phi CO_{2max}$) was not different between WT and VPZ lines, averaging 0.092 $CO_2$/absorbed photon (Fig. 4A). Fluctuating light decreased $\Phi CO_{2max}$ to 0.058 $CO_2$/absorbed photon in the WT plants (Fig. 4B), whereas $\Phi CO_{2max}$ in the VPZ lines showed a far smaller depression to 0.066 $CO_2$/absorbed photon ($P$ < 0.05). Similarly, under fluctuating light, the maximum quantum yield of whole-chain electron transport ($\Phi PSII_{max}$) declined from an average value of 0.73 (Fig. 4C) to 0.54 $e^-$/absorbed photon in the WT plants (Fig. 4D), compared with 0.60 $e^-$/absorbed photon in the VPZ lines ($P$ < 0.05). Thus, under these fluctuating conditions, average $\Phi CO_{2max}$ and average $\Phi PSII_{max}$ of the VPZ lines were 11.3 and 14.0% higher than WT, respectively. These differences were also confirmed in plants grown under field conditions (fig. S6, A and B) and were not caused by a difference in photosynthetic capacity, as shown by the lack of differences in $\Phi CO_{2max}$ and $\Phi PSII_{max}$ between VPZ lines and WT when measured at steady state (Fig. 4, A and C). There were also no differences in the maximum carboxylation capacity ($V_{cmax}$) or ribulose bisphosphate regeneration capacity ($J_{max}$) derived from $CO_2$ response curves (table S1), nor were there differences in the levels and stoichiometry of the major photosynthetic complexes (fig. S7). Instead, the differences under fluctuating conditions corresponded to the faster relaxation of NPQ resulting from VPZ overexpression. Steady-state NPQ below 400 µmol photons $m^{-2}$ $s^{-1}$ was very low (Fig. 4E and fig. S5G) and did not differ between WT and VPZ lines. However, under fluctuating light intensity, NPQ was significantly higher in the WT compared with the VPZ lines at low light ($P$ < 0.05) (Fig. 4F), whereas NPQ in high light did not differ between WT and VPZ lines (fig. S5, G and H).

### *Productivity under field conditions*

Whether this greater photosynthetic efficiency during shading events would affect productivity was evaluated under field conditions in a randomized block design with 12 blocks (Fig. 5D and fig. S8). Plants from VPZ lines exhibited greater total dry weight per plant by 14 to 20% relative to that of WT (Fig. 5A), which was evident in increases in leaf, stem, and root weights (fig. S9, A to C). Additionally, plants from VPZ lines showed increases in leaf area (Fig. 5B) and plant height (Fig. 5C), relative to WT. Similar productivity increases were found under greenhouse conditions (fig. S10, A to F).

Downloaded from http://science.sciencemag.org/ on November 24, 2016

**Table 1. Xanthophyll cycle pigment concentrations and DES.** Samples were taken from greenhouse-grown fully expanded leaves of wild-type *N. tabacum* (WT) and three lines overexpressing *AtVDE*, *AtPsbS*, and *AtZEP* (VPZ) in dark-acclimated state or after exposure to constant 400 or 2000 μmol photons $m^{-2}$ $s^{-1}$ (when steady-state photosynthesis was reached) or three cycles of 3 min 2000/3 min 200 μmol photons $m^{-2}$ $s^{-1}$. Pigment concentrations (mean ± SEM, $n$ = 3 to 6 biological replicates) were normalized by chlorophyll a content (mmol $mol^{-1}$). Asterisks indicate significant differences between VPZ lines and WT ($\alpha$ = 0.05). Vio, violaxanthin; Ant, antheraxanthin; Zea, zeaxanthin; DES (%), (Zea + 0.5Ant)/(Zea + Ant + Vio); n.d., not detected.

| Light treatment | Pigment | WT | VPZ-23 | VPZ-34 | VPZ-56 |
|---|---|---|---|---|---|
| Dark-acclimated | Vio | 68.6 ± 1.5 | 52.1 ± 1.7 | 48.5 ± 0.6 | 51.6 ± 1.7 |
| | Ant | 0.1 ± 0.0 | 0.0 ± 0.0 | 0.0 ± 0.0 | 0.0 ± 0.0 |
| | Zea | n.d. | n.d. | n.d. | n.d. |
| | DES | 0 | 0 | 0 | 0 |
| Constant at 400 μmol photons $m^{-2}$ $s^{-1}$ | Vio | 53.0 ± 1.7 | 54.1 ± 6.2 | 56.9 ± 1.1 | 53.2 ± 1.2 |
| | Ant | 0.2 ± 0.1 | 0.1 ± 0.0 | 0.1 ± 0.0 | 0.1 ± 0.0 |
| | Zea | 1.7 ± 0.8 | 0.0 ± 0.0 | 0.4 ± 0.4 | 0.0 ± 0.0 |
| | DES | 3.0 ± 1.5 | 0.0 ± 0.0 | 0.7 ± 0.7 | 0.1 ± 0.0 |
| Constant at 2000 μmol photons $m^{-2}$ $s^{-1}$ | Vio | 29.0 ± 1.3 | 36.7 ± 4.5 | 30.1 ± 1.4 | 34.3 ± 0.4 |
| | Ant | 0.5 ± 0.0 | 0.6 ± 0.1 | 0.5 ± 0.0 | 0.6 ± 0.1 |
| | Zea | 26.3 ± 1.8 | *11.1 ± 3.6 | *11.3 ± 2.6 | *14.1 ± 3.8 |
| | DES | 46.3 ± 2.7 | *22.7 ± 7.5 | *26.0 ± 5.3 | *27.7 ± 5.2 |
| Fluctuating between 2000 and 200 μmol photons $m^{-2}$ $s^{-1}$ | Vio | 21.0 ± 0.6 | *35.8 ± 1.2 | *28.7 ± 1.6 | *31.9 ± 0.9 |
| | Ant | 0.8 ± 0.1 | *0.5 ± 0.0 | 0.7 ± 0.1 | *0.4 ± 0.1 |
| | Zea | 24.9 ± 2.1 | *4.7 ± 0.3 | *11.4 ± 3.8 | *6.6 ± 1.0 |
| | DES | 52.4 ± 2.4 | *11.3 ± 0.5 | *25.5 ± 7.0 | *16.4 ± 1.9 |

### *Xanthophyll cycle de-epoxidation as a function of different light treatments*

In dark-acclimated leaves from both WT and VPZ lines, the xanthophyll-cycle pool was completely epoxidated—entirely in the form of violaxanthin (Table 1). Exposure to 400 μmol photons $m^{-2}$ $s^{-1}$ constant light did not lead to substantial de-epoxidation, but 2000 μmol photons $m^{-2}$ $s^{-1}$ constant light led to accumulation of antheraxanthin and especially zeaxanthin. VPZ lines retained more violaxanthin and accumulated less zeaxanthin and antheraxanthin compared with that of WT, which led DES in the VPZ lines to be about half that of WT (26 versus 46%). Exposure to fluctuating light led to similar results as high light exposure, but with even less xanthophyll de-epoxidation in the VPZ lines, relative to WT (18 versus 53%), and field-grown plants of VPZ-23 showed significantly lower DES than that of WT throughout a diurnal period ($P$ < 0.05) (fig. S11). Because of the lower DES in the VPZ lines, a concern was that they would be more vulnerable to photoinhibition. However, photoprotection in seedlings after 2 hours exposure to excessive light ($\lambda_{max}$ = 470 nm, 2000 μmol photons $m^{-2}$ $s^{-1}$) appeared to be equal (VPZ-56) or even higher (VPZ-23 and VPZ-34; $P$ < 0.05) than that in WT (fig. S12).

## Discussion

How does introduction of the VPZ construct accelerate NPQ relaxation on transfer of leaves from high to low light, as would occur in a shading event? NPQ is a compound variable, encompassing several quenching mechanisms with contrasting relaxation kinetics (*22*). Whereas PsbS is exclusively associated with rapidly relaxing qE, the xanthophyll cycle is involved in multiple components of NPQ, especially qE and qZ. Even though VPZ lines had a lower xanthophyll DES under high and fluctuating light intensity (Table 1), levels of NPQ were similar to those of WT at high light (figs. S3B and S5H), implying that the relationship between xanthophyll DES and NPQ has been altered by PsbS overexpression, allowing for higher NPQ at lower DES. The presence of zeaxanthin correlates with faster induction and slower relaxation of NPQ, with respect to qZ and qE (*4*, *20*, *23*). Consistent with the lower DES in the VPZ lines, relaxation of both qE ($\tau_1$) and qZ ($\tau_2$) was accelerated by the VPZ overexpression. The faster relaxation of NPQ by VPZ overexpression can thus be explained by two parallel manipulations of NPQ. Combined overexpression of VDE and ZEP decreased xanthophyll DES, which in turn increased the NPQ relaxation rate through qZ, qE, and zeaxanthin-associated effects on NPQ kinetics. Second, the overexpression of PsbS led to an increase in qE, which more than offset the decrease due to lower DES (fig. S3B).

The hypothesis that photosynthetic efficiency could be increased through acceleration of NPQ relaxation (*8*, *24*) relies on the inverse correlation between NPQ and photosynthetic efficiency. Under fluctuating light, the VPZ lines showed faster and greater decreases in NPQ after transitions from high to low light, relative to that of WT (Fig. 4F and fig. S5H), which increased the quantum yield of $CO_2$ assimilation by 14% (Fig. 4B), providing proof that on transition from high to low light, NPQ does indeed limit photosynthetic efficiency. Xanthophyll DES is correlated with NPQ (*19*), which suggests that limiting violaxanthin de-epoxidation may also increase the NPQ relaxation rate. However, decreased zeaxanthin formation through antisense *VDE* expression in tobacco in previous studies did not lead to an increase in photosynthetic efficiency and growth (*25*, *26*). Reduction in NPQ amplitude (*27*) and antioxidant capacity (*28*) leads to greater sensitivity to damage by excessive light in mutants with reduced zeaxanthin (*29*). In the current work, expression of VDE and PsbS was increased to balance the up-regulation of ZEP and avoid such damage (fig. S12). This conservation of photoprotection in the VPZ lines most likely originates from an increase in qE, reflecting the positive correlation between photoprotection and PsbS content (*18*).

About 50% of canopy carbon gain in crops occurs under light limitation (*5*). Efficiency of photosynthesis in the shade declines even further with rapid light transitions caused by clouds and wind-driven movement of overshadowing leaves. Higher yields have followed increased planting densities, which also caused denser canopies and increased the proportion of partially shaded leaves, leading to more irregular light conditions for each leaf. Even on a clear day, diurnal changes in sun angle cause dynamic shading of leaves within the canopy by those at the top. At the level of the individual chloroplast, these changes from sun to shade are almost instantaneous (*7*). Thus, light conditions in the field are anything but steady state. Under steady-state light, the VPZ lines evaluated here would have shown no yield advantage over WT. Their yield advantage becomes apparent under more realistic, irregular, lighting conditions.

Because the xanthophyll cycle and PsbS are common to all vascular plants (*11*, *19*), we expect that similar results would pertain to all major crops. Although this work has focused on crop light-use efficiency, stomatal conductance also remains high during the first few minutes after transfer to shade. Increasing the rate of relaxation of NPQ will therefore not only increase net carbon gain but also increase crop water-use efficiency. This may be an important attribute, given forecast climate change impacts on future crop production (*30*).

Transgenic expression of *Arabidopsis* VDE, PsbS, and ZEP (VPZ) in combination in tobacco led to a marked and statistically significant acceleration of NPQ relaxation on transfer of leaves from high light to shade. As hypothesized, this led to a more rapid recovery of the efficiency of photosynthetic $CO_2$ assimilation in the shade. Results from field and greenhouse experiments showed that this corresponded to increased productivity in terms of final dry mass. Increases in crop productivity of 15%, as obtained here, demonstrate a potential means to achieve the increases in crop yield that are forecast to be necessary by 2050 (*31*, *32*).

Downloaded from http://science.sciencemag.org/ on November 24, 2016

## REFERENCES AND NOTES

1. D. R. Ort *et al.*, *Proc. Natl. Acad. Sci. U.S.A.* **112**, 8529–8536 (2015).
2. Z. Li, S. Wakao, B. B. Fischer, K. K. Niyogi, *Annu. Rev. Plant Biol.* **60**, 239–260 (2009).
3. P. Müller, X.-P. Li, K. K. Niyogi, *Plant Physiol.* **125**, 1558–1566 (2001).
4. M. L. Pérez-Bueno, M. P. Johnson, A. Zia, A. V. Ruban, P. Horton, *FEBS Lett.* **582**, 1477–1482 (2008).
5. S. P. Long, S. Humphries, P. G. Falkowski, *Annu. Rev. Plant Biol.* **45**, 633–662 (1994).
6. C. Werner, R. J. Ryel, O. Correia, W. Beyschlag, *Plant Cell Environ.* **24**, 27–40 (2001).
7. X.-G. Zhu, D. R. Ort, J. Whitmarsh, S. P. Long, *J. Exp. Bot.* **55**, 1167–1175 (2004).
8. E. H. Murchie, K. K. Niyogi, *Plant Physiol.* **155**, 86–92 (2011).
9. C. D. P. Duffy, A. V. Ruban, *J. Photochem. Photobiol. B* **152** (pt. B), 215–226 (2015).
10. C. A. Wraight, A. R. Crofts, *Eur. J. Biochem.* **17**, 319–327 (1970).
11. M. D. Brooks, S. Jansson, K. K. Niyogi, in *Non-Photochemical Quenching and Energy Dissipation in Plants Algae and Cyanobacteria* (Springer, 2014), vol. 40, pp. 297–314.
12. X.-P. Li *et al.*, *Nature* **403**, 391–395 (2000).
13. B. Demmig-Adams, *Biochim. Biophys. Acta* **1020**, 1–24 (1990).
14. H. Y. Yamamoto, T. O. M. Nakayama, C. O. Chichester, *Arch. Biochem. Biophys.* **97**, 168–173 (1962).
15. S. Hubbart, O. O. Ajigboye, P. Horton, E. H. Murchie, *Plant J.* **71**, 402–412 (2012).
16. X.-P. Li, A. M. Gilmore, K. K. Niyogi, *J. Biol. Chem.* **277**, 33590–33597 (2002).
17. A. Zia, M. P. Johnson, A. V. Ruban, *Planta* **233**, 1253–1264 (2011).
18. X.-P. Li, P. Muller-Moule, A. M. Gilmore, K. K. Niyogi, *Proc. Natl. Acad. Sci. U.S.A.* **99**, 15222–15227 (2002).
19. B. Demmig-Adams, W. W. Adams III, *Planta* **198**, 460–470 (1996).
20. M. Nilkens *et al.*, *Biochim. Biophys. Acta* **1797**, 466–475 (2010).
21. M. P. Johnson, P. A. Davison, A. V. Ruban, P. Horton, *FEBS Lett.* **582**, 262–266 (2008).
22. A. V. Ruban, *Plant Physiol.* **170**, 1903–1916 (2016).
23. P. Horton, A. V. Ruban, R. G. Walters, *Annu. Rev. Plant Physiol. Plant Mol. Biol.* **47**, 655–684 (1996).
24. S. P. Long, X.-G. Zhu, S. L. Naidu, D. R. Ort, *Plant Cell Environ.* **29**, 315–330 (2006).
25. S.-H. Chang, R. C. Bugos, W.-H. Sun, H. Y. Yamamoto, *Photosynth. Res.* **64**, 95–103 (2000).
26. W.-H. Sun, A. S. Verhoeven, R. C. Bugos, H. Y. Yamamoto, *Photosynth. Res.* **67**, 41–50 (2001).
27. K. K. Niyogi, A. R. Grossman, O. Björkman, *Plant Cell* **10**, 1121–1134 (1998).
28. M. Havaux, L. Dall'osto, R. Bassi, *Plant Physiol.* **145**, 1506–1520 (2007).
29. N. Wang *et al.*, *Physiol. Plant.* **132**, 384–396 (2008).
30. D. R. Ort, S. P. Long, *Science* **344**, 484–485 (2014).
31. J. Kromdijk, S. P. Long, *Proc. Biol. Sci.* **283**, 20152578 (2016).
32. D. Tilman, M. Clark, *Daedalus* **144**, 8–23 (2015).



## ACKNOWLEDGMENTS

We thank D. Drag and B. Harbaugh for plant management in greenhouse and field studies; M. Kobayashi for performing the high-performance liquid chromatography analysis of pigments from the field-grown plants; and K. Kucera, M. Steiner, and S. Gillespie for general assistance during laboratory- and fieldwork. We also thank T. Clemente for initial help with tobacco transformation. This research was supported by Bill and Melinda Gates Foundation grant OPP1060461, titled "RIPE—Realizing increased photosynthetic efficiency for sustainable increases in crop yield." K.K.N. is an investigator of the Howard Hughes Medical Institute and the Gordon and Betty Moore Foundation (through grant GBMF3070). The data reported in this paper have been tabulated in the supplementary materials. Plants and constructs reported are available from the University of Illinois and University of California, Berkeley, for research purposes, subject to the conditions of the Uniform Biological Material Transfer Agreement. The University of Illinois has submitted a provisional patent on behalf of J.K., K.G., L.L., K.K.N., and S.P.L on aspects of the findings.


## SUPPLEMENTARY MATERIALS

www.sciencemag.org/content/354/6314/857/suppl/DC1
Materials and Methods
Figs. S1 to S14
Tables S1 to S3
Data Sets 1 to 21
References (*33*–*49*)

29 August 2016; accepted 28 September 2016
10.1126/science.aai8878

REPORTS

SOLAR CELLS

# Perovskite-perovskite tandem photovoltaics with optimized band gaps

**Giles E. Eperon,[1,2]* Tomas Leijtens,[3]* Kevin A. Bush,[3] Rohit Prasanna,[3] Thomas Green,[1] Jacob Tse-Wei Wang,[1] David P. McMeekin,[1] George Volonakis,[4] Rebecca L. Milot,[1] Richard May,[2] Axel Palmstrom,[5] Daniel J. Slotcavage,[3] Rebecca A. Belisle,[3] Jay B. Patel,[1] Elizabeth S. Parrott,[1] Rebecca J. Sutton,[1] Wen Ma,[6] Farhad Moghadam,[6] Bert Conings,[1,7] Aslihan Babayigit,[1,7] Hans-Gerd Boyen,[7] Stacey Bent,[5] Feliciano Giustino,[4] Laura M. Herz,[1] Michael B. Johnston,[1] Michael D. McGehee,[2]† Henry J. Snaith[1]†**

**We demonstrate four- and two-terminal perovskite-perovskite tandem solar cells with ideally matched band gaps. We develop an infrared-absorbing 1.2–electron volt band-gap perovskite, $FA_{0.75}Cs_{0.25}Sn_{0.5}Pb_{0.5}I_3$, that can deliver 14.8% efficiency. By combining this material with a wider–band gap $FA_{0.83}Cs_{0.17}Pb(I_{0.5}Br_{0.5})_3$ material, we achieve monolithic two-terminal tandem efficiencies of 17.0% with >1.65-volt open-circuit voltage. We also make mechanically stacked four-terminal tandem cells and obtain 20.3% efficiency. Notably, we find that our infrared-absorbing perovskite cells exhibit excellent thermal and atmospheric stability, not previously achieved for Sn-based perovskites. This device architecture and materials set will enable "all-perovskite" thin-film solar cells to reach the highest efficiencies in the long term at the lowest costs.**

Metal halide perovskites [$ABX_3$, where A is typically Cs, methylammonium (MA), or formamidinium (FA); B is Pb or Sn; and X is I, Br, or Cl] have emerged as an extremely promising photovoltaic (PV) technology owing to their rapidly increasing power conversion efficiencies (PCEs) and low processing costs. Single-junction perovskite devices have reached a certified 22% PCE (*1*), but the first commercial iterations of perovskite PVs will likely be as an "add-on" to silicon (Si) PVs. In a tandem configuration, a perovskite with a band gap of ~1.75 eV can enhance the efficiency of the silicon cell. (*2*) An all-perovskite tandem cell could deliver lower fabrication costs, but requires band gaps that have not yet been realized. The highest-efficiency tandem devices would require a rear cell with a band gap of 0.9 to 1.2 eV and a front cell with a band gap of 1.7 to 1.9 eV. Although materials such as $FA_{0.83}Cs_{0.17}Pb(I_xBr_{1-x})_3$ deliver appropriate band gaps for the front cell (*2*), Pb-based materials cannot be tuned to below 1.48 eV for the rear cell. Completely replacing Pb with Sn can shift the band gap to ~1.3 eV (for $MASnI_3$) (*3*), but the tin-based materials are notoriously air sensitive and difficult to process, and PV devices based on them have been limited to ~6% PCE. (*3*, *4*) An anomalous band-gap bowing in mixed tin-lead perovskite systems ($MAPb_{0.5}Sn_{0.5}I_3$) has given band gaps of ~1.2 eV but mediocre performance (~7% PCE). Very recently, PCE of >14% has been reported with $MA_{0.5}FA_{0.5}Pb_{0.75}Sn_{0.25}I_3$ cells, for band gaps >1.3 eV and all-perovskite four-terminal tandem cells with 19% efficiency (*5*, *6*, *7*). Here, we demonstrate a stable, 14.8% efficient perovskite solar cell based on a ~1.2-eV band gap $FA_{0.75}Cs_{0.25}Pb_{0.5}Sn_{0.5}I_3$ absorber. We measure open-circuit voltages ($V_{oc}$'s) of up to 0.83 V in these cells, which represents a smaller voltage deficit between band gap and $V_{oc}$ than measured for the highest-efficiency lead-based perovskite cells. We then combined these with 1.8-eV $FA_{0.83}Cs_{0.17}Pb(I_{0.5}Br_{0.5})_3$ perovskite cells to demonstrate current-matched and efficient (17.0% PCE) monolithic all-perovskite two-terminal tandem solar cells on small areas and 13.8% PCE on large areas, with $V_{oc}$ >1.65 V. Finally, we fabricated 20.3% efficient small-area and 16.0% efficient 1-$cm^2$ all-perovskite four-terminal tandems using a semitransparent 1.6-eV $FA_{0.83}Cs_{0.17}Pb(I_{0.83}Br_{0.17})_3$ front cell.

[1]Department of Physics, University of Oxford, Clarendon Laboratory, Parks Road, Oxford OX1 3PU, UK. [2]Department of Chemistry, University of Washington, Seattle, WA, USA. [3]Department of Materials Science, Stanford University, Lomita Mall, Stanford, CA, USA. [4]Department of Materials, University of Oxford, Parks Road, Oxford OX1 3PH, UK. [5]Department of Chemical Engineering, Stanford University, Via Ortega, Stanford, CA, USA. [6]SunPreme, Palomar Avenue, Sunnyvale, CA, USA. [7]Institute for Materials Research, Hasselt University, Diepenbeek, Belgium.
*These authors contributed equally to this work. **†Corresponding author. Email: mmcgehee@stanford.edu (M.D.M.); henry.snaith@physics.ox.ac.uk (H.J.S.)**

Downloaded from http://science.sciencemag.org/ on November 24, 2016

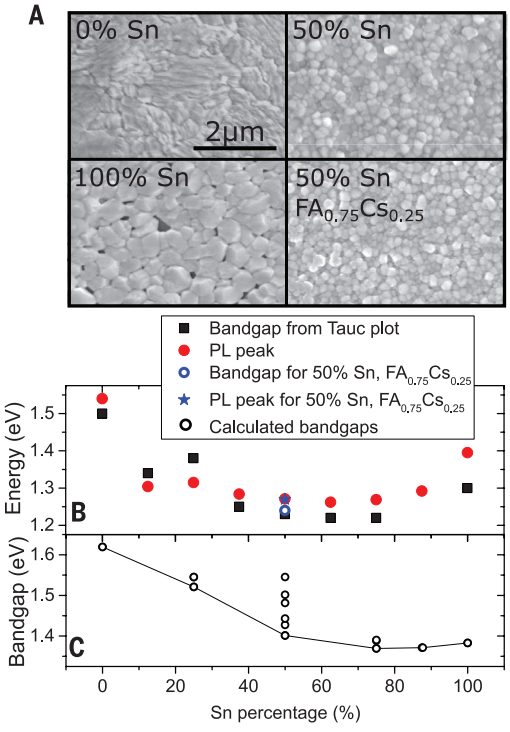


**Fig. 1. Tin-lead alloying.** (**A**) Scanning electron micrographs showing the top surface of $FASn_xPb_{1-x}I_3$ films with different Sn percentages and $FA_{0.75}Cs_{0.25}Pb_{0.5}Sn_{0.5}I_3$ ("50% Sn, $FA_{0.75}Cs_{0.25}$"), fabricated by PAI deposition. The 0% Sn films were annealed at 170°C, and the other films were annealed at 70°C. (**B**) Plot of experimentally estimated band gap as a function of Sn percentage, determined from absorption onset in a Tauc plot (assuming direct band gap) of the absorption (black); PL peak positions are given in red. (**C**) Band gaps for Sn-Pb perovskite alloys calculated from first principles using a supercell containing eight $BX_6$ octahedra, where the Sn and Pb atoms are ordered relative to each other (see supplementary materials for full details). Points plotted represent all possible band gaps for a particular composition, based on all possible Sn-Pb configurations; a solid line is drawn through the lowest band-gap options as a comparison to experiment.

It has proved difficult to fabricate smooth, pinhole-free layers of tin-based perovskites on planar substrates (fig. S1) (*3*, *4*). We developed a technique, precursor-phase antisolvent immersion (PAI), to deposit uniform layers of tin-containing perovskites, $FASn_xPb_{1-x}I_3$, that combines two previous methods: the use of low–vapor pressure solvents to retard crystallization by forming precursor complexes and an antisolvent bath to crystallize the film with only gentle heating (*4*, *8*). Rather than using neat dimethyl sulfoxide (DMSO) as a solvent (*4*), a mixture of DMSO and dimethylformamide (DMF) allowed spin-coating of a uniform transparent precursor film that was not yet fully crystallized. Immersion of the films immediately in an antisolvent bath (anisole) (fig. S2) rapidly changed the film to a deep red. (*9*) Subsequent annealing at 70°C removed residual DMSO (fig. S7) to form smooth, dark, highly crystalline and uniform $FASn_xPb_{1-x}I_3$ films over the entire range of values of $x$ = 0 to 1 (Fig. 1A). Only the neat Pb perovskite required heating at a higher temperature (170°C) to convert the film from the yellow room-temperature phase to the black phase (*10*).

Photoluminescence (PL) spectra and absorption spectra of a range of compositions (fig. S4) allowed us to estimate the optical band gap from Tauc plots (from absorption, as discussed in the supplementary materials) and the PL peak positions (Fig. 1B) (*9*). The band gap narrowed between the two composition end points, similar to the observations of Kanatzidis *et al.* with the MA system (*5*), and between 50 and 75% Sn, was almost 1.2 eV. X-ray diffraction (XRD) spectra (fig. S5) for the whole series revealed a single dominant perovskite phase (table S1).

To understand this anomalous band-gap trend, we performed first-principles calculations of band gaps as a function of the tin-lead ratio (details in the supplementary materials) (*9*). For a disordered solid solution with Pb and Sn in random locations, the calculated band gap decreased monotonically (fig. S8). For an ordered structure, we placed the Sn and Pb atoms in specific positions relative to each other within a repeating lattice unit of eight octahedra in a "supercell." Here, if we take the lowest band gaps for each ratio, an anomalous band-gap trend emerges (Fig. 1C). For compositions with >50% Sn, a specific type of short-range order in the Pb-Sn positions allowed the band gap to dip below the end points. Im *et al.* attributed a similar band-gap trend observed for $MAPb_xSn_{1-x}I_3$ to the competition between spin-orbit coupling and distortions of the lattice (*11*), but if this was the case here, we should have observed it in the random solid solution approach. The energetic difference between the various Pb-Sn configurations was on the order of 2 meV, so at room temperature, the materials are likely to contain various combinations of the configurations that we show in fig. S7, but the absorption and emission onsets reflect the regions with the smallest gap.

To determine the charge-carrier diffusion length, mobility, and recombination lifetimes of these materials, we performed optical pump-probe terahertz (THz spectroscopy) on $FASnI_3$ and $FASn_{0.5}Pb_{0.5}I_3$. The fluence dependence of the THz transients for $FASn_{0.5}Pb_{0.5}I_3$ (fig. S9) exhibited faster decays at higher intensities as the result of increased bimolecular and Auger recombination (*12*). We calculated recombination rate constants and charge-carrier mobilities of 22 and 17 $cm^2 V^{-1} s^{-1}$ for $FASnI_3$ and $FASn_{0.5}Pb_{0.5}I_3$, respectively, comparable to values for Pb perovskite films (*12*, *13*). In comparison, for $MASnI_3$, the value was only 2 $cm^2 V^{-1} s^{-1}$ (*3*, *14*). For charge-carrier densities typical under solar illumination, charge-carrier diffusion lengths of ~300 nm were obtained for $FASn_{0.5}Pb_{0.5}I_3$ (details in the supplementary materials). Although lower than that for the best reported perovskite materials, it is equivalent to the typical thickness required to absorb most incident light (~300 to 400 nm) (*15*).

We fabricated a series of planar heterojunction devices in the "inverted" p-i-n architecture (*16*) comprising indium-tin-oxide (ITO)/poly(3,4-ethylenedioxythiophene)-poly(styrenesulfonate) (PEDOT:PSS)/$FASn_xPb_{1-x}I_3$/$C_{60}$/bathocuproine (BCP) capped with an Ag or Au electrode (Fig. 2A). The current density–voltage (*J-V*) curves and external quantum efficiency (EQE) measurements for the whole compositional series are shown in fig. S10. The onset of the EQEs closely matched that of the absorption of the materials, with light harvested out to ~1020 nm in the 50 to 75% Sn compositions. The highest efficiencies are generated from the devices with 50% Sn, within the lowest band-gap region; thus, we used this material to optimize our low-gap solar cells.

A small addition of Cs boosts the performance and stability of Pb-based perovskites (*17*–*19*). Substituting 25% of the FA with Cs in our films had little impact on band gap, morphology, PL, crystal structure, and charge carrier diffusion lengths (Fig. 1 and figs. S4 and S7), but device performance was enhanced (Fig. 2, B to D). The best $FASn_{0.5}Pb_{0.5}I_3$ device yields 10.9% PCE, whereas the best $FA_{0.75}Cs_{0.25}Sn_{0.5}Pb_{0.5}I_3$ device exhibited an impressive short-circuit current of 26.7 mA $cm^{-2}$, 0.74 V $V_{oc}$, and 0.71 fill factor (FF) to yield 14.1% PCE. The processing of each composition was optimized separately. These devices did not exhibit appreciable rate-dependent hysteresis, and the stabilized power output (14.8%) matched the scanned performance well. This efficiency was comparable with that of the best solution-processed low–band gap copper-indium-gallium-diselenide (CIGS) solar cells. (*20*) Thus, $FA_{0.75}Cs_{0.25}Pb_{0.5}Sn_{0.5}I_3$ is well

**Table 1. Device parameters corresponding to the *J-V* curves in Fig. 2B.**

| | $J_{SC}$ (mA $cm^{-2}$) | $V_{OC}$ (V) | FF | PCE (%) | SPO (%) |
|---|---|---|---|---|---|
| $FASn_{0.5}Pb_{0.5}I_3$ | 21.9 | 0.70 | 0.66 | 10.2 | 10.9 |
| $FA_{0.75}Cs_{0.25}Sn_{0.5}Pb_{0.5}I_3$ | 26.7 | 0.74 | 0.71 | 14.1 | 14.8 |

Downloaded from http://science.sciencemag.org/ on November 22, 2016

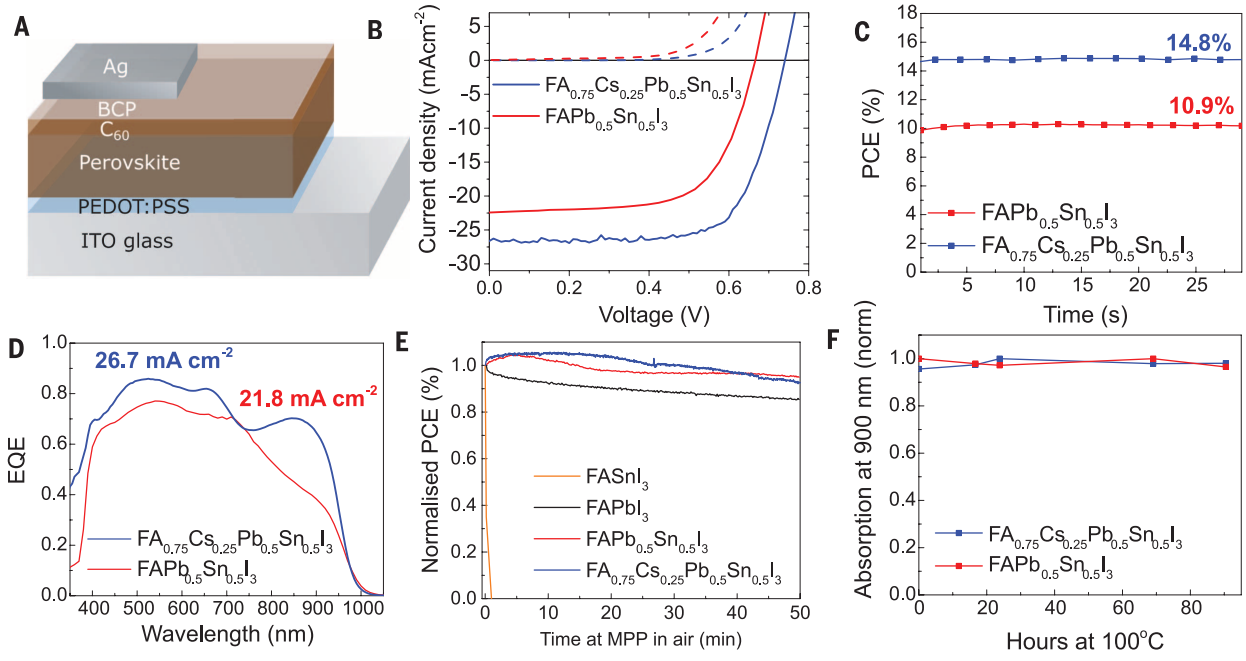


**Fig. 2. Performance and stability of $FASn_{0.5}Pb_{0.5}I_3$ and $FA_{0.75}Cs_{0.25}Sn_{0.5}Pb_{0.5}I_3$ perovskite solar cells.** (**A**) Schematic of the device architecture for narrow-gap single-junction perovskite solar cells. (**B**) Current-voltage characteristics under AM1.5G illumination for the best $FASn_{0.5}Pb_{0.5}I_3$ and $FA_{0.75}Cs_{0.25}Sn_{0.5}Pb_{0.5}I_3$ devices under illumination (solid lines) and in the dark (dashed lines), measured at 0.1 V/s with no prebiasing or light soaking. (**C**) Stabilized power output for the best solar cells, measured via a maximum power point tracking algorithm. (**D**) External quantum efficiency for the best devices of each material with the integrated current values shown providing a good match to the *J-V* scan $J_{sc}$. (**E**) PCE as a function of time for three compositions of $FASn_xPb_{1-x}I_3$ ($x$ = 0, 0.5, 1) as well as $FA_{0.75}Cs_{0.25}Sn_{0.5}Pb_{0.5}I_3$, measured by holding the cell at maximum power point in air under AM1.5G illumination. (**F**) Thermal stability of $FASn_{0.5}Pb_{0.5}I_3$ and $FA_{0.75}Cs_{0.25}Sn_{0.5}Pb_{0.5}I_3$ films, quantified by heating the samples at 100°C and monitoring their absorption at 900 nm as a function of time.

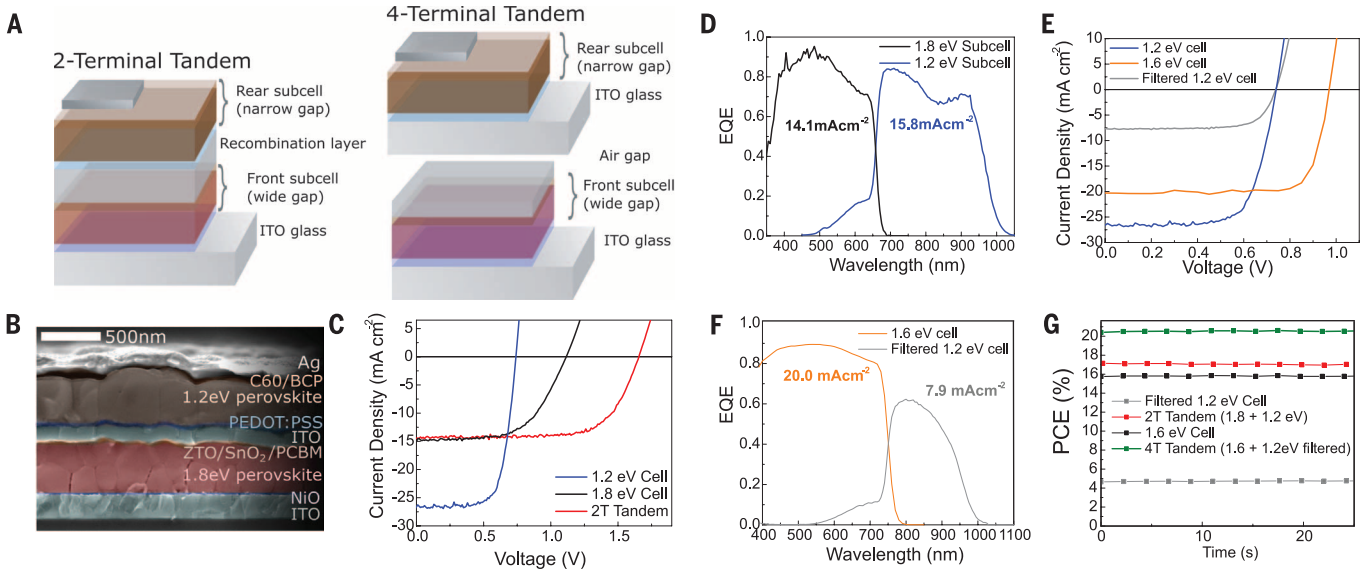


**Fig. 3. Perovskite-perovskite tandems.** (**A**) Schematics showing 2T and 4T tandem perovskite solar cell concepts. In this image, devices would be illuminated from below. (**B**) Scanning electron micrograph of the 2T perovskite-perovskite tandem. (**C**) Scanned current-voltage characteristics under AM 1.5G illumination, of the two-terminal perovskite-perovskite tandem, the 1.2-eV solar cell, and the ITO-capped 1.8-eV solar cell. (**D**) External quantum efficiency spectra for the subcells. (**E**) *J-V* curves of a 1.2-eV perovskite, of the same solar cell filtered by an ITO-capped 1.6-eV perovskite solar cell, and of the ITO-capped 1.6-eV perovskite solar cell, used to determine the mechanically stacked tandem efficiency. (**F**) External quantum efficiency spectra for the mechanically stacked tandem. (**G**) The stabilized power output tracked over time at maximum power point for the 2T perovskite solar cell, the 1.2-eV perovskite solar cell filtered by an ITO-capped 1.6-eV perovskite solar cell, the ITO-capped 1.6-eV perovskite solar cell, and the mechanically stacked tandem under AM1.5G illumination. The stabilized power output (SPO) for the 1.8-eV subcell is plotted in fig. S14 and given in Table 2.

Downloaded from http://science.sciencemag.org/ on November 22, 2016

**Table 2. Solar cell performance parameters corresponding to the *J-V* curves shown in Fig. 3.** Cell active areas are 0.20 or 1 $cm^2$. SPO, stabilized power output from maximum power point tracking. Large-area tandem data are plotted in fig. S19.

| | $J_{sc}$ (mA $cm^{-2}$) | $V_{oc}$ (V) | FF | PCE (%) | SPO (%) |
|---|---|---|---|---|---|
| 1.2-eV cell | 26.7 | 0.74 | 0.71 | 14.1 | 14.8 |
| 1.8-eV cell | 15.1 | 1.12 | 0.58 | 9.8 | 9.5 |
| 2T tandem | 14.5 | 1.66 | 0.70 | 16.9 | 17.0 |
| Filtered 1.2-eV cell | 7.9 | 0.74 | 0.73 | 4.4 | 4.5 |
| ITO-capped 1.6-eV cell | 20.3 | 0.97 | 0.79 | 15.7 | 15.8 |
| 4T tandem | – | – | – | 20.1 | 20.3 |
| 1-$cm^2$ 2T tandem | 13.5 | 1.76 | 0.56 | 13.3 | 13.8 |
| 1-$cm^2$ 4T tandem | – | – | – | 16.4 | 16.0 |

suited for a rear junction in a solution-processed tandem solar cell, without the need for high-temperature thermal processing.

We performed ultraviolet photoelectron spectroscopy (UPS) and x-ray photoelectron spectroscopy (XPS) measurements to determine the energetic positions of the conduction and valence bands (fig. S11). The band levels for $FASn_{0.5}Pb_{0.5}I_3$ are well matched for C60 and PEDOT:PSS as electron and hole acceptors. The Cs-containing material showed an energetically shallower valance band and mild p-type doping (*21*, *22*).

The electronic losses in a solar cell are reflected by the difference in energy between the band gap of the absorber and $V_{oc}$ (the loss in potential) (*23*). For crystalline silicon PV cells, which generate a record $V_{oc}$ of 0.74 V and have a band gap of 1.12 eV, this loss is 0.38 V (*24*). Some of our $FA_{0.75}Cs_{0.25}Sn_{0.5}Pb_{0.5}I_3$ devices, with a thinner active layer, displayed $V_{oc}$'s up to 0.83 V (fig. S11), with a 1.24-eV band gap, exhibiting a comparable loss in potential of 0.41 eV.

Tin-based perovskites have previously been observed to be extremely unstable in air (*25*), so we carried out a simple aging test on the $FASn_{0.5}Pb_{0.5}I_3$ and $FA_{0.75}Cs_{0.25}Pb_{0.5}Sn_{0.5}I_3$ devices, comparing to $FASnI_3$ and $FAPbI_3$. We held the devices at maximum power point under 100 mW $cm^{-2}$ illumination and measured power output over time in ambient air with a relative humidity of 50 ± 5% (Fig. 2E). The $FAPbI_3$ device maintained its performance relatively well, with a small drop observed over the time (to 85% of initial PCE over 50 min), possibly associated with photo-oxidation and hydration of the unencapsulated perovskite layer, or a partial reversion to the yellow room-temperature phase (*17*, *26*). Both the $FASn_{0.5}Pb_{0.5}I_3$ and $FA_{0.75}Cs_{0.25}Sn_{0.5}Pb_{0.5}I_3$ showed a stability similar to or even better than the neat Pb material. We also subjected bare perovskite films to thermal stress, heating for 4 days at 100°C under nitrogen; there were no changes in absorption spectra, a monitor of optical quality and hence stability (Fig. 2F) (*27*). We also monitored the performance of full devices at 85°C over several months (fig. S13) and found that the Sn:Pb material displays device stability similar to that of the neat Pb material. The contribution of both Sn and Pb orbitals to the valence band minimum may reduce the propensity of $Sn^{2+}$ to oxidize to $Sn^{4+}$.

A 1.2-eV perovskite is ideally suited as the rear cell in either monolithic two-terminal (2T) tandem solar cells or mechanically stacked four-terminal (4T) tandem solar cells (Fig. 3A). The subcells in a 2T tandem must be current matched to deliver optimum performance, and connected with a recombination layer. A 4T tandem operates the two cells independently but requires an extra transparent electrode, which can result in more absorption losses and higher cost. Theoretical efficiencies using a 1.2-eV rear cell (fig. S14) show that the 2T architecture requires the use of a top cell with a ~1.75- to 1.85-eV band gap, whereas the 4T architecture has a much more relaxed requirement of 1.6 to 1.9 eV.

We can obtain efficient and stable perovskites with appropriate wide band gaps for front cells in tandem architectures by using a mixture of FA and Cs cations (*2*) and control the band gap by tuning the Br:I ratio; $FA_{0.83}Cs_{0.17}Pb(I_{0.5}Br_{0.5})_3$ has a 1.8-eV band gap that is ideally suited for the 2T tandem. However, their higher losses in potential compared with the more commonly used 1.6-eV perovskites (*28*) make the latter better suited for the 4T tandem. We prepared both of these perovskites in the p-i-n structure depicted in Fig. 3A, using $NiO_x$ and phenyl-C61-butyric acid methyl ester (PCBM) as the hole and electron contacts, respectively. We applied PAI deposition to form smooth and thick perovskite layers, obtaining efficient devices with appropriate photocurrents and voltages up to 1.1 V (see fig. S14) (*9*).

For the recombination layer in the 2T cell, we used layers of tin oxide and zinc-tin-oxide (ZTO) coated with sputter-coated ITO (*29*). This ITO layer completely protects the underlying perovskite solar cell from any solvent damage (fig. S16), meaning that we could fabricate the 1.2-eV $FA_{0.75}Cs_{0.25}Sn_{0.5}Pb_{0.5}I_3$ solar cell directly on top. We plot the *J-V* curves of the best single-junction 1.2-eV cells and single-junction 1.8-eV cell, and that of the best 2T tandem device, in Fig. 3C. We observed good performance for the 2T tandem solar cells, exceeding either of the individual subcells despite the somewhat non-optimized 1.8-eV top cell. The photocurrent of the tandem solar cell was 14.5 mA $cm^{-2}$; voltage is an appropriate addition of the two subcells (1.66 V); and the fill factor is 0.70, yielding an overall performance of 16.9% via a scanned *J-V* curve and of 17.0% when stabilized at its maximum power point. None of the devices exhibit substantial hysteresis in the *J-V* curves (Fig. 3G and fig. S17).

The photocurrent is notably high when compared to the photocurrent density of the best reported monolithic perovskite-silicon tandems (*30*, *31*). External quantum efficiency (EQE) measurements (Fig. 3D) demonstrate that the two subcells are fairly well matched, with the wide-gap subcell limiting the current. One benefit of a tandem architecture, which we observe here, is that the FF tends not to be limited to the lowest value of the individual subcells, owing to the reduced impact of series resistance on a higher-voltage cell (*32*). Furthermore, we held a 2T tandem at its maximum power point under illumination in nitrogen for more than 18 hours, and it showed effectively no performance drop (fig. S18).

For a 4T tandem, we used an efficient 1.6-eV band gap $FA_{0.83}Cs_{0.17}Pb(I_{0.83}Br_{0.17})_3$ perovskite, similar to that reported by McMeekin *et al.* but in p-i-n configuration (*2*) with a transparent ITO top contact. We obtained a 15.8% efficient solar cell with a $V_{oc}$ ~1 V, and when we use it to filter a 14.8% $FA_{0.75}Cs_{0.25}Sn_{0.5}Pb_{0.5}I_3$ cell, we can still extract substantial photocurrent (7.9 mA $cm^{-2}$) from the low–band gap device. We plot the *J-V* curves and EQE spectra of the 1.6- and 1.2-eV cells in the 4T tandem in Fig. 3, E and F, and obtain an additional 4.5% PCE from the 1.2-eV rear cell, yielding an overall stabilized tandem efficiency of 20.3% (Fig. 3G).

The above results were for 0.2-$cm^2$ devices. We also made large-area (1 $cm^2$) versions of the single junctions and 2T and 4T tandems. The current-voltage characteristics of these devices are shown in Table 2 and fig. S18, with 2T tandem 1-$cm^2$ devices exhibiting 13.8% stabilized PCE and 4T tandems 16.0%. The 17.0% PCE 2T and 20.3% 4T tandems, which are for devices that could be further optimized, already far exceed the best tandem solar cells made with other similarly low-cost semiconductors, such as those made with organic small molecules (world record is 13%) or amorphous and microcrystalline silicon (13.5%) (*1*, *24*). Notably, our results illustrate that the tandem cell should be at least 4 to 5% more efficient than the best 1.6-eV single-junction perovskite cells, indicating that as the efficiency of the single-junction cells increases, then the tandem approach will enable this low temperature–processed polycrystalline thin-film technology to surpass the 30% efficiency barrier.

Downloaded from http://science.sciencemag.org/ on November 22, 2016

## REFERENCES AND NOTES

1. National Renewable Energy Laboratory, *Best Research-Cell Efficiencies*, www.nrel.gov/pv/assets/images/efficiency_chart.jpg (2016).
2. D. P. McMeekin *et al.*, *Science* **351**, 151–155 (2016).
3. N. K. Noel *et al.*, *Energy Environ. Sci.* **7**, 3061–3068 (2014).
4. F. Hao *et al.*, *J. Am. Chem. Soc.* **137**, 11445–11452 (2015).
5. F. Hao, C. C. Stoumpos, R. P. H. Chang, M. G. Kanatzidis, *J. Am. Chem. Soc.* **136**, 8094–8099 (2014).
6. L. Zhu *et al.*, *Nanoscale* **8**, 7621–7630 (2016).
7. Z. Yang *et al.*, *Adv. Mater.* 10.1002/adma.201602696 (2016).
8. Y. Zhou *et al.*, *J. Mater. Chem. A Mater. Energy Sustain.* **3**, 8178–8184 (2015).
9. See supplementary materials on *Science* Online.
10. C. C. Stoumpos, C. D. Malliakas, M. G. Kanatzidis, *Inorg. Chem.* **52**, 9019–9038 (2013).
11. J. Im, C. C. Stoumpos, H. Jin, A. J. Freeman, M. G. Kanatzidis, *J. Phys. Chem. Lett.* **6**, 3503–3509 (2015).
12. L. M. Herz, *Annu. Rev. Phys. Chem.* **67**, 65–89 (2016).
13. W. Rehman *et al.*, *Adv. Mater.* **27**, 7938–7944 (2015).
14. E. S. Parrott *et al.*, *J. Phys. Chem. Lett.* **7**, 1321–1326 (2016).
15. M. B. Johnston, L. M. Herz, *Acc. Chem. Res.* **49**, 146–154 (2016).
16. P. Docampo, J. M. Ball, M. Darwich, G. E. Eperon, H. J. Snaith, *Nat. Commun.* **4**, 2761 (2013).
17. Z. Li *et al.*, *Chem. Mater.* **28**, 284–292 (2016).
18. J.-W. Lee *et al.*, *Adv. Energy Mater.* **5**, 1501310 (2015).
19. C. Yi *et al.*, *Energy Environ. Sci.* **9**, 656–662 (2016).
20. T. K. Todorov, O. Gunawan, T. Gokmen, D. B. Mitzi, *Prog. Photovolt. Res. Appl.* **21**, 82–87 (2013).
21. P. Schulz *et al.*, *Energy Environ. Sci.* **7**, 1377–1381 (2014).
22. C. Wang *et al.*, *Appl. Phys. Lett.* **106**, 111603 (2015).
23. H. J. Snaith, *Adv. Funct. Mater.* **20**, 13–19 (2010).
24. M. A. Green, K. Emery, Y. Hishikawa, W. Warta, E. D. Dunlop, *Prog. Photovolt. Res. Appl.* **23**, 1–9 (2015).
25. F. Hao, C. C. Stoumpos, D. H. Cao, R. P. H. Chang, M. G. Kanatzidis, *Nat. Photonics* **8**, 489–494 (2014).
26. T. Leijtens *et al.*, *Adv. Energy Mater.* **5**, 1500963 (2015).
27. B. Conings *et al.*, *Adv. Energy Mater.* **5**, 1500477 (2015).
28. M. Saliba *et al.*, *Science* **354**, 206–209 (2016).
29. K. A. Bush *et al.*, *Adv. Mater.* **28**, 3937–3943 (2016).
30. J. Werner *et al.*, *J. Phys. Chem. Lett.* **7**, 161–166 (2016).
31. S. Albrecht *et al.*, *Energy Environ. Sci.* **9**, 81–88 (2015).
32. A. Hadipour *et al.*, *Adv. Funct. Mater.* **16**, 1897–1903 (2006).



## ACKNOWLEDGMENTS

We thank M. T. Hörantner for performing the Shockley-Queisser calculation. The research leading to these results has received funding from the Graphene Flagship (Horizon 2020 grant no. 696656 - GrapheneCore1), the Leverhulme Trust (grant RL-2012-001), the UK Engineering and Physical Sciences Research Council (grant EP/J009857/1 and EP/M020517/1), and the European Union Seventh Framework Programme (FP7/2007-2013) under grant agreement nos. 239578 (ALIGN) and 604032 (MESO). T.L. is funded by a Marie Sklodowska Curie International Fellowship under grant agreement H2O2IF-GA-2015-659225. A.B. is financed by IMEC (Leuven) in the framework of a joint Ph.D. program with Hasselt University. B.C. is a postdoctoral research fellow of the Research Fund Flanders (FWO). We also acknowledge the U.S. Office of Naval Research for support. We acknowledge the use of the University of Oxford Advanced Research Computing (ARC) facility (http://dx.doi.org/10.5281/zenodo.22558) and the ARCHER UK National Super-computing Service under the "AMSEC" Leadership project. We thank the Global Climate and Energy Project (GCEP) at Stanford University. All data pertaining to the conclusions of this work can be found in the main paper and the supplementary materials.


## SUPPLEMENTARY MATERIALS

www.sciencemag.org/content/354/6314/861/suppl/DC1
Materials and Methods
Supplementary Text
Figs. S1 to S21
Tables S1 and S2
References (*33*–*43*)


27 April 2016; resubmitted 15 August 2016
Accepted 4 October 2016
Published online 20 October 2016
10.1126/science.aaf9717


ORGANIC CHEMISTRY

# Asymmetric synthesis of batrachotoxin: Enantiomeric toxins show functional divergence against $Na_V$


**Matthew M. Logan,* Tatsuya Toma,† Rhiannon Thomas-Tran,‡ J. Du Bois§**



**The steroidal neurotoxin (−)-batrachotoxin functions as a potent agonist of voltage-gated sodium ion channels ($Na_V$s). Here we report concise asymmetric syntheses of the natural (−) and non-natural (+) antipodes of batrachotoxin, as well both enantiomers of a C-20 benzoate–modified derivative. Electrophysiological characterization of these molecules against $Na_V$ subtypes establishes the non-natural toxin enantiomer as a reversible antagonist of channel function, markedly different in activity from (−)-batrachotoxin. Protein mutagenesis experiments implicate a shared binding side for the enantiomers in the inner pore cavity of $Na_V$. These findings motivate and enable subsequent studies aimed at revealing how small molecules that target the channel inner pore modulate $Na_V$ dynamics.**


The phenotypic effects of acute poisons found among the rich pharmacopeia of terrestrial and marine life have been documented from antiquity. Isolation and characterization of toxic compounds have made available important chemical reagents for studying complex biochemical circuits (*1*). Studies of this type have revealed a large number of peptide and small-molecule agents that target voltage-gated sodium ion channels ($Na_V$s), an obligatory class of membrane proteins for bioelectrical signaling (*1*–*4*). Among the collection of known $Na_V$ modulators are three structurally related agents, (−)-batrachotoxin [(−)-BTX], veratridine, and aconitine (Fig. 1A)—sterically large, lipophilic amine derivatives believed to share a common binding locus in the inner pore region of $Na_V$ (*3*) (site 2, Fig. 1B). The influence of these toxins on ion gating, however, differs distinctly. On one extreme, (−)-BTX, the primary toxic constituent of Colombian poison dart frogs (genus *Phyllobates*), is a full $Na_V$ agonist, causing the channel to open more readily at hyperpolarized membrane potentials and blocking fast inactivation (among other characteristic effects) (*3*–*5*). Conversely, the activities of veratridine and aconitine are best described as partial agonism and inhibition of channel function, respectively (*5*). Despite recent insights from structural biology into the three-dimensional architecture of prokaryotic $Na_V$s (*6*–*9*), a molecular understanding of the influence of the site 2 toxins on ion conduction and ion gating kinetics is lacking. Toxin structure-activity studies, in combination with protein mutagenesis experiments, can address questions related to the dynamical nature of channel function and may guide the rational design of small-molecule modulators of $Na_V$ activity (*1*). The potency of (−)-BTX (*10*), its storied history as the archetypal small-molecule site 2 probe (*4*), and its unparalleled effects on channel gating render it an optimal "lead" compound for such investigations.

(−)-BTX binding to $Na_V$s alters every aspect of channel function, resulting in a hyperpolarized shift in the voltage dependence of activation, inhibition of both fast and slow inactivation, a decrease in single-channel conductance, and reduction of ion selectivity (*3*, *4*). The utility of this natural product as a $Na_V$ activator has led to a substantial depletion in the world supply, which once exceeded 1 g but was less than 170 mg as of 2009 (*11*, *12*). Since the toxin was first isolated in 1963 by Märki and Witkop from poisonous frogs collected in the northern rain forest of Colombia (*13*), *Phyllobates* has been placed on the endangered species list, and thus collection of natural (−)-BTX from this source is restricted. (−)-BTX has also been identified in select species of birds (genus *Pitohui* and *Ifrita*) (*14*) and beetles (genus *Choresine*) (*15*), but only in small quantities (e.g., ~1.8 μg of (−)-BTX per beetle). Although semi- (*16*) and racemic syntheses (*17*) of BTX-A (Fig. 1C), a compound lacking the C-20 pyrrole ester, have been disclosed, the length of each of these works (>45 linear steps) precludes the facile production of (−)-BTX or select analogs. Accordingly, our desire to use BTX and modified forms thereof for examining channel dynamics and ion gating mechanisms has motivated our efforts to obtain the natural product through de novo synthesis.

Retrosynthetic analysis of (−)-BTX led us to outline a plan that would enable late-stage assembly of the homomorpholine E ring and elaboration of the C-20 allylic ester (Fig. 1C), thereby facilitating access to modified forms of the toxin. Previous structure-activity relationship studies using a small number of semisynthetic BTX derivatives (*10*, *18*) and C/D/E-ring BTX analogs (*19*) revealed the importance of the C-20 ester, tertiary amine, and tetracyclic skeleton for $Na_V$


Department of Chemistry, Stanford University, Stanford, CA 94305-5080, USA.
*Present address: Gilead Sciences, Foster City, CA 94404, USA.
†Present address: Graduate School of Pharmaceutical Sciences, Nagoya University, Furo-cho, Chikusa-ku, Nagoya 464-8601, Japan.
‡Present address: Arcus Biosciences, Hayward, CA 94545, USA.
**§Corresponding author. Email: jdubois@stanford.edu**


Downloaded from http://science.sciencemag.org/ on November 22, 2016

agonist activity. Unraveling BTX-A exposes a steroid-like frame **1**, the assembly of which is confounded by two angular groups at C/D-ring junction, the C-11 *exo*-methylene and the C-8/C-9 alkene. To maximize convergence in our synthetic plan, we conceived a disconnection strategy for **1** across the C ring. This idea would reduce the problem of constructing **1** into two fragments, one expressing the A/B-ring system (*3*, *20*) and a second comprising the D-ring cyclopentane (*4*, *21*). The successful execution of this scheme could produce the desired toxin through a sequence of linear steps totaling no more than 20 to 25.

Our synthesis of (−)-BTX commenced with the coupling of methylenecyclopentanone **4** (*21*) (fig. S1A) and vinyl bromide **3**, accessed from (*S*)-(+)-Hajos-Parrish ketone through a modified sequence of steps originally outlined by Parsons and co-workers (*20*) (fig. S1B). Conjoining fragments **3** and **4** to generate the linked A/B/D-tricycle **5** presented the first in a series of process development challenges. An initial attempt to effect this transformation involved Li-Br exchange of **3** with *n*-BuLi (Bu, butyl) and sequential addition of enone **4**. Although **5** was delivered under these conditions, product yields never exceeded 30%. Deuterium quenching experiments with $D_2O$ validated our hypothesis that α-deprotonation of **4** was competitive with the desired ketone addition pathway. Transmetalation reactions of the vinyl-lithium species with $ZnCl_2$, $ZnBr_2$, $MgBr_2{\bullet}OEt_2$ (Et, ethyl), $CeCl_3$, $Yb(OTf)_3$ (Tf, trifluoromethansulfonate), $CeCl_3{\bullet}2LiCl$, and $LaCl_3{\bullet}2LiCl$ were examined, but none of these measures proved effective (*22*, *23*). The addition of one equivalent of anhydrous LiBr to the reaction media of **3** improved the coupling efficiency by >20% (*24*). Following this lead, an optimized protocol using 2.1 equivalents of *t*-BuLi, which presumably generates one equivalent of LiBr in situ, reproducibly afforded **5** as a single diastereomer in 65% yield on a multigram scale. The ease of synthesis of this material and its desilylated form **6** enabled subsequent efforts to identify conditions for tandem annulation of the C ring and installation of the quaternary C-13 center.

An evaluation of available methods for ring closure of 1,6-enynes led us to consider radical-initiated processes (*25*). Under such conditions, an incipient C-13 3° radical could be intercepted to forge the angular aminomethylene unit (or a suitable surrogate). Efforts to first examine C-ring formation on **6**, however, revealed the potential fallacy of this plan. Using *n*-$Bu_3SnH$ and triethylborane ($Et_3B$) to promote the cyclization event resulted in the generation of two isomers, **7** and **8**, in a 1:5 ratio favoring the undesired product (Fig. 2A). Studies by Stork and Beckwith and co-workers have demonstrated that substrate concentration and reaction temperature can influence the mode of cyclization (i.e., 5-*exo*-trig versus 6-*endo*-trig) in radical-mediated enyne reactions (*26*, *27*). At elevated temperature (130°C) and with fivefold dilution of **6**, a reversal in selectivity was observed, affording a slight excess of the desired tetracycle (1.3:1 ratio of **7** to **8**; Fig. 2A). The combined product yield of this transformation exceeded 90%, thus encouraging further exploration of this chemistry, despite the modest selectivity results.

Repeated attempts to capture the intermediate C-13 radical with oxime and hydrazone derivatives generated from formaldehyde failed to deliver the expected aminomethylation product (*28*). Forced to consider alternative solutions, we recognized that a modified silyl ether group appended from the neighboring C-14 alcohol would be aptly positioned to intercept the 3° radical (*29*). Based on available precedent, an alkynylsilyl chloride, $Me_3SiC{\equiv}CSiEt_2Cl$ (Me, methyl), was selected for modification of the C-14 alcohol in **6** (*30*, Fig. 2A). Treatment of the resulting silylether (**9**) with *n*-$Bu_3SnH$ and $Et_3B$ at 150°C resulted in a cyclization cascade to give pentacycle **10** as the exclusive product (*31*). Within the limits of proton nuclear magnetic resonance ($^1H$ NMR) detection, none of the corresponding five-membered C-ring isomer was generated in this process. Our preliminary efforts to understand the role of C-14 substituent groups on reaction selectivity suggest that silyl protection of the alcohol (along with the elevated reaction temperatures) favors 6-*endo*-trig ring closure. Although additional studies are warranted to appreciate these structure-selectivity data, our enyne cyclization cascade offers a convergent approach for synthesizing substituted steroid scaffolds and should facilitate access to a wide range of such compounds.

Close inspection of the radical cyclization products derived from either **6** or **9** revealed an unexpected outcome pertaining to the structure of the resulting organostannane moiety (Fig. 2, A and B). Carbostannylation of the alkyne group should afford a vinyl-tin product, as noted in the reaction of **6**. Unexpectedly, when **9** was subjected to the reaction conditions, allylstannane **10** was the sole product, a result confirmed by both NMR and x-ray crystallography. Formation of allylstannane **10** can be rationalized through a mechanism involving 1,4-H-atom transfer of an intermediate vinyl radical (*32*) (Fig. 2B), a proposal supported by a deuterium labeling experiment (fig. S5). Although this result was unplanned, the efficiency and selectivity of the cyclization reaction compelled our decision to advance this material. Looking forward, the versatility of the allylstannane group should serve future efforts to prepare C ring–modified BTXs.

The availability of **10** in nine steps from the Hajos-Parrish ketone enabled the production of

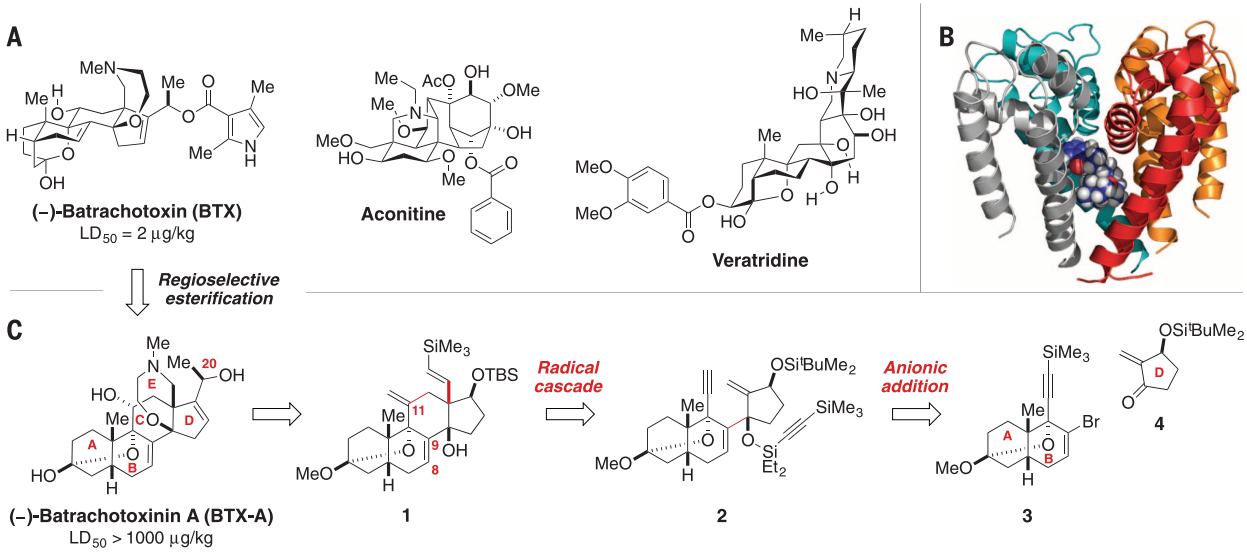


**Fig. 1. Background and synthetic plan.** (**A**) The structures of lipophilic site 2 toxins (−)-batrachotoxin (BTX), aconitine, and veratridine. (**B**) A pore model of $Na_V$ with (−)-BTX (depicted as spheres) docked at site 2. The structure is based on *Magnetococcus marinus* $Na_V$ crystallographic data (Protein Data Bank accession code 4F4L) (*9*, *19*). Domain I, orange; domain II, red; domain III, gray; domain IV, teal. (**C**) Retrosynthetic analysis of BTX and BTX C-20 ester analogs. $LD_{50}$, half-maximal lethal dose; Me, methyl; $^t$Bu, *tert*-butyl; Et, ethyl; TBS, *tert*-butyldimethylsilyl.

Downloaded from http://science.sciencemag.org/ on November 22, 2016

substantial quantities of material to complete the target synthesis. Excision of the bridging silyl ether in **10** was accomplished with excess *n*-$Bu_4NF$, revealing a diol intermediate that was subsequently advanced to **11** through 2-iodoxybenzoic acid–mediated alcohol oxidation and chemoselective vinylsilane cleavage (57%; Fig. 2B). Conversion of aldehyde **11** to chloroacetamide **12** was performed by following a three-step, single-flask sequence (*16*, *33*). From **12,** efficient closure of the homomorpholinamide ring with NaOEt (92%) (*17*) provided a versatile intermediate for modification of both the C- and D-ring units. The latter could be achieved through the D-ring enol triflate, prepared using $KN(SiMe_3)_2$ and $PhNTf_2$.

Introduction of the C-11α alcohol from the C-ring allylstannane **13** presented one of the more difficult challenges in our approach to BTX (Fig. 2B). Although protodestannylation of **13** to generate the corresponding C-11 *exo*-methylenecyclohexane had limited success (*34*), all subsequent attempts to oxidize this compound to ketone **15** (i.e., $O_3$, $OsO_4$, and $RuO_4$) failed to give product. Inspired by a report from Kim and Fuchs, we attempted to convert **13** to the corresponding allyl chloride by using $CuCl_2$ (*35*). Fortuitously, conducting this reaction in dioxane under aerobic conditions delivered enal **14** in 85% yield with only a minor amount of the chlorinated product (~10%). Although the mechanistic details of this transformation remain unclear, we are aware of only one other documented example of such an oxidation reaction, which uses a vanadium catalyst and $O_2$ (*36*). Enal **14** is suitably disposed for conversion to C-11 ketone **15** by following a series of functional group interconversion steps highlighted by a Curtius rearrangement (*37*). The absence of a viable chromophore on batrachotoxinin A (BTX-A) makes purification of this material difficult; accordingly, in the sequence leading to **15**, the C-3 methoxy acetal was exchanged with *p*-methoxyphenethyl alcohol.

Completion of the carbon skeleton of (–)-BTX was accomplished through a palladium-catalyzed cross-coupling of tributyl(1-ethoxyvinyl)tin to vinyl triflate **15** (Fig. 3A) (*38*). In situ hydrolysis of the incipient enol ether with 1 M oxalic acid supplied enone **16** (77%). Following an extensive screen of reducing agents, successful stereoselective global reduction of enone **16** was accomplished in 33% yield by treatment with freshly prepared $AlH_3$ (*39*). We hypothesize that the Lewis-basic lactam (or a reduced form) acts as a pivotal stereocontrolling element, as treatment of enone **15** with alternative hydride reducing agents [e.g., $AlH_3$•$NMe_2Et$, $NaBH_4$, $NH_3$•$BH_3$, (*S*)-Me-CBS-oxazaborolidine/$BH_3$, or L-selectride] delivered the undesired C-11β alcohol exclusively. The use of $AlH_3$ also favored generation of the correct C-20 allylic alcohol epimer, a sterochemical outcome that can be rationalized through a model invoking chelation control (*38*). Deprotection of the product from $AlH_3$ reduction under acidic conditions afforded (–)-BTX-A in 83% yield (*17*). Finally, by employing a modification of Tokuyama, Daly, and Witkop's (–)-BTX-A acylation protocol with the mixed anhydride prepared from ethyl chloroformate and 2,4-dimethyl-pyrrole-3-carboxylic acid (*10*), the synthesis of 2 mg of (–)-BTX was completed [79%, 0.25% overall yield, 24 steps from (*S*)-(+)-Hajos-Parish ketone]. The product was identical in all respects [as assessed by high-resolution mass spectrometry, thin-layer chromatography, and high-performance liquid chromatography (HPLC) coinjection] with a sample of the natural material and with previously recorded spectroscopic data (*40*, *41*). Our synthetic plan also enabled milligram-scale preparation of the unnatural toxin antipode, (+)-BTX, the known benzoate ester of (–)-BTX-A (BTX-B; Fig. 3B) (*42*, *43*), and the enantiomer of this compound (*ent*-BTX-B).

Electrophysiological characterization of synthetic (–)-BTX and BTX-B against rat $Na_V1.4$ ($rNa_V1.4$) confirmed that the latter also functions as an agonist and is similar in potency to the natural product (fig. S6 and table S12). Previous reports and our own studies indicate that the ester group of BTX-B

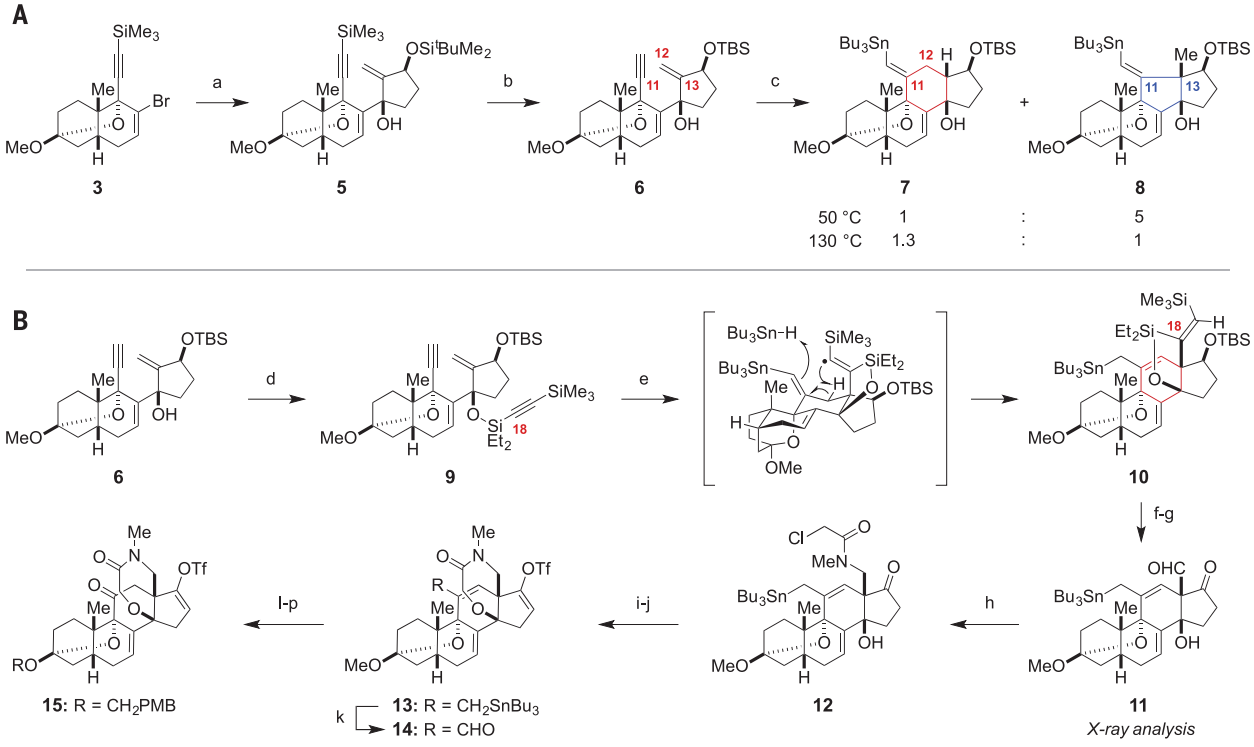


**Fig. 2. Enyne radical cyclization to furnish the steroidal core of BTX.** Reagents, conditions, and product yields for steps a to p are as follows: (**A**) a, *t*-BuLi, THF, –90°C, then **4** (see Fig. 1) (65%); b, $K_2CO_3$, MeOH (94%); c, $Et_3B$, air, *n*-$Bu_3SnH$. (**B**) d, $Me_3SiC{\equiv}CSiEt_2Cl$, imidazole, $CH_2Cl_2$ (93%); e, $O_2$, *n*-$Bu_3SnH$, $Et_3B$, $Ph_2O$, 150°C (75%); f, *n*-$Bu_4NF$, THF, 60°C (94%); g, 2-iodoxybenzoic acid, *t*-BuOH, 65°C, then $OsO_4$ [7 mol %], $NaIO_4$, pyridine, $H_2O$ (57%); h, $MeNH_2$, $CH_2Cl_2$; $NaB(O_2CCF_3)_3H$, $CH_2Cl_2$, –78°C, then $ClCH_2COCl$, 2,6-lutidine, –78 to 0°C (52%); i, NaOEt, EtOH, 1:1 THF/$C_6H_6$ (92%); j, $KN(SiMe_3)_2$, $PhNTf_2$, THF, –78 to 0°C (94%); k, $CuCl_2$, $O_2$, 1,4-dioxane, 73°C (85%); l, $NaClO_2$, $NaH_2PO_4$, dimethyl sulfoxide/$H_2O$; m, $SOCl_2$, pyridine, $CH_2Cl_2$; n, $NaN_3$, acetone/$H_2O$; o, aqueous AcOH, 1,4-dioxane, 90°C (57% over four steps); p, *p*-TsOH, 4-Å molecular sieves, *p*-methoxyphenethyl alcohol ($PMBCH_2OH$), $C_6H_6$ (89%). THF, tetrahydrofuran; Ph, phenyl; Tf, trifluoromethansulfonate; Ts, *p*-toluenesulfonate; Ac, acetate.

Downloaded from http://science.sciencemag.org/ on November 22, 2016

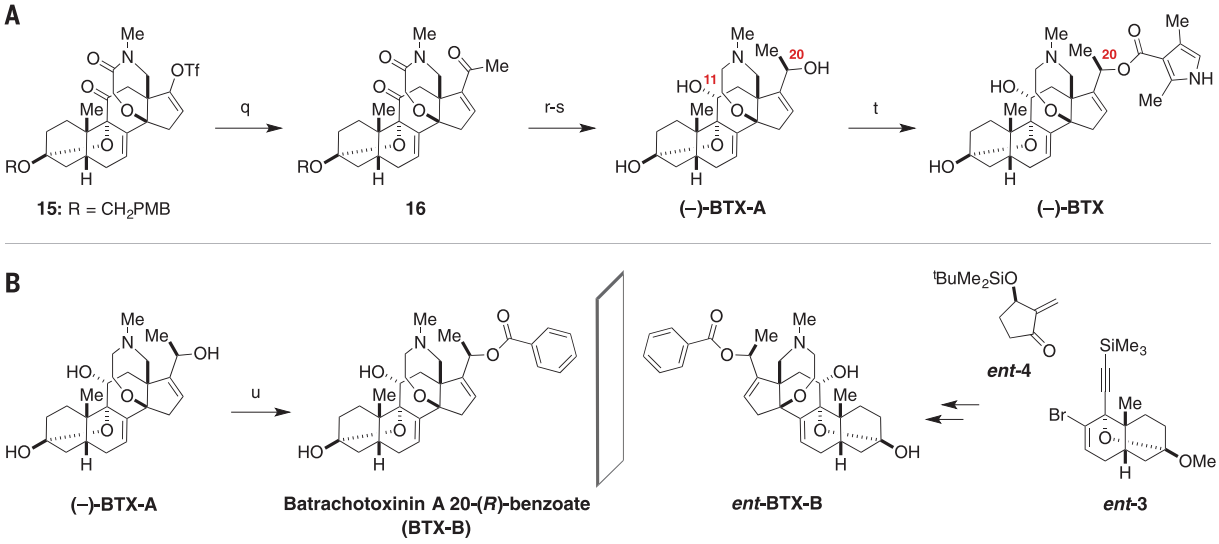


**Fig. 3. Completion of the synthesis.** Reagents, conditions, and product yields for the preparation of (**A**) (–)-BTX (steps q to t) and (**B**) BTX-B and its enantiomer (steps q to s, then u) are as follows: q, LiCl, CuCl, $Pd(PPh_3)_4$, tributyl(1-ethoxyvinyl)tin, THF, 60°C, then 1 M oxalic acid, 0°C (77%); r, $AlH_3$, THF, –78 to 0°C (33%); s, *p*-TsOH, 3:2 acetone/$H_2O$ (83%); t, (ethyl carbonic)-2,4-dimethyl-1*H*-pyrrole-3-carboxylic anhydride, $Et_3N$, $C_6H_6$, 45°C (79%); u, benzoic (ethyl carbonic) anhydride, $Et_3N$, $C_6H_6$, 45°C (70%).

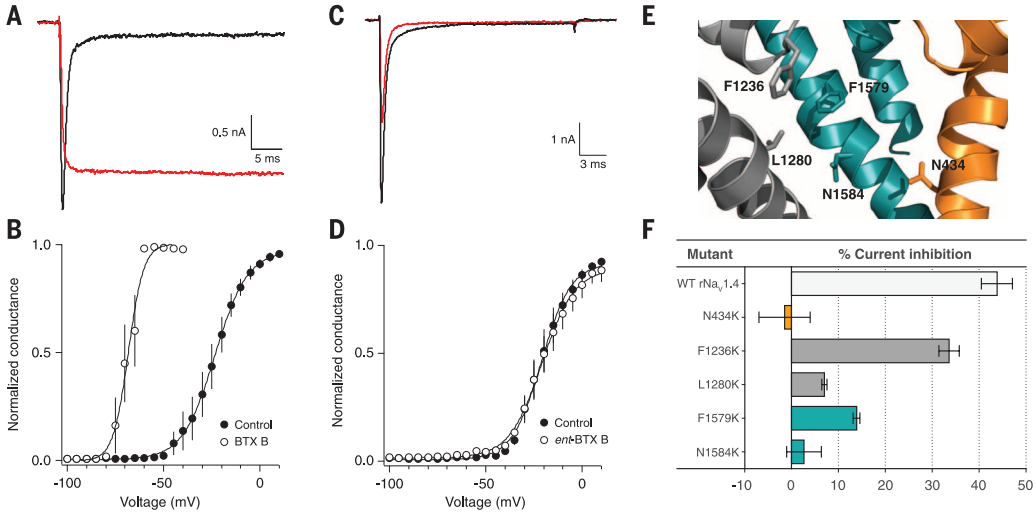


**Fig. 4. Effects of synthetic BTX-B and *ent*-BTX-B on wild-type rat $Na_V1.4$ function.** (**A**) Representative trace for rat $Na_V1.4$ ($rNa_V1.4$) current before (black) and after (red) steady-state binding of 10 μM BTX-B. Current was evoked by a 150-ms test pulse from –120 to 0 mV after establishment of steady-state inhibition by repetitive depolarizing pulses to 0 mV. (**B**) Voltage dependence of activation for $rNa_V1.4$ in the presence of 10 μM BTX-B (open circles) compared with control conditions (filled circles) for $n \geq 3$ cells (mean ± SD). (**C**) Representative trace for $rNa_V1.4$ current before (black) and after (red) steady-state binding of 5 μM *ent*-BTX-B. Current was evoked by a 24-ms test pulse from –120 to 0 mV after establishment of steady-state inhibition by repetitive depolarizing pulses to 0 mV. (**D**) Voltage dependence of activation for $rNa_V1.4$ in the presence of 10 μM *ent*-BTX-B (open circles) compared with control conditions (filled circles) for $n \geq 3$ cells (mean ± SD). (**E**) $rNa_V1.4$ homology model highlighting residues that have previously been shown to abolish (–)-BTX activity. (**F**) Percent current inhibition of $rNa_V1.4$ mutants by 5 μM *ent*-BTX-B (mean ± SD). WT, wild type; F, phenylalanine; K, lysine; L, leucine; N, asparagine.

is more stable than the oxidatively sensitive acylpyrrole of BTX; thus, additional experiments were performed with the former compound (*42*, *43*). Synthetic BTX-B was tested against a subset of representative $Na_V$ isoforms including $rNa_V1.4$, human $Na_V1.5$, and human $Na_V1.7$. Application of 10 μM BTX-B to Chinese hamster ovary cells expressing a single $Na_V$ subtype resulted in sustained sodium current in all cases (Fig. 4A and figs. S7 and S8). Use-dependent agonism of $Na_V$ isoforms by BTX-B prevented steady-state inactivation of >80% of the sodium channel population (Fig. 4A and fig. S8). BTX-B also induced a characteristic hyperpolarizing shift (–44.9 to –51.5 mV) in the half-maximal voltage ($V_{0.5}$) of activation of wild-type $Na_V$ isoforms (Fig. 4B and table S13). The similarity of these data is consistent with the high protein sequence conservation between $Na_V$ subtypes in the inner pore–lining S6 helices that form the putative toxin binding site (fig. S9).

Following earlier work from our laboratory (*19*) and others (*44*, *45*), we questioned whether the enantiomer form of BTX would bind with high affinity to $Na_V$ with analogous functional effects. Such a question can only be answered with the availability of a de novo synthesis of the toxin. Accordingly, electrophysiological recordings with *ent*-BTX-B were performed against $rNa_V1.4$. These data revealed *ent*-BTX-B to be a use- and state-dependent channel antagonist, with a measured half-maximal inhibitory concentration of 5.3 ± 0.6 μM [Fig. 4C and fig. S10; (+)-BTX also displays antagonistic activity (fig. S11)]. The concentration for half-maximal inhibition of $Na_V$ by *ent*-BTX-B is similar in magnitude to the half-maximal effective concentration for BTX-B agonism (1.0 ± 0.1 μM; fig. S10) measured under identical conditions. Notably, unlike the natural antipode, *ent*-BTX-B binding caused only a minimal shift in the $V_{0.5}$ of activation and the $V_{0.5}$ of steady-state inactivation (table S14). In

Downloaded from http://science.sciencemag.org/ on November 22, 2016

addition, channel block was fully reversible by this inhibitor.

To determine whether BTX-B and *ent*-BTX-B share an overlapping binding site within the inner pore region of $Na_V$, *ent*-BTX-B was tested against five $rNa_V1.4$ single-point mutants that have been shown previously to destabilize BTX binding (Fig. 4, E and F, and fig. S12) (*19*). Mutation of N434 (*46*), L1280 (*47*), F1579 (*48*), and N1584 (*48*) to lysine resulted in a ~3- to 30-fold decrease in current block by 5 μM *ent*-BTX-B. Against F1236K (*49*), however, *ent*-BTX-B retained significant activity (33.6 ± 2.1% current inhibition). The evident difference between *ent*-BTX-B and BTX-B indicates an overlapping, but nonidentical, binding region within the inner pore cavity. It would seem that the open channel is sufficiently large to accommodate lipophilic tertiary amine ligands (*19*, *45*, *50*). Subtle alterations in the binding pose of these ligands appear to dramatically alter the functional response of the protein. Future investigations will be directed at delineating the precise channel-toxin interactions that distinguish activation from inhibition by BTX derivatives and related lipophilic toxins.

## REFERENCES AND NOTES


1. M. de Lera Ruiz, R. L. Kraus, *J. Med. Chem.* **58**, 7093–7118 (2015).
2. A. P. Thottumkara, W. H. Parsons, J. Du Bois, *Angew. Chem. Int. Ed. Engl.* **53**, 5760–5784 (2014).
3. S. Y. Wang, G. K. Wang, *Cell. Signal.* **15**, 151–159 (2003).
4. B. I. Khodorov, *Prog. Biophys. Mol. Biol.* **45**, 57–148 (1985).
5. W. A. Catterall, *J. Biol. Chem.* **252**, 8669–8676 (1977).
6. J. Payandeh, T. Scheuer, N. Zheng, W. A. Catterall, *Nature* **475**, 353–358 (2011).
7. J. Payandeh, T. M. Gamal El-Din, T. Scheuer, N. Zheng, W. A. Catterall, *Nature* **486**, 135–139 (2012).
8. X. Zhang *et al.*, *Nature* **486**, 130–134 (2012).
9. E. C. McCusker *et al.*, *Nat. Commun.* **3**, 1102–1110 (2012).
10. T. Tokuyama, J. Daly, B. Witkop, *J. Am. Chem. Soc.* **91**, 3931–3938 (1969).
11. T. Tokuyama, *Heterocycles* **79**, 3–8 (2009).
12. H. M. Garraffo, T. F. Spande, *Heterocycles* **79**, 195–205 (2009).
13. F. Märki, B. Witkop, *Experientia* **19**, 329–338 (1963).
14. J. P. Dumbacher, B. M. Beehler, T. F. Spande, H. M. Garraffo, J. W. Daly, *Science* **258**, 799–801 (1992).
15. J. P. Dumbacher *et al.*, *Proc. Natl. Acad. Sci. U.S.A.* **101**, 15857–15860 (2004).
16. R. Imhof *et al.*, *Helv. Chim. Acta* **55**, 1151–1153 (1972).
17. M. Kurosu, L. R. Marcin, T. J. Grinsteiner, Y. Kishi, *J. Am. Chem. Soc.* **120**, 6627–6628 (1998).
18. B. I. Khodorov *et al.*, *Cell. Mol. Neurobiol.* **12**, 59–81 (1992).
19. T. Toma, M. M. Logan, F. Menard, A. S. Devlin, J. Du Bois, *ACS Chem. Neurosci.* **7**, 1463–1468 (2016).
20. P. Lacrouts, P. J. Parsons, C. S. Penkett, A. R. Raza, *Synlett* **18**, 2767–2768 (2005).
21. S. Takano, T. Yamane, M. Takahashi, K. Ogasawara, *Synlett* **1992**, 410–412 (1992).
22. G. A. Molander, *Chem. Rev.* **92**, 29–68 (1992).
23. A. Krasovskiy, F. Kopp, P. Knochel, *Angew. Chem. Int. Ed. Engl.* **45**, 497–500 (2006).
24. P. E. Van Rijn, S. Mommers, R. G. Visser, H. D. Verkruijsse, L. Brandsma, *Synthesis* **1981**, 459–460 (1981).
25. G. Stork, R. Mook Jr., *J. Am. Chem. Soc.* **109**, 2829–2831 (1987).
26. G. Stork, R. Mook Jr., *Tetrahedron Lett.* **27**, 4529–4532 (1986).
27. A. L. J. Beckwith, D. M. O'Shea, *Tetrahedron Lett.* **27**, 4525–4528 (1986).
28. D. J. Hart, F. L. Seely, *J. Am. Chem. Soc.* **110**, 1631–1633 (1988).
29. G. Stork, H. Suh, G. Kim, *J. Am. Chem. Soc.* **113**, 7054–7056 (1991).
30. R. Bürli, A. Vasella, *Helv. Chim. Acta* **79**, 1159–1168 (1996).
31. K. Nozaki, K. Oshima, K. Utimoto, *J. Am. Chem. Soc.* **109**, 2547–2549 (1987).
32. M. Gulea, J. M. Lopez-Romero, L. Fensterbank, M. Malacria, *Org. Lett.* **2**, 2591–2594 (2000).
33. G. W. Gribble, *Chem. Soc. Rev.* **27**, 395–404 (1998).
34. M. Andrianome, B. Delmond, *J. Chem. Soc. Chem. Commun.* **1985**, 1203–1204 (1985).
35. S. Kim, P. L. Fuchs, *J. Am. Chem. Soc.* **115**, 5934–5940 (1993).
36. T. Hirao, C. Morimoto, T. Takada, H. Sakurai, *Tetrahedron Lett.* **42**, 1961–1963 (2001).
37. R. L. Snowden, S. M. Linder, M. Wüst, *Helv. Chim. Acta* **72**, 892–905 (1989).
38. A. Sloan Devlin, J. Du Bois, *Chem. Sci.* **4**, 1059–1063 (2013).
39. A. I. Meyers, L. E. Burgess, *J. Org. Chem.* **56**, 2294–2296 (1991).
40. A 10-μg sample of authentic (−)-BTX was purchased from Santa Cruz Biotech.
41. T. Tokuyama, J. W. Daly, *Tetrahedron* **39**, 41–47 (1983).
42. G. B. Brown, S. C. Tieszen, J. W. Daly, J. E. Warnick, E. X. Albuquerque, *Cell. Mol. Neurobiol.* **1**, 19–40 (1981).
43. W. A. Catterall, C. S. Morrow, J. W. Daly, G. B. Brown, *J. Biol. Chem.* **256**, 8922–8927 (1981).
44. S. Mehrotra *et al.*, *J. Nat. Prod.* **77**, 2553–2560 (2014).
45. C. Nau, S. Y. Wang, G. R. Strichartz, G. K. Wang, *Mol. Pharmacol.* **56**, 404–413 (1999).
46. S. Y. Wang, G. K. Wang, *Proc. Natl. Acad. Sci. U.S.A.* **95**, 2653–2658 (1998).
47. S. Y. Wang, C. Nau, G. K. Wang, *Biophys. J.* **79**, 1379–1387 (2000).
48. S. Y. Wang, G. K. Wang, *Biophys. J.* **76**, 3141–3149 (1999).
49. S. Y. Wang, J. Mitchell, D. B. Tikhonov, B. S. Zhorov, G. K. Wang, *Mol. Pharmacol.* **69**, 788–795 (2006).
50. B. S. Zhorov, D. B. Tikhonov, *Trends Pharmacol. Sci.* **34**, 154–161 (2013).



## ACKNOWLEDGMENTS

We are grateful to M. Maduke (Stanford University) for generous use of her laboratory space and equipment. We thank S. Lynch (Stanford University) for assistance with NMR experiments and analysis, Y. Kishi (Harvard University) for graciously providing NMR spectra of synthetic BTX-A, J. K. Maclaren (Stanford Nano Shared Facilities) for solving the crystal structure of **11** (supported by the NSF under award ECCS-1542152), G. Dick (Stanford University) for assistance with HPLC coinjection of natural and synthetic BTX, and the Vincent Coates Foundation Mass Spectrometry Laboratory, Stanford University Mass Spectrometry (https://mass-spec.stanford.edu). Metrical parameters for the structure of compound **11** are available free of charge from the Cambridge Crystallographic Data Centre under reference number CCDC-1509206. This work was supported in part by the NIH (R01NS045684) and by gifts from Pfizer and Amgen. T.T. was sponsored as a Japan Society for the Promotion of Science Fellow for research abroad. R.T.-T. is a NSF predoctoral fellow. M.M.L. and T.T. contributed to the synthesis of BTX, and R.T.-T. was responsible for electrophysiology experiments. The manuscript was prepared by M.M.L., R.T.-T., and J.D.B. J.D.B. is a cofounder of and owns equity shares in SiteOne Therapeutics, a pharmaceutical startup company aimed at developing sodium channel subtype–selective inhibitors as antinociceptive agents.


## SUPPLEMENTARY MATERIALS

www.sciencemag.org/content/354/6314/865/suppl/DC1
Materials and Methods
Figs. S1 to S12
Tables S1 to S14
References (*51*–*58*)

13 June 2016; accepted 14 October 2016
10.1126/science.aag2981

GEOPHYSICS

# Coseismic rupturing stopped by Aso volcano during the 2016 $M_w$ 7.1 Kumamoto earthquake, Japan

**A. Lin,[1]* T. Satsukawa,[1] M. Wang,[1] Z. Mohammadi Asl,[1] R. Fueta,[1] F. Nakajima[2]**

**Field investigations and seismic data show that the 16 April 2016 moment magnitude ($M_w$) 7.1 Kumamoto earthquake produced a ~40-kilometer-long surface rupture zone along the northeast-southwest–striking Hinagu-Futagawa strike-slip fault zone and newly identified faults on the western side of Aso caldera, Kyushu Island, Japan. The coseismic surface ruptures cut Aso caldera, including two volcanic cones inside it, but terminate therein. The data show that northeastward propagation of coseismic rupturing terminated in Aso caldera because of the presence of magma beneath the Aso volcanic cluster. The seismogenic faults of the 2016 Kumamoto earthquake may require reassessment of the volcanic hazard in the vicinity of Aso volcano.**

Large earthquakes and active volcanoes are closely related natural phenomena resulting from plate tectonic processes (*1*–*3*). Large earthquakes often accompany or precede volcanic eruptions (*4*, *5*). Seismic analyses and geological observations reveal that the distribution and segmentation of active faults are mainly controlled by the presence of magma bodies in volcanic regions (*6*) and that fault segment boundaries play important roles in a number of aspects of earthquake behavior, including rupture initiation and termination (*7*). Fault segment boundaries generally are associated with a buildup of heterogeneous fault stress (*8*) and large changes in earthquake-induced surface offset (*9*). In volcanic regions, a magma chamber may affect seismicity and the rupture process of an earthquake through the presence of a high-temperature area (*10*), a heterogeneous fault plane on a crater wall (*11*), and/or rectified diffusion (*12*). However, because of a lack of geological data, it is unknown whether a volcano can affect coseismic fault rupturing processes and mechanisms. The 16 April 2016 Kumamoto earthquake of moment magnitude

[1]Department of Geophysics, Graduate School of Science, Kyoto University, Kyoto 606-8502, Japan. [2]CTI Engineering International, Kotou-ku, Tokyo 136-0071, Japan.
*Corresponding author. Email: slin@kugi.kyoto-u.ac.jp

Downloaded from http://science.sciencemag.org/ on November 22, 2016

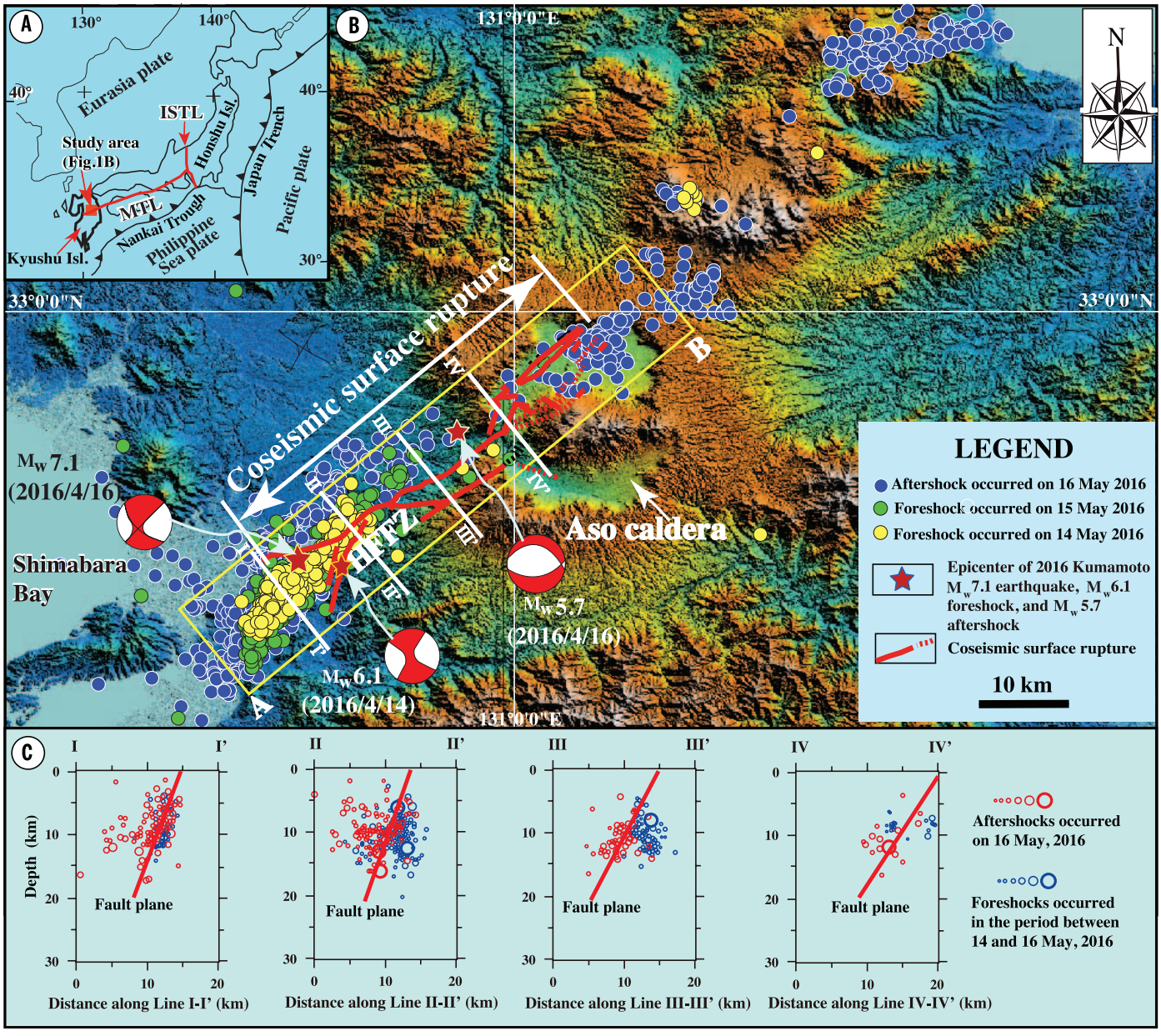


**Fig. 1. Map of the study area.** (**A**) Tectonic setting. (**B**) Color-shaded relief map. (**C**) Seismic profiles (I–I′ to IV–IV′) across the Hinagu–Futagawa fault zone (HFFZ). The distribution of coseismic surface ruptures, foreshocks, and aftershocks during the period of 14 to 16 May 2016 are shown. Active fault data are from the Research Group for Active Faults of Japan (1991) (*16*). Epicenter data and focal mechanisms are from the Disaster Information Laboratory, National Research Institute for Earth Science and Disaster Resilience (2016) (9). Dip angles of fault planes shown in profiles I–I′ to IV–IV′ are inferred from the seismic data. MTL, Median Tectonic Line; ISTL, Itoigawa–Shizuoka Tectonic Line; Isl., island. Profile A–B is shown in Fig. 2C.

($M_w$) 7.1 ($M_j$ 7.3 on the Japan Meteorological Agency intensity scale) provided an opportunity to study the relationship between seismogenic fault processes and crustal structures beneath the Aso volcano cluster, Kyushu Island, southwestern Japan.

Mount Aso, one of the largest active volcanoes in the world, contains a large caldera up to 380 $km^2$ in cross-sectional area. The $M_w$ 7.1 Kumamoto earthquake occurred ~30 km southwest of Aso caldera on 16 April 2016 (Fig. 1) (*13*). The main earthquake was preceded by four large foreshocks of $M \geq 5.5$, including a $M_w$ 6.2 shock that occurred one day before the main shock, and followed by four large aftershocks of $M \geq 5.0$ that occurred within 6 hours of the main shock (*13*, *14*). A maximum seismic intensity of 7 on the Japanese 7-point seismic intensity scale was observed at the epicenter of the $M_w$ 6.2 foreshock on 14 April and at the epicenter of the main earthquake. The earthquakes caused widespread damage throughout central Kyushu Island, including in the Aso caldera region.

Our survey group travelled to the area of the epicenter 1 day after the main event and conducted field investigations for 10 days to determine the sense of motion on the seismogenic fault, the extent of ground deformation features, and the relationship between coseismic rupturing processes and crustal structure at Aso caldera. We found a ~40-km-long coseismic surface rupture zone along the southwest segment of the preexisting Hinagu–Futagawa fault zone (HFFZ) and three newly identified faults in the northeast segment of the HFFZ, which cut the west-southwest side of Aso caldera and terminate at its opposite (northeast) edge (Figs. 1B and 2) (*15*, *16*). The HFFZ is composed of two main active faults, the Hinagu and Futagawa faults. The Hinagu fault strikes

Downloaded from http://science.sciencemag.org/ on November 22, 2016

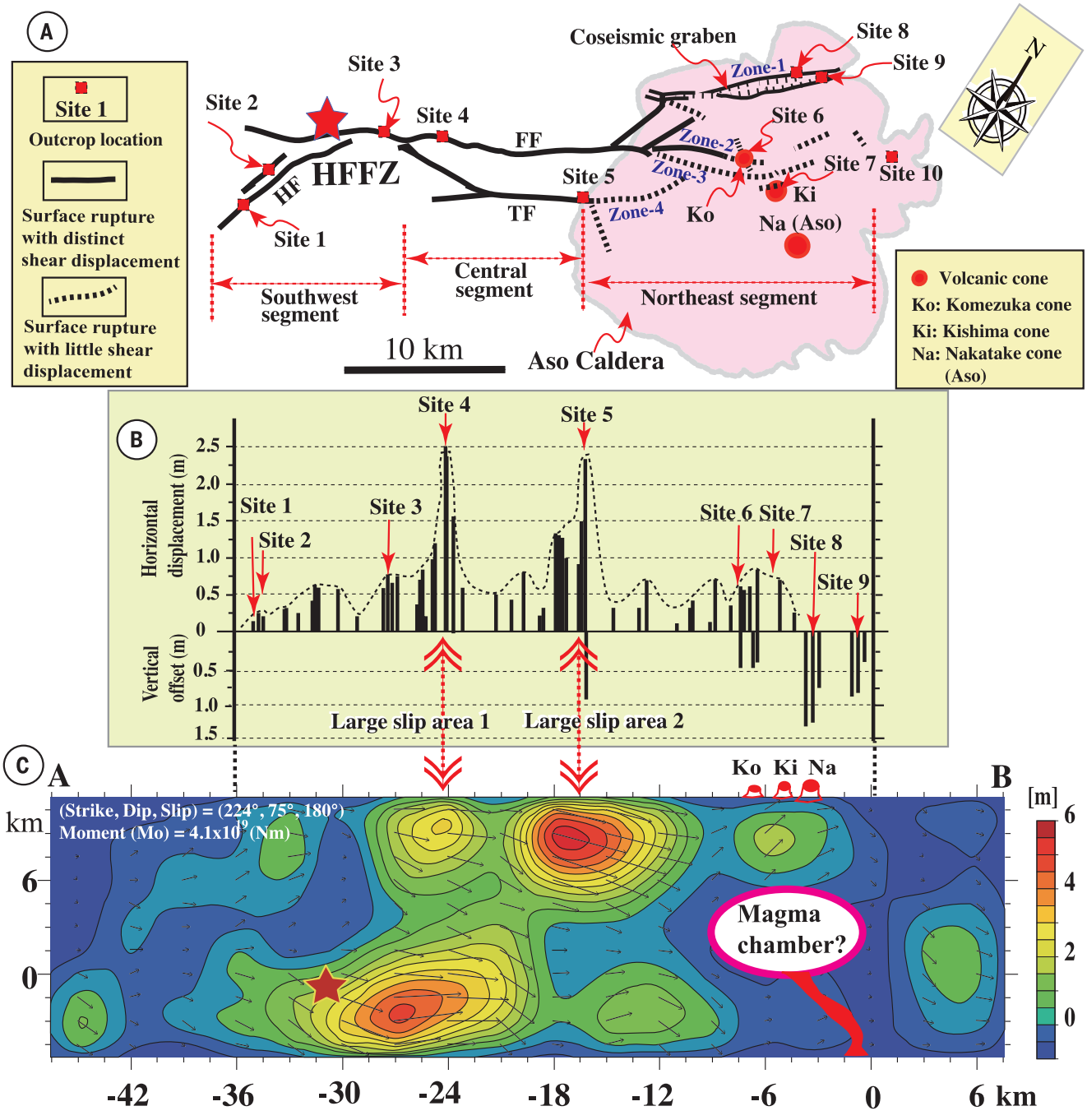


**Fig. 2. Distribution of rupture traces and rupture displacements in the coseismic surface rupture zone.** (**A**) Map of the coseismic surface rupture zone with locations of the main study sites (1 to 10). (**B**) Distribution of coseismic displacements. (**C**) Seismic inversion results for seismic slip (in meters) on the seismogenic fault plane [modified from Koketsu *et al*. (*15*); see Fig. 1B for the surface location of profile A–B]. The fault length (horizontal axis) and width (vertical axis) are 54 and 16.5 km, respectively. The location of the magma chamber is inferred from previous studies (*23*, *24*, *26*–*28*). The red star indicates the epicenter. Areas of large slip in the field measurements (B) are comparable to those obtained from seismic inversion (C).

northeast-southwest and extends for ~81 km, and the Futagawa Fault strikes north-northeast–south-southwest and extends for ~64 km. The Hinagu fault merges obliquely with the Futagawa fault in the northeast (Fig. 2A) (*14*). Both faults are dominantly right-lateral strike-slip faults with uplift to the southeast (*17*).

The coseismic surface ruptures were generally concentrated in a zone that can be divided into three segments (southwest, central, and northeast) on the basis of structural features and spatial distribution (Fig. 2A). The southwest segment parallels the main fault traces of the Hinagu and Futagawa faults. The central segment branches into two parallel surface rupture zones, one along the Futagawa fault and the other along a newly identified fault located ~2 to 3 km east of the Futagawa fault (Fig. 2A). The southwest and central segments consist mainly of distinct shear faults, left-stepping echelon cracks, and additional tracks constrained to a zone 3 to 50 m wide (average width, 5 to 10 m) (Fig. 3 and figs. S1 and S2). Distinct shear faults striking N30°E to N70°E and dipping 75° to 90° to the northwest occur parallel to the general trend of the rupture zone; the shear faults are dominated by right-lateral strike-slip displacement. Horizontal striations

Downloaded from http://science.sciencemag.org/ on November 22, 2016

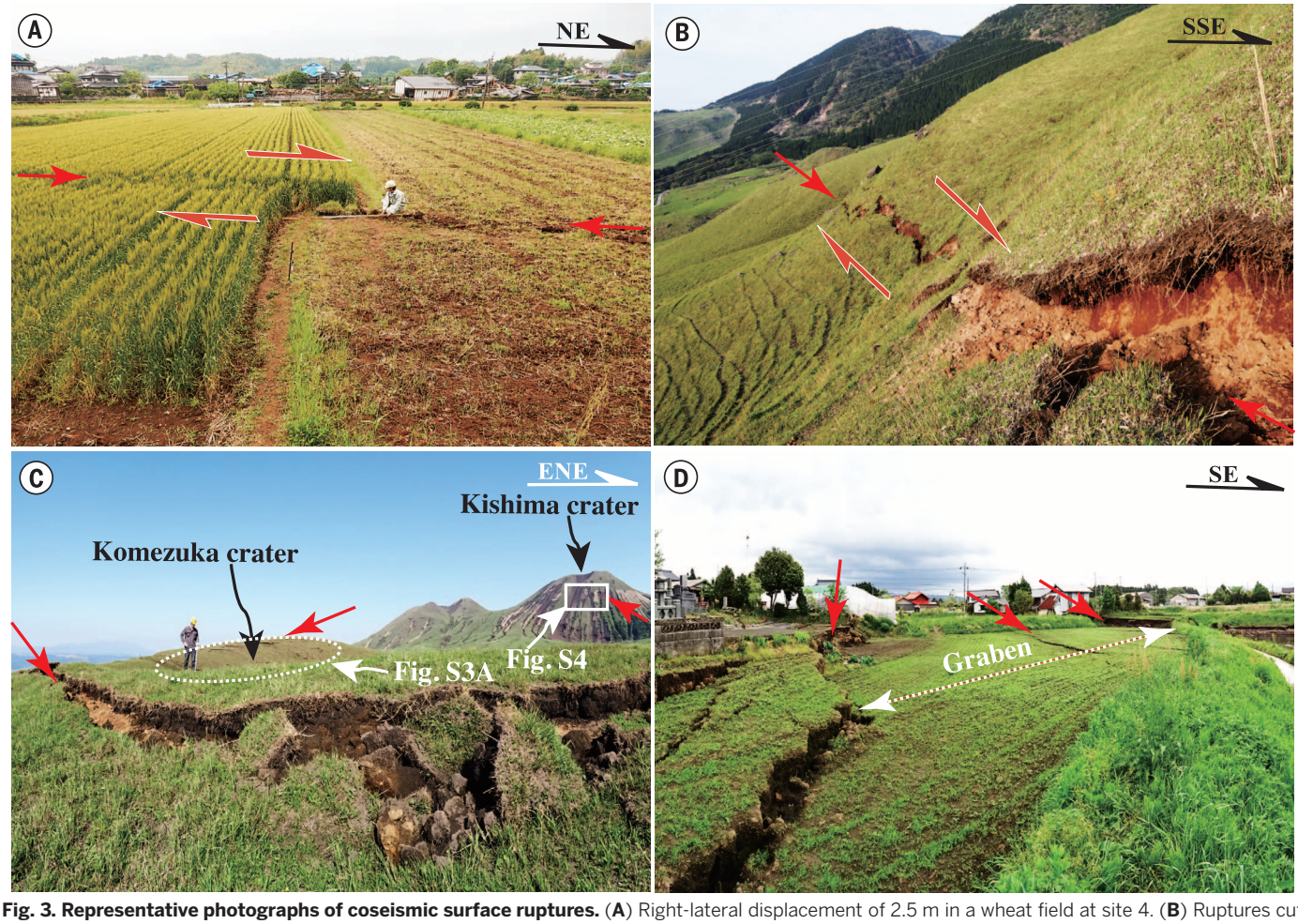


**Fig. 3. Representative photographs of coseismic surface ruptures.** (**A**) Right-lateral displacement of 2.5 m in a wheat field at site 4. (**B**) Ruptures cut the slope of the rim of Aso caldera at site 5. (**C**) Tensional cracks on Kometsuka crater at site 6. (**D**) Coseismic graben structure at site 8. Red arrows indicate the coseismic surface ruptures, with half arrows indicating the direction of fault motion.

on slickensides were observed on shear fault planes; the striations are marked by parallel lineations with some grooves and steps in unconsolidated clay (fig. S1C). Extensional cracks, which commonly show a left-stepping en echelon pattern indicating a right-lateral sense of shear, are widespread along the surface rupture zone (fig. S1B). The coseismic deformation of surface markers and slickensides on fault planes reveal a right-lateral strike-slip motion of the seismogenic fault at the surface along the central and southwest segments, as reported previously (*18*, *19*).

In contrast, the northeast segment of the rupture zone shows a more complex rupture distribution over a broad area. We found four subrupture zones (zones 1 to 4) that are parallel or subparallel to the general trend of the rupture zone, all of which cut the southwest and northeast sides of Aso caldera (Fig. 2A). The rupture zones occur in a region with no previously reported faults. Zone 1 extends for ~10 km along the northwestern edge of Aso caldera and consists mainly of normal faults and extensional cracks (Figs.1 and 2 and figs. S1 to S5). The normal faults, striking N50°E to N70°E and with dips of 75° to 85° to the northwest and southeast, form a typical graben structure that varies in width from 20 to 100 m (generally, 30 to 50 m), with vertical offsets of up to 1.3 m on both sides of the graben (Fig. 3D and fig. S5). Zone 2 is a northeastward extension of the HFFZ and cuts the southwest rim of Aso caldera and the Komezuka volcanic cone (located within the caldera), with a conjugate geometry pattern of ruptures striking N50°E to N60°E and N60°E to N70°W, respectively (Figs. 1, 2A, and 3C and fig. S3). The surface ruptures also occur around both the crater and foot of the Komezuka cone in doughnut-shaped patterns, in which both the crater and the cone are uplifted by 30 to 50 cm relative to the slopes surrounding the cone (fig. S3). This zone is composed mainly of extensional cracks with an opening width of up to 50 cm and distinct shear faults striking N50°E to N60°E and N60°W to N70°W. A right-lateral strike-slip displacement of up to 60 cm and a left-lateral strike-slip displacement of up to 50 cm are observed along the northeast- and northwest-striking faults, respectively (Fig. 3C and fig. S3). These displacements indicate that the northeast- and northwest-striking rupture zones cut the volcanic cone by conjugate rupturing under an east-west compressive stress, coinciding with that revealed by seismic data and geodetic measurements (*20*). Zone 3, which is parallel to the general trend of zone 2 but separated by a distance of ~3 km, cuts the southwest side of Aso caldera and the Kishima volcanic cone (which is located inside Aso caldera and bounded by the Nakatake cone to the east and the Komezuka cone to the west) and terminates at the northeast edge of Aso caldera (Fig. 2A and fig. S4), where Aso Shrine collapsed as a result of strong shaking at the northeast end of the surface rupture zone (fig. S6). Zone 4 is a northeastern extension of the central segment and occurs along a newly identified fault. Zone 4 was difficult to access because it is in a mountainous area where many landslides occurred and roads were heavily damaged by the 2016 event. However, we identified ruptures in high-resolution Google Earth images acquired on 16 April 2016, about half a day after the main shock (figs. S3A and S5A). Ground deformation features and the distribution of the coseismic surface ruptures in the northeast segment reveal that the Komezuka and Kishima cones and the southwest-northeast rim of Aso caldera are cut by coseismic ruptures, and that the propagation of seismogenic rupturing terminated within Aso caldera.

We measured displacements along ruptures by using offsets of linear surface markers, such as roads,

Downloaded from http://science.sciencemag.org/ on November 22, 2016

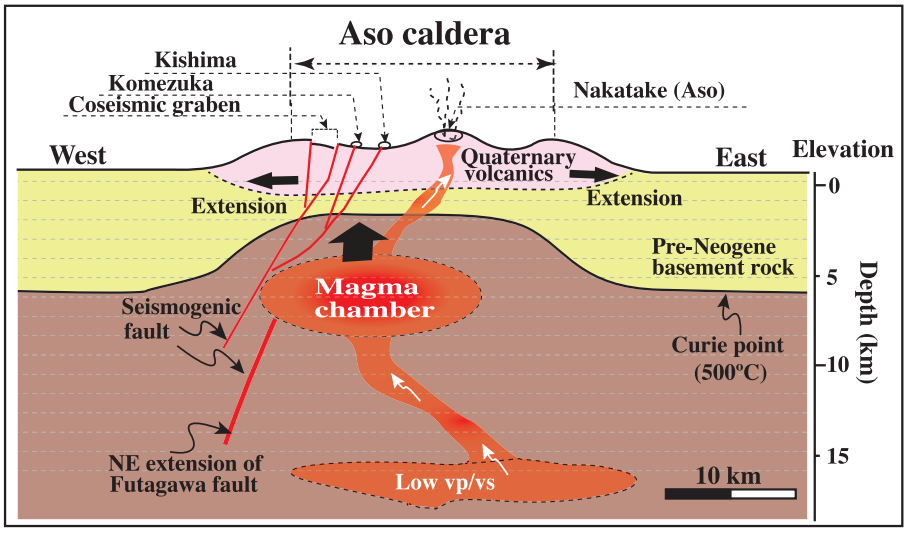


**Fig. 4. Schematic model of the relationship between the crustal structure of Aso caldera and the northeast segment of the 2016 Kumamoto seismogenic fault.** Geological structures are inferred from this study and a previous study (*29*). The Curie point and location of the magma chamber are based on data from previous studies (*23*–*28*). White arrows indicate the magma intrusion conduit of the 2003 eruption of Aso volcano, inferred from geophysical observations (*27*). vp/vs, ratio of *P*-wave to *S*-wave velocity.

paths, gullies, terrace risers, and river channels (Fig. 3, A and B, and figs. S1 to S3 and S5), which were measured at more than 50 sites (Fig. 2B). The maximum right-lateral displacement of 2.45 m, with a vertical component of 0.9 m, was measured along a 3-m-wide zone composed of three parallel surface ruptures on the slope of the southwest rim of Aso caldera (site 5; fig. S2B). We measured another large right-lateral displacement of up to 2.4 m (with no observed vertical component) in a wheat field at site 4 (Fig. 3A). The areas of large displacements that we observed in the field are comparable to those obtained from seismic inversion (Fig. 2, B and C). The northeast end of the rupture zone inside Aso caldera is dominated by vertical displacements with only small horizontal components.

In focal mechanism solutions, the main shock and foreshocks exhibited a strike-slip–dominated mechanism on a fault striking northeast-southwest and dipping 60° to 85° to the northwest with an east-west compression axis, which is consistent with observations in the field (Fig. 1, B and C) (*13*, *20*, *21*). However, the focal mechanism solutions of the $M_w$ 5.7 ($M_j$ 5.9) aftershock, which occurred in the boundary area between the central and northeast segments at ~20 min after the main shock, indicate a normal fault mechanism (Fig. 1B), consistent with the structural features of the coseismic graben that we observed in the field. The foreshocks and aftershocks show a spatial migration of epicenters from southwest to northeast during the 3-day period from 14 May to 16 May 2016, mostly along the coseismic surface ruptures that cut Aso caldera (Fig. 1B).

Our analysis of seismic waves and geophysical observations reveals that the crustal structure beneath Aso caldera is characterized by a zone of ascending magma with an upper boundary of pre-Neogene basement rocks (Fig. 4) (*22*–*28*). This boundary is coincident with the depth of the Curie point, which ranges from 580° to 400°C on the back-arc side of the Japanese Islands and is ~500°C under Aso caldera (Fig. 4) (*29*). Seismic wave analyses also show that the low-velocity region (i.e., the magma chamber), which is located in the area between the Nakatake cone and the northern part of Aso caldera, extends downward from a depth of 6 km below the ground surface (Figs. 2 and 4) (*22*). The Futagawa fault extends to zones 2 and 3, which respectively cut the Komezuka and Kishima cones, but which terminate at the inner northeast edge of Aso caldera (Figs. 1 and 2). The seismic inversion results show that a fault slip of up to 1 to 2 m occurred at shallow depths of <2 km, but that no distinct slip occurred along the fault plane at depths of >6 km under Aso caldera (Fig. 2C) (*15*). This result indicates that seismogenic fault rupturing propagated to the northeast edge of Aso caldera in near-surface regions, where surface ruptures were observed in the field, but ceased at depths of >6 km, which is the inferred location of the magma chamber beneath Aso caldera (Figs. 2C and 4). The presence of the magma chamber likely induced an upward pressure, resulting in localized east-west extensional stresses and the generation of the coseismic graben inside the caldera (Fig. 4). The stress field perturbation due to the mechanical heterogeneity in the vicinity of the volcanic region could create a local stress concentration around the magma chamber (*30*). The newly formed coseismic ruptures under Aso caldera are potential new channels for magma venting, thus changing the spatial heterogeneity and mechanical properties of Aso volcano.

Seismic analyses have shown that mechanical heterogeneities in fault zones control the seismicity of megathrust zones and the initiation and termination of ruptures in large earthquakes (*31*–*35*). Fault heterogeneities could affect the nucleation of interplate earthquakes, seismicity patterns, source rupture processes, strong ground motion (*31*, *32*), and recurrence behavior of fault segments (*11*). Spatial heterogeneity in the vicinity of a volcanic region would have an effect on the mechanical properties around the magma chamber (*30*). Accordingly, we conclude that the magma chamber below Aso caldera had an important role in terminating the propagation of the seismogenic rupture through the volcano during the 2016 $M_w$ 7.1 Kumamoto earthquake. Therefore, the 2016 coseismic surface ruptures provide new insight into the mechanical heterogeneity of seismogenic faults that could be important in reassessing the volcanic hazard in the vicinity of Aso volcano.

## REFERENCES AND NOTES


1. D. P. Hill, F. Pollitz, C. Newhall, *Phys. Today* **55**, 41–47 (2002).
2. S. Eggert, T. R. Walter, *Tectonophysics* **471**, 14–26 (2009).
3. D. Delle Donne, A. J. L. Harris, M. Ripepe, R. Wright, *Geology* **38**, 771–774 (2010).
4. C. G. Newhall, R. S. Punongbayan, Eds., *FIRE and MUD: Eruptions and Lahars of Mount Pinatubo, Philippines* (Philippine Institute of Volcanology and Seismology, Univ. of Washington Press, 1996).
5. T. R. Walter *et al.*, *Geophys. Res. Lett.* **34**, L05304 (2007).
6. S. Prejean, W. Ellsworth, M. Zoback, F. Waldhauser, *J. Geophys. Res.* **107**, ESE 9-1 (2002).
7. G. King, J. Nabecaronlek, *Science* **228**, 984–987 (1985).
8. B. Duan, D. D. Oglesby, *J. Geophys. Res.* **111**, B05309 (2006).
9. G. E. Hilley, J. R. Arrowsmith, E. Stone, *Bull. Seismol. Soc. Am.* **91**, 427–440 (2001).
10. Y. Yagi *et al.*, *Earth Planets Space* **68**, 118 (2016).
11. K. Aki, *J. Geophys. Res.* **89**, 5867–5872 (1984).
12. E. E. Brodsky, B. Sturtevant, H. Kanamori, *J. Geophys. Res.* **103**, 23827–23838 (1998).
13. Japan Meteorological Agency, "Report on the Heisei 28 (2016) Kumamoto earthquake (no. 10)," 2016; www.jma.go.jp/jma/press/1604/16g/201604161530.html [in Japanese].
14. Disaster Information Laboratory, National Research Institute for Earth Science and Disaster Resilience, "Report on the Heisei 28 (2016) Kumamoto earthquake (no. 21)," 2016; http://ecom-plat.jp/nied-cr/index.php?gid=10153 [in Japanese].
15. K. Koketsu, H. Kobayashi, H. Miyake, "Generation process of the 14th and 16th April 2016 Kumamoto earthquakes," 2016; http://taro.eri.u-tokyo.ac.jp/saigai/2016kumamoto/index.html#C [in Japanese].
16. Research Group for Active Faults of Japan, *Active Faults in Japan—Sheet Maps and Inventories* (Univ. of Tokyo Press, revised ed., 1991).
17. Headquarters for Earthquake Research Promotion, "Evaluation of Heisei 28 (2016) Kumamoto earthquake," 2016; www.mext.go.jp/component/a_menu/science/detail/__icsFiles/afieldfile/2016/04/15/1285728_001_1.pdf [in Japanese].
18. A. Lin, S. Uda, *Isl. Arc* **5**, 1–15 (1996).
19. A. Lin *et al.*, *Science* **296**, 2015–2017 (2002).
20. Geospatial Information Authority of Japan, "Information concerning with the 2016 Kumamoto earthquake," 2016; www.gsi.go.jp/BOUSAI/H27-kumamoto-earthquake-index.html [in Japanese].
21. National Research Institute for Earth Science and Disaster Prevention, "16 April 2016 Kumamoto earthquake and its aftershock distribution," 2016; www.jishin.go.jp/main/chousa/13apr_awaji/p03.htm [in Japanese].
22. Y. Sudo, *Bull. Volcanol. Soc. Jpn.* **33**, 130–134 (1988).
23. Y. Sudo, *Bull. Volcanol.* **53**, 99–111 (1991).
24. Y. Sudo, L. Kong, *Bull. Volcanol.* **63**, 326–344 (2001).
25. Y. Okubo, H. Tsu, K. Ogawa, *Tectonophysics* **159**, 279–290 (1989).
26. T. Tsutsui, Y. Sudo, *J. Volcanol. Geotherm. Res.* **131**, 33–58 (2004).
27. K. Unglert, M. K. Savage, N. Fournier, T. Ohkura, Y. Abe, *J. Geophys. Res.* **116**, B11203 (2011).
28. Y. Abe, T. Ohkura, T. Shibutani, K. Hirahara, M. Kato, *J. Volcanol. Geotherm. Res.* **195**, 1–12 (2010).
29. Y. Okubo, A. Shibuya, *J. Volcanol. Geotherm. Res.* **55**, 337–350 (1993).


Downloaded from http://science.sciencemag.org/ on November 22, 2016

30. J. Takekawa, H. Mikada, T. Goto, *Nat. Hazards Earth Syst. Sci.* **13**, 231–237 (2013).
31. F. Tajima, H. Kanamori, *Geophys. Res. Lett.* **12**, 345–348 (1985).
32. H. Kanamori, *Annu. Rev. Earth Planet. Sci.* **14**, 293–322 (1986).
33. M. Simons *et al.*, *Science* **332**, 1421–1425 (2011).
34. D. Zhao, Z. Huang, U. Umino, A. Hasegawa, H. Kanamori, *Geophys. Res. Lett.* **38**, L17308 (2011).
35. F. Tajima, B. L. N. Kennett, *Geophys. Res. Lett.* **39**, L05307 (2012).

**ACKNOWLEDGMENTS**

We thank K. Sado, S. Takahashi, S. Hirata, and K. Osono for assistance in the field; M. Miyawaki for discussions during this study; and B. Di and N. Akiyama for help in arranging the field work and processing the images. We acknowledge the Disaster Information Laboratory (DIL), National Research Institute for Earth Science and Disaster Resilience for kindly providing seismic data. The raw data for focal mechanisms, foreshocks, and aftershocks are available directly from DIL. This work was partially supported by a Science Project (no. 15K01248) of the Ministry of Education, Culture, Sports, Science and Technology of Japan.

**SUPPLEMENTARY MATERIALS**

www.sciencemag.org/content/354/6314/869/suppl/DC1
Figs. S1 to S6

30 June 2016; accepted 7 October 2016
Published online 20 October 2016
10.1126/science.aah4629

NANOMATERIALS

# Single-particle mapping of nonequilibrium nanocrystal transformations

**Xingchen Ye,[1]* Matthew R. Jones,[1]* Layne B. Frechette,[1] Qian Chen,[1,2] Alexander S. Powers,[1] Peter Ercius,[7] Gabriel Dunn,[3] Grant M. Rotskoff,[5] Son C. Nguyen,[1] Vivekananda P. Adiga,[3] Alex Zettl,[3,6,8] Eran Rabani,[1,6,9] Phillip L. Geissler,[1] A. Paul Alivisatos[1,4,6,8]†**

**Chemists have developed mechanistic insight into numerous chemical reactions by thoroughly characterizing nonequilibrium species. Although methods to probe these processes are well established for molecules, analogous techniques for understanding intermediate structures in nanomaterials have been lacking. We monitor the shape evolution of individual anisotropic gold nanostructures as they are oxidatively etched in a graphene liquid cell with a controlled redox environment. Short-lived, nonequilibrium nanocrystals are observed, structurally analyzed, and rationalized through Monte Carlo simulations. Understanding these reaction trajectories provides important fundamental insight connecting high-energy nanocrystal morphologies to the development of kinetically stabilized surface features and demonstrates the importance of developing tools capable of probing short-lived nanoscale species at the single-particle level.**

Nanoscience relies on the ability to create nonequilibrium states of matter in which metastable materials are spatially organized in close proximity to yield desired properties. As a result, much effort is currently dedicated to understanding and controlling the complex pathways of formation (*1*), transformation (*2*–*5*), and dissolution (*6*, *7*) of individual nanoscale building blocks. The majority of studies on the evolution of nanocrystal-based chemical reactions have relied on methods to isolate intermediates and characterize them by electron microscopy or probe the ensemble with spectroscopic techniques. Although these approaches have provided new fundamental knowledge, their time-resolution is severely limited and/or the ensemble averaging can obscure the details of individual pathways.

Methods for the direct imaging of the evolution of individual nanoparticle species in a liquid environment are under active development because they enable the preservation of dynamic processes present in the native colloid (*1*, *8*–*14*). Recently, our group has developed transmission electron microscopy (TEM) liquid cells based on the trapping of thin fluids between sheets of graphene (Fig. 1A) (*15*). The superior electron transparency of these windows has allowed for detailed tracking of nucleation and growth phenomena as well as atomistic reconstruction of nanocrystals (*15*, *16*).

The majority of liquid-phase electron microscopy studies of transient nanoscale phenomena have focused on beam-induced nucleation and growth processes (*1*, *9*, *10*, *15*, *17*, *18*). These studies often produce an ill-defined set of randomly oriented nanoparticles that requires atomic resolution to deduce crystallographically meaningful information about liquid-phase phenomena (*1*, *15*). If, on the other hand, one monitors the dissolution of presynthesized particles with a well-defined crystallographic habit (vis-à-vis their shape), far more information is available regarding nonequilibrium processes because the orientation, zone axis, and exposed crystal facets can be known ahead of time and can be monitored kinetically through the evolution of particle shape over time.

We use graphene liquid cell TEM to monitor in real time single-particle, nonequilibrium structural transformations of anisotropic gold nanocrystals as they undergo oxidative dissolution in their native aqueous environment (Fig. 1 and figs. S1 to S3). $FeCl_3$ is introduced as the primary oxidative etchant, the concentration of which allows for a controlled rate of etching in the presence of the electron beam, with virtually no etching in the absence of the beam (Fig. 1A). This occurs because additional oxidizing species formed as radiolysis products by the electron beam, such as OH radicals, can be used to locally trigger nanoparticle etching (figs. S4 to S9 and movie S3) (*17*, *19*). Monte

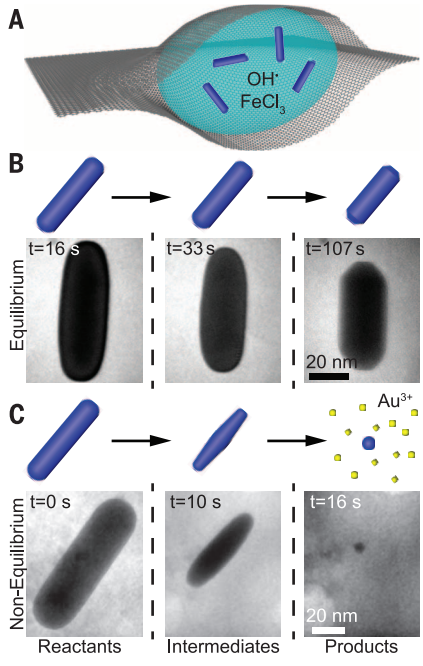


**Fig. 1. Real-time observation of near-equilibrium and nonequilibrium nanocrystal species in a graphene liquid cell.** (**A**) Schematic liquid cell encapsulating a solution of gold nanocrystals. (**B**) Idealized reaction pathway and TEM images extracted from movie S1 showing the reaction to generate near-equilibrium rods with flat {100} facets at the tips. (**C**) Idealized reaction pathway and TEM images extracted from movie S2 showing the transition from rods to a nonequilibrium ellipsoidal intermediate with sharp tips.

[1]Department of Chemistry, University of California, Berkeley, Berkeley, CA 94720, USA. [2]Miller Institute for Basic Research in Science, University of California, Berkeley, Berkeley, CA 94720, USA. [3]Department of Physics, University of California, Berkeley, Berkeley, CA 94720, USA. [4]Department of Materials Science and Engineering, University of California, Berkeley, Berkeley, CA 94720, USA. [5]Biophysics Graduate Group, University of California, Berkeley, Berkeley, CA 94720, USA. [6]Materials Sciences Division, Lawrence Berkeley National Laboratory, Berkeley, CA 94720, USA. [7]Molecular Foundry, Lawrence Berkeley National Laboratory, Berkeley, CA 94720, USA. [8]Kavli Energy NanoScience Institute, University of California, Berkeley, and Lawrence Berkeley National Laboratory, Berkeley, CA 94720, USA. [9]Raymond and Beverly Sackler Center for Computational Molecular and Materials Science, Tel Aviv University, Tel Aviv 69978, Israel.
*These authors contributed equally to this work. **†Corresponding author. Email: alivis@berkeley.edu**

Downloaded from http://science.sciencemag.org/ on November 22, 2016

Carlo simulations corroborate the observation of nonequilibrium nanocrystal reaction pathways and shed light on their mechanistic underpinnings.

These methods are illustrated first with a simple shape, rods (Fig. 1). At low $FeCl_3$ concentrations, reactions proceed slowly and show the development of low-energy facets (Fig. 1B and movies S1 and S4). In this scenario, the rate of etching is slow compared to the rate at which the particle is able to restructure and adopt a shape that is close to equilibrium (*20*). At high $FeCl_3$ concentrations, however, fast-reaction kinetics constantly drive the system out of equilibrium and the nanocrystal transiently adopts an ellipsoidal shape (Fig. 1C and movie S2). Previous ex situ studies have investigated the etching of gold nanorods but have primarily observed tip-selective shortening (*21*).

The distinguishing feature of the nonequilibrium rod reaction is the change in the relative proportions of the particle through the development of tips that are sharper than the diameter—i.e., the formation of ellipsoids (Fig. 2A, fig. S10, and movie S5). Analysis of the longitudinal dissolution rate and tip curvature changes over time show that periods during which the rod tips become sharper are well correlated with accelerated etching of the particle (Fig. 2B and fig. S11). To better understand the spatiotemporal details of the reaction, we constructed time-domain contour plots: cross-sectional outlines of a changing nanocrystal extracted from frames that are equally spaced in time and colored based on calculation of the in-plane local curvature (Fig. 2C and figs. S12 and S13) (*22*). These data are consistent with the expectation that, because the rod tips are curved along two orthogonal dimensions while the sides are curved along one, the tips possess a lower areal ligand density and are therefore more chemically accessible and etch faster (fig. S14) (*22*–*24*); this interpretation is supported by Monte Carlo simulations of rod etching (fig. S15 and movie S6). Whereas in the near-equilibrium case, atoms at the tips have an opportunity to relax (e.g., via surface diffusion) (fig. S16 and movie S7) (*20*, *23*), the persistent oxidative environment reacts with these species selectively, accelerating the reaction and driving the transient stabilization of the ellipsoidal intermediate. Etching reactions conducted on rods with synthetically blunted tips follow the same reaction trajectory (ellipsoidal intermediate), albeit with slower initial kinetics corresponding to selective removal of the blunt features (Fig. 2, D to F; figs. S12 and S13; and movies S8 and S9). Qualitatively similar dependencies on tip dimensionality and tip curvature are observed for other nanocrystal shapes as well as when a rod and blunted rod pair are etched in the same field of view under identical conditions (figs. S17 and S18 and movies S10 to S16).

The etching of pseudo–one-dimensional nanocrystals demonstrates that persistent and selective etching at high-energy local features drives the formation of nonequilibrium intermediate shapes. However, for this class of particles the surface faceting is not easily characterized or agreed upon in the literature (*25*); therefore, deducing a more detailed, atomistic understanding of far-from-equilibrium reactions is challenging. To address this, single-crystalline polyhedral gold nanocrystals with definitive surface faceting were subjected to the oxidative environment in the liquid cell and were observed to transition through crystallographically well-defined intermediate shapes.

We describe results for a {100}-faceted cube (movies S17 and S18). The square cross-section indicative of the ⟨100⟩ zone axis of a cube is observed to transition through a faceted intermediate before adopting an isotropic shape and being oxidized completely (Fig. 3, A and B). To determine a crystallographic assignment for the intermediate shape, the angles between candidate {hkl} crystal facets viewed along the ⟨100⟩ zone axis were calculated and compared to those measured in the TEM images (Fig. 3, C and D). This analysis reveals a transformation to high-energy {310} facets, indicative of a tetrahexahedron (THH)–shaped nanocrystal as the longest-lived intermediate (*26*, *27*).

We observe a similar shape transformation in Monte Carlo simulations of a schematic kinetic model for nanocrystal etching (Fig. 3, B and D, and movies S19 and S20). We take Au atoms to reside on sites of a face-centered cubic (fcc) lattice and adopt rate constants $k(n)$ for etching of surface-exposed atoms that depend only on their coordination number, $n$. Despite its simplicity, this model produces a THH intermediate for a broad range of parameter values (fig. S19). This

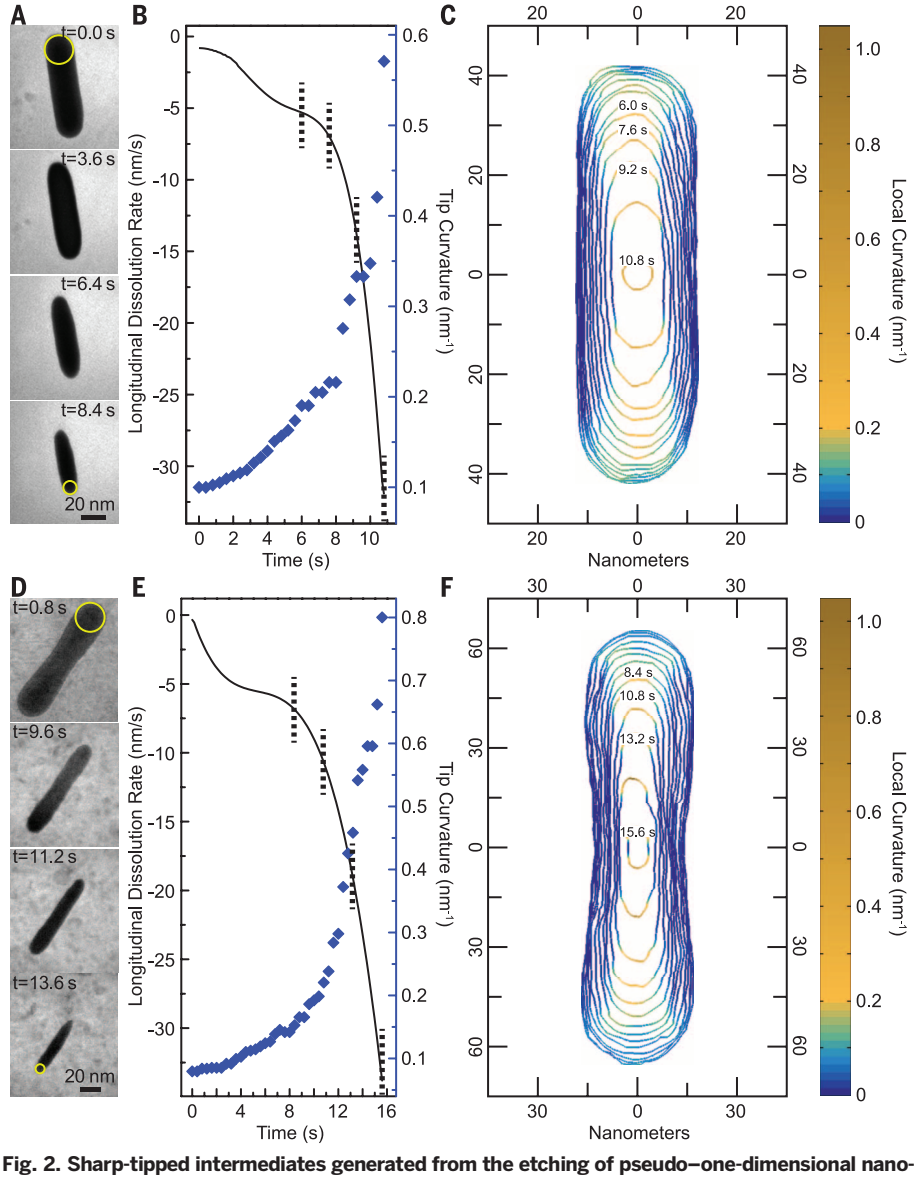


**Fig. 2. Sharp-tipped intermediates generated from the etching of pseudo–one-dimensional nanocrystals.** Dissolution of a gold rod (**A** to **C**) and blunted rod (**D** to **F**) under nonequilibrium conditions. Selected time-lapse TEM images extracted from movies S5 (A) and S8 (D), plots of longitudinal dissolution rate and tip curvature as a function of time [(B) and (E)], and time-domain contour plots [(C) and (F)]. Yellow circles in (A) and (D) highlight the extrema of cross-sectional tip curvature. Vertical dotted lines in (B) and (E) correspond to the time-labeled contours in (C) and (F). Contour lines are spaced in time by 0.8 s in (C) and 1.2 s in (F).

Downloaded from http://science.sciencemag.org/ on November 22, 2016

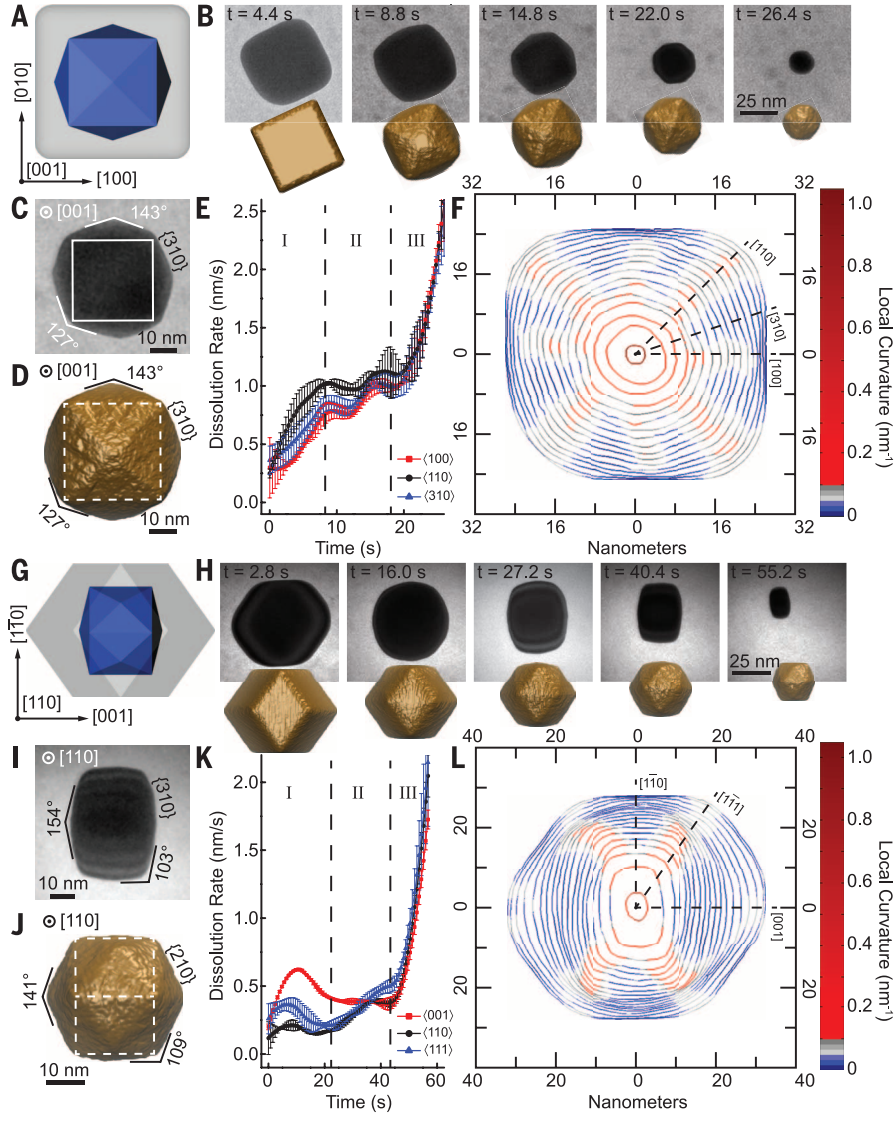


**Fig. 3. Crystallographically well-defined intermediates generated from polyhedral nanocrystals.** Transition of a cube (**A** to **F**) and rhombic dodecahedron (**G** to **L**) to a tetrahexahedron during nonequilibrium etching. [(A) and (G)] Model of a crystallographically oriented particle (gray) with intermediate tetrahexahedra shown internally (blue). [(B) and (H)] Time-lapse TEM images and corresponding snapshots from Monte Carlo simulations extracted from movies S17 and S19 (B) and S27 and S29 (H). Tetrahexahedron intermediates with labeled zone axis and calculated {hk0} facet angles are shown for the cube [(C) and (D)] and rhombic dodecahedron [(I) and (J)] reactions for experiment [(C) and (I)] and simulation [(D) and (J)]. [(E) and (K)] Crystallographic dissolution rates extracted from contour plots, averaged over several symmetric directions. [(F) and (L)] Time-domain contour plots with relevant crystallographic directions labeled as dotted lines. Contour lines are spaced in time by 1.6 s in (F) and (L).

nonequilibrium structure is unlikely to be a consequence of the electron beam, the particular oxidation chemistry employed in the liquid cell, or the presence of surface-bound ligands, because these effects are not explicitly considered in the simulation. When the driving force for oxidation is reduced in experiments, cubes transform into truncated octahedra (fig. S20 and movies S21 and S22) (*28*), the expected equilibrium Wulff shape for an fcc lattice (fig. S21) (*20*, *23*). This same equilibrium transformation is observed in simulations when mechanisms of surface relaxation are introduced (figs. S19 and S22 and movies S23 to S25; see supplementary materials).

Because the particles do not visibly rotate throughout the etching reaction, the crystallographic zone axis is constant and can be known beforehand by the cross-sectional appearance of the initial nanocrystals. This allows for the quantification of dissolution rates along specific [uvw] directions from time-domain contour maps (Fig. 3, E and F, and figs. S23 to S25). These data represent an experimental manifestation of the so-called kinetic Wulff construction (*23*) but provide additional insight because they allow one to extract the time dependence of crystallographic dissolution rates (Fig. 3E and fig. S26). The ⟨110⟩ edges of the cubic nanocrystal exhibit the fastest initial etching rates, revealing the {310} THH facets that then experience a period of transient metastability (region II, Fig. 3E) before all rates accelerate at small particle sizes (region III, Fig. 3, E and F).

The formation of a well-defined THH intermediate is driven primarily by a coordination number ($n$)–dependent etching process (see supplementary materials). When the rate of deletion of surface atoms with $n = 6$ is much slower than surface relaxation, the equilibrium truncated octahedron is observed (fig. S19 and movies S24 and S25). However, when the rate of removal of surface atoms with $n = 6$ is faster than both surface relaxation and the removal of $n \geq 7$ atoms, the nonequilibrium THH intermediate is observed (Fig. 3, B and D; fig. S19; and movies S24 and S25). This occurs through the lateral recession of sequential {100} layers via etching of the peripheral edge atoms that tend to have $n \leq 6$ (Fig. 4A, fig. S27, and movie S26). This results in the gradual transition from {100} facets on the initial cube to a series of vicinal {hk0} facets and is corroborated by measurement of the facet h-index in both experiment and simulation (Fig. 4B). Because vicinal {hk0} facets consist of a series of {100} terraces ($n = 8$) separated by steps ($n = 6$) (Fig. 4, C and D), continued removal of $n = 6$ atoms eventually results in a far-from-equilibrium condition in which a series of stepped terraces are receding via their edges at a constant rate, resulting in the transient existence of the THH intermediate (Fig. 4E). This mechanism, known as step-recession (*29*, *30*), is the reverse of the well-known step-flow growth process (*31*, *32*) which occurs in many examples of crystal growth and serves as a foundation for continuum models of nanoparticle shape development (e.g., kinetic Wulff construction) and modern thin-film fabrication techniques (e.g., molecular beam epitaxy) (*23*, *32*).

To determine the generality of these observations, single-crystalline rhombic dodecahedron (RD) nanocrystals were etched under similar conditions (Fig. 3, G to L, and movies S27 to S30). Indeed, the elongated hexagonal projection of the RD is observed to transition through a THH intermediate (viewed edge-on as a result of the ⟨110⟩ zone axis) before being oxidized completely (Fig. 3, G and H). Although the experimental results show a {310} THH as the final kinetic product, simulations show a {210} THH (Fig. 3, I and J; fig. S28; and movies S31 to S34), suggesting that additional factors that are not considered in simulations (e.g., ligand binding to the larger {100} terrace area of {310} facets) (Fig. 4, C and D) may be important in dictating the precise facet morphology. (A similar discrepancy between the experiment and simulations for tip-selective nanorod etching supports the idea that ligand binding can modulate relative facet stability; see above, fig. S15, and movie S6.) Nonetheless, the qualitative observation of a period of transient metastability of a THH intermediate is confirmed and can be quantified through similar kinetic Wulff construction and time-domain contour plot analysis techniques (Fig. 3, K and L, and figs. S23 to S26). The appearance of THH intermediates is also observed from a rhombic dodecahedron and

Downloaded from http://science.sciencemag.org/ on November 22, 2016

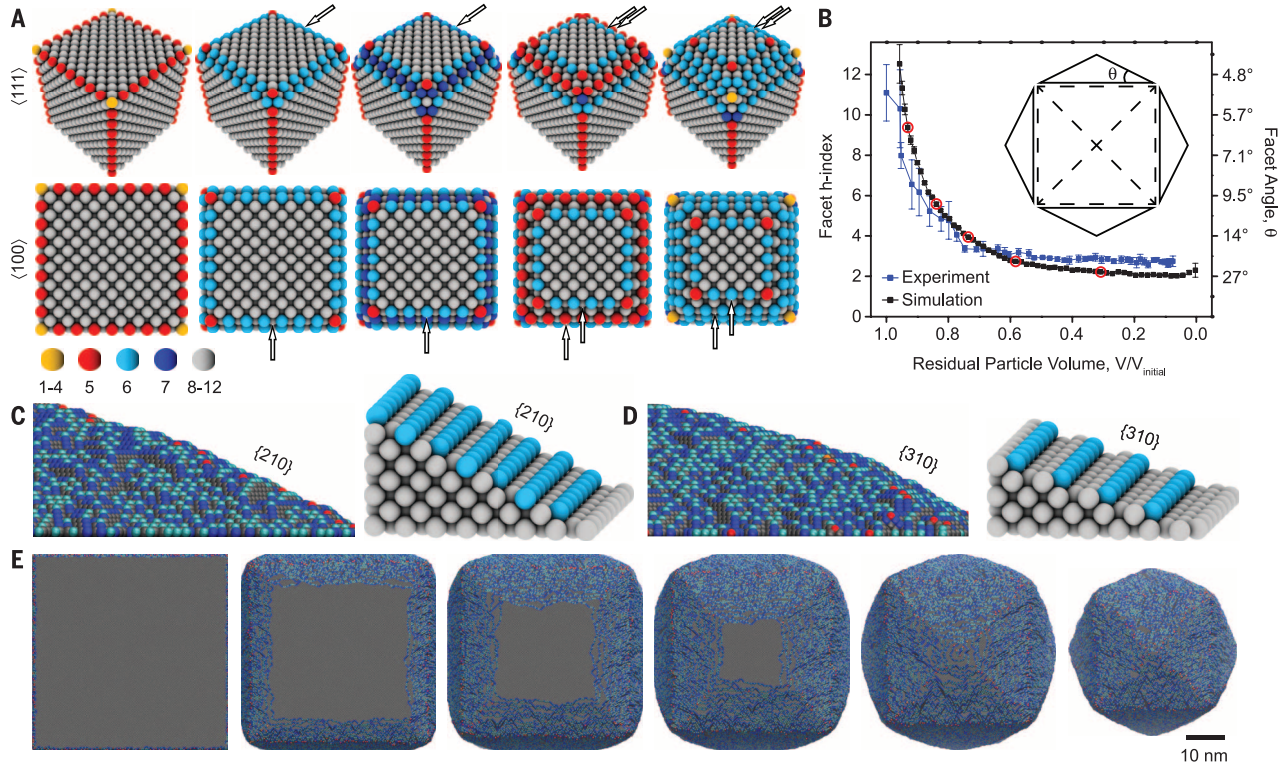


**Fig. 4. Coordination number and step-recession–based formation mechanism of intermediate nanocrystals.** (**A**) Idealized etching of a cubic nanocrystal shown from two crystallographic perspectives wherein atoms with coordination number ($n$) ≤ 6 are deterministically removed at each step (movie S26). Arrows denote the presence of {100} terraces that recede via removal of atoms at their step edges. Color-coded legend for $n$ is shown at bottom left. (**B**) Time evolution of the vicinal facet effective h-index via measurement of the facet angle in both experiment and simulation (movies S17 and S19). Red circles correspond to the snapshots in (E). (**C** and **D**) Simulation snapshot (left) and perfect model facet (right) of {210} (C) and {310} (D) facets. (**E**) Simulation snapshots of the progression of a cube to a nonequilibrium THH with atoms color-coded according to coordination number (movie S20).

cube pair, etched in the same field of view under identical conditions (movie S35).

Our results suggest that the formation of a THH nanocrystal is a general property of fcc metals under a broad range of conditions that favor kinetic products. This may explain the observation that the synthetic nanocrystal literature contains a preponderance of reports of structures bounded by {hk0} rather than other, ostensibly equally likely, {hkl} facets (*26*, *27*). Additional nanocrystal shapes exhibited driving-force–dependent near-equilibrium and nonequilibrium transformation pathways, highlighting the generality of the observations described above (fig. S29 and movies S36 to S39).

In the chemistry of atoms and molecules, the study of reactive intermediates is key to understanding molecular reaction mechanisms, and new tools for observing such intermediates are constantly sought. An analogy is often made between nanocrystals and artificial atoms and molecules. Liquid cell TEM provides for observation and mechanistic understanding of transient intermediates in the formation of nanostructures at the relevant time and length scales. This will add to our rapidly developing ability to create and control artificial nanoscale building blocks with high precision.

## REFERENCES AND NOTES


1. H. Zheng *et al.*, *Science* **324**, 1309–1312 (2009).
2. D. H. Son, S. M. Hughes, Y. Yin, A. P. Alivisatos, *Science* **306**, 1009–1012 (2004).
3. Y. Sun, Y. Xia, *Science* **298**, 2176–2179 (2002).
4. S. H. Tolbert, A. P. Alivisatos, *Science* **265**, 373–376 (1994).
5. P. Buffat, J. P. Borel, *Phys. Rev. A* **13**, 2287–2298 (1976).
6. M. J. Mulvihill, X. Y. Ling, J. Henzie, P. Yang, *J. Am. Chem. Soc.* **132**, 268–274 (2010).
7. M. N. O'Brien, M. R. Jones, K. A. Brown, C. A. Mirkin, *J. Am. Chem. Soc.* **136**, 7603–7606 (2014).
8. M. J. Williamson, R. M. Tromp, P. M. Vereecken, R. Hull, F. M. Ross, *Nat. Mater.* **2**, 532–536 (2003).
9. N. de Jonge, F. M. Ross, *Nat. Nanotechnol.* **6**, 695–704 (2011).
10. D. Li *et al.*, *Science* **336**, 1014–1018 (2012).
11. E. Sutter *et al.*, *Nat. Commun.* **5**, 4946 (2014).
12. Q. Chen *et al.*, *ACS Cent. Sci.* **1**, 33–39 (2015).
13. J. Wu *et al.*, *Nano Lett.* **15**, 2711–2715 (2015).
14. F. M. Ross, *Science* **350**, aaa9886 (2015).
15. J. M. Yuk *et al.*, *Science* **336**, 61–64 (2012).
16. J. Park *et al.*, *Science* **349**, 290–295 (2015).
17. T. J. Woehl, J. E. Evans, I. Arslan, W. D. Ristenpart, N. D. Browning, *ACS Nano* **6**, 8599–8610 (2012).
18. H.-G. Liao *et al.*, *Science* **345**, 916–919 (2014).
19. N. M. Schneider *et al.*, *J. Phys. Chem. C* **118**, 22373–22382 (2014).
20. Y. Xia, X. Xia, H.-C. Peng, *J. Am. Chem. Soc.* **137**, 7947–7966 (2015).
21. C.-K. Tsung *et al.*, *J. Am. Chem. Soc.* **128**, 5352–5353 (2006).
22. D. Alpay, L. Peng, L. D. Marks, *J. Phys. Chem. C* **119**, 21018–21023 (2015).
23. L. D. Marks, L. Peng, *J. Phys. Condens. Matter* **28**, 053001 (2016).
24. Z. Nie *et al.*, *Nat. Mater.* **6**, 609–614 (2007).
25. B. Goris *et al.*, *Nat. Mater.* **11**, 930–935 (2012).
26. X. Ye *et al.*, *Nano Lett.* **13**, 2163–2171 (2013).
27. M. L. Personick, M. R. Langille, J. Zhang, C. A. Mirkin, *Nano Lett.* **11**, 3394–3398 (2011).
28. M. Liu, Y. Zheng, L. Zhang, L. Guo, Y. Xia, *J. Am. Chem. Soc.* **135**, 11752–11755 (2013).
29. A. Feltz, U. Memmert, R. J. Behm, *Chem. Phys. Lett.* **192**, 271–276 (1992).
30. C. Y. Nakakura, E. I. Altman, *J. Vac. Sci. Technol. A* **15**, 2359–2368 (1997).
31. W. K. Burton, N. Cabrera, F. C. Frank, *Philos. Trans. R. Soc. London A* **243**, 299–358 (1951).
32. J. Krug, in *Multiscale Modeling in Epitaxial Growth*, A. Voigt, Ed. (Birkhäuser Basel, Basel, 2005), pp. 69–95.


## ACKNOWLEDGMENTS

This work was supported in part by the King Abdulaziz City for Science and Technology (KACST), Kingdom of Saudi Arabia, which provided for nanocrystal synthesis; the Defense Threat Reduction Agency (DTRA) under award HDTRA1-13-1-0035, which provided for nanocrystal etching, postdoctoral support, and TEM instrumentation; the NSF-BSF International Collaboration in Chemistry program, NSF grant CHE-1416161 and BSF grant 2013/604, which provided for computational resources; and the Director, Office of Science, Office of Basic Energy Sciences, Materials Sciences and Engineering Division of the U.S. Department of Energy under contract DE-AC02-05CH11231 within the sp2-bonded Materials Program (KC2207), which provided for graphene growth, cell fabrication, and student support. This work made use of the Molecular Foundry, Lawrence Berkeley National Laboratory, which is supported by the U.S. Department of Energy under contract DE-AC02-05CH11231. Q.C. was supported by a Miller fellowship from Miller Institute for Basic Research in Science at UC Berkeley. G.M.R. acknowledges the NSF for a Graduate Research Fellowship. M.R.J. acknowledges the Arnold and Mabel Beckman Foundation for a postdoctoral fellowship.

## SUPPLEMENTARY MATERIALS

www.sciencemag.org/content/354/6314/874/suppl/DC1
Materials and Methods
Figs. S1 to S36
Movies S1 to S43
References (*33*–*54*)

27 June 2016; accepted 14 October 2016
10.1126/science.aah4434

Downloaded from http://science.sciencemag.org/ on November 22, 2016

GEOLOGY

# The formation of peak rings in large impact craters

Joanna V. Morgan,[1]* Sean P. S. Gulick,[2] Timothy Bralower,[3] Elise Chenot,[4] Gail Christeson,[2] Philippe Claeys,[5] Charles Cockell,[6] Gareth S. Collins,[1] Marco J. L. Coolen,[7] Ludovic Ferrière,[8] Catalina Gebhardt,[9] Kazuhisa Goto,[10] Heather Jones,[3] David A. Kring,[11] Erwan Le Ber,[12] Johanna Lofi,[13] Xiao Long,[14] Christopher Lowery,[2] Claire Mellett,[15] Rubén Ocampo-Torres,[16] Gordon R. Osinski,[17,18] Ligia Perez-Cruz,[19] Annemarie Pickersgill,[20] Michael Poelchau,[21] Auriol Rae,[1] Cornelia Rasmussen,[22] Mario Rebolledo-Vieyra,[23] Ulrich Riller,[24] Honami Sato,[25] Douglas R. Schmitt,[26] Jan Smit,[27] Sonia Tikoo,[28] Naotaka Tomioka,[29] Jaime Urrutia-Fucugauchi,[19] Michael Whalen,[30] Axel Wittmann,[31] Kosei E. Yamaguchi,[32,33] William Zylberman[17,34]

**Large impacts provide a mechanism for resurfacing planets through mixing near-surface rocks with deeper material. Central peaks are formed from the dynamic uplift of rocks during crater formation. As crater size increases, central peaks transition to peak rings. Without samples, debate surrounds the mechanics of peak-ring formation and their depth of origin. Chicxulub is the only known impact structure on Earth with an unequivocal peak ring, but it is buried and only accessible through drilling. Expedition 364 sampled the Chicxulub peak ring, which we found was formed from uplifted, fractured, shocked, felsic basement rocks. The peak-ring rocks are cross-cut by dikes and shear zones and have an unusually low density and seismic velocity. Large impacts therefore generate vertical fluxes and increase porosity in planetary crust.**

Impacts of asteroids and comets play a major role in planetary evolution by fracturing upper-crustal lithologies, excavating and ejecting material from the impact site, producing melt pools, and uplifting and exposing subsurface rocks. The uplift of material during impact cratering rejuvenates planetary surfaces with deeper material. Complex impact craters on rocky planetary bodies possess a central peak or a ring of peaks internal to the crater rim, and the craters with these features are termed central-peak and peak-ring craters, respectively (*1*). Most known peak-ring craters occur on planetary bodies other than Earth, prohibiting assessment of their physical state and depth of origin. Here, we address the question of how peak rings are formed, using geophysical data, numerical simulations, and samples of the Chicxulub peak ring obtained in a joint drilling expedition by the International Ocean Discovery Program (IODP) and International Continental Scientific Drilling Program (ICDP).

Upon impact, a transient cavity is initially formed, which then collapses to produce a final crater that is both shallower and wider than the transient cavity (*1*). Dynamic uplift of rocks during the collapse of the transient cavity in the early stages of crater formation (Fig. 1, B and C) likely forms central peaks (*2*). The dynamic collapse model of peak-ring formation attributes the origin of peak rings to the collapse of overheightened central peaks (*3*). The observational evidence for this model is most obvious on Venus, where central peaks gradually evolve into peak rings with increasing crater size (*4*). The peak-ring-diameter–to–crater-rim-diameter ratio increases with crater size on Venus but does not get much larger than ~0.5. The lack of any further increase in this ratio led to the suggestion that in larger craters, the outward collapse of peak-ring material is halted when it meets the collapsing transient cavity rim (*4*).

A different concept for peak-ring formation—the nested melt-cavity hypothesis—evolved from observations of peak-ring craters on the Moon and Mercury (*5*–*7*). This alternative hypothesis envisions that the uppermost central uplift is melted during impact, and an attenuated central uplift remains below the impact melt sheet and does not overshoot the crater floor during the modification stage. Hence, in contrast to the dynamic collapse model (Fig. 1), this nested melt-cavity hypothesis would not predict outward thrusting of uplifted rocks above the collapsed transient cavity rim material. The origin and shock state of rocks that form a peak ring are less clear in the nested melt-cavity hypothesis because they have not been evaluated with numerical simulations. Head, however, postulated that material in the outer margin of the melt cavity forms the peak ring and therefore should be close to melting (*6*). This requires shock pressures of just below 60 GPa. In contrast, Baker *et al.* propose that peak rings are formed from inwardly slumped rotated blocks of transient cavity rim material originating at shallow depths and thus should have experienced lower average shock pressures than simulated in the dynamic collapse model (*7*).

The transition from central-peak to peak-ring craters with increasing crater size scales inversely with gravity (*1*), suggesting that the same transition diameter of ~30 km found on Venus (*4*) should also hold for Earth, and that craters >30 km in diameter should possess a peak ring. Craters on Earth often display internal ring-like structures, but complications and uncertainties owing to target heterogeneity, erosion, and sedimentation make it difficult to distinguish peak rings that are genetically linked to their extraterrestrial counterparts (*8*, *9*). Seismic reflection data across the ~200-km-diameter Chicxulub multi-ring impact structure revealed it to be the

Downloaded from http://science.sciencemag.org/ on November 22, 2016

[1]Department of Earth Science and Engineering, Imperial College London, SW7 2AZ, UK. [2]Institute for Geophysics, Jackson School of Geosciences, University of Texas at Austin, TX 78758-4445, USA. [3]Department of Geosciences, Pennsylvania State University, University Park, PA 16802, USA. [4]Biogéosciences Laboratory, UMR 6282 CNRS, Université de Bourgogne-Franche Comté, Dijon 21000, France. [5]Analytical, Environmental and Geo-Chemistry, Vrije Universiteit Brussel, Pleinlaan 2,Brussels 1050, Belgium. [6]Centre for Astrobiology, School of Physics and Astronomy, University of Edinburgh, Edinburgh EH9 3FD, UK. [7]Department of Chemistry, WA-Organic and Isotope Geochemistry Centre (WA-OIGC), Curtin University, Bentley, WA 6102, Australia. [8]Natural History Museum, Burgring 7, 1010 Vienna, Austria. [9]Alfred Wegener Institute Helmholtz Centre of Polar and Marine Research, Bremerhaven, 27568, Germany. [10]Tohoku University, International Research Institute of Disaster Science, Aoba 468-1 E303, Sendai 980-0845, Japan. [11]Lunar and Planetary Institute, 3600 Bay Area Boulevard, Houston, TX 77058, USA. [12]Department of Geology, University of Leicester, Leicester, LE1 7RH, UK. [13]Géosciences Montpellier, Université de Montpellier, 34095 Montpellier Cedex05, France. [14]China University of Geosciences (Wuhan), School of Earth Sciences, Planetary Science Institute, 388 Lumo Rd. Hongshan Dist., China. [15]British Geological Survey, The Lyell Centre, Research Avenue South, Edinburgh, EH14 4AP, UK. [16]Groupe de Physico-Chimie de l´Atmosphère, L'Institut de Chimie et Procédés pour l'Énergie, l'Environnement et la Santé (ICPEES), UMR 7515 Université de Strasbourg–CNRS 1 rue Blessig, 67000 Strasbourg, France. [17]Centre for Planetary Science and Exploration and Department of Earth Sciences, University of Western Ontario, London, ON, N6A 5B7, Canada. [18]Department of Physics and Astronomy, University of Western Ontario, London, ON, N6A 5B7, Canada. [19]Instituto de Geofísica, Universidad Nacional Autónoma de México, Cd. Universitaria, Coyoacán Ciudad de México, C. P. 04510, México. [20]School of Geographical and Earth Sciences, University of Glasgow, Gregory, Lilybank Gardens, Glasgow, G12 8QQ, UK. [21]University of Freiburg, Geology, Albertstraße 23b, Freiburg, 79104, Germany. [22]University of Utah, Department of Geology and Geophysics, 115 S 1460 E (FASB), Salt Lake City, UT 84112, USA. [23]Unidad de Ciencias del Agua, Centro de Investigación, Científica de Yucatán, A.C., Cancún, Quintana Roo, C.P. 77500, México. [24]Institut für Geologie, Universität Hamburg, Bundesstrasse 55, Hamburg, 20146, Germany. [25]Japan Agency for Marine-Earth Science and Technology, 2-15, Natsushima-cho, Yokosuka-city, Kanagawa, 237-0061, Japan. [26]Department of Physics, University of Alberta, Edmonton, Alberta, T6G 2E1, Canada. [27]Faculty of Earth and Life Sciences (FALW), Vrije Universiteit Amsterdam, de Boelelaan 1085, Amsterdam, 1018HV, Netherlands. [28]Rutgers University New Brunswick, Earth and Planetary Sciences, Piscataway Township, NJ 08854, USA. [29]Kochi Institute for Core Sample Research, Japan Agency for Marine-Earth Science and Technology, 200 Monobe Otsu, Nankoku, Kochi, 783-8502, Japan. [30]Department of Geosciences, University of Alaska Fairbanks, 900 Yukon Drive, Fairbanks, AK 99775, USA. [31]Arizona State University, LeRoy Eyring Center for Solid State Science, Physical Sciences, Tempe, AZ 85287-1704, USA. [32]Department of Chemistry, Toho University, Funabashi, Chiba 274-8510, Japan. [33]NASA Astrobiology Institute, USA. [34]Aix Marseille Université, CNRS, Institut pour la Recherche et le Développement, Coll France, CEREGE, Aix-en-Provence, France.
*Corresponding author. Email: j.morgan@imperial.ac.uk

only terrestrial crater with an unequivocal and intact peak ring, with the same morphological structure as peak-ring craters on Venus, Mercury, the Moon, and other rocky bodies (*10*–*14*). These seismic data and previous drilling also revealed a terrace zone formed from slump blocks of Mesozoic sedimentary rocks, with the innermost blocks lying directly underneath or close to the outer edge of the peak ring (Fig. 1G). This observation supported the idea that peak rings in larger craters could be created through the interaction of two collapse regimes, with the peak-ring rocks being formed from uplifted crustal basement that had collapsed outward and been emplaced above the collapsed transient cavity rim (*15*).

Numerical shock-physics simulations (Fig. 1) are consistent with the dynamic collapse model in that they reproduce this mode of peak-ring formation as well as other crater features, such as the observed mantle uplift and terrace zone (*16*–*20*). For the simulation in Fig. 1, we used well and geophysical data to construct the preimpact target, which is composed of a 33-km-thick crust with ~3 km of sedimentary rocks above the basement (*21*). We tracked the material that eventually forms the Chicxulub peak ring and show that it originates from mid-crustal basement (8- to 10-km depth) that is shocked to pressures >10 GPa (Fig. 1A). The peak-ring rocks first move outward and upward as the initial transient cavity forms (Fig. 1B), then progress inward to form part of the zone of central uplift (Fig. 1C), and finally collapse outward to be emplaced above collapsed transient cavity rim material composed of sedimentary rocks (Fig. 1C, light gray) that were originally between 0- and 3-km depth (Fig. 1, D to F). The dynamic collapse model therefore predicts that the Chicxulub peak ring is formed from uplifted crystalline basement rocks. Structural data

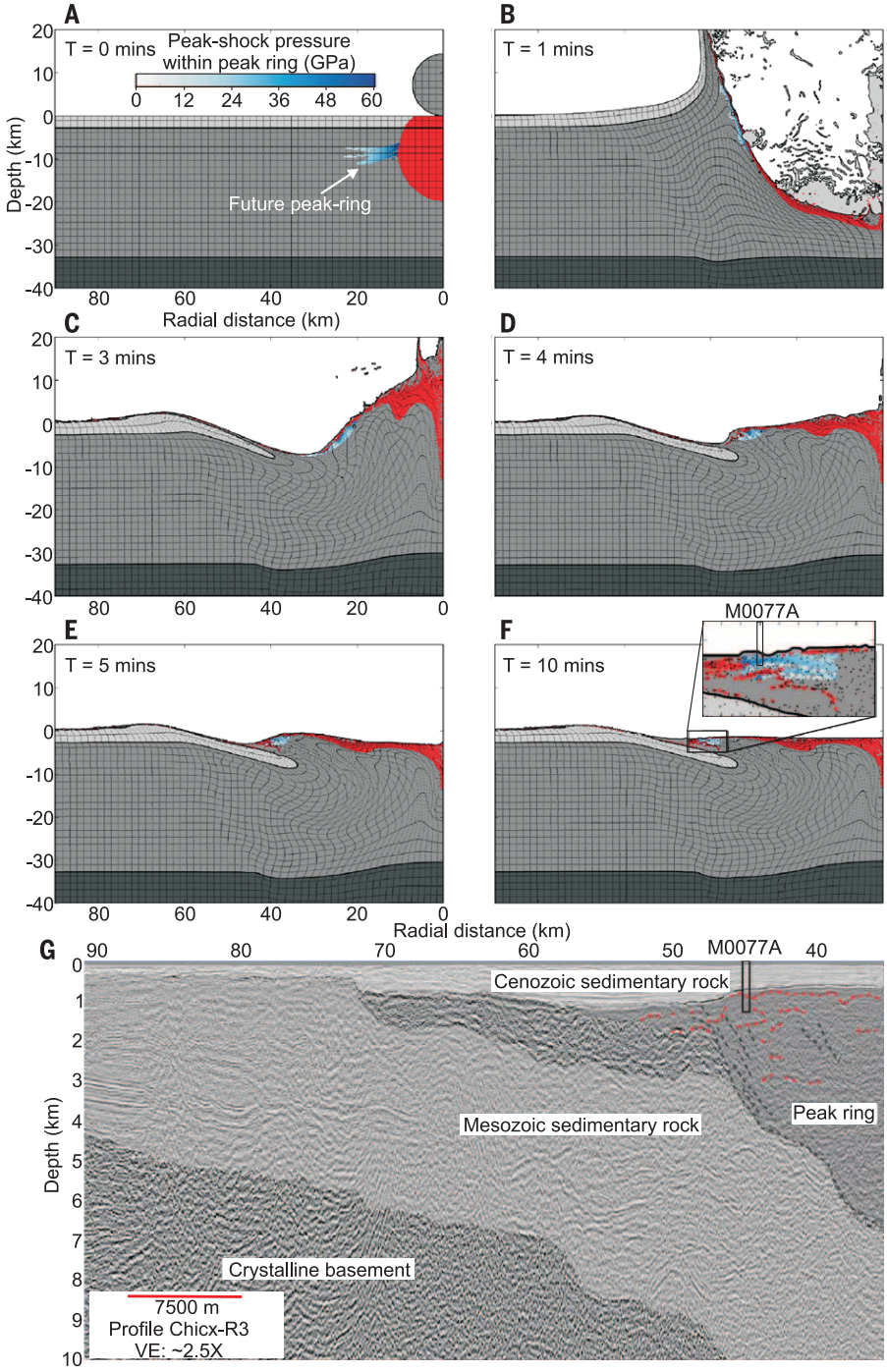


**Fig. 1. Dynamic collapse model of peak-ring formation.** (**A** to **F**) Numerical simulation of the formation of Chicxulub (*18*) at 0, 1, 3, 4, 5, and 10 min tracking the material that eventually forms the peak ring [indicated by the arrow in (A)] and records the maximum shock pressure (blue color scale) to which the peak-ring rocks were exposed during passage of the shock wave. The red color indicates zones of impact melt, for which shock pressures have exceeded 60 GPa. The preimpact target rocks are composed of sediments (light gray), crust (medium gray), and mantle (dark gray). (**G**) Depth-converted, time-migrated seismic profile ChicxR3 (*13*). ChicxR3 is a radial profile (roughly west-northwest) that passes ~200 m from the location of M0077A. For comparison with the simulation, shading is added to match the final crater shown in (F), with light gray for inward-collapsed sedimentary rock, dark gray for peak-ring material, and white for Cenozoic sedimentary cover (*21*). Black dashed lines indicate dipping reflectors at the outer boundary of the peak ring, and red dashed lines mark reflectors that may be consistent with zones of impact melt rock in (F). IODP/ICDP Site M0077A is shown in (G) and placed in a similar position on the magnified inset of the model in (F). VE, vertical exaggeration.

Downloaded from http://science.sciencemag.org/ on November 22, 2016

from a number of exposed terrestrial impact structures supports the idea of dynamic collapse of the central uplift (*9*, *22*–*24*) and that, in larger craters, the peak ring is formed from the interaction of two collapse regimes (*25*). In the simulation, the final crater (Fig. 1F) has the same key features as the upper 10 km of the Chicxulub crater, as imaged on a radial, depth-converted seismic reflection profile (Fig. 1G) (*21*). Specifically, a suite of dipping reflectors mark the boundary between Mesozoic sedimentary rocks and peak-ring rocks, with evidence of discrete melt zones within the peak ring (especially in the upper few hundred meters).

Before drilling, not all of the geophysical data appeared to be consistent with the hypothesis that the Chicxulub peak ring was formed from uplifted crustal basement. Gravity models and seismic refraction data indicated that the peak-ring rocks had a relatively low density (2.2-2.3 g $cm^{-3}$) (*26*) and seismic *P* wave velocity (3.9 to 4.5 km $s^{-1}$) (*27*). The seismic velocity of crustal basement rock outside the central crater is >5.6 km $s^{-1}$ (*28*), making it difficult to explain how crustal rocks within the peak ring could have such a strongly reduced seismic velocity. The inferred physical properties have been explained by the peak ring being formed either from a thickened section of allochthonous impact breccia (*26*), which is a typical cover of crater floors, or from megabreccia (allochthonous breccia with large clasts >10 m), as seen in one of the annular rings at the Popigai impact structure in Siberia (*8*).

In April to May 2016, a joint effort by IODP and ICDP drilled the Chicxulub peak ring offshore during Expedition 364 at site M0077A (21.45° N, 89.95° W) (Fig. 2A). The drill site is located at ~45.6 km radial distance, using a previously selected nominal center for the Chicxulub structure of 21.30° N, 89.54° W (*10*). We recovered core between 505.7 and 1334.7 m below the seafloor (mbsf). We made visual descriptions through a transparent liner, while samples from the end of the core barrel (core catcher) were available for direct inspection. We made 114 smear slides and 51 thin sections from the core-catcher samples, which were taken at regular intervals throughout the drill core. We measured petrophysical properties at the surface using a Multi-Sensor Core Logger (MSCL) and acquired a suite of wireline logging data from the seafloor to the bottom of the hole (*21*).

The upper part of the cored section from 505 to 618 mbsf consists of a sequence of hemipelagic and pelagic Paleogene sediments. We reached the top of the peak ring at 618 mbsf (Fig. 2, A and B). The uppermost peak ring is composed of ~130 m of breccia, with impact melt fragments that overlie clast-poor impact melt rock (Fig. 2B). We encountered felsic basement rocks between 748 and 1334.7 mbsf that were intruded by preimpact mafic and felsic igneous dikes as well as impact-generated dikes. We recovered one particularly thick impact breccia and impact melt rock sequence between 1250 and 1316 mbsf. The entire section of felsic basement exhibits impact-induced deformation on multiple scales. There are many fractures (Fig. 3A), foliated shear zones (Fig. 3B), and cataclasites (Fig. 3C), as well as signs of localized hydrothermal alteration (Fig. 3D). The felsic basement is

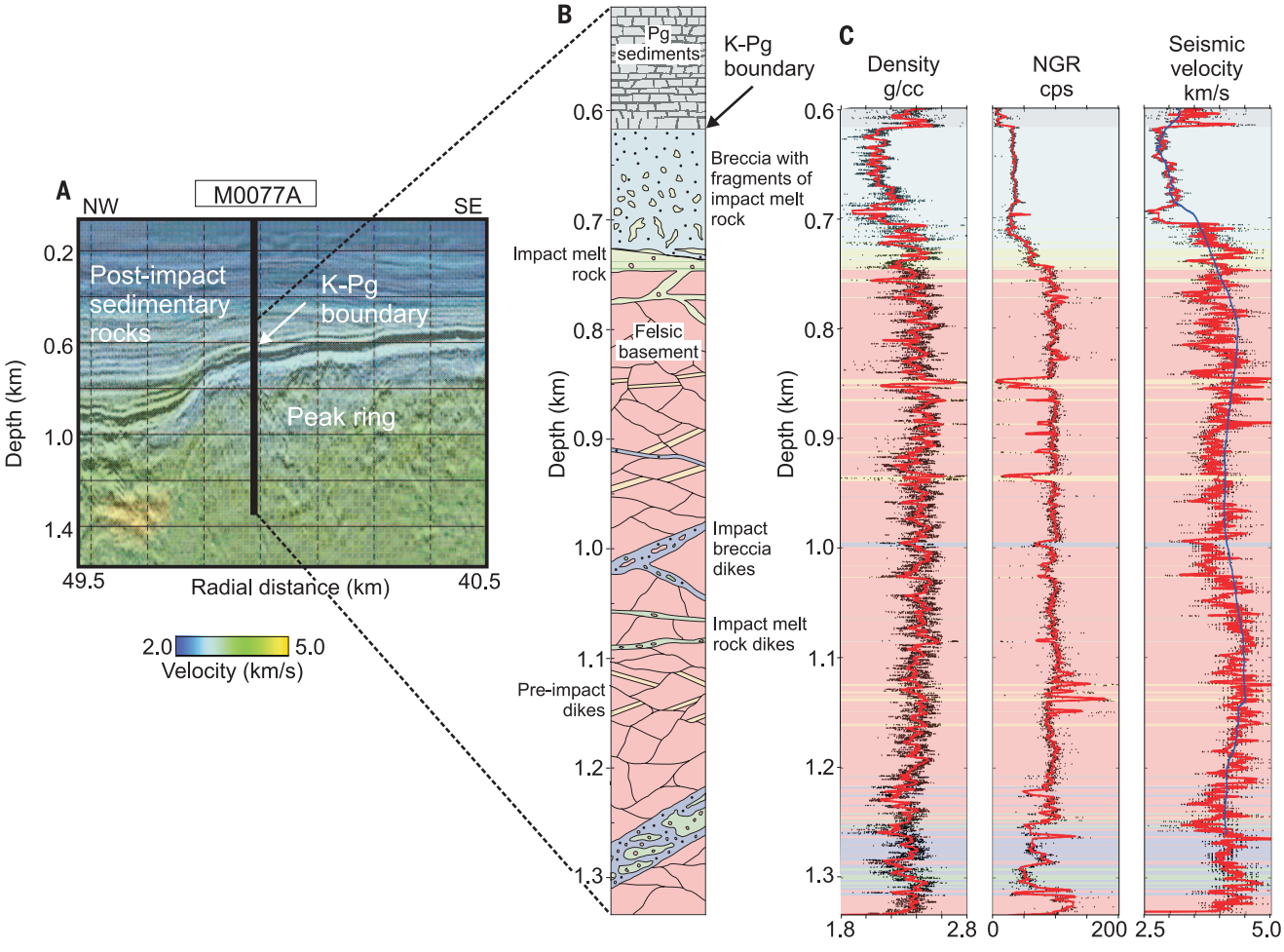


**Fig. 2. IODP/ICDP Expedition 364.** (**A**) Location of Site M0077A on depth-converted seismic reflection profile ChicxR3 (*13*, *14*), overlain by seismic *P* wave velocity (*27*). (**B**) Lithology encountered at Site M0077A from 600 m to total depth, with Paleogene sediments (gray), breccia with impact melt fragments (blue), impact melt rock (green), felsic basement (pink), and preimpact dikes (yellow). In order to indicate a possible difference in origin, the blue and green color within the breccia is slightly lighter than in the dikes. (**C**) Corresponding petrophysical properties: gamma density [grams per cubic centimeter (g/cc)] and NGR [counts per second (cps)] measured on the cores using a MSCL, and seismic *P* wave velocity (km/s) obtained from sonic (red) and VSP (blue) wireline logging data (*21*).

Downloaded from http://science.sciencemag.org/ on November 22, 2016

predominantly a coarse-grained, roughly equigranular granitic rock (Fig. 3E) that is locally aplitic or pegmatitic and, in a few cases, syenitic. The basement rocks in the peak ring differ from basement in nearby drill holes encountered immediately below the Mesozoic sedimentary rocks, suggesting a source of origin that was deeper than 3 km (*21*).

In total, 18 of the smear slides and 17 of the thin sections were prepared from the felsic basement and viewed with an optical microscope. Evidence of shock metamorphism is pervasive throughout the entire basement, with quartz crystals displaying up to four sets of decorated planar deformation features (Fig. 3F). We observed shatter cone fragments in preimpact dikes between 1129 and 1162 mbsf, as well as within the breccia (Fig. 3G). Jointly, the observed shock metamorphic features suggest that the peak ring rocks were subjected to shock pressures of ~10 to 35 GPa (*29*). No clear systematic variation in shock metamorphism was observed with depth. Impact melt, which is formed at shock pressures of >60 GPa, is also a component of the peak ring (Fig. 2B).

The formation of the Chicxulub peak ring from felsic basement (Fig. 2) confirms that crustal rocks lie directly above Mesozoic sedimentary rocks (Fig. 1G), which is consistent with the dynamic collapse model of peak-ring formation (Fig. 1, A to F). On the contrary, the nested melt-cavity hypothesis does not predict this juxtaposition of units at the peak ring. In the numerical simulation shown in Fig. 1, the majority of the rocks that form the peak ring are subjected to peak-shock pressures in the 10 to 35 GPa range, with some zones of melt rock (Fig. 1, red), which is also consistent with our drill-core observations. Conversely, in the nested melt-cavity hypothesis, the peak-ring rocks are expected to be subjected to either higher (*6*) or lower average shock pressures (*7*) than we observed.

We investigated the physical properties of the peak-ring rocks using (i) core-based MSCL natural gamma ray (NGR) and gamma density logs and (ii) downhole sonic logs and vertical seismic profile (VSP) data that determine *P* wave velocity surrounding the borehole (Fig. 2C) (*21*). The drilling data confirm that the peak-ring rocks have low densities and seismic velocities, as suggested by geophysical models (*26*, *27*). The density of the felsic basement varies between 2.10 and 2.55 g $cm^{-3}$, with a mean of 2.41 g $cm^{-3}$, and *P* wave velocities vary between 3.5 and 4.5 km $s^{-1}$, with a mean of 4.1 km $s^{-1}$. These values are unusually low for felsic basement, which typically has densities of >2.6 g $cm^{-3}$ and seismic velocities of >5.5 km $s^{-1}$. We found that samples of the peak ring were variable in strength, locally quite hard, or friable. We also observed distinct variations in the rate of drill bit penetration over short distances (<1 m), with some sections seeming mechanically weaker than others. Fracturing, shock metamorphism, and other factors such as hydrothermal alteration may contribute to the reduction in seismic velocity and density of the felsic basement. Dilation during brittle deformation is observed in central uplifts in other large terrestrial impact craters (*30*, *31*), and dilatancy is predicted to increase fracture porosity in the peak-ring rocks by between 1 and 5% (*32*). Shock metamorphism can also reduce density, as shown in experiments (*33*) and in nature (*34*).

One of the most enigmatic and enduring fundamental unknowns in impact cratering is how bowl-shaped transient cavities collapse to form larger, relatively flat final craters (*1*). To do so requires a temporary reduction in cohesive strength and internal friction (*35*, *36*). In the model shown in Fig. 1, the rocks in the peak ring have moved a large distance (>20 km) during crater formation; hence, these units may well provide clues to the transient weakening mechanism that allows large craters to collapse.

The confirmation of the dynamic collapse model (Fig. 1, A to F) by the Expedition 364 results provides predictions about shock deformation, density reduction, and the kinematics of peak-ring formation. These predictions can be tested and refined through drill-core investigations of physical properties, paleomagnetism, structural data, and shock metamorphism. We anticipate improvement in constraints on impact energy and the sizes of the transient and excavation

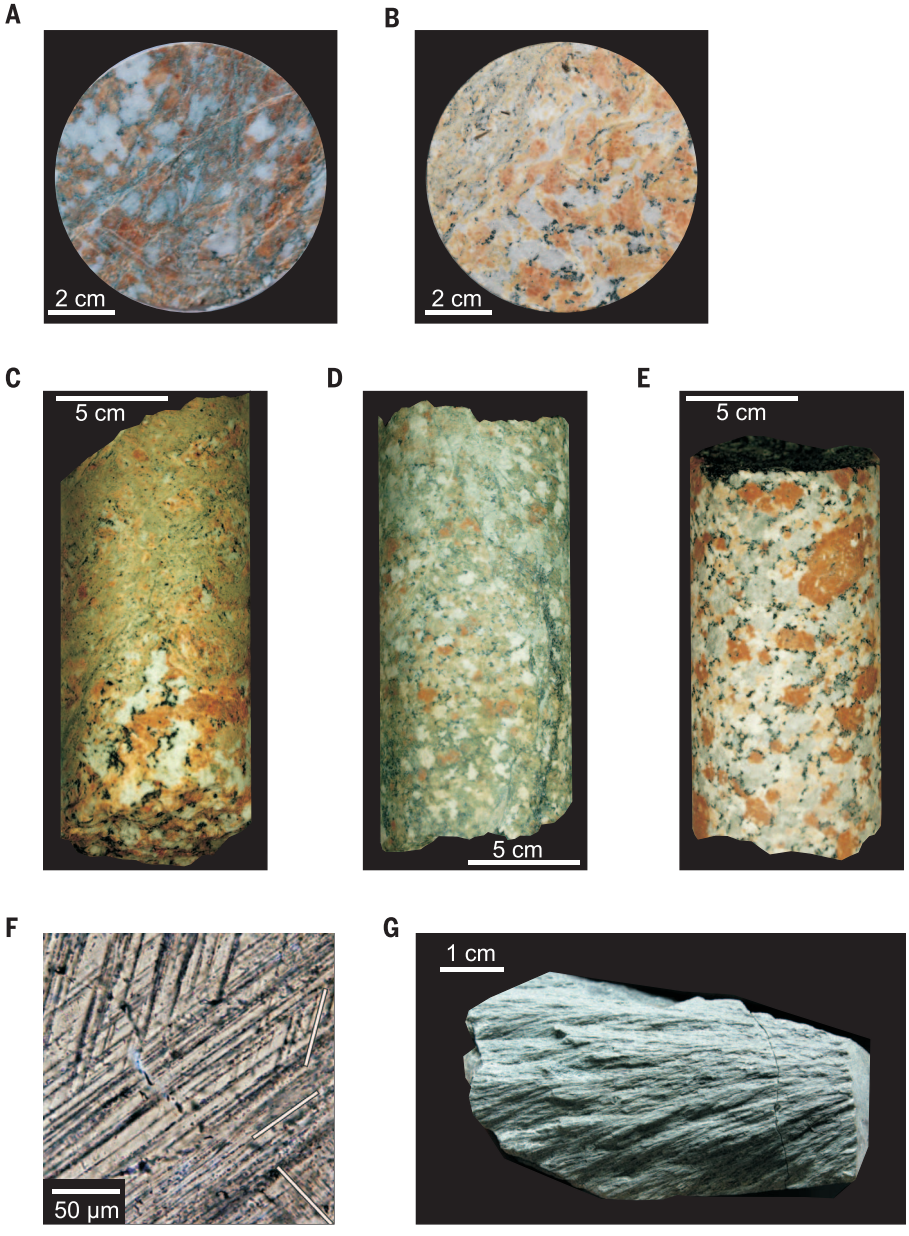


**Fig. 3. Photographs from Expedition 364.** (**A** to **E**) Felsic basement displaying (A) brittle faulting at 749.5 mbsf, (B) a foliated shear zone at 963.5 mbsf, (C) a cataclastic shear zone at 957.4 mbsf, (D) hydrothermal alteration at 930 mbsf, and (E) typical granitic basement with large crystals of red/brown potassium feldspar at 862.3 mbsf. (**F**) Shocked quartz from 826.9 mbsf in cross-polarized light, displaying three sets of planar deformation features (indicated by the solid white bars). (**G**) Shatter cone fragment from an amphibolite clast in the breccia at 708.5 mbsf.

Downloaded from http://science.sciencemag.org/ on November 22, 2016

cavities. As a consequence, the volumes of environmental pollutants released by the K-Pg impact will be better constrained, together with its role in causing the end-Cretaceous mass extinction (*37*). Because the deep subsurface biosphere is influenced by fracturing and mineralogical changes in host rocks induced by shock and post-impact hydrothermal activity, understanding how impact craters are formed and modify the environment will advance our understanding of deep subsurface life on Earth and potential habitability elsewhere.

The validation of the dynamic collapse model also strengthens confidence in simulations of large-crater formation on other planetary bodies. These simulations suggest that as crater size increases, the rocks that form peak rings originate from increasingly deeper depths (*38*). This relationship means that the composition of the peak-ring lithology provides information on the crustal composition and layering of planetary bodies and may be used to verify formation models, such as for the Moon (*6*, *38*, *39*). One of the principal observations used to support a version of the nested melt-cavity hypothesis in Baker *et al*. (*7*) is that peak rings within basins of all sizes on the Moon contain abundant crystalline anorthosite and must, therefore, originate from the upper crust, if indeed the lower crust is noritic. Our results suggest a deeper origin for peak-ring rocks and thus are more in accordance with alternative models for the composition of a heterogeneous lunar crust in which an anorthositic layer extends regionally to deeper depths (*40*, *41*). The dynamic collapse model and Expedition 364 results predict density reduction through shock and shear fracturing within the uplifted material (*33*), which is consistent with the recent Gravity Recovery and Interior Laboratory (GRAIL) mission results of a highly porous lunar crust (*42*) and the presence of mid-crustal rocks juxtaposed by shear zones in the peak ring at the Schrödinger crater (*38*). This linkage between deformation and overturning of material at the scales >10 km implies that over an extended period of time, impact cratering greatly increases the porosity of the subsurface and causes vertical fluxes of materials within the crust.

## REFERENCES AND NOTES


1. H. J. Melosh, *Impact Cratering* (Oxford Univ. Press, 1989).
2. W. S. Hale, R. A. F. Grieve, *J. Geophys. Res.* **87** (S01), A65 (1982).
3. J. B. Murray, *Moon Planets* **22**, 269–291 (1980).
4. J. S. Alexopoulos, W. B. McKinnon, *Spec. Pap. Geol. Soc. Am.* **293**, 29 (1994).
5. M. J. Cintala, R. A. F. Grieve, *Meteorit. Planet. Sci.* **33**, 889–912 (1998).
6. J. W. Head, *Geophys. Res. Lett.* **37**, L02203 (2010).
7. D. M. H. Baker, J. W. Head, G. S. Collins, R. W. K. Potter, *Icarus* **273**, 146 (2016).
8. P. M. Vermeesch, J. V. Morgan, *Meteorit. Planet. Sci.* **39**, 1019–1034 (2004).
9. G. R. Osinski, J. G. Spray, *Meteorit. Planet. Sci.* **40**, 1813–1834 (2005).
10. A. Camargo-Zanoguera, G. Suarez-Reynoso, *Bol. Asoc. Mex. Geof. Expl.* **34**, 1 (1994).
11. J. V. Morgan *et al*., *Nature* **390**, 471 (1997).
12. A. R. Hildebrand *et al*., *Spec. Publ. Geol. Soc. Lond.* **140**, 155 (1998).
13. S. P. S. Gulick *et al*., *Nat. Geosci.* **1**, 131–135 (2008).
14. S. P. S. Gulick *et al*., *Rev. Geophys.* **51**, 31–52 (2013).
15. J. Brittan, J. Morgan, M. Warner, L. Marin, *Spec. Pap. Geol. Soc. Am.* **339**, 269 (1999).
16. J. V. Morgan, M. R. Warner, G. S. Collins, H. J. Melosh, G. L. Christeson, *Earth Planet. Sci. Lett.* **183**, 347–354 (2000).
17. B. Ivanov, *Sol. Syst. Res.* **39**, 381–409 (2005).
18. G. S. Collins *et al*., *Earth Planet. Sci. Lett.* **270**, 221–230 (2008).
19. G. L. Christeson *et al*., *Earth Planet. Sci. Lett.* **284**, 249–257 (2009).
20. L.E. Senft, S. T. Stewart, *Earth Planet. Sci. Lett.* **287**, 471–482 (2009).
21. Materials and methods are available as supplementary materials on *Science* Online.
22. T. Kenkmann, I. von Dalwigk, *Meteorit. Planet. Sci.* **35**, 1189–1201 (2000).
23. T. Kenkmann, G. S. Collins, K. Wünnemann, The modification stage of impact crater formation, *Impact Cratering* (Wiley-Blackwell, 2013).
24. A. Jahn, U. Riller, *Spec. Pap. Geol. Soc. Am.* **518**, 85–97 (2015).
25. R. A. F. Grieve, W. U. Reimold, J. Morgan, U. Riller, M. Pilkington, *Meteorit. Planet. Sci.* **43**, 855–882 (2008).
26. M. Pilkington, A. Hildebrand, C. Ortiz-Aleman, *J. Geophys. Res.* **99** (E6), 13147 (1994).
27. J. V. Morgan *et al*., *J. Geophys. Res.* **116** (B6), B06303 (2011).
28. G. Christeson, Y. Nakamura, R. T. Buffler, J. Morgan, M. Warner, *J. Geophys. Res.* **106** (B10), 21751–21769 (2001).
29. R. A. F. Grieve, F. Langenhorst, D. Stöffler, *Meteorit. Planet. Sci.* **31**, 6–35 (1996).
30. D. Lieger, U. Riller, R. L. Gibson, *Earth Planet. Sci. Lett.* **279**, 53–64 (2009).
31. U. Riller, D. Lieger, R. L. Gibson, R. A. F. Grieve, D. Stöffler, *Geology* **38**, 619–622 (2010).
32. G. S. Collins, *J. Geophys. Res.* **119**, 2600–2619 (2014).
33. F. Langenhorst, A. Deutsch, *Earth Planet. Sci. Lett.* **125**, 407–420 (1994).
34. A. C. Singleton, G. R. Osinski, P. J. A. McCausland, D. E. Moser, *Meteorit. Planet. Sci.* **46**, 1774–1786 (2011).
35. H. J. Melosh, *Impact and Explosion Cratering* (Pergamon Press, 1977).
36. W. B. McKinnon, *Lunar Planet. Sci. Conf. Proc.* **9**, 3965 (1978).
37. P. R. Renne *et al*., *Science* **339**, 684–687 (2013).
38. D. A. Kring, G. Y. Kramer, G. S. Collins, *Nat. Commun.* 10.1038/ncomms13161 (2016).
39. G. Y. Kramer, D. A. Kring, A. L. Nahm, C. M. Pieters, *Icarus* **223**, 131–148 (2013).
40. S. Yamamoto *et al*., *Geophys. Res. Lett.* **39**, L13201 (2012).
41. T. Arai, H. Takeda, A. Yamaguchi, M. Ohtake, *Earth Planets Space* **60**, 433–444 (2008).
42. M. A. Wieczorek *et al*., *Science* **339**, 671–675 (2013).


## ACKNOWLEDGMENTS

This research used samples and data provided by IODP. Samples can be requested at http://web.iodp.tamu.edu/sdrm after the end of the moratorium on 19 October 2017. Expedition 364 was jointly funded by the European Consortium for Ocean Research Drilling (ECORD) and the International Continental Scientific Program, with contributions and logistical support from the Yucatan State Government and Universidad Nacional Autónoma de México (UNAM). G.S.C. was funded by UK Science and Technology Facilities Council grant ST/N000803/1. S.P.S.G. acknowledges his Fellowship at the Hanse-Wissenschaftkolleg, Germany. This is UTIG Contribution #3018.

## SUPPLEMENTARY MATERIALS

www.sciencemag.org/content/354/6314/878/suppl/DC1
Material and Methods
Table S1
References (*43*–*63*)

27 July 2016; accepted 14 October 2016
10.1126/science.aah6561

ACTIVE MATTER

# Command of active matter by topological defects and patterns

**Chenhui Peng,* Taras Turiv,* Yubing Guo, Qi-Huo Wei, Oleg D. Lavrentovich†**

**Self-propelled bacteria are marvels of nature with a potential to power dynamic materials and microsystems of the future. The challenge lies in commanding their chaotic behavior. By dispersing swimming *Bacillus subtilis* in a liquid crystalline environment with spatially varying orientation of the anisotropy axis, we demonstrate control over the distribution of bacterial concentration, as well as the geometry and polarity of their trajectories. Bacteria recognize subtle differences in liquid crystal deformations, engaging in bipolar swimming in regions of pure splay and bend but switching to unipolar swimming in mixed splay-bend regions. They differentiate topological defects, heading toward defects of positive topological charge and avoiding negative charges. Sensitivity of bacteria to preimposed orientational patterns represents a previously unknown facet of the interplay between hydrodynamics and topology of active matter.**

Swimming rodlike bacteria such as *Bacillus subtilis* show a distinct ability to sense and navigate their environment in search of nutrients. They propel in viscous fluids by rotating appendages called flagella, which are composed of bundles of thin helical filaments. Flagella can also steer the bacterium in a new direction by momentarily untangling the filaments and causing the bacterium to tumble (*1*). Alternating runs and tumbles of bacteria form a random trajectory reminiscent of a Brownian walk. The flows of the surrounding fluid created by bacteria cause their interactions and collective dynamics (*2*). Locally, the bacteria swim parallel to each other but globally this orientational order is unstable, showing seemingly chaotic patterns in both alignment of bacterial bodies and their velocities (*3*, *4*). Similar out-of-equilibrium patterns are met in many other systems, universally called "active matter" and defined as collections of interacting self-propelled particles, each converting internally stored or ambient energy into a systematic movement and generating coordinated collective motion (*5*–*7*). To extract useful work from the

Liquid Crystal Institute and Chemical Physics Interdisciplinary Program, Kent State University, Kent, OH 44242, USA.
*These authors contributed equally to this work. **†Corresponding author. Email: olavrent@kent.edu**

Downloaded from http://science.sciencemag.org/ on November 22, 2016

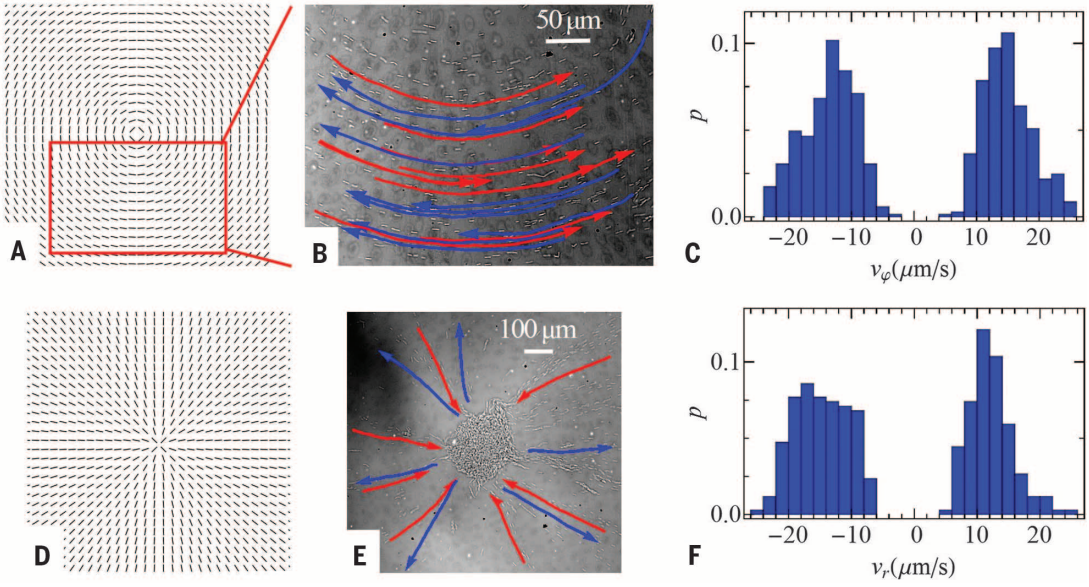


**Fig. 1. Bipolar locomotion of bacteria in patterns of pure bend and pure splay.** (**A**) Director pattern of a pure bend. (**B**) Circular trajectories of bacteria in the bend region. (**C**) Probability distribution ($p$) of azimuthal velocity ($v_\varphi$) of bacteria in the bend pattern. (**D**) Director field of pure splay. (**E**) Radial trajectories of bacteria moving toward and away from the center. (**F**) Probability distribution of radial velocities ($v_r$) of bacteria swimming in the splay pattern.

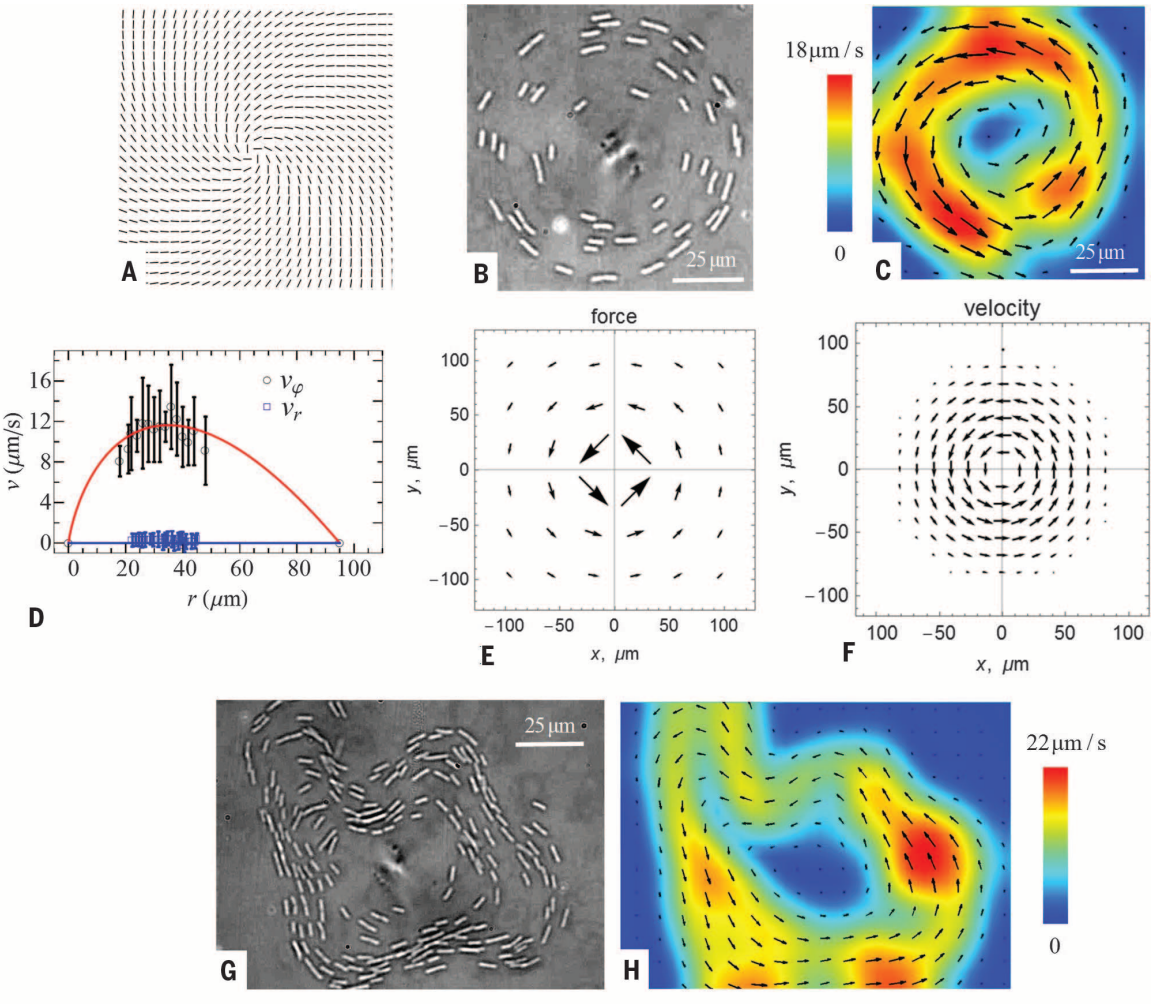


**Fig. 2. Unipolar circular flow of bacteria around a spiraling vortex.** (**A**) Mixed splay-bend director deformation of the vortex. (**B**) Circular bacterial swarm enclosing the vortex center. (**C**) Map of bacterial velocities. (**D**) Radial dependence of the azimuthal and radial velocities of the bacteria. Solid curves are predictions from Eq. 2. Error bars indicate SD taken for 40 bacteria. (**E**) Active force calculated from Eq. 1. (**F**) Velocity map calculated from Eq. 2. (**G**) Undulation instability of the circular swarm. (**H**) Velocity map in the undulating swarm.

chaotic dynamics of bacteria (or any other active matter) (*8*, *9*), one needs to learn how to control the spatial distribution of particles, as well as the geometry and polarity of their trajectories.

Placing swimming bacteria in an anisotropic environment of a nontoxic liquid crystal (*10*–*12*) might be one of the strategies to command active matter. Liquid crystals are anisotropic fluids, with a well-defined nonpolar axis of anisotropy called the director: $\hat{\mathbf{n}} \equiv -\hat{\mathbf{n}}$. A sphere moving in a liquid crystal parallel to the director enjoys the lowest viscous resistance (*13*, *14*). It has already been demonstrated

Downloaded from http://science.sciencemag.org/ on November 22, 2016

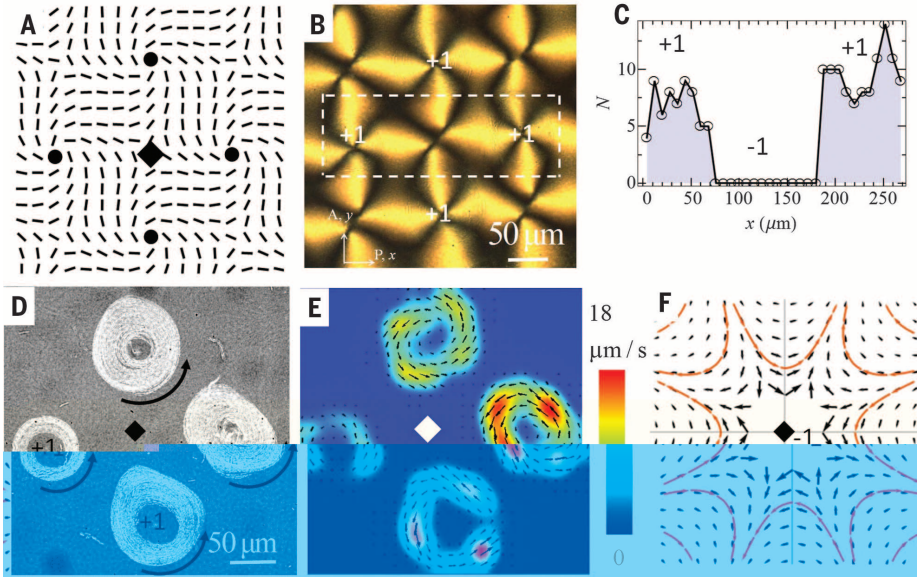


**Fig. 3. Unipolar circular flows of bacteria in the periodic pattern of defects.** (**A**) Director pattern with +1 (cores marked by circles) and –1 defects (one core marked by a diamond). (**B**) Polarizing optical microscopy texture of the pattern. A, analyzer; P, polarizer. (**C**) Spatial modulation of the number of bacteria (*N*) within the rectangular region in (B). (**D**) Counterclockwise trajectories of bacteria around four +1 spiraling vortices. (**E**) Map of corresponding velocities. (**F**) Active force calculated from Eq. 1 for a –1 defect.

that the liquid crystal director, either uniform (*10*–*12*) or spatially distorted (*11*, *15*), serves as an easy swimming pathway for bacteria. In particular, Zhou *et al.* (*11*) demonstrated curvilinear trajectories of bacteria around obstacles in a liquid crystal, while Mushenheim *et al.* (*15*) rectified the bacterial flows by using nematic cells with the so-called hybrid alignment at the opposite bounding plates. Liquid crystals were also used by Guillamat *et al.* (*16*) as an adjacent layer to an aqueous dispersion of active microtubules to align their active flows. Theoretical models of active systems with orientational order predict that a nonuniform director might cause polar flows (*17*, *18*). In particular, Green, Toner, and Vitelli (GTV) suggested that unidirectional flows in active nematics can be triggered by mixed splay-bend director deformations (*18*).

In this work, we produce spatially varying patterns of a liquid crystal anisotropic environment for swimming bacteria through controlled surface alignment of the director. The patterns are designed with well-defined deformations, either pure bend, pure splay, or mixed splay-bend. These preimposed patterns command the self-propelled bacteria dispersed in such a liquid crystal in a number of ways by controlling (i) geometry of trajectories, (ii) polarity of locomotion, and (iii) spatial distribution of bacterial concentration. Bacteria distinguish subtle differences in director deformations that occur over length scales much larger than their bodies. Namely, their swimming is bipolar in the pure-bend and pure-splay regions but unipolar in the mixed splay-bend case, matching the predictions of the GTV model (*18*). The bacteria also sense the topological charges of defects in the patterns, moving closer to defects of a positive topological charge and avoiding negative charges.

The patterned anisotropic environment represents thin (thickness $d$ = 5 μm) slabs of a lyotropic chromonic liquid crystal (LCLC) confined between two flat glass plates. The LCLC is an aqueous dispersion of nontoxic disodium chromoglycate (*19*). The bounding plates are pretreated to impose the desired surface alignment of the adjacent LCLC (*20*–*22*). First, they are coated with a layer of photosensitive molecules. This layer is then irradiated with a light beam of linear polarization that changes from point to point, forcing the photosensitive molecules to align in accordance with local polarization. The photoaligned surface molecules align the director of the LCLC. The patterns are the same on the top and bottom plates so that the director is two-dimensional (2D).

In a homogeneously aligned liquid crystal, bacteria swim along $\hat{\mathbf{n}}$ in a bipolar fashion, half to the left and half to the right, so that there is no net flow (*11*, *12*, *15*). In the patterned cells with a pure bend (Fig. 1A) or a pure splay (Fig. 1D), the bacterial locomotion is very similar to the uniform case, being bipolar and parallel to the local $\hat{\mathbf{n}}$ (Fig. 1, B and E, and movies S1 to S3). When the number of bacteria in the radial splay configuration is low, they enter and leave the central region freely (movie S2), but if it is high, they accumulate into a concentrated immobilized

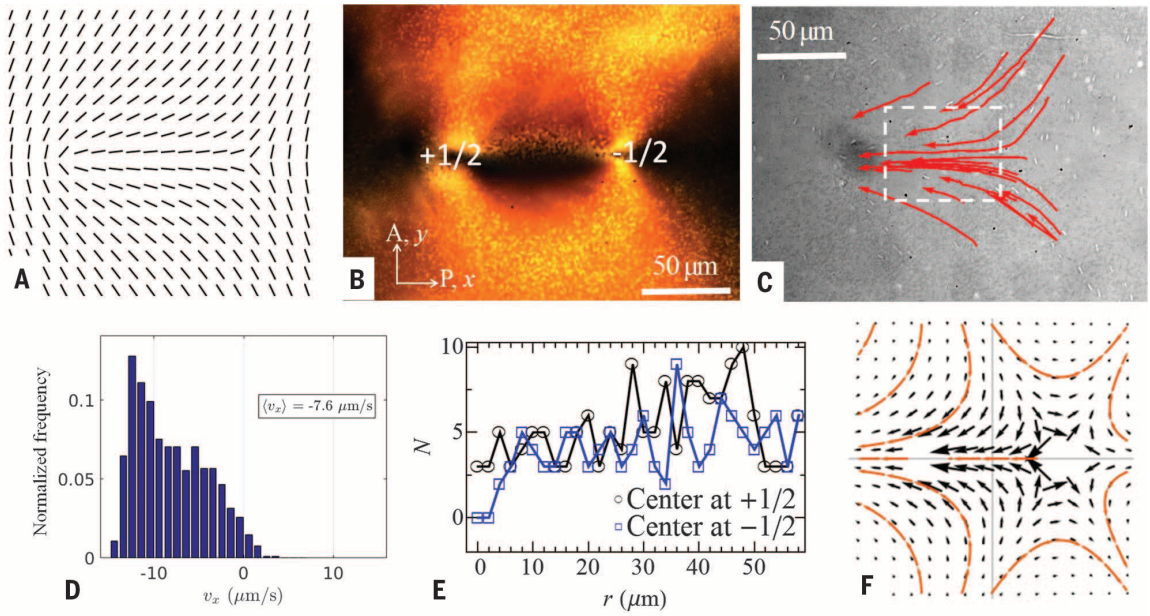


**Fig. 4. Motion of bacteria controlled by a pair of semi-integer defects.** (**A**) Predesigned director field. (**B**) Polarizing microscope texture of the defect pair. (**C**) Trajectories of bacteria moving predominantly from the –½ defect toward the +½ defect. (**D**) Polar character of velocities within the rectangular area shown in (C). (**E**) Concentration of bacteria versus radial distance from the center of the +½ and –½ defects. (**F**) Active force calculated for the pair, using Eq. 1.

Downloaded from http://science.sciencemag.org/ on November 22, 2016

disk-like colony (Fig. 1E and movie S3). In contrast, centers of circular bend remain bacteria-free (Fig. 1B and movie S1).

The bipolar swimming changes to unipolar when the bacteria encounter a pattern in the form of a spiraling vortex with mixed splay and bend (Fig. 2A and fig. S1). At any point, the local director $\hat{\mathbf{n}}$ makes an angle 45° with the radius-vector $\hat{\mathbf{r}}$, spiraling clockwise as one moves away from the center. The vortex is chiral, as it cannot be superimposed on its mirror image. The clockwise spiraling vortex forces counterclockwise circumnavigation of bacteria, producing a net flow (Fig. 2C and movie S4). The unipolar locomotion is along circular trajectories—that is, at 45° with respect to the surface-imposed $\hat{\mathbf{n}}$ (Fig. 2B)—which is in contrast to the cases of uniform, splayed, and bent director fields, where swimming is along $\hat{\mathbf{n}} \equiv -\hat{\mathbf{n}}$ (Fig. 1).

The spiraling vortex also controls bacterial concentration by attracting the bacteria to a circular annulus of a finite width. For example, a swarm of 50 bacteria occupies a region between radius $r \approx 15$ and 50 μm (Fig. 2B). The azimuthal velocity $v_\varphi$ within the band is maximized at $r \approx 35$ μm (Fig. 2, C and D). As the number $N$ of bacteria in the swarm increases (through the attraction of bacteria from outside regions) above a threshold of about $N_c = 110$, the circular trajectories start to undulate (Fig. 2, G and H). The undulations are similar to the periodic bend instability described for highly concentrated bacterial dispersions in a uniformly aligned LCLC (*11*).

Each spiraling vortex is a point defect of a topological charge $m = 1$ (*23*). The charge $m$ is defined as the number of times the director rotates by $2\pi$ when one circumnavigates the defect (*23*); its sign reflects the direction of rotation with respect to the direction of circumnavigation. A periodic pattern of spiraling vortices with $m = 1$ and point defects with $m = -1$ is shown in Figure 3, A and B. The bacteria gather into circulating swarms around the $m = 1$ cores, all of which exhibit the same counterclockwise flow (Fig. 3, D and E, and movie S5).

Unipolar locomotion can also be designed as linear rather than circular. A defect pair with $m_1 = +½$ and $m_2 = -½$ is shown in Figure 4, A and B. The bacteria prefer to swim from the −½ defect toward the +½ defect rather than in the opposite direction (Fig. 4, C and D, and movie S6). The +½ defect is enriched with the bacteria, whereas the −½ defect is deprived of them (Fig. 4E).

The bacterial dynamics in a patterned LCLC shows a marked departure from the simple bipolar "swimming along $\hat{\mathbf{n}}$" behavior: (i) Bacteria can swim at some angle to the surface-imposed director (Figs. 2B and 3D). (ii) The locomotion becomes unipolar with the net flows of circular (Figs. 2, B and C, and 3, D and E) and linear (Fig. 4, C and D) type. Equally important is that (iii) the bacterial concentration varies in space substantially, being high around defects of positive topological charge and low at negative defects (Figs. 3C and 4E).

The emergence of unipolar locomotion in mixed splay-bend regions (Figs. 2 to 4) is in qualitative agreement with the GTV model (*18*), despite that fact that the model deals with an incompressible system whereas the experiment shows variation of bacterial concentration across the patterns. A combination of splay $\nabla\cdot\hat{\mathbf{n}}$ and bend $\hat{\mathbf{n}}\times\nabla\times\hat{\mathbf{n}}$ that satisfies the condition $\nabla\times[\hat{\mathbf{n}}\nabla\cdot\hat{\mathbf{n}}-\hat{\mathbf{n}}\times(\nabla\times\hat{\mathbf{n}})]\neq 0$ is predicted to produce a local guiding force (*18*)

$$\mathbf{f} = \alpha[\hat{\mathbf{n}}\nabla\cdot\hat{\mathbf{n}} - \hat{\mathbf{n}}\times(\nabla\times\hat{\mathbf{n}})] \qquad (1)$$

where $\alpha = c\sigma$ is the activity, defined by the concentration $c$ of bacteria and the force dipole $\sigma$ exerted by each swimmer on the fluid. For *B. subtilis*, $\sigma$ is negative and estimated to be $\sigma \approx -1$ pN·μm in an aqueous environment (*24*). Although $c$ varies across the patterns, we assume it is constant for a qualitative consideration. Eq. 1 applied to the clockwise spiral vortex in Fig. 2A, $\hat{\mathbf{n}} = \{\cos\theta, \sin\theta\}$, where $\theta = \tan^{-1}y/x - \pi/4$ ($x$ and $y$ are Cartesian coordinates), yields $\mathbf{f} = \{0, -\alpha/r\}$ [written in polar coordinates $(r, \varphi)$: $r = \sqrt{x^2+y^2}$] (Fig. 2E). The flow velocity $\mathbf{v} = \{v_r, v_\varphi\}$ is obtained by balancing f with the viscous drag $\eta\nabla^2\mathbf{v}$

$$\mathbf{v} = \left\{0, \frac{\alpha r}{2\eta}\log\left(\frac{r}{r_0}\right)\right\} \qquad (2)$$

where $r_0$ is the distance at which the velocity vanishes, and $\eta$ is the effective viscosity. When $\alpha < 0$, Eq. 2 predicts a counterclockwise circulation of bacteria around a clockwise vortex (Fig. 2F), which is in line with our observations (Figs. 2, B and C, and 3, D and E). The velocity field (Eq. 2) is similar to the velocity around an active gel vortex (*25*) and yields a nonmonotonous $v_\varphi(r)$, with a maximum $v_{max} = -\alpha r_0/2e\eta$ at $r = r_0/e$, matching qualitatively the experiment, in which $r_0/e = 35$ μm and $v_{max} \approx 12$ μm/s (Fig. 2D). The activity/viscosity ratio estimated from Eq. 2 is $\alpha/\eta \approx -0.7\ s^{-1}$.

The force (Eq. 1) calculated for the pair in Fig. 4F is directed from the −½ defect toward the ½ defect, reflecting the observed unipolar swimming from −½ to +½ in Fig. 4C. The force around the −1 defect deflects away from its center (Fig. 3F), again in a qualitative agreement with the observed bacterial avoidance of negative topological charges. For pure splay and pure bend 2D samples, the GTV model (*18*) predicts $\mathbf{f} = 0$ and, thus, no net flows, as in Fig. 1, which shows only bipolar swimming. A more detailed analysis should account for spatial variations of concentration and activity, potential flow-induced realignment of the director, anisotropy, and variations of effective viscosities.

The unipolar locomotion of bacteria is observed at relatively low concentration and, thus, low activity. For example, in the circulating swarm in Figs. 2B and 3D, $c \approx 1.4 \times 10^{15}\ m^{-3}$. This concentration is well below the critical threshold of instabilities described by Zhou *et al.* (*11*) for highly concentrated bacterial dispersions that exhibit undulations and topological turbulence. As the circular swarms attract more bacteria, increasing $c$ by a factor of 2 or 3, the trajectories start to develop bend undulations (Fig. 2G), signaling that the activity overcomes the stabilizing liquid crystal elasticity (*11*).

To summarize, we demonstrate an approach to control active matter through a patterned anisotropic environment. Self-propelled bacteria sense the imposed patterns of orientational order by adapting their spatial distribution, heading toward topological defects of positive charge and avoiding negative charges, and switching from bipolar locomotion in splayed and bent environments to unipolar locomotion in mixed splay-bend regions. The demonstrated command of active matter by a spatially varying anisotropic environment opens opportunities for designing out-of-equilibrium spatiotemporal behavior, with the goal of developing new dynamic materials and systems.

## REFERENCES AND NOTES


1. E. Lauga, *Annu. Rev. Fluid Mech.* **48**, 105–130 (2016).
2. D. L. Koch, G. Subramanian, *Annu. Rev. Fluid Mech.* **43**, 637–659 (2011).
3. C. Dombrowski, L. Cisneros, S. Chatkaew, R. E. Goldstein, J. O. Kessler, *Phys. Rev. Lett.* **93**, 098103 (2004).
4. A. Sokolov, I. S. Aranson, J. O. Kessler, R. E. Goldstein, *Phys. Rev. Lett.* **98**, 158102 (2007).
5. T. Vicsek, A. Czirók, E. Ben-Jacob, I. Cohen, O. Shochet, *Phys. Rev. Lett.* **75**, 1226–1229 (1995).
6. J. Toner, Y. H. Tu, S. Ramaswamy, *Ann. Phys.* **318**, 170–244 (2005).
7. D. Nishiguchi, K. H. Nagai, H. Chaté, M. Sano, https://arxiv.org/abs/1604.04247 (2016).
8. A. Sokolov, M. M. Apodaca, B. A. Grzybowski, I. S. Aranson, *Proc. Natl. Acad. Sci. U.S.A.* **107**, 969–974 (2010).
9. R. Di Leonardo *et al.*, *Proc. Natl. Acad. Sci. U.S.A.* **107**, 9541–9545 (2010).
10. A. Kumar, T. Galstian, S. K. Pattanayek, S. Rainville, *Mol. Cryst. Liq. Cryst.* **574**, 33–39 (2013).
11. S. Zhou, A. Sokolov, O. D. Lavrentovich, I. S. Aranson, *Proc. Natl. Acad. Sci. U.S.A.* **111**, 1265–1270 (2014).
12. P. C. Mushenheim, R. R. Trivedi, H. H. Tuson, D. B. Weibel, N. L. Abbott, *Soft Matter* **10**, 88–95 (2014).
13. J. C. Loudet, P. Hanusse, P. Poulin, *Science* **306**, 1525 (2004).
14. T. Turiv *et al.*, *Science* **342**, 1351–1354 (2013).
15. P. C. Mushenheim *et al.*, *Soft Matter* **11**, 6821–6831 (2015).
16. P. Guillamat, J. Ignés-Mullol, F. Sagués, *Proc. Natl. Acad. Sci. U.S.A.* **113**, 5498–5502 (2016).
17. R. Voituriez, J. F. Joanny, J. Prost, *Europhys. Lett.* **70**, 404–410 (2005).
18. R. Green, J. Toner, V. Vitelli, https://arxiv.org/abs/1602.00561 (2016).
19. C. J. Woolverton, E. Gustely, L. Li, O. D. Lavrentovich, *Liq. Cryst.* **32**, 417–423 (2005).
20. See supplementary materials on *Science* Online.
21. Y. Guo *et al.*, *Adv. Mater.* **28**, 2353–2358 (2016).
22. C. Peng *et al.*, *Phys. Rev. E* **92**, 052502 (2015).
23. M. Kleman, O. D. Lavrentovich, *Soft Matter Physics: An Introduction* (Springer, 2003).
24. K. Drescher, J. Dunkel, L. H. Cisneros, S. Ganguly, R. E. Goldstein, *Proc. Natl. Acad. Sci. U.S.A.* **108**, 10940–10945 (2011).
25. K. Kruse, J. F. Joanny, F. Jülicher, J. Prost, K. Sekimoto, *Phys. Rev. Lett.* **92**, 078101 (2004).


## ACKNOWLEDGMENTS


We thank S. Zhou and G. Cukrov for help with experiments and I. Aronson and A. Sokolov for discussions. This work was supported by NSF grants DMR-1507637 (design and development of patterned alignment), DMS-1434185 (analysis of dynamics), and CMMI-1436565 (design and fabrication of metamasks). C.P. and T.T. performed the experiments. O.D.L. conceived and directed the research. Y.G. and Q.-H.W. provided the metamasks. C.P., T.T., and O.D.L. analyzed the data. All authors participated in discussing and writing the manuscript.


## SUPPLEMENTARY MATERIALS

www.sciencemag.org/content/354/6314/882/suppl/DC1
Materials and Methods
Supplementary Text
Figs. S1 and S2
References (*26–29*)
Movies S1 to S6


1 August 2016; accepted 21 October 2016
10.1126/science.aah6936


Downloaded from http://science.sciencemag.org/ on November 22, 2016

PLANT SCIENCE

# Phytochromes function as thermosensors in *Arabidopsis*

Jae-Hoon Jung,[1]* Mirela Domijan,[1]* Cornelia Klose,[2]* Surojit Biswas,[1]*† Daphne Ezer,[1]* Mingjun Gao,[1] Asif Khan Khattak,[3]‡ Mathew S. Box,[1] Varodom Charoensawan,[1]§ Sandra Cortijo,[1] Manoj Kumar,[1] Alastair Grant,[3] James C. W. Locke,[1,4] Eberhard Schäfer,[2,5] Katja E. Jaeger,[1] Philip A. Wigge[1,6]‖

**Plants are responsive to temperature, and some species can distinguish differences of 1°C. In *Arabidopsis*, warmer temperature accelerates flowering and increases elongation growth (thermomorphogenesis). However, the mechanisms of temperature perception are largely unknown. We describe a major thermosensory role for the phytochromes (red light receptors) during the night. Phytochrome null plants display a constitutive warm-temperature response, and consistent with this, we show in this background that the warm-temperature transcriptome becomes derepressed at low temperatures. We found that phytochrome B (phyB) directly associates with the promoters of key target genes in a temperature-dependent manner. The rate of phyB inactivation is proportional to temperature in the dark, enabling phytochromes to function as thermal timers that integrate temperature information over the course of the night.**

Plant development is responsive to temperature, and the phenology and distribution of crops and wild plants have already altered in response to climate change (*1*, *2*). In *Arabidopsis thaliana*, warm temperature–mediated elongation growth and flowering are dependent on the basic helix-loop-helix transcription factors PHYTOCHROME INTERACTING FACTOR4 (PIF4) and PIF5 (*3*–*6*). Growth at 27°C reduces the activity of the evening complex (EC), resulting in greater *PIF4* transcription. The EC is a transcriptional repressor made up of the proteins EARLY FLOWERING3 (ELF3), ELF4, and LUX ARRHYTHMO (LUX) (*7*–*9*). To test whether the EC is also required for hypocotyl elongation responses below 22°C, we examined the behavior of *elf3-1* and *lux-4* at 12° and 17°C. Hypocotyl elongation in *elf3-1* and *lux-4* is largely suppressed at lower temperatures (Fig. 1, A and B), which is consistent with cold temperatures being able to suppress *PIF4* overexpression phenotypes (*10*). Because *PHYTOCHROME B* (*PHYB*) was identified as a quantitative trait locus for thermal responsiveness and PIF4 activity is regulated by phytochromes (*8*, *11*), we investigated whether these red light receptors control hypocotyl elongation in the range 12° to 22°C. phyABCDE, lacking phytochrome activity (*12*) shows constitutively long hypocotyls at 12° and 17°C. Thus, phytochromes are essential for responding to temperature (Fig. 1, C and D, and fig. S1).

We used transcriptome analysis to determine whether disrupted thermomorphogenesis in *phyABCDE* is specific for temperature signaling or is a consequence of misregulated growth pathways. To capture diurnal variation in thermoresponsiveness, we sampled seedlings over 24 hours at 22° and 27°C. Clustering analysis revealed 20 groups of transcripts (Fig. 2A and fig. S3; described in supplement). Thermomorphogenesis occurs predominantly at night and is driven by *PIF4*. Consistent with this, we observed that *PIF4* is present in cluster 20, which is more highly expressed at 27°C during darkness. Clusters 15 and 16 represent the other major groups of nighttime thermally responsive genes, and these are strongly induced in *phyABCDE*. These clusters are enriched for genes involved in hormone signaling and elongation growth (*YUCCA8*, *YUCCA9*, *BRASSINOSTEROID INSENSITIVE2*, *LIKE AUXIN RESISTANT1*, *AUXIN RESPONSE FACTOR7* and *9*, *BIG*, and *TRANSPORT INHIBITOR1*) (data S2 and S3). These results indicate that the nighttime warm-temperature transcriptome is specifically affected when phytochrome activity is altered.

We used principal components analysis to investigate the overall responses of the transcriptome to temperature and phytochromes. For principal component PC1, which explains 40.8% of the expression variance, *phyABCDE* at 22°C occupies a similar position to the wild type at 27°C (Fig. 2B). At nighttime, there is a positive correlation between gene expression changes in response to temperature and in response to *phyABCDE*; this relationship is lost during the day (Fig. 2C). Phytochromes are interconvertible photoreceptors (*13*–*15*): phyB switches between an inactive Pr state and an active Pfr state upon absorbing red and far-red light, respectively. In a thermal relaxation reaction, Pfr in the dark spontaneously reverts to the Pr state (*16*–*18*). We hypothesized

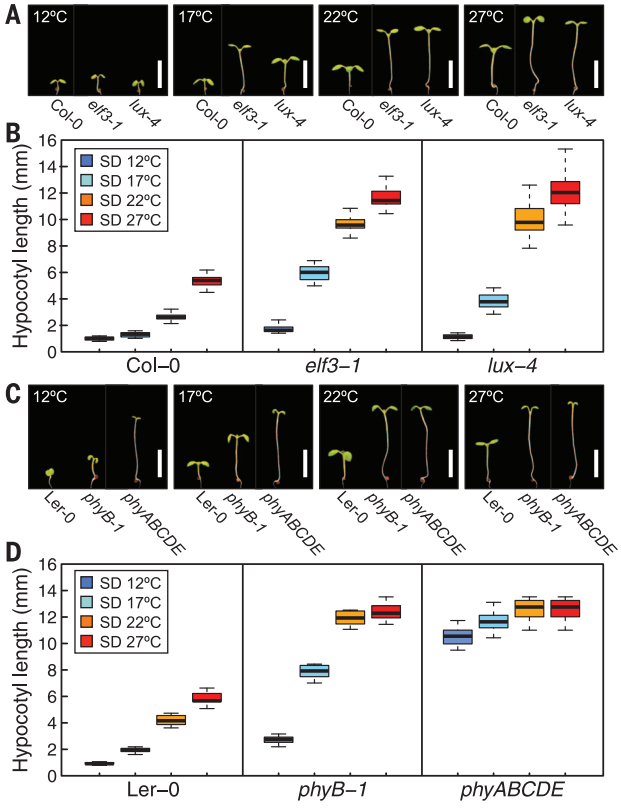


**Fig. 1. Phytochromes are essential for correct thermomorphogenesis at lower temperatures.** (**A**) Seedlings for Col-0, *elf3-1*, and *lux-4* (left to right in each panel) were grown at the indicated temperatures for 8 days under short photoperiods. Scale bars, 5 mm. (**B**) Hypocotyl length box plots for the indicated genotypes grown at different temperatures as in (A). (**C**) Seedlings for Ler, *phyB-1*, and *phyABCDE* (left to right in each panel) were grown at the indicated temperatures for 8 days under short photoperiods. Scale bars, 5 mm. (**D**) Hypocotyl length box plots for the indicated genotypes grown at different temperatures as in (C). In (B) and (D), each box is bounded by the lower and upper quartiles, the central bar represents the median, and the whiskers indicate minimum and maximum values.

[1]Sainsbury Laboratory, University of Cambridge, Cambridge CB2 1LR, UK. [2]Institut für Biologie II, University of Freiburg, D-79104 Freiburg, Germany. [3]School of Environmental Sciences, University of East Anglia, Norwich, UK. [4]Department of Biochemistry, University of Cambridge, Cambridge CB2 1GA, UK. [5]BIOSS Centre for Biological Signalling Studies, University of Freiburg, 79104 Freiburg, Germany. [6]Department of Plant Sciences, University of Cambridge, Cambridge CB2 3EA, UK.
*These authors contributed equally to this work. †Present address: Division of Medical Sciences, Harvard Medical School, Boston, MA, USA. ‡Present address: Department of Environmental Sciences, University of Peshawar, 25120 Peshawar, Pakistan. §Present address: Department of Biochemistry, Faculty of Science, and Integrative Computational BioScience Center, Mahidol University, Bangkok 10400, Thailand. ‖Corresponding author. Email: philip.wigge@slcu.cam.ac.uk

Downloaded from http://science.sciencemag.org/ on November 22, 2016

that the reversion of Pfr to the inactive Pr state may contribute to the subsequent increase in expression of the warm-temperature transcriptome during the night. We therefore examined plants containing a constitutively active version of phyB. The $Tyr^{276} \rightarrow$ His point mutation in phyB (YHB) prevents the dark reversion reaction (*19*, *20*), locking phyB in the active Pfr state. This results in constitutive repression of the warm-temperature transcriptome throughout the night (Fig. 2A and fig. S3). *YHB* plants also phenocopy cool-grown plants, showing little thermoresponsive elongation growth even at 27°C (fig. S2). Across the time course, we found that 79% of the temperature transcriptome is misregulated in *phyABCDE*, *YHB*, or both backgrounds (Fig. 2D).

PhyA is able to bind promoters (*21*), and PIF3 can recruit phyB to G-boxes, motifs bound by PIFs, in vitro (*22*), so we tested whether phyB controls temperature-responsive genes directly. Chromatin immunoprecipitation of epitope-tagged phyB (phyB-Myc) coupled with sequencing (ChIP-seq) revealed phyB to bind >100 sites (~95 promoters), with more targets bound at 17°C than at 27°C (Fig. 3A). Phytochrome signaling is reduced at warmer temperatures, and even for the 33 sites bound by phyB at both temperatures, less binding occurred at 27°C (Fig. 3B). Most phyB target genes are expressed at night in response to temperature (fig. S4). It has been suggested

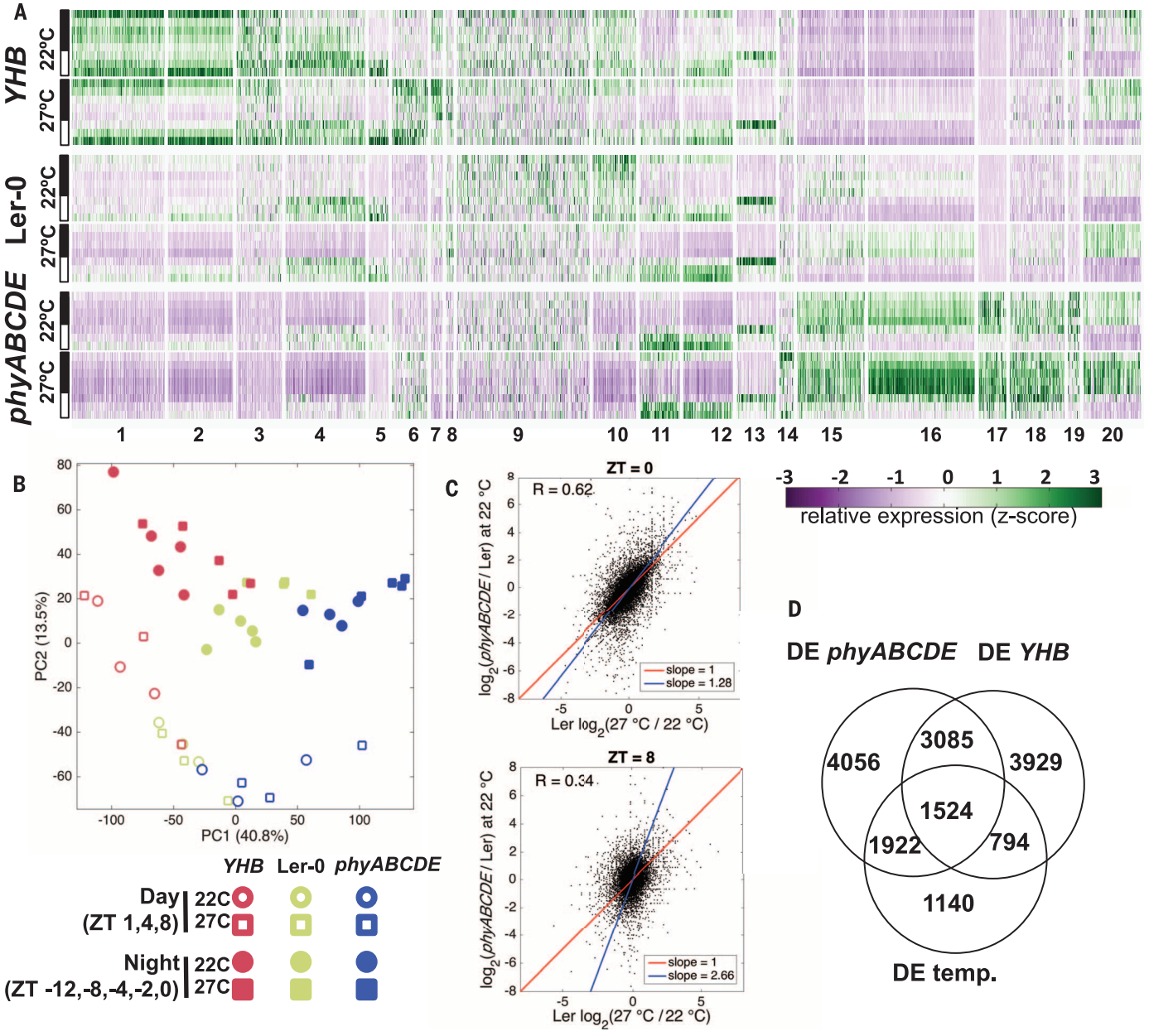


**Fig. 2. Phytochromes control the temperature transcriptome at night.** (**A**) Clustering of all RNA sequencing (RNA-seq) time course samples for *phyABCDE*, Ler-0, and *YHB* at two different temperatures, 22°C and 27°C. Samples were collected every 4 hours from ZT (zeitgeber time) = 0 with additional time points at ZT = 1 and ZT = 22. Black bars (far left) indicate night, white bars day. Clustering was performed on the expression-filtered data set using a Gaussian mixture model. The number of clusters was assumed to be a random variable and was automatically learned using an empirical Bayes approach (variational Bayesian inference). (**B**) Principal components analysis on the expression-filtered data set using genes as features. (**C**) Transcripts up-regulated in the *phyABCDE* background correlated positively with genes induced by temperature at dawn (ZT = 0, top) but not at dusk (ZT = 8, bottom). (**D**) Sets of differentially expressed (DE) genes from phytochrome and temperature transcriptomes overlap.

Downloaded from http://science.sciencemag.org/ on November 22, 2016

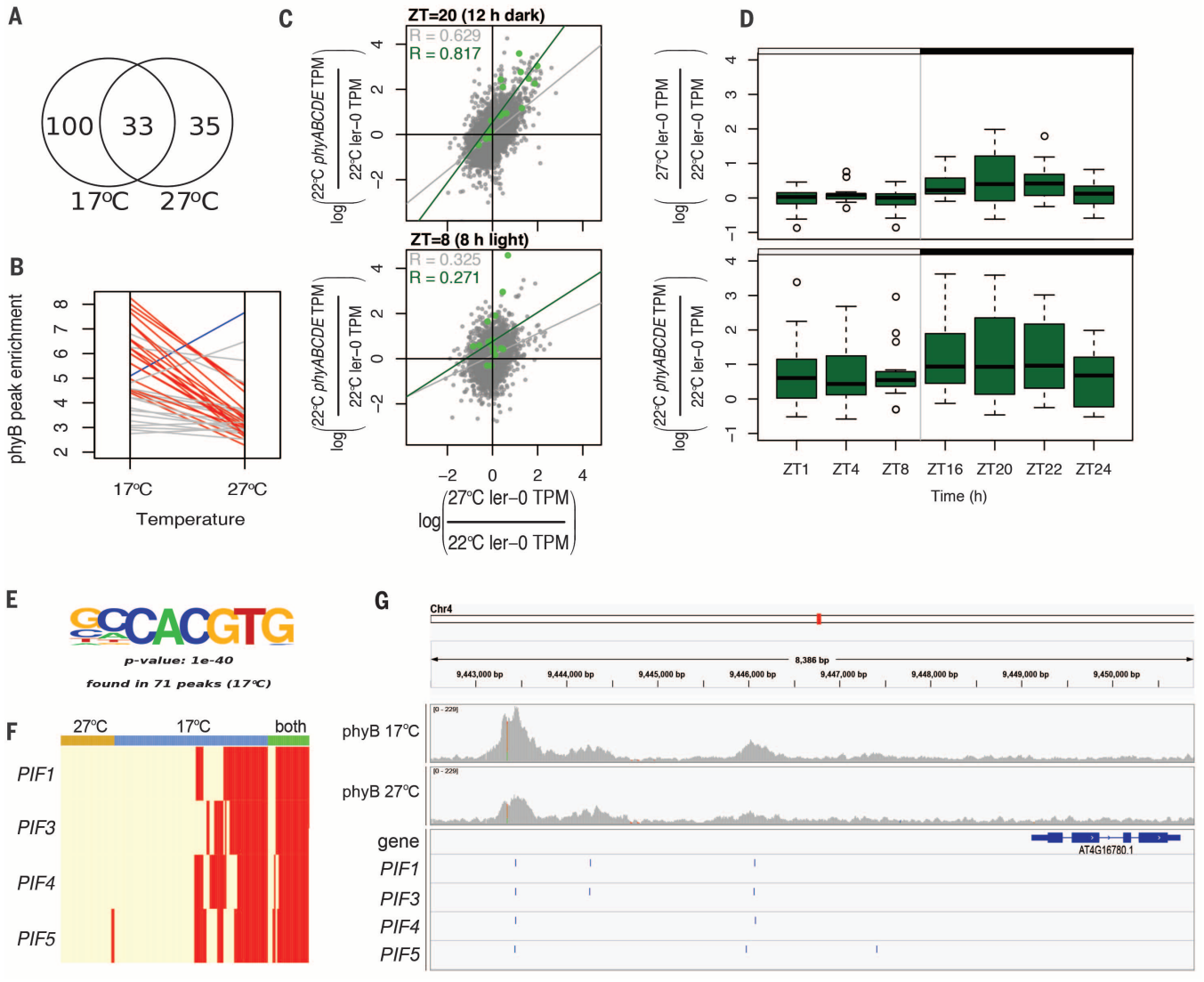


**Fig. 3. phyB binds to promoters of temperature-responsive genes.** (**A**) Comparison of phyB-Myc ChIP-seq peaks identified at 17° and 27°C using model-based analysis of ChIP-seq (MACS2). In six instances, a single broad 17°C peak was identified as two smaller peaks at 27°C, each of which is considered separately in the subsequent analysis. (**B**) Among the 33 peaks that were found at both 17° and 27°C, we compared the phyB-Myc peak enrichment [calculated as the logarithm of change relative to input (log-fold change) by MACS2] at 17° and 27°C. Values that decreased by >50% are colored red, those that increased by >50% are blue, and the remainder are gray. (**C**) Log-fold change in expression in *phyABCDE* compared to log-fold change in expression caused by elevated temperature (27°C versus 22°C), at two time points (ZT = 8 and 20) in the RNA-seq time course from Fig. 2. The green points depict the transcripts of the 15 genes that are adjacent to the 33 peaks that are found in both 17°C and 27°C. Pearson's *R* is calculated for all genes (gray) and the phyB target genes (green). TPM denotes transcripts per million. (**D**) Distributions of log-fold change in expression caused by *phyABCDE* and temperature elevation for 15 phyB target genes. Open circles represent outliers (greater than the upper quartile value by more than 1.5 times the interquartile domain, and vice versa for points of low value). The horizontal lines represent the largest and smallest points that fall within this range. (**E**) From the 17°C peaks (127, considering the six broad peaks as a single peak), a G-box was the strongest de novo motif identified by Homer2 software for motif analysis, using shuffled sequence to form the background distribution. (**F**) Each column represents a different phyB peak, sorted by whether it was found at 27°C, 17°C, or both; a red bar indicates that this peak overlaps with the center of the reported PIF binding site (*23*). All but three of the peaks found at both 17° and 27°C are bound by multiple PIFs; almost none of the peaks found only at 27°C are bound by PIFs. (**G**) Integrated Genomics Viewer browser view of the *ATHB2* promoter, showing overlap between phyB-Myc peaks at 17° and 27°C and the PIF1, 3, 4, and 5 peaks previously described (*23*).

that phyB may modulate transcription (*22*), and our results indicate that it acts as a transcriptional repressor; most targets were up-regulated under conditions that reduce phytochrome activity during the night, whereas during daytime this relationship was lost (Fig. 3, C and D, and figs. S6 and S9). We did not observe a change in *PHYB* expression or phyB protein levels in response to temperature, consistent with the effect of temperature on phyB being direct (fig. S11).

Most of the phyB-bound peaks contained G-boxes (Fig. 3E and fig. S7). We found overlap between phyB peaks and reported binding sites for PIF1, 3, 4, and 5 (*23*–*25*) (Fig. 3, E and F). phyB-preferring sites that are bound by all four PIFs were enriched at both 17° and 27°C. [Only 7% of the identified peaks are shared among all four PIFs in (*23*).] Of the loci that were bound by phyB at both 17° and 27°C, only three were not bound by PIFs. Relative to other sites, phyB at PIF binding sites showed stronger enrichment (fig. S5). These loci likely represent sites for facilitated PIF binding and coenrichment for phyB. The *ATHB2* promoter illustrates how phyB binding correlates to the binding sites of PIFs (Fig. 3G and fig. S8). To further resolve the phyB peaks, we used cross-linking ChIP (X-ChIP) (*26*). Verified multiple PIF-bound sites corresponded to phyB-bound sites (fig. S10). Although light induces degradation of PIFs, readily detectable levels of

Downloaded from http://science.sciencemag.org/ on November 22, 2016

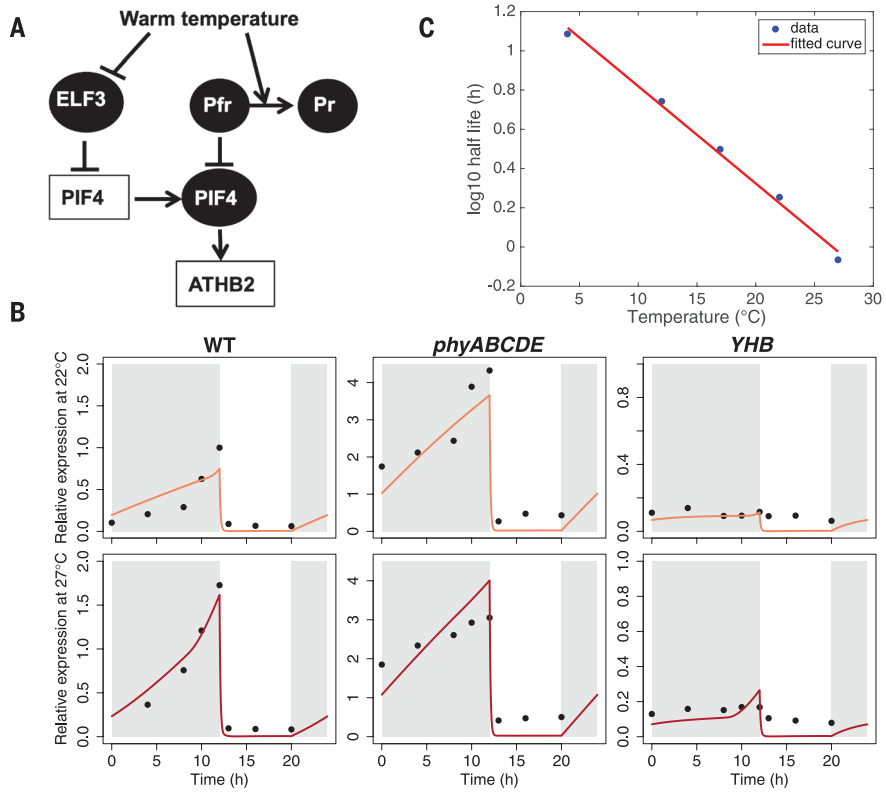


**Fig. 4. A thermoresponsive gene expression network.** (**A**) Regulatory network integrating temperature information through ELF3 activity and Pfr dark reversion. Temperature information is integrated through activity of ELF3 (which acts as a repressor of PIF4) and deactivation of phyB (active Pfr state switching to inactive Pr state). Ovals and rectangles denote proteins and squares, respectively. (**B**) Modeled gene expression (orange and red lines) agrees with measured values (black dots). (**C**) The phyB Pfr half-life varies exponentially with temperature (assayed in etiolated seedlings). At lower temperatures, active Pfr persists at the end of the night, whereas at higher temperatures most Pfr is depleted within a few hours.

natively expressed PIF4 were seen during the daytime (*27*). Thus, phyB at promoters may recruit or modulate the action of other regulators, providing a mechanism to increase the dynamic range of the transcriptional regulation of target genes. Precedent exists for a transcriptional activator being converted into a repressor by a ligand; for example, FD (ATBZIP14) is an activator when bound to FLOWERING LOCUS T and a repressor when bound to TERMINAL FLOWER1 (*28*).

Changes in the activity of a transcriptional repressor, R, can explain the thermoresponsive expression of *PIF4* and *LUX*, and the thermal responsiveness of R can be accounted for by *ELF3* (*8*). However, transcripts of PIF4 target genes such as *ATHB2* cluster separately from *PIF4* and show greater responsiveness to phytochrome signaling (Fig. 2A). This led us to conclude that phytochromes provide additional temperature-dependent regulation of PIF4. Thus, active phytochromes (Pfr) repress the activity of PIF4 and its ability to activate *ATHB2* (Fig. 4A). In the dark, the amount of Pfr is determined by the dark reversion rate, *b*. We used *ATHB2* expression data from L*er*, *phyABCDE*, and *YHB* to calibrate this model (fig. S12). Using parameters from the previous model (*8*), we allowed the model to determine which values of *b* are consistent with the thermoresponsive gene expression profiles (table S1). The model selects values of *b* that vary as a function of temperature: The half-life of Pfr is 2.09 hours at 22°C and 1.53 hours at 27°C. If *b* is not allowed to vary with temperature, the model does not fit the data as well (fig. S13). Our model recapitulates *ATHB2* expression in response to temperature, which suggests that dual control of *PIF4* at transcriptional and posttranslational levels explains regulation of gene expression to control expansion growth (Fig. 4B).

Our model infers a temperature-responsive half-life for Pfr. Dark reversion of phytochromes from various species is a thermal relaxation reaction (*14*). We observed that the in vivo dark reversion rate of phyB:phyB$_{Pfr}$, in terms of half-life ($t_{1/2}$), showed an exponential relationship to temperature over one order of magnitude between 4° and 27°C [$t_{1/2} = 10^{(-0.0496T + 1.315)}$, where $T$ is temperature (°C); $R^2 = 0.99$] (Fig. 4C and fig. S14). The half-lives at 22° and 27°C ($t_{1/2}$ = 1.79 hours and 0.86 hours, respectively) are comparable to those seen in the model.

Phytochromes are central regulators of plant responses to the environment; hence, their acquisition of a thermally responsive behavior suggests an evolutionary route to integrate temperature information into development. Because single amino acid changes as well as posttranslational modifications can alter the dark reversion rate, sequence diversification among phytochromes may afford diversity in thermal responsiveness for different climates (*18*, *20*, *29*–*31*). The Pfr dark reversion rate represents a sensitive mechanism for integrating small differences in temperature during the night in order to make developmental decisions.

## REFERENCES AND NOTES


1. C. G. Willis, B. Ruhfel, R. B. Primack, A. J. Miller-Rushing, C. C. Davis, *Proc. Natl. Acad. Sci. U.S.A.* **105**, 17029–17033 (2008).
2. D. S. Battisti, R. L. Naylor, *Science* **323**, 240–244 (2009).
3. W. M. Gray, A. Ostin, G. Sandberg, C. P. Romano, M. Estelle, *Proc. Natl. Acad. Sci. U.S.A.* **95**, 7197–7202 (1998).
4. K. J. Halliday, M. G. Salter, E. Thingnaes, G. C. Whitelam, *Plant J.* **33**, 875–885 (2003).
5. M. A. Koini *et al.*, *Curr. Biol.* **19**, 408–413 (2009).
6. S. V. Kumar *et al.*, *Nature* **484**, 242–245 (2012).
7. T. Mizuno *et al.*, *Plant Cell Physiol.* **55**, 958–976 (2014).
8. M. S. Box *et al.*, *Curr. Biol.* **25**, 194–199 (2015).
9. A. Raschke *et al.*, *BMC Plant Biol.* **15**, 197 (2015).
10. S. V. Kumar *et al.*, *Nature* **484**, 242–245 (2012).
11. S. Lorrain, T. Allen, P. D. Duek, G. C. Whitelam, C. Fankhauser, *Plant J.* **53**, 312–323 (2008).
12. W. Hu *et al.*, *Proc. Natl. Acad. Sci. U.S.A.* **110**, 1542–1547 (2013).
13. H. A. Borthwick, S. B. Hendricks, M. W. Parker, E. H. Toole, V. K. Toole, *Proc. Natl. Acad. Sci. U.S.A.* **38**, 662–666 (1952).
14. W. L. Butler, H. C. Lane, H. W. Siegelman, *Plant Physiol.* **38**, 514–519 (1963).
15. M. Chen, J. Chory, C. Fankhauser, *Annu. Rev. Genet.* **38**, 87–117 (2004).
16. L. Hennig, E. Schäfer, *J. Biol. Chem.* **276**, 7913–7918 (2001).
17. C. Klose *et al.*, *Nat. Plants* **1**, 15090 (2015).
18. U. Sweere *et al.*, *Science* **294**, 1108–1111 (2001).
19. W. Hu, Y. S. Su, J. C. Lagarias, *Mol. Plant* **2**, 166–182 (2009).
20. Y. S. Su, J. C. Lagarias, *Plant Cell* **19**, 2124–2139 (2007).
21. F. Chen *et al.*, *Plant Cell* **26**, 1949–1966 (2014).
22. J. F. Martínez-García, E. Huq, P. H. Quail, *Science* **288**, 859–863 (2000).
23. A. Pfeiffer, H. Shi, J. M. Tepperman, Y. Zhang, P. H. Quail, *Mol. Plant* **7**, 1598–1618 (2014).
24. Y. Zhang *et al.*, *PLOS Genet.* **9**, e1003244 (2013).
25. P. Hornitschek *et al.*, *Plant J.* **71**, 699–711 (2012).
26. P. J. Skene, S. Henikoff, *eLife* **4**, e09225 (2015).
27. T. Yamashino *et al.*, *Plant Signal. Behav.* **8**, e23390 (2013).
28. K. E. Jaeger, N. Pullen, S. Lamzin, R. J. Morris, P. A. Wigge, *Plant Cell* **25**, 820–833 (2013).
29. M. Medzihradszky *et al.*, *Plant Cell* **25**, 535–544 (2013).
30. D. L. Filiault *et al.*, *Proc. Natl. Acad. Sci. U.S.A.* **105**, 3157–3162 (2008).
31. J. N. Maloof *et al.*, *Nat. Genet.* **29**, 441–446 (2001).


## ACKNOWLEDGMENTS

We thank C. Dean for insightful discussions. We dedicate this study to J. Chory. The data reported in this paper are deposited in the NCBI Sequence Read Archive (accession number SUB1572336) and are also in the supplementary materials. Supported by a Churchill Scholarship from the Winston Churchill Foundation of the United States (S.B.); Gatsby Foundation fellowship GAT3272/GLC (J.C.W.L.); Biotechnology and Biological Sciences Research Council responsive mode grants BB/I013350/1 and BB/N010248/1, European Research Council grant EC FP7 ERC 243140, and Gatsby Foundation fellowship GAT3273/GLB (P.A.W.); and Deutsche Forschungsgemeinschaft grant SCHA 303/16-1 (C.K., via E.S.).

## SUPPLEMENTARY MATERIALS

www.sciencemag.org/content/354/6314/886/suppl/DC1
Model Description
Gene Expression Cluster Descriptions
Materials and Methods
Figs. S1 to S14
Table S1
Data S1 to S6
References (*32*–*40*)

3 March 2016; accepted 31 August 2016
Published online 27 October 2016
10.1126/science.aaf6005

Downloaded from http://science.sciencemag.org/ on November 22, 2016

PLANT SCIENCE

# Characterization of a dynamic metabolon producing the defense compound dhurrin in sorghum

Tomas Laursen,[1,2,3,4,5] Jonas Borch,[2,6] Camilla Knudsen,[1,2,3,4] Krutika Bavishi,[1,2,3,4] Federico Torta,[7] Helle Juel Martens,[4] Daniele Silvestro,[4] Nikos S. Hatzakis,[2,8] Markus R. Wenk,[7,9] Timothy R. Dafforn,[10,11] Carl Erik Olsen,[1,2,3] Mohammed Saddik Motawia,[1,2,3,4] Björn Hamberger,[1,2] Birger Lindberg Møller,[1,2,3,4,12]* Jean-Etienne Bassard[1,2,3,4]*

Metabolic highways may be orchestrated by the assembly of sequential enzymes into protein complexes, or metabolons, to facilitate efficient channeling of intermediates and to prevent undesired metabolic cross-talk while maintaining metabolic flexibility. Here we report the isolation of the dynamic metabolon that catalyzes the formation of the cyanogenic glucoside dhurrin, a defense compound produced in sorghum plants. The metabolon was reconstituted in liposomes, which demonstrated the importance of membrane surface charge and the presence of the glucosyltransferase for metabolic channeling. We used in planta fluorescence lifetime imaging microscopy and fluorescence correlation spectroscopy to study functional and structural characteristics of the metabolon. Understanding the regulation of biosynthetic metabolons offers opportunities to optimize synthetic biology approaches for efficient production of high-value products in heterologous hosts.

Plants produce a plethora of specialized metabolites to fend off attack from herbivores and pests and to adapt to abiotic stresses. One class of specialized metabolites is the cyanogenic glucosides, such as dhurrin, which is present in *Sorghum bicolor* (*1*). Dhurrin is produced from the amino acid L-tyrosine and synthesized by three membrane-anchored proteins—the NADPH (reduced nicotinamide adenine dinucleotide phosphate)–dependent cytochrome P450 oxidoreductase (POR) and two cytochrome P450 enzymes (CYP79A1 and CYP71E1)— and by a soluble UDP (uridine diphosphate)–glucosyltransferase (UGT85B1) (*2*) (Fig. 1A). When cellular integrity is disrupted, such as by a chewing insect, dhurrin is hydrolyzed, which results in the release of toxic hydrogen cyanide (Fig. 1A) (*1*).

[1]Plant Biochemistry Laboratory, Department of Plant and Environmental Science, University of Copenhagen, DK-1871 Frederiksberg C, Denmark. [2]bioSYNergy, Center for Synthetic Biology, DK-1871 Frederiksberg C, Denmark. [3]VILLUM Research Center for Plant Plasticity, DK-1871 Frederiksberg C, Denmark. [4]Copenhagen Plant Science Center, University of Copenhagen, DK-1871 Frederiksberg C, Denmark. [5]Feedstocks Division, Joint BioEnergy Institute, Emeryville, CA 94608, USA. [6]VILLUM Center For Bioanalytical Sciences, Department of Biochemistry and Molecular Biology, University of Southern Denmark, DK-5230 Odense M, Denmark. [7]Department of Biochemistry, Yong Loo Lin School of Medicine, National University of Singapore, Singapore 117597, Singapore. [8]Department of Chemistry, Nano-Science Center, University of Copenhagen, DK-2100 Copenhagen, Denmark. [9]Department of Biological Sciences, Yong Loo Lin School of Medicine, National University of Singapore, Singapore 117597, Singapore. [10]School of Biosciences, University of Birmingham, Birmingham B15 2TT, UK. [11]Department of Business, Energy and Industrial Strategy, Her Majesty's Government, UK. [12]Carlsberg Research Laboratory, DK-1799 Copenhagen V, Denmark.
*Corresponding author. Email: blm@plen.ku.dk (B.L.M.); jbassard@outlook.com (J.-E.B.)

The dhurrin content of 3-day-old etiolated seedlings reaches 30% of their dry weight (*3*), even though the enzymes involved in dhurrin biosynthesis constitute less than 1% of the total membrane protein content (*4*). This efficiency may be governed by metabolon formation. Metabolon disassembly would result in the release of an aldoxime intermediate, which has been proposed to act as an antifungal agent (*5*). Several biosynthetic pathways have been proposed to involve the formation of metabolons, which are often depicted as static entities composed of equimolar protein components (*2, 6–8*). Here we report protein-protein interactions (including oligomer formation), protein dynamics, and functional regulation of the metabolon that catalyzes dhurrin synthesis.

The isolation of dynamic membrane-embedded metabolons is hampered by their destabilization and dissociation upon detergent solubilization of the lipid bilayer. The use of the styrene maleic acid (SMA) copolymer circumvents these issues. The SMA polymer spontaneously integrates into the lipid bilayer and carves out discrete lipid particles (SMALPs) containing the resident membrane proteins and the surrounding lipids (*9*). We used the SMALP technology in combination with affinity chromatography to isolate the dynamic dhurrin metabolon (fig. S1).

Application of the SMA polymer to microsomes prepared from etiolated sorghum seedlings resulted in the formation of discrete SMALPs ranging from 10 to 25 nm in diameter ($n$ = 242) (Fig. 1B). These particles were larger than previously reported SMA particles obtained from pure lipids or harboring a single protein (10 nm on average) (*9*). POR is the common electron donor to all microsomal P450s (*10*). The SMALPs were purified by 2′,5′ADP (adenosine diphosphate)–Sepharose affinity chromatography, based on the NADPH cofactor requirement of POR, for copurification of POR-associated proteins (fig. S2). We analyzed the protein content in the course of SMALP purification by quantitative mass spectrometry (Fig. 1C, fig. S3, and data S1 and S2) (*11*). As a control, the same purification was carried out using the anionic detergent cholate instead of the SMA polymer. The protein enrichment was determined on the basis of the content of the three POR isoforms (POR2a to -c), the P450 proteins, and other enzymes including UGT85B1, dhurrinase, cytochrome $b_5$ ($Cytb_5$), and $Cytb_5$ reductase (table S1). Microsomal and SMA-solubilized fractions had similar protein content (fig. S3). After affinity chromatography, 132 proteins were quantified in the SMALPs, with the P450s CYP79A1 and CYP71E1 among the eight most abundant proteins (Fig. 1C). In contrast, no P450 enrichment was observed in the cholate sample (table S1). The soluble UGT85B1 was identified in all samples but could not be quantified in the purified SMALP sample, most likely because of the extensive washing steps during microsome preparation and affinity chromatography. The strong enrichment of the entire complement of membrane-bound dhurrin pathway enzymes in the affinity-purified SMALPs demonstrates that these enzymes are assembled in a metabolon.

Functional regulation of dhurrin biosynthesis as a response to environmental stresses (*1*) likely involves dynamic assembly and disassembly of the metabolon. Therefore, we studied the effect of UGT85B1 on the channeling of L-tyrosine toward dhurrin by in vitro reconstitution of the dhurrin enzymes in liposomes. Catalytic activities of P450s were determined based on the amounts of aldoxime (CYP79A1-mediated) and cyanohydrin (CYP71E1-mediated) produced after administration of radiolabeled L-tyrosine substrate (Fig. 2A). In the absence of UGT85B1, 50% of the produced aldoxime was further converted into the cyanohydrin, corresponding to a catalytic rate constant for CYP79A1 ($k_{cat}^{CYP79A1}$) of 80 $min^{-1}$ and a $k_{cat}^{CYP71E1}$ of 40 $min^{-1}$. When supplemented with UGT85B1 in the absence of UDP-glucose, UGT85B1 interacted with the two P450s (fig. S4), increasing their catalytic properties ($k_{cat}^{CYP79A1}$ = 100 $min^{-1}$ and $k_{cat}^{CYP71E1}$ = 80 $min^{-1}$) and thus demonstrating an increased flux of L-tyrosine through the P450s and improved channeling (80%; Fig. 2A). Addition of UDP-glucose did not further increase the catalytic efficiency of the two P450s or the channeling of the aldoxime. Additionally, UGT85B1 did not stimulate CYP71E1 activity, as observed by administration of aldoxime as a substrate (Fig. 2A). Therefore, we propose that UGT85B1 binds specifically to both P450s and augments the flux and channeling of L-tyrosine toward dhurrin.

The impact of membrane lipid composition on the catalytic activities of the dhurrin pathway P450s was examined by reconstitution experiments in liposomes, using different ratios of phospholipids based on the enrichment observed in the purified SMALP samples (fig. S5 and data S3 to S5). CYP79A1 activity was marginally influenced by the phospholipid composition. In contrast, the

Downloaded from http://science.sciencemag.org/ on November 24, 2016

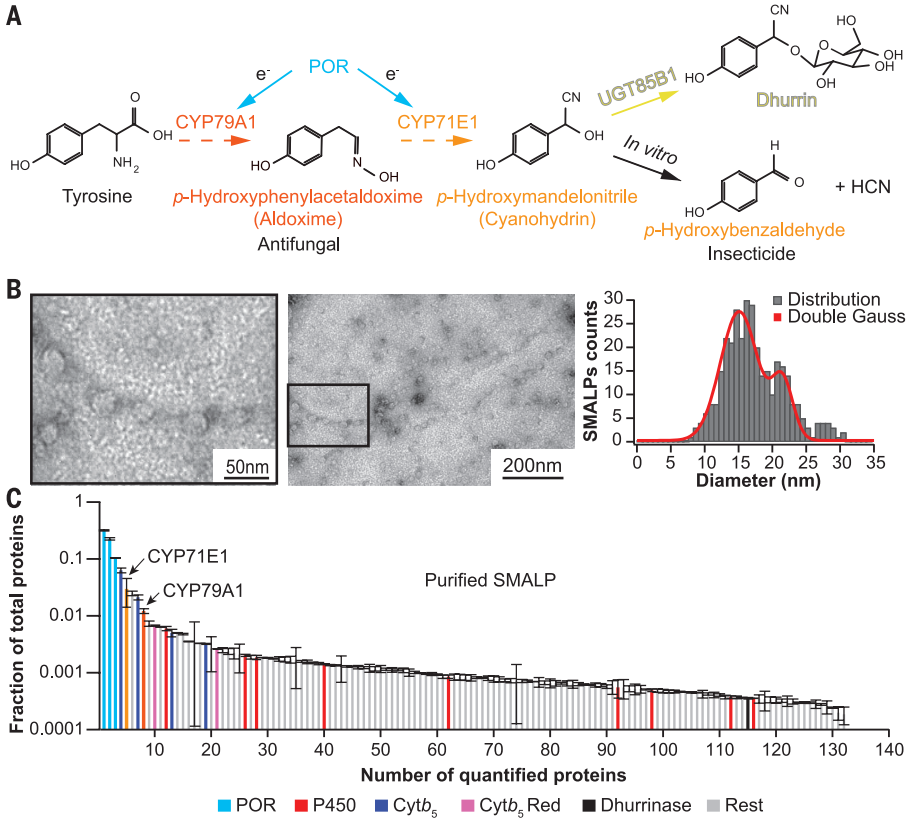


**Fig. 1. Detergent-free isolation of the dhurrin metabolon, including the surrounding lipids.** (**A**) The dhurrin biosynthetic pathway. HCN, hydrogen cyanide. (**B**) Negative-stain transmission electron microscopy images of affinity-purified SMALPs (left) and the distribution of particle sizes (right). (**C**) Quantitative mass spectrometry of the protein content of affinity-purified SMALPs. Proteins related to dhurrin biosynthesis and other P450 enzymes are highlighted. Data are represented as the fraction of the total protein content (mean values of three independent measurements ± SD). Red, reductase.

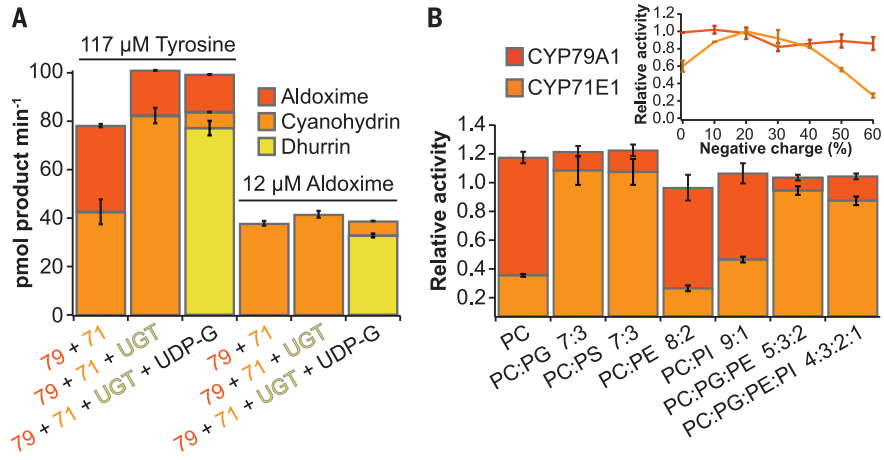


**Fig. 2. Protein-protein and protein-lipid interactions stimulate channeling.** (**A**) POR2b, CYP79A1, and CYP71E1 were reconstituted in liposomes from a total lipid extract from sorghum microsomes. The catalytic activity of CYP79A1 ("79") and CYP71E1 ("71") was measured in the absence of or after supplementation with UGT85B1 ("UGT") and/or UDP-glucose ("UDP-G"), using radiolabeled L-tyrosine or aldoxime as the substrate. (**B**) POR2b, CYP79A1, and CYP71E1 were reconstituted in liposomes with different lipid mixtures of POPC, POPG, POPS, POPE, and PI. The catalytic activity of CYP79A1 and CYP71E1 was measured and compared with that measured in (A) (relative activity). The inset shows the relative catalytic activity for a titration of PG lipids and P450 activities. All functional data are averages of biological triplicates, and error bars indicate ±SD. PC, 1-palmitoyl-2-oleoyl-*sn*-glycero-3-phosphocholine; PS, 1-palmitoyl-2-oleoyl-*sn*-glycero-3-phospho-L-serine; PG, 1-palmitoyl-2-oleoyl-*sn*-glycero-3-phospho-(1′-rac-glycerol); PI, L-α-phosphatidylinositol; PE, 1-palmitoyl-2-oleoyl-*sn*-glycero-3-phosphoethanolamine.

catalytic efficiency of CYP71E1 was highly sensitive to the lipid environment and dependent on the total concentration of negative charges derived from the lipid headgroups of PG, PS, and PI, with an optimum efficiency in liposomes containing 20 to 30% negatively charged phospholipids (Fig. 2B). This matches the observed enrichment of PG in the purified SMALPs.

To study the organization of the dhurrin pathway enzymes in planta, we transiently expressed CYP79A1, CYP71E1, UGT85B1, POR2b, and different combinations of these (including control proteins) in *Nicotiana benthamiana* leaf epidermal cells (*11*), the most suitable plant expression system for in planta fluorescence lifetime imaging microscopy (FLIM) and fluorescence correlation spectroscopy (FCS). The expression levels of the heterologous proteins in *N. benthamiana* were quantitatively comparable to those in *S. bicolor* seedlings (table S2 and data S6).

Upon coexpression of CYP79A1 and CYP71E1, several byproducts of the dhurrin pathway and some dhurrin accumulated (Fig. 3A). The formation of dhurrin reflects the inherent capability of *N. benthamiana* to glycosylate exogenous compounds (*12*). Coexpression of UGT85B1 with the two P450s and without *S. bicolor* POR2b resulted in the accumulation of 263% more dhurrin and a reduction of byproduct release to 9% of the level observed in the absence of UGT85B1 (table S3). The efficient channeling of intermediates achieved upon coexpression of UGT85B1 supports the assembly of a metabolon in planta and confirms that endogenous *N. benthamiana* POR is sufficient to provide reducing equivalents to the P450s.

To further evaluate dhurrin metabolon formation, we expressed CYP79A1, CYP71E1, UGT85B1, and POR2b as fusion proteins with different fluorescent proteins suitable for in planta FLIM and FCS (figs. S6 to S8) (*11*). First, the functionality of the target enzymes after fusion was assessed. All possible combinations with enhanced green fluorescent protein (eGFP) fused to two of the three target proteins produced similar amounts of dhurrin and byproducts (Fig. 3A and table S3). No apparent difference between the use of N- and C-terminally tagged UGT85B1 was observed, and here we present only the data obtained for N-terminal fusion constructs. The tracking of fluorescent fusion constructs of the dhurrin enzymes with confocal microscopy techniques (movies S1 and S2) illustrated their fast movement in the plant cell along the endoplasmic reticulum (ER) network, as has also been observed in studies of other metabolons (*7*, *8*, *13*). Quantified by FCS, the average diffusion coefficients of individual dhurrin enzymes decreased upon coexpression of the two other partners, whereas the diffusion of the POR2b:eGFP fusion protein was not influenced by coexpression of dhurrin enzymes (Fig. 3, B and C; fig. S9; and tables S4 and S5).

The fluorescence (Förster) resonance energy transfer (FRET) efficiencies from pairwise combinations of all target fluorescent fusion proteins were calculated to gain a more detailed knowledge of the organization of the dhurrin metabolon (fig. S10). The in planta FRET results demonstrated that

Downloaded from http://science.sciencemag.org/ on November 24, 2016

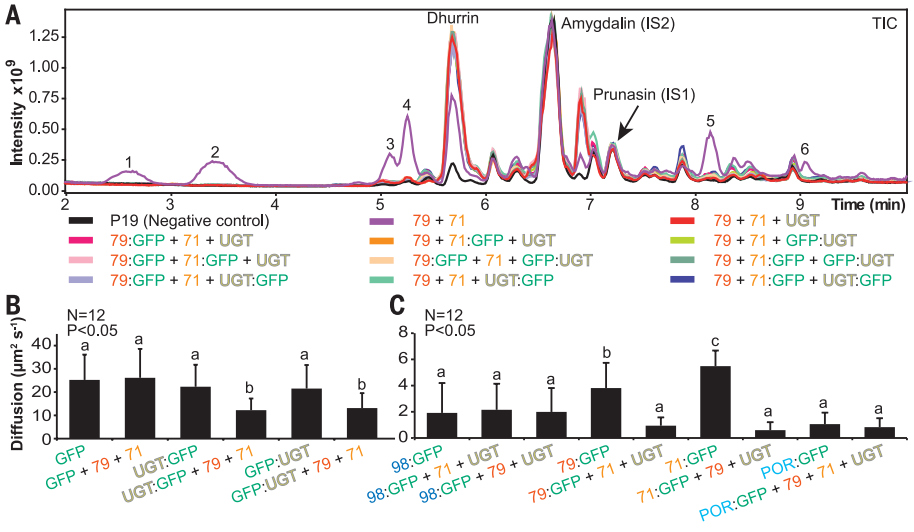


**Fig. 3. Functional fluorescence labeling of dhurrin biosynthetic enzymes and control proteins for in planta studies.** (**A**) Liquid chromatography–mass spectrometry data for dhurrin biosynthesis in *N. benthamiana* upon expression of CYP79A1, CYP71E1, and UGT85B1. Metabolite profiles were monitored as total ion chromatograms (TICs). Peaks 1 to 6 are byproducts of dhurrin intermediates. Prunasin was used as a primary internal standard and amygdalin as a secondary internal standard. The combination of CYP79A1 and CYP71E1 ("79 + 71") was used as a reference (100%) for the total level of accumulated byproducts. (**B**) Apparent diffusion of eGFP-labeled soluble proteins and (**C**) ER proteins measured by in planta FCS onto ER. CYP98A1:eGFP and free eGFP were used as controls. The CYP98 family of P450 enzymes belongs to the CYP71 clan, like CYP79A1 and CYP71E1. CYP98 catalyzes the introduction of hydroxyl groups at the meta position of phenylpropanoid-derived esters and was chosen as a control because it is not involved in dhurrin metabolism. Letters indicate statistically significant similarities for the recorded values, based on *t* test pairwise comparisons with $P < 0.05$. Error bars indicate ±SD.

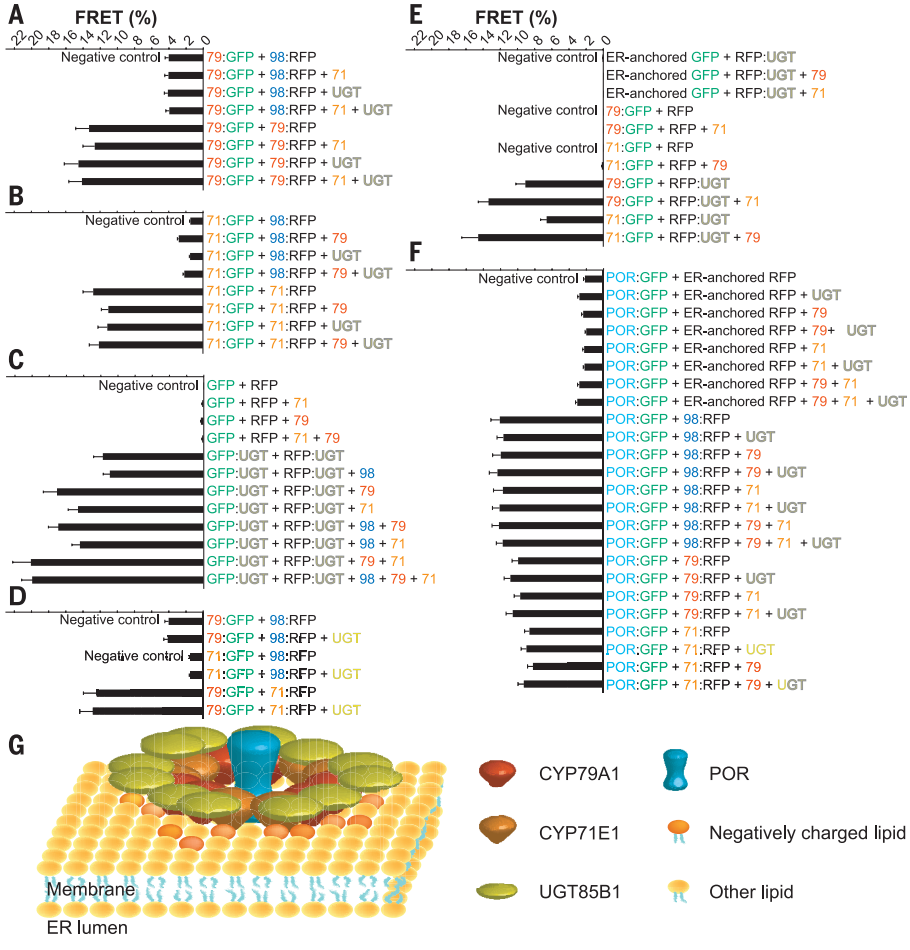


**Fig. 4. Protein-protein interactions in planta reveal formation of multienzyme clusters.** Pairwise protein association of the dhurrin enzymes was monitored in *N. benthamiana* by FLIM with eGFP- and mRFP1 (monomeric red fluorescent protein 1)–labeled proteins. FRET percentages reflecting the proximity and the frequency of association between protein constructs were calculated from the recorded eGFP lifetime. Error bars indicate ±SD. The effect of coexpression of the third dhurrin enzyme was determined by FRET measurements between the combinations (**A**) CYP79A1-CYP79A1, (**B**) CYP71E1-CYP71E1, (**C**) UGT85B1-UGT85B1, (**D**) CYP79A1-CYP71E1, (**E**) CYP79A1-UGT85B1 and CYP71E1-UGT85B1, and (**F**) POR2b-P450. (**G**) Model of the dhurrin metabolon involving higher-order clusters and enrichment of negatively charged phospholipids.

CYP79A1, CYP71E1, and UGT85B1 all form homo- and hetero-oligomers with FRET values higher than those of the controls (Fig. 4, A to E, and tables S6 to S10). FRET signals for CYP79A1-CYP79A1, CYP71E1-CYP71E1, and CYP79A1-CYP71E1 complexes were unaffected by coexpression of UGT85B1. In contrast, UGT85B1-UGT85B1 oligomerization was enhanced by coexpression of either CYP79A1 or CYP71E1, with the highest FRET signal observed when the entire dhurrin pathway was expressed, suggesting recruitment of UGT85B1 by the P450s (Fig. 4C). We therefore

Downloaded from http://science.sciencemag.org/ on November 24, 2016

conclude that the soluble UGT85B1 interacts with both CYP79A1 and CYP71E1, but that it is not necessary for CYP79A1-CYP71E1 complex formation (Fig. 4E). CYP79A1, CYP71E1, CYP98A1, and POR2b are situated very close together at the ER surface and have comparable pairwise FRET values (Fig. 4F and table S11). All microsomal P450s require electron donation from POR; therefore, it is not surprising that CYP98A1 is proximal to the dhurrin biosynthetic enzymes (Fig. 4, A, B, and D). UGT85B1 was situated close to the nonpartner ER membrane proteins, CYP98A1 and POR2b, when CYP79A1 and CYP71E1 were coexpressed (table S12).

A prerequisite to understanding how cells coordinate diverse metabolic activities is to understand how the enzyme systems catalyzing these reactions are organized and their possible enrollment as part of dynamic metabolons. Efforts to maximize product yield from genetically engineered pathways (*14*–*17*) would benefit from this information. In this study, we showed that the dhurrin pathway forms an efficient metabolon. CYP79A1 and CYP71E1 form homo- and hetero-oligomers, which enable recruitment of the cytosolic soluble UGT85B1 (Fig. 4G). UGT85B1 regulates the flux of L-tyrosine and stimulates channeling between CYP79A1 and CYP71E1. Efficient metabolic flux and channeling require an overall negatively charged lipid surface and may provide an additional means for regulating the dynamic assembly necessary to respond swiftly to environmental challenges. A similar organization may characterize the biosynthetic pathways of other specialized metabolites as well.

## REFERENCES AND NOTES


1. R. M. Gleadow, B. L. Møller, *Annu. Rev. Plant Biol.* **65**, 155–185 (2014).
2. T. Laursen, B. L. Møller, J. E. Bassard, *Trends Plant Sci.* **20**, 20–32 (2015).
3. B. A. Halkier, B. L. Møller, *Plant Physiol.* **90**, 1552–1559 (1989).
4. O. Sibbesen, B. Koch, B. A. Halkier, B. L. Møller, *Proc. Natl. Acad. Sci. U.S.A.* **91**, 9740–9744 (1994).
5. B. L. Møller, *Science* **330**, 1328–1329 (2010).
6. K. Jørgensen *et al.*, *Curr. Opin. Plant Biol.* **8**, 280–291 (2005).
7. S. An, R. Kumar, E. D. Sheets, S. J. Benkovic, *Science* **320**, 103–106 (2008).
8. K. Mohr, E. Kostenis, *Nat. Chem. Biol.* **7**, 860–861 (2011).
9. S. C. Lee *et al.*, *Nat. Protoc.* **11**, 1149–1162 (2016).
10. T. Laursen *et al.*, *ACS Chem. Biol.* **9**, 630–634 (2014).
11. Materials and methods are available as supplementary materials on *Science* Online.
12. H. M. Ting *et al.*, *New Phytol.* **199**, 352–366 (2013).
13. J. E. Bassard *et al.*, *Plant Cell* **24**, 4465–4482 (2012).
14. I. Wheeldon *et al.*, *Nat. Chem.* **8**, 299–309 (2016).
15. C. Singleton, T. P. Howard, N. Smirnoff, *J. Exp. Bot.* **65**, 1947–1954 (2014).
16. G. Farré *et al.*, *Annu. Rev. Plant Biol.* **65**, 187–223 (2014).
17. J. E. Dueber *et al.*, *Nat. Biotechnol.* **27**, 753–759 (2009).


## ACKNOWLEDGMENTS


This research was supported by the VILLUM Research Center for Plant Plasticity; by the bioSYNergy program of Center for Synthetic Biology (University of Copenhagen Excellence Program for Interdisciplinary Research); by a European Research Council Advanced Grant to B.L.M. (ERC-2012-ADG_20120314); and by funding from the VILLUM Foundation Young Investigator Programme to N.S.H. T.L. is recipient of a fellowship awarded by the VILLUM Foundation (project no. 95-300-73023). K.B. was supported by the P4FIFTY Marie Curie Initial Training Network (European Union's 7th Framework Programme). D.S. acknowledges funding from Innovation Fund Denmark (project no. 001-2011-4). F.T. and M.R.W. were supported by grants from the National Research Foundation of Singapore (NRFI2015-05) and a Biomedical Research Council–Science and Engineering Research Council joint grant (112 148 0006) from the Singapore Agency for Science, Technology and Research. T.R.D. acknowledges Biological and Biotechnology Science Research Council grants (BB/J017310/1 and BB/K004441/1). Imaging data were collected at the Center for Advanced Bioimaging, University of Copenhagen. We thank B. A. Halkier, C. Martin, A. Schulz, D. Werck-Reichhart, and anonymous reviewers for critical review of this manuscript. The supplementary materials contain additional data.


## SUPPLEMENTARY MATERIALS

www.sciencemag.org/content/354/6314/890/suppl/DC1
Materials and Methods
Figs. S1 to S10
Tables S1 to S14
References (*18*–*30*)
Movies S1 and S2
Data S1 to S6


27 May 2016; accepted 4 October 2016
10.1126/science.aag2347


NEURODEVELOPMENT

# The sacral autonomic outflow is sympathetic


**I. Espinosa-Medina,[1]* O. Saha,[1]* F. Boismoreau,[1] Z. Chettouh,[1] F. Rossi,[1] W. D. Richardson,[2] J.-F. Brunet[1]†**



**A kinship between cranial and pelvic visceral nerves of vertebrates has been accepted for a century. Accordingly, sacral preganglionic neurons are considered parasympathetic, as are their targets in the pelvic ganglia that prominently control rectal, bladder, and genital functions. Here, we uncover 15 phenotypic and ontogenetic features that distinguish pre- and postganglionic neurons of the cranial parasympathetic outflow from those of the thoracolumbar sympathetic outflow in mice. By every single one, the sacral outflow is indistinguishable from the thoracolumbar outflow. Thus, the parasympathetic nervous system receives input from cranial nerves exclusively and the sympathetic nervous system from spinal nerves, thoracic to sacral inclusively. This simplified, bipartite architecture offers a new framework to understand pelvic neurophysiology as well as development and evolution of the autonomic nervous system.**


The allocation of the sacral autonomic outflow to the parasympathetic division of the visceral nervous system—as the second tier of a "cranio-sacral outflow"—has an ancient origin, yet a simple history: It is rooted in the work of Gaskell (*1*), was formalized by Langley (*2*), and has been universally accepted ever since [as in (*3*)]. The argument derived from several similarities of the sacral outflow with the cranial outflow: (i) anatomical—a target territory less diffuse than that of the thoracolumbar outflow, a separation from it by a gap at limb levels, and a lack of projections to the paravertebral sympathetic chain (*1*); (ii) physiological—an influence on some organs opposite to that of the thoracolumbar outflow (*4*); and (iii) pharmacological—an overall sensitivity to muscarinic antagonists (*2*). However, analysis of cellular phenotype was lacking. Here, we define differential genetic signatures and dependencies for parasympathetic and sympathetic neurons, both pre- and postganglionic. When we reexamine the sacral autonomic outflow of mice in this light, we find that it is better characterized as sympathetic than parasympathetic.


[1]Institut de Biologie de l'École Normale Supérieure (IBENS), INSERM, CNRS, École Normale Supérieure, Paris Sciences et Lettres Research University, Paris, 75005 France. [2]Wolfson Institute for Biomedical Research, University College London, London, UK.
*These authors contributed equally to this work †Corresponding author. Email: jfbrunet@biologie.ens.fr


Cranial parasympathetic preganglionic neurons are born in the "pMNv" progenitor domain of the hindbrain (*5*) that expresses the homeogene *Phox2b* and produces, in addition, branchiomotor neurons (*6*). The postmitotic precursors migrate dorsally (*7*) to form nuclei (such as the dorsal motor nucleus of the vagus nerve) and project through dorsolateral exit points (*7*) in several branches of the cranial nerves to innervate parasympathetic and enteric ganglia. In contrast, thoracic and upper lumbar (hereafter "thoracic") preganglionic neurons, which are sympathetic, are thought to have a common origin with somatic motoneurons (*8*, *9*). By implication, they would be born in the pMN progenitor domain (just dorsal to p3)—thus from progenitors that express the basic helix-loop-helix (bHLH) transcription factor Olig2 (*10*). The sympathetic preganglionic precursors then segregate from somatic motoneurons to form the intermediolateral column in mammals (*11*), project in the ventral roots of spinal nerves together with axons of somatic motoneurons, and, via the white rami communicantes, synapse onto neurons of the paravertebral and prevertebral sympathetic ganglia.

We sought to compare the genetic makeup and dependencies of lower lumbar and sacral (hereafter "sacral") preganglionic neurons with that of cranial (parasympathetic) and thoracic (sympathetic) ones. As representative of cranial preganglionic neurons, we focused on the dorsal motor nucleus of the vagus nerve, a cluster of

Downloaded from http://science.sciencemag.org/ on November 24, 2016

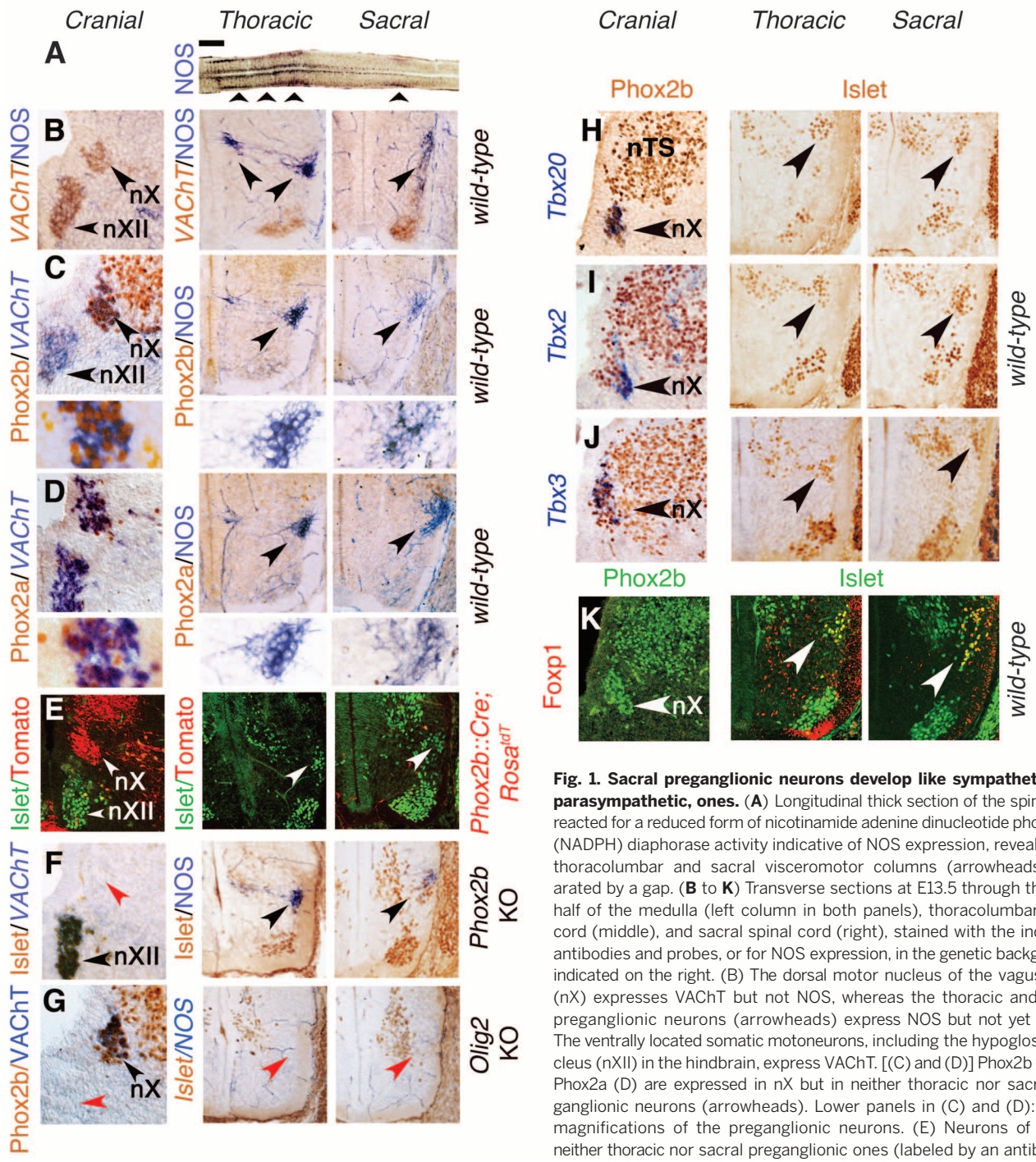


**Fig. 1. Sacral preganglionic neurons develop like sympathetic, not parasympathetic, ones.** (**A**) Longitudinal thick section of the spinal cord reacted for a reduced form of nicotinamide adenine dinucleotide phosphate (NADPH) diaphorase activity indicative of NOS expression, revealing the thoracolumbar and sacral visceromotor columns (arrowheads) separated by a gap. (**B** to **K**) Transverse sections at E13.5 through the right half of the medulla (left column in both panels), thoracolumbar spinal cord (middle), and sacral spinal cord (right), stained with the indicated antibodies and probes, or for NOS expression, in the genetic backgrounds indicated on the right. (B) The dorsal motor nucleus of the vagus nerve (nX) expresses VAChT but not NOS, whereas the thoracic and sacral preganglionic neurons (arrowheads) express NOS but not yet VAChT. The ventrally located somatic motoneurons, including the hypoglossal nucleus (nXII) in the hindbrain, express VAChT. [(C) and (D)] Phox2b (C) and Phox2a (D) are expressed in nX but in neither thoracic nor sacral preganglionic neurons (arrowheads). Lower panels in (C) and (D): higher magnifications of the preganglionic neurons. (E) Neurons of nX but neither thoracic nor sacral preganglionic ones (labeled by an antibody to Islet1/2, white arrowheads) derive from Phox2b$^{+}$ precursors, permanently labeled in a Phox2b::Cre;Rosa$^{tdT}$ background. (F) nX is missing in Phox2b knockouts (red arrowhead), but thoracic and sacral preganglionic neurons are spared (black arrowheads). (G) nX is spared in Olig2 knockouts (black arrowhead), but thoracic and sacral preganglionic neurons are missing (red arrowheads). nXII is also missing, as expected of a somatic motor nucleus (red arrowhead). [(H) to (J)] Tbx20, Tbx2, and Tbx3 are expressed in all or a subset of nX neurons (arrowheads in panels of the left column) but in no thoracic or sacral preganglionic neuron (arrowheads in panels of the middle and right columns). (K) Foxp1 is not expressed in the nX (arrowhead in left column) but is a marker of both thoracic and sacral preganglionic neurons (arrowheads in middle and right columns). nTS, nucleus of the solitary tract. Scale bars: 1 mm (A), 100 μm [(B) to (K)].

neurons already well delineated at 13.5 days of embryonic development (E13.5), that expresses the vesicular acetylcholine transporter (VAChT) (Fig. 1B). Thoracic and sacral preganglionic neurons, which both form a mediolateral column in the spinal cord, did not express VAChT at this stage despite their eventual cholinergic nature. To localize them, we thus used their common marker nitric oxide synthase (NOS) (*12*) (Fig. 1, A and B), which was absent from the dorsal motor nucleus of the vagus nerve at E13.5 (Fig. 1B) or later (fig. S1). Thus, NOS expression characterizes thoracic and sacral, but not cranial, preganglionic neurons.

In contrast to cranial (parasympathetic) preganglionic neurons, thoracic (sympathetic) ones

Downloaded from http://science.sciencemag.org/ on November 22, 2016

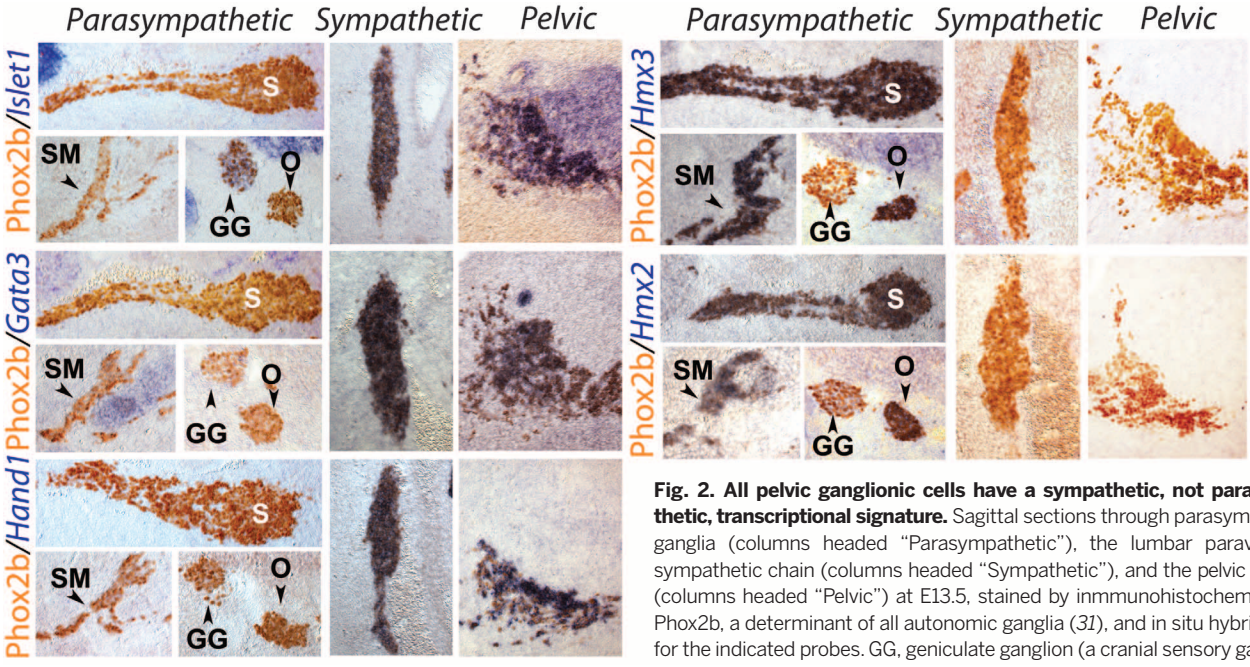


**Fig. 2. All pelvic ganglionic cells have a sympathetic, not parasympathetic, transcriptional signature.** Sagittal sections through parasympathetic ganglia (columns headed "Parasympathetic"), the lumbar paravertebral sympathetic chain (columns headed "Sympathetic"), and the pelvic ganglion (columns headed "Pelvic") at E13.5, stained by inmmunohistochemistry for Phox2b, a determinant of all autonomic ganglia (*31*), and in situ hybridization for the indicated probes. GG, geniculate ganglion (a cranial sensory ganglion); O, otic ganglion; S, sphenopalatine ganglion; SM, submandibular ganglion (all parasympathetic ganglia).

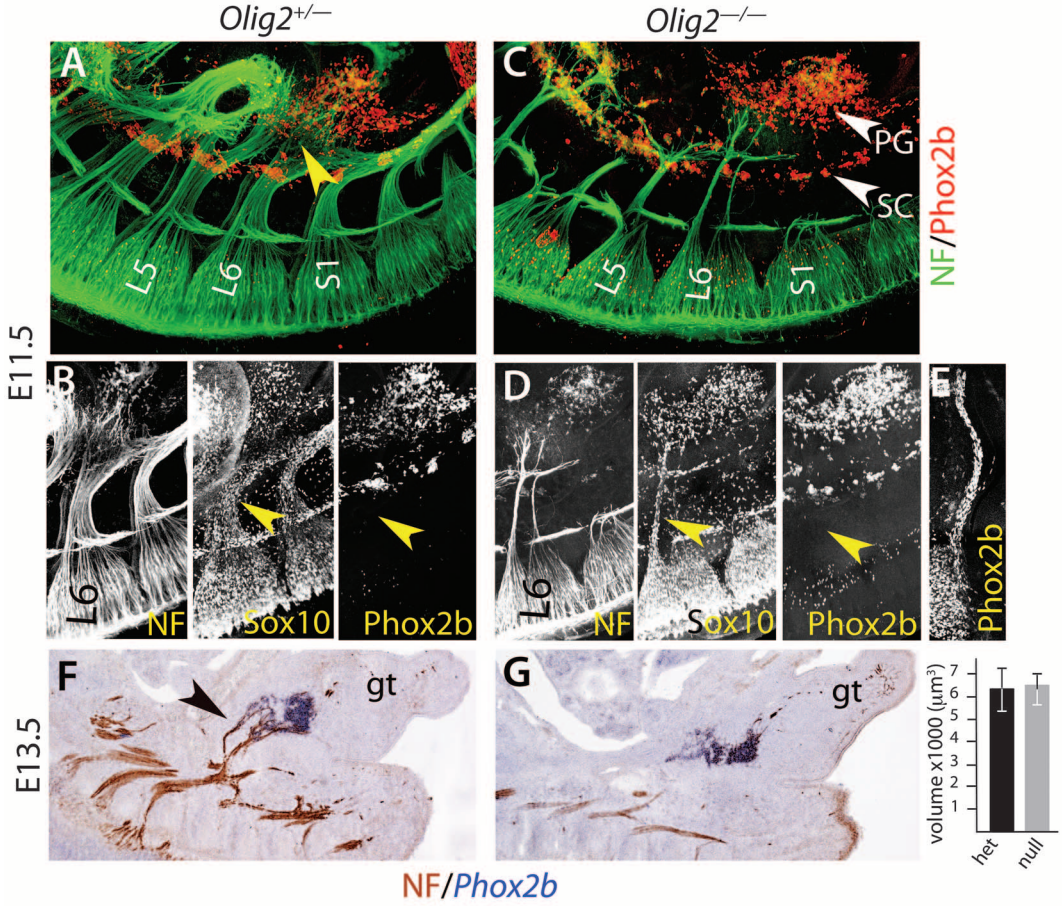


**Fig. 3. The pelvic ganglion forms independently of its nerve, like sympathetic and unlike parasympathetic ones.** (**A** and **C**). Whole-mount immunofluorescence with the indicated antibodies on E11.5 embryos either heterozygous (A) or homozygous (C) for an *Olig2* null mutation. The nascent pelvic nerves [yellow arrowhead in (A)] seem to derive mostly from the L6 nerve at that stage. The Olig2 null mutation (C) spares two thin sensory pelvic projections. The pelvic ganglion (PG) lies ahead of most fibers in both heterozygous and mutant background. (**B** and **D**). View of the L6 nerve, covered with Sox10$^+$ cells but no Phox2b$^+$ cells (yellow arrowheads), unlike cranial nerves that give rise to parasympathetic ganglia at the same stage [Jacobson's nerve in (**E**)]. (**F** and **G**) In situ hybridization for Phox2b and immunohistochemistry for neurofilament (NF) on heterozygous and homozygous Olig2 knockouts at E13.5, when parasympathetic ganglia have formed elsewhere in the body. Graph: the pelvic ganglion has the same volume whether its preganglionic nerve is present [black arrowhead in (F)] or not (6369 µm$^3$ ± 1066 versus 6441 µm$^3$ ± 919, $P = 0.96$, $n = 5$ embryos). gt, genital tubercle; L5 and L6, 5th and 6th lumbar roots; S1, 1st sacral root; SC, sympathetic chain.

Downloaded from http://science.sciencemag.org/ on November 22, 2016

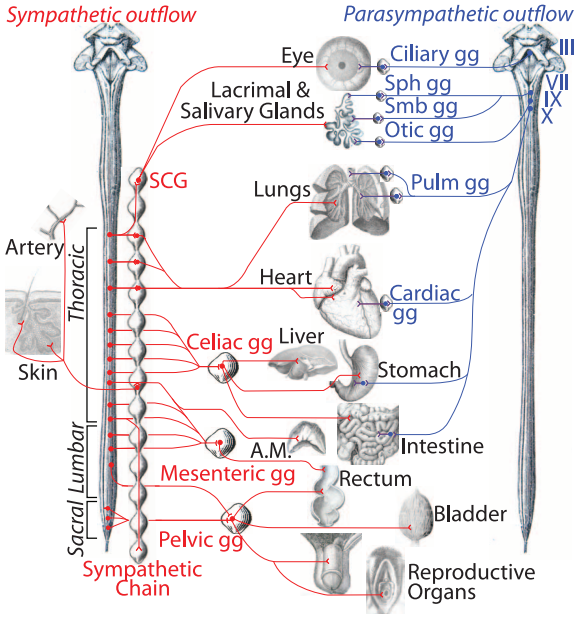


**Fig. 4. Revised anatomy of the autonomic nervous system.** The efferent path of the autonomic nervous system is made up of a spinal sympathetic outflow (left, in red) and a cranial parasympathetic outflow (right, in blue). Sympathetic targets in the skin other than arteries are piloerector muscles and sweat glands. III, oculomotor nerve; VII, facial nerve; IX, glossopharyngeal nerve; X, vagus nerve; A.M., adrenal medulla; gg, ganglion; Pulm, pulmonary; SCG, superior cervical ganglion; Sph, sphenopalatine; Smb, submandibular. For a larger version, see fig. S11.

not only failed to express Phox2b or its paralogue Phox2a at E13.5 but also arose from Phox2b-negative progenitors and did not depend on Phox2b for their differentiation (Fig. 1, C to F, left and middle columns) but instead depended on Olig2 (Fig. 1G). Sacral preganglionic neurons shared all these features with thoracic ones (Fig. 1, C to G, middle and right columns). At E13.5, the T-box transcription factors Tbx20, Tbx2, and Tbx3 were expressed by cranial (parasympathetic) neurons but by neither thoracic (sympathetic) nor sacral preganglionic ones (Fig. 1, H to J, and fig. S2). The F-box transcription factor Foxp1, a determinant of thoracic preganglionic neurons (*13*), was expressed by sacral but not cranial preganglionic neurons (Fig. 1K). Differential expression of Phox2b, Tbx20, and FoxP1 between cranial and all spinal preganglionic neurons, thoracic and sacral, was still observed at E16.5 (fig. S3). In sum, the ontogeny and transcriptional signature of sacral preganglionic neurons was indistinguishable from that of thoracic ones and therefore sympathetic as well.

Thoracic and sacral preganglionic neurons share a settling site in the mediolateral region of the spinal cord and a ventral exit point for their axons, whereas cranial preganglionics have a less systematized topography and a dorsal axonal exit point. These similarities of thoracic with sacral, and differences of both with cranial, are at odds with the notion of craniosacral outflow since its first description (*1*).

The targets of the sacral preganglionic neurons are in the pelvic plexus (figs. S4 and S5) and are considered, by definition, parasympathetic (*14*). Because a proportion of pelvic ganglionic neurons receive input from upper lumbar levels [half of them in rats (*15*)] and thus from sympathetic preganglionic neurons, the pelvic ganglion is considered mixed sympathetic and parasympathetic (*16*). This connectivity-based definition runs into a conundrum for cells that receive a dual lumbar/sacral input (*17*). The sympathetic identity of both thoracic and sacral preganglionic neurons that we unveil here makes the issue moot. Regardless, we looked for a cell-intrinsic criterion that would corroborate the sympathetic nature of all pelvic ganglionic cells in the form of genes differentially expressed in sympathetic versus parasympathetic ganglionic cells elsewhere in the autonomic nervous system. Neurotransmitter phenotypes do not map on the sympathetic/parasympathetic partition because cholinergic neurons in the pelvic ganglion comprise both "parasympathetic" and "sympathetic" ganglionic cells, as defined by connectivity (*14*), and bona fide sympathetic neurons of the paravertebral chain are cholinergic [reviewed in (*18*)]. However, we found that three transcription factors expressed and required in the sympathoadrenal lineage—Islet1 (*19*), Gata3 (*20*), and Hand1 (*21*)—were not expressed in parasympathetic ganglia such as the sphenopalatine, the submandibular, or the otic ganglia (Fig. 2 and fig. S6) [although Islet1 is expressed in ciliary ganglia (*22*) and Gata3 in cardiac ones (*20*), which thus diverge from the canonical parasympathetic molecular signature]. Conversely, we found that the two paralogous homeobox genes *Hmx2* and *Hmx3* are specific markers of all parasympathetic versus sympathetic ganglia and adrenal medulla (Fig. 2 and figs. S6 and S7). All cells of the pelvic ganglion were Islet1$^+$, Gata3$^+$, Hand1$^+$, Hmx3$^-$, and Hmx2$^-$ at E13.5 (Fig. 2) and at E16.5 (fig. S8), as were smaller scattered ganglia of the pelvic organs (fig. S8). Thus, all had a sympathetic transcriptional fingerprint. Similarly, the chicken ganglion of Remak, classically considered parasympathetic (*23*), displayed an Islet1$^+$, Hand1$^+$, Hmx3$^-$ signature, and thus is sympathetic (fig. S9).

Finally, we tested the pelvic ganglion for the contrasted modes of development of sympathetic and parasympathetic ganglia. Parasympathetic ganglia, unlike sympathetic ones, arise through the migration of Sox10$^+$/Phox2b$^+$ Schwann cell precursors along their future preganglionic nerve toward the site of ganglion formation and do not form if these nerves are absent (*24*, *25*). At E11.5, the lumbosacral plexus, which gives rise to the pelvic nerve, extended some fibers that reached the lateral and rostral edge of the pelvic ganglion anlagen, most of which was already situated well ahead of them (Fig. 3A and movie S1). These fibers were coated with Sox10$^+$ cells, none of which, though, expressed Phox2b (Fig. 3B), in contrast to the cranial nerves that produce parasympathetic ganglia at the same stage (Fig. 3E). Deletion of all motor fibers in Olig2$^{-/-}$ embryos spared only two thin, presumably sensory, projections from the lumbosacral plexus (Fig. 3C), also devoid of Phox2b$^+$ cells (Fig. 3D and fig. S10). Despite this massive atrophy, the pelvic ganglion appeared intact (Fig. 3C, fig. S10, and movie S2). This was verified quantitatively at E13.5 (Fig. 3, F and G). Thus, even though 50% of its cells are postganglionic to the pelvic nerve, the pelvic ganglion forms before and independently of it, as befits a sympathetic ganglion but contrary to parasympathetic ones.

Thus, the sacral visceral nervous system is the caudal outpost of the sympathetic outflow (Fig. 4 and fig. S11), the autonomic nervous system being divided in a cranial and a spinal autonomic system, in line with certain evolutionary speculations (*26*). This new understanding of the anatomy accounts for many data that were at odds with the previous one. For example, although schematics generally represent the sacral pathway to the rectum as disynaptic—i.e., vagal-like—[e.g., (*3*)], it is in fact predominantly (*27*) if not exclusively (*28*) trisynaptic—i.e., sympathetic-like (*29*). Despite the dogma of lumbosacral antagonism on the bladder detrusor muscle, the lumbar inhibition is experimentally absent (*4*) or of dubious functional relevance (*30*). The synergy of the lumbar and sacral pathway for vasodilatation in external sexual organs [reviewed in (*29*)] shows a continuity of action—rather than antagonism, as the old model suggested—across the gap between the thoracolumbar and sacral outflows.

The sympathetic identity of all sacral and pelvic autonomic neurons, which our data unveil, provides a new framework for discoveries on pelvic neuroanatomy and physiology.

## REFERENCES AND NOTES


1. W. H. Gaskell, *J. Physiol.* **7**, 1–80.9 (1886).
2. J. N. Langley, *The Autonomic Nervous System: Part I* (W. Heffer, Cambridge, 1921).
3. E. Kandel, J. Schwartz, T. Jessell, S. Siegelbaum, A. J. Hudspeth, *Principles of Neural Science, Fifth Edition* (McGraw-Hill Professional, 2012).
4. J. N. Langley, H. K. Anderson, *J. Physiol.* **19**, 71–139 (1895).
5. J. Briscoe *et al.*, *Nature* **398**, 622–627 (1999).
6. A. Pattyn, M. Hirsch, C. Goridis, J. F. Brunet, *Development* **127**, 1349–1358 (2000).
7. S. Guthrie, *Nat. Rev. Neurosci.* **8**, 859–871 (2007).
8. A. Prasad, M. Hollyday, *J. Comp. Neurol.* **307**, 237–258 (1991).
9. J. A. Markham, J. E. Vaughn, *J. Neurobiol.* **22**, 811–822 (1991).
10. W. A. Alaynick, T. M. Jessell, S. L. Pfaff, *Cell* **146**, 178–178.e1 (2011).
11. P. E. Phelps, R. P. Barber, J. E. Vaughn, *J. Comp. Neurol.* **330**, 1–14 (1993).
12. C. R. Anderson, *Neurosci. Lett.* **139**, 280–284 (1992).


Downloaded from http://science.sciencemag.org/ on November 22, 2016

13. J. S. Dasen, A. De Camilli, B. Wang, P. W. Tucker, T. M. Jessell, *Cell* **134**, 304–316 (2008).
14. J. R. Keast, *Int. Rev. Cytol.* **248**, 141–208 (2006).
15. J. R. Keast, *Neuroscience* **66**, 655–662 (1995).
16. A. Kuntz, R. L. Moseley, *J. Comp. Neurol.* **64**, 63–75 (1936).
17. W. C. De Groat, A. M. Booth, J. Krier, in *Integrative Functions of the Autonomic Nervous System*, C. M. Brooks, K. Koizumi, A. Sato, Eds. (University of Tokyo Press, Tokyo, 1979), pp. 234–245.
18. U. Ernsberger, H. Rohrer, *Cell Tissue Res.* **297**, 339–361 (1999).
19. K. Huber *et al.*, *Dev. Biol.* **380**, 286–298 (2013).
20. K. Tsarovina *et al.*, *Development* **131**, 4775–4786 (2004).
21. E. Doxakis, L. Howard, H. Rohrer, A. M. Davies, *EMBO Rep.* **9**, 1041–1047 (2008).
22. L. Huber, M. Ferdin, J. Holzmann, J. Stubbusch, H. Rohrer, *Dev. Biol.* **363**, 219–233 (2012).
23. C. L. Yntema, W. S. Hammond, *J. Exp. Zool.* **129**, 375–413 (1955).
24. V. Dyachuk *et al.*, *Science* **345**, 82–87 (2014).
25. I. Espinosa-Medina *et al.*, *Science* **345**, 87–90 (2014).
26. S. Nilsson, in *Autonomic Nerve Function in the Vertebrates*, *Zoophysiology*, vol. 13, D. S. Farner, Ed. (Springer-Verlag, New York, 1983), chap. 2.
27. C. Olsson *et al.*, *J. Comp. Neurol.* **496**, 787–801 (2006).
28. K. Fukai, H. Fukuda, *J. Physiol.* **362**, 69–78 (1985).
29. W. Jänig, *The Integrative Action of the Autonomic Nervous System: Neurobiology of Homeostatis* (Cambridge Univ. Press, Cambridge, UK, 2006).
30. W. C. de Groat, W. R. Saum, *J. Physiol.* **220**, 297–314 (1972).
31. A. Pattyn, X. Morin, H. Cremer, C. Goridis, J. F. Brunet, *Nature* **399**, 366–370 (1999).

**ACKNOWLEDGMENTS**

We thank the Imaging Facility of Institut de Biologie de l'École Normale Supérieure (IBENS), which is supported by grants from Fédération pour la Recherche sur le Cerveau, Région Ile-de-France DIM NeRF 2009 and 2011 and France-BioImaging. We thank A. Shihavuddin and A. Genovesio for help with image analysis, the animal facility of IBENS, C. Goridis for helpful comments on the manuscript, and all the members of the Brunet laboratory for discussions. This study was supported by the Centre National de la Recherche Scientifique, the Ecole Normale Supérieure, Institut National de la Santé et de la Recherche Médicale, Agence Nationale de la Recherche (ANR) award ANR-12-BSV4-0007-01 (to J.-F.B), Fondation pour la Recherche Médicale (FRM) award DEq. 2000326472 (to J.-F.B.), the Investissements d'Avenir program of the French government implemented by the ANR (referenced ANR-10-LABX-54 MEMO LIFE and ANR-11-IDEX-0001-02 Paris Sciences et Lettres Research University). I.E.-M. was supported by the French Ministry of Higher Education and Research and the FRM award FDT20160435297. Work in W.D.R.'s laboratory is supported by the European Research Council (grant agreement 293544) and Wellcome (100269/Z/12/Z). The supplementary materials contain additional data.

**SUPPLEMENTARY MATERIALS**

www.sciencemag.org/content/354/6314/893/suppl/DC1
Materials and Methods
Figs. S1 to S11
Movies S1 and S2
References (*32*–*43*)

12 July 2016; accepted 14 October 2016
10.1126/science.aah5454

PLANT SCIENCE

# Phytochrome B integrates light and temperature signals in *Arabidopsis*

**Martina Legris,[1] Cornelia Klose,[2]* E. Sethe Burgie,[3]* Cecilia Costigliolo Rojas,[1]* Maximiliano Neme,[1] Andreas Hiltbrunner,[2,4] Philip A. Wigge,[5] Eberhard Schäfer,[2,4]† Richard D. Vierstra,[3]† Jorge J. Casal[1,6]‡**

**Ambient temperature regulates many aspects of plant growth and development, but its sensors are unknown. Here, we demonstrate that the phytochrome B (phyB) photoreceptor participates in temperature perception through its temperature-dependent reversion from the active Pfr state to the inactive Pr state. Increased rates of thermal reversion upon exposing *Arabidopsis* seedlings to warm environments reduce both the abundance of the biologically active Pfr-Pfr dimer pool of phyB and the size of the associated nuclear bodies, even in daylight. Mathematical analysis of stem growth for seedlings expressing wild-type phyB or thermally stable variants under various combinations of light and temperature revealed that phyB is physiologically responsive to both signals. We therefore propose that in addition to its photoreceptor functions, phyB is a temperature sensor in plants.**

Plants have the capacity to adjust their growth and development in response to light and temperature cues (*1*). Temperature-sensing helps plants determine when to germinate, adjust their body plan to protect themselves from adverse temperatures, and flower. Warm temperatures as well as reduced light resulting from vegetative shade promote stem growth, enabling seedlings to avoid heat stress and canopy shade from neighboring plants. Whereas light perception is driven by a collection of identified photoreceptors—including the red/far-red light-absorbing phytochromes; the blue/ultraviolet-A (UV-A) light–absorbing cryptochromes, phototropins, and members of the Zeitlupe family; and the UV-B–absorbing UVR8 (*2*)—temperature sensors remain to be established (*3*). Finding the identity (or identities) of temperature sensors would be of particular relevance in the context of climate change (*4*).

Phytochrome B (phyB) is the main photoreceptor controlling growth in *Arabidopsis* seedlings exposed to different shade conditions (*5*). Like others in the phytochrome family, phyB is a homodimeric chromoprotein, with each subunit harboring a covalently bound phytochromobilin chromophore. phyB exists in two photo-interconvertible forms: a red light–absorbing Pr state that is biologically inactive and a far-red light–absorbing Pfr state that is biologically active (*6*, *7*). Whereas Pr arises upon assembly with the bilin, formation of Pfr requires light, and its levels are strongly influenced by the red/far-red light ratio. Consequently, because red light is absorbed by photosynthetic pigments, shade light from neighboring vegetation has a strong impact on Pfr levels by reducing this ratio (*8*). phyB Pfr also spontaneously reverts back to Pr in a light-independent reaction called thermal reversion (*9*–*11*). Traditionally, thermal reversion was assumed to be too slow relative to the light reactions to affect the Pfr status of phyB, even under moderate irradiances found in natural environments, but two observations contradict this view. First, the formation of phyB nuclear bodies, which reflects the status of Pfr, is affected by light up to irradiances much higher than expected if thermal reversion were slow (*12*). Second, it is now clear that thermal reversion occurs in two steps. Although the first step, from the Pfr:Pfr homodimer (D2) to the Pfr:Pr heterodimer (D1), is slow ($k_{r2}$), the second step, from the Pfr:Pr heterodimer to the Pr:Pr homodimer (D0), is almost two orders of magnitude faster ($k_{r1}$) (Fig. 1A) (*11*).

Physiologically relevant temperatures could change the magnitude of $k_{r1}$ and consequently affect Pfr and D2 levels, even under illumination (Fig. 1A). To test this hypothesis, we used in vitro and in vivo spectroscopy and analysis of phyB nuclear bodies by means of confocal microscopy. For the first of these approaches, we produced recombinant full-length phyB bearing its phytochromobilin chromophore. When irradiated under continuous red light, the in vitro absorbance at 725 nm reached lower values at higher temperatures, which is indicative of reduced steady-state levels of Pfr (Fig. 1, B and C). We calculated the differences between the steady-state absorbance spectra in darkness and continuous red light (Δ absorbance). The amplitude between the maximum and minimum peaks of Δ absorbance, which represents the amount of Pfr, strongly decreased between 10 and 30°C (Fig. 1, D and E). This characteristic of phyB differs from the typical behavior

[1]Fundación Instituto Leloir, Instituto de Investigaciones Bioquímicas de Buenos Aires–Consejo Nacional de Investigaciones Científicas y Técnicas (CONICET), 1405 Buenos Aires, Argentina. [2]Institut für Biologie II, University of Freiburg, Schaenzlestrasse 1, D-79104 Freiburg. [3]Department of Biology, Washington University in St. Louis, Campus Box 1137, One Brookings Drive, St. Louis, MO 63130, USA. [4]BIOSS Centre for Biological Signaling Studies, University of Freiburg, Schaenzlestrasse 18, 79104 Freiburg, Germany. [5]Sainsbury Laboratory, Cambridge University, 47 Bateman Street, Cambridge CB2 1LR, UK. [6]Instituto de Investigaciones Fisiológicas y Ecológicas Vinculadas a la Agricultura (IFEVA), Facultad de Agronomía, Universidad de Buenos Aires and CONICET, Avenida San Martín 4453, 1417 Buenos Aires, Argentina.
*These authors contributed equally to this work. †These authors contributed equally to this work. ‡**Corresponding author. Email: casal@ifeva.edu.ar**

Downloaded from http://science.sciencemag.org/ on November 22, 2016

Corrected 17 November 2016. See full text.

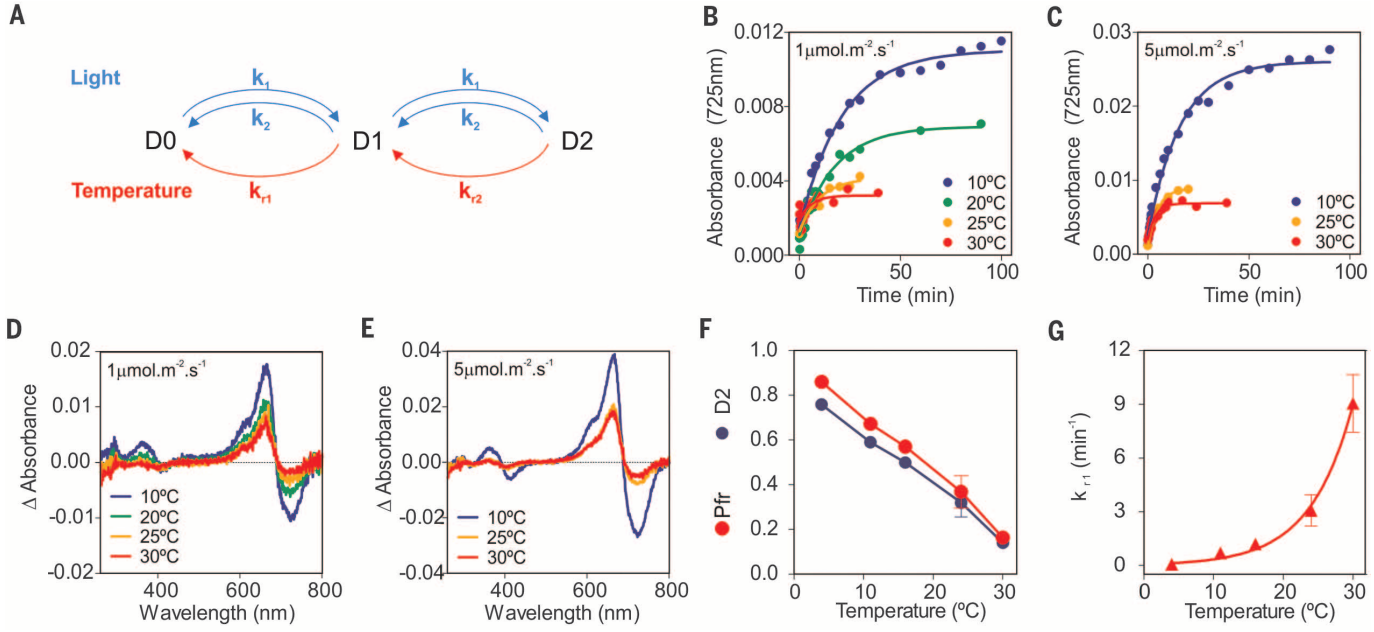


**Fig. 1. The status of phyB responds to light and temperature.** (**A**) Three-stage model of phyB (*11*). Our working hypothesis is that D2 integrates light cues (via $k_1$ and $k_2$) and temperature cues (via $k_{r2}$ and mainly $k_{r1}$). (**B** to **E**) Warm temperatures reduce Pfr levels of full-length recombinant phyB exposed in vitro to 1 [(B) and (D)] or 5.1 [(C) and (E)] µmol $m^{-2}$ $s^{-1}$ of continuous red light. [(B) and (C)] Absorbance kinetics (maximal absorption decreased with temperature, $P < 0.05$). [(D) and (E)] Δ absorbance in samples incubated in darkness or exposed to continuous red light to reach a steady state. The difference between Δ absorbance at 665 and 725 nm decreased with temperature ($P < 0.01$). (**F**) Warm temperatures reduce the levels of Pfr and D2 in vivo measured in *phyA* mutant seedlings overexpressing phyB (*9*) exposed to 1 µmol $m^{-2}$ $s^{-1}$ red light. Means ± SE of three biological replicates. (**G**) Warm temperatures increase $k_{r1}$ [calculated from (F), $P < 0.001$].

of enzymes, which exhibit increased activity over the same temperature range (*13*).

We also measured with in vivo spectroscopy the steady-state levels of phyB Pfr in seedlings irradiated with continuous red or white light at different temperatures (applied only during the irradiation). Increasing temperatures reduced both the total pool of Pfr and that of D2 (Fig. 1F and fig. S1), which is considered to be the physiologically relevant species for phyB (*11*). Using these data, we determined $k_{r1}$, which increased with temperature (Fig. 1G).

phyB nuclear body formation increases with irradiance and red/far-red light ratio (*12*, *14*) because it depends on D2 (*11*). As a proxy for temperature impact on D2, we used the difference in nuclear body formation in lines of the *phyB-9*–null mutant rescued with unmodified phyB [phyB–yellow fluorescent protein (YFP)] or either of two chromophore pocket mutants that suppress Pfr thermal reversion in vitro with little to no effect on photoconversion ($phyB^{Y361F}$-YFP and $phyB^{R582A}$-YFP) (*15*, *16*). De-etiolated (green) seedlings were transferred to the different light conditions (irradiances and red/far-red light ratios) representative of unfiltered sunlight, canopy shade, or cloudy days, in combination with different temperatures applied only during the light treatments (fig. S2). The nuclear body size of $phyB^{Y361F}$-YFP and $phyB^{R582A}$-YFP was not significantly affected by irradiance (fig. S3) and strongly affected by the red/far-red ratio (fig. S4). This is consistent with the notion that irradiance responses depend on $k_{r1}$ and $k_{r2}$ (*11*), which are affected in the mutants. The size of phyB nuclear bodies varied quadratically with temperature and

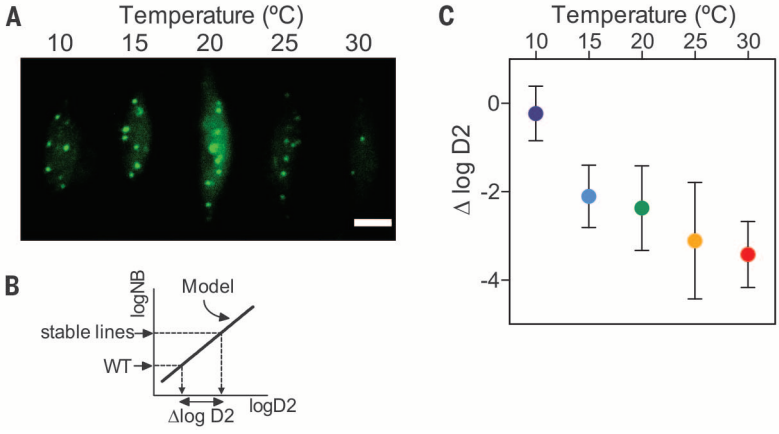


**Fig. 2. phyB nuclear bodies respond to light and temperature.** (**A**) Dual response of phyB-YFP nuclear bodies to temperature (white light, 10 µmol $m^{-2}$ $s^{-1}$). Scale bar, 5 µm. (**B**) Estimation of D2 in the wild type by using its average phyB nuclear body size (NB) as input in the model relating NB to D2 in lines expressing stabilized phyB ($phyB^{Y361F}$-YFP and $phyB^{R582A}$-YFP). (**C**) Impact of temperature on D2. Difference in log-transformed D2 averaged for 5 to 11 conditions (±SE) covering a wide range of irradiances and red/far-red ratios (temperature effect, $P < 0.05$).

was largest at ~20°C (Fig. 2A and fig. S5). We tested the hypothesis that the negative phase of this response to temperature is the manifestation of enhanced thermal reversion reducing D2. Toward this aim, we modeled the average size of the $phyB^{Y361F}$-YFP and $phyB^{R582A}$-YFP nuclear bodies (tables S1 and S2) as a function of both D2 (*11*) and temperature effects not mediated by changes in D2 (fig. S6). Then, we used this restricted model to predict D2 levels from phyB nuclear body sizes in wild-type lines (Fig. 2B). The difference between the apparent log D2 in wild-type and the log D2 of $phyB^{Y361F}$ and $phyB^{R582A}$ in the same light condition is shown in Fig. 2C (difference averaged for all light conditions). The results indicate that high temperatures decrease the apparent D2 for the wild-type phyB under a wide range of light conditions.

By using the three approaches above, we showed that the activity of phyB decreases with increasing temperature (Figs. 1 and 2), suggesting two possible biological outcomes. One is that downstream

Downloaded from http://science.sciencemag.org/ on November 24, 2016

Corrected 17 November 2016. See full text.



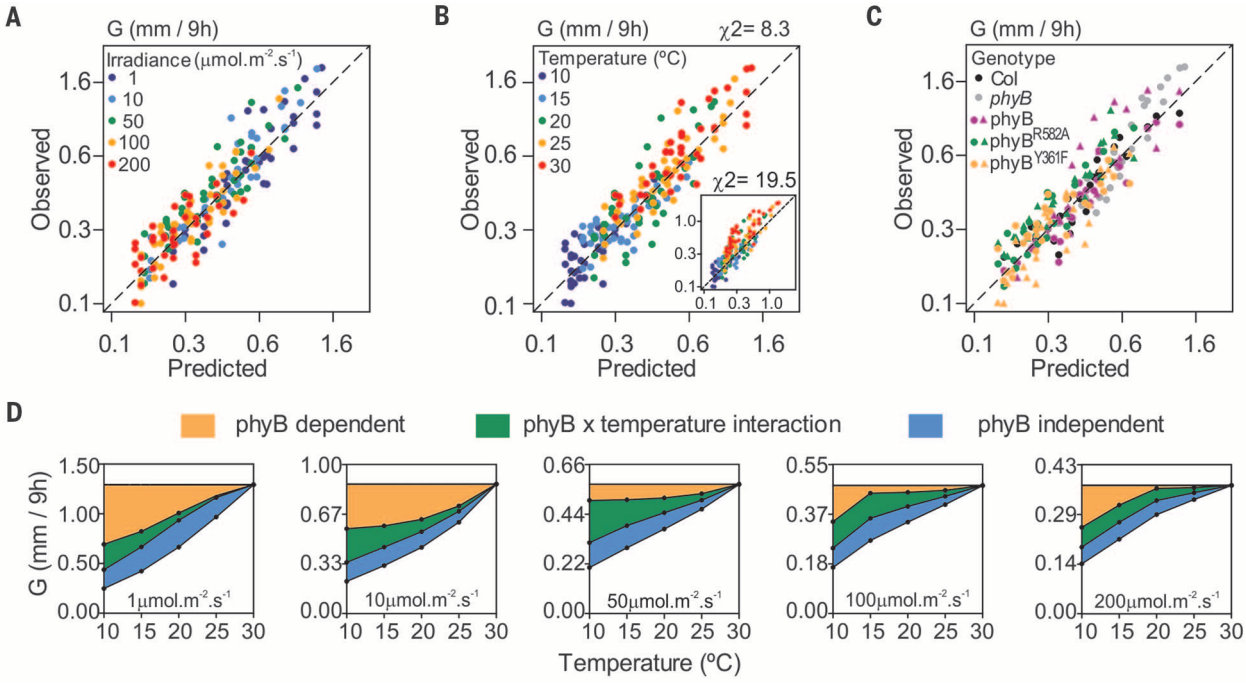


**Fig. 3. phyB mediates growth responses to light and temperature.** (**A** to **C**) Observed values of hypocotyl growth (*G*) in white light–grown seedlings of eight genotypes exposed to 25 combinations of irradiance and temperature versus the values predicted by the growth model. The different irradiances (A), temperatures (B), and genotypes (C) are color-coded to show that the relationship between observed and predicted values is not biased for any of these factors (within the range tested here). Col, Columbia wild type; *phyB*, phyB null mutant; phyB, $phyB^{Y361F}$, and $phyB^{R582A}$, transgenic lines expressing wild-type or mutated phyB in the *phyB* null mutant background. [(B), inset] The goodness of fit of the model (Pearson's $\chi^2$ test) is greatly deteriorated when temperature effects on D2 are not incorporated (both versions of the model have the same number of parameters). (**D**) Contribution to the inhibition of growth of each one of the three temperature-dependent terms of the growth model. Topmost line is the horizontal base line of no low-temperature effects (*G* incorporating only light effects at 30°C). Downward, the lines indicate *G* calculations successively incorporating the phyB-dependent temperature effects, the phyB-temperature interaction, and the phyB-independent temperature effect. The colored areas highlight the contribution of each additional term incorporated in the calculations.

changes in phyB signaling compensate for the temperature effect. The circadian clock provides an example of temperature compensation (*17*). The other is that phyB perception of temperature cues controls the physiological output. A prediction of the latter hypothesis is that phyB activity (D2) should similarly affect growth independently of whether it is altered by light, temperature, or mutations that stabilize phyB. To test this prediction, we cultivated *Arabidopsis* seedlings (including phyB genetic variants) at the same irradiance and temperature, sorted them to the different light and temperature environments (fig. S2), and modeled growth under these conditions (table S3) as a function of D2.

The growth responses to temperature (fig. S7) and light (*18*) are not exclusively mediated by phyB (D2). Thus, we built the model in two steps: first, fitting univariate submodels describing the relationship between growth and the individual factors (D2, temperature effects not mediated by changes in D2, and activity of other photo-sensory receptors), and then combining those components in the final model. To quantify the contribution of D2 (fig. S8), we used growth at 30°C (no low-temperature inhibition of growth) (fig. S9) of all genotypes, including the stabilized phyB variants and the *phyB*-null mutant (D2 = 0). To quantify the effects of temperature not mediated by changes in D2 (fig. S9B), we used the *phyB* mutant (no phyB-mediated inhibition) at 1 µmol $m^{-2}$ $s^{-1}$ (at this irradiance, and at 30°C, growth is maximal, indicating that other photoreceptors do not make a strong contribution). To quantify the contribution of other photoreceptors (fig. S10), we used the *phyB* mutant (no phyB-mediated inhibition) at a range of irradiances at 30°C (no low-temperature growth inhibition). The only statistically significant interaction among these terms was between D2 and temperature effects not mediated by changes in D2 (table S4). Therefore, in the final model, growth was inversely related to terms representing the actions of D2, low temperatures (not mediated by changes in D2), other photo-sensory receptors, and the synergistic interaction between D2 and low temperature (not mediated by changes in D2).

We then fitted to the model growth for all 200 light-temperature-genotype combinations. The relationship between observed and predicted data showed no systematic deviation from the 1:1 correlation for the different light (Fig. 3A), temperature (Fig. 3B), or genetic variants with altered Pfr stability (Fig. 3C). Predicted data were obtained with D2 values affected by light, temperature, and genotype. To test the significance of temperature effects mediated by changes in the status of phyB, we recalculated growth by using D2 modified by light and genotype but not by temperature (constant 10°C). This adjustment reduced the growth model goodness of fit (Fig. 3B, inset), indicating that the contribution of phyB-mediated temperature effects on growth is statistically significant and should not be neglected. Because we estimated the effect of D2 using data from a single temperature (fig. S8), our growth model is not based on the assumption that D2 changes with temperature, thus providing confidence that the latter conclusion is genuine.

We used the growth model to compare the contribution of each of the three temperature-dependent terms to the inhibition of growth by low temperatures. phyB-mediated effects of temperature contribute to the overall temperature response (Fig. 3D). The effects were large at low irradiances, decreased with intermediate irradiances (light reactions become increasingly important), and increased again at higher irradiances because now D2 affects growth more strongly.

Phytochromes were discovered and have been studied on the basis of their roles as light receptors in plants (*6*, *7*). However, our observations that temperature alters the amount of D2 for phyB (Figs. 1 and 2) and its physiological output in a manner similar to light (Fig. 3) indicate that phyB should also be defined as a temperature cue receptor. phyB requires light to comply with this temperature function by needing light to initially generate the unstable but bioactive Pfr state. Temperature affects the Pfr status of phyB mainly via $k_{r1}$ in the light (Fig. 1) and via $k_{r2}$ during the night (*19*). Receptors are often activated by their

Downloaded from http://science.sciencemag.org/ on November 24, 2016

Corrected 17 November 2016. See full text.

ligands; although phyB is activated by red light, it is inactivated by far-red light and high temperatures. This combination of light and temperature perception would serve to integrate the signals controlling photo- and thermo-morphogenesis in ways that optimize the growth of plants exposed to a wide range of environments.

## REFERENCES AND NOTES


1. J. J. Casal, C. Fankhauser, G. Coupland, M. A. Blázquez, *Trends Plant Sci.* **9**, 309–314 (2004).
2. V. C. Galvão, C. Fankhauser, *Curr. Opin. Neurobiol.* **34**, 46–53 (2015).
3. M. Quint *et al.*, *Nat. Plants* **2**, 15190 (2016).
4. D. S. Battisti, R. L. Naylor, *Science* **323**, 240–244 (2009).
5. J. J. Casal, *Annu. Rev. Plant Biol.* **64**, 403–427 (2013).
6. P. H. Quail *et al.*, *Science* **268**, 675–680 (1995).
7. E. S. Burgie, R. D. Vierstra, *Plant Cell* **26**, 4568–4583 (2014).
8. M. G. Holmes, H. Smith, *Photochem. Photobiol.* **25**, 539–545 (1977).
9. U. Sweere *et al.*, *Science* **294**, 1108–1111 (2001).
10. É. Ádám *et al.*, *PLOS ONE* **6**, e27250 (2011).
11. C. Klose *et al.*, *Nat. Plants* **1**, 15090 (2015).
12. S. A. Trupkin, M. Legris, A. S. Buchovsky, M. B. Tolava Rivero, J. J. Casal, *Plant Physiol.* **165**, 1698–1708 (2014).
13. M. E. Salvucci, K. W. Osteryoung, S. J. Crafts-Brandner, E. Vierling, *Plant Physiol.* **127**, 1053–1064 (2001).
14. E. K. Van Buskirk, P. V. Decker, M. Chen, *Plant Physiol.* **158**, 52–60 (2012).
15. J. Zhang, R. J. Stankey, R. D. Vierstra, *Plant Physiol.* **161**, 1445–1457 (2013).
16. E. S. Burgie, A. N. Bussell, J. M. Walker, K. Dubiel, R. D. Vierstra, *Proc. Natl. Acad. Sci. U.S.A.* **111**, 10179–10184 (2014).
17. P. A. Salomé, D. Weigel, C. R. McClung, *Plant Cell* **22**, 3650–3661 (2010).
18. R. Sellaro *et al.*, *Plant Physiol.* **154**, 401–409 (2010).
19. J.-H. Jung *et al.*, *Science* **354**, 886–889 (2016).


## ACKNOWLEDGMENTS

We thank F. Venezia (University of Freiburg) for his valuable help with the analytical equations. This work was supported by Agencia Nacional de Promoción Científica y Tecnológica (grants PICT 2012-1396 and PICT 2013-1444 to J.J.C.), Alexander von Humboldt-Foundation (J.J.C.), Universidad de Buenos Aires (grant 20020100100437 to J.J.C.), Fundación Rene Baron (J.J.C.), the Excellence Initiative of the German Federal and State Governments (EXC 294, project C 20 to E.S. and A.H.), the German Research Foundation (DFG; SCHA 303/16-1 and HI 1369/5-1 to E.S. and A.H.), and the U.S. National Science Foundation (MCB-1329956 to R.D.V.). R.D.V and E.S.B. and the University of Wisconsin–Madison have filed U.S. patent application P140220US02, which relates to the use of mutants phyB$^{Y361F}$ and phyB$^{R582A}$ in agriculture. The supplementary materials contain additional data.

## SUPPLEMENTARY MATERIALS

www.sciencemag.org/content/354/6314/897/suppl/DC1
Materials and Methods
Figs. S1 to S11
Tables S1 to S4
References (*20*–*26*)

9 March 2016; accepted 16 September 2016
Published online 27 October 2016
10.1126/science.aaf5656

SYNTHETIC BIOLOGY

# A synthetic pathway for the fixation of carbon dioxide in vitro

**Thomas Schwander,[1] Lennart Schada von Borzyskowski,[1,2] Simon Burgener,[1,2] Niña Socorro Cortina,[1] Tobias J. Erb[1,2,3]***

**Carbon dioxide ($CO_2$) is an important carbon feedstock for a future green economy. This requires the development of efficient strategies for its conversion into multicarbon compounds. We describe a synthetic cycle for the continuous fixation of $CO_2$ in vitro. The crotonyl–coenzyme A (CoA)/ethylmalonyl-CoA/hydroxybutyryl-CoA (CETCH) cycle is a reaction network of 17 enzymes that converts $CO_2$ into organic molecules at a rate of 5 nanomoles of $CO_2$ per minute per milligram of protein. The CETCH cycle was drafted by metabolic retrosynthesis, established with enzymes originating from nine different organisms of all three domains of life, and optimized in several rounds by enzyme engineering and metabolic proofreading. The CETCH cycle adds a seventh, synthetic alternative to the six naturally evolved $CO_2$ fixation pathways, thereby opening the way for in vitro and in vivo applications.**

Autotrophic carbon fixation transforms more than 350 gigatons of $CO_2$ annually. More than 90% of the carbon is fixed by the Calvin-Benson-Bassham (CBB) cycle in plants, algae, and microorganisms. The rest is converted through alternative autotrophic $CO_2$ fixation pathways (*1*, *2*). Despite this naturally existing diversity, the application of $CO_2$-fixing enzymes and pathways for converting $CO_2$ into value-added multicarbon products has been limited in chemistry (*3*, *4*) and biotechnology (*5*). Natural $CO_2$ fixation delivers mainly biomass and not a dedicated product. Moreover, under optimal conditions, biological $CO_2$ fixation is often directly affected by the inefficiency of the $CO_2$-fixing enzymes and pathways. For instance, the CBB cycle's carboxylase, RuBisCO (ribulose-1,5-bisphosphate carboxylase/oxygenase), is a slow catalyst that shows a strong side reaction with oxygen, which leads to the loss of fixed carbon and thus photosynthetic energy by up to 30% in a process called photorespiration (*6*).

Attempts to improve biological $CO_2$ fixation (*7*) have included evolving RuBisCO toward higher reaction rate and specificity (*8*, *9*), engineering more efficient photorespiration (*10*, *11*), and transplanting natural $CO_2$ fixation pathways into non-autotrophic organisms such as *Escherichia coli* (*12*–*14*). In contrast to these efforts, which showed only limited success, the emerging field of synthetic biology provides an alternative approach to create designer $CO_2$ fixation pathways. By freely combining different enzymatic reactions from various biological sources, completely artificial $CO_2$ fixation routes may be constructed that are kinetically or thermodynamically favored relative to the naturally evolved $CO_2$ fixation pathways. Several synthetic routes for $CO_2$ fixation have been theoretically considered (*15*). However, the gap between theoretical design and experimental realization in synthetic biology has impeded the realization of such artificial pathways. For example, attempts to directly assemble synthetic pathways in living organisms are challenged by limited understanding of the complex interplay among the different enzymes used in these synthetic networks, as well as interference of the synthetic networks in the complex background of the host organism, which can lead to undesired effects such as side reactions and toxicity. Therefore, the realization of synthetic pathways requires novel strategies that first allow their testing and optimization in more defined conditions (*16*–*19*). To overcome these limitations, we decided to take a radically different, reductionist approach by assembling a synthetic $CO_2$ fixation cycle from its principal components in a bottom-up fashion (fig. S1).

A known bottleneck in natural $CO_2$ fixation is the efficiency of a carboxylating enzyme in a given pathway (*20*–*22*). To identify a suitable $CO_2$ fixation reaction for our synthetic cycle, we first compared the different biochemical and kinetic properties of all known major carboxylase classes (*23*) (table S1). On the basis of this analysis, we decided to rely on coenzyme A (CoA)–dependent carboxylases, and enoyl-CoA carboxylases/reductases (ECRs) in particular, because of their favorable catalytic properties. ECRs are a recently discovered class of carboxylases that operate in secondary metabolism, as well as in central carbon metabolism of α-proteobacteria and *Streptomycetes*, but notably not in any autotrophic $CO_2$ fixation pathway known so far (*24*). Relative to other carboxylases, including RuBisCO, ECRs span a broad substrate spectrum (*25*), are oxygen-insensitive, do not accept molecular oxygen as substrate, require only the ubiquitous redox cofactor NADPH (reduced nicotinamide adenine dinucleotide phosphate), and catalyze the fixation of $CO_2$ with high catalytic efficiency (i.e., on average better than RuBisCO by a factor of 2 to 4) (table S1) (*26*).

We conceived several theoretical $CO_2$ fixation routes that (i) start with a given ECR reaction, (ii) regenerate the carboxylation substrate to allow for continuous cycling, and (iii) feature a dedicated output reaction to channel the fixed carbon into a product (fig. S2). In contrast to earlier approaches (*15*, *27*), we did not restrict our design to known

[1]Biochemistry and Synthetic Biology of Microbial Metabolism Group, Max Planck Institute for Terrestrial Microbiology Marburg, D-35043 Marburg, Germany. [2]Institute for Microbiology, ETH Zürich, CH-8093 Zürich, Switzerland. [3]LOEWE Center for Synthetic Microbiology, Universität Marburg, D-35037 Marburg, Germany.
*Corresponding author. Email: toerb@mpi-marburg.mpg.de

Downloaded from http://science.sciencemag.org/ on November 24, 2016

enzymes; rather, we considered all reactions that seemed biochemically feasible (i.e., fall into one of the standard reaction classes defined by the Enzyme Commission). We obtained several prospective cycles, of which seven were considered further (fig. S2, A to G).

We first evaluated the thermodynamic feasibility of these theoretical cycles by calculating their Gibbs free energy profile ($\Delta_r G'$) under biologically relevant conditions and estimating the presumable consumption of adenosine triphosphate (ATP) and NADPH in each cycle per $CO_2$ molecule converted (fig. S2 and supplementary text). Our calculations show that the synthetic cycles were generally more energy-efficient than a stand-alone CBB cycle and were also more energy-efficient than the core sequence of other naturally existing, oxygen-insensitive $CO_2$ fixation pathways, such as the 3-hydroxypropionate (3HP) bicycle and the 3-hydroxypropionate/4-hydroxybutyrate (3HP/4HB) cycle (table S2). As an example, four of our synthetic cycles required on average one-third less ATP per $CO_2$ converted into phosphoglycerate, relative to the core sequence of the CBB cycle. This would translate to at least seven fewer photons per phosphoglycerate formed from $CO_2$ in a theoretical photosynthetically coupled process (Table 1 and figs. S3 and S4). In summary, these calculations suggested that our synthetic cycles could provide promising solutions to an efficient C-C bond formation under aerobic conditions that compete with naturally existing metabolic pathways.

Next, we searched bioinformatic databases for enzymes that could sustain our drafts (fig. S2). For the crotonyl-CoA/ethylmalonyl-CoA/hydroxybutyryl-CoA (CETCH) cycle (fig. S2A), we were able to identify one or more potential enzyme candidates for each reaction of its core sequence. We purified, tested, and characterized these candidates and selected a set of 12 enzymes, each with a specific activity of >1 U $mg^{-1}$ protein at 250 μM substrate concentration (table S3), to experimentally realize the CETCH cycle as a proof of principle. To demonstrate the feasibility of the CETCH cycle, we first reconstituted its central $CO_2$ fixation reaction sequence stepwise. We provided cofactors and the chemically synthesized intermediate propionyl-CoA in a buffer containing $NaHCO_3$. To this mixture, propionyl-CoA carboxylase (Pcc) was added first, followed by the subsequent addition of the other 11 enzymes. High-performance liquid chromatography–mass spectrometry (HPLC-MS) analysis demonstrated the stepwise transformation of propionyl-CoA into key intermediates of the pathway (fig. S5), indicating that this first version of the CETCH cycle (CETCH 1.0) was in principle functional.

To test for continuous operation of CETCH 1.0, we provided all enzymes, cofactors, and the artificial electron acceptor ferrocenium from the beginning and started the cycle by addition of propionyl-CoA (fig. S6A). To follow the dynamics of the cycle, we used $NaH^{13}CO_3$ as the $CO_2$ source for this and all subsequent experiments. Because of the constant incorporation of $CO_2$ during the course of the cycle, we could use enrichment of the $^{13}C$ isotope in the intermediates to follow flux through the CETCH cycle in the continuous mode and under apparent steady-state conditions (fig. S7). However, the conversion of CoA esters stopped before a complete turn of the cycle at the level of methylsuccinyl-CoA, which indicated that the methylsuccinyl-CoA dehydrogenase (Mcd) (*28*) enzyme reaction used in the cycle was rate-limiting (fig. S6, B and C, and supplementary text).

Mcd belongs to the family of flavin adenine dinucleotide (FAD)–dependent acyl-CoA dehydrogenases, which are coupled via electron transfer flavoproteins to the membrane-bound ubiquinone pool and eventually to the respiratory chain. In the stepwise reconstitution of CETCH 1.0, we had added the artificial electron acceptor ferrocenium together with Mcd to substitute for the electron transfer cascade. Under continuous conditions, the use of the artificial electron acceptor from the beginning was limited to 0.1 mM, because higher concentrations caused other enzymes in the assay to precipitate. At 0.1 mM, however, the spontaneous reduction of ferrocenium to ferrocene by NADPH (*29*), as well as the slow reoxidation rate of ferrocene, most likely prevented effective cycling of CETCH 1.0.

To overcome the limitations caused by Mcd, we engineered the enzyme to directly use molecular oxygen as electron acceptor. On the basis of structural considerations (Fig. 1 and supplementary text), we introduced three point mutations—$Thr^{317}$ → Gly (T317G), $Glu^{377}$ → Asn (E377N), and $Trp^{315}$ → Phe (W315F)—to convert the dehydrogenase into a functional methylsuccinyl-CoA oxidase (Mco) that catalyzes the oxygen-dependent oxidation

**Table 1. Comparison of selected theoretical and synthetic $CO_2$ fixation cycles with the core sequence of naturally existing, aero-tolerant $CO_2$ fixation pathways.** Shown are the number of reaction steps and the numbers of NAD(P)H, ATP, and $FADH_2$ molecules required (negative numbers) or generated (positive numbers) during conversion of $CO_2$ into one molecule of phosphoglycerate. These values were normalized to ATP equivalents required per $CO_2$ molecule fixed into phosphoglycerate, or alternatively to the number of photons per $CO_2$ fixed into phosphoglycerate in a theoretical photosynthetically coupled process (see supplementary text and figs. S3 and S4 for a more detailed analysis). Number of reaction steps does not take into account stereochemical conversions such as racemization or epimerization. For ATP per $CO_2$ conversions, a P/O ratio of 2.5 for NAD(P)H and 1.5 for $FADH_2$ was assumed (*38*). For photons per $CO_2$ conversions, the number of biologically generated photons required for the generation of the NADPH and ATP in each cycle was calculated, assuming a stoichiometry of 1 NADPH and 1.28 ATP per 4 photons (*39*). The photon energy left is given in ATP equivalents. These calculations do not consider the additional generation of ATP through any $FADH_2$ generated through a given pathway. HOPAC, hydroxypropionyl-CoA/acrylyl-CoA; FUMES, fumaryl-CoA/methylmalyl-CoA/succinyl-CoA; HITME, hydroxycrotonyl-CoA/itaconyl-CoA/methylmalonyl-CoA; n.c., not calculated.

| Pathway | Status | Number of reaction steps | $\Sigma_{NAD(P)H}$ | $\Sigma_{ATP}$ | $\Sigma_{FADH_2}$ | ATP equivalents per $CO_2$ | Photons per $CO_2$ (additional ATP left) |
|---|---|---|---|---|---|---|---|
| CETCH cycle* | Theoretical | 11 | −4 | −4 | 2 | −6.2 | 16 (+2.1 ATP) |
| HOPAC cycle* | Theoretical | 12 | −4 | −3 | 1 | −6.5 | 16 (+1.1 ATP) |
| FUMES cycle* | Theoretical | 11 | −4 | −3 | 1 | −6.5 | 16 (+2.1 ATP) |
| HITME cycle* | Theoretical | 12 | −4 | −3 | 1 | −6.5 | 16 (+2.1 ATP) |
| CBB cycle | Natural | 13 | −5 | −8 | 0 | −6.8 | 21 (+0.1 ATP) |
| CBB cycle (+$O_2$)† | Natural | 13 | −5 | −8 | 0 | −8.2 | 24 (n.c.) |
| 3HP bicycle‡ | Natural | 15 | −6 | −7 | 1 | −6.8 | 24 (+0.7 ATP) |
| 3HP/4HB cycle§ | Natural | 13 | −7 | −8 | 1 | −8.0 | 28 (+1.0 ATP) |
| CETCH 2.0–4.0*‖ | Synthetic | 11 | −4 | −4 | 0 / 1# | −7.5 / −6.5# | 16 (+2.1 ATP) |
| CETCH 5.0–5.4*‖ | Synthetic | 13 | −5 | −2 | 0 / 2# | −8.5 / −6.5# | 20 (+4.4 ATP) |

*Transformation of the initial $CO_2$ fixation product glyoxylate into phosphoglycerate was calculated via glyoxylate carboligase (*40*). †Assuming a loss of 20% photosynthetic energy due to photorespiration. ‡Transformation of the initial $CO_2$ fixation product pyruvate was calculated via pyruvate synthase. §Transformation of the initial $CO_2$ fixation product acetyl-CoA via pyruvate:water dikinase. ‖Transformation of the initial $CO_2$ fixation product acetyl-CoA via acetyl/propionyl-CoA carboxylase and phosphoenolpyruvate carboxykinase. #Calculations for a process, where the electrons from the two oxidase reactions could be conserved via a respiratory chain.

Downloaded from http://science.sciencemag.org/ on November 22, 2016

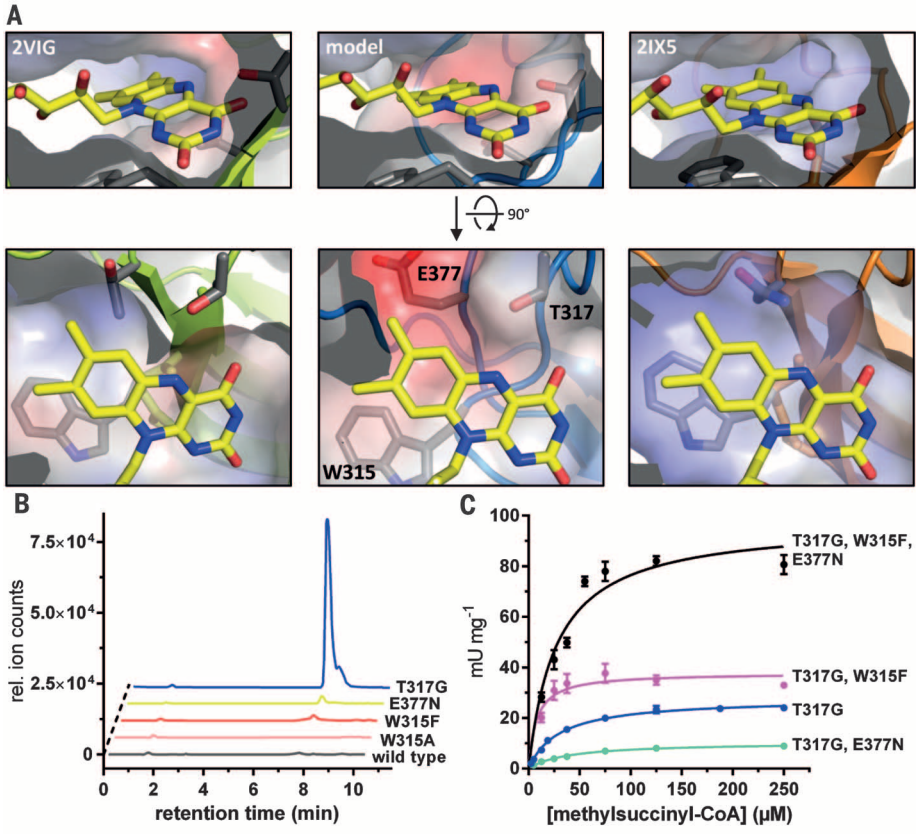


**Fig. 1. Structure-guided engineering of Mcd into a Mco.** (**A**) Active-site comparison of the human short-chain acyl-CoA dehydrogenase (green backbone; PDB ID 2VIG) with a model of Mcd from *Rhodobacter sphaeroides* (blue backbone; modeled by the SWISS-MODEL server with 2VIG as template) and the short-chain acyl-CoA oxidase 4 from *Arabidopsis thaliana* (orange backbone; PDB ID 2IX5). The three residues that were targeted to introduce oxidase activity into Mcd are highlighted. (**B**) HPLC-MS–based analysis of wild-type and different single active-site mutants for oxidation of methylsuccinyl-CoA into mesaconyl-CoA with molecular oxygen as electron acceptor. The screen identified three substitutions (W315F, T317G, and E377N) that were combined into double and triple mutants. (**C**) Michaelis-Menten graphs of single, double, and triple mutants characterized in more detail. The triple mutant showed the best kinetic parameters.

of methylsuccinyl-CoA with a maximal catalytic rate $v_{max}$ of 97 ± 6 mU mg$^{-1}$ and an apparent Michaelis-Menten constant $K_M$ of 27 ± 5 μM. In version 2.0 of the CETCH cycle, we replaced Mcd with the engineered Mco. Fractional labeling of intermediates showed that CETCH 2.0 was turning at least twice within 45 min (fig. S8).

After successful demonstration of the CETCH core cycle under continuous conditions, we next optimized its reaction sequence. We established a readout module to directly quantify $CO_2$ fixation (fig. S9A). Starting from propionyl-CoA, the CETCH cycle converts two molecules of $CO_2$ per turn into one molecule of glyoxylate. To measure glyoxylate formation, we used a malate synthase (Mas) from *E. coli*, which condenses glyoxylate with externally added acetyl-CoA to yield malate. From here on, we used the malate production rate as a readout—in combination with CoA ester analysis—to improve $CO_2$ fixation efficiency of the CETCH cycle stepwise (CETCH 2.0–5.4; see supplementary text).

During the optimization phase, we added enzymes for ATP and NADPH regeneration, provided chemical and enzymatic protection against oxidative damage from $H_2O_2$-producing enzymes, and dealt with unwanted side reactions that prevented effective cycling. The CETCH cycle includes enzymes from very different biological sources. The combination of such diverse enzymes into a synthetic pathway poses the challenge that these enzymes face metabolites to which they were never exposed in their native metabolic context, causing undesired side reactions. Inspired by principles of natural metabolism, we pursued different strategies to overcome this problem (supplementary text and figs. S9 to S12). We replaced the original pathway design with alternative reaction sequences, used enzyme engineering to minimize side reactions of promiscuous enzymes, and introduced proofreading enzymes to correct for the formation of dead-end metabolites. Whereas the first two of these strategies are applied in biotechnology and synthetic biology to improve productivity (*30*, *31*), the concept of metabolic proofreading has only rarely been considered for synthetic pathway design (*16*), although proofreading apparently exists in naturally evolved pathways (*32*). We believe that this design principle should be included more systematically in metabolic engineering in the future.

Over the course of the optimization, $CO_2$ fixation efficiency in the CETCH cycle improved by almost a factor of 20 until version 5.4 (Fig. 2). CETCH 5.4 represents an in vitro enzyme network that is able to fix $CO_2$ at a rate of 5 nmol min$^{-1}$ mg$^{-1}$ of core cycle proteins (Fig. 2C). This is comparable to the few reported attempts to measure the CBB cycle in cell extracts (1 to 3 nmol min$^{-1}$ mg$^{-1}$ CBB cycle protein, assuming that CBB cycle enzymes account for 30% of the proteome) (*33*). However, we note that cell extracts represent a more complex environment than our reductionist in vitro system.

In total, the 13 core reactions of CETCH 5.4, together with the auxiliary proofreading and cofactor regeneration processes, are catalyzed by 17 enzymes from nine different organisms and all three domains of life, including bacteria, archaea, plants, and humans. In addition, the cycle features three reactions that were created by rational active-site engineering of existing enzyme scaffolds to catalyze the desired activities, such as Mco and Pco. Notably, CETCH 5.4 relies solely on the reductive carboxylation of enoyl-CoA esters. Although ECRs belong to the most efficient $CO_2$-fixing group of enzymes known to date, they were not selected for autotrophic $CO_2$ fixation during evolution, as far as we know. The reallocation of reductive carboxylation as a key reaction for a synthetic autotrophic $CO_2$ fixation cycle thus goes beyond simply improving or reshuffling naturally existing autotrophic $CO_2$ fixation reactions and pathways. The CETCH cycle expands the diversity of the six naturally evolved $CO_2$ fixation strategies by a seventh, synthetic alternative that did not require the serendipity of evolution to bring together all components in space and time (*34*).

The successful in vitro reconstitution of a synthetic enzymatic network for the conversion of $CO_2$ into organic products that is superior to chemical processes and competes with naturally existing $CO_2$-fixing solutions in vitro opens the door for several future applications. These could include the in vivo transplantation of synthetic $CO_2$ fixation cycles into lithotrophic or photosynthetic organisms, paving the way to improved $CO_2$ fixation (*35*); the use of synthetic $CO_2$ fixation cycles in the development of artificial photosynthetic processes (e.g., in combination with photovoltaics or artificial leaves) (*36*); and the

Downloaded from http://science.sciencemag.org/ on November 22, 2016

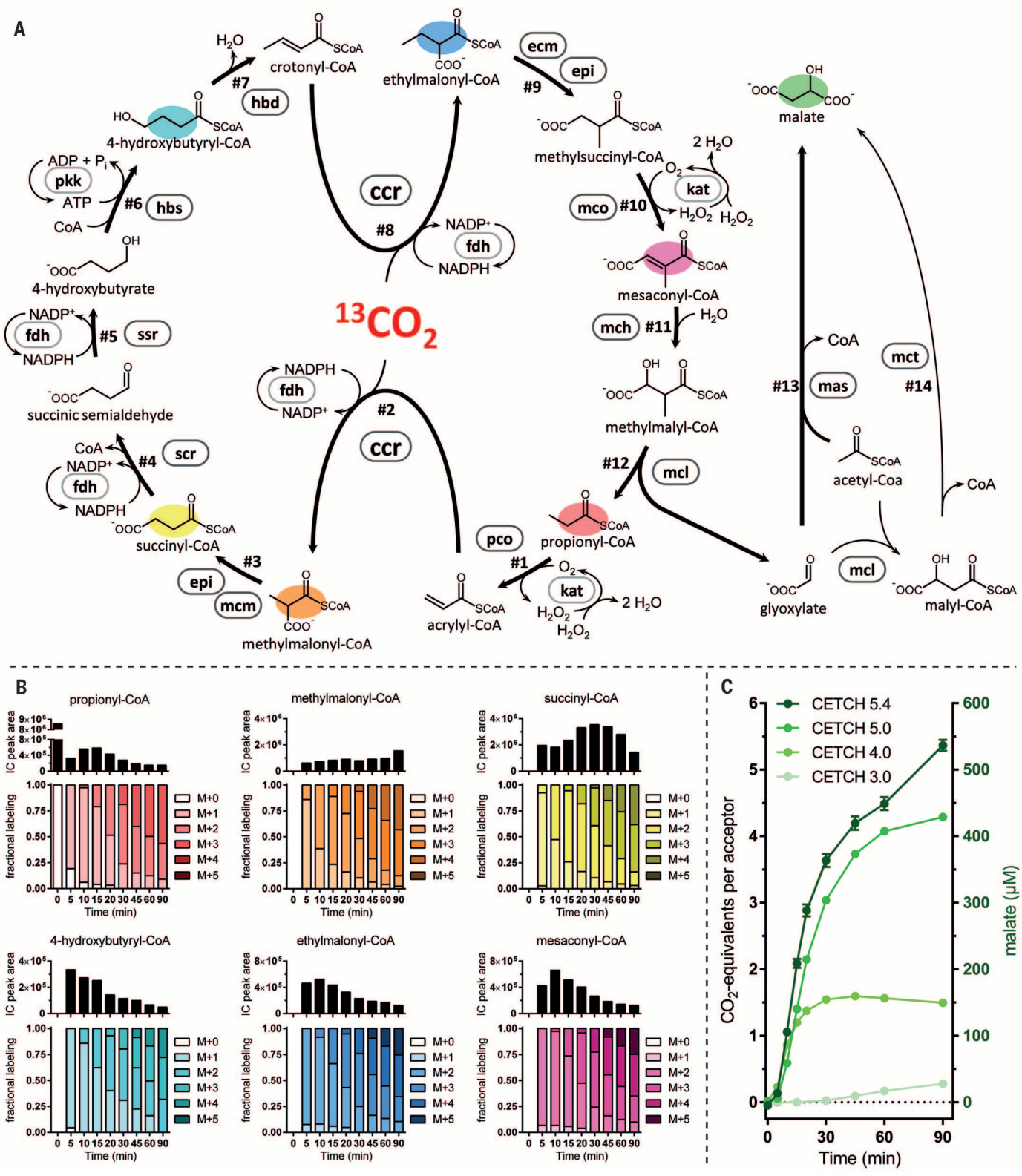


**Fig. 2. The CETCH cycle.** (**A**) Topology of the CETCH cycle (version 5.4), including proofreading and cofactor regenerating enzymes. See table S3 for numbering of reaction steps and enzyme abbreviations. (**B**) Dynamics of key intermediates of CETCH 5.4 over 90 min. Shown are the levels of six different intermediates, as well as their fractional labeling patterns from the incorporation of $^{13}CO_2$ for each turn of the cycle (see fig. S7 for the expected labeling pattern). Intermediates are colored as in (A). (**C**) Left *y* axis: $CO_2$ fixation efficiency of the CETCH cycle over the course of its optimization (see supplementary text). $CO_2$ fixation efficiency is defined as $CO_2$ equivalents fixed per acceptor molecule in the cycle (i.e., starting amount of propionyl-CoA). Right *y* axis: Absolute malate concentration formed over the course of 90 min in CETCH 5.4. The final assay (0.52 ml) contained 2.3 mg $ml^{-1}$ protein of cycle core enzymes plus 0.8 mg $ml^{-1}$ auxiliary enzymes and produced 540 μM malate over 90 min, which corresponds to 1080 μM fixed $CO_2$.

Downloaded from http://science.sciencemag.org/ on November 22, 2016

design of a self-sustained, completely synthetic carbon metabolism in artificial or minimal cells (*37*).

## REFERENCES AND NOTES


1. I. A. Berg, *Appl. Environ. Microbiol.* **77**, 1925–1936 (2011).
2. G. Fuchs, *Annu. Rev. Microbiol.* **65**, 631–658 (2011).
3. M. Aresta, in *Greenhouse Gases: Mitigation and Utilization, CHEMRAWN-XVII and ICCDU-IX Conference, July 8 to 12, 2007*, E. Buncel, Ed. (Queen's University, Kingston, Ontario, Canada, 2009), pp. 123–149.
4. S. M. Glueck, S. Gümüs, W. M. F. Fabian, K. Faber, *Chem. Soc. Rev.* **39**, 313–328 (2010).
5. L. Rosgaard, A. J. de Porcellinis, J. H. Jacobsen, N. U. Frigaard, Y. Sakuragi, *J. Biotechnol.* **162**, 134–147 (2012).
6. B. J. Walker, A. VanLoocke, C. J. Bernacchi, D. R. Ort, *Annu. Rev. Plant Biol.* **67**, 107–129 (2016).
7. T. J. Erb, J. Zarzycki, *Curr. Opin. Chem. Biol.* **34**, 72–79 (2016).
8. D. N. Greene, S. M. Whitney, I. Matsumura, *Biochem. J.* **404**, 517–524 (2007).
9. N. E. Kreel, F. R. Tabita, *PLOS ONE* **10**, e0138351 (2015).
10. P. M. Shih, J. Zarzycki, K. K. Niyogi, C. A. Kerfeld, *J. Biol. Chem.* **289**, 9493–9500 (2014).
11. R. Kebeish *et al.*, *Nat. Biotechnol.* **25**, 593–599 (2007).
12. M. Mattozzi, M. Ziesack, M. J. Voges, P. A. Silver, J. C. Way, *Metab. Eng.* **16**, 130–139 (2013).
13. M. W. Keller *et al.*, *Proc. Natl. Acad. Sci. U.S.A.* **110**, 5840–5845 (2013).
14. N. Antonovsky *et al.*, *Cell* **166**, 115–125 (2016).
15. A. Bar-Even, E. Noor, N. E. Lewis, R. Milo, *Proc. Natl. Acad. Sci. U.S.A.* **107**, 8889–8894 (2010).
16. P. H. Opgenorth, T. P. Korman, J. U. Bowie, *Nat. Chem. Biol.* **12**, 393–395 (2016).
17. S. Billerbeck, M. Bujara, C. Hold, R. Pellaux, S. Panke, *FEBS J.* **277** (suppl. 1), 23 (2010).
18. C. E. Hodgman, M. C. Jewett, *Metab. Eng.* **14**, 261–269 (2012).
19. J. A. Rollin, T. K. Tam, Y. H. P. Zhang, *Green Chem.* **15**, 1708–1719 (2013).
20. S. P. Long, E. A. Ainsworth, A. Rogers, D. R. Ort, *Annu. Rev. Plant Biol.* **55**, 591–628 (2004).
21. R. J. Spreitzer, M. E. Salvucci, *Annu. Rev. Plant Biol.* **53**, 449–475 (2002).
22. M. Könneke *et al.*, *Proc. Natl. Acad. Sci. U.S.A.* **111**, 8239–8244 (2014).
23. L. Schada von Borzyskowski, R. G. Rosenthal, T. J. Erb, *J. Biotechnol.* **168**, 243–251 (2013).
24. T. J. Erb *et al.*, *Proc. Natl. Acad. Sci. U.S.A.* **104**, 10631–10636 (2007).
25. D. M. Peter *et al.*, *Angew. Chem. Int. Ed.* **54**, 13457–13461 (2015).
26. T. J. Erb, V. Brecht, G. Fuchs, M. Müller, B. E. Alber, *Proc. Natl. Acad. Sci. U.S.A.* **106**, 8871–8876 (2009).
27. M. Volpers *et al.*, *PLOS ONE* **11**, e0157851 (2016).
28. T. J. Erb, G. Fuchs, B. E. Alber, *Mol. Microbiol.* **73**, 992–1008 (2009).
29. B. W. Carlson, L. L. Miller, *J. Am. Chem. Soc.* **105**, 7453–7454 (1983).
30. V. de Lorenzo, A. Sekowska, A. Danchin, *FEMS Microbiol. Rev.* **39**, 96–119 (2015).
31. C. Lerma-Ortiz *et al.*, *Biochem. Soc. Trans.* **44**, 961–971 (2016).
32. C. L. Linster *et al.*, *J. Biol. Chem.* **286**, 42992–43003 (2011).
33. N. L. Gale, J. V. Beck, *J. Bacteriol.* **94**, 1052–1059 (1967).
34. F. Jacob, *Science* **196**, 1161–1166 (1977).
35. D. R. Ort *et al.*, *Proc. Natl. Acad. Sci. U.S.A.* **112**, 8529–8536 (2015).
36. R. K. Yadav *et al.*, *J. Am. Chem. Soc.* **134**, 11455–11461 (2012).
37. C. A. Hutchison III *et al.*, *Science* **351**, aad6253 (2016).
38. P. C. Hinkle, *BBA Bioenergetics* **1706**, 1–11 (2005).
39. D. M. Kramer, J. R. Evans, *Plant Physiol.* **155**, 70–78 (2011).
40. L. Schada von Borzyskowski, M. Remus-Emsermann, R. Weishaupt, J. A. Vorholt, T. J. Erb, *ACS Synth. Biol.* **4**, 430–443 (2015).


## ACKNOWLEDGMENTS

We thank G. Fuchs for introducing us to the fundamental principles of microbial $CO_2$ fixation. We thank U. Oppermann for the expression plasmid p2BP1, K. Castiglione for the expression plasmid of Fdh (D221A), J. Andexer for the expression plasmid for Pkk2 and the purified enzyme, and J. Zarzycki and B. Vögeli for contributions during pathway design. The work conducted by the U.S. Department of Energy Joint Genome Institute, a DOE Office of Science User Facility, is supported under contract DE-AC02-05CH11231. Also supported by European Research Council grant ERC 637675 "SYBORG," Swiss National Science Foundation Ambizione grant PZ00P3_136828/1, ETH Zürich grant ETH-41 12-2, and the Max Planck Society. Supporting data are available in the supplementary materials. Author contributions: T.J.E. conceived the project; T.J.E., L.S.v.B., and T.S. designed the experiments, analyzed the data, and wrote the manuscript; T.J.E., T.S., and L.S.v.B. performed experiments; S.B. assisted in experiments; and N.S.C. performed mass spectrometry and analyzed the data.

## SUPPLEMENTARY MATERIALS

www.sciencemag.org/content/354/6314/900/suppl/DC1
Materials and Methods
Supplementary Text
Figs. S1 to S14
Tables S1 to S8
References (*41*–*63*)

8 July 2016; accepted 5 October 2016
10.1126/science.aah5237

NEURODEGENERATION

# Site-specific phosphorylation of tau inhibits amyloid-β toxicity in Alzheimer's mice

**Arne Ittner,[1]* Sook Wern Chua,[1] Josefine Bertz,[1] Alexander Volkerling,[1] Julia van der Hoven,[1] Amadeus Gladbach,[1] Magdalena Przybyla,[1] Mian Bi,[1] Annika van Hummel,[1,2] Claire H. Stevens,[1] Stefania Ippati,[1] Lisa S. Suh,[1,3] Alexander Macmillan,[4] Greg Sutherland,[3] Jillian J. Kril,[3] Ana P. G. Silva,[5] Joel Mackay,[5] Anne Poljak,[6] Fabien Delerue,[1,7] Yazi D. Ke,[2] Lars M. Ittner[1,7,8]***

**Amyloid-β (Aβ) toxicity in Alzheimer's disease (AD) is considered to be mediated by phosphorylated tau protein. In contrast, we found that, at least in early disease, site-specific phosphorylation of tau inhibited Aβ toxicity. This specific tau phosphorylation was mediated by the neuronal p38 mitogen-activated protein kinase p38γ and interfered with postsynaptic excitotoxic signaling complexes engaged by Aβ. Accordingly, depletion of p38γ exacerbated neuronal circuit aberrations, cognitive deficits, and premature lethality in a mouse model of AD, whereas increasing the activity of p38γ abolished these deficits. Furthermore, mimicking site-specific tau phosphorylation alleviated Aβ-induced neuronal death and offered protection from excitotoxicity. Our work provides insights into postsynaptic processes in AD pathogenesis and challenges a purely pathogenic role of tau phosphorylation in neuronal toxicity.**

Alzheimer's disease (AD), the most prevalent form of dementia, is neuropathologically characterized by extracellular amyloid-β (Aβ) plaques and intracellular tau-containing neurofibrillary tangles (*1*, *2*). Growing evidence suggests that Aβ and tau together orchestrate neuronal dysfunction in AD (*3*), although their molecular connections remain poorly understood. Aberrant tau phosphorylation is the first step in a cascade leading to its deposition and to cognitive dysfunction (*4*, *5*). Aβ is thought to trigger toxic events, including tau phosphorylation (*6*). Accordingly, the depletion of tau prevents Aβ toxicity in AD models (*7*–*9*). Aβ-induced neuronal network and synaptic dysfunction is associated with aberrant glutamatergic synaptic transmission (*10*). *N*-methyl-D-aspartate (NMDA)–type glutamatergic receptors (NRs) drive glutamate-induced neuronal excitotoxicity (*11*) and mediate Aβ toxicity by downstream responses that promote neuronal dysfunction (*12*).

Multiple factors, including p38 kinases, contribute to NR-mediated toxicity (*12*). Although inhibition of p38α and p38β improves Aβ-induced long-term potentiation deficits (*13*, *14*), it increases hyperexcitability in Aβ precursor protein (APP) transgenic mice (*15*). However, the specificity of p38 inhibitors remains debatable (*16*, *17*). Other p38 kinases, p38γ and p38δ, have not been studied in AD. To understand the roles of p38 kinases in AD, we induced excitotoxic seizures with pentylenetetrazole (PTZ), an approach widely used for studying excitotoxicity in AD mouse models (*8*, *9*). We used mice with individual deletion of *p38α*, *p38β*, *p38γ*, or *p38δ* (fig. S1). Surprisingly, only *p38γ* depletion ($p38\gamma^{-/-}$), but not systemic *p38β*, *p38δ*, or neuronal *p38α* ($p38\alpha^{\Delta neu}$)

[1]Dementia Research Unit, School of Medical Sciences, University of New South Wales (UNSW), Sydney, New South Wales 2052, Australia. [2]Motor Neuron Disease Unit, School of Medical Sciences, UNSW, Sydney, New South Wales 2052, Australia. [3]Discipline of Pathology, Sydney Medical School, University of Sydney, Sydney, New South Wales 2050, Australia. [4]Biomedical Imaging Facility, Mark Wainwright Analytical Centre, UNSW, Sydney, New South Wales 2052, Australia. [5]School of Molecular Bioscience, University of Sydney, Sydney, New South Wales 2050, Australia. [6]Biomedical Mass Spectrometry Facility, Mark Wainwright Analytical Centre, UNSW, Sydney, New South Wales 2052, Australia. [7]Transgenic Animal Unit, Mark Wainwright Analytical Centre, UNSW, Sydney, New South Wales 2052, Australia. [8]Neuroscience Research Australia, Sydney, New South Wales 2031, Australia.
***Corresponding author. Email: a.ittner@unsw.edu.au (A.I.); l.ittner@unsw.edu.au (L.M.I.)**

Downloaded from http://science.sciencemag.org/ on November 22, 2016

knockout, changed PTZ-induced seizures (Fig. 1A and fig. S2). Pan-p38 inhibition in wild-type (WT) mice augmented seizures, similar to the effects of *p38γ* depletion (fig. S3). Consistent with a postsynaptic role, only p38γ localized to dendritic spines and postsynaptic densities (PSDs) of neurons and was enriched in PSD preparations (Fig. 1B and fig. S4). Hence, of all p38 kinases, only p38γ localized to postsynapses and limited excitotoxicity.

To test whether $p38\gamma^{-/-}$ augments Aβ-induced deficits, we crossed $p38\gamma^{-/-}$ with Aβ-forming APP23 mice. APP23 mice present with premature mortality, memory deficits, neuronal circuit aberrations with epileptiform brain activity,

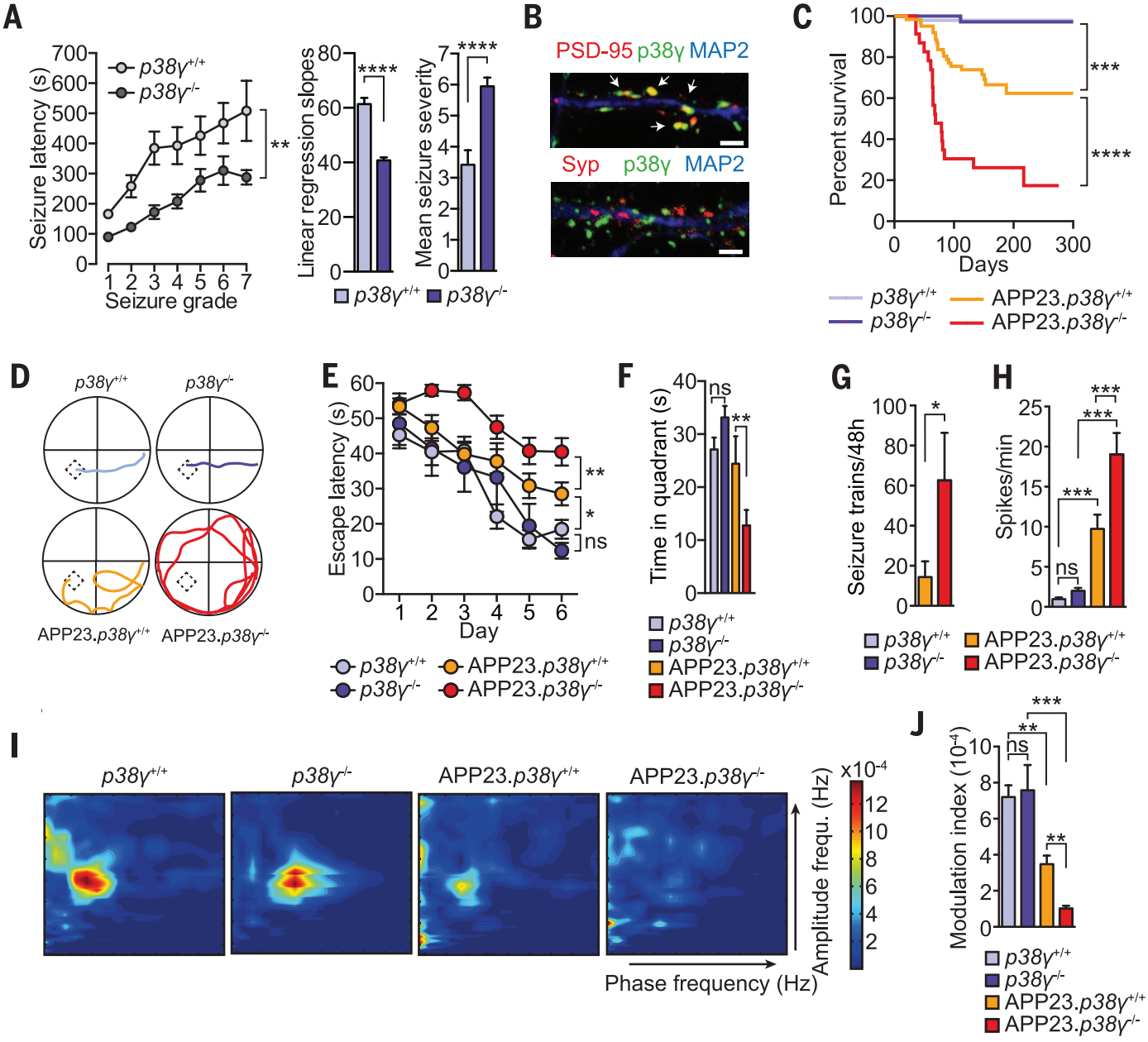


**Fig. 1. Depletion of postsynaptic p38γ exacerbates excitotoxicity and deficits in APP transgenic mice.** (**A**) Reduced seizure latency (linear regression slopes) and increased seizure severity in $p38\gamma^{-/-}$ mice compared with $p38\gamma^{+/+}$ animals injected with 30 mg/kg pentylenetetrazole (PTZ) ($n$ = 10 to 12 mice). (**B**) Colocalization of p38γ and postsynaptic PSD-95 (arrows), but not presynaptic synaptophysin (Syp), in neurons. Scale bars, 1 μm. (**C**) Mortality in APP23.$p38\gamma^{+/+}$ mice was further augmented in APP23.$p38\gamma^{-/-}$ animals, whereas $p38\gamma^{+/+}$ and $p38\gamma^{-/-}$ mice survived normally ($n$ = 43 to 62). (**D** to **F**) Memory deficits in 4-month-old APP23.$p38\gamma^{+/+}$ and APP23.$p38\gamma^{-/-}$ mice (memory deficits were exacerbated in the APP23.$p38\gamma^{-/-}$ animals). Morris water maze (MWM) test: (D) Representative MWM path traces to a hidden platform. (E) Increased escape latency and (F) reduced time in the target quadrant during probe trials in APP23.$p38\gamma^{+/+}$ and, more so, APP23.$p38\gamma^{-/-}$ mice compared with $p38\gamma^{+/+}$ and $p38\gamma^{-/-}$ mice ($n$ = 8 to 10). (**G** to **H**) Increased (G) spike train and (H) spike frequency in APP23.$p38\gamma^{+/+}$ and APP23.$p38\gamma^{-/-}$ mice but not $p38\gamma^{+/+}$ and $p38\gamma^{-/-}$ mice ($n$ = 6 to 8). (**I**) Representative phase-amplitude comodulograms of interictal hippocampal local field potential recordings showed reduced and virtually lost cross-frequency coupling (CFC) (~8 Hz) in APP23.$p38\gamma^{+/+}$ and APP23.$p38\gamma^{-/-}$ mice, respectively, compared with $p38\gamma^{+/+}$ and $p38\gamma^{-/-}$ mice. (**J**) Reduced modulation index in APP23.$p38\gamma^{+/+}$ mice and, more so, in APP23.$p38\gamma^{-/-}$ mice compared with $p38\gamma^{+/+}$ and $p38\gamma^{-/-}$ animals ($n$ = 6 to 8). For (A), (C), (E) to (H), and (J): ****$P$ < 0.0001, ***$P$ < 0.001, **$P$ < 0.01, *$P$ < 0.05; ns, not significant. Error bars indicate SEM.

Downloaded from http://science.sciencemag.org/ on November 22, 2016

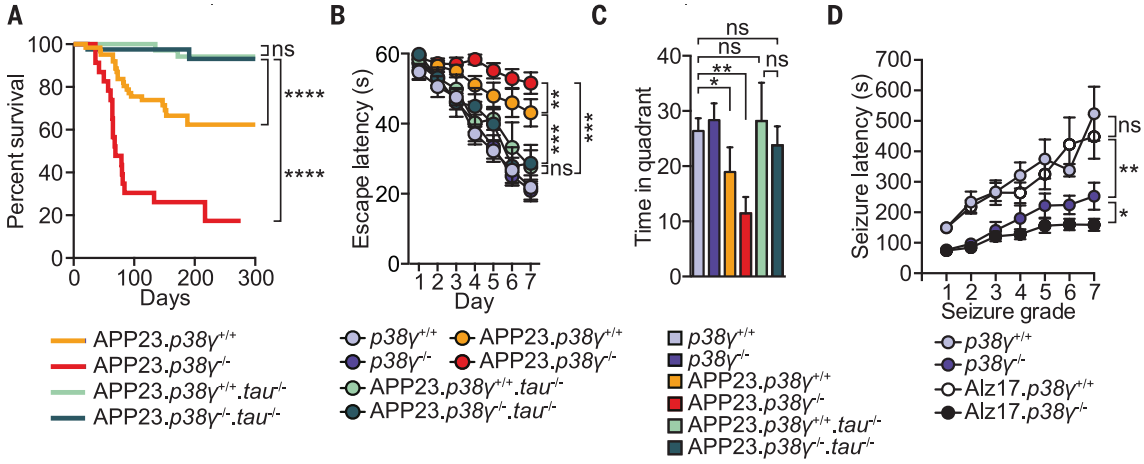


**Fig. 2. Tau is required for p38γ-mediated inhibition of Aβ and excitotoxicity.** (**A**) Normal survival of APP23.$p38\gamma^{-/-}$.$tau^{-/-}$ compared with APP23.$p38\gamma^{-/-}$ and APP23.$p38\gamma^{+/+}$ mice ($n$ = 42 to 62). (**B** and **C**) Normal memory in 12-month-old APP23.$p38\gamma^{-/-}$.$tau^{-/-}$ mice compared with APP23.$p38\gamma^{-/-}$ and APP23.$p38\gamma^{+/+}$ mice ($n$ = 10 to 12). MWM test: (B) Escape latency and (C) time in target quadrant during probe trials. (**D** to **F**) (D) Further reduction in seizure latencies, shown by linear regression analysis (E). (F) Further enhanced mean seizure severity following 30 mg/kg PTZ in Alz17.$p38\gamma^{-/-}$ mice versus those already reduced in $p38\gamma^{-/-}$ compared with $p38\gamma^{+/+}$ and Alz17.$p38\gamma^{+/+}$ mice ($n$ = 10 to 12). (**G** to **I**) (G) Seizure latencies after 30 mg/kg PTZ were reduced, as shown by linear regression analysis (H), and mean seizure severity was increased in $tau^{+/+}$.$p38\gamma^{-/-}$ compared with $tau^{+/+}$.$p38\gamma^{+/+}$ mice (I). However, latencies were markedly increased (G) and severities similarly reduced (I) in both $tau^{-/-}$.$p38\gamma^{+/+}$ and $tau^{-/-}$.$p38\gamma^{-/-}$ mice ($n$ = 10 to 12). For all panels: ****$P$ < 0.0001, ***$P$ < 0.001, **$P$ < 0.01, *$P$ < 0.05; ns, not significant. Error bars indicate SEM.

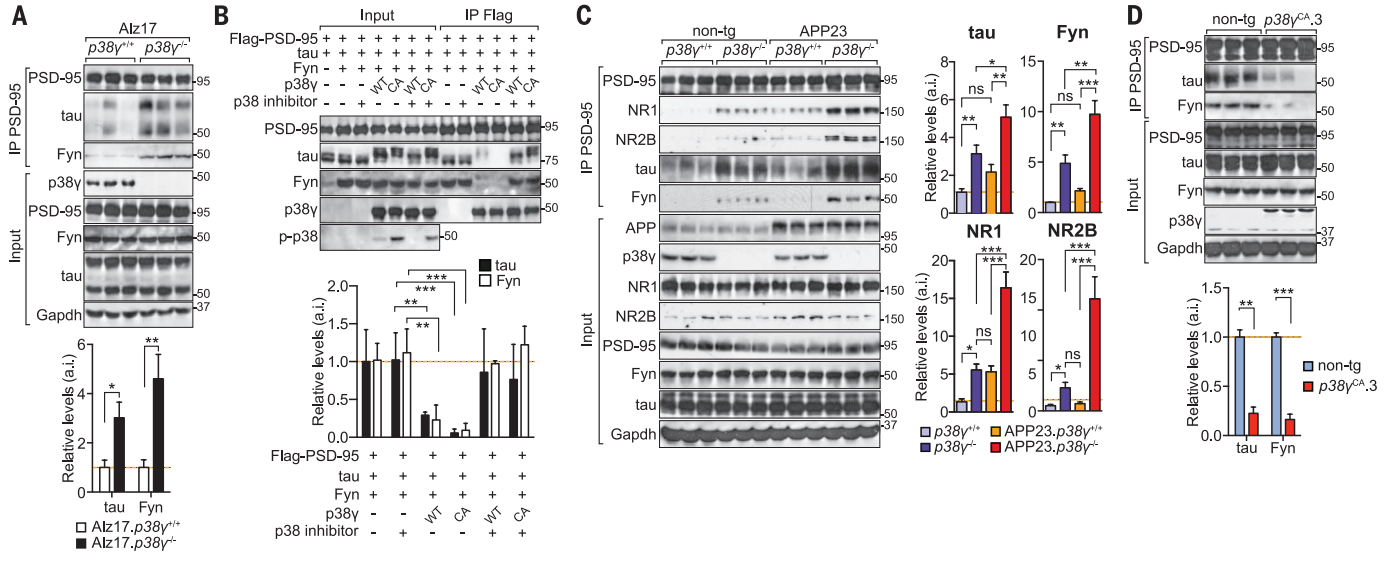


**Fig. 3. Active p38γ dissociates PSD-95/tau/Fyn/NR complexes.** (**A**) Immunoprecipitation (IP) analysis. More PSD-95/tau/Fyn complexes were immunoprecipitated from the brains of Alz17.$p38\gamma^{-/-}$ than Alz17.$p38\gamma^{+/+}$ animals, despite comparable total protein levels. Detection of glyceraldehyde-3-phosphate dehydrogenase (GAPDH) confirmed equal loading ($n$ = 6). Numbers at right indicate molecular weight. a.i., arbitrary index. (**B**) p38γ (WT) and $p38\gamma^{CA}$ (CA) failed to disrupt PSD-95/tau/Fyn complexes in the presence of the p38 inhibitor ($n$ = 6). p38 inhibition reduces phosphorylated active p38 levels (p-p38). (**C**) More tau, Fyn, and NMDA receptor subunits 1 (NR1) and 2B (NR2B) were immunoprecipitated with PSD-95 from $p38\gamma^{-/-}$ versus $p38\gamma^{+/+}$ brains. This result was further enhanced in APP23.$p38\gamma^{-/-}$ mice compared with APP23.$p38\gamma^{+/+}$ animals, without changes to total protein levels ($n$ = 6 to 8). (**D**) Virtually no PSD-95/tau/Fyn complexes were immunoprecipitated from the brains of $p38\gamma^{CA}$-expressing mice ($n$ = 6). For all panels: Representative blots are shown. Quantification of IP bands relative to PSD-95 IP. ***$P$ < 0.001; **$P$ < 0.01; *$P$ < 0.05. Error bars indicate SEM.

Downloaded from http://science.sciencemag.org/ on November 22, 2016

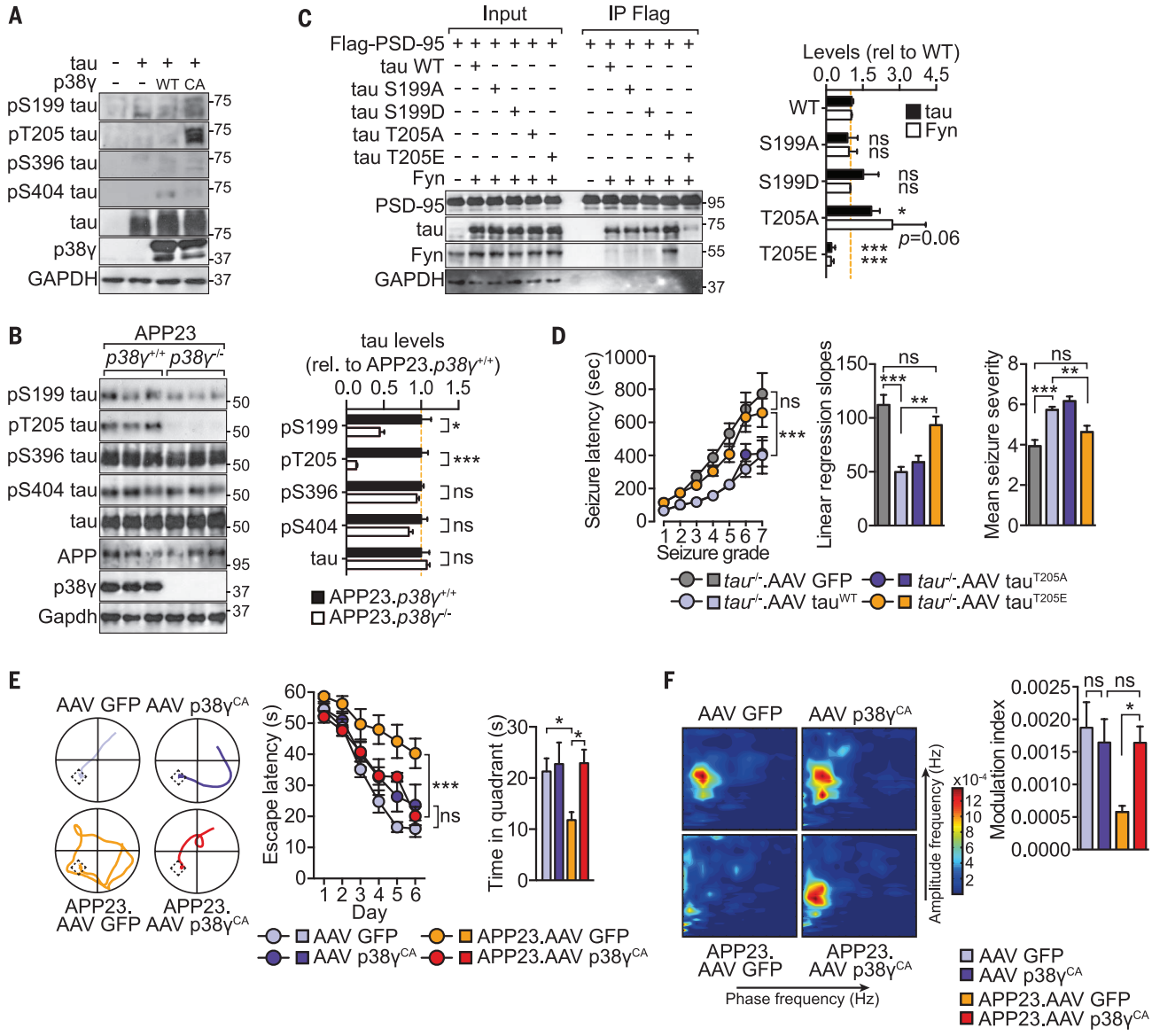


**Fig. 4. Site-specific tau phosphorylation disrupts PSD-95/tau/Fyn interaction and inhibits Aβ toxicity.** (**A**) Coexpression of p38γ (WT) or p38γ$^{CA}$ (CA) with tau showed phosphorylation at T205, less at S199, and virtually none at S396 or S404. Detection of GAPDH confirmed equal loading. (**B**) Compared with APP23.*p38γ*$^{+/+}$ animals, APP23.*p38γ*$^{-/-}$ mice showed a lack of T205 tau phosphorylation ($n$ = 6). Other sites remained phosphorylated. Graph shows quantification of tau phosphorylation. (**C**) Coexpression of T205E disrupted PSD95/tau/Fyn IP, whereas T205A tau increased it ($n$ = 6). S199 mutations had no effect. Graph shows quantification of tau/Fyn bound to PSD-95. D, Asp. (**D**) AAV-mediated expression of WT and T205A, but not T205E or GFP, restored susceptibility of *tau*$^{-/-}$ to 50 mg/kg PTZ-induced seizures, with reduced latency (linear regression) and higher severity ($n$ = 12). (**E**) Improved memory in APP23 mice upon AAV-mediated p38γ$^{CA}$ expression (APP23.AAV$^{p38\gamma CA}$). MWM test: (Left) Example traces; (middle) escape latencies; (right) time in target quadrant during probe trials ($n$ = 8 to 10). (**F**) Rescued CFC in APP23.AAV$^{p38\gamma CA}$ compared with APP23.AAV$^{GFP}$ mice ($n$ = 5 to 6). For (B) to (F): ***$P$ < 0.001; **$P$ < 0.01; *$P$ < 0.05; ns, not significant. Error bars indicate SEM.

and Aβ pathology (*9*, *15*, *18*). Compared with APP23.*p38γ*$^{+/+}$ mice, APP23.*p38γ*$^{-/-}$ animals had increased sensitivity to PTZ-induced seizures (fig. S5). Aβ pathology was comparable in the brains of APP23.*p38γ*$^{-/-}$ and APP23.*p38γ*$^{+/+}$ mice (fig. S6), but *p38γ* deletion aggravated premature mortality and memory deficits of APP23 mice (Fig. 1, C to F, and fig. S7). *p38γ*$^{-/-}$ mice showed no deficits and had normal motor function (fig. S8). Electroencephalography showed enhanced spontaneous epileptiform activity and interictal hypersynchronous discharges in APP23.*p38γ*$^{-/-}$ compared with APP23.*p38γ*$^{+/+}$ mice (Fig. 1, G and H, and fig. S9). Hippocampal theta and gamma oscillations and cross-frequency coupling (CFC) through theta-phase modulation of gamma power are measures of network activity related to memory, including in humans (*19*–*22*). These measures are compromised in APP transgenic mice (*15*). Compromised spectral power and CFC of APP23.*p38γ*$^{+/+}$ mice were significantly more affected in APP23.*p38γ*$^{-/-}$ recordings (Fig. 1, I and J, and fig. S9). Recordings of *p38γ*$^{-/-}$ and *p38γ*$^{+/+}$ mice were indistinguishable. In summary, p38γ depletion exacerbated excitotoxicity, neuronal circuit synchronicity, mortality, and memory deficits in APP23 mice, without changes in Aβ pathology. In addition, p38γ levels were reduced in aged APP23 and APP$^{NL\text{-}G\text{-}F}$ mice and humans with AD (fig. S10), further suggesting that the loss of p38γ-mediated neuroprotection may contribute to AD pathogenesis.

To determine whether the Aβ toxicity–limiting effects of p38γ were tau-dependent, we crossed

Downloaded from http://science.sciencemag.org/ on November 22, 2016

APP23.$p38\gamma^{-/-}$ with $tau^{-/-}$ mice. The exacerbating effects of p38γ loss on reduced survival, memory deficits, and neuronal network dysfunction of APP23 mice were virtually abolished in APP23.$p38\gamma^{-/-}$.$tau^{-/-}$ mice (Fig. 2, A to C, and fig. S11). These data also showed that, compared with APP23 mice, APP23.$p38\gamma^{-/-}$ animals had aggravated memory deficits that persisted with aging. In contrast, increasing tau levels in $p38\gamma^{-/-}$ mice [brought about by crossing with nonmutant tau-expressing Alz17 mice (*23*)] significantly enhanced PTZ-induced seizures in Alz17.$p38\gamma^{-/-}$ mice (Fig. 2, D to F). Conversely, when compared to $tau^{-/-}$.$p38\gamma^{+/+}$ mice, $tau^{-/-}$.$p38\gamma^{-/-}$ animals showed similar protection from PTZ-induced seizures (Fig. 2, G to I). Taken together, the effects of p38γ on excitotoxicity and Aβ toxicity were tau-dependent.

We have previously shown that postsynaptic PSD-95/tau/Fyn complexes mediate Aβ-induced excitotoxicity (*9*). PSD-95/tau/Fyn interaction was enhanced in Alz17.$p38\gamma^{-/-}$ animals versus Alz17.$p38\gamma^{+/+}$ mice (Fig. 3A and fig. S12). Conversely, no PSD-95/tau/Fyn complexes were isolated from $tau^{-/-}$ and $tau^{-/-}$.$p38\gamma^{-/-}$ brains (fig. S12). Increasing p38γ levels compromised PSD-95/tau/Fyn interaction in cells, and expression of a constitutively active p38γ variant ($p38\gamma^{CA}$) completely abolished this interaction (Fig. 3B and fig. S13). Pan-p38 inhibition stopped p38γ/$p38\gamma^{CA}$-induced disruption of PSD-95/tau/Fyn complexes (Fig. 3B). PSD-95 copurified more tau and Fyn from $p38\gamma^{-/-}$ versus $p38\gamma^{+/+}$ brains, and even more from APP23.$p38\gamma^{-/-}$ compared with APP23.$p38\gamma^{+/+}$ and $p38\gamma^{-/-}$ brains (Fig. 3C). Conversely, PSD-95/tau/Fyn interaction was reduced in transgenic mice with neuronal expression of $p38\gamma^{CA}$ (Fig. 3D and fig. S14). PTZ transiently increased PSD-95/tau/Fyn complex formation in $p38\gamma^{+/+}$ animals; this effect was even more noticeable in $p38\gamma^{-/-}$ mice (fig. S12). Fyn-mediated NR2B phosphorylation at $Tyr^{1472}$ (Y1472) facilitates PSD-95/NR2B interaction (*24*). Consistent with increased PSD-95/tau/Fyn complex formation, NR2B phosphorylation at Y1472 was increased in $p38\gamma^{-/-}$ brains (fig. S15). Conversely, cellular expression of p38γ and $p38\gamma^{CA}$—but not $p38\alpha^{CA}$, $p38\beta^{CA}$, or $p38\delta^{CA}$—reduced Y1472 phosphorylation of NR2B (fig. S15). Hence, p38γ regulated PSD-95/tau/Fyn complexes, likely at the level of PSD-95/tau interaction (fig. S16).

Although p38γ hyperphosphorylates tau during long-term in vitro kinase assays (*25*), the temporal profile of p38γ-induced tau phosphorylation in acute signaling remains unknown. Short-term in vitro kinase reactions using phosphorylation site–specific tau antibodies revealed phosphorylation at $Ser^{199}$ (S199), $Thr^{205}$ (T205), S396, and S404 (fig. S17). Mass spectrometric analysis confirmed these and 14 additional, though low-abundant, sites (figs. S17C and S18 and table S4). Coexpression of p38γ or $p38\gamma^{CA}$ and tau in cells revealed tau phosphorylation (p) at T205, less at S199, and hardly any at S396 or S404 (Fig. 4A). Similarly, T205 (and, less so, S199 and S396) were phosphorylated in $p38\gamma^{CA}$ transgenic mice (fig. S19). pT205 increased after PTZ in $p38\gamma^{+/+}$ animals but was virtually abolished in $p38\gamma^{-/-}$ mice, whereas pS199, pS396, and pS404 were induced in both $p38\gamma^{+/+}$ and $p38\gamma^{-/-}$ mice (fig. S19). Similarly, pT205 was markedly reduced in APP23.$p38\gamma^{-/-}$ animals compared with APP23.$p38\gamma^{+/+}$ mice (Fig. 4B). In primary neurons, pT205 (but not p199) was markedly reduced by pan-p38 inhibition (fig. S20). Taken together, these findings indicate that pT205 was a primary p38γ site in tau.

Next, we showed that a phosphorylation-mimicking $Thr^{205}$→$Glu^{205}$ (T205E) tau variant coprecipitated significantly less with PSD-95 as compared with nonmutant and T205A (A, Ala) tau (Fig. 4C and fig. S21). In contrast, phosphorylation-mimicking mutants of all other identified sites had no effect on PSD-95/tau/Fyn interaction (fig. S18). Microscale thermophoresis and glutathione *S*-transferase–pulldown in vitro and fluorescence-lifetime imaging microscopy (FLIM)–fluorescence resonance energy transfer (FRET) analysis in live cells confirmed the markedly compromised interaction of T205E tau with PSD-95 (fig. S22). The T205E mutation did not hinder tau/Fyn interaction (fig. S21). Phosphorylation of T205 by $p38\gamma^{CA}$ was required for disrupting PSD-95/tau/Fyn complexes (fig. S21). Hence, p38γ regulated PSD-95/tau/Fyn complexes via phosphorylating tau at T205.

The disruption of NR/PSD-95/tau/Fyn complexes prevents excitotoxicity and Aβ toxicity (*9*). Hence, phosphorylation of tau at T205 should similarly mitigate neurotoxicity. Aβ caused cell death in WT and T205A neurons but significantly less in T205E tau-expressing neurons (fig. S23). Similarly, neurons expressing p38γ and, more so, $p38\gamma^{CA}$ were significantly more resistant to Aβ-induced cell death than controls (fig. S24). PTZ-induced seizures are reduced in $tau^{-/-}$ mice (*8*, *9*). Adeno-associated virus (AAV)–mediated expression of WT and T205A neurons, but not T205E tau or green fluorescent protein (GFP), in the forebrains of $tau^{-/-}$ mice enhanced PTZ-induced seizures (Fig. 4D and fig. S25). In contrast, expression of $p38\gamma^{CA}$ in WT mice using AAV or in Thy1.2-$p38\gamma^{CA}$ transgenic mice decreased PTZ-induced seizures (fig. S25). AAV-mediated $p38\gamma^{CA}$ expression in APP23 mice rescued memory deficits and network aberrations; the same was true for crossing APP23 with Thy1.2-$p38\gamma^{CA}$ mice (Fig. 4, E and F, and figs. S26 and S27). In summary, the levels of active p38γ kinase and tau phosphorylation at T205 determined susceptibility to excitotoxicity and Aβ toxicity.

Here we have shown that T205 phosphorylation of tau is part of an Aβ toxicity–inhibiting response. This is contrary to the current view that tau phosphorylation downstream of Aβ toxicity is a pathological response (*3*). However, this finding is in line with the idea that tau is involved in normal physiologic NR signaling events in neurons (*12*). Finally, we found that tau-dependent Aβ toxicity was modulated by site-specific tau phosphorylation, which inhibited postsynaptic PSD-95/tau/Fyn complexes, revealing an Aβ toxicity–limiting role of p38γ in AD that is distinct and opposite to the effects of p38α and p38β (*11*, *13*, *14*).

## REFERENCES AND NOTES


1. C. Ballatore, V. M. Lee, J. Q. Trojanowski, *Nat. Rev. Neurosci.* **8**, 663–672 (2007).
2. C. Haass, D. J. Selkoe, *Nat. Rev. Mol. Cell Biol.* **8**, 101–112 (2007).
3. L. M. Ittner, J. Götz, *Nat. Rev. Neurosci.* **12**, 67–72 (2011).
4. K. Iqbal, F. Liu, C.-X. Gong, A del C. Alonso, I. Grundke-Iqbal, *Acta Neuropathol.* **118**, 53–69 (2009).
5. E. M. Mandelkow, E. Mandelkow, *Cold Spring Harb. Perspect. Med.* **2**, a006247 (2012).
6. E. S. Musiek, D. M. Holtzman, *Nat. Neurosci.* **18**, 800–806 (2015).
7. M. Rapoport, H. N. Dawson, L. I. Binder, M. P. Vitek, A. Ferreira, *Proc. Natl. Acad. Sci. U.S.A.* **99**, 6364–6369 (2002).
8. E. D. Roberson *et al.*, *Science* **316**, 750–754 (2007).
9. L. M. Ittner *et al.*, *Cell* **142**, 387–397 (2010).
10. J. J. Palop, L. Mucke, *Nat. Neurosci.* **13**, 812–818 (2010).
11. G. E. Hardingham, H. Bading, *Nat. Rev. Neurosci.* **11**, 682–696 (2010).
12. L. Mucke, D. J. Selkoe, *Cold Spring Harb. Perspect. Med.* **2**, a006338 (2012).
13. Q. Wang, D. M. Walsh, M. J. Rowan, D. J. Selkoe, R. Anwyl, *J. Neurosci.* **24**, 3370–3378 (2004).
14. S. Li *et al.*, *J. Neurosci.* **31**, 6627–6638 (2011).
15. A. A. Ittner, A. Gladbach, J. Bertz, L. S. Suh, L. M. Ittner, *Acta Neuropathol. Commun.* **2**, 149 (2014).
16. M. A. Fabian *et al.*, *Nat. Biotechnol.* **23**, 329–336 (2005).
17. M. B. Menon, S. Dhamija, A. Kotlyarov, M. Gaestel, *Autophagy* **11**, 1425–1427 (2015).
18. C. Sturchler-Pierrat *et al.*, *Proc. Natl. Acad. Sci. U.S.A.* **94**, 13287–13292 (1997).
19. G. Buzsáki, E. I. Moser, *Nat. Neurosci.* **16**, 130–138 (2013).
20. R. Goutagny, J. Jackson, S. Williams, *Nat. Neurosci.* **12**, 1491–1493 (2009).
21. R. T. Canolty *et al.*, *Science* **313**, 1626–1628 (2006).
22. A. B. Tort, R. W. Komorowski, J. R. Manns, N. J. Kopell, H. Eichenbaum, *Proc. Natl. Acad. Sci. U.S.A.* **106**, 20942–20947 (2009).
23. A. Probst *et al.*, *Acta Neuropathol.* **99**, 469–481 (2000).
24. M. Aarts *et al.*, *Science* **298**, 846–850 (2002).
25. M. Goedert *et al.*, *FEBS Lett.* **409**, 57–62 (1997).


## ACKNOWLEDGMENTS


We thank the staff of the Biological Resources Centre of UNSW for animal care, E. Hinde for help with FLIM-FRET experiments, D. Sullivan and T. Foo for *APOE* genotyping of human samples, and T. Saito and T. C. Saido for $APP^{NL-G-F}$ mice. The data from mass spectrometry experiments can be found in the supplementary materials. This work was funded by the National Health and Medical Research Council (grants 1081916, 1037746, and 1003083), the Australian Research Council (grants DP130102027 and DE130101591), Alzheimer's Association (grant NIRG000070035), Alzheimer's Australia (grants DGP14-39 and DGP14-95), the NIH (grant R28AA012725), and UNSW Australia. A.I. and L.M.I. are inventors on Australian patent application number APO/2016/900764, submitted by UNSW, which covers increasing p38γ activity to prevent neuronal toxicity.


## SUPPLEMENTARY MATERIALS

www.sciencemag.org/content/354/6314/904/suppl/DC1
Materials and Methods
Figs. S1 to S27
Tables S1 to S5
References (*26*–*53*)


22 July 2016; resubmitted 9 October 2016
Accepted 19 October 2016
10.1126/science.aah6205


Downloaded from http://science.sciencemag.org/ on November 22, 2016

DNA METHYLATION

# The DNA methyltransferase DNMT3C protects male germ cells from transposon activity

Joan Barau,[1] Aurélie Teissandier,[1,2] Natasha Zamudio,[1*] Stéphanie Roy,[3] Valérie Nalesso,[4,5,6] Yann Hérault,[4,5,6] Florian Guillou,[3] Déborah Bourc'his[1†]

**DNA methylation is prevalent in mammalian genomes and plays a central role in the epigenetic control of development. The mammalian DNA methylation machinery is thought to be composed of three DNA methyltransferase enzymes (DNMT1, DNMT3A, and DNMT3B) and one cofactor (DNMT3L). Here, we describe the discovery of *Dnmt3C*, a de novo DNA methyltransferase gene that evolved via a duplication of *Dnmt3B* in rodent genomes and was previously annotated as a pseudogene. We show that DNMT3C is the enzyme responsible for methylating the promoters of evolutionarily young retrotransposons in the male germ line and that this specialized activity is required for mouse fertility. DNMT3C reveals the plasticity of the mammalian DNA methylation system and expands the scope of the mechanisms involved in the epigenetic control of retrotransposons.**

Genome defense via transcriptional silencing of transposable elements has been proposed to be a driving force for the evolution of DNA methylation (*1*). Retrotransposons occupy half of mammalian genomic space, and their control is of paramount importance in the germ line: Their activity can damage the hereditary material with an impact on fertility and the fitness of subsequent generations (*2*). In mammals, after germline epigenetic reprogramming, small RNA-directed DNA methylation establishes life-long epigenetic silencing of retrotransposons during the perinatal period of spermatogenesis (*3*). Piwi-interacting RNAs (piRNAs) are the cleavage products of retrotransposon transcripts and guide DNA methylation to the promoters of these elements through homology recognition (*4*, *5*). Mammals have specifically evolved a catalytically inactive DNA methyltransferase (DNMT) cofactor, DNMT3L, which acts downstream of the piRNA pathway (*6*, *7*). The inactivation of DNMT3L or PIWI-pathway proteins invariably results in hypomethylation and reactivation of retrotransposons, meiotic failure, azoospermia, and male sterility marked by small testis size (hypogonadism) (*8*).

To gain insights into the biology of retrotransposon silencing in the germ line, we screened a collection of hypogonadal male mice generated through *N*-ethyl-*N*-nitrosourea (ENU) mutagenesis for ectopic retrotransposon activity (fig. S1, A and B). Five independent positive lines were obtained, but all showed linkage to the same genomic interval on chromosome 2 (fig. S1C), suggesting that they shared a spontaneous, ENU-independent mutation. Whole-genome sequencing revealed a de novo insertion of an IAPEz element, a subclass of inracisternal A-particle (IAP) retrotransposon, in the last intron of the *Gm14490* gene (Fig. 1A and fig. S1, D to F). *Gm14490* maps 9 kilobases (kb)

[1]Institut Curie, PSL Research University, INSERM, CNRS, 75005 Paris, France. [2]Ecole des Mines, 75005 Paris, France. [3]PRC, INRA, CNRS, IFCE, Tours University, 37380 Nouzilly, France. [4]Institut de Génétique et Biologie Moléculaire et Cellulaire, Strasbourg University, 67404 Illkirch, France. [5]Centre National de la Recherche Scientifique, UMR7104, Illkirch, France. [6]Institut National de la Santé et de la Recherche Médicale, U964, Illkirch, France.
*Present address: The Walter and Eliza Hall Institute of Medical Research, Parkville, Victoria, Australia. †Corresponding author. Email: deborah.bourchis@curie.fr

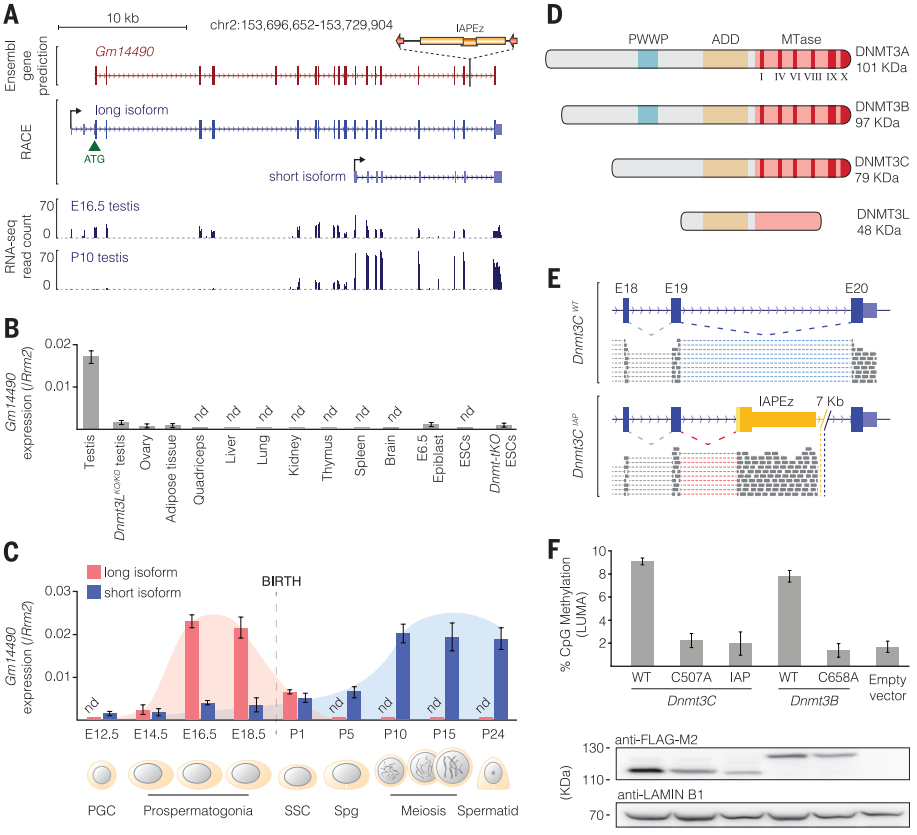


**Fig. 1. *Gm14490* encodes a male germ cell–specific de novo DNA methyltransferase, DNMT3C.** (**A**) Structure of *Gm14490* (*Ensembl 2011*) and position of the IAPEz insertion (antisense orientation). RACE and RNA-seq analysis of E16.5 and P10 testis identifies a long isoform with coding potential (ATG, green triangle). (**B**) *Gm14490* is detected in testis by reverse transcription–quantitative polymerase chain reaction (RT-qPCR), but not in germ cell–depleted testis from *Dnmt3L*$^{KO/KO}$ animals. Tissues from 10-week-old mice, unless otherwise specified. (**C**) RT-qPCR of the two *Gm14490* isoforms during testis development. Predominant germ cell populations are represented. Primordial germ cells (PGC), spermatogonial stem cells (SSC), and spermatogonia (Spg). (**D**) DNMT3C shows characteristics of DNMT3 proteins—conserved methyltransferase (MTase) motifs and an ADD domain, but no PWWP domain. (**E**) RNA-seq supporting wild-type and mutant *Dnmt3C* $^{IAP}$ splicing events in E16.5 testis. (**F**) LUminometric methylation assay (LUMA) of global CpG methylation in *Dnmt-tKO* ESCs that transiently express *Dnmt3C*- and *Dnmt3B-3XFLAG* alleles. Data are mean ± SD from three technical replicates in (B) and (C) and from three biological replicates in (F). nd, not detectable.

Downloaded from http://science.sciencemag.org/ on November 22, 2016

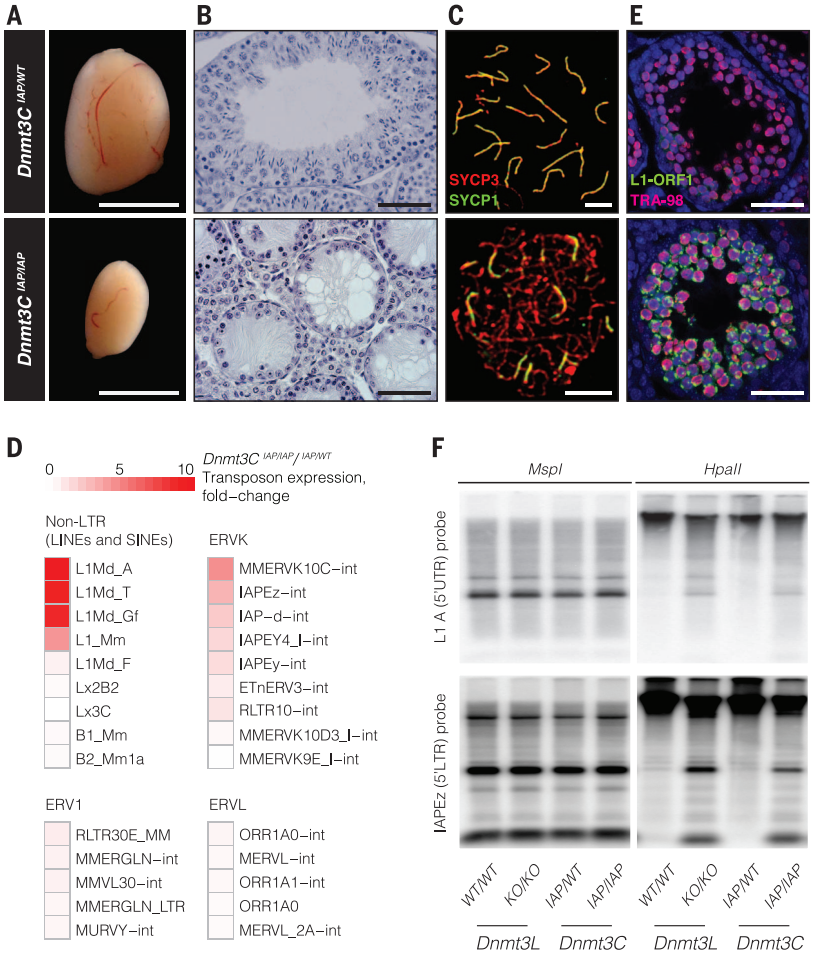


**Fig. 2. Phenotype of *Dnmt3C*$^{IAP/IAP}$ males.** (**A**) Hypogonadism (6-week-old mice). Scale bars, 5 mm. (**B**) Severe germ cell loss in testis sections (11-week-old mice). Scale bars, 100 μm. (**C**) Impaired chromosome synapsis at meiosis as detected by immunofluorescence against synaptonemal complex proteins (SYCP1 and SYCP3). Scale bars, 4 μm. (**D**) RNA-seq heatmap shows overexpression of young L1 and specific ERVK types in *Dnmt3C*$^{IAP/IAP}$ compared to *Dnmt3C*$^{IAP/WT}$ testis at P20. Annotations from RepeatMasker. (**E**) Aberrant expression of L1-ORF1 proteins in *Dnmt3C*$^{IAP/IAP}$ germ cells (TRA98-positive) at P20. Scale bars, 50 μm. (**F**) L1A-5′UTR and IAPEz-5′LTR are hypomethylated in *Dnmt3C*$^{IAP/IAP}$ testis DNA at P20, as in *Dnmt3L*$^{KO/KO}$ testis. Southern blot analysis after methyl-sensitive Hpa II digestion. Msp I is used as a digestion control.

downstream of the *Dnmt3B* gene and was annotated as a nonfunctional tandem duplication of *Dnmt3B*, based on lack of transcription and recognizable open reading frames (ORFs) (*9*).

We found that *Gm14490* was exclusively expressed in male germ cells (Fig. 1B and fig. S2A). Using RNA sequencing (RNA-seq) and rapid amplification of cDNA ends (RACE), we annotated two transcript isoforms, whose expression was tightly regulated during spermatogenesis (Fig. 1, A and C). The short, noncoding isoform was expressed in postnatal testes. However, the long isoform (2.8 kb) possessed a 709-codon ORF, and its expression sharply peaked around embryonic day 16.5 (E16.5), coinciding with male germline de novo DNA methylation (*5*, *10*). In comparison, *Dnmt3B* is expressed in germ cells, early embryos, and somatic tissues of both sexes (*11*, *12*). Using discriminating primers, we showed independent regulation of *Dnmt3B* and *Gm14490* during spermatogenesis (fig. S2B). The coding potential and specific developmental regulation of *Gm14490* led us to reconsider it as a functional paralog of *Dnmt3B* rather than a pseudogene, and thus we renamed it *Dnmt3C*.

The long *Dnmt3C* isoform encodes a protein with an organization characteristic of DNMT3 enzymes: six methyltransferase motifs (I, IV, VI, VIII, IX, and X) in C-terminal position and an N-terminal ATRX-DNMT3L-DNMT3A (ADD) domain, which binds unmethylated lysine 4 residues of histone H3 (H3K4) (Fig. 1D and fig. S2C) (*13*). However, DNMT3C lacks the Pro-Trp-Trp-Pro (PWWP) domain, which targets DNMT3 proteins to gene bodies through recognition of H3K36 trimethylation (H3K36me3) (*14*, *15*). Overall, DNMT3C exhibits 70% identity with DNMT3B, while DNMT3A and DNMT3B are 46% identical. In hypogonadal mutants, the IAP insertion did not affect *Dnmt3C* transcript levels but provided an alternative splice acceptor site, which led to the exclusion of *Dnmt3C* last exon in favor of the retrotransposon sequence in a chimeric *Dnmt3C-IAP* mRNA (Fig. 1E and fig. S2, D and E). Its predicted translation product lacks motifs IX and X (fig. S2C), which are essential for the AdoMet-dependent methyltransferase fold and for the binding of the methyl donor *S*-adenosyl methionine, respectively (*16*).

To demonstrate that DNMT3C is catalytically active, we performed an in vivo DNA methylation assay. *Dnmt3C* is not expressed in mouse embryonic stem cells (ESCs) (Fig. 1B). By transfecting constructs driving *Dnmt3C* expression in DNA methylation-free ESCs (*Dnmt1*, *Dnmt3A*, and *Dnmt3B* triple-knockout; *Dnmt*-tKO) (*17*), we observed a gain of CpG methylation (10 to 20%), similar to that observed upon *Dnmt3B* transfection (Fig. 1F and fig. S2, F and G). The mutant *Dnmt3C*$^{IAP}$ allele failed to raise CpG methylation levels, as did *Dnmt3C* and *Dnmt3B* mutant alleles with a missense mutation in the catalytic site (DNMT3C C507A and DNMT3B C658A, in which cysteine at position 507 and 658 is replaced by alanine). An in vitro DNA methylation assay using the DNMT3C methyltransferase domain showed concordant results (fig. S2, H and I). These findings demonstrate that DNMT3C is an enzymatically active member of the DNMT3 family of de novo DNA methyltransferases.

*Dnmt3C*$^{IAP/IAP}$ animals were somatically normal, and only males were sterile (fig. S3A). Hypogonadism was linked to azoospermia with interruption of spermatogenesis at the pachytene stage of meiosis I, in the context of impaired chromosome synapsis (Fig. 2, A to C). The developmental phenotype of *Dnmt3C* mutant mice was similar to that observed in *Dnmt3L*$^{KO/KO}$ males (*7*, *18*), suggesting that DNMT3C could be involved in transposon silencing during spermatogenesis. Indeed, the same set of retrotransposons were up-regulated in *Dnmt3C*$^{IAP/IAP}$ and *Dnmt3L*$^{KO/KO}$ testes at P20 (postnatal day 20) (Fig. 2D and fig. S3B) (*18*). Long interspersed nuclear elements (LINEs or L1s) showed the strongest reactivation, and more specifically evolutionarily young subfamilies: type A, T, and Gf transcripts were increased by 10-fold in *Dnmt3C*$^{IAP/IAP}$ testes, in association with accumulation of L1-encoded ORF1 proteins (Fig. 2E). Among endogenous retroviruses (ERVs), reactivation was specific to some ERVK families (MMERVK10C, IAPEz, and IAPEy). As in the case of the *Dnmt3L* mutation, L1 and IAPEz derepression was linked to a DNA methylation defect in *Dnmt3C*$^{IAP/IAP}$ testes (Fig. 2F), despite normal expression of piRNA/DNA methylation genes and piRNA production during fetal spermatogenesis (fig. S3, C to F). Finally, we confirmed DNMT3C function by generating a *Dnmt3C* knockout mouse through CRISPR-Cas9–mediated deletion (fig. S4A). The *Dnmt3C*$^{KO}$ allele recapitulated the *Dnmt3C*$^{IAP/IAP}$ developmental and molecular phenotypes in homozygous *Dnmt3C*$^{KO/KO}$ males and failed to complement the *Dnmt3C*$^{IAP}$ allele in *Dnmt3C*$^{IAP/KO}$ compound heterozygous males (fig. S4, B to E).

To assess the contribution of DNMT3C to male germline methylation, we performed whole-genome bisulfite sequencing (WGBS) in sorted

Downloaded from http://science.sciencemag.org/ on November 22, 2016

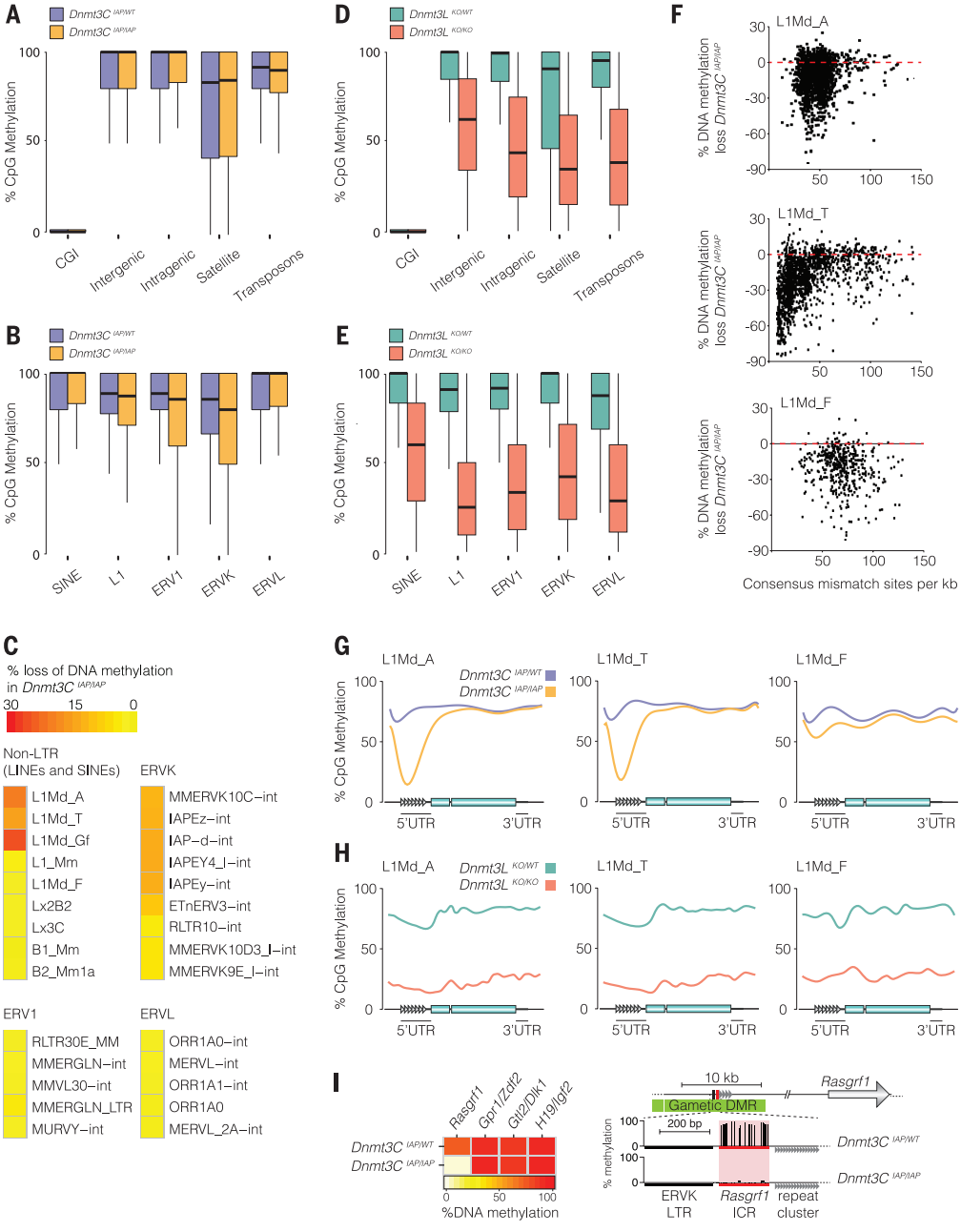


**Fig. 3. DNMT3C methylates evolutionarily young retrotransposon promoters.** (**A** and **B**) Tukey box-plot representation of CpG methylation content as determined by WGBS over different (A) genomic compartments and (B) retrotransposon classes in control *Dnmt3C* $^{IAP/WT}$ (purple) and mutant *Dnmt3C* $^{IAP/IAP}$ (yellow) germ cells at P10. (**C**) Percentage of DNA methylation loss within individual retrotransposon families in *Dnmt3C*$^{IAP/IAP}$ samples. (**D** and **E**) As in (A) and (B) but for *Dnmt3L*$^{KO/WT}$ (green) and *Dnmt3L*$^{KO/KO}$ (red) germ cells. (**F**) Plotting of DNA methylation loss over individual copies of L1 families according to genetic distance from consensus sequences. (**G** and **H**) Metaplots of DNA methylation over full-length L1s (>5 kb) comparing (G) *Dnmt3C*$^{IAP/IAP}$ and (*H*) *Dnmt3L*$^{KO/KO}$ versus control samples. (**I**) Left: Heatmap of *Dnmt3C*$^{IAP/IAP}$ and control DNA methylation levels across paternally imprinted loci. Right: Methylation maps at the *Rasgrf1* locus.

germ cells from testes at P10, when de novo DNA methylation is completed. Overall CpG methylation levels of *Dnmt3C*$^{IAP/IAP}$ mutant cells were not markedly different from the *Dnmt3C*$^{IAP/WT}$ control (77.7 versus 78.5%). A slight decrease was only apparent when focusing on transposons (81.5 versus 84.2%), and more specifically on LINEs, ERVK, and ERV1 (Fig. 3, A and B). Accordingly, there was only a limited number (264) of differentially methylated regions (DMRs) in *Dnmt3C*$^{IAP/IAP}$ versus *Dnmt3C*$^{IAP/WT}$ germ cells (fig. S5A); all reflected hypomethylation in the mutant, and most overlapped with LINEs (34%) and ERVs (48%). RepeatMasker annotations further highlighted that the same families that were transcriptionally derepressed were hypomethylated in *Dnmt3C*$^{IAP/IAP}$ testes; namely, young L1s and specific ERVKs (Fig. 2D and Fig. 3C). By comparison, deletion of DNMT3L had a stronger and broader impact: *Dnmt3L*$^{KO/KO}$ germ cells exhibited only 39% of global CpG methylation, and all genomic compartments and retrotransposon classes were affected (Fig. 3, D and E, and fig. S5B).

The DNA methylation defect in *Dnmt3C* mutants only reached 30% at the most for young L1s (Fig. 3C). We reasoned that DNMT3C selectively affects transcriptionally active retrotransposon copies, as these are targets of piRNA-dependent DNA methylation during fetal spermatogenesis (*4*, *5*). Indeed, individual L1-A and -T elements with a 5′ promoter (length >5 kb) and the highest similarity toward the consensus sequence showed the greatest DNA methylation loss in *Dnmt3C*$^{IAP/IAP}$ cells (Fig. 3F and fig. S4C). Additionally, DNMT3C-dependent DNA methylation was not evenly distributed across the length of these transcriptionally competent elements, but rather focalized to their promoters [5′ untranslated region (UTR)] (Fig. 3G), in a pattern previously observed in piRNA-deficient *Mili*$^{KO/KO}$ males (fig. S5D) (*4*). Older L1-F elements did not show such trends (Fig. 3F and fig. S5C). By contrast, *Dnmt3L* deficiency caused demethylation of L1s independently of their age and throughout their sequence (Fig. 3H).

ERVKs exhibited milder methylation loss (10%) than LINEs in *Dnmt3C*$^{IAP/IAP}$ cells (Fig. 3C), and this was not related to the size or the sequence conservation of individual copies (fig. S5, C and E). ERVKs partially resist the genome-wide erasure of methylation that occurs in the

Downloaded from http://science.sciencemag.org/ on November 22, 2016

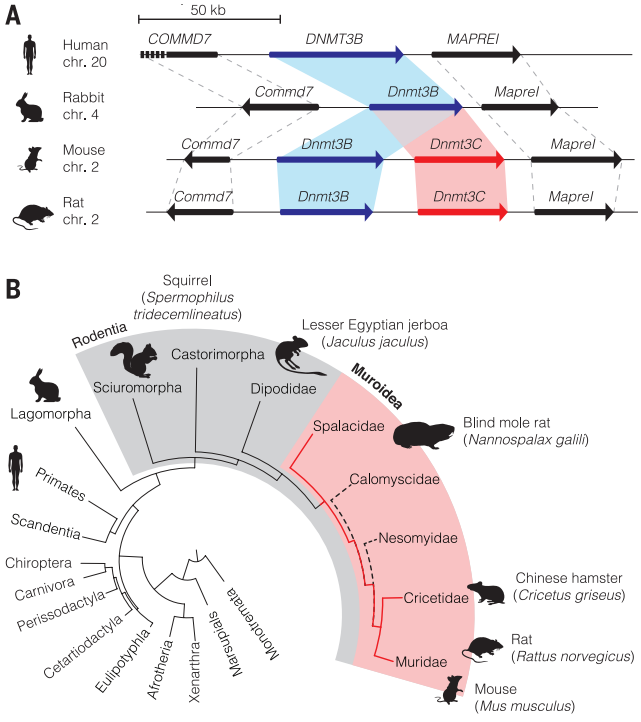


**Fig. 4. Phylogenetic distribution of *Dnmt3C*.** (**A**) Locus organization and synteny around the *Dnmt3B* (blue) and *Dnmt3C* (red) genes in human, rabbit, mouse, and rat genomes. (**B**) *Dnmt3C* distribution in the mammalian phylogenetic tree with a focus on the Rodentia order. Species in detail have available sequenced genomes. Red branches: Muroidea families in which *Dnmt3C* was identified; dashed branches: Muroidea families without available genome sequence.

fetal germ line (*19*, *20*); this likely explains their limited dependency toward DNMT3C remethylation activity. Nevertheless, DNMT3C dependency was still greatest over regulatory long-terminal repeat (LTR) sequences of MMERVK10C (fig. S5F) and IAPEz elements when highly conserved copies were analyzed by bisulfite pyrosequencing (fig. S4E). Finally, among paternally methylated imprinted loci, only the *Rasgfr1* imprinting control region (ICR) was hypomethylated in *Dnmt3C*$^{IAP/IAP}$ germ cells (Fig. 3I). This ICR includes an ERVK LTR fragment, which acquires DNA methylation in a piRNA-dependent manner during spermatogenesis (*21*). This highlights again the genomic convergence between piRNA and DNMT3C targeting in fetal male germ cells.

DNMT3C is highly specialized at methylating young retrotransposon promoters in the male germ line. In comparison, DNMT3B is not involved in germ cell development but establishes somatic methylation patterns genome-wide in the early embryo (*11*, *22*, *23*). DNMT3C has therefore evolved its own regulatory pattern and genomic targets, which have diverged from the ancestral DNMT3B copy. Despite the strict requirement of DNMT3C in the mouse, the *Dnmt3C* duplication is not universal among mammals but occurred ~46 million years ago in the last common ancestor of the muroid rodents (Fig. 4, A and B, and fig. S6, A and B). These represent the largest mammalian superfamily, with 1518 species accounting for 28% of all extant mammals (fig. S5C) (*24*), and include the two primary models for biomedical research, particularly in reproduction and endocrinology: the mouse and the rat. The genomes of Muroidea carry a heavy burden in young transposons: 25% have integrated in the last 25 million years with currently thousands of active copies (*25*). In comparison, most human transposons became extinct during that time (*26*).

The lack of transposon methylation defects in the germ cells of *Dnmt3A* or *Dnmt3B* mutant mice had been previously interpreted as a sign of functional redundancy between these two enzymes (*23*, *27*). We show here that this function relies instead on an additional de novo DNMT. The mammalian DNA methylation members should now be considered as a quintet: DNMT1, 3A, 3B, 3C, and 3L. The two most recent evolutionary additions are linked to reproduction: The eutherian DNMT3L cofactor stimulates germline methylation genome-wide, and the muroid DNMT3C enzyme methylates young retrotransposons during spermatogenesis. Future research should resolve the biochemical mechanism that designates specific sequences for DNMT3C-dependent DNA methylation. Its PWWP-free status may prevent it from targeting H3K36me3-enriched gene bodies and redirect it to retrotransposon promoters. In conclusion, our discovery of DNMT3C raises a new set of challenges to the current views of the remarkable evolution of DNA methyltransferases, the regulation of the de novo methylation process, and its tight links with the selective pressure to epigenetically control transposons in the germ line.

## REFERENCES AND NOTES


1. J. A. Yoder, C. P. Walsh, T. H. Bestor, *Trends Genet.* **13**, 335–340 (1997).
2. J. L. Goodier, H. H. Kazazian Jr., *Cell* **135**, 23–35 (2008).
3. A. A. Aravin, D. Bourc'his, *Genes Dev.* **22**, 970–975 (2008).
4. S. A. Manakov *et al.*, *Cell Reports* **12**, 1234–1243 (2015).
5. A. Molaro *et al.*, *Genes Dev.* **28**, 1544–1549 (2014).
6. A. A. Aravin *et al.*, *Mol. Cell* **31**, 785–799 (2008).
7. D. Bourc'his, T. H. Bestor, *Nature* **431**, 96–99 (2004).
8. N. Zamudio, D. Bourc'his, *Heredity (Edinb)* **105**, 92–104 (2010).
9. D. J. Lees-Murdock *et al.*, *Genomics* **84**, 193–204 (2004).
10. H. Kobayashi *et al.*, *Genome Res.* **23**, 616–627 (2013).
11. M. Okano, D. W. Bell, D. A. Haber, E. Li, *Cell* **99**, 247–257 (1999).
12. S. La Salle *et al.*, *Dev. Biol.* **268**, 403–415 (2004).
13. S. K. T. Ooi *et al.*, *Nature* **448**, 714–717 (2007).
14. T. Baubec *et al.*, *Nature* **520**, 243–247 (2015).
15. A. Dhayalan *et al.*, *J. Biol. Chem.* **285**, 26114–26120 (2010).
16. S. Klimasauskas, S. Kumar, R. J. Roberts, X. Cheng, *Cell* **76**, 357–369 (1994).
17. A. Tsumura *et al.*, *Genes Cells* **11**, 805–814 (2006).
18. N. Zamudio *et al.*, *Genes Dev.* **29**, 1256–1270 (2015).
19. P. Hajkova *et al.*, *Mech. Dev.* **117**, 15–23 (2002).
20. S. Seisenberger *et al.*, *Mol. Cell* **48**, 849–862 (2012).
21. T. Watanabe *et al.*, *Science* **332**, 848–852 (2011).
22. G. Auclair, S. Guibert, A. Bender, M. Weber, *Genome Biol.* **15**, 545 (2014).
23. M. Kaneda *et al.*, *Nature* **429**, 900–903 (2004).
24. J. Michaux, A. Reyes, F. Catzeflis, *Mol. Biol. Evol.* **18**, 2017–2031 (2001).
25. R. H. Waterston *et al.*, *Nature* **420**, 520–562 (2002).
26. R. Cordaux, M. A. Batzer, *Nat. Rev. Genet.* **10**, 691–703 (2009).
27. Y. Kato *et al.*, *Hum. Mol. Genet.* **16**, 2272–2280 (2007).


## ACKNOWLEDGMENTS

We thank members of D.B.'s laboratory, especially M. Greenberg and M. Walter. We are grateful to T. H. Bestor, V. Colot, E. Heard, and E. Mulugeta for advice; S. Fouchécourt, B. Fumel, L. Mourao, and B. Piegu for technical help; A. Bortvin and S. Tajima for antibodies; C. Jouhanneau for excellent mouse husbandry; E. Desale and PHENOMIN-TAAM for the mutagenesis program; and PICT-IBiSA (France–Bioimaging, ANR-10-INSB-04), the Flow Cytometry and Animal Platforms of the Institut Curie. This research was supported by grants from European Research Council (ERC-Cog EpiRepro), Agence Nationale pour la Recherche (ANR TranspoFertil, ANR-10-LABX-0030-INRT, and ANR-10-INBS-07 PHENOMIN). D.B.'s laboratory is part of the Laboratoire d'Excellence (LABEX) DEEP (11-LBX0044). J.B. was a recipient of a postdoctoral fellowship from Agence Nationale de Sécurité Sanitaire (Anses). The Institut Curie ICGex NGS platform was supported by ANR-10-EQPX-03 (Equipex) and ANR-10-INBS-09-08 (France Génomique Consortium) grants and by the Canceropôle Ile-de-France. Mouse line distribution under uniform biological material transfer agreement. All sequencing data sets are available at the National Center for Biotechnology Information Gene Expression Omnibus database under GSE84141.

## SUPPLEMENTARY MATERIALS

www.sciencemag.org/content/354/6314/909/suppl/DC1
Materials and Methods
Figs. S1 to S6
Tables S1 to S7
References (*28*–*54*)

8 July 2016; accepted 19 October 2016
10.1126/science.aah5143

Downloaded from http://science.sciencemag.org/ on November 22, 2016

**Genomic Data Analysis Software**
Illumina's NGS-based CytoSeq assay extends beyond traditional microarray-based cytogenetics assays for detection of copy number variation (CNV) and absence of heterozygosity (AOH), but also adds the ability to identify single-nucleotide variation, all in a single assay. Coupled with BioDiscovery's $N_x$Clinical software for analysis and interpretation of genomic events, the new solution will offer customers a powerful and cost-effective research tool for studying CNVs, AOH, and mutations in genetic disorders. The $N_x$Clinical software will be offered with the CytoSeq assay, providing an easy-to-use, interactive instrument for visualization and interpretation of genomic events. The $N_x$Clinical software will directly read CytoSeq results to process sample data and provide results.
**BioDiscovery**
For info: 310-414-8100
www.biodiscovery.com

**Inductively Coupled Plasma Optical Emission Spectrometry**
The Agilent 5110 inductively coupled plasma optical emission spectrometer (ICP-OES) will enable scientists to perform faster, more precise ICP-OES analysis than ever before in food, environmental, and pharmaceutical testing as well as in mining and industrial applications. The new system builds on the company's breakthrough 5100 ICP-OES, which captures axial and radial views of plasma in a single measurement, enabling laboratories to use half as much argon in the process, and saving both time and money. The new system is also a dual-view system. Unlike ICP-OES systems from other vendors, the 5110 enables laboratories to increase throughput without compromising on precision. It includes a fully integrated advanced valve system with unique hardware and software technologies that enable ultrahigh throughput with excellent precision and ease of use. IntelliQuant measurement is used for rapid sample screening and simple method development. Lastly, new diagnostic capabilities maximize instrument uptime and simplify troubleshooting.
**Agilent Technologies**
For info: 800-227-9770
www.agilent.com

**LCMS Pretreatment Module**
The Clinical Laboratory Automation Module (CLAM-2000) automatically performs all the processes necessary for analyzing blood and other biological samples, from scanning information from blood collection tubes to sample pretreatment and LCMS analysis. The CLAM-2000 is directly attached to the LCMS system, thus enabling a very safe, simple means for lab personnel to process and analyze samples. A variety of functions help ensure the precision of analytical results, including management of reagents, calibration curves, and controls, as well as system maintenance management. The CLAM-2000 module automatically processes individual samples successively in parallel, which gives researchers uniform pretreatment times and allows more efficient use of the mass spectrometer. By automating operations such as dispensing, stirring, filtering, heating, and sample transfer, the system effectively improves data accuracy and achieves the reproducibility needed for clinical research for new drug discovery and monitoring of drugs in the blood.
**Shimadzu Scientific Instruments**
For info: 800-477-1227
www.ssi.shimadzu.com

**Zika Virus Antibody**
To help accelerate progress toward a vaccine or treatment for this global health threat, a Zika virus antibody from Vanderbilt University and Kerafast is now available. Thought to be the cause of microcephaly in newborn babies, the disease is spread by the mosquito genus *Aedes* as well as by sexual contact. By sharing data and materials research, institutions can help to address the current Zika outbreak and minimize its effects on the global population. The Zika polyclonal antibody recognizes the human Zika envelope (E) protein and can be utilized for a range of applications to study the virus and its function. Since its founding in 2011, Kerafast has partnered with more than 130 prominent academic research institutions internationally that provide thousands of rare and unique "Reagents for the Greater Good" for the benefit of the scientific community working toward the cure of disease in 52 countries on 6 continents.
**Kerafast**
For info: 800-546-1760
www.kerafast.com

**PD-1 Cell Lines**
AMS Biotechnology has introduced cell lines for programmed cell death protein-1 (PD-1) research, and for testing inhibitors of the PD-1/PD-L1 (PD-ligand 1) pathway. The binding of PD-1, a receptor expressed on activated T-cells, to its ligands (PD-L1 and PD-L2) negatively regulates immune responses. PD-1 ligands are highly expressed in many cancers, and their interaction inhibits T-cell activity, allowing cancer cells to escape immune surveillance. The PD-1/PD-L pathway is also involved in regulating autoimmune responses, making these proteins therapeutic targets for a number of cancers, as well as multiple sclerosis, arthritis, lupus, and type I diabetes. A PD-1/NFAT Reporter–Jurkat Cell Line is available for screening of activators or inhibitors of PD-1 signaling. An accompanying T-cell receptor activator/PD-L1–CHO Recombinant Cell Line is also designed for screening for activators or inhibitors of PD-1 signaling as well as screening PD-L1 antibodies for their binding affinity.
**AMS Biotechnology**
For info: +44-(0)-1235-828200
www.amsbio.com

Electronically submit your new product description or product literature information! Go to www.sciencemag.org/about/new-products-section for more information.

Newly offered instrumentation, apparatus, and laboratory materials of interest to researchers in all disciplines in academic, industrial, and governmental organizations are featured in this space. Emphasis is given to purpose, chief characteristics, and availability of products and materials. Endorsement by *Science* or AAAS of any products or materials mentioned is not implied. Additional information may be obtained from the manufacturer or supplier.

Downloaded from http://science.sciencemag.org/ on November 22, 2016

# life science EXPERT and e-commerce leader

The life science leaders of
**EMD Millipore + Sigma-Aldrich**
have joined together and, with our agile e-commerce and global distribution, we can help to simplify your world.
So you can focus with confidence on tackling life science's biggest challenges.

MilliporeSigma now offers:

- **An extended global network** across more than 66 countries
- **A world-class e-commerce platform** to simplify transactions
- **A vast portfolio** that has grown to over 300,000 products

Our combined strengths will deliver the **knowledge, know-how, and best-in-class resources.**

Learn more at **milliporesigma.com**

The life science business of Merck KGaA, Darmstadt, Germany operates as MilliporeSigma in the U.S. and Canada.

EMD Millipore, MilliporeSigma and the vibrant M are trademarks of Merck KGaA, Darmstadt, Germany and its affiliates.
Sigma-Aldrich is a trademark of Sigma-Aldrich Co. LLC and its affiliates.
Copyright © 2016 EMD Millipore Corporation. All Rights Reserved.

MilliporeSigma

# life science EXPERT and e-commerce leader

The life science leaders of
**Merck Millipore + Sigma-Aldrich**
have joined together and, with our
agile e-commerce and global distribution,
we can help to simplify your world.
So you can focus with confidence on
tackling life science's biggest challenges.

The life science business of Merck now offers:

- **An extended global network** across more than 66 countries
- **A world-class e-commerce platform** to simplify transactions
- **A vast portfolio** that has grown to over 300,000 products

Our combined strengths will deliver the **knowledge, know-how, and best-in-class resources.**

Learn more at **merckgroup.com/life-science**

The life science business of Merck operates as MilliporeSigma in the U.S. and Canada.

Merck, Merck Millipore and the vibrant M are trademarks of Merck KGaA and its affiliates.
Sigma-Aldrich is a trademark of Sigma-Aldrich Co. LLC and its affiliates.
Copyright © 2016 Merck KGaA. All Rights Reserved.

MERCK

eppendorf

# More Capacity

**Centrifuge 5920 R**

The new Centrifuge 5920 R delivers extraordinary high capacity in a very compact and ergonomic product design. Its state-of-the-art refrigeration system provides excellent cooling performance and keeps your temperature sensitive samples safe.

> Max. capacity: 4 × 1000 mL or 52 × 50 mL conical
> Outstanding rotor versatility
> Space-saving design
> Advanced temperature management
> NEW: Eppendorf Conical Tubes, 15 mL and 50 mL

www.eppendorf.com/centrifugation

Eppendorf® and the Eppendorf logo are registered trademarks of Eppendorf AG, Germany. U.S. Design Patents are listed on www.eppendorf.com/ip
All rights reserved, including graphics and images. Copyright © 2016 by Eppendorf AG.

Watch video!

*See the Total Solar Eclipse August 21, 2017*

## Sun Valley Idaho Eclipse

***Tetons & Yellowstone • August 18-26, 2017***

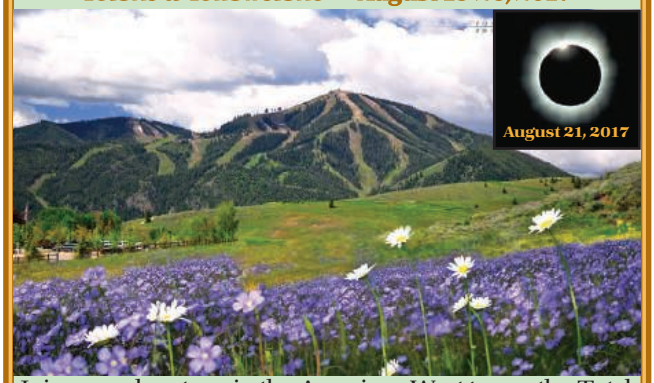


Join our adventure in the American West to see the Total Solar Eclipse overlooking Sun Valley, Idaho! Discover prehistoric sites from Boise to the Tetons. Follow the Snake River to an important fossil site. Ride in cable cars with an incredible 360-degree view of Jackson Hole, the Tetons, and Yellowstone National Park. Trip fee: $4,595 + air.

**AAAS *Travels***

***For a detailed brochure, call (800) 252-4910***
All prices are per person twin share + air

BETCHART EXPEDITIONS Inc.
17050 Montebello Rd, Cupertino, CA 95014
*Email:* AAASInfo@betchartexpeditions.com
www.betchartexpeditions.com



## WILL YOUR RESEARCH LEAD TO BETTER LIVES FOR PATIENTS?

Gopinath Sutendra and Evangelos D. Michelakis, "Pulmonary Arterial Hypertension: Challenges in Translational. Research and a Vision for Change", *Sci. Transl. Med.* 5, 208sr5 (2013) Credit: *Science* Source

Science Translational Medicine | AAAS
INTEGRATING SCIENCE, ENGINEERING, AND MEDICINE

Find out more about the scope of the journal and submit your research today. **ScienceTranslationalMedicine.org**

# 2017
## AAAS MARTIN AND ROSE WACHTEL CANCER RESEARCH AWARD

Recognize the work of an early career scientist who has performed outstanding work in the field of cancer research. Award nominees must have received their Ph.D. or M.D. within the last 10 years. The winner will deliver a public lecture on his or her research, receive a cash award of **$25,000**, and publish a Focus article in *Science Translational Medicine*.

For more information visit
www.aaas.org/aboutaaas/awards/wachtel
or e-mail wachtelprize@aaas.org.
Deadline for submission: March 1, 2017.

Science Translational Medicine | AAAS

# Xi'an Jiaotong University
# Welcome Distinguished Scholars From Home and Abroad

## *XJTU Introduction*

Xi'an Jiaotong University is a key university which is directly administered by the Chinese Education Ministry and is one of the oldest current institutions of higher education in China. Xi'an Jiaotong University, as one of the first universities entering the seventh and eighth five-plan, as well as China's "211 Project" and "985 Project", is selected to be developed into a global first-class university.

Currently Xi'an Jiaotong University is a comprehensive research university with scientific focus. It is composed of 10 branches of learning, namely: science, engineering, medicine, economics, management, literature, law, philosophy, education and art. The university, currently, consists of 28 full-time colleges and schools, 8 schools for undergraduates and 12 affiliated teaching hospitals. It boasts a high-level staff of 5,696, including 3,006 full-time teachers, among which are 1,800 professors and associated professors.

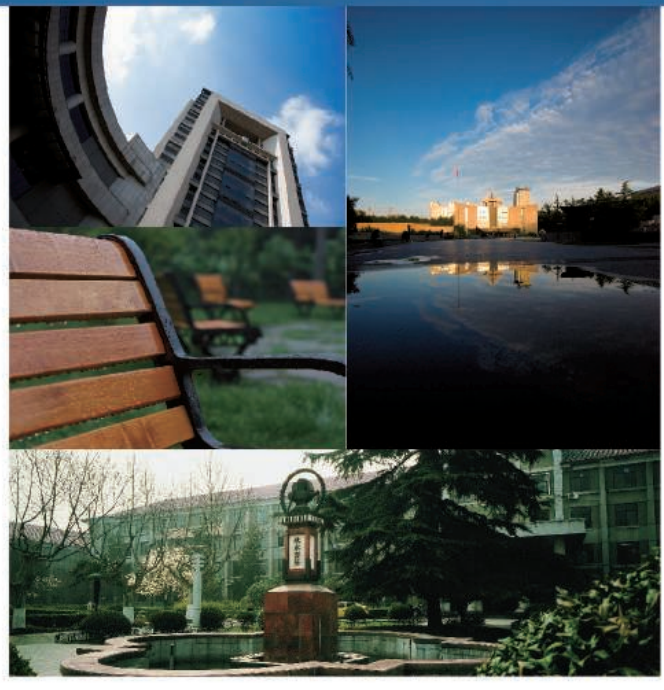

XJTU has 29 academicians of the Chinese Academy of Sciences and the Chinese Academy of Engineering, of which 17 are doubled-hired academicians. There are 6 national-level teachers, 57 Changjiang Scholars, 35 Outstanding Young Investigator Award laureates, 20 national experts with outstanding contribution to the country, 41 nation-level candidates of the National Talents Project, and the 21st Century National Talents Project, 19 leaders of the Program for Changjiang Scholars and Innovative Research Team, 234 personnel of 21st Century Excellent Talents Training Plan proposed by the Ministry of Education, and 535 experts who have made outstanding contributions and enjoy special governmental allowances.

In this new century, Xi'an Jiaotong University continues to renew itself to adapt to the ever-changing landscape of higher education, domestically and internationally, gradually evolving a model of higher education that is suited to international developments, while constructing at the same time a modern scientific approach to policy-making, policy execution and supervision, so as to provide the university with a management structure meeting international standards. Together, the two lay a firm foundation for building Xi'an Jiaotong University into a top-flight international university.

## *Recruitment Requirements*

*Leading Scholars Program*

1.Academicians of CAS and CAE, selected candidates of National Thousand Talents Program, Tens of Thousands of People Plan, Changjiang Scholars Program, The National Science Fund for Distinguished Young Scholars, etc.
2. Professors or other specialists with equivalent academic level who work in famous universities or research institutes at home and abroad
3.Excellent scholars who in charge of national important research tasks and make significant academic achievements

*Young Talents Support Plan*

1.Applicants should have obtained PhD degree and under the age of 40; Outstanding applicants under 45 can be also be considered & recruited;
2.Applicants should have extensive academic horizon and innovative thinking, and have the potential to become future leaders in relevant areas.
3.Applicants should have outstanding academic achievements in their chosen fields, be prominent among peers and have obtained high recognition from academia.

## *How to Apply*

Please email a CV to our contacts listed below. After reaching agreement, we will have designated staff to help with applying to the different talent programs. Please include basic personal data, contact information, education and work experience, and major academic achievements including publications, research projects, grants, patents, awards and so forth in the CV.

## *Contact Information*

*Teacher Xie, 86-29-82668975, bjxie@mail.xjtu.edu.cn*
*Teacher Liu, 86-29-82668975, lybobo@mail.xjtu.edu.cn*

CELL SIGNALING TECHNOLOGY

# Rooted In Science

As a company rooted in science we are committed to producing and rigorously validating our products in house. This ensures they will work in your experiments and be worthy of the important research efforts they support.

We are proud to be recognized by scientists for our efforts to be leaders in key validation areas.*

*#1 Rank: *2015 Biocompare Antibody Market Report* • www.cellsignal.com/**rooted**

16PADSCORP0090ENG

**For Research Use Only. Not For Use In Diagnostic Procedures.**

© 2016 Cell Signaling Technology, Inc. Cell Signaling Technology, and CST are trademarks of Cell Signaling Technology, Inc.

Cell Signaling TECHNOLOGY®

# *Science* Careers Advertising

For full advertising details, go to ScienceCareers.org and click For Employers, or call one of our representatives.

**Tracy Holmes**
Worldwide Associate Director
*Science* Careers
Phone: +44 (0) 1223 326525

THE AMERICAS

E-mail: advertise@sciencecareers.org
Fax: +1 (202) 289 6742

**Tina Burks**
Phone: +1 (202) 326 6577

**Nancy Toema**
Phone: +1 (202) 326 6578

**Online Job Posting Questions**
Phone: +1 (202) 312 6375

EUROPE / INDIA / AUSTRALIA / NEW ZEALAND / REST OF WORLD

E-mail: ads@science-int.co.uk
Fax: +44 (0) 1223 326532

**Sarah Lelarge**
Phone: +44 (0) 1223 326527

**Kelly Grace**
Phone: +44 (0) 1223 326528

**Online Job Posting Questions**
Phone: +44 (0) 1223 326528

JAPAN

**Katsuyoshi Fukamizu** (Tokyo)
E-mail: kfukamizu@aaas.org
Phone: +81 3 3219 5777

**Hiroyuki Mashiki** (Kyoto)
E-mail: hmashiki@aaas.org
Phone: +81 75 823 1109

CHINA / KOREA / SINGAPORE / TAIWAN / THAILAND

**Danny Zhao**
E-mail: dzhao@aaas.org
Phone: +86 131 4114 0012

All ads submitted for publication must comply with applicable U.S. and non-U.S. laws. *Science* reserves the right to refuse any advertisement at its sole discretion for any reason, including without limitation for offensive language or inappropriate content, and all advertising is subject to publisher approval. *Science* encourages our readers to alert us to any ads that they feel may be discriminatory or offensive.

ScienceCareers
FROM THE JOURNAL SCIENCE AAAS

ScienceCcareers.org

## Faculty Search
## Endowed Chair in Energy Sustainability

The Georgia Institute of Technology seeks applications from outstanding faculty candidates with national and international stature, who will lead science and technology programs at the forefront of energy sustainability. Candidates should have a track record of well-funded research, broadly cited publications, collaboration, entrepreneurial spirit, and professional qualifications consistent with appointment as a tenured, full professor.

Located in Atlanta, the Georgia Institute of Technology is among the top ten public universities in the nation. Georgia Tech aims to meet several grand challenges associated with energy sustainability based upon current strengths and areas of growth. Research in this interdisciplinary field at Georgia Tech benefits from strong interactions among faculty from diverse disciplines across the College of Sciences and the College of Engineering. It is our expectation that the person selected for this position will continue to build strong ties amongst diverse faculty across both colleges.

Additional information is available from Dr. Elsa Reichmanis, chair of the search committee (ereichmanis@chbe.gatech.edu). Nominations should be directed to the chair of the search committee. Applications, including a cover letter, curriculum vitae, statement of research interests and plans, and names and contact information for three references, should be sent via email to **chairsearch@chbe.gatech.edu**.

Review of applications begins **December 1, 2016** and will continue until the position is filled.

*Georgia Tech is a unit of the University System of Georgia and an Affirmative Action/Equal Opportunity Employer and requires compliance with the Immigration Control Reform Act of 1986.*

Georgia Institute of Technology

## Herman Ostrow School of Dentistry of USC

### CENTER FOR CRANIOFACIAL MOLECULAR BIOLOGY

The Herman Ostrow School of Dentistry of USC's Center for Craniofacial Molecular Biology (CCMB) http://ccmb.usc.edu seeks outstanding candidates for a tenure-track faculty position at the rank of assistant professor in the Division of Biomedical Sciences to conduct cutting-edge research in the areas of cell and developmental biology, tissue regeneration, cell signaling, gene regulation, computational modeling and human diseases using genetic and genomic approaches. The CCMB and the University of Southern California offer an exciting and supportive environment in which to conduct collaborative, basic, clinical and translational research.

Candidates must have a Ph.D. in developmental biology, stem cell biology or molecular biology and a strong record of high-quality research with significant publications in their field. Candidates with K99/R00 or other independent support are strongly encouraged to apply. Candidates with both a Ph.D. and a D.D.S./D.M.D. degree are also encouraged to apply.

Interested applicants should submit a cover letter, complete curriculum vitae, statement of current and future research plans, selected recent publications, and arrange to have at least four letters of reference sent to: **Dr. Yang Chai, Search Committee Chair, Center for Craniofacial Molecular Biology, Herman Ostrow School of Dentistry of USC, c/o Ms. Patricia Thompson, 2250 Alcazar Street, CSA 103, Los Angeles, CA 90033; Email: pathomps@usc.edu**. For more information and/or to apply: **http://jobs.usc.edu/postings/78304**. Consideration of applicants will begin immediately and will continue until the position is filled.

*USC is an Equal-Opportunity Educator and Employer, proudly pluralistic and firmly committed to providing equal opportunity for outstanding persons of every race, gender, creed and background. The university particularly encourages members of underrepresented groups, veterans and individuals with disabilities to apply. USC will make reasonable accommodations for qualified individuals with known disabilities unless doing so would result in an undue hardship. Further information is available by contacting uschr@usc.edu.*

## PennState
## Eberly College of Science

## Eberly Research Fellows
## at Penn State University

The Eberly College of Science at Penn State University invites nominees for the Eberly Research Fellowship program. Eberly Fellowships are designed to attract exceptional early career scientists to Penn State to enhance their career goals in the vibrant, highly collaborative environment of the Eberly College of Science and the broader STEM community of Penn State University. The Eberly College of Science which includes the Departments of Astronomy & Astrophysics, Biology, Biochemistry & Molecular Biology, Chemistry, Mathematics, Physics, and Statistics, ranks in the top 10 universities in the U.S. and has annual research expenditures exceeding $106M. Each of the seven departments is expecting to appoint one or more Eberly Fellows. Nominations for early career scientists with exceptional promise in basic research in physics, chemistry, biology, molecular biology, astronomy, mathematics, and statistics and/or applied research in health, energy, materials, or the environment are encouraged. Interdisciplinary as well as traditional disciplinary research is encouraged. Fellows who wish to also gain training and experience in teaching may elect to receive mentored teaching experience. Eberly Fellow advisors must hold their primary appointment in one of the seven departments of the Eberly College of Science. Co-advisors and cross-disciplinary research are also supported.

### Eligibility and Appointment

Applicants must have received a doctoral degree in one of the sciences, statistics, or mathematics within the past three years. Current doctoral students and postdoctoral fellows at Penn State are not eligible. Eberly Research Fellowships may be held from 1-3 years with annual appointments conditional on satisfactory performance. Fellows will receive a stipend of $65,000 and $5,000 per year in discretionary funds, which can be used for travel and other research expenses.

### Nomination and Applications

Nominations will be accepted from faculty advisors, graduate program chairs, department chairs, or others who can attest to the nominee's potential as a scientist. Nominations of women and under-represented minorities are strongly encouraged. The nomination deadline is December 15 for appointments beginning 6-12 months later. Nominations should sent to research-fellows@psu .edu

The Eberly Research Fellowship Selection Committee will select the nominees who will then be requested to submit their applications by January 15, 2017. Applications will include (1) a biographical sketch – including publications, accepted, and submitted manuscripts, (2) three letters of reference including one from the doctoral advisor, (3) research statement summarizing research accomplishments and research that you intend to pursue at Penn State, (4) names of one or more potential faculty advisors among the faculty in the seven department of the Eberly College of Science, Penn State University.

CAMPUS SECURITY CRIME STATISTICS: For more about safety at Penn State, and to review the Annual Security Report which contains information about crime statistics and other safety and security matters, please go to http://www.police.psu.edu/clery/, which will also provide you with detail on how to request a hard copy of the Annual Security Report.

Penn State is an equal opportunity, affirmative action employer, and is committed to providing employment opportunities to all qualified applicants without regard to race, color, religion, age, sex, sexual orientation, gender identity, national origin, disability or protected veteran status. U.Ed. SCI 17-37

ScienceCareers online @sciencecareers.org

ScienceCareers online @sciencecareers.org

# Breakthrough of the Year

## Special Editorial Feature: December 23, 2016

Reserve ad space by December 6

Ads accepted until December 16 on a first-come, first-served basis

For recruitment in science, there's only one Science

## This December, reach an additional 50,000 scientists at no extra cost!

**Content:** Each year, the *Science* editorial team reviews the most exciting discoveries of the past 12 months in the eagerly awaited "Breakthrough of the Year" issue.

**Reach:** Reach our 400,000 worldwide readers as well as a special group of 50,000 scientists carefully selected for their demographic similarities to *Science*'s current audience.

**Special Offer:** Advertisers who place an ad both in print and online will get their job featured in one of our January Career Path Newsletters. Online postings will also be refreshed in January so that they appear at the top of job search results and are included again in the new job alerts for the new year.

**Celebrate your own breakthrough this holiday season by reaching nearly 450,000 potential employees!**

SCIENCECAREERS.ORG

ScienceCareers
FROM THE JOURNAL SCIENCE AAAS

To book your ad: advertise@sciencecareers.org

The Americas
202-326-6577

Europe/RoW
+44 (0) 1223 326500

Japan
+81 3 3219-5777

China/Korea/Singapore/Taiwan
+86 131 4114 0012

The University of Illinois at Chicago, Department of Chemistry seeks an internationally renowned scientist with exceptional records of research accomplishment, vibrant externally funded research programs, visibility, and vision to fill a newly established **ENDOWED CHAIR** in Chemistry. Leaders in all areas of the chemical sciences who complement our existing research strengths, push disciplinary boundaries and are committed to developing stellar academic programs are sought. The rank of the appointment is to be Associate or Full Professor. For fullest consideration, please submit an online application, including a cover letter, curriculum vitae, brief summary of past research and plans for future research, and the names and email addresses of three references by **January 17, 2017.** Please go to website: **https://jobs.uic.edu/job-board/job-details?jobID=72707&job=associate-or-full-professor-endowed-chair-chemistry** to apply. Review of applications will begin **January 18, 2017.**

*The University of Illinois at Chicago is an affirmative action/equal opportunity employer, dedicated to the goal of building a culturally diverse pluralistic faculty and staff committed to teaching in a multicultural environment. We strongly encourage applications from women, minorities, individuals with disabilities and covered veterans. The University of Illinois may conduct background checks on all job candidates upon acceptance of a contingent offer. Background checks will be performed in compliance with the Fair Credit Reporting Act.*

---

**CARDIOVASCULAR RESEARCH in TEXAS**

**POSTDOCTORAL TRAINING** positions in cardiovascular research are immediately available at the University of Texas Health Science Center at San Antonio. Available positions are funded by a National Institutes of Health training program (T32) with training opportunities in the fields of atherosclerosis, cerebrovascular diseases, myocardial infarction and hypertension. Information about the training program and its faculty can be found at website: **www.CVtrainingTexas.org**. Highly motivated early-career scientists and physicians with interests in basic cardiovascular biology and mechanisms of disease are encouraged to apply. Successful applicants will receive training in cutting edge technologies prominent in modern research. At the time of appointment, trainees must hold an advanced academic/professional degree (e.g. DDS, DVM, MD or PhD) and be a U.S. citizen or green card holder. San Antonio is the nation's 7th largest city and offers rich multicultural heritage, attractive quality of life and low cost of living. The University of Texas Health Science Center is a Tier I Research Institution situated between downtown and recreational areas in the beautiful Texas hill country. To apply, please send a curriculum vitae and cover letter, which includes a brief statement of interest and qualifications and the names of three professional referees, to **Ms. Mila Grinshpan at e-mail: Grinshpan@uthscsa.edu.**

All postdoctoral appointments are designated as security sensitive positions. *The University of Texas Health Science Center at San Antonio is an Equal Employment Opportunity/Affirmative Action Employer, including protected veterans and persons with disabilities.*

---

FLORIDA STATE UNIVERSITY

**The Wyatt/Green Endowed Chair in Physics**

The Department of Physics at Florida State University seeks to fill this endowed chair with an individual who will enhance research within the Department and foster collaborations with other researchers across the University. We seek a physicist with an international reputation for outstanding scholarship and leadership and a commitment to undergraduate, graduate and postdoctoral education. The successful candidate will be hired at the Full Professor level.

Applications should include a CV and summary of current and future research plans including possible collaborations within the department and university and will be accepted until the position is filled. For further information on this Endowed Chair, contact Professor Kirby Kemper, Search Committee Chair at **kkemper@fsu.edu**.

*Florida State University is an Equal Opportunity/Access/Affirmative Action/Pro Disabled & Veteran Employer. FSU's Equal Opportunity Statement can be viewed at: http://www.hr.fsu.edu/PDF/Publications/diversity/EEO_Statement.pdf.*

---

Northeastern University
College of Engineering

With **169** tenured/tenure-track faculty (**57** hired since 2013), and **12** federally-funded research centers, Northeastern's College of Engineering is in a period of dynamic growth. Our emphasis on interdisciplinary, use-inspired research—tied to Northeastern's unique history of industry collaboration via the university's signature cooperative education program—enables partnerships with academic institutions, medical research centers, and companies near our centrally located Boston campus and around the globe.

**The college seeks outstanding faculty candidates in all five departments.**

Particular consideration will be given to candidates at the associate or full professor level; successful applicants will lead internationally recognized research programs aligned with one or more of the college's strategic research initiatives. Exceptional candidates at the assistant professor level will also be considered.

**Learn more and apply at coe.neu.edu/faculty/positions**

Northeastern University is an Equal Opportunity, Affirmative Action Educational Institution and Employer, Title IX University, committed to excellence through diversity.

---


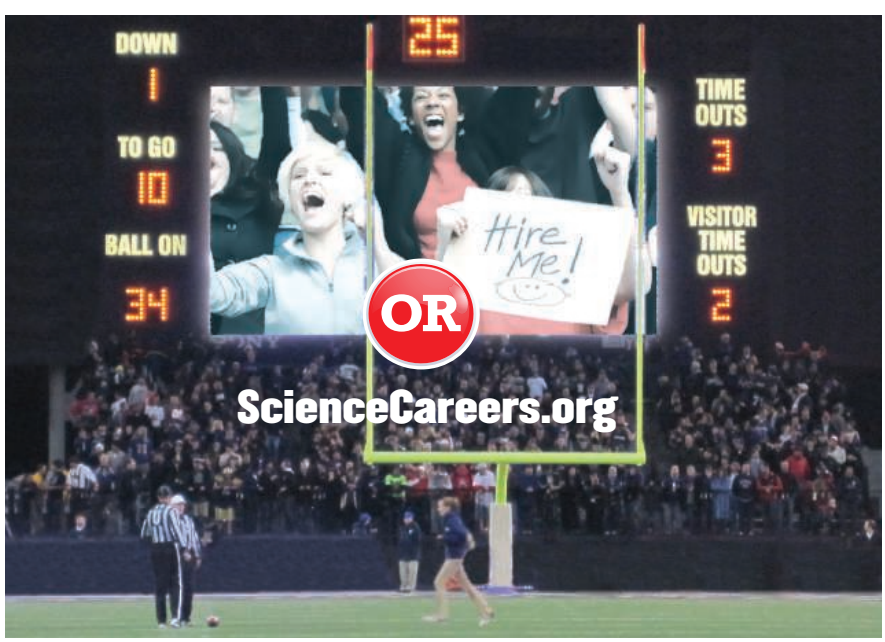


**Keep your job search out of the cheap seats.**

Target your job search using relevant resources on **ScienceCareers.org**.

ScienceCareers
FROM THE JOURNAL SCIENCE AAAS

CHINA

聚焦“一带一路，西部大学”

# A Convergence of Topnotch Talents Serving *“One Belt, One Road”*

**Zhimin Li**
**Director of Center for Science and Technology Development**
**Ministry of Education, People's Republic of China**

“One Belt, One Road” is the slogan for the Silk Road and 21st Century Maritime Economic Belts, which were decreed by Chinese President Jinping Xi on Sep. 2013 to accelerate the economic integration of Eurasia. Marked by the historic signs of the ancient Silk Road, “One Belt, One Road” runs throughout the Eurasian continent, spanning the active East Asian and developed European economic rims. The countries within this broad area have tremendous development potential.

Western China is an important area for implementation of the “One Belt, One Road” strategy. However its economic development is critically dependent on educational development, which is in turn dependent on strategic and balanced allocation of educational resources. In recent years, China has begun to carry out The Higher Education Rejuvenation Program for Central and Western China, which aims to strengthen the "slant force" of educational resource allocation, and to take full advantage of the assets in the western region. In May 2015, the talents and scientific payoffs from the “One Belt, One Road” strategy was on display when nearly a hundred universities from 22 countries convened in Xi’an, jointly issuing the “Xi’an Declaration” which officially launched the “University Association of New Silk Road” under the co-sponsorship of 21 universities, including Xi' an Jiaotong University. 128 universities from 31 countries have joined this association to date, including Harbin Institute of Technology, The University of Hong Kong, Bauman Moscow State Technical University, Kazakhstan National University, Kirghizia National Normal University, Ecole Supérieure d'Electricité, Politecnico di Milano, University of Liverpool (UK), Pakistan University of Sciences and Technology, National University of Singapore, Busan University (South Korea), Chiang Mai University, and Tampere University of Technology (Finland).

In May 2016, “Guidance for Accelerating the Education Development in the Midwest” was issued by the General Office of the State Council of the People's Republic of China. Emphasizing China’s continued implementation of the “The Higher Education Rejuvenation Program for Central and Western China”, the guidance proposes to strengthen resource allocation, introduce high level talents to the region, and support the construction of first-class universities and disciplines in China’s mid-western universities. For provinces not under the direct supervision of the Ministry of Education, western universities will be boosted by construction of 14 universities in strategic locations and using innovative practices, according to the principle of “One Province, One Provincial University”.

In addition to the above programs, China will also continue to improve foundational capabilities in mid-western universities. Comprehensive universities will be developed with disciplines that correspond to plans for existing local industry and regional development. These undergraduate universities will provide important support for local economic and social development, by developing disciplines and professions that are of strategic importance for the different regions. Specifically, the construction of basic facilities will be strengthened, including teaching laboratories, well-equipped research laboratories, comprehensive training centers, and library and information centers. In addition, the abilities of teachers and their treatment will be improved by strengthening practical teaching links, constructing experimental teaching teams, and training of teachers and laboratory personnel. Thus the “One Belt, One Road” strategy is a rare opportunity for western universities to become talent magnets that will in turn generate a “super magnetic cluster effect”, whereby development of western universities will be accelerated by provision of intellectual support cultivation of talent. To fulfill this promising future, western universities are thirsty for ingenuity, and now is the time to welcome this talent!

**Fengyou Wang**
**Director-General of Guizhou Provincial Department of Education**

Guizhou, China’s 2nd Inland Opening-up Pilot Economic Zone and the country’s Pilot Eco-civilization Development Zone, is now in its flourishing period of economic and social development. With “Big Data” Industry, large-scale poverty-relief projects, and local ecological and tourist resources as its developmental backbones, Guizhou is witnessing dramatic and prosperous changes. Guizhou is also well-recogized for its favorable climate, fresh air and high popularity. We sincerely welcome all the ambitious talents who wish to make contribution to the development of southwest China to come to Guizhou, and to start your business, develop your career and enjoy your life here. I am expecting you in Guizhou!

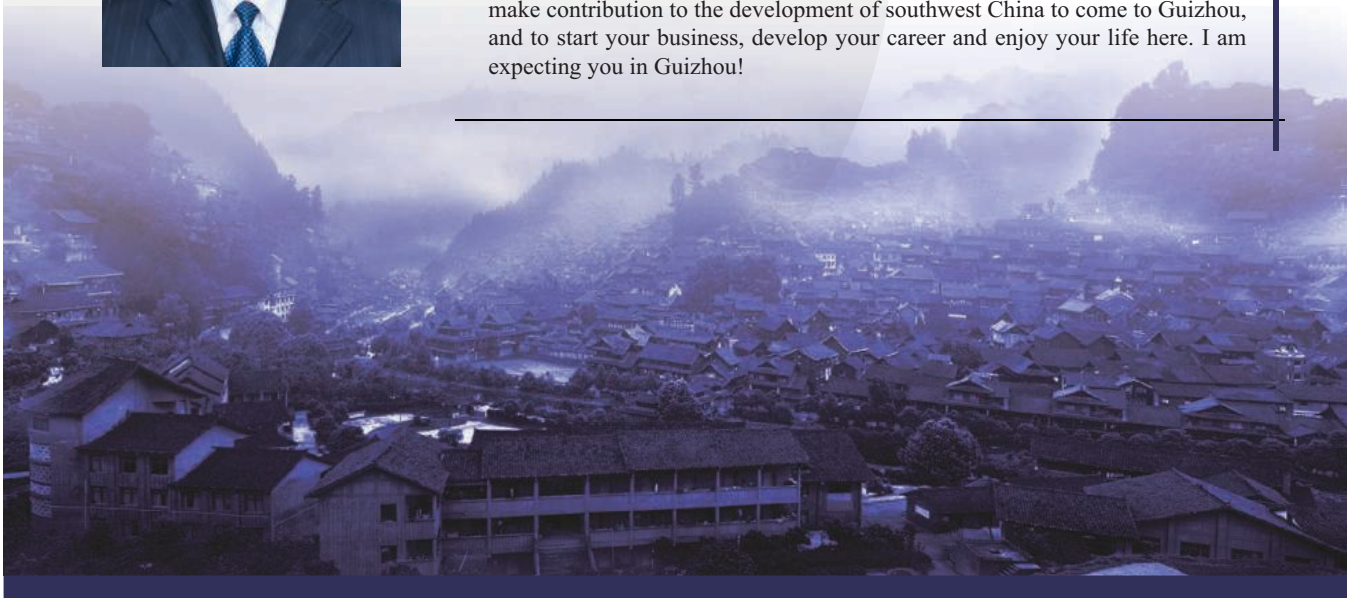



Science Careers online @sciencecareers.org

## Heping Xie
**President of Sichuan University**

Sichuan University, located in one of the regions along "One Belt, One Road" Initiative, is one of China's premier institutions with high-level teaching and research facilities and faculties. We embrace a "people-oriented, academic-advocated and excellence pursuit" mission, which pictures a blueprint for the University in a new era. We invite you to join the SCU Talent Pool, and work with us to forge a World-class University in West China.

## Shuguo Wang
**President of Xi`an Jiaotong University**

Outstanding talents are the driving force for sustainable development of Xi'an Jiaotong University. The University welcomes all kinds of talents to join us, and commits itself to employing talents without any restraint of styles. Great efforts will be made to create an exceptional environment where first-class talents can gather.

## Xuhong Zhou
**President of Chongqing University**

Chongqing University warmly invites global talents to broaden the development prospect in Chongqing, the Significant Central City in China, and to join the team of Chongqing University to do academic research, bring up talents, bless township and achieve vibration guide society.

## Qiang Zheng
**President of Guizhou University**

Guizhou is a province with fantastic ecology, which is as intoxicating as the taste of Moutai, the most famous Chinese liquor.
After approved to be one of the key "211 Project" universities in 2005, Guizhou University was listed as one of the "14 National Key Construction Universities in the Central and West Region of China" in 2016 by the central government. This enables GZU to obtain the financial support of over 5 billion RMB from the central government and Guizhou Province. GZU has invested 4 billion RMB to construct the new campus, making it one of the most beautiful campuses in China. In recent 3 years, over 300 Ph.D graduates from Europe and America as well as other domestic universities have joined GZU.
I heartily welcome you to realize your dreams in Guizhou!

## Wenxun Lin
**President of Yunnan University**

In the grand cause of building a first-class university with first-class disciplines of the world, we are implementing the strategies of "upgrading the University academically, and strengthening the University with professionals." We earnestly invite professionals of all fields to join us for a brilliant future.

## Ying He
**President of Heilongjiang University**

The construction of "Double tops" promotes our development in connation, feature and innovation.
The construction of "Double tops" brings Chinese Higher Educationworld golden opportunities and powerful drive to further enhance our educational level and comprehensive strength. Distinguishingly featured by servicing Sino-Russian relation development and regarding as our own duty people enlightening, knowledge dissemination, and truth seeking, Heilongjiang University has been further implementing strategies of Russia-oriented educational approach, top-level discipline and underlying talents cultivation. Allying talents from home and abroad, we are committed to constructing a top comprehensive university with unique features, high educational level and modernized conditions.

## Xiaojun Liu

**President of Xi'an University of Architecture and Technology**

The strategy of building the Silk Road economic belt has provided XAUAT with a good opportunity for development. XAUAT will adhere to the concept of a human-oriented and teacher-centered education and strengthening the university with talents. With the advantages of building Xi'an into an international metropolis, XAUAT will enhance its recruitment ability of high-level talents and create favorable working conditions and environment for global talents.

## Shuzhi Yao

**President of Shaanxi University of Science & Technology**

The Silk Road has opened cultural and economic relations between the civilizations since ancient China and has been a bridge for cultural interaction connecting the East and West. Located in Xi'an, a vibrant and inspirational place where the Silk Road starts, SUST has initiated light industry higher education with paper, leather and ceramic engineering, inheriting Chinese civilization with modern technologies. SUST welcomes global talents to Shaanxi for academic interaction in research areas of Bio-resources Chemical &Material Engineering, Materials Science & Engineering, Environmental Science & Engineering, Food & Biology. SUST sincerely expects excellent scholars to join us and contribute to the Four First Rate higher education by achieving first class academic accomplishments.

## Boming Tang

**President of Chongqing Jiaotong University**

As an important base for cultivation of students and scientific and technological innovation in the fields of traffic and transport, Chongqing Jiaotong University warmly welcomes outstanding talents from home and abroad. Encouraged by the motto and spirit of "Virtues make you go afar, and traffic and transport help you better communicate with the world ", the university will provide platform for opportunity and success.

## Fangcheng Sun

**President of Chongqing Technology and Business University**

CTBU is a key beneficiary of the China' s Middle and West Universities Basic Capacity Enhancement Program and a cradle of talents for Chongqing' s West China Financial Highland Initiative, located below the Nanshan Mountain and by the Yangtze River, boasting a garden-like campus. Illuminated by the spirit of encompassing all, strengthening self, prospering the nation and benefiting the society, CTBU sincerely invites you to join us in the pursuit of glorious chapters.

## Zhixu He

**President of Guizhou Medcial University**

At new era the higher education in medicine should be treated as elite education rather than education for all, fully embrace the fruits of technological progress, strengthen student-centered concept and the training for hands-on and innovation capacity, enhance the quality of teaching and education, and produce high-quality medical professionals to meet social needs.

To help China's top-ranked universities attract high-level talent from overseas, CERNET has partnered with Science to launch a print and online media campaign. Many of China's top universities are recognized as world-class and are doing first-class research but the aim is to build on this and establish worldwide acclaim for all of China's top universities in both institute and discipline rankings.
Researchers, interested in working in China, are invited to consider applying for jobs published in the following special section "Opportunities in China" and online at **http://jobs.sciencecareeres.org/**

Further information can also be located at **www.edu.cn/jjxb**



Science Careers online @sciencecareers.org

ScienceCareers online @sciencecareers.org
OPPORTUNITIES IN CHINA

四川大學
SICHUAN UNIVERSITY

# SICHUAN UNIVERSITY CALLS FOR GLOBAL TALENTS

## About Sichuan University

Sichuan University (SCU) is one of China's key universities under the direct supervision of Ministry of Education. Located in Chengdu, Sichuan Province in West China, the hometown of the Giant panda, the SCU has 34 academic colleges and is identified as a prominent high-level comprehensive research university under National Project 985 and Project 211. The SCU has won national recognition for the excellence of its faculty.

We offer a package of Talents Program for different talents. On entering one of the following programs, we will accordingly provide starting research funds, equipment, daily expenses and fees for international academic exchanges. We will also provide support in terms of salaries, housing, offices, laboratories, postdoctor, research assistants and graduate students. We look forward to you joining the ranks of the renowned scholars and researchers who make the SCU an outstanding university.

## Join Us!

### *I. Chief Scientists*

***Related Fields:*** New Energy and Low Carbon Technology and Engineering, Industrial Internet, Aircraft engine and Combustion Kinetics, Aerospace Mechanics, Advanced Navigation and Flight Simulation, Cyberspace Security, Computer Science and Technology, Software Engineering.

***Qualifications:*** Obtained professorship or equivalent position at high level universities or research institutions, or experts with strong academic influence both domestically and internationally; excellent ability in academic team organization and noticeable social influence.

***Compensation:***

(1) Annual salary: *RMB 600,000 - 1,000,000*

(2) Research start-up fund: *RMB 400,000 - 800,000* for humanities and social sciences; *RMB 2,000,000 - 6,000,000* for natural science and engineering science

(3) Supporting packages: Budget for academic research assistants and personnel costs for academic team according to the disciplines construction

(4) Priority of being recommended by SCU to apply for national talent programs, including the "1000 Talents Plan" and the "Chang Jiang Scholars Program".

### *II. International Faculty Program (Full-time or Part-time)*

This program aims at attracting two levels of teachers with a non-Chinese nationality. The foreign teachers can work full or part time under a 3 to 5-year-contract at a fix or non-fix time every year (the working time at Sichuan University shall be no less than ONE month per year for the part-time foreign teachers).

***Level 1: Full time or Part time High-end Foreign Teachers***

We are looking for renowned professors in world-class universities or research institutes. We provide them competitive salary(*400,000 Yuan to 1250,000 Yuan per year* for the full-times and *30,000 Yuan to 100,000 Yuan per month* for part-times), local insurance, fee for international travel and accommodation in the SCU, and a research assistant for each who is also a young full teacher in the SCU.

***Level 2: Full-time Foreign Teachers***

We are looking for foreign teachers with doctorate of the renowned international universities or research institutes with years of teaching or research experiences in university or research institutes. Salary scale will be within the range of *100,000 Yuan to 600,000 Yuan per year for the full time.*

### *III. Young Scholars Program（Full-time）*

For this program, we are looking for excellent talents from renowned universities or institutions, in the area of Natural Science, Medicine, Engineering, Liberal Art and Social Science.

A. We encourage and support all the qualified candidates to apply the "*Young 1000 Talents Program*" and they will be given an academic title of Distinguished Researcher. Highly competitive salary（*350,000-500,000 Yuan per year*） and generous start-up funding（no less than 1500,000 Yuan）as well as housing allowance will be provided for each successful applicant.

B. Who have a doctorate from the top 100 international universities or research institutes (or from top 30 disciplines in the world) will be given an academic title of Researcher with *annual salary pay 250,000 Yuan* and *200,000-600,000 Yuan as starting research fund.*

C. We support Associate Researcher with *annual salary pay 180,000 Yuan* and *starting research fund 150,000-300,000 Yuan.*

## Contact Information

Address: Sichuan University, No.24 South Section 1, Yihuan Road, Chengdu, Sichuan, P. R. China. 610065
Contacts:Ms.Du,Ms.Wang
E-mail: ***recruitment@scu.edu.cn***
Tel: 0086-028-8540-5390

**This Job Advertisement Is Long-term Effective.**

# CHONGQING UNIVERSITY CALLS FOR GLOBAL TALENTS

## Chongqing University Profiles

*Chongqing University, founded in 1929, is a national "Project 985" and "Project 211" comprehensive key university directly governed by the Ministry of Education, China. Located in Chongqing, the significant Central City with the fastest GDP growth, Chongqing University aims to contribute to the national strategic research, municipal social and economic growth. Chongqing University has highly academic reputation, cultural richness and history deposits, known for advanced disciplines of Mechanical Engineering, Power Engineering, Material Science and Engineering, Information Science, Biology, and Economics and Business Administration, and the high-level disciplines of Architecture, Civil Engineering, and Resources and Environmental Science. The university consists of 6 faculties, namely, Faculty of Arts and Humanities, Faculty of Social Science, Faculty of Science, Faculty of Engineering, Faculty of Built Environment, Faculty of Information Science, and 34 colleges. As the best university in the western China, Chongqing University warmly invites global talents to broaden the development prospect here!*

## Brief Introduction to Tenure Track Recruitment System

*Chongqing University carries out the tenure track recruitment system with reference to international recruitment system of foreign universities and the academic evaluation of peer review, strives for providing the guarantees of talents team building, converses the outstanding talents home and abroad, promotes the sustainable development for school construction, and is featured as full implementation, independent system, and international academic standard.*

## What We Offer

*According to the educational background and working experience, successful candidates will be employed as the Full Professor, Associate Professor or Assistant Professor by the university with preferential treatments as follows:*

- Appointed as the doctoral advisor and master's advisor;
- Incentive high salary;
- Competitive settling-in allowance;
- Sufficient research start-up fund;
- Purchasable talent apartment with less-than-market price.

## How to Apply

*Qualified applicants are strongly suggested to submit application materials electronically on http://121.43.192.253:8086/login/login.html?id=59 or email to cqurczp@cqu.edu.cn with a comprehensive CV, certificates of academic degrees, 5 samples of major publications and 3 references.*

## Contact Information

*Home Page of Personnel Department: http://rsc.cqu.edu.cn*
*Tel: 0086-23-65112823*
*Email: cqurczp@cqu.edu.cn*
*Address: No. 174, Shazheng Street, Chongqing, PRC*

**This Job Advertisement Is Long-term Effective.**

ScienceCareers online @sciencecareers.org
OPPORTUNITIES IN CHINA

# Brief Introduction to Guizhou University

*Founded in 1902, Guizhou University (GZU) has a long history and profound culture. Located along the picturesque Huaxi River, it covers a total area of 407.844 hectares. It is one of the key "211 Project" universities, "14 National Key Construction Universities in the Central and West Region of China" and one of the universities of "One Top University; One Province" project.*

## Disciplines

The university consists of 39 colleges and 2 public education departments, covering 12 disciplines such as literature, history, philosophy, science, engineering, agriculture, medicine, economics, administration laws, education as well as liberal arts.

The university has 1 state-level key subject, i.e. Pesticide Science, 8 key subjects of "211 projects", 28 provincial key subjects, 23 featured provincial subjects, 8 postdoctoral research stations. GZU offers 9 First-level and 47 Second-level Disciplines for PhD granting, 46 First-level and 197 Second-level Disciplines for Master's Degree Granting, and 13 Master's programs for specialized subjects.

## Faculty

At present, GZU has a full-time enrollment of 46,237 undergraduates, 7,202 postgraduates. Among the staff of 4,024, there are 2,739 full-time teachers, including 717 PhD owners, 1,173 Master degree owners, 495 full professors, 1,156 associate professors, 2 academicians of The Chinese Academy of Engineering, 4 distinguished (chair) professors of Cheung Kong Scholars Programme of China, 1 owner of National Science Fund for Distinguished Young Scholars (NSFDYS), 3 leading scholars of "Ten Thousand Talents Plan", 1 "Global Highly Cited Researchers", 1 scholar of "Thousand Young Talents", 1 member of discipline appraisal group of the Academic Degree Committee of the State Council, 8 scholars with the honor of "Young Experts with Outstanding Contributions, 7 candidates of state-level New Century Million-and-10-Million-Talents Project, 20 members of Steering Committee of Higher Education of Ministry of Education, 14 new century outstanding science and technology talents, 14 first-batch key provincial experts and 51 province-managed experts.

## Scientific research

The university has 1 national center of engineering technology, 1 breeding base of national key laboratories, 4 engineering laboratories co-constructed by the state and GZU, 7 key laboratories or centers affiliated to the Ministry of Education, 49 provincial key laboratories or centers, 12 provincial innovation centers, and 9 provincial research centers of humanities and social sciences.

## Featured Subjects

GZU has laid much emphasis on developing featured subjects closely related to the regional economic and social development of Guizhou. It had set up research Institute of Big Data Industry of Guizhou, Liquor Research Institute, International Folk Art Research Institute, Ethnology Research Institute (Hmong Studies Research Institute of China), Karst Landform Museum, Ethnic Museum of South-west Region, Yangming Culture Research Institute, ASEAN Research Institute, Long March Culture Research Institute and Youth Mental Health Research Center in the West Region.

## International Cooperation and Exchanges

GZU always places importance on developing international cooperation and exchanges. So far, the University has established cooperative relations with more than 140 academic institutions in over 40 countries and regions. GZU is a base of international education aid authorized by the Ministry of Education, an institution offering Chinese Government Scholarship Programs, and a base of international cooperation in science and technology authorized by the Ministry of Science and Technology. GZU established Guizhou's first Confucius Institute in Presbyterian College, U.S. The university also plays an important role in such international organizations as IAUP and AUAP. Since 2008, nine sessions of "China-ASEAN Educational Cooperation Week" have been successfully organized by GZU.

Upholding the motto of "Illustrious virtue, utmost goodness, extensive learning and earnest practice", GZU laid great emphasis on educating and cultivating talents to serve the economic and social development of Guizhou Province.

We are making efforts to build GZU into a high level university with its own features. We sincerely welcome the talents of the world to join us in building a better GZU.

## Job vacancies:

We need the scholars, experts and doctors studying literature, history, philosophy, science, engineering, agriculture, medicine, economics, administration laws, education as well as liberal arts.

The talents studying Big Data are Medicines are particularly needed.

## Salary & Benefits

- 1)Housing subsidy: 0.15million—1million RMB
- 2)Researching fund: 1million –5 million RMB
- 3)Fund for Research Platform Construction：2.5million-10million RMB
- 4)Annual salary for the first employment term: 300 thousand -500 thousand RMB ( doctors' salary is equivalent to the salary of associate professor in the first 3 years)

The salary and benefits is individually different. Please contact us for an interview and negotiation.

For further details, please visit ***http://hr.gzu.edu.cn***
Tel: 0086-851-88291959
Fax: 0086-851--88292278
E-mail:***pe@gzu.edu.cn***
Address: Huaxi District, Guiyang, Guizhou Province, China 550025
Official accounts:gzuniversity

# Yunnan University Recruits High-end Professionals

## I. Brief Introduction

Yunnan University, one of the earliest comprehensive universities in southwest China, was founded in 1923 and is located in Kunming, a city renowned for its spring-like weather all the year round. In 1946, it was listed in ***Concise Encyclopedia Britannica*** as one of the 15 Chinese universities of world fame. It is among the first universities to win the membership of "Project 211." A recent ***Nature*** ranking indicates that Yunnan University ranks the 65th among the 200 top Chinese research institutes and universities. In terms of the number of publications on ***Nature*** and ***Science***, Yunnan University ranks the 15th among Chinese research institutes and universities, and the 9th among Chinese universities. Yunnan University now recruits global talents. We will provide you with excellent environment in which your academic talent will be rewarded. We cordially invite you to join us for a better future.

## II. Qualifications and Requirements

1.High-end Professionals include academicians of Chinese Academy of Sciences, academicians of Chinese Academy of Engineering, "Ten Thousand Talents Program" fellows, "Thousand Talent Program" fellows, distinguished professors of the "Yangtze River Scholar Award Plan," winners of National Science Funds for Distinguished Young Scholars, and other high-end leading professionals.

2. Priority Disciplines: history, ethnology, law, economics, finance, mathematics, physics, astronomy, chemistry, paleobiology, ecology, micro-biology, material science.

## III. Salary and Benefits

1. The annual salary, housing subsidy and scientific research funding for academicians of Chinese Academy of Sciences/Engineering are negotiable.

2. Welfare package for other high-end professionals:

(1) Housing subsidy: 400 thousand RMB to 3 million RMB

(2) Scientific research funding: 300 thousand RMB to 10 million RMB

(3) The "Tier 2" professionals referred to in the "Yunnan University Interim Regulations on Talent Recruitment" can enjoy an annual salary of no less than 800 thousand RMB.

3. Yunnan University will recruit team members for high-end professionals.

**More details available at :**
**http://www.rsc.ynu.edu.cn/rules/2015-05-15/0-7-672.html**

ScienceCareers online @sciencecareers.org
OPPORTUNITIES IN CHINA

OPPORTUNITIES IN CHINA
ScienceCareers online @sciencecareers.org

# Northwest University
# Calls for Talents All Over the World

Established in 1902 and located in Xi'an, China, Northwest University (NWU) currently has been selected as one of the leading universities sponsored by the national "211 Project" and under the joint administration of the Ministry of Education and Shaanxi province. NWU sincerely invites talents home and abroad to join us, and warmly welcome distinguished talents declare the talents programme, for instance, the national "Thousand Talents Plan", "Changjiang Scholars Program" and Shannxi"Excellent One Hundred Talents" Project.

**Requirements:**

**A. Academic Leading Talents:**

1. Under the Age of 55.

2a. Full Professor in Overseas University.

2b.Candidates should be qualified to be listed in talents programs such as "Thousand Talents Plan", "Tens of Thousands of People Plan", "Changjiang Scholars Program", "The National Distinguished Young Scholars", etc.

**B. Youth Top-notch Talents:**

1. Under the age of 45;

2a. In the formal position for teaching and scientific research overseas, or the PHD graduates from international top universities, with excellent achievements;

2b. Candidates are preferable to be listed or qualified for the following programs: "Youth Thousand Talents Plan", "Ten Thousand Distinguished Young Talents", "Youth Yangtze River Scholar", "Outstanding Youth" or published papers in top academic journals (like Science). Scientists with outstanding achievements.

**C. Youth Academic Backbone Talents:**

1. Under the age of 35;

2a. Overseas post-doctor or excellent PHD graduates;

2b. Domestic excellent scientific research personnel, PHD graduates, with outstanding research achievement or achieved important awards for teaching and scientific research.

**D. Chair Professor Position for Level-A Part-time Candidates**

We sincerely welcome excellent talents home and abroad to join us and salary negotiate.

**Website:** http://www.nwu.edu.cn/
**Email:** rcb@nwu.edu.cn
**Contact Person:** Yibo Shen
**Tel:** (86) 29-88305288
**Address:** High-level talent project office, Northwest University, 229 North Taibai Road, Beilin District, Xi'an, 710069,Shaanxi Province, China

---

# Southwest Jiaotong University, Chengdu, China
# Invites Applications for the Academic Positions

Southwest Jiaotong University (SWJTU), founded in 1896 and located in Chengdu, the capital of Sichuan province--China's dynamically growing West. SWJTU is an elite university with national key multidisciplinary "211" and "985 Feature" projects directly managed by the Ministry of Education.SWJTU is currently on the strategic "Developing and Strengthening the University by Introducing and Cultivating talents" campaign. Thus, you are cordially invited to apply for the following academic positions. More information is available at **http://www.swjtu.edu.cn/**

## Positions and Requirements

**A. High-level Talented Leaders:** Candidates should be qualified to be listed in national top talents programs such as Program of Global Experts, Top Talents of National Special Support Program, "Chang Jiang Scholars", China National Funds for Distinguished Young Scientists and National Award for Distinguished Teacher.

**B. Young Leading Scholars:** Candidates are preferable to be listed or qualified for the following programs: National Thousand Young Talents Program.The Top Young Talents of National Special Support Program (Program for Supporting Top Young Talents), Science Foundation for the Excellent Youth Scholars.

**C. Excellent Young Academic Backbones**

**D. Excellent Doctors and Post Doctoral Fellows**

Please contact Mr. Yu Wang, Ms. Ye Zeng
Telephone number: +86-28-66367238/66366202
Email: talent@swjtu.edu.cn
Address: Human Resources Department, SWJTU, Western Park of High-Tech Zone, Chengdu, Sichuan, China, 611756

西安建筑科技大学

XI'AN UNIVERSITY OF ARCHITECTURE AND TECHNOLOGY

# XI'AN UNIVERSITY OF ARCHITECTURE AND TECHNOLOGY CALLS FOR TALENTS ALL OVER THE WORLD

Located in the ancient city of Xi'an, XAUAT (Xi'an University of Architecture and Technology) is one of the eight well-known architecture and civil engineering universities in China and the key university affiliated to the former Ministry of Metallurgy. XAUAT started from the earliest Civil Engineering, Architecture and Environment majors in China and boasted a history of 120 years. Ever since its founding in 1956, XAUAT has developed into a multidisciplinary university specialized in Architecture, Civil Engineering, Environment, Municipal Engineering, Material Science, Metallurgy and other related disciplines and featured by the coordinated development of Humanities, Science, Economics, Management, Art and Law.

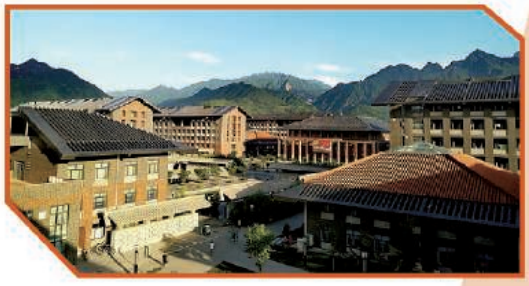

As one of the first universities authorized by the State Council of PRC to confer master and doctoral degrees, XAUAT has 3 national key disciplines, 34 provincial key disciplines, and a postgraduate school that can confer doctoral degrees for 7 first-level disciplines. XAUAT also has an excellent faculty and research team led by academicians, outstanding professionals, national renowned teachers, members of the "Ten Thousand Talents Program"(High-level program sponsored by State Council), winners of Chang Jiang Scholars Program ( Sponsored by Ministry of Education and Li Ka Shing Foundation)and winners of the National Science Fund for Distinguished Young Scholars.

As a key high-level university in Shaanxi province, XAUAT is now under the joint construction of Shaanxi province and the Ministry of Housing and Urban-Rural Development.

XAUAT supports the national strategy of innovation-driven development and the guidance of One Belt, One Road. It insists on a high-quality education featuring specialized disciplines, talents and openness and strives for an outstanding university with an international fame.

We dedicate ourselves to the highest quality of education and exert our effort in pursuit of academic excellence. Currently, we are actively seeking distinguished talents from all over the world. High-level research platforms and decent compensation for work and living will be provided.

You are welcome to join us in the following fields: Civil Engineering, Architecture, Environment Science and Engineering, Management Science and Engineering, Material Science and Engineering, Metallurgy Engineering, Mechanical Engineering, Computer Science and Technology, Chemistry Engineering and Technology, Science, Art, Foreign Languages, Law, etc.

## Contact Us:


Department of Personnel, XAUAT
Contacts: Chuantao Pang, Wei He
Tel: +86-29-82202184
Fax: +86-29-82202329
Email: *zhaopin@xauat.edu.cn*
Address: #13, Yangta Rd. Xi'an, Shaanxi
Zip Code: 710055
Our website: *http://www.xauat.edu.cn*

ScienceCareers online @sciencecareers.org
OPPORTUNITIES IN CHINA

# Open Faculty Positions
# Shaanxi University of Science and Technology

*Shaanxi University of Science and Technology (SUST) is a multidisciplinary university featuring light industry research. SUST is supported by National University Basic Ability Construction Project-Mid and West, and Shaanxi Province Advanced Level University Construction Project. SUST has developed 6 provincial level key disciplines, 17 research centers of national and ministry level, 1 discipline supported by Shaanxi Province Social Science Construction Project. We are now sincerely inviting distinguished talents to join in SUST. Multiple faculty positions at different levels in the following disciplines are open for application.*

***1. Bio-resources Chemical & Material Engineering;2. Materials Science & Engineering;3. Environmental Science & Engineering;4. Food & Biological Engineering;5. Chemistry & Chemical Engineering;6. Mechanical & Electrical Engineering;7. Electrical & Information;8. Economics & Management;9. Managerial Science and Engineering.***

## Level 1 Disciplinary Leading Talents

***Qualification :***

National Thousand Talents Plan Members, including Long Term Innovative Talents Plan, Short Term Innovative Talents Plan, Foreign Experts Plan, Topnotch Talents and Teams Plan.

***Salary & Benefits (pre-tax)***

*1 Relocation :* Free housing on campus (apartment ~180m$^2$); relocation allowance : CNY800000

*2 Research Start-up Fund :* Science & Engineering : CNY10000000 to 15000000; Social Science: CNY3000000 to 5000000.

*3 Faculty Position :* Level 2 Professorship or above, PhD candidate adviser.

*4 Annual Salary :* Faculty position salary plus CNY 1000000 to 1200000.

*5 Graduate Recruiting :* SUST will assist in building up the research team through internal or external recruiting, and afford the salaries of team members. The priority in graduate recruiting is guaranteed.

*6 Short Term Innovative Talents Plan Members :* Negotiated according to above standard, length of service and international level.

## Level 2 Distinguished Professors

***Qualification :***

Applicants for Distinguished Professors, who will be qualified for National Thousand Talents Plan(under 50), must hold a PhD degree with a top overseas university or research institution, and should have been working as professors or equivalent positions at a well-known overseas university or research institution with excellent publication record. SUST offers assistance to successful applicants in applications for National Thousand Talents Plan and the government talents' allowance.

***Salary & Benefits (pre-tax)***

*1 Relocation :* Free housing on campus (apartment ~140m$^2$); Relocation allowance: CNY600000.

*2 Research Start-up Fund :* Science & Engineering: CNY3000000 to 6000000 ; Social Science: CNY1000000 to 2000000.

*3 Faculty Position :* Level 3 Professorship or above, PhD candidate adviser.

*4 Annual Salary :* Faculty position salary plus CNY 600000 to 800000.

*5 Graduate Recruiting :* SUST will assist in building up the research team through internal or external recruiting, and afford the salaries of team members. The priority in graduate recruiting is guaranteed.

*6 Part-time Faculty Positions :* Negotiated according to above standard, length of service and international level.

## Level 3 National Thousand Youth Talents Plan or Equivalent

***Qualifications :***

1. Thousand Youth Talents Plan members.

2. Applicants who will be qualified for National Thousand Youth Talents Plan (under 40), must hold a PhD degree and have no less than three consecutive years of overseas research experience. The applicants should have worked in official positions in overseas universities or research institutes with the top-notch talents in their research fields and the potential to become future leaders in relevant areas. SUST offers assistance to successful applicants in applications for National Thousand Youth Talents Plan and the government talents' allowance.

***Salary & Benefits (pre-tax)***

*1 Relocation :* Free housing (apartment: 120m$^2$) on campus; Relocation allowance: CNY450000.

*2 Research Start-up Fund :* Science & Engineering: CNY1500000 to 3000000; Social Science: CNY800000 to 1000000.

*3 Faculty Position :* Level 4 Professorship or above, PhD/Master candidate adviser.

*4 Annual Salary :* Faculty position salary plus CNY 300000 to 400000.

*5 Graduate Recruiting :* Priority in graduate recruiting.

## Level 4 Excellent Young Scholars

***Qualifications :***

Applicants (under 35), must hold a PhD degree or have a post-doctoral research experience with a top overseas university or research institution with strong research potential and leadership, and meet one of the following requirements:

(1) Publication of 1 ESI high citation paper, or 2 SCI JCR-Q1 papers, or 5 SCI JCR-Q2 papers or 5 papers with impact factor above 3.0 as the first author in recent 5 years, and major research projects experience;

(2) 2 years of experience at overseas universities, research institutions or top enterprises with assistant professorship or post-doctoral fellowship.

***Salary & Benefits (pre-tax)***

*1 Relocation :* Entitled to buy an apartment on campus (100-120m$^2$); Relocation allowance: CNY300000.

*2 Research Start-up Fund :* Science & Engineering: CNY600000; Social Science: CNY300000.

*3 Faculty Position :* Level 6 Associate Professorship, Master student adviser.

*4 Annual Salary :* Minimum: CNY 150000

*5 Graduate Recruiting :* Priority in graduate recruiting.

## Level 5 Excellent PhD

***Qualifications :***

Applicants (under 32), must hold a PhD degree or have a post-doctoral experience with a top overseas university or research institution, and meet one of the following requirements:

(1) Publication of SCI JCR-Q1 paper, or 3 SCI JCR-Q2 papers or 3 papers with impact factor above 3.0, or 6 SCI /EI journal papers as the first author in recent 5 years, and research projects experience;

(2) Experience at overseas university, research institution with assistant professorship or post-doctoral fellowship.

***Salary & Benefits (pre-tax)***

*1 Relocation :* Entitled to buy an apartment on campus (100-120m$^2$); Relocation allowance: CNY200000.

*2 Research Start-up Fund :* Science & Engineering : CNY200000; Social Science: CNY150000.

*3 Faculty Position :* Level 7 Associate Professorship.

*4 Annual Salary :* Minimum: CNY 120000

## Location: Xi'an, China

***Application:***

For questions regarding the positions, please contact Qiao Mingzhe at +86-29-86168062(tel/fax) or mobile +86-13572186963, or via email: ***hr@sust.edu.cn***

The review of applications and nominations is underway and will continue until positions are filled. For more information about SUST please visit ***http://www.sust.edu.cn/***.

# Guizhou Medical University

On March 1, 1938, National Guiyang Medical College was founded as one of nine national medical colleges affiliated with Ministry of Education. The first president was Dr. Li Zongen, expert in tropical diseases and educator, who graduated from University of Glasgow (UK) and worked in Union Medical College. In the beginning of the college, over 40 professors from the most famous medical colleges taught in Guizhou Medical College, including Zhang Xiaoqian, President of Xiang Ya School of Medicine and medicine scientist; Professor Shen Kefei, President of Central Hospital of Chinese National Government; Zhong Shifan, Vice President of Central Hospital of Chinese National Government and podiatrist; Li Ruilin, gynecologist; Guo Bingkuan, ophthalmologist; Lin Shaowen, biologist; and Wang Jiwu, epidemiologist, etc. The college had nearly two-thirds of faculty coming from Beijing Union Medical College, followed the Britain and American teaching systems, and learned from successful operation experience of Beijing Union Medical College, all of which made National Guiyang Medical College be the widely recognized "Small Union Medical College" then.

张涤霄教授，著名医学教育家和内科学专家，先后任北京协和医学院内科学教授，湘雅医学院院长、贵阳医学院特约内科学教授。

王季午教授，著名内科学、传染病学专家和医学教育家。1947 年任贵阳医学院院长兼附院主任。

Following 78 years of development, Guizhou Medical University (hereinafter referred to as GMU) now has two campuses, i.e. a south one and a north one, covering an area of 1868 mu. GMU is featured by beautiful campus environment, powerful faculty capacity, complete teaching facilities, advanced instrument and equipment. GMU has 1.74 million real books and 430,000 electronic books in the library. There are over 19,000 students on both campuses. GMU has 20 teaching units accommodating seven disciplines, i.e. Medicine, Science, Laws, Pedagogy, Arts, Technology and Management, consisting of 30 undergraduate specialties. GMU is authorized to award master's degrees in Medicine, Science and Pedagogy, and Psychology, and doctoral degree in Medicine.

By always upholding the operation philosophy of "Adapting to the needs of the era and local needs", GMU has made outstanding achievements with respect to pathogenic biology, research in endemic diseases, research and development of traditional Chinese medicine and ethic medicines based on its own advantages and features. GMU's honorable president is Academician Zhong Nanshan, world famous expert in respiratory diseases. In addition, a number of domestic and international famous scholars, including scholars from Cornell University, University of Washington, University of Wisconsin, University of Toronto, and Karolinska Institute, scholars of Recruitment Program of Global Experts, chair professors of Chang Jiang Scholars program, and honorable professors, are now teaching in GMU. GMU boasts 12 scientific research platforms of Ministry of Science and Technology and Ministry of Education such as State Key Laboratory for Natural Medicine, National Research Center for Engineering Technology of Miao Ethic Medicines, and 2 national experimental teaching and demonstration centers; GMU now holds 9 affiliated hospitals under its direct jurisdiction, 10 affiliated hospitals under its indirect jurisdiction, 11 teaching hospitals, and 9 contracted community healthcare centers.

Since the new century, GMU adoptes the development philosophy of "open-minded and inclusive for everything" strengthens foreign cooperation and exchange, and exerts great efforts in developing and recruiting top talents. GMU has established and maintained scientific research and teaching cooperation with top universities and scientific research institutions from 30+ countries and regions including US, UK, Japan, South Korea and Taiwan, thereby fully promoting the sustainable healthy development of GMU. In November 2015, Professor Bary Marshall, winner of Nobel Prize in Physiology or Medicine, and GMU's open Clinical Medical Research Center of international standard established a cooperation laboratory.

Protecting human's health is our common concern, fostering high-quality medical talent is our common duty, and driving the progress of medical science is our common responsibility. At Guizhou Medical University, we open up our mind and welcome medical institutions and talent from around the world to cooperate and exchange with us.

***Address: No.9 Beijing Road, Guiyang City, Guizhou Province, China***

**Website: *http://www.gmc.edu.cn/***
**Tel: 86-851-88416081, 86-851-88416080**
**WeChat account: gmc1938,**

More and more academics returning to China

WHAT ARE YOU WAITING FOR?

10,000+ academic job vacancies in China
Free one-to-one consultation service

consultant@acabridge.edu.cn

北京理工大学 东南大学 暨南大学 浙江大学
西南交通大学 国防科技大学 哈尔滨工业大学

上海交通大学
SHANGHAI JIAO TONG UNIVERSITY

**MULTIPLE FACULTY POSITIONS IN ULTRAFAST SCIENCES / ELECTRON MICROSCOPY**
**SHANGHAI JIAO TONG UNIVERSITY, SHANGHAI, CHINA**

Shanghai Jiao Tong University is establishing a world-class research Center for Ultrafast Sciences in physics, chemistry, materials and biology with integration of both experimental and theoretical efforts. The Center will provide state-of-the-art ultrafast laser spectroscopy, electron diffraction and microscopy, and excellent multi-disciplinary environment for cutting-edge research.

The Center invites applications for a number of open-rank faculty positions to begin in the spring of 2017 (or earlier). Applicants should have a Ph.D. degree, preferably with postdoctoral experience in a closely related field, and a strong record of research accomplishments. Previous experimental and/or theoretical experience in electron microscopy and ultrafast sciences is favorable. The successful candidates will be expected to develop world-class research programs and teach classes at both undergraduate and graduate levels. The University will provide competitive annual salary, start-up fund, housing allowance and other benefits.

All applicants should send a cover letter, a curriculum vitae with a publication list, a research proposal (3-4 pages) and a statement of teaching interest in a single pdf file by Dec. 31, 2016 to Dr. Jie Chen, Shanghai Jiao Tong University, Shanghai 200240, China through e-mail to ultrafast@sjtu.edu.cn. Please also arrange three reference letters directly to the above e-mail address. Applications after the deadline could be reviewed until the positions are filled.

长江师范学院

***Yangtze Normal University Invites Outstanding Talents from Home and Abroad***

Yangtze Normal University (hereafter as YZNU) is a full-time institution of higher education under the leadership of Chongqing Municipal Government of P. R. China, and a member of China Association of Universities ( Colleges ) of Applied Science. Covering an area of over 133 hectares (2,000 mu) with a total construction area of 900,000 square meters, YZNU offers 51 undergraduate programs for more than 20, 000 students.

***Advantageous location and convenient traffic.***

YZNU is located in Fuling, Chongqing, which is world famous for "Former Capital of Ba Kingdom" and "Town of Zhacai (hot pickled mustard tuber)" and holds an important position in Chongqing's social and economic development. YZNU is just three minutes' car ride to Fuling High Speed Railway Station which leads directly to Beijing, Shanghai, Guangzhou, Chengdu, 30 minutes' high-speed-train ride to Chongqingbei Railway station, 2 minutes' car ride to the entrance to expressways, and 50 minutes' car ride to Chongqing city proper.

***Complete facilities and supportive platform.***

YZNU has teaching and research instruments worth a total value of 200 million RMB, 1.5 million paper books and 50 TB digital resources in the library. It has constructed a five-discipline specialty cluster adapted to the local leading industries and socio-economic development. It has two key municipal disciplines of Chongqing and eleven innovative platforms at provincial level.

***Adequate housing and favorable working conditions.***

YZNU provides each talent with doctoral degree an apartment of 160m2 with parking space at the price of 2800RMB/m2, transportation subsidy, free working lunch, fees for visiting family in accordance with the relevant regulations. YZNU assists children of the talents with doctoral degree to study in the best schools in Fuling.

*An opening Chongqing appeals to talents, and the developing YZNU promotes the growth of talents.*
*We sincerely invite you to join us to create a bright future!*

Contact: Mr. Yang
Tel: +86-023-72791177, 72791222
Email: *rscrc@yznu.cn*
Website: *http://www.yznu.cn/*

Effective Connection Full Service 三城三校高效联动 人才顾问全程陪同

Endorsed by 中国教育在线 www.eol.cn Organizers 暨南大學 JINAN UNIVERSITY 東南大學 SOUTHEAST UNIVERSITY 北京理工大學 BEIJING INSTITUTE OF TECHNOLOGY

# 海外学者中国行

## *Overseas Chinese Scholars' Visit to Top Chinese Universities*

**Date:**
**Dec. 21st to 29th, 2016;**
**Universities:**
**Jinan University (Guangdong);**
**Southeast University (Nanjing);**
**Beijing Institute of Technology (Beijing)**

**The sponsors will cover all costs during this activity and provide high subsidies of international flight for successful candidates.**

**FULL SERVICE & SUPPORT FOR YOU!**

### Jinan University

It is a multi-disciplinary university with a special emphasis on Life Science, Medicine, Pharmacy, Environmental Science, Information Science, Applied Economics and Journalism and Communication.

### Southeast University

It is a comprehensive and research-oriented university featuring the coordinated development of multi-disciplines with engineering as its focus. Among it, 9 disciplines including Engineering, Computer Science, and Material Science, etc. rank among the first 1% of global ESI database.

### Beijing Institute of Technology

BIT is the first university of science and engineering established by the Communist Party of China (CPC). Its disciplines are colored with peculiar characteristics, especially Aerospace Engineering, Mechanical Engineering, Optoelectronics and Informatics.

## Applications

**Requirements:**
Applicants should have a doctoral degree in the relevant research field and have at least 3-year overseas working experience in overseas universities and institutes. The restrictions can be relaxed for extraordinary excellent ones.

**Methods:**
Please refer to the website www.edu.cn/zgx to apply and send your CV directly to consultant@acabridge.edu.cn.

**Deadline:**
Nov. 20th, 2016. Please apply early as seats are limited. We will officially send successful candidates Invitation Letters via email.

## Contacts


| | | | | | |
|---|---|---|---|---|---|
| Jia Zhao | zhaojia@eol.cn | +86-10-62603373 | Bei Jiang | jiangbei@eol.cn | +86-10-62603770 |
| Lu Zhang | zhanglu@eol.cn | +86-10-62603334 | Pingping Ma | mapingping@eol.cn | +86-10-62603667 |


ScienceCareers online @sciencecareers.org
OPPORTUNITIES IN CHINA

ScienceCareers online @sciencecareers.org

AMERICAN ASSOCIATION FOR THE ADVANCEMENT OF SCIENCE

# Career Development Center

## Career Development Center

**Meet career challenges head-on with online courses designed for scientists**

- Public engagement
- R&D funding analysis
- Effective communication
- Proposal writing
- Career development
- Science policy and advocacy

**REGISTER TODAY**
**CareerDevelopment.aaas.org**

AAAS

# 10 ways that *Science* Careers can help advance your career

1. Register for a free online account on **ScienceCareers.org**.
2. Search thousands of job postings and find your perfect job.
3. Sign up to receive e-mail alerts about job postings that match your criteria.
4. Upload your resume into our database and connect with employers.
5. Watch one of our many webinars on different career topics such as job searching, networking, and more.
6. Download our career booklets, including Career Basics, Careers Beyond the Bench, and Developing Your Skills.
7. Complete an interactive, personalized career plan at "my IDP."
8. Visit our Career Forum and get advice from career experts and your peers.
9. Research graduate program information and find a program right for you.
10. Read relevant career advice articles from our library of thousands.

Visit **ScienceCareers.org** today — all resources are free

SCIENCECAREERS.ORG

ScienceCareers

FROM THE JOURNAL SCIENCE AAAS

*By* **Kevin F. Boehnke**

# *Selling out science?*

A year ago, a faculty member sent an email to the recipients of our university's Dow Sustainability Fellowships, referencing an article reporting that Dow Chemical Company had provided apparently contradictory information to U.S. regulatory agencies about one of its pesticides. The faculty member implied that he thought it was hypocritical for a company that he believed was harming the environment to fund sustainability research. As a recipient of this fellowship and a scientist studying water quality, his email got me thinking about the implications of accepting money from Dow and other funding sources. Given my desire to protect public health, had I sold out when I accepted financial support from a chemical company that has at times violated environmental regulations?

I learned about the fellowship a year into my doctoral program. I considered the ethical issues around applying for industry money and was encouraged to learn that the fellowship was administered through an independent foundation. Dow did not decide which research was funded, nor did it have authority to directly influence or censor the researchers it supported. Before I applied, I also spoke with a friend who had received the fellowship. He felt that although the program administrators had a pro-Dow bent, they didn't interfere with his scientific integrity, and the funding helped him do good science.

So I decided to apply, and was excited to receive the fellowship. The funding allowed me to collect extra water samples and perform experiments that gave better insight into the problems I study. It also gave me flexibility to pursue other projects that are personally and professionally enriching, such as blogging about science and traveling to conferences. By accepting Dow's money and doing good science, I've added to the collective body of scientific knowledge and benefited my career. And I have not felt restricted or censored in any way.

But I acknowledge that this arrangement also benefits Dow. The company can rightfully trumpet that it is improving public health and sustainability by funding impactful research. My work can be referenced in promotional materials, and my research findings during this fellowship will be stamped "funded by Dow Chemical." Although I'm not working for Dow, the company profits when I take its money.

This situation makes me a little uncomfortable, but I've come to realize that other funding sources come with their own complications. Government money, for example, is often viewed as more respectable than corporate funds, but it, too, has strings attached. Relying on government money can mean shoehorning research into the priorities of the funding program. The pressure to win government grants may contribute to the disturbing number of nonreplicable studies and tactics like mining data for statistical significance, regardless of actual biological or social relevance. All of these factors can compromise the integrity of the research process—if scientists let them.

***"I considered the ethical issues around applying for industry money."***

To me, selling out means losing agency or compromising ethical standards for the sake of personal gain. By this definition, I acknowledge that I am currently selling out, because I disagree with many of Dow's practices and my work is helping the company "greenwash" its image. Realistically, though, I think I would have had to sell out a little bit no matter where I got my funding. As long as researchers are dependent on external funding, we will be, in some way, subject to our funding source's agenda.

I'm thankful that the faculty member provoked me into pursuing this line of thinking. I've become more aware of the implications of accepting funding and the need to reflect on the perceptions and potential conflicts associated with different funding sources. But in the end, science costs money, and it is important not to sacrifice the good done by research in pursuit of the "perfect" funding source. Otherwise, the work might never get done at all. ■

*Kevin F. Boehnke is a doctoral candidate at the University of Michigan in Ann Arbor. Send your career story to SciCareerEditor@aaas.org.*

ILLUSTRATION: ROBERT NEUBECKER

Downloaded from http://science.sciencemag.org/ on November 22, 2016



Published by AAAS